Computational homogenisation of thermomechanical problems

von der Fakultät Maschinenbau
der Technischen Universität Dortmund
zur Erlangung des akademischen Grades

Doktor-Ingenieur (Dr.-Ing.)

genehmigte Dissertation

von

Dipl.-Ing. Rolf Berthelsen

aus Kleve

Referent:	Prof. Dr.-Ing. habil. A. Menzel
Korreferenten:	Prof. Dr.-Ing. habil. D. Balzani
	Prof. Dr.-Ing. Dipl.-Wirt.Ing. W. Tillmann
Tag der Einreichung:	19.08.2019
Tag der mündlichen Prüfung:	22.11.2019

Bibliografische Information Der Deutschen Bibliothek
Die Deutsche Bibliothek verzeichnet diese Publikation in der Deutschen Nationalbibliografie; detaillierte bibliografische Daten sind im Internet über **http://dnb.ddb.de** abrufbar.

Bibliographic information published by Die Deutsche Bibliothek
Die Deutsche Bibliothek lists this publication in the Deutsche Nationalbibliografie; detailed bibliographic data is available in the Internet at **http://dnb.ddb.de**.

Schriftenreihe des Instituts für Mechanik

Herausgeber: Institut für Mechanik
Fakultät Maschinenbau
Technische Universität Dortmund
Leonhard-Euler-Str. 5
D-44227 Dortmund

Druck: Koffler DruckManagement GmbH

Als Manuskript gedruckt. Printed in Germany.

ISSN 2191-0022
ISBN 978-3-947323-19-7

To Anna, Clara and Anton

Acknowledgements

The research related to this work was carried out between 2011 and 2019 during my time as a research assistant at the Intitute of Mechanics at TU Dortmund University. At this point I should like to express my thanks to the people who contributed to the final success of my research work and therefore to this thesis and my doctoral degree in mechanical engineering.

First of all, I want to thank my doctoral adviser Professor Andreas Menzel for offering me the chance to graduate in his research group as well as for his continuous support during all the years of collaboration. The excellent working atmosphere, in combination with the remarkable freedom granted to deal with the individual research challenges, let me accumulate specialised knowledge in the field of mechanics and numerical methods and let me develop further in my personality. In this respect I would also like to express my thanks to Professor Jörn Mosler who likewise contributed to the most favorable and enjoyable working conditions at the Institute of Mechanics.

Furthermore, my thanks go to Professor Daniel Balzani for his interest in my research as well as for acting as co-referee of my thesis. Similarly, I want to thank Professor Wolfgang Tillmann for acting as third referee of my thesis. Moreover, I should thank Dr. Andreas Zabel who agreed to serve as the chairman of the examination committee.

Special thanks go to Professor Ralf Denzer who contributed significantly to my decision to change from Ruhr-Universität Bochum to TU Dortmund University. I am thankful for the many scientific and technical discussions and, particularly, for the ongoing interest in my work, even beyond his engagement as senior researcher in Dortmund.

Besides the scientific and rather technical issues of working life, research at an university also involves puzzling administrative tasks and plenty of formalities which have to be followed. My sincere thanks go to Kerstin Walter and Christina McDonagh who where always helpful and managed the organisational aspects not only of my work but of the work of all colleagues at the institute. Apart from these necessary conditions for successful research work, they both contributed to the great working atmosphere by means of organising social events like excursions, mutual breakfasts as well as Christmas parties.

Working in the field of computational mechanics, one requires reliable hardware and software to develop, test and run code in order to hopefully obtain meaningful results. Therefore, my thanks go to Matthias Weiss and his assistants for providing the hardware to work on and for maintaining the rock stable Linux environment to work with. Without such a platform, the work related to this thesis could not have been accomplished.

Accordingly, I should also express my gratitude to the LiDo-Team which operates the high performance cluster of TU Dortmund University. Some of the numerical examples shown in this thesis have been carried out on this cluster.

On this occasion, of course, I would also like to thank my former colleagues for the extraordinary team spirit and for the many scientific as well as "popular scientific" discussions we have had throughout the years. I gladly do remember our business trips which evolved from family trips to mass events during this time while the group was growing. Big thanks go to senior engineer Dr. Thorsten Bartel who always was, even though formally part of the administrative staff, more a colleague and with whom I had plenty of professional and personal conversations. Concurrently, my sincere thanks go to Dr. Alexander Bartels for his outstanding collegiality and the many long working days as well as leisure activities we have shared. Concerning this, I also want to particularly thank Dr. Karsten Buckmann, Dr. Dinesh Dusthakar, Dr. Tim Heitbreder, Dr. Raphael Holtermann, Dr. Richard Ostwald, Robin Schulte and Christian Sievers. Furthermore, I would like to thank my former office colleagues Dr. Maniprakash Subramanian, Lars Rose as well as Dr. Tobias Kaiser for their kind company. Further special thanks go to my former long-term student assistants Markus Schewe and Hendrik Wilbuer for their various contributions to research topics as well as educational material. I am very pleased that both of them became research assistants at the Institute of Mechanics. For the exceptional solidarity and mutual support during all the time in Dortmund, I also want to thank Serhat Aygün, Dr. Till Clausmeyer, Guillermo Diaz Ph.D., Volker Fohrmeister, Tim Furlan, Professor Björn Kiefer, Dr. Patrick Kurzeja, Henning Lammen, Kai Langenfeld, Isabelle Noll, Cesar Polindara Ph.D., Leon Sprave, Dr. Tobias Waffenschmidt and Tillmann Wiegold.

Last but not least, I want to deeply thank my family and my friends for the moral support over the whole period of time. Their enduring patience during the periodic phases of high workload and their forgiving acceptance of my absence at the one or other mutual activity are not self-evident and let me feel the necessary support to complete this thesis.

My greatest possible gratitude finally belongs to my wife Anna and to our children Clara and Anton. Their love, patience and support are the most significant non-technical contribution to my work. This thesis is dedicated to them.

Dortmund, March 2020 Rolf Berthelsen

Zusammenfassung

Die vorliegende Arbeit behandelt die Modellierung von Wärmeeintrag und Massenauftrag beim thermischen Spritzen sowie schwerpunktmäßig die Bestimmung des effektiven Materialverhaltens von Mikrostrukturen unter der Berücksichtigung von Inelastizität im Rahmen thermo-mechanischer Kontinua. Der Wärmeeintrag beim thermischen Spritzen wird hierbei durch konvektive Wärmeübertragung sowie durch Strahlung im Rahmen eines nicht-linearen starren Wärmeleiters modelliert und in Form eines Finite Elemente Programms implementiert. Dieses Modell des starren Wärmeleiters wird anschließend weiterentwickelt, um den Massenauftrag in Form von heißen Partikeln thermodynamisch konsistent mithilfe eines neuartigen Ansatzes abzubilden. Der inhaltliche Schwerpunkt liegt im weiteren Verlauf der Arbeit auf der Entwicklung eines thermo-mechanisch gekoppelten zweiskaligen Finite-Elemente-Programms, wobei das effektive Materialverhalten von zugrunde liegenden Mikrostrukturen, unter Anwendung numerischer Homogenisierung, unmittelbar in die Lösung von Randwertproblemen auf der übergeordneten Bauteilskala einfließt. Die Umsetzung erfolgt in Form eines nicht-linearen Rahmens für kleine sowie große Deformationen, wobei jeweils ein thermo-viskoplastisches Materialmodell beispielhaft für inelastisches Materialverhalten Anwendung findet. Darüber hinaus werden neuartige Randbedingungen für die Lösung von thermo-mechanisch gekoppelten Randwertproblemen auf der Ebene der zugrunde liegenden Mikrostruktur erarbeitet. Die Möglichkeiten der entwickelten Finite Elemente Programme sowie der darin enthaltenen neuen Methoden werden anhand von numerischen Simulationen anschaulich dargestellt.

Abstract

The thesis at hand deals with the modelling of heat input and mass deposition during thermal spraying and especially with the capturing of the effective material behaviour of microstructures under consideration of inelasticity in the framework of thermo-mechanical continua. The heat input during thermal spraying is modelled by means of convective heat transfer as well as radiation in the framework of a non-linear rigid heat conductor which is implemented into a finite element programme. This model is subsequently extended in order to capture mass deposition via hot particles by a novel thermodynamically consistent ansatz. As this work proceeds, the main emphasis of this thesis is on the development of a thermo-mechanically coupled two-scale finite element programme. Here, the effective material behaviour of underlying microstructures is directly used in the solution of boundary value problems at the upper scale of application by means of numerical homogenisation. The implementation is carried out in the framework of small as well as finite deformations. In both cases, a thermo-viscoplastic material model is applied in order to exemplarily represent non-linear inelastic material behaviour. Furthermore,

novel boundary conditions are elaborated for the solution of thermo-mechanically coupled boundary values problems at the scale of the underlying microstructure. The capabilities of the developed finite element frameworks as well as of the novel methods included therein are shown by means of descriptive numerical simulations.

Publications

The following articles were submitted or published during the preparation of this thesis and therefore represent the significant part of the thesis at hand.

[20] R. Berthelsen, T. Wiederkehr, R. Denzer, A. Menzel and H. Müller. Efficient Simulation of Nonlinear Heat Transfer during Thermal Spraying of Complex Workpieces, *World Journal of Mechanics*, 4(9):289–301, 2014.

[22] R. Berthelsen, D. Tomath, R. Denzer and A. Menzel. Finite element simulation of coating-induced heat transfer: application to thermal spraying processes, *Meccanica*, 51(2):291–307, 2016.

[24] R. Berthelsen, P. Oppermann, R. Denzer and A. Menzel. Computational homogenisation for thermoviscoplasticity: application to thermally sprayed coatings, *Computational Mechanics*, 60(5):739–766, 2017.

[18] R. Berthelsen and A. Menzel. Computational homogenisation for thermo-viscoplastic composites: Large strain formulation and weak micro-periodicity, *Computer Methods in Applied Mechanics and Engineering*, 348:575–603, 2019.

For the articles listed, the author of this thesis has contributed essential aspects with regard to the underlying theories as well as the algorithmic formulation. Regarding the peer-reviewed contribution [20], the author of this thesis elaborated the theory, algorithmic framework and implementation in the shape of a research Matlab code and prepared the respective parts of the article. The Matlab code was re-implemented into a GPGPU code by the co-author of the respective publication, Dr. Thomas Wiederkehr. Hence, the shown numerical results of this peer-reviewed article are carried out with the GPGPU implementation. The development of the underlying geometrical simulation framework is discussed in the dissertation [190] wherein the collaborative research work [20] is not included. For the peer-reviewed journal articles [22, 24] as well as for the submitted article [18], the author of this thesis contributed essential aspects with regard to the outline of the theory, carried out all of the numerical implementations and simulations, and prepared the articles.

In addition, the following contributions were published during and alongside the preparation of this thesis.

[178] R. Denzer, R. Berthelsen, B. Klusemann and A. Menzel. Aspects of thermomechanical homogenization. In: W. Tillmann and J. Nebel (eds). *4. öffentliches Kolloquium – SFB 708*, pp. 127–136, 2011

[179] R. Berthelsen, R. Denzer and A. Menzel. A thermodynamical consistent finite-element-framework for rigid heat conduction. In: W. Tillmann and J. Nebel (eds). *5. öffentliches Kolloquium – SFB 708*, pp. 123–132, 2012

[177] R. Berthelsen, R. Denzer and A. Menzel. Multi-scale modelling and simulation of the material behaviour of thermal-sprayed coatings. In: W. Tillmann and I. Baumann (eds). *6. öffentliches Kolloquium – SFB 708*, pp. 139–150, 2013

[19] R. Berthelsen, R. Denzer and A. Menzel. Thermo-mechanical homogenisation – application to HVOF thermal-aprayed WC-Co coatings. *Proceedings in Applied Mathematics and Mechanics*, 14(1):583–584, 2014.

[21] R. Berthelsen, D. Tomath, R. Denzer and A. Menzel. Towards a finite element simulation of coating by means of thermal spraying. *Proceedings in Applied Mathematics and Mechanics*, 15(1):277–278, 2015.

[23] R. Berthelsen, H. Wilbuer, R. Holtermann and A. Menzel. Computational modelling of wear – application to structured surfaces of elastoplastic tools. *GAMM-Mitteilungen*, 39(2):210–228, 2016.

Contributions [177–179] represent annual progress reports of the collaborative research center (SFB) 708 founded by the German research foundation (DFG). For the contributed article [178], the author of this thesis only contributed to the preparation of the article. The scientific part was elaborated in Klusemann et al. [95] without participation of the author of this thesis and is therefore not included within the thesis at hand. For the contributed articles [177, 179], the author of this thesis has contributed essential aspects with regard to the outline of the theory, carried out all of the related programming tasks as well as the numerical simulations and prepared the articles. The Proceedings [19, 21] result from conference participations of the author of this thesis. Here, the author of the thesis has contributed essential aspects with regard to the outline of the theory, prepared the presentation slides, carried out all of the related numerical implementations as well as the numerical simulations and prepared the proceedings. Related to this thesis, the contributions [21, 179] represent preliminary work which is included in the peer-reviewed articles [20, 22] and [19, 177] represent preliminary work which is included within the peer-reviewed journal articles [18, 24]. The peer-reviewed journal article [23] is collaborative research which represents preliminary studies for a project within the transregional collaborative research center (Transregio) 73, the content of which is not included within this thesis.

Contents

1 Introduction

The present thesis is based on the author's research carried out at the *Institute of Mechanics* at *TU Dortmund University*. During the initial phase, the research was carried out within *Project B6*

Multiscale modelling and simulation of the material behaviour
of thermally sprayed coatings

—

Mehrskalige Modellierung und Simulation des Materialverhaltens
thermisch gespritzter Beschichtungen

as part of the *Collaborative Research Centre SFB 708* where collaborative and interdisciplinary research dealt with *3d-surface engineering for sheet metal forming tools — 3D-Surface Engineering für Werkzeugsysteme der Blechformteilefertigung*. In particular, thermal spraying was studied as a flexible and comparatively cheap coating technology to improve the wear resistance of metal sheet forming tools by the application of hard material coatings. The collaboration was between researchers from different disciplines, namely mechanical engineering, computer sciences, mathematics as well as statistics. During the later phase and after the funding period was over, the research initiated so far was further followed and finally resulted in this thesis.

1.1 Motivation and state of the art

Conventional sheet metal forming tools are made of cold working steels — such as e.g. X153CrMoV12-1[1] — which are, relative to the sheets to be formed, exceptionally wear resistant against abrasive and adhesive wear due to the high amount of hard carbides. As outlined in Berns and Theisen [16], the application of the exemplary mentioned steel as deep drawing tool for steel sheets in the automobile industry yields a service live of approximately 15 000 deep drawn parts. A significant improvement to approximately

[1] Material number 1.2379: C 1.55 %, Cr 12.00 %, Mo 0.80 %, V 0.90 % where % represents mass-%. Source: Material data sheet of Dörrenberg Edelstahl GmbH (https://www.doerrenberg.de).

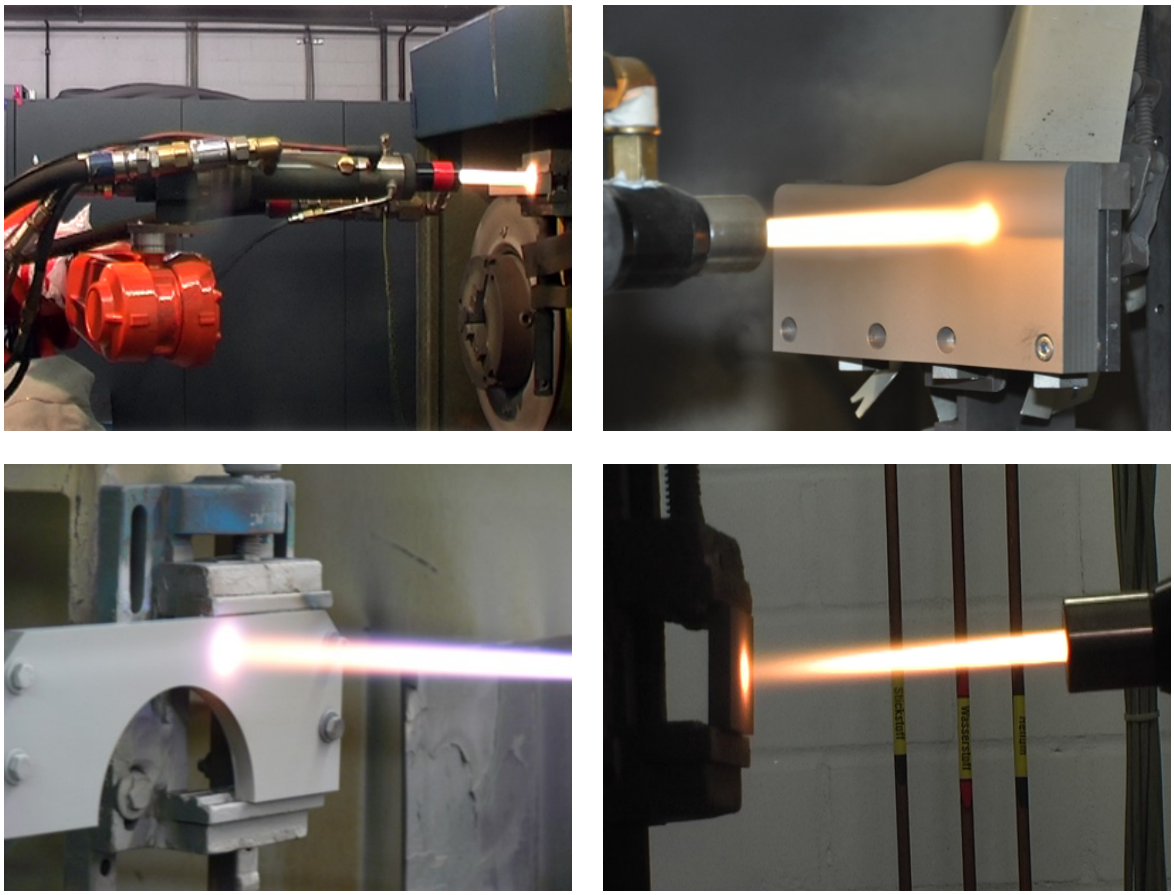

Figure 1.1: HVOF spraying process. The photographs are kindly provided by LWT, TU Dortmund.

600 000 parts can be achieved by the application of an additional CVD TiN/TiCN/TiC-sandwich coating, [16], which represents a service life extension by factor 40. Hence, coating of sheet metal forming tools appears to be economically very attractive for the application in mass production scenarios.

Within the Collaborative Research Centre SFB 708, the goal was to produce free-form surface sheet metal forming tools with tailored coatings by means of thermal spraying as a flexible and simultaneously cost-efficient coating technique. The vision was to locally adjust the friction behaviour of the applied coating to favour or restrain material flow of the deep drawn metal sheets into particular directions. Beside the challenge of the local adjustment of friction behaviour, another important requirement to the thermal spraying processes is the near net shape precision of the applied coating in order to avoid time consuming and expensive subsequent dressing procedures to meet the required manufacturing tolerances. This is especially important due to the fact that the subsequent dressing is limited to the thickness of the thermally sprayed coating (150 μm to 300 μm) on the one hand as well as due to the wear resistance of the applied hard material such as tungsten carbide (WC) cobalt (Co) on the other. To encounter

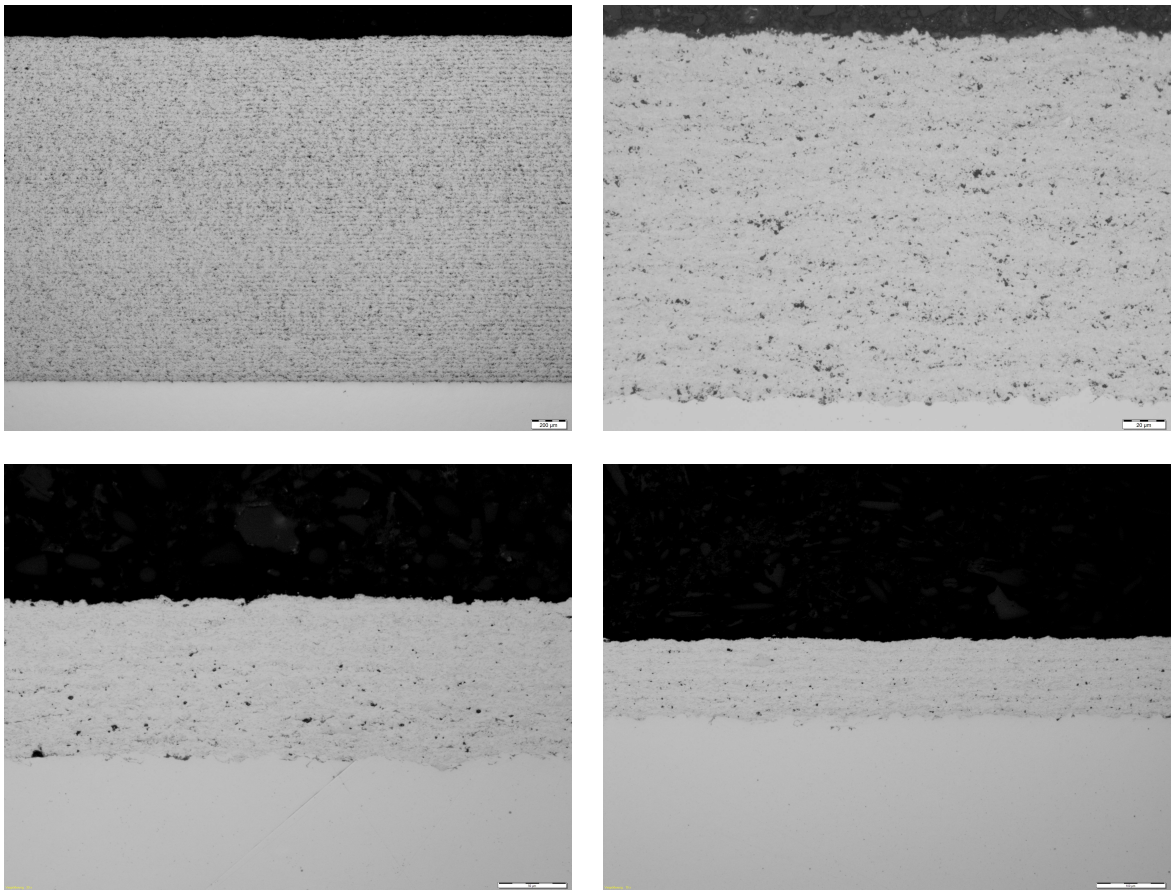

Figure 1.2: Polished micrograph sections of WC-Co coatings applied to steel substrate. The different coating layers which are observable in the respective pictures stem from different HVOF gun passovers. The photographs are kindly provided by LWT, TU Dortmund.

this challenge, researchers of the Collaborative Research Centre SFB 708 worked on an integrated process simulation tool which shall be able to capture the whole free surface forming tool production process chain from the CAD design via the production procedures up to the thermally sprayed and finally dressed metal sheet forming tool. The thermal spraying process under consideration was the high velocity oxygen fuel (HVOF) process which is depicted in Fig. 1.1. Here, hard material powder is partly molten by the HVOF gun flame and subsequently accelerated to the substrate where the heterogeneous coating is built, cf. Fig. 1.2 where polished micrograph sections of WC-Co coatings are depicted. Further magnification by means of an electron microscope allows the observation of the single constituents of the coating as shown in Fig. 1.3 where WC particles are embedded into an Co matrix. The research within Project B6 was related to the modelling of the heat input (Fig. 1.1) and mass deposition (Fig. 1.2) in the context of the finite element method as well as to the prediction of the effective thermo-mechanical material behaviour of the heterogeneous coating (Fig. 1.3) by numerical homogenisation

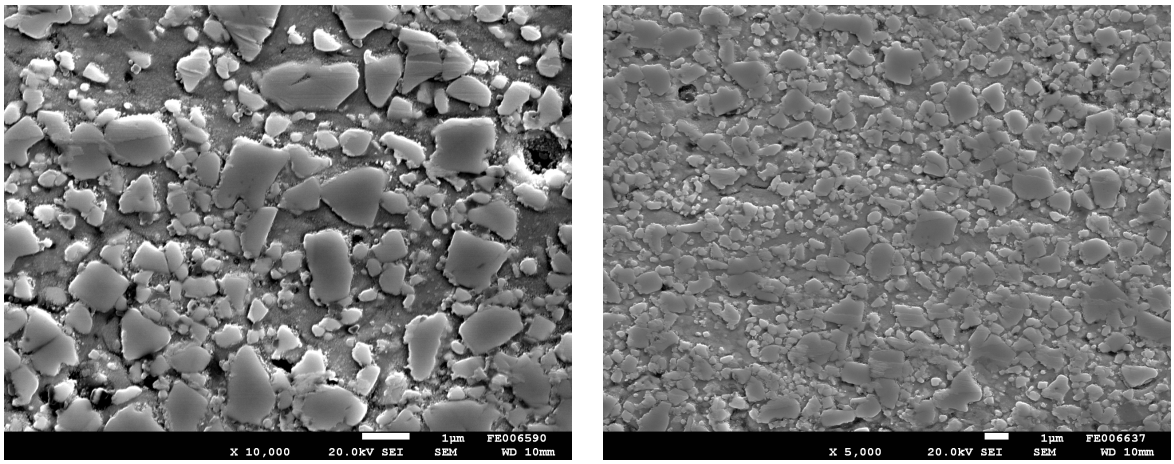

Figure 1.3: Electron micrographs of WC particles embedded into an Co matrix. The photographs are kindly provided by LWT, TU Dortmund.

within a thermo-mechanically coupled finite element framework. The following sections provide an overview of the modelling of thermal spraying processes and of numerical homogenisation frameworks as well as related fields of research.

1.1.1 Thermal spraying and its modelling

For the coating of forming tools, e.g. HVOF thermally sprayed hard material coatings of WC and Co are used because of their superior wear-resistance compared to chrome (Cr) and nickel (Ni) coatings as outlined in Sahraoui et al. [147]. The basic mode of operation of an HVOF spray gun which is used for the coating process is sketched in Fig. 1.4 for illustration purposes. For an overview of HVOF thermal spraying as well as its application, the reader is referred to the works of, e.g., Fauchais et al. [53], Gérard [63], Hanson et al. [71], Thorpe and Richter [174]. As a disadvantage, the HVOF thermal spraying process induces thermal energy into the usually heterogeneous coating as well as into the substrate which leads to a complex transient thermo-mechanical problem. Since the coating generally has different properties from the substrate and since the substrate is typically coated at significantly lower temperatures than the temperature of the HVOF gun, residual stresses – or more precisely, residual lattice strains which are used to calculate residual stresses – occur during the subsequent quenching procedure. These lattice strains caused by thermal spraying are for instance investigated by means of curvature measurements by Gill and Clyne [65], Kuroda and Clyne [102]. Moreover, Totemeier and Wright [181] compared curvature models and X-ray techniques in oder to determine residual lattice strains in HVOF thermal sprayed coatings, and Oladijo et al. [129] measured residual lattice strains in WC-Co coatings by X-ray diffraction. In order to investigate the HVOF technology with respect to complex workpiece geometries, curved workpieces were coated by researchers from LWT, TU Dortmund. Results of

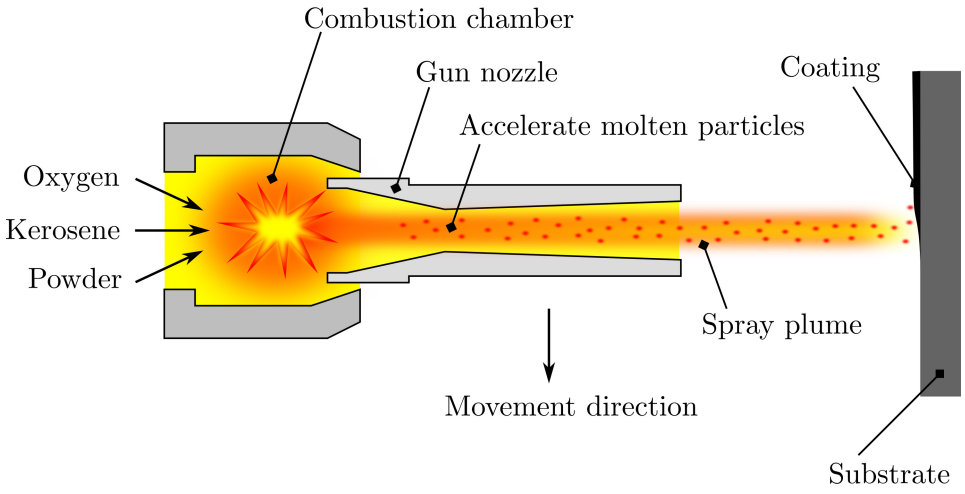

Figure 1.4: Schematic sketch of a HVOF spray gun which is used to apply wear resistant coatings, cf. Fig. 1.1.

some of these experiments are depicted in Fig. 1.5 where delamination of the applied coating can be observed. Besides insufficient connection of the coating to the substrate on the one hand, a further reason for the delamination could be residual lattice strains due to the quenching after coating. In order to replace other coating techniques like CVD for the production of wear resistant surfaces of metal sheet forming tools, the HVOF thermal spraying process must reliably produce adhering coatings of high quality. Besides process know-how and experience in application of the coating technique itself, modelling approaches can help to obtain a deeper understanding of the underlying process and might help to optimise the process or the process application with regard to desired parameters, e.g. the reduction of residual lattice strains (residual stresses). With regard to the modelling of the thermal spraying process, there is no existent modelling framework which captures the whole process in any aspect and, depending on the thermal spraying process at hand, simulation frameworks must be adapted. In the case of the HVOF process, the simulation of melting the hard material powder and its transport by the hot gas into the direction of the substrate represents the first challenging part of a coating simulation framework. A finite volume method based framework using the commercial CFD software ANSYS for the modelling of the combustion of HVOF and high-velocity suspension flamespraying (HVSFS) processes is e.g. proposed by Dongmo et al. [49] in order to render possible combustion chamber optimisation on the basis of the numerical results. Another numerical study with the commercial CFD code Fluent was made to investigate the influence of nozzle throat diameter, combustion chamber size as well as the influence of fuel droplet size, cf. Tabbara and Gu [166]. Due to the high numerical

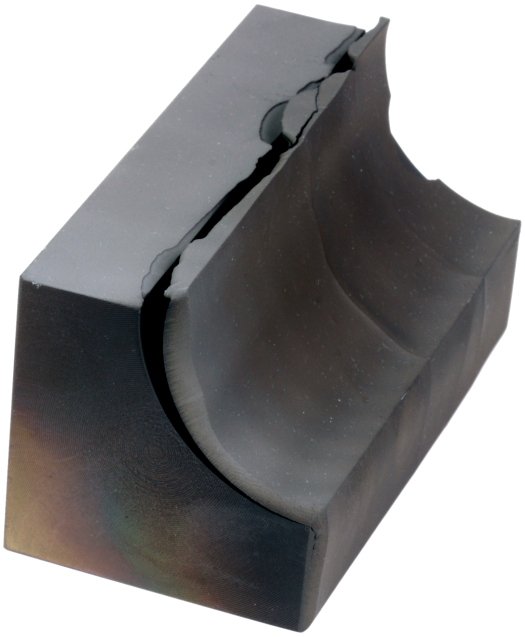

(a) Coated workpiece with a radius.

(b) Coated surface with a ridge.

(c) Close up of a coated workpiece with a radius.

(d) Coated workpiece with a sharp radius.

Figure 1.5: Delamination of a WC-Co coating from (a,c,d) a workpiece with a radius, (b) a plain surface with a ridge. The samples are kindly provided by LWT, TU Dortmund.

cost of fluid dynamical analyses, there is a need for the development of efficient solution methods which are applicable in order to solve boundary value problems of the entire thermal spraying processes. Gurris et al. [68] propose a semi-implicit finite element framework which captures two phases in order to model a particle-laden gas flow. In a further work, cf. Gurris et al. [69], an implicit finite element framework for the solution of compressible Euler equations is developed and applied to gun nozzle flow simulations. To capture the separation of droplets of molten hard-material powder within a gas flow, Neittaanmäki et al. [123] proposed a finite element based level set approach which was subsequently developed in order to simulate droplet generation in nozzles, see Mierka and Turek [119].

Another aspect of thermal spraying processes is the deposition of the molten or partly molten hard material powder at the substrate. Here, the accelerated droplets impact the substrate with a process dependent velocity which leads to a splatting of the hard material droplets at the substrate. From a modelling point of view, this yields a highly non-linear problem where contact formulations as well as large deformations within a short period of time — similar to crash simulations in the automobile industry — have to be taken into account. Furthermore, the hot droplets solidify at the surface of the substrate where the total of all the hard material splats form the hard material coating. Here, phenomena like phase transitions or phase transformations can occur, dependent on the coating material at hand. The modelling of these phenomena leads to thermo-mechanically coupled formulations which must be capable of accounting for the complex constitutive behaviour as well as for a large temperature range. Bertagnolli et al. [17] numerically investigated the impact of hot spherical ceramic particles on a cool flat substrate by means of a three dimensional finite element framework in the context of plasma spraying where much higher temperatures are reached than during HVOF processes. Besides the impact simulation, the solidification of the splat and the influence of the substrate material – here, steel and zirconia – as well as the influence of convective boundary conditions on the temperature evolution of the ceramic splat is investigated. Assuming an axisymmetric impact problem, Aalami-Aleagha et al. [1] investigate the droplet deformation in a thermal spraying process with the help of the commercial finite element solver LS-DYNA and present their results in a comparison to results from references cited therein.

The above mentioned frameworks are able to capture the combustion of a thermal spraying process including the chemical reactions taking place, the particle transport due to the gas flow, or can capture the influence of the nozzle geometry on the gas flow and therefore on the resulting particle or hard material droplet velocity. Other mentioned frameworks propose promising solution techniques for large scale simulations of computational fluid dynamics or take into account the impact of the molten hard material droplets on the substrate as well as the temperature evolution of the resulting splats on the cool substrate. However, the simulation of a single hard material droplet impact is far away from the simulation of the entire process at the scale of application since the coating — which is of technological interest as a whole not as a single splat — results

from so many single splats so that different frameworks are required which predict the final geometry of the coating applied in order to model the whole thermal spraying procedure of a metal sheet forming tool or other workpieces. A framework which predicts the thickness distribution of a thermally sprayed coating which is based on parameters like the spray gun position and orientation relative to the modelled surface to be coated is presented in Sadovoy [145]. This framework is implemented into the commercial software tool RobCad and shows realistic predictions of the coating thickness of free-form surfaces. Within the collaborative research centre SFB 708, experimental investigations of characteristic thermal spray gun footprints where used as input for a geometric deposition model which is published by Wiederkehr et al. [188]. The framework presented therein is applied to arc spraying but could be adapted to other spraying techniques like HVOF thermal spraying in order to obtain a geometrical representation of the respective coatings. Further effort would be necessary in order to obtain a multi-phase finite element discretisation which is suitable for subsequent finite element analyses. An alternative approach where two-dimensional slices stemming from successive grinding and microscopy analyses of thermally sprayed coatings is published in Wiederkehr et al. [189]. In that work, the two-dimensional images which represent slices of the produced coating are processed to a three-dimensional finite element mesh by means of an image morphing algorithm. The resulting three-dimensional finite element mesh holds information about pore networks within the thermally sprayed coating analysed and can be used for further finite element analyses. More details on the geometric modelling of thermal spraying as well as the related experiments carried out in context of the collaborative research centre SFB 708 are summarised in detail in Wiederkehr [190].

The extension of existing thermal spraying modelling frameworks by means of finite element formulations based on fundamental balance equations requires frameworks which are capable of adding elements to an existing discretisation in order to account for the additionally applied mass. When e.g. the temperature is considered to be a degree of freedom in a finite element approach, the adding of elements to an existing system with a different temperature formally leads to a temperature jump. Two promising methods for the thermodynamically consistent simulation of mass deposition by means of the finite element method were proposed in the literature. One option is the use of discontinuous Galerkin methods. Finite element implementations of discontinuous Galerkin methods are used for many different applications such as gas dynamics, cf. Baumann and Oden [12], the solution of Hamilton-Jacobi equations, see Hu et al. [82], or solid mechanics as proposed in Engel et al. [50]. In the framework of continuous Galerkin methods, another possibility is the use of interface elements which are well established for thermo-mechanical analysis, see e.g. the works of Fagerstrom and Larsson [52], Fleischhauer et al. [56], Steinmann and Häsner [165].

To recapitulate, different modelling frameworks related to thermal spraying exist and each of these frameworks is able to capture different aspects of the process. The mentioned frameworks of Wiederkehr are promising with regard to the modelling of the entire thermal spraying process and therefore contribute to an integrated process

simulation tool in the spirit of the goal of SFB 708. His simulation framework is calibrated based on experiments and can have a flexible application programming interface (API) since it is software written by himself. Consequently, the framework developed by Wiederkehr is a good candidate to be integrated into a larger software tool. However, the geometry simulation so far does not account for balance equations for heat or momentum which would be fundamentally necessary in order to optimise the process at hand with respect to, e.g., residual lattice strains or temperature peaks. With respect to the modelling of thermal spraying by means of the finite element method, a further challenge is the consistent consideration of the arising jumps of the nodal degrees of freedom by means of suitable methods. In addition, the effective material behaviour of the thermally sprayed coating would be essential to be known. One possibility of obtaining the effective behaviour of heterogeneous media, cf. Fig. 1.3, is the application of homogenisation techniques.

1.1.2 Homogenisation of thermo-mechanical problems

The behaviour of many technologically interesting materials is determined by the composition of different constituents at different length scales or by inherent textures at length scales far below the scale of technological application. When talking about different length scales, the length scale of technological applications is often denoted as the upper scale or as the macro-scale — an example would be a sheet metal forming tool. The scale where the heterogeneities are observed is often denoted as the lower scale or as the micro-scale – an example would be the wear resistant coating applied to a sheet metal forming tool. The subdivision into different length scales is not limited to two different scales, but in the framework of this thesis only an upper scale as well as a lower scale with heterogeneities will be considered. The macro-scale is the scale where typically strength calculations or other kinds of analyses are performed and where the constitutive behaviour of the underlying material — the micro-scale — needs to be known. Hence, simulative predictions of e.g. workpiece behaviour during application, workpiece interactions within assembly groups or workpiece service life during operation require a deep understanding of the processes within the material at the micro-scale and, therefore, fundamentally, give an answer to the question: what is the effective material behaviour that results from a certain micro-structure? The mathematical procedure to determine the effective material behaviour in this context is denoted as *homogenisation* for which particular assumptions must be made. Although homogenisation is applied to thermo-mechanically coupled problems in this thesis, this section additionally discusses pioneering works for purely mechanical problems as well as homogenisation frameworks for different physical phenomena.

With respect to the effective mechanical behaviour of a heterogeneous material, Voigt [185] assumed that a strain field is uniform within a given RVE that captures the heterogeneous material at the micro-scale. Complementarily to the homogenisation-procedure of Voigt, Reuss [140] proposed the stress field to be uniform within a given

RVE. As shown by Hill [75], the effective behaviour which results from the procedure proposed by Reuss is weaker than the effective behaviour obtained via the procedure of Voigt while the true effective behaviour lies somewhere in between. Improved bounds which are based on variational principles have been developed by Hashin and Shtrikman [72, 73] where the upper and lower bounds for the effective elastic properties are between the Reuss and Voigt bounds, while the true effective elastic behaviour lies between the so-called upper and lower Hashin-Shtrikman bounds. The bounds for the effective elastic properties mentioned so far do not account for the topology of the micro-structure which can be rather complex in reality, cf. Fig. 1.3, but only depend on the volume fractions of the respective constituents. Eshelby [51] proposed a framework to determine the uniform stress field (and therefore the uniform strain field) in a single ellipsoidal inclusion embedded into an infinite matrix under a uniform stress field (and therefore resulting in a uniform strain field) far from the inclusion embedded into a matrix. As depicted in Fig. 1.3, inclusions are typically not embedded into an infinite matrix but are located quite close to one another, such that the inhomogeneities influence each other. To account for this, Mori and Tanaka [120] proposed a framework which captures the interaction of inclusions. An overview of the mentioned analytical methods/bounds can be found in the textbooks of, e.g., Mura [122], Nemat-Nasser and Hori [124] or Zohdi and Wriggers [193]. With respect to two-phase micro-structures, the plots shown in Mura [122, p. 437] or Zohdi and Wriggers [193, p. 57] where the different methods/bounds are compared with each other might be of particular interest to the interested reader.

Further development in the field of homogenisation led to the asymptotic homogenisation analysis which dates back to the works of e.g. Babuška [7], Bensoussan et al. [14], Sanchez-Palencia [148] as well as Bakhvalov and Panasenko [8] and which was applied early to the solution of thermal problems by Auriault [6] or to thermo-mechanically coupled problems in the framework of linear thermo-elasticity by Francfort [58]. In this method, the solution of a given two-scale problem with periodic micro-structure is written as a so-called asymptotic expansion such that the problem to be solved explicitly depends on the unknown field(s) on the involved scales. The method has since been developed further to capture inelastic material behaviour in terms of elasto-plasticity by Ghosh et al. [64]. More recent works on the development of asymptotic expansion based homogenisation frameworks are in the fields of, e.g., thermo-elasticity, cf. Savatorova et al. [150], Temizer [169], of inelasticity applied to composites of shape memory alloys, cf. Chatzigeorgiou et al. [37, 38], or of hygro-thermo-mechanically coupled problems, cf. Bosco et al. [31]. In Bobzin et al. [27], the asymptotic homogenisation method was used to determine the effective properties of thermally sprayed coatings and was thereby successfully compared – with quite good agreement – to finite element based virtual tensile tests as well as to experimental investigations.

With increasing computational power of high performance clusters and even desktop workstations, the computational cost of two-scale frameworks became affordable. In these frameworks, boundary value problems are solved at the scale of technological application, while the effective constitutive response is obtained from the solution of

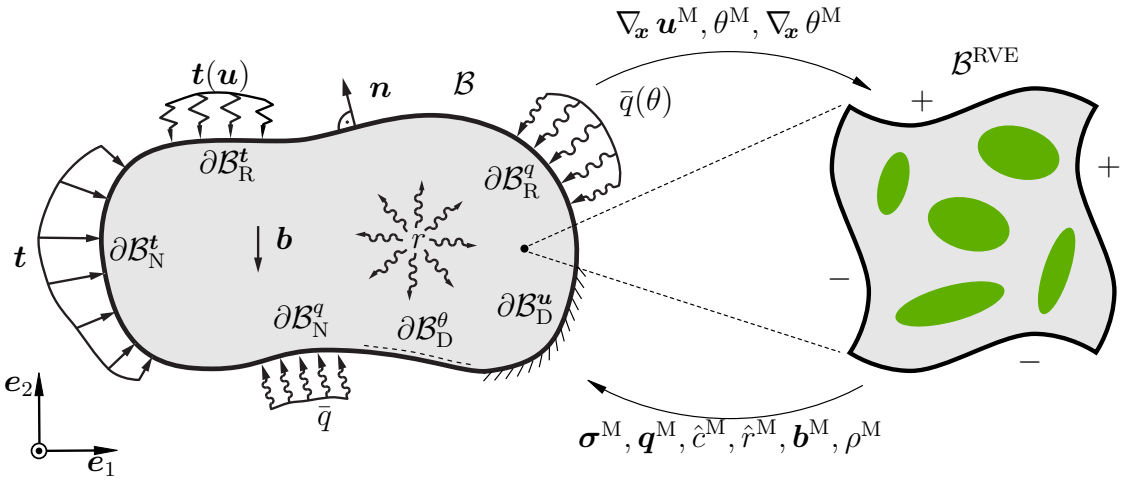

Figure 1.6: Body $\mathcal{B}$ at the macro-scale where the effective material behaviour is determined by the underlying heterogeneous micro-structure of the material represented by a RVE $\mathcal{B}^{\mathrm{RVE}}$. – The figure constitutes a lookahead to Chapters 5 and 6 where the details are discussed.

appropriate boundary value problems at the lower scale. One example of such two-scale frameworks is the so-called FE^2-method, see e.g. Feyel and Chaboche [54], Kouznetsova et al. [98], Miehe et al. [116], which also is applied in this thesis. In this method, the finite element method is used to solve an initial boundary value problem at the upper scale, as well as to solve boundary value problems at a lower scale where representative volume elements (RVE) capture the information of the lower scale as indicated by Fig. 1.6: Here, the boundary value problems at the lower scale (micro-scale) are set up in dependence of the unknown field variables at the upper scale (macro-scale). After solution of the micro-scale boundary value problem, the effective material behaviour is obtained in terms of the homogenised fluxes at RVE level and therefore at integration point level at the macro-scale. The scale bridging between the macro-scale and the underlying micro-scale is thereby achieved by the application of macro-homogeneity conditions which connect the fields and fluxes or balance equations of the both scales involved, dependent on the chosen condition. The presumably most widely applied macro-homogeneity condition in FE^2-frameworks found in literature is the so-called Hill-Mandel criterion of work equivalence at both scales, cf. Hill [76, 77]. For a comprehensive overview, a detailed discussion and derivation of the criterion, the interested reader is referred to the textbook of Nemat-Nasser and Hori [124]. In addition, there also are other homogenisation frameworks based on the Irving-Kirkwood procedure, cf. Irving and Kirkwood [86], Mandadapu et al. [110], Mercer et al. [114], where conditions similar to the Hill-Mandel conditions are derived from relating the macro-scale balance equations to the micro-scale balance equations. Another approach is called the "boundary driven approach to computational homogenisation", Fleischhauer et al. [57], where the balance equations themselves are homogenised.

The advantage of the FE^2-method is that it is applicable to frameworks with any kind of non-linearity, as long as proper boundary conditions can be formulated for the micro-scale boundary value problem with respect to the chosen macro-homogeneity condition, and as long as one is aware of instabilities which might arise due to non-linearities. Consequently, thermo-dynamically consistent, cf. Coleman and Noll [40], constitutive models in the spirit of the one proposed by Simo [161, 162] for metal plasticity at large deformations can be used, to name just one important work on constitutive modelling for inelastic material behaviour in a geometric exact computational frame. In the following, the literature overview is limited to homogenisation frameworks. For background information on the respective balance equations involved as well as on related constitutive theories, the reader is referred to the references of the respective contributions.

The already mentioned works of Feyel and Chaboche [54], Kouznetsova et al. [98], Miehe et al. [116] represent FE^2-frameworks for mechanical boundary value problems which are based on the balance of linear momentum. Feyel and Chaboche deal with elasto-viscoplasticity within a geometric linearised setting, whereas Kouznetsova et al. and Miehe et al. deal with inelastic constitutive models in a geometric exact framework. Within the Hill-Mandel criterion based frameworks, three different well-established kinds of boundary conditions exist: linear displacement boundary conditions (LN), periodic boundary conditions (PR) and uniform traction boundary conditions (UT). Out of these three different types of boundary conditions, LN yields the stiffest effective material behaviour, UT yields the weakest effective material behaviour, whereas the effective material behaviour of PR lies in between. A comparison of the boundary conditions with an emphasis on the implementation as well as the macro-scale tangent computation within a small strain framework can be found in the work of Miehe and Koch [115]. A large deformation two-scale framework for second-order homogenisation is proposed in Kouznetsova [99], Kouznetsova et al. [100] in order to take into account macroscopic localisation phenomena as well as size effects due to the inherent length scale of the applied RVE. Localisation is a material instability and is studied in the context of a large deformation two-scale framework in Miehe et al. [117]. In addition, buckling effects are investigated as an instability on a structural level which may occur during analyses. The framework is also discussed in Schröder [152] where many demonstrative examples are elaborated, not only with respect to instabilities but also with respect to finite inelasticity as well as to the derivative of the consistent algorithmic tangent modulus. Another approach which accounts for size effects in homogenisation is proposed by Hirschberger et al. [78], Hirschberger [79]. In this framework, a classic continuum is applied at the macro-scale, whereas a micropolar continuum is assumed at the micro-scale in order to capture size effects while determining the effective behaviour of thin material interfaces at the macro-scale based on the macroscopic displacement jump. The homogenisation framework is extended in the works of Javili et al. [89], McBride et al. [113] by accounting for a surface energy of the considered interfaces. As an alternative to the established boundary conditions mentioned above, Larsson et al. [104] proposed the concept of weak micro-periodicity where the Hill-Mandel macro homogeneity condition

is fulfilled in a weak sense. With this framework at hand, the meshes of periodic RVEs do not need to have identically discretised opposing boundaries. Depending on the micro-structure to be discretised, this can be an advantage, e.g. with respect to mesh quality in those cases where inhomogeneities are close to one of the RVE boundaries and where a coarser boundary discretisation is desired at the opposing face in order to save computation time. The FE^2-method for purely mechanical problems has also been used in the context of the analysis of dual phase steel, cf. Schröder et al. [155] where initial volumetric strains are assumed to account for the residual stresses which stem from the dual phase steel production process. Another contribution which deals with stability analysis and homogenisation is proposed by Miehe et al. [118]. In this work, limit points in the local constitutive response as well as buckling of micro-fibers are investigated by means of an energy based framework. Recently, in Tikarrouchine et al. [175], a two-scale finite element framework was implemented into the commercial finite element solver ABAQUS/Standard. The framework captures inelastic material behaviour at small strains and is compared with semi-analytical solutions as well as with the Mori-Tanaka method which was mentioned above.

The two-scale finite element method is also applied to other balance equations such as the balance of energy in terms of the temperature rate equation. Within the framework proposed by Özdemir et al. [131], transient heat conduction is considered at the macro-scale, and an instantaneous micro-scale response is assumed to obtain the effective quantities. Hereby, the effective thermal response is not dependent on the RVE size as long as no temperature dependent quantities are involved, as will be discussed in the following. In contrast to this framework, Larsson et al. [105] account for the RVE size in their work on variationally consistent homogenisation of diffusion type problems. The framework is exemplarily applied to transient heat flow. In the limit case of infinitesimally small RVEs, the framework of Özdemir et al. is recovered.

The FE^2-method is also applied to coupled analyses where the coupling between two or more balance equations is considered. One of the most important couplings in mechanical engineering applications is the coupling of the mechanical problem with the temperature in both directions. Since many of the displacement and/or temperature driven engineering processes and applications are influenced by — and moreover also influence — the micro-structure of the material involved, thermo-mechanically coupled FE^2-frameworks have been developed. In Özdemir et al. [132], a staggered thermo-mechanically coupled two-scale framework is developed as an extension of the purely thermal framework, [131], mentioned above. The framework accounts for inelastic material behaviour as well as for temperature dependent material properties at the micro-scale, whereas the microscopic temperature field is connected to the macro-scale temperature gradient which is used to apply the boundary conditions to the RVE. This leads to the evaluation of temperature dependent quantities with the locally varying micro-scale temperature θ^{m}. In Temizer and Wriggers [172], a thermodynamically consistent staggered homogenisation procedure for finite thermo-elasticity is introduced, where temperature dependent properties are evaluated at the macro-scale temperature θ^{M} to ensure that, e.g. the effective

macroscopic mechanical behaviour depends on the macro-scale temperature gradient. A monolithic thermo-mechanically coupled two-scale framework applied to the modelling of shape memory alloys within a geometrically exact setting is proposed in the work of Sengupta et al. [157]. The focus of this contribution is on the derivation of the algorithmically consistent tangent moduli in material as well as spatial formulation. Within the framework, temperature dependent quantities are evaluated at θ^{m}. A thermo-mechanical homogenisation framework based on [132] which deals with the effective behaviour of lamellar cast iron is proposed in the work of Pina et al. [136] where the graphite crystallites at the micro-scale are explicitly resolved in order to study the influence of anisotropy of graphite. Another work, cf. Sahraee [146], deals with homogenisation in finite thermo-viscoplasticity with an application to heterogeneous compressible rubber-like materials. More recent works on thermo-mechanical homogenisation deal with the determination of elastic and thermal metal matrix composite materials, see Schindler et al. [151], or with the implementation of a fully coupled thermo-viscoplastic FE^2-framework into the commercial software ABAQUS/Standard, cf. Tikarrouchine et al. [176] which represents the thermo-mechanical extension of [175].

Apart from homogenisation frameworks for mechanical, thermal or thermo-mechanically coupled problems, homogenisation frameworks also exist for other underlying balance equations or other coupled problems such as the two-scale framework for electro-mechanically coupled problems proposed by Schröder and Keip [153] which is applied to non-linear material behaviour within a geometrically linearised setting. The mentioned framework is conceptually enhanced to a finite deformation framework for the modelling of electro-active materials in Keip et al. [93] using the example of finite electro-elasticity. Magneto-mechanical coupling is strongly related to the modelling of electro-mechanically coupled problems is the. In this regard, Javili et al. [88] developed a large deformation homogenisation framework for composites with magneto-mechanically coupled constitutive behaviour. Another magneto-mechanically coupled homogenisation framework is presented in the work of Chatzigeorgiou et al. [36], with an emphasis on the modelling of magneto-rheological elastomers undergoing large deformations. A kind of union of the both aforementioned couplings represents the magneto-electro-mechanically coupled two-scale finite element scheme proposed by Schröder et al. [156] as well as Labusch et al. [103] where emphasis is laid on the analysis of the strain-induced magneto-electric coefficient for different micro-structures with simultaneous consideration of different constitutive models. In some way related to the homogenisation of thermal problems is the diffusion problem which has been addressed in Rocha et al. [143] where the emphasis is on diffusion induced microscopic material degradation. In this framework, the homogenisation of the Fick's law based diffusion problem is avoided due to the assumption of constant concentration at the micro-scale. This implies that the effective diffusivity tensor is constant. In contrast to this, the large deformation framework for chemo-mechanically coupled problems proposed in Kaessmair and Steinmann [92] accounts for both balance equations at the lower scale while the macro-scale tangent terms are computed numerically. A characteristic of the framework is that transient

micro-scale problems are considered where the two scales are not clearly separated due to the definition of the macroscopic flux which induces a size effect.

Apart from the further development of the homogenisation frameworks for different balance equations and couplings between different balance equations themselves, investigations regarding the size of the RVEs, cf. Khisaeva and Ostoja-Starzewski [94], or effective tangent computations, cf. Balzani et al. [10], Temizer and Wriggers [171], have been carried out. Other works deal with multi-scale contact problems, cf. De Lorenzis and Wriggers [45] where the developed framework is applied to determine the effective friction coefficient of structured surfaces, or the works of Temizer [168, 170] which deal with homogenisation of thermo-mechanical contact problems. Furthermore, in the work of Fillep et al. [55], a homogenisation framework for periodic woven structures is presented where multiple contact zones are involved at the lower scale. Beyond this, works exist which deal with localisation phenomena at the lower scale in context of the X-FEM as proposed by Bosco et al. [30], or which deal with the algorithmic treatment of lower scale boundary conditions, cf. Javili et al. [90]. Since RVEs can be of any complexity which yields finite element meshes with a very high number of elements, the concept of so-called statistically similar representative volume elements (SSRVE) has been developed in the works of Balzani et al. [9], Schröder et al. [154] where RVEs showing finite plastic material behaviour are considered. Such an SSRVE represents an RVE with reduced complexity to significantly save computation time while showing the same effective behaviour as the much more complex original RVE. In a way, the topic has also already been adressed in the work of Temizer and Zohdi [173] with a focus on linear as well as non-linear elasticity. However, the use of the finite element method at both scales constitutes only one possible approximation framework amongst others. Recently, e.g. the combination of a macro-scale finite element framework with FFT-based micro-scale-simulations has been proposed, Kochmann et al. [96], which can be more computationally cost efficient. In the recent work of Brassart and Stainier [32], a semi-analytical mean field approach for transient diffusion problems at the lower scale is presented. The latter mentioned contributions try to reduce the computational cost of the presented homogenisation frameworks compared to the computational cost of the FE^2-frameworks mainly discussed so far.

Although high performance clusters are available which are able to handle the computational extensive frameworks discussed above, it would still be desirable to reduce computation time. Though it would be misleading not to mention at least some of the works which avoid the high computational effort of full-field approaches such as the reduced basis homogenisation framework proposed by Fritzen and Böhlke [60] which is applied to visco-elasticity, and where the modes of the local inelastic field are assumed to be known, whereas the precise determination of these modes is a task of its own. The presented framework is compared with finite element method based solutions to demonstrate the capability of the method. In other works of Fritzen et al. [61], Leuschner and Fritzen [106], reduced order modelling schemes are developed where the solution of multi-scale problems is performed during a so-called "online"-phase, whereas the modes

of the inelastic local fields are pre-analysed during the so-called "offline"-phase. As a consequence, the actual analysis is performed at a far lower computational cost compared to FE^2-approaches, but at the expense of the time spent for pre-selecting and pre-calculating the modes of the local fields. The recent work of van Tuijl et al. [184] deals with a wavelet-reduced order modelling framework for mechanical problems that is compared to a reduced order modelling frame as well as to a full-field finite element solution by means of a one-dimensional elasto-plastic boundary value problem at which the developed method shows a quite good performance.

As a concluding remark regarding this section it should be mentioned that only a small subset of the literature dealing with homogenisation is summarised above. For a broader overview, the interested reader is referred to the review paper of Geers et al. [62] and especially to the rather recent review article of Matouš et al. [112] where different homogenisation approaches, applications and future directions are referred to and discussed.

1.2 Objective of this work

This thesis follows two different objectives which are founded on the research carried out within Project B6 of SFB 708 as well as during the years after the funding period was over. The first objective is the development of a simulation framework for the thermal spraying process which is, on the one hand, capable of displaying the whole thermal spraying procedure and which is able to predict the temperature evolution in the coated workpiece based on fundamental balance laws on the other. The second objective is the development of a computational homogenisation framework for thermo-mechanically coupled problems in order to predict the effective thermo-mechanical behaviour of heterogeneous materials such as the coatings produced during thermal spraying processes. With regard to the weight of the content, the latter was also chosen to be eponymous for this work: Computational homogenisation of thermomechanical problems.

Both objectives are realised as thermodynamical consistent finite element frameworks based on the governing equations of continuum thermodynamics in the sense of Coleman and Noll [40]. Hence, the notation applied in this thesis as well as the kinematics and balance equations are summarised in **Chapter 2** which thereby represents the continuum mechanical basis of the subsequent chapters.

Different aspects of the development of a simulation framework for thermal spraying processes are outlined in Chapters 3 and 4. In **Chapter 3**, a simulation framework for the computation of the temperature development for a given workpiece during the thermal spraying process is presented. The developed simulation framework consists of two parts, an "outer" part as well as an "inner" part. Therein, the "outer" part of the framework

deals with the discrete time stepping, the spray gun movement and it computes the time-dependent input boundary conditions for the "inner" simulation module, which evaluates a thermodynamically consistent transient and non-linear heat conduction formulation for a rigid heat conductor. The surface area of the modelled workpiece which is affected by the gun flame stemming from the spray gun is assumed to be exposed to heat transfer due to radiation as well as to forced convection, whereas the remaining surface area is assumed to be exposed to natural convection at ambient conditions. For complex workpieces, the setup of the input boundary conditions itself is a computationally expensive procedure since the modelled gun flame load distribution on the workpiece surface is not locally restricted and may affect a large fraction of the workpiece. As already stated in the preface, this chapter comprises the collaborative work of the author of this thesis and Dr. Thomas Wiederkehr who contributed the GPGPU–C++–reimplementation of the developed framework into the geometrical simulation framework which is discussed in the previous section. The performance of the developed combined novel framework is presented by means of demonstrative computational examples where a spray gun is moved across a deep drawing tool along a predefined gun movement path.

In **Chapter 4**, the software tool for the simulation of heat transfer during thermal spraying developed in Chapter 3 is extended with respect to mass deposition within the framework of a non-linear rigid heat conductor where the temperature is the degree of freedom. As previously discussed in Section 1.1.1, adding elements to an existing rigid heat conductor formally leads to a temperature jump. Two techniques to encounter the temperature jump previously discussed are the discontinuous Galerkin method, [12, 50, 82], as well as as interface elements within a continuous Galerkin framework, [52, 56, 165]. This chapter presents a novel approach for the thermodynamically consistent modelling of mass deposition for a rigid heat conductor in the framework of continuous Galerkin methods. The analysis is therefore restricted to the energy balance in form of the temperature rate equation, and newly added mass has to satisfy a continuous temperature distribution. Practically, the considered rigid heat conductor as well as the newly applied mass are both represented by finite elements where the temperature is the only degree of freedom which is present during the analysis. We overcome this problem by introducing internal heat sources which ensure the conservation of energy. Therefore, existing degrees of freedom remain unchanged during the procedure of adding additional finite elements. If elements with different temperature values are added, the energy difference is computed and finally compensated by a corresponding volumetric heat source. The algorithmic treatment of the internal heat sources as well as the implementation into a non-linear finite element framework is discussed in detail. The performance of the developed framework is shown by means of various numerical examples. The material parameters are therefore fitted to experimental data.

The main emphasis of this thesis is on the development of a computational homogenisation framework for thermo-mechanically coupled problems which is discussed in Chapters 5 and 6, whereby the upper scale is denoted as the "macro-scale" and the lower scale is denoted as the "meso-scale". Note that this lower scale is often denoted as the

micro-scale such as within the overview given in the previous section. Within this work, however, we shall denote this scale as meso-scale since its respective constituents may possess further, even smaller scales. In **Chapter 5**, a thermo-mechanically fully coupled FE^2-framework for inelastic material behaviour in a geometrically linearised setting is developed. The framework is implemented monolithically where the balance of linear momentum as well as the balance of energy are solved simultaneously in order to obtain solutions for the displacements and the temperature which are the degrees of freedom. The scale-bridging is based on the application of the Hill–Mandel criterion. For the sake of comparison, the previously mentioned θ^{m}-approach from [132] as well as the θ^{M}-approach from [172] are applied. The hard material which is deposited by the HVOF spray gun consists of the ceramic WC which shows brittle behaviour and which is modelled as a thermo-elastic phase, as well as of Co which acts as a ductile binding phase, cf. Fig. 1.3. In order to account for the viscous behaviour of Co at higher temperatures, a thermo-viscoplastic material model including non-linear thermal softening is presented in detail and applied in the FE^2-framework. For demonstration purposes, results obtained from the θ^{m}-approach and the θ^{M}-approach are compared with each other and discussed. Furthermore, the performance of the two-scale framework is shown by its comparison with one-scale simulations of the same problem where quite a good agreement of the results is obtained under adiabatic as well as non-adiabatic boundary conditions. For the simulation of quenching, Robin boundary conditions are applied in order to simulate cooling due to natural convection of the surrounding air at ambient conditions. These boundary conditions are introduced within Chapters 3 and 4 and are as well applied for the multi-scale 2d–analysis of the quenching of a WC–Co coated steel radius.

In **Chapter 6**, the thermo-mechanically coupled FE^2-framework developed in Chapter 5 is extended to a geometrically exact framework. Emphasis is laid on the thermo-mechanical extension of the "weak micro-periodicity"-concept which was initially proposed by [104] for mechanical problems as discussed above and which was further extended to diffusion problems by [149]. The weak format of the periodicity constraints for thermo-mechanical problems allows for the interpolation between uniform traction as well as uniform heat flux boundary conditions and "true" periodic boundary conditions for both fields under consideration. A thermo-viscoplastic constitutive model for finite deformations is derived as a benchmark model for inelastic material behaviour including heat production via dissipation. The implementation of the two-scale finite element framework for large deformations is briefly recapitulated with the focus on the algorithmic handling of the novel thermo-mechanical weak micro-periodicity constraints which are enforced by Lagrange multipliers. The performance of the developed weak micro-periodic boundary conditions are shown by means of descriptive numerical examples where the weak boundary conditions are compared to linear displacement, periodic as well as uniform flux boundary conditions. However, RVE level simulations as well as full FE^2-simulations are carried out. In addition and in contrast to Chapter 5, the multi-scale analysis of the quenching of a WC–Co coated steel radius is performed in three-dimensional space here.

The thesis closes with a brief summary and a discussion on possible extensions as well as future directions in **Chapter 7**. The appendix provides additional information regarding Chapters 3 to 6. In **Appendix A**, equations and definitions regarding the implementation of the finite element method which are omitted in the remaining chapters are summarised. Furthermore, the homogenisation related **Appendix B** provides comments on the Hill–Mandel criterion as well as comments on the algorithmic implementation of the so-called well-established boundary conditions. In **Appendix C**, some auxiliary calculations are collated which are necessary for the implementation of the thermo-viscoplastic material models that are used within this thesis.

2 Continuum thermodynamics of thermo-inelasticity

The purpose of this chapter is to introduce the continuum thermodynamical basics. They are applied in the following chapters of this thesis to thermal and thermo-mechanically coupled initial boundary value problems in the context of continuum mechanics where the motion of particles as well as the related physics are described by means of tensors and tensor functions. The contents of the respective sections within this chapter do not represent new findings but are adopted from the literature.

In order to introduce the notation which is applied throughout the whole thesis, Section 2.1 gives an overview of the definition of the symbolic and index notation of tensors of different order as well as the definition of tensor products and special tensors of second and fourth order. The notation originates from the community of computational mechanics and the given overview leaves out many details regarding precise mathematical definitions and tensor calculus. For a comprehensive introduction to tensor calculus, the interested reader is therefore referred to the textbooks of Itskov [87] and de Boer [43].

In dependence of the application at hand, a temperature field is considered in the framework of a so-called rigid heat conductor, cf. Chapters 3 and 4, or a field which represents the deformation of a deformable heat conductor is considered alongside with the temperature which represents a thermo-mechanically coupled problem, cf. Chapters 5 and 6. The deformation can be considered finite, i.e. observable with the naked eye, or infinitesimally small. The theory of a deformable heat conductor which undergoes finite deformations is the most general case considered within the present thesis. Therefore, the kinematics of large deformations are briefly summarised in Section 2.2 and, subsequently in Section 2.3, the underlying balance equations of a finite deformable heat conductor are collated. In conclusion, the initial boundary value problem of a deformable heat conductor at finite deformations is summarised in Section 2.4 and, in addition, the reduction to a deformable heat conductor at small deformations as well as the reduction to a rigid heat conductor is briefly described.

2.1 Notation

Throughout this thesis, tensor operations are performed to describe the motion of material in physical space and in time. Within this section, the tensor notation is briefly summarised. For the sake of simplicity, this thesis is restricted to the n-dimensional Euclidean space $\mathbb{E}^n$ spanned by the Cartesian basis vectors $\{\boldsymbol{e}_i\}, i = 1, \ldots, n$, whereby the examples within this thesis will either be located in two-dimensional space, $n = 2$, or three-dimensional space, $n = 3$. In a n-dimensional space, a tensor of order m has n^m components. The tensors used in this thesis are of the order $m \in [\,0\,,1\,,2\,,3\,,4\,]$ and are typically written in the following typesetting

$$\alpha \,, \qquad \text{(zero-order tensor, i.e. scalar)} \tag{2.1}$$

$$\boldsymbol{a} = a_i \, \boldsymbol{e}_i \;\; , \qquad \text{(first-order tensor, i.e. vector)} \tag{2.2}$$

$$\boldsymbol{A} = A_{ij} \, \boldsymbol{e}_i \otimes \boldsymbol{e}_j \;\; , \qquad \text{(second-order tensor)} \tag{2.3}$$

$$\mathbf{A} = \mathrm{A}_{ijk} \, \boldsymbol{e}_i \otimes \boldsymbol{e}_j \otimes \boldsymbol{e}_k \;\, , \qquad \text{(third-order tensor)} \tag{2.4}$$

$$\mathsf{A} = \mathsf{A}_{ijkl} \, \boldsymbol{e}_i \otimes \boldsymbol{e}_j \otimes \boldsymbol{e}_k \otimes \boldsymbol{e}_l \;\; . \qquad \text{(fourth-order tensor)} \tag{2.5}$$

If not stated otherwise, according to the above equations, non-bold italic letters are used for scalars, bold-face italic lower-case letters denote first-order tensors, bold-face italic upper-case letters are used for second-order tensors, bold-face upright upper-case letters denote third-order tensors and fourth order-tensors are expressed by sans-serif bold-face upper-case letters. In the above equations as well as in the following, Einstein's summation convention is applied to indicate summation over duplicate indices, cf. [43, p. 4] or [81, p. 4].

The scalar product of two orthonormal base vectors $\boldsymbol{e}_i$ and $\boldsymbol{e}_j$ defines the so-called Kronecker delta

$$\boldsymbol{e}_i \cdot \boldsymbol{e}_j = \delta_{ij} = \begin{cases} 1 & \text{if } i = j \\ 0 & \text{else} \end{cases} \;\; , \tag{2.6}$$

which is useful to indicate contractions between base vectors. The scalar product of two vectors $\boldsymbol{a}$ and $\boldsymbol{b}$ can be written as

$$\alpha = \boldsymbol{a} \cdot \boldsymbol{b} = a_i \, b_j \, \boldsymbol{e}_i \cdot \boldsymbol{e}_j = a_i \, b_j \, \delta_{ij} = a_i \, b_i \;\, , \tag{2.7}$$

where the Kronecker property is utilised to replace index j by index i. Other contractions between tensors which are also denoted as inner tensor products in this thesis are defined as

$$\boldsymbol{a} = \boldsymbol{B} \cdot \boldsymbol{c} \qquad\qquad a_i = B_{ij} \, c_j \;\, , \tag{2.8}$$

$$\boldsymbol{A} = \boldsymbol{B} \cdot \boldsymbol{C} \qquad\qquad A_{ij} = B_{ik} \, C_{kj} \;\, , \tag{2.9}$$

$$\alpha = \boldsymbol{A} : \boldsymbol{B} \qquad \alpha = A_{ij}\, B_{ij} \ , \tag{2.10}$$

$$\boldsymbol{A} = \mathsf{B} : \boldsymbol{C} \qquad A_{ij} = \mathsf{B}_{ijkl}\, C_{kl} \ . \tag{2.11}$$

The expressions on the left hand sides of the above equations, e.g. $\boldsymbol{B} \cdot \boldsymbol{c}$, are referred to as absolute notation or as symbolic notation, whereas the right hand sides, e.g. $B_{ij}\, c_j$, are referred to as index notation.

Dyadic products which are also denoted as outer tensor products are already introduced by the definition of tensors in Eqs. (2.1) to (2.5) where the so-called standard dyadic product symbol $\otimes$ is used between tensor base vectors. Applied to tensors in general, the standard dyadic product, denoted by symbol $\otimes$, and non-standard dyadic products, denoted by symbols $\overline{\otimes}$ as well as $\underline{\otimes}$, are defined as

$$\boldsymbol{A} = \boldsymbol{b} \otimes \boldsymbol{c} \qquad A_{ij} = b_i\, c_j \ , \tag{2.12}$$

$$\mathsf{A} = \boldsymbol{B} \otimes \boldsymbol{C} \qquad \mathsf{A}_{ijkl} = B_{ij}\, C_{kl} \ , \tag{2.13}$$

$$\mathsf{A} = \boldsymbol{B} \,\overline{\otimes}\, \boldsymbol{C} \qquad \mathsf{A}_{ijkl} = B_{ik}\, C_{jl} \ , \tag{2.14}$$

$$\mathsf{A} = \boldsymbol{B} \,\underline{\otimes}\, \boldsymbol{C} \qquad \mathsf{A}_{ijkl} = B_{il}\, C_{jk} \ . \tag{2.15}$$

Consequently, the outer tensor product of two first-order tensors results in second-order tensors and the outer tensor products of two second-order tensors yield fourth-order tensors.

Special tensors are so-called identity tensors which have the property to map a tensor onto itself or to extract a particular part of a tensor. The identity tensors used in this work are

$$\boldsymbol{I} = \delta_{ij}\, \boldsymbol{e}_i \otimes \boldsymbol{e}_j \qquad I_{ij} = \delta_{ij} \ , \tag{2.16}$$

$$\mathsf{I} = \boldsymbol{I} \,\overline{\otimes}\, \boldsymbol{I} \qquad \mathsf{I}_{ijkl} = \delta_{ik}\, \delta_{jl} \ , \tag{2.17}$$

$$\mathsf{I}^{\mathrm{sym}} = \frac{1}{2}\, [\, \boldsymbol{I} \,\overline{\otimes}\, \boldsymbol{I} + \boldsymbol{I} \,\underline{\otimes}\, \boldsymbol{I} \,] \qquad \mathsf{I}^{\mathrm{sym}}_{ijkl} = \frac{1}{2}\, [\, \delta_{ik}\, \delta_{jl} + \delta_{il}\, \delta_{jk} \,] \ , \tag{2.18}$$

$$\mathsf{I}^{\mathrm{vol}} = \frac{1}{3}\, [\, \boldsymbol{I} \otimes \boldsymbol{I} \,] \qquad \mathsf{I}^{\mathrm{vol}}_{ijkl} = \frac{1}{3}\, \delta_{ij}\, \delta_{kl} \ , \tag{2.19}$$

$$\mathsf{I}^{\mathrm{dev}} = \mathsf{I} - \mathsf{I}^{\mathrm{vol}} \qquad \mathsf{I}^{\mathrm{dev}}_{ijkl} = \delta_{ik}\, \delta_{jl} - \frac{1}{3}\, \delta_{ij}\, \delta_{kl} \ , \tag{2.20}$$

$$\mathsf{I}^{\mathrm{sym}}_{\mathrm{dev}} = \mathsf{I}^{\mathrm{sym}} - \mathsf{I}^{\mathrm{vol}} \qquad [\, \mathsf{I}^{\mathrm{sym}}_{\mathrm{dev}} \,]_{ijkl} = \frac{1}{2}\, [\, \delta_{ik}\, \delta_{jl} + \delta_{il}\, \delta_{jk} \,] - \frac{1}{3}\, \delta_{ij}\, \delta_{kl} \ , \tag{2.21}$$

whereby the second-order identity tensor $\boldsymbol{I}$ maps a first-order tensor $\boldsymbol{a}$ onto itself, i.e. $\boldsymbol{a} = \boldsymbol{I} \cdot \boldsymbol{a}$, and in analogy, the fourth-order identity tensor I maps a second-order tensor $\boldsymbol{A}$ onto itself, i.e. $\boldsymbol{A} = \mathsf{I} : \boldsymbol{A}$. The fourth-order symmetric identity $\mathsf{I}^{\mathrm{sym}}$ extracts the

symmetric part of second-order tensor $\boldsymbol{A}$, i.e. $\boldsymbol{A}^{\mathrm{sym}} = \mathbf{I}^{\mathrm{sym}} : \boldsymbol{A}$, whereas the volumetric part of a second-order tensor $\boldsymbol{A}$ is extracted with help of the volumetric fourth-order identity $\mathbf{I}^{\mathrm{vol}}$, i.e. $\boldsymbol{A}^{\mathrm{vol}} = \mathbf{I}^{\mathrm{vol}} : \boldsymbol{A}$. Analogously, the deviatoric part or symmetric deviatoric part of a second-order tensor is extracted by double contraction with the deviatoric fourth-order identity $\mathbf{I}^{\mathrm{dev}}$ or the symmetric deviatoric fourth-order identity $\mathbf{I}^{\mathrm{sym}}_{\mathrm{dev}}$.

In continuum mechanics, the inverse or transpose of a second-order tensor is often needed. Hereby, the inverse tensor $\boldsymbol{A}^{-1}$ of a second-order tensor $\boldsymbol{A}$ is defined as

$$\boldsymbol{A} \cdot \boldsymbol{A}^{-1} = \boldsymbol{I} \qquad A_{ik} \left[A^{-1}\right]_{kj} = \delta_{ij} \ , \tag{2.22}$$

such that the single contraction of the tensor itself with its inverse results in the identity. The transpose $\boldsymbol{A}^{\mathrm{t}}$ of a second-order tensor $\boldsymbol{A}$ is defined as

$$\boldsymbol{A}^{\mathrm{t}} \cdot \boldsymbol{b} = \boldsymbol{b} \cdot \boldsymbol{A} \qquad \left[A^{\mathrm{t}}\right]_{ij} b_j = b_j A_{ji} \ , \tag{2.23}$$

where $\boldsymbol{b} \in \mathbb{E}^n$ is an arbitrary vector in Euclidean space.

In this thesis, vector and matrix operations are also performed whereby a vector $\underline{\mathbf{v}}$ with n components is written as

$$\underline{\mathbf{v}} = \left[\, v_1 \quad v_2 \quad \dots \quad v_n \,\right]^{\mathrm{t}} \quad \in \ \mathbb{R}^{n \times 1} \ , \tag{2.24}$$

and a matrix $\underline{\underline{\mathbf{M}}}$ with $n \times m$ components is written as

$$\underline{\underline{\mathbf{M}}} = \begin{bmatrix} \mathrm{M}_{11} & \mathrm{M}_{12} & \cdots & \mathrm{M}_{1n} \\ \mathrm{M}_{21} & \mathrm{M}_{22} & \cdots & \mathrm{M}_{2n} \\ \vdots & \vdots & \ddots & \vdots \\ \mathrm{M}_{m1} & \mathrm{M}_{m2} & \cdots & \mathrm{M}_{mn} \end{bmatrix} \quad \in \ \mathbb{R}^{m \times n} \ . \tag{2.25}$$

Products between vectors and matrices are defined as

$$\alpha = \underline{\mathbf{v}}^{\mathrm{t}} \cdot \underline{\mathbf{w}} \quad \in \ \mathbb{R} \qquad \alpha = \mathrm{v}_i \, \mathrm{w}_i \ , \tag{2.26}$$

$$\underline{\mathbf{w}} = \underline{\underline{\mathbf{M}}} \cdot \underline{\mathbf{v}} \quad \in \ \mathbb{R}^n \qquad \mathrm{w}_i = \mathrm{M}_{ij} \, \mathrm{v}_j \tag{2.27}$$

$$\underline{\underline{\mathbf{M}}} = \underline{\mathbf{v}} \otimes \underline{\mathbf{w}} \quad \in \ \mathbb{R}^{n \times m} \qquad \mathrm{M}_{ij} = \mathrm{v}_i \, \mathrm{w}_j \ , \tag{2.28}$$

$$\underline{\underline{\mathbf{M}}} = \underline{\underline{\mathbf{A}}} \cdot \underline{\underline{\mathbf{B}}} \quad \in \ \mathbb{R}^{n \times m} \qquad \mathrm{M}_{ij} = \mathrm{A}_{ik} \, \mathrm{B}_{kj} \ . \tag{2.29}$$

The identity matrix as well as the inverse of a square matrix with $n \times n$ components are defined as

$$\underline{\underline{\mathbf{I}}} = \begin{bmatrix} 1 & 0 & \cdots & 0 \\ 0 & 1 & \ddots & \vdots \\ \vdots & \ddots & \ddots & 0 \\ 0 & \cdots & 0 & 1 \end{bmatrix} \quad \in \mathbb{R}^{n\times n} \qquad \mathrm{I}_{ij} = \delta_{ij} \ , \tag{2.30}$$

$$\underline{\underline{\mathbf{M}}} \cdot \underline{\underline{\mathbf{M}}}^{-1} = \underline{\underline{\mathbf{I}}} \quad \in \mathbb{R}^{n\times n} \qquad \mathrm{M}_{ik} \left[\mathrm{M}^{-1}\right]_{kj} = \delta_{ij} \ . \tag{2.31}$$

For algorithmic implementation of tensor operations, it is sometimes convenient to write second-order and fourth-order tensors in a second order base system $\mathbb{E}^3 \otimes \mathbb{E}^3$ which is defined as

$$\begin{aligned} \boldsymbol{E}_1 &= \boldsymbol{e}_1 \otimes \boldsymbol{e}_1 \ , & \boldsymbol{E}_2 &= \boldsymbol{e}_2 \otimes \boldsymbol{e}_2 \ , & \boldsymbol{E}_3 &= \boldsymbol{e}_3 \otimes \boldsymbol{e}_3 \ , \\ \boldsymbol{E}_4 &= \boldsymbol{e}_1 \otimes \boldsymbol{e}_2 \ , & \boldsymbol{E}_5 &= \boldsymbol{e}_2 \otimes \boldsymbol{e}_3 \ , & \boldsymbol{E}_6 &= \boldsymbol{e}_1 \otimes \boldsymbol{e}_3 \ , \\ \boldsymbol{E}_7 &= \boldsymbol{e}_2 \otimes \boldsymbol{e}_1 \ , & \boldsymbol{E}_8 &= \boldsymbol{e}_3 \otimes \boldsymbol{e}_2 \ , & \boldsymbol{E}_9 &= \boldsymbol{e}_3 \otimes \boldsymbol{e}_1 \ . \end{aligned} \tag{2.32}$$

With the above base system at hand, a second-order tensor $\boldsymbol{A}$ in three-dimensional space can be written as

$$\boldsymbol{A} = A_i \, \boldsymbol{E}_i \ , \quad i = 1, \ldots, 9 \ , \tag{2.33}$$

$$[\boldsymbol{A}] = [\, A_{11}, \, A_{22}, \, A_{33}, \, A_{12}, \, A_{23}, \, A_{13}, \, A_{21}, \, A_{32}, \, A_{31} \,]^{\mathrm{t}} \ , \tag{2.34}$$

and a fourth-order tensor $\mathbf{A}$ in three-dimensional space is represented by

$$\mathbf{A} = \mathsf{A}_{ij} \, \boldsymbol{E}_i \otimes \boldsymbol{E}_j \ , \quad i, j = 1, \ldots, 9 \ , \tag{2.35}$$

$$[\mathbf{A}] = \begin{bmatrix} \mathsf{A}_{1111} & \mathsf{A}_{1122} & \mathsf{A}_{1133} & \mathsf{A}_{1112} & \mathsf{A}_{1123} & \mathsf{A}_{1113} & \mathsf{A}_{1121} & \mathsf{A}_{1132} & \mathsf{A}_{1131} \\ \mathsf{A}_{2211} & \mathsf{A}_{2222} & \mathsf{A}_{2233} & \mathsf{A}_{2212} & \mathsf{A}_{2223} & \mathsf{A}_{2213} & \mathsf{A}_{2221} & \mathsf{A}_{2232} & \mathsf{A}_{2231} \\ \mathsf{A}_{3311} & \mathsf{A}_{3322} & \mathsf{A}_{3333} & \mathsf{A}_{3312} & \mathsf{A}_{3323} & \mathsf{A}_{3313} & \mathsf{A}_{3321} & \mathsf{A}_{3332} & \mathsf{A}_{3331} \\ \mathsf{A}_{1211} & \mathsf{A}_{1222} & \mathsf{A}_{1233} & \mathsf{A}_{1212} & \mathsf{A}_{1223} & \mathsf{A}_{1213} & \mathsf{A}_{1221} & \mathsf{A}_{1232} & \mathsf{A}_{1231} \\ \mathsf{A}_{2311} & \mathsf{A}_{2322} & \mathsf{A}_{2333} & \mathsf{A}_{2312} & \mathsf{A}_{2323} & \mathsf{A}_{2313} & \mathsf{A}_{2321} & \mathsf{A}_{2332} & \mathsf{A}_{2331} \\ \mathsf{A}_{1311} & \mathsf{A}_{1322} & \mathsf{A}_{1333} & \mathsf{A}_{1312} & \mathsf{A}_{1323} & \mathsf{A}_{1313} & \mathsf{A}_{1321} & \mathsf{A}_{1332} & \mathsf{A}_{1331} \\ \mathsf{A}_{2111} & \mathsf{A}_{2122} & \mathsf{A}_{2133} & \mathsf{A}_{2112} & \mathsf{A}_{2123} & \mathsf{A}_{2113} & \mathsf{A}_{2121} & \mathsf{A}_{2132} & \mathsf{A}_{2131} \\ \mathsf{A}_{3211} & \mathsf{A}_{3222} & \mathsf{A}_{3233} & \mathsf{A}_{3212} & \mathsf{A}_{3223} & \mathsf{A}_{3213} & \mathsf{A}_{3221} & \mathsf{A}_{3232} & \mathsf{A}_{3231} \\ \mathsf{A}_{3111} & \mathsf{A}_{3122} & \mathsf{A}_{3133} & \mathsf{A}_{3112} & \mathsf{A}_{3123} & \mathsf{A}_{3113} & \mathsf{A}_{3121} & \mathsf{A}_{3132} & \mathsf{A}_{3131} \end{bmatrix} . \tag{2.36}$$

For symmetric second-order and fourth-order tensors, a similar notation is applied which is denoted as the Kelvin notation. Here, the second order base system is defined as

$$\begin{aligned} \boldsymbol{E}_1^{\mathrm{Kel}} &= \boldsymbol{e}_1 \otimes \boldsymbol{e}_1 \,, & \boldsymbol{E}_4^{\mathrm{Kel}} &= \frac{1}{\sqrt{2}} \left[\boldsymbol{e}_1 \otimes \boldsymbol{e}_2 + \boldsymbol{e}_2 \otimes \boldsymbol{e}_1 \right] \,, \\ \boldsymbol{E}_2^{\mathrm{Kel}} &= \boldsymbol{e}_2 \otimes \boldsymbol{e}_2 \,, & \boldsymbol{E}_5^{\mathrm{Kel}} &= \frac{1}{\sqrt{2}} \left[\boldsymbol{e}_2 \otimes \boldsymbol{e}_3 + \boldsymbol{e}_3 \otimes \boldsymbol{e}_2 \right] \,, \\ \boldsymbol{E}_3^{\mathrm{Kel}} &= \boldsymbol{e}_3 \otimes \boldsymbol{e}_3 \,, & \boldsymbol{E}_6^{\mathrm{Kel}} &= \frac{1}{\sqrt{2}} \left[\boldsymbol{e}_1 \otimes \boldsymbol{e}_3 + \boldsymbol{e}_3 \otimes \boldsymbol{e}_1 \right] \,. \end{aligned} \tag{2.37}$$

With this base system, a symmetric second-order tensor $\boldsymbol{S}$ in three-dimensional space can be written as

$$\boldsymbol{S} = S_i^{\mathrm{Kel}} \, \boldsymbol{E}_i^{\mathrm{Kel}} \,, \quad i = 1, \ldots, 6 \,, \tag{2.38}$$

$$[\boldsymbol{S}]^{\mathrm{Kel}} = \left[S_{11}, \, S_{22}, \, S_{33}, \, \sqrt{2}\, S_{12}, \, \sqrt{2}\, S_{23}, \, \sqrt{2}\, S_{13} \right]^{\mathrm{t}} \,, \tag{2.39}$$

and a symmetric fourth-order tensor S in three-dimensional space is represented by

$$\mathsf{S} = \mathsf{S}_{ij} \, \boldsymbol{E}_i^{\mathrm{Kel}} \otimes \boldsymbol{E}_j^{\mathrm{Kel}} \,, \quad i, j = 1, \ldots, 6 \,, \tag{2.40}$$

$$[\mathsf{S}]^{\mathrm{Kel}} = \begin{bmatrix} \mathsf{S}_{1111} & \mathsf{S}_{1122} & \mathsf{S}_{1133} & \sqrt{2}\,\mathsf{S}_{1112} & \sqrt{2}\,\mathsf{S}_{1123} & \sqrt{2}\,\mathsf{S}_{1113} \\ \mathsf{S}_{2211} & \mathsf{S}_{2222} & \mathsf{S}_{2233} & \sqrt{2}\,\mathsf{S}_{2212} & \sqrt{2}\,\mathsf{S}_{2223} & \sqrt{2}\,\mathsf{S}_{2213} \\ \mathsf{S}_{3311} & \mathsf{S}_{3322} & \mathsf{S}_{3333} & \sqrt{2}\,\mathsf{S}_{3312} & \sqrt{2}\,\mathsf{S}_{3323} & \sqrt{2}\,\mathsf{S}_{3313} \\ \sqrt{2}\,\mathsf{S}_{1211} & \sqrt{2}\,\mathsf{S}_{1222} & \sqrt{2}\,\mathsf{S}_{1233} & 2\,\mathsf{S}_{1212} & 2\,\mathsf{S}_{1223} & 2\,\mathsf{S}_{1213} \\ \sqrt{2}\,\mathsf{S}_{2311} & \sqrt{2}\,\mathsf{S}_{2322} & \sqrt{2}\,\mathsf{S}_{2333} & 2\,\mathsf{S}_{2312} & 2\,\mathsf{S}_{2323} & 2\,\mathsf{S}_{2313} \\ \sqrt{2}\,\mathsf{S}_{1311} & \sqrt{2}\,\mathsf{S}_{1322} & \sqrt{2}\,\mathsf{S}_{1333} & 2\,\mathsf{S}_{1312} & 2\,\mathsf{S}_{1323} & 2\,\mathsf{S}_{1313} \end{bmatrix} . \tag{2.41}$$

2.2 Kinematics

In this section, the motion of a deformable heat conductor in a geometrically non-linear setting is considered for all points in time $t \in [\, t_0, t_{\mathrm{end}} \,]$. The deformable heat conductor is hereby seen as a continuum which is defined as a set of material points X that is continuous in space at all points in time, cf. [66, 74, 135]. The set of material points X is limited by a boundary or by neighbouring sets of material points. Each material point, often also denoted as a particle, has physical properties such as mass density or temperature which are described by means of fields, [39, 74]. A bounded region of material points at a point in time $t = \tau$ is denoted as a body with a configuration $\mathcal{B}_\tau$ while each material point X has coordinates $\boldsymbol{x}_\tau(X)$ in physical space. The reference configuration of the deformable heat conductor at time $t = t_0$ is denoted by $\mathcal{B}_0$ and the current configuration at time t is denoted by $\mathcal{B}_t$. We consider reference placements

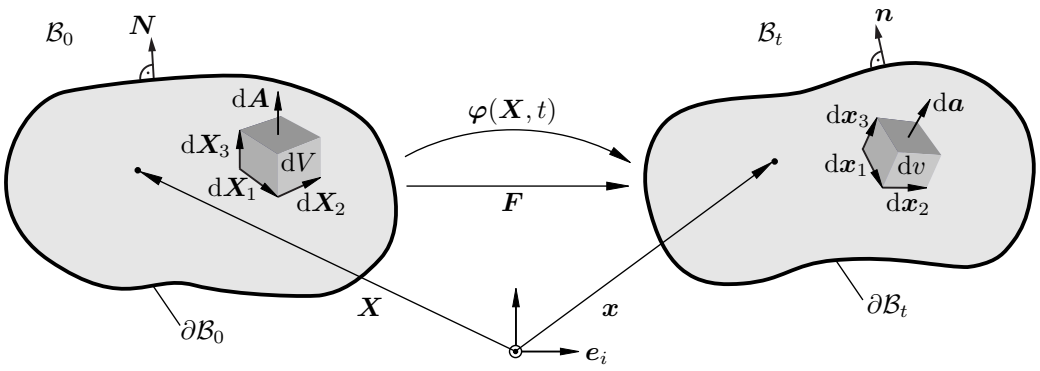

Figure 2.1: Reference configuration $\mathcal{B}_0$ and current configuration $\mathcal{B}_t$ of a deformable body.

$\boldsymbol{X} \in \mathcal{B}_0$ as well as current placements $\boldsymbol{x} \in \mathcal{B}_t$ which are connected via the non-linear deformation map $\boldsymbol{\varphi}(\boldsymbol{X},t)$, such that the current placements

$$\boldsymbol{x} = \boldsymbol{\varphi}(\boldsymbol{X},t) \; , \tag{2.42}$$

in current configuration $\mathcal{B}_t$ are a function of the material placements $\boldsymbol{X}$ in reference configuration $\mathcal{B}_0$ and the time $t \in [\, t_0 \,,\; t_{\text{end}} \,]$. A Taylor series, [33], of $\boldsymbol{\varphi}(\boldsymbol{X},t)$ in material space around a point $\boldsymbol{X}_0$ yields the linear approximation

$$\boldsymbol{\varphi}(\boldsymbol{X},t) \approx \boldsymbol{\varphi}(\boldsymbol{X}_0,t) + \frac{\partial \boldsymbol{\varphi}(\boldsymbol{X}_0,t)}{\partial \boldsymbol{X}} \cdot [\, \boldsymbol{X} - \boldsymbol{X}_0 \,] + \mathcal{O}(2) \; , \tag{2.43}$$

where the first gradient of the deformation map is required and usually is denoted as the deformation gradient

$$\boldsymbol{F} = \frac{\partial \boldsymbol{\varphi}}{\partial \boldsymbol{X}} = \nabla_{\boldsymbol{X}} \boldsymbol{\varphi} \; , \qquad\qquad F_{iJ} = \frac{\partial \varphi_i}{\partial X_J} = \varphi_{i,J} \; , \tag{2.44}$$

which is a second-order tensor. When written in index notation, an upper-case index shall indicate an index which refers to the reference configuration and a lower-case index represents an index which refers to the current configuration. The deformation gradient therefore is a so-called two-point tensor since it has one basis related to the material configuration and one basis related to the spatial configuration, cf. [111, p. 48].

The deformation map between reference configuration $\mathcal{B}_0$ and current configuration $\mathcal{B}_t$ of a deformable heat conductor is depicted in Fig. 2.1. Here, the reference configuration $\mathcal{B}_0$ is bounded by the referential boundary $\partial\mathcal{B}_0$ with its outward normal unit vector $\boldsymbol{N}$. Analogously, the current configuration $\mathcal{B}_t$ is bounded by the current boundary $\partial\mathcal{B}_t$ with its outward normal unit vector $\boldsymbol{n}$. The usual convention is that upper-case symbols represent quantities in reference configuration, whereas lower-case symbols indicate quantities related to the current configuration. Exceptions from this convention are in this case explicitly mentioned. From Eq. (2.43) it follows that the deformation gradient $\boldsymbol{F}(\boldsymbol{X}_0,t)$

is a first-order approximation of $\boldsymbol{\varphi}(\boldsymbol{X},t)$ close to $\boldsymbol{\varphi}(\boldsymbol{X}_0,t)$, [108]. For infinitesimally small material distances $\mathrm{d}\boldsymbol{X} = \boldsymbol{X} - \boldsymbol{X}_0$, the deformation gradient transforms infinitesimal line elements

$$\mathrm{d}\boldsymbol{x} = \boldsymbol{F} \cdot \mathrm{d}\boldsymbol{X} \ , \tag{2.45}$$

between the current configuration, where the infinitesimal line element symbols $\mathrm{d}\boldsymbol{X}$ (material) and $\mathrm{d}\boldsymbol{x}$ (current) follow the convention met above. Since the deformation map $\boldsymbol{\varphi}(\boldsymbol{X},t)$ is a bijective mapping, [33, 108], $\boldsymbol{F}$ is not allowed to be singular such that the determinant of the deformation gradient $J = \det(\boldsymbol{F})$ cannot be zero. Furthermore, inverting the infinitesimal volume of a material point is unphysical such that the determinant of the deformation gradient

$$J = \det(\boldsymbol{F}) > 0 \ , \tag{2.46}$$

must be greater than zero. Beside infinitesimal line elements, infinitesimal surface elements, $\mathrm{d}\boldsymbol{A} = \boldsymbol{N}\,\mathrm{d}A$ and $\mathrm{d}\boldsymbol{a} = \boldsymbol{n}\,\mathrm{d}a$, as well as infinitesimal volume elements, $\mathrm{d}V$ and $\mathrm{d}v$, can also be transformed by means of the deformation gradient $\boldsymbol{F}$. Via the so-called *Nanson* formula, [81, 128],

$$\mathrm{d}\boldsymbol{a} = \mathrm{cof}(\boldsymbol{F}) \cdot \mathrm{d}\boldsymbol{A} \ , \tag{2.47}$$

infinitesimal area elements are transformed by means of the cofactor of the deformation gradient, $\mathrm{cof}(\boldsymbol{F}) = \partial J/\partial \boldsymbol{F} = J\,\boldsymbol{F}^{-\mathrm{t}}$, and infinitesimal volume elements transform with

$$\mathrm{d}v = J\,\mathrm{d}V \ . \tag{2.48}$$

See, e.g., [108, p. 3] for a concise proof of Eqs. (2.47) and (2.48). For illustration purposes, the infinitesimal line, area and volume elements of both configurations considered are sketched within Fig. 2.1.

In the following, not only the deformation in terms of the deformation gradient $\boldsymbol{F}$ itself is of interest but also the rate of deformation. In order to formulate rates of quantities of interest, the material time derivative of a quantity $(\bullet)$

$$\dot{(\bullet)} = \left.\frac{\mathrm{d}\,(\bullet)}{\mathrm{d}t}\right|_{\boldsymbol{X}} \ , \tag{2.49}$$

is introduced. With this at hand, the deformation rate is written as $\dot{\boldsymbol{F}}$. Apart from the formulation of motion in terms of absolute placements $\boldsymbol{X}$ and $\boldsymbol{x}$, it is sometimes convenient to describe the motion relative to the reference configuration. Therefore, the displacement $\boldsymbol{u}(\boldsymbol{X},t)$ is introduced as

$$\boldsymbol{u}(\boldsymbol{X},t) = \boldsymbol{x}(\boldsymbol{X},t) - \boldsymbol{X} \ , \tag{2.50}$$

and the material gradient of the displacement is written as

$$\boldsymbol{H} = \frac{\partial \boldsymbol{u}(\boldsymbol{X},t)}{\partial \boldsymbol{X}} = \frac{\partial \boldsymbol{\varphi}(\boldsymbol{X},t)}{\partial \boldsymbol{X}} - \frac{\partial \boldsymbol{X}}{\partial \boldsymbol{X}} = \boldsymbol{F} - \boldsymbol{I} \ . \tag{2.51}$$

Further kinematic properties needed in this thesis are the velocity

$$\dot{\boldsymbol{\varphi}}(\boldsymbol{X},t) = \frac{\mathrm{d}\boldsymbol{\varphi}(\boldsymbol{X},t)}{\mathrm{d}t} = \boldsymbol{v}(\boldsymbol{X},t) \ , \tag{2.52}$$

as well as the acceleration

$$\ddot{\boldsymbol{\varphi}}(\boldsymbol{X},t) = \frac{\mathrm{d}\dot{\boldsymbol{\varphi}}(\boldsymbol{X},t)}{\mathrm{d}t} \ . \tag{2.53}$$

With the velocity defined in Eq. (2.52), the deformation rate mentioned above reads

$$\dot{\boldsymbol{F}} = \frac{\mathrm{d}}{\mathrm{d}t}\left[\frac{\partial \boldsymbol{\varphi}(\boldsymbol{X},t)}{\partial \boldsymbol{X}}\right] = \frac{\partial \dot{\boldsymbol{\varphi}}(\boldsymbol{X},t)}{\partial \boldsymbol{X}} \ , \tag{2.54}$$

which can also be denoted as the material velocity gradient. In constitutive modelling, in some cases the spatial velocity gradient $\boldsymbol{l}$ is involved which can be expressed in terms of the deformation rate $\dot{\boldsymbol{F}}$ and the deformation gradient $\boldsymbol{F}$, i.e.

$$\boldsymbol{l} = \frac{\partial \dot{\boldsymbol{\varphi}}}{\partial \boldsymbol{x}} = \frac{\partial \dot{\boldsymbol{\varphi}}}{\partial \boldsymbol{X}} \cdot \frac{\partial \boldsymbol{X}}{\partial \boldsymbol{x}} = \dot{\boldsymbol{F}} \cdot \boldsymbol{F}^{-1} = \nabla_{\boldsymbol{x}}\, \boldsymbol{v} \ , \tag{2.55}$$

where the chain rule is applied.

In the context of the formulation of constitutive relations at large deformations, the polar decomposition of the deformation gradient

$$\boldsymbol{F} = \boldsymbol{R} \cdot \boldsymbol{U} = \boldsymbol{V} \cdot \boldsymbol{R} \ , \tag{2.56}$$

into an orthogonal rotational part $\boldsymbol{R}$, with $\boldsymbol{R}^{\mathrm{t}} = \boldsymbol{R}^{-1}$, and the so-called right stretch tensor $\boldsymbol{U}$ or the left stretch tensor $\boldsymbol{V}$ is of essential significance, since an arbitrary rotation can be interpreted as a change of the perspective while observing a deformation process.

In order to eliminate the rotational part of $\boldsymbol{F}$, the so-called *right Cauchy-Green deformation tensor*

$$\boldsymbol{C} = \boldsymbol{F}^{\mathrm{t}} \cdot \boldsymbol{F} = \boldsymbol{U}^{\mathrm{t}} \cdot \boldsymbol{R}^{\mathrm{t}} \cdot \boldsymbol{R} \cdot \boldsymbol{U} = \boldsymbol{U}^{\mathrm{t}} \cdot \boldsymbol{R}^{-1} \cdot \boldsymbol{R} \cdot \boldsymbol{U} = \boldsymbol{U}^{\mathrm{t}} \cdot \boldsymbol{U} \ , \tag{2.57}$$

is often introduced. As a consequence of the composition of $\boldsymbol{C}$, the right Cauchy-Green deformation tensor is a purely material tensor. In analogy to $\boldsymbol{C}$, the so-called *left Cauchy-Green deformation tensor* or *Finger tensor*

$$\boldsymbol{b} = \boldsymbol{F} \cdot \boldsymbol{F}^{\mathrm{t}} = \boldsymbol{V} \cdot \boldsymbol{R} \cdot \boldsymbol{R}^{\mathrm{t}} \cdot \boldsymbol{V}^{\mathrm{t}} = \boldsymbol{V} \cdot \boldsymbol{R} \cdot \boldsymbol{R}^{-1} \cdot \boldsymbol{V}^{\mathrm{t}} = \boldsymbol{V} \cdot \boldsymbol{V}^{\mathrm{t}} \ , \tag{2.58}$$

is introduced which is a purely spatial deformation measure.

With the above definitions at hand, the quantities necessary for the description of the kinematics of finite deformations in the framework of this thesis are introduced. However, in Chapter 5 a geometrically linearised setting is applied where the deformation is described by an infinitesimal strain tensor $\boldsymbol{\varepsilon}$ which will briefly be discussed in the following. So far, deformation tensors ($\boldsymbol{F}$, $\boldsymbol{C}$, $\boldsymbol{b}$) are defined which all result in the identity for an undeformed state. Deformation measures which vanish in an undeformed state are often denoted as *strain tensors*. A material is *strained* when a line element $\mathrm{d}\boldsymbol{X}$ is changed after deformation into a line segment $\mathrm{d}\boldsymbol{x} \neq \mathrm{d}\boldsymbol{X}$, [128]. With Eq. (2.45) the expression

$$\mathrm{d}\boldsymbol{x} \cdot \mathrm{d}\boldsymbol{x} - \mathrm{d}\boldsymbol{X} \cdot \mathrm{d}\boldsymbol{X} = [\,\boldsymbol{C} - \boldsymbol{I}\,] : [\,\mathrm{d}\boldsymbol{X} \otimes \mathrm{d}\boldsymbol{X}\,] = \left[\,\boldsymbol{U}^2 - \boldsymbol{I}\,\right] : [\,\mathrm{d}\boldsymbol{X} \otimes \mathrm{d}\boldsymbol{X}\,] \;, \quad (2.59)$$

is obtained which measures the difference of a material line element $\mathrm{d}\boldsymbol{X}$ and its deformed spatial counterpart $\mathrm{d}\boldsymbol{x}$. The inverse of the exponent of $\boldsymbol{U}$, here 2, is taken as factor in the so-called *Green-Lagrange strain tensor*

$$\boldsymbol{E} = \frac{1}{2}\,[\,\boldsymbol{C} - \boldsymbol{I}\,] \;, \quad (2.60)$$

which is a symmetric tensor that vanishes in the case of an undeformed state and which does not include rigid body rotations. The generalisation of the strain measure with different exponents of $\boldsymbol{U}$ is, e.g., discussed in the textbook of Ogden [128, p. 118].

With the displacement gradient introduced in Eq. (2.51), the Green-Lagrange strain tensor reads

$$\boldsymbol{E} = \frac{1}{2}\,\left[\,\boldsymbol{H} + \boldsymbol{H}^{\mathrm{t}} + \boldsymbol{H}^{\mathrm{t}} \cdot \boldsymbol{H}\,\right] \;, \quad (2.61)$$

where the term which is quadratic in $\boldsymbol{H}$ can be neglected if it is small compared to $\boldsymbol{H}$, i.e. $\boldsymbol{H}^{\mathrm{t}} \cdot \boldsymbol{H} \ll \boldsymbol{H}$. Including this assumption, the Green-Lagrange strain tensor reduces to the infinitesimal strain tensor

$$\boldsymbol{\varepsilon} = \frac{1}{2}\,\left[\,\boldsymbol{H} + \boldsymbol{H}^{\mathrm{t}}\,\right] \;, \quad (2.62)$$

mentioned above which represents the symmetric part of the displacement gradient $\boldsymbol{H}$.

2.3 Balance equations

In this section, the underlying balance equations used within the thesis are summarised and key-aspects of the underlying derivations are recaptured from the literature. Following the textbooks of Liu [108, pp. 31] and Hutter [85, pp. 51], the body introduced in the previous section is subdivided into subregions $\Omega_\tau \subset \mathcal{B}_\tau$, with $\tau \in \{0\,,\; t\}$, whereby region

Ω_τ is bounded by its bounding surface $\partial\Omega_\tau$. According to the convention met above, the material subregion Ω_0 is written as Ω and the spatial subregion Ω_t is abbreviated with ω, cf.Fig. 2.2. According to [85, 108], the general form of all balance equations is

$$\dot{\mathcal{G}} = \mathcal{P}_\mathcal{G} + \mathcal{S}_\mathcal{G} + \mathcal{F}_\mathcal{G} \ , \tag{2.63}$$

where the rate of the physical variable $\mathcal{G}(t)$ in terms of its material time derivative is the sum of production $\mathcal{P}_\mathcal{G}$ and supply $\mathcal{S}_\mathcal{G}$ within Ω_τ as well as the flux $\mathcal{F}_\mathcal{G}$ via the surface $\partial\Omega_\tau$. The physical quantity to be balanced is computed by means of its density

$$\mathcal{G}(t) = \int_\Omega \Gamma(\boldsymbol{X}, t)\, \mathrm{d}V = \int_\omega \gamma(\boldsymbol{x}, t)\, \mathrm{d}v \ , \tag{2.64}$$

where $\Gamma(\boldsymbol{X}, t)$ represents the material density of $\mathcal{G}(t)$ and $\gamma(\boldsymbol{x}, t)$ is the spatial density of $\mathcal{G}(t)$. In analogy, the production, supply and flux terms are computed by the integrals

$$\mathcal{P}_\mathcal{G}(t) = \int_\Omega \Pi_\Gamma(\boldsymbol{X}, t)\, \mathrm{d}V \quad = \int_\omega \pi_\gamma(\boldsymbol{x}, t)\, \mathrm{d}v \ , \tag{2.65}$$

$$\mathcal{S}_\mathcal{G}(t) = \int_\Omega \Sigma_\Gamma(\boldsymbol{X}, t)\, \mathrm{d}V \quad = \int_\omega \sigma_\gamma(\boldsymbol{x}, t)\, \mathrm{d}v \ , \tag{2.66}$$

$$\mathcal{F}_\mathcal{G}(t) = \int_{\partial\Omega} \bar{\Phi}_\Gamma(\boldsymbol{X}, t, \boldsymbol{N})\, \mathrm{d}A = \int_{\partial\omega} \bar{\phi}_\gamma(\boldsymbol{x}, t, \boldsymbol{n})\, \mathrm{d}a \ , \tag{2.67}$$

where $\Pi_\Gamma(\boldsymbol{X}, t)$ and $\pi_\gamma(\boldsymbol{x}, t)$ represent the production densities in material and spatial form, $\Sigma_\Gamma(\boldsymbol{X}, t)$ and $\Sigma_\gamma(\boldsymbol{x}, t)$ are the supply densities in material and spatial form and where $\bar{\Phi}_\Gamma(\boldsymbol{X}, t, \boldsymbol{N})$ as well as $\bar{\phi}_\gamma(\boldsymbol{x}, t, \boldsymbol{n})$ are the surface fluxes in material and spatial form, whereby the flux terms are assumed to depend on the outward surface normals $\boldsymbol{N}$ and $\boldsymbol{n}$. Subscript Γ (γ) indicates the respective field to be balanced in material (spatial) representation of the balance equation. The so-called global forms of the balance equations then read

$$\frac{\mathrm{d}}{\mathrm{d}t} \int_\Omega \Gamma(\boldsymbol{X}, t)\, \mathrm{d}V = \int_\Omega \left[\, \Pi_\Gamma(\boldsymbol{X}, t) + \Sigma_\Gamma(\boldsymbol{X}, t) \,\right] \mathrm{d}V - \int_{\partial\Omega} \boldsymbol{\Phi}_\Gamma(\boldsymbol{X}, t) \cdot \boldsymbol{N}\, \mathrm{d}A \ , \tag{2.68}$$

$$\frac{\mathrm{d}}{\mathrm{d}t} \int_\omega \gamma(\boldsymbol{x}, t)\, \mathrm{d}v = \int_\omega \left[\, \pi_\gamma(\boldsymbol{x}, t) + \sigma_\gamma(\boldsymbol{x}, t) \,\right] \mathrm{d}v - \int_{\partial\omega} \boldsymbol{\phi}_\gamma(\boldsymbol{x}, t) \cdot \boldsymbol{n}\, \mathrm{d}a \ , \tag{2.69}$$

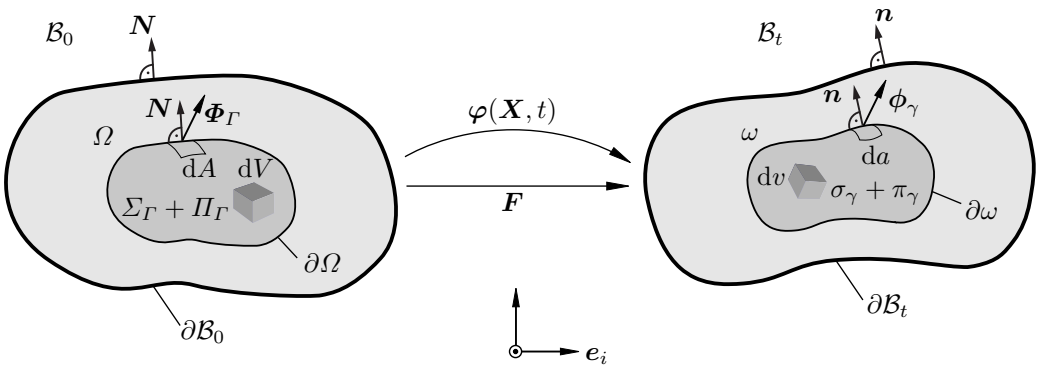

Figure 2.2: Reference configuration $\mathcal{B}_0$ and current configuration $\mathcal{B}_t$ of a deformable body.

wherein $\boldsymbol{\Phi}_\Gamma(\boldsymbol{X},t)$ and $\boldsymbol{\phi}_\gamma(\boldsymbol{x},t)$ are surface flux fields related to the respective fields. In the above equations, the Cauchy theorem is applied which is commented on in the following remark.

Remark 2.3.1 (Cauchy theorem) *According to Hutter [85, pp. 55] or Liu [108, pp. 44], the surface densities $\bar{\Phi}_\Gamma$ and $\bar{\phi}_\gamma$ depend linearly on $\boldsymbol{N}$ and $\boldsymbol{n}$ respectively. Hence, one obtains the relations*

$$\bar{\Phi}_\Gamma(\boldsymbol{X},t,\boldsymbol{N}) = -\,\boldsymbol{\Phi}_\Gamma(\boldsymbol{X},t)\cdot\boldsymbol{N} \qquad \textit{and} \qquad \bar{\phi}_\gamma(\boldsymbol{x},t,\boldsymbol{n}) = -\,\boldsymbol{\phi}_\gamma(\boldsymbol{x},t)\cdot\boldsymbol{n}\;.$$

Here, the surface flux fields $\boldsymbol{\Phi}_\Gamma(\boldsymbol{X},t)$ and $\boldsymbol{\phi}_\gamma(\boldsymbol{x},t)$ represent tensors which are of one tensorial order higher than the balanced quantity $\Gamma(\boldsymbol{X},t)$ or $\gamma(\boldsymbol{x},t)$. By means of contraction with the appropriate outward surface normal $\boldsymbol{N}$ or $\boldsymbol{n}$, the tensorial order of the balanced quantity is met. This rather general definition found in Hutter [85] is throughout the literature often related to the so-called "Cauchy stress theorem", see e.g. Holzapfel [81, p. 111] or de Boer [43, p. 30], or to the so-called "Stokes' heat flux theorem", cf. Holzapfel [81, p. 162]. Both of the mentioned specifications will be used in what follows.

The transformations of the volume related quantities, namely the balanced quantity, the production contribution and the supply contribution follow from Eqs. (2.64) to (2.66) together with Eq. (2.48) such that

$$\Gamma = J\,\gamma\;, \qquad \Pi_\Gamma = J\,\pi_\gamma\;, \qquad \Sigma_\Gamma = J\,\sigma_\gamma\;, \tag{2.70}$$

and the surface flux contribution according to Eq. (2.67) transforms by application of Eq. (2.47) such that

$$\boldsymbol{\Phi}_\Gamma = \boldsymbol{\phi}_\gamma\cdot\operatorname{cof}(\boldsymbol{F})\;. \tag{2.71}$$

In order to obtain the so-called local form of the general balance equations Eqs. (2.68) and (2.69), according to Hutter [85, p. 59], the time differentiation and integration over

the respective domain Ω or ω has to be interchanged, and the surface integral terms must be transformed to volume integrals such that finally a volume integral can be written in residual form which holds true if the integrand vanishes. The material time derivative of the physical quantity $\mathcal{G}(t)$ results in

$$\dot{\mathcal{G}} = \int_{\Omega} \dot{\Gamma}(\boldsymbol{X}, t)\, \mathrm{d}V \ , \tag{2.72}$$

since the integration domain is constant and the spatial form results from the so-called *Reynolds transport theorem*, cf. Hutter [85, pp. 59] or Liu [108, pp. 32], such that

$$\dot{\mathcal{G}} = \int_{\omega} \left[\, \dot{\gamma}(\boldsymbol{x}, t) + \gamma\ \nabla_{\boldsymbol{x}} \cdot \boldsymbol{v}(\boldsymbol{x}, t) \,\right] \mathrm{d}v \ . \tag{2.73}$$

The surface integrals in Eqs. (2.68) and (2.69) are transformed via the divergence theorem

$$\int_{\partial\Omega} \boldsymbol{\Phi}_{\Gamma} \cdot \boldsymbol{N}\, \mathrm{d}A = \int_{\Omega} \nabla_{\boldsymbol{X}} \cdot \boldsymbol{\Phi}_{\Gamma}\, \mathrm{d}V \ , \tag{2.74}$$

$$\int_{\partial\omega} \boldsymbol{\phi}_{\gamma} \cdot \boldsymbol{n}\, \mathrm{d}a = \int_{\omega} \nabla_{\boldsymbol{x}} \cdot \boldsymbol{\phi}_{\gamma}\, \mathrm{d}v \ . \tag{2.75}$$

Inserting Eqs. (2.72) to (2.75) into Eqs. (2.68) and (2.69) yields the global balance equations

$$0 = \int_{\Omega} \left[\, \dot{\Gamma} - \Pi_{\Gamma} - \Sigma_{\Gamma} + \nabla_{\boldsymbol{X}} \cdot \boldsymbol{\Phi}_{\Gamma} \,\right] \mathrm{d}V \ , \tag{2.76}$$

$$0 = \int_{\omega} \left[\, \dot{\gamma} + \gamma\ \nabla_{\boldsymbol{x}} \cdot \boldsymbol{v} - \pi_{\gamma} - \sigma_{\gamma} + \nabla_{\boldsymbol{x}} \cdot \boldsymbol{\phi}_{\gamma} \,\right] \mathrm{d}v \ , \tag{2.77}$$

which result in the local forms

$$\dot{\Gamma} = \Pi_{\Gamma} + \Sigma_{\Gamma} - \nabla_{\boldsymbol{X}} \cdot \boldsymbol{\Phi}_{\Gamma} \ , \tag{2.78}$$

$$\dot{\gamma} + \gamma\ \nabla_{\boldsymbol{x}} \cdot \boldsymbol{v} = \pi_{\gamma} + \sigma_{\gamma} - \nabla_{\boldsymbol{x}} \cdot \boldsymbol{\phi}_{\gamma} \ . \tag{2.79}$$

In the following subsections, the underlying balance equations are specified with respect to the material formulation, i.e. with respect to the reference configuration $\Omega \subset \mathcal{B}_0$. The corresponding representations with respect to the deformed configuration for instance are discussed in Hutter [85] and Liu [108] which served as main references for this section, and also in other textbooks on continuum mechanics such as, amongst others,

Marsden and Hughes [111], Šilhavý [159], Holzapfel [81] or Haupt [74]. It shall be clarified that the quantities in the balance equations Eqs. (2.78) and (2.79) are interpreted as "placeholder" for physical quantities. Consequently, if a scalar quantity is to be balanced, the corresponding production as well as supply terms are also scalars and the flux is represented by a vector. If a vector-valued quantity is balanced, the corresponding production and supply terms are vectors and the flux of the respective vector-field is a second-order tensor.

2.3.1 Balance of mass

The material mass density $\rho_0(\boldsymbol{X}, t) > 0$ is the physical quantity balanced when Eq. (2.78) is specified with regard to balancing the mass of a referential element Ω. Within this thesis it is assumed that mass is neither produced ($\mathit{\Pi}_{\rho_0} = 0$) nor supplied ($\mathit{\Sigma}_{\rho_0} = 0$) within Ω and that no mass flows through $\partial\Omega$ ($\boldsymbol{\Phi}_{\rho_0} = \boldsymbol{0}$). This coincides with the assumptions made in Hutter [85, p. 64]. As a consequence, the material local form of the balance of mass reads

$$\dot{\rho}_0(\boldsymbol{X}, t) = \dot{\rho}_0(\boldsymbol{X}) = 0 \, . \tag{2.80}$$

In the following, the material mass density $\rho_0(\boldsymbol{X})$ will only be a function of the material placement $\boldsymbol{X}$ as indicated by the above equation. The mass of a material element Ω is obtained by the volume integral of the mass density

$$m_\Omega = \int_\Omega \rho_0(\boldsymbol{X}) \, \mathrm{d}V \, , \tag{2.81}$$

which is constant due to Eq. (2.80).

2.3.2 Balance of momentum

With regard to the linear momentum of a material element Ω, the physical field is the momentum $[\, \rho_0 \, \dot{\boldsymbol{\varphi}} \,]$. Hence, with respect to linear momentum, Eq. (2.78) specifies to a vector-valued balance equation. Since it is postulated that linear momentum is a conserved quantity, see [85, p. 66], no momentum is produced within Ω, i.e. $\mathit{\Pi}_{\rho_0 \, \dot{\boldsymbol{\varphi}}} = \boldsymbol{0}$. The supply term with respect to linear momentum corresponds to the volume force $\mathit{\Sigma}_{\rho_0 \, \dot{\boldsymbol{\varphi}}} = \rho_0 \, \boldsymbol{b}$ and the momentum flux via the surface is a second-order tensor $\boldsymbol{\Phi}_{\rho_0 \, \dot{\boldsymbol{\varphi}}} = -\boldsymbol{P}$ which is introduced with a negative sign in order to obtain the local balance of linear momentum in its established material form by inserting the discussed terms into Eq. (2.78) under consideration of Eq. (2.80)

$$\frac{\mathrm{d}}{\mathrm{d}t} \, [\, \rho_0 \, \dot{\boldsymbol{\varphi}} \,] = \rho_0 \, \ddot{\boldsymbol{\varphi}} = \nabla_{\boldsymbol{X}} \cdot \boldsymbol{P} + \rho_0 \, \boldsymbol{b} \, , \tag{2.82}$$

where $\boldsymbol{P}$ is the unsymmetric Piola stress tensor which defines the surface traction vector $\boldsymbol{t}_0 = \boldsymbol{P} \cdot \boldsymbol{N}$ via the Cauchy theorem, cf. Remark 2.3.1, where the negative sign is considered which was formally introduced above. The Piola stress tensor $\boldsymbol{P}$ is, in analogy to the deformation gradient $\boldsymbol{F}$, introduced in Eq. (2.44), a two-point tensor with the first basis located in the current configuration and the second basis located in the reference configuration, cf. [111, p. 135]. Hence, the surface traction $\boldsymbol{t}_0$ represents a spatial stress vector referred to referential surface area and is sometimes also denoted as the *nominal stress vector* and $\boldsymbol{P}$ as *nominal stress tensor*, Altenbach [2].

The stress measure which arises in the spatial analogue to Eq. (2.82) is the Cauchy stress tensor $\boldsymbol{\sigma}$ which is related to Piola tensor $\boldsymbol{P}$ via Eq. (2.71), i.e. $\boldsymbol{\sigma} = \boldsymbol{P} \cdot \operatorname{cof}(\boldsymbol{F}^{-1})$, and is a purely spatial tensor so that both basis vectors are related to the current configuration. The resulting surface traction vector $\boldsymbol{t}_t = \boldsymbol{\sigma} \cdot \boldsymbol{n}$ which is a spatial stress vector referred to the current cross surface area. Hence, stress vector $\boldsymbol{t}_t$ is also denoted as *true stress vector* and the Cauchy stresses $\boldsymbol{\sigma}$ as *true stress tensor*, Altenbach [2].

Remark 2.3.2 (Balance of angular momentum) *The balance of angular momentum which is the physical quantity* $[\,\boldsymbol{\varphi} \times \rho_0\,\dot{\boldsymbol{\varphi}}\,]$ *to be inserted into Eq.* (2.78) *is not discussed in detail in the context of this work. Instead, the interested reader is referred to, e.g. Hutter [85, pp. 69–71], Marsden and Hughes [111, p. 138] or Holzapfel [81, pp. 142–147]. For a classic Boltzmann continuum, the essential result is that the Piola stress tensor* $\boldsymbol{P}$ *has to fulfill the relation* $\boldsymbol{P} \cdot \boldsymbol{F}^{\mathrm{t}} = \left[\,\boldsymbol{P} \cdot \boldsymbol{F}^{\mathrm{t}}\,\right]^{\mathrm{t}} = \boldsymbol{F} \cdot \boldsymbol{P}^{\mathrm{t}}$. *In view of the spatial form of the balance of linear momentum, where the Cauchy stress tensor* $\boldsymbol{\sigma} = \boldsymbol{P} \cdot \operatorname{cof}(\boldsymbol{F}^{-1})$ *is related to the momentum flux, the mentioned relation results in the requirement of symmetric Cauchy stresses* $\boldsymbol{\sigma} = \boldsymbol{\sigma}^{\mathrm{t}}$. *Within the underlying thesis, this restriction will automatically be fulfilled since the constitutive relations considered do not induce volume moments.*

2.3.3 Balance of energy

The balance of energy represents the so-called first law of thermodynamics where all kinds of energies under consideration are mutually conserved in Ω. In the present work, mechanical and thermal energies are considered, whereby the energy stored within a part of a body is composed of the sum of the kinetic energy, $\mathcal{K} = \frac{1}{2}\,\rho_0\,\dot{\boldsymbol{\varphi}} \cdot \dot{\boldsymbol{\varphi}}$, and the internal energy, $\mathcal{E} = \rho_0\,e$, where e is the internal energy density. Thus, the physical quantity to be balanced referred to Eq. (2.78) in context of the balance of energy is $\mathit{\Gamma} = \mathcal{K} + \mathcal{E}$. According to Hutter [85, p. 72] it is postulated that no energy is produced within Ω since the energy is a conserved quantity, i.e. $\mathit{\Pi}_{\mathcal{K}+\mathcal{E}} = 0$. The volume related supply of energy is assembled from the external power of volume forces, $\mathit{\Sigma}^{\mathrm{mech}}_{\mathcal{K}+\mathcal{E}} = \rho_0\,\dot{\boldsymbol{\varphi}} \cdot \boldsymbol{b}$, and the externally induced volume related heat source, $\mathit{\Sigma}^{\mathrm{therm}}_{\mathcal{K}+\mathcal{E}} = \rho_0\,r$, where r is the thermal energy supply density. The supply of energy then results in $\mathit{\Sigma}_{\mathcal{K}+\mathcal{E}} = \rho_0\,\dot{\boldsymbol{\varphi}} \cdot \boldsymbol{b} + \rho_0\,r$. The mechanical energy flux via the surface is represented by the power of the momentum flux introduced in the previous subsection, $\boldsymbol{\Phi}^{\mathrm{mech}}_{\mathcal{K}+\mathcal{E}} = -\dot{\boldsymbol{\varphi}} \cdot \boldsymbol{P}$, and the thermal energy flux is

the referential heat flux, $\boldsymbol{\Phi}^{\text{therm}}_{\mathcal{K}+\mathcal{E}} = \boldsymbol{Q}$. Consequently, the total energy flux via the surface is $\boldsymbol{\Phi} = -\dot{\boldsymbol{\varphi}} \cdot \boldsymbol{P} + \boldsymbol{Q}$. Inserting all these terms into Eq. (2.78) yields

$$\frac{\mathrm{d}}{\mathrm{d}t}\left[\frac{1}{2}\,\rho_0\,\dot{\boldsymbol{\varphi}}\cdot\dot{\boldsymbol{\varphi}} + \rho_0\,e\right] = \rho_0\,\dot{\boldsymbol{\varphi}}\cdot\boldsymbol{b} + \nabla_{\boldsymbol{X}}\cdot[\,\dot{\boldsymbol{\varphi}}\cdot\boldsymbol{P}\,] + \rho_0\,r - \nabla_{\boldsymbol{X}}\cdot\boldsymbol{Q}\;. \tag{2.83}$$

Together with the balance of mass Eq. (2.80), relation $\nabla_{\boldsymbol{X}}\cdot[\,\dot{\boldsymbol{\varphi}}\cdot\boldsymbol{P}\,] = \boldsymbol{P} : \dot{\boldsymbol{F}} + \dot{\boldsymbol{\varphi}}\cdot[\,\nabla_{\boldsymbol{X}}\cdot\boldsymbol{P}\,]$ and the balance of linear momentum Eq. (2.82), the above equation simplifies to the local balance of energy equation used within this thesis

$$\rho_0\,\dot{e} = \boldsymbol{P} : \dot{\boldsymbol{F}} + \rho_0\,r - \nabla_{\boldsymbol{X}}\cdot\boldsymbol{Q}\;, \tag{2.84}$$

where the rate of the internal energy density $\dot{e}$ is related with the so-called stress power $\boldsymbol{P} : \dot{\boldsymbol{F}}$, with the heat supply $\rho_0\,r$ as well as with the material divergence of the referential heat flux $\boldsymbol{Q}$.

2.3.4 Balance of entropy

The balance equations summarised so far dealt with quantities which are conserved such that their production terms are zero, i.e. $\mathit{\Pi}_{\rho_0} = 0$, $\mathit{\Pi}_{\rho_0\,\dot{\boldsymbol{\varphi}}} = \boldsymbol{0}$, $\mathit{\Pi}_{\boldsymbol{\varphi}\times\rho_0\,\dot{\boldsymbol{\varphi}}} = \boldsymbol{0}$ and $\mathit{\Pi}_{\mathcal{K}+\mathcal{E}} = 0$. While observing real processes it turns out that such processes (in many cases) possess a direction which cannot be reversed without further extent and are therefore often denoted as *irreversible* processes. In order to account for the direction of a thermodynamical process, the specific entropy s is introduced as a non-conserved quantity. The entropy $\rho_0\,s$ is balanced, whereby according to Coleman and Noll [40] the entropy supply is assumed to be proportional to the thermal energy supply $\mathit{\Sigma}^{\text{therm}}_{\mathcal{K}+\mathcal{E}}$, i.e. $\mathit{\Sigma}_s = \rho_0\,r/\theta$, and the entropy flux is assumed to be proportional to the heat flux, i.e. $\boldsymbol{\Phi}_s = \boldsymbol{Q}/\theta$, whereby $\theta > 0$ is the absolute temperature. For every admissible thermo-mechanical process in $\mathit{\Omega}$, the production of entropy

$$\mathit{\Pi}_s \geq 0\;, \tag{2.85}$$

must be greater or equal to zero which represents the *second law of thermodynamics* in form of the so-called *Clausius-Duhem inequality*. Insertion of the above-mentioned assumptions made for the entropy supply as well as for the entropy flux yields, together with the balance of mass Eq. (2.80), the relation $\nabla_{\boldsymbol{X}}\cdot[\,\boldsymbol{Q}/\theta\,] = \nabla_{\boldsymbol{X}}\cdot\boldsymbol{Q}/\theta - \nabla_{\boldsymbol{X}}\theta\cdot\boldsymbol{Q}/\theta^2$, after multiplication with the absolute temperature $\theta > 0$, results in the local material representation of the Clausius-Duhem inequality

$$\rho_0\,\theta\,\dot{s} - \rho_0\,r + \nabla_{\boldsymbol{X}}\cdot\boldsymbol{Q} - \frac{\nabla_{\boldsymbol{X}}\theta\cdot\boldsymbol{Q}}{\theta} \geq 0\;. \tag{2.86}$$

The above inequality is further transformed by inserting the the balance of energy Eq. (2.84), i.e. $-\rho_0\, r + \nabla_{\boldsymbol{X}} \cdot \boldsymbol{Q} = \boldsymbol{P} : \dot{\boldsymbol{F}} - \rho_0\, \dot{e}$, such that the inequality

$$\rho_0\, \theta\, \dot{s} + \boldsymbol{P} : \dot{\boldsymbol{F}} - \rho_0\, \dot{e} - \frac{\nabla_{\boldsymbol{X}} \theta \cdot \boldsymbol{Q}}{\theta} \geq 0 \,, \tag{2.87}$$

is obtained, whereby a further assumption made is that the two parts defined as the mechanical dissipation

$$\mathcal{D}_{\text{mech}} = \rho_0\, \theta\, \dot{s} + \boldsymbol{P} : \dot{\boldsymbol{F}} - \rho_0\, \dot{e} \geq 0 \,, \tag{2.88}$$

as well as the thermal dissipation

$$\mathcal{D}_{\text{therm}} = -\frac{\nabla_{\boldsymbol{X}} \theta \cdot \boldsymbol{Q}}{\theta} \geq 0 \,, \tag{2.89}$$

shall be fulfilled independent from each other. The latter is also denoted as Fourier's inequality. A thermodynamical process fulfilling the restrictions given by Eqs. (2.88) and (2.89) is denoted as an admissible process or also as *thermodynamical consistent*.

2.3.5 Hyperelastic format for thermo-inelasticity

The specific entropy s introduced in the previous subsection represents a useful concept for modelling purposes but has the disadvantage that it is a quantity which is hard to interprete with regard to experimental investigations. In order to dispense with the entropy s as a variable which arises explicitly, a Legendre transform is carried out

$$\Psi = e - \theta\, s \quad \rightarrow \quad \dot{e} = \dot{\Psi} + \dot{\theta}\, s + \theta\, \dot{s} \,, \tag{2.90}$$

where Ψ is denoted as the Helmholtz free energy density which is assumed to be a function of the deformation gradient $\boldsymbol{F}$, the temperature θ as well as further variables $\boldsymbol{k}$ which describe the state of the material, $\Psi = \Psi(\boldsymbol{F}, \theta, \boldsymbol{k})$, such that the material time derivative yields

$$\dot{\Psi} = \frac{\partial \Psi}{\partial \boldsymbol{F}} : \dot{\boldsymbol{F}} + \frac{\partial \Psi}{\partial \theta}\, \dot{\theta} + \frac{\partial \Psi}{\partial \boldsymbol{k}} \circ \dot{\boldsymbol{k}} \,, \tag{2.91}$$

where the symbol "$\circ$" indicates an appropriate scalar-valued contraction of the last term of the above equation. Inserting the relations Eqs. (2.90) and (2.91) into the mechanical dissipation Eq. (2.88) yields the inequality

$$\left[\boldsymbol{P} - \rho_0\, \frac{\partial \Psi}{\partial \boldsymbol{F}} \right] : \dot{\boldsymbol{F}} + \left[-\rho_0\, s - \rho_0\, \frac{\partial \Psi}{\partial \theta} \right] \dot{\theta} - \rho_0\, \frac{\partial \Psi}{\partial \boldsymbol{k}} \circ \dot{\boldsymbol{k}} \geq 0 \,, \tag{2.92}$$

from which so-called hyperelastic definitions for the Piola stresses

$$\boldsymbol{P} = \rho_0 \frac{\partial \Psi}{\partial \boldsymbol{F}} \,, \tag{2.93}$$

as well as the entropy

$$\rho_0 \, s = -\rho_0 \frac{\partial \Psi}{\partial \theta} \,, \tag{2.94}$$

are obtained. This means that a thermodynamical process – in this thesis this means a thermo-mechanical process – is thermodynamically consistent if the Piola stresses $\boldsymbol{P}$ and the specific entropy s can be computed on the basis of an appropriately defined Helmholtz free energy function $\Psi(\boldsymbol{F}, \theta, \boldsymbol{k})$ under the further restriction that the so-called reduced dissipation inequality

$$\mathcal{D}_{\text{int}}^{\text{red}} = -\rho_0 \frac{\partial \Psi}{\partial \boldsymbol{k}} \circ \dot{\boldsymbol{k}} = \boldsymbol{\kappa} \circ \dot{\boldsymbol{k}} \geq 0 \,, \tag{2.95}$$

holds. In the above equation, $\boldsymbol{\kappa}$ is introduced as dual quantity of $\boldsymbol{k}$. If a thermo-mechanical process is inelastic, so-called evolution equations for $\boldsymbol{k}(\boldsymbol{k}, \boldsymbol{F}, \theta)$ must satisfy the inequality above. A material whose constitutive relations are derived from a stored energy function is known as hyperelastic material, cf. [182, p. 182] where the term is introduced for elastic materials. In the context of the modelling of thermo-inelastic materials, the term hyperelasticity is adopted whenever a stored energy function of the form $\Psi(\boldsymbol{F}, \theta, \boldsymbol{k})$ is used. The Helmholtz energies of the material models in this thesis are formulated in the form $\Psi(\boldsymbol{C}(\boldsymbol{F}), \theta, \boldsymbol{k})$. This has the advantage that the principle of *material objectivity* or *material frame indifference* is fulfilled. For a detailed discussion see e.g. the textbooks of Marsden and Hughes [111], Chadwick [35] or Gurtin et al. [70]. The definition of such a stored energy function is a broad field of research on its own and is not discussed in further detail at this point. Apart from a considerable amount of journal articles on constitutive modelling, the interested reader is referred to the textbooks of Simo and Hughes [160], Neto et al. [125], Ottosen and Ristinmaa [130] or Holzapfel [81] for an introduction to constitutive modelling of elastic and inelastic material behaviour.

In the framework of this thesis, the Fourier inequality, given by Eq. (2.89) in referential form, is fulfilled by a relation such as

$$\boldsymbol{Q} = -\boldsymbol{K}_0 \cdot \nabla_{\boldsymbol{X}} \theta \,, \tag{2.96}$$

where $\boldsymbol{K}_0$ is a positive semi-definite heat conductivity tensor, cf. Liu [108, p. 133]. Inserting the above equation into Eq. (2.89) shows that the Fourier inequality via this ansatz is automatically fulfilled. For a review on non-Fourier heat conduction the reader is referred to, e.g., the works of Atefi and Talaee [5], Talaee and Atefi [167].

Remark 2.3.3 (Heat flux definition) *Within this thesis, the referential heat flux* $\boldsymbol{Q}$ *given by Eq.* (2.96) *with a material constant isotropic heat conductivity tensor* $\boldsymbol{K}_0 = \Lambda_0 \boldsymbol{I}$ *will be used within large deformation applications. Analogous to the Piola stresses (or nominal stresses)* $\boldsymbol{P}$ *and the Cauchy stresses (or true stresses)* $\boldsymbol{\sigma}$ *discussed in Section 2.3.2, the referential heat flux* $\boldsymbol{Q}$ *(or nominal heat flux) is related to a material surface element, whereas the spatial heat flux (or true heat flux)* $\boldsymbol{q}$ *is related to a spatial surface element, see Holzapfel [81, p. 162]. By carrying out the procedure above related to spatial formulation, the spatial counterpart of Fourier inequality Eq.* (2.89) *is fulfilled by*

$$\boldsymbol{q} = -\boldsymbol{k}_0 \cdot \nabla_{\boldsymbol{x}} \theta \ ,$$

where $\boldsymbol{k}_0$ *is a positive-semidefinite tensor. Analogous to the case applied in this thesis, a spatial constant isotropic heat conductivity tensor* $\boldsymbol{k}_0 = \Lambda \boldsymbol{I}$ *can be defined. This is often said to be isotropic heat conduction in the framework of large deformation thermo-mechanics. However, the relation Eq.* (2.96) *will be applied for simplicity, since it solely depends on the referential temperature gradient* $\nabla_{\boldsymbol{X}} \theta$*. Consideration of the spatial Fourier's law of heat conduction induces a dependence of the referential heat flux* $\boldsymbol{Q}$ *on the deformation gradient via Eq.* (2.71)*, i.e.*

$$\boldsymbol{Q} = \boldsymbol{q} \cdot \operatorname{cof}(\boldsymbol{F}) = -J\, \boldsymbol{k}_0 \cdot \nabla_{\boldsymbol{x}} \theta \cdot \boldsymbol{F}^{-\mathrm{t}} = -J\, \boldsymbol{F}^{-1} \cdot \boldsymbol{k}_0 \cdot \boldsymbol{F}^{-\mathrm{t}} \cdot \nabla_{\boldsymbol{X}} \theta \ ,$$

as e.g. outlined in Holzapfel [81, p. 171]. For isotropic heat conduction, the above expression simplifies to $\boldsymbol{Q} = -J\, \Lambda\, \boldsymbol{C}^{-1} \cdot \nabla_{\boldsymbol{X}} \theta$*.*

2.3.6 Heat equation

From the local relation of the entropy in hyperelastic form, cf. Eq. (2.97), together with mass conservation, cf. Eq. (2.80), the local rate of the entropy is obtained as

$$\rho_0\, \dot{s} = -\rho_0\, \frac{\partial \dot{\Psi}}{\partial \theta} = -\frac{\partial \boldsymbol{P}}{\partial \theta} : \dot{\boldsymbol{F}} + \rho_0\, \frac{\partial s}{\partial \theta}\, \dot{\theta} + \frac{\partial \boldsymbol{\kappa}}{\partial \theta} \circ \dot{\boldsymbol{k}} \ . \tag{2.97}$$

Inserting this relation into Eq. (2.90) multiplied by the mass density ρ_0 and further considering the relation Eq. (2.91) as well as the energy balance Eq. (2.84), the expression

$$\begin{aligned} \rho_0\, \dot{e} &= \rho_0\, \dot{\theta}\, s + \rho_0 \left[\frac{\partial \Psi}{\partial \boldsymbol{F}} : \dot{\boldsymbol{F}} + \frac{\partial \Psi}{\partial \theta}\, \dot{\theta} + \frac{\partial \Psi}{\partial \boldsymbol{k}} \circ \dot{\boldsymbol{k}} \right] \\ &\quad + \theta \left[-\frac{\partial \boldsymbol{P}}{\partial \theta} : \dot{\boldsymbol{F}} + \rho_0\, \frac{\partial s}{\partial \theta}\, \dot{\theta} + \frac{\partial \boldsymbol{\kappa}}{\partial \theta} \circ \dot{\boldsymbol{k}} \right] \\ &= \boldsymbol{P} : \dot{\boldsymbol{F}} + \rho_0\, r - \nabla_{\boldsymbol{X}} \cdot \boldsymbol{Q} \ , \end{aligned} \tag{2.98}$$

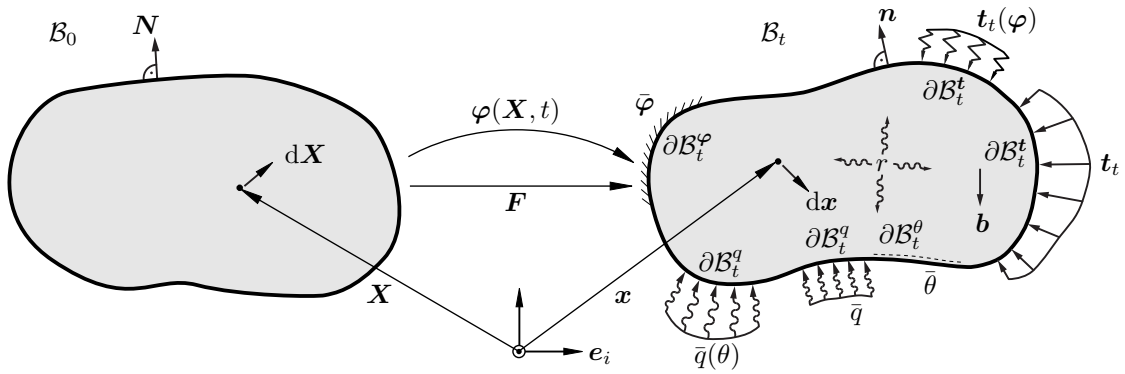

Figure 2.3: Reference configuration $\mathcal{B}_0$ and current configuration $\mathcal{B}_t$ of a deformable body.

is obtained. Combining the above terms yields

$$-\boldsymbol{\kappa}\circ\dot{\boldsymbol{k}}-\theta\,\frac{\partial\boldsymbol{P}}{\partial\theta}:\dot{\boldsymbol{F}}+\rho_0\,\theta\,\frac{\partial s}{\partial\theta}\,\dot{\theta}+\theta\,\frac{\partial\boldsymbol{\kappa}}{\partial\theta}\circ\dot{\boldsymbol{k}}=\rho_0\,r-\nabla_{\boldsymbol{X}}\cdot\boldsymbol{Q}\;, \tag{2.99}$$

and thus with the definition of the heat capacity

$$c_0=\rho_0\,\theta\,\frac{\partial s}{\partial\theta}=-\rho_0\,\frac{\partial^2\Psi}{\partial\theta^2}\;, \tag{2.100}$$

the local heat equation in material form is finally obtained as

$$c_0\,\dot{\theta}=\theta\,\frac{\partial\boldsymbol{P}}{\partial\theta}:\dot{\boldsymbol{F}}+\rho_0\,r-\nabla_{\boldsymbol{X}}\cdot\boldsymbol{Q}+\left[\,\boldsymbol{\kappa}-\theta\,\frac{\partial\boldsymbol{\kappa}}{\partial\theta}\,\right]\circ\dot{\boldsymbol{k}}\;, \tag{2.101}$$

wherein the rate of the temperature $\dot{\theta}$ weighted by the heat capacity c_0 is related to the elastic cooling due to the Gough-Joule effect $\theta\,\partial\boldsymbol{P}/\partial\theta:\dot{\boldsymbol{F}}$, to the volume related heat supply $\rho_0\,r$, the material divergence of the material heat flux $\boldsymbol{Q}$ as well as to structural heating due to evolution of internal variables $[\,\boldsymbol{\kappa}-\theta\,\partial\boldsymbol{\kappa}/\partial\theta\,]\circ\dot{\boldsymbol{k}}$.

2.4 Summary of thermo-inelasticity

In the previous sections, the underlying kinematics where discussed and the fundamental balance equations as well as related assumptions for a deformable heat conductor were summarised. In a nutshell, two fields will be considered within the thermo-mechanically

coupled framework, namely placements $\boldsymbol{\varphi}$ as well as temperature θ. The balance equations are the balance of linear momentum and the energy balance

$$\rho_0 \, \ddot{\boldsymbol{\varphi}} = \nabla_{\boldsymbol{X}} \cdot \boldsymbol{P} + \rho_0 \, \boldsymbol{b} \; , \tag{2.102}$$

$$c_0 \, \dot{\theta} = \theta \, \frac{\partial \boldsymbol{P}}{\partial \theta} : \dot{\boldsymbol{F}} + \rho_0 \, r - \nabla_{\boldsymbol{X}} \cdot \boldsymbol{Q} + \left[\boldsymbol{\kappa} - \theta \, \frac{\partial \boldsymbol{\kappa}}{\partial \theta} \right] \circ \dot{\boldsymbol{k}} \; , \tag{2.103}$$

in their local material forms according to Eqs. (2.82) and (2.101), where thermodynamical consistency is ensured via a suitably chosen Helmholtz free energy $\Psi(\boldsymbol{F}, \theta, \boldsymbol{k})$ together with holding the thermal and reduced dissipation inequalities, cf. Eqs. (2.89) and (2.95). As discussed in Section 2.3, all parts Ω represent the reference configuration $\mathcal{B}_0$ of the deformable heat conductor under consideration with its referential boundary representation $\partial\mathcal{B}_0$ as depicted in Fig. 2.3. The boundary of the current configuration of the body $\mathcal{B}_t$ is denoted by $\partial\mathcal{B}_t$. The two balance equations are solved for given initial conditions at the initial point in time t_0 and boundary conditions are applied to the considered deformable heat conductor. In order to formulate boundary conditions for both fields, the boundaries are formally split into disjoint parts,

$$\partial\mathcal{B}_t = \partial\mathcal{B}_t^{\boldsymbol{\varphi}} \cup \partial\mathcal{B}_t^{\boldsymbol{t}} \qquad \text{with} \qquad \partial\mathcal{B}_t^{\boldsymbol{\varphi}} \cap \partial\mathcal{B}_t^{\boldsymbol{t}} = \emptyset \; , \tag{2.104}$$

$$\partial\mathcal{B}_t = \partial\mathcal{B}_t^{\theta} \cup \partial\mathcal{B}_t^{\boldsymbol{q}} \qquad \text{with} \qquad \partial\mathcal{B}_t^{\theta} \cap \partial\mathcal{B}_t^{\boldsymbol{q}} = \emptyset \; , \tag{2.105}$$

a Dirichlet and a Neumann part for each field, whereby $\partial\mathcal{B}_t^{\boldsymbol{\varphi}}$ is the spatial Dirichlet boundary of the placement field, $\partial\mathcal{B}_t^{\boldsymbol{t}}$ represents the spatial Neumann boundary of the placement field, $\partial\mathcal{B}_t^{\theta}$ is the spatial Dirichlet boundary of the temperature field and where $\partial\mathcal{B}_t^{\boldsymbol{q}}$ is the spatial Neumann boundary of the temperature field. On the respective Dirichlet boundaries the field variables themselves are prescribed, whereby the corresponding flux terms are prescribed on the Neumann boundaries. Although, from a physical perspective, boundary conditions are applicable only to the current configuration $\mathcal{B}_t$, it is formally possible to relate the current load to the reference state, and Eqs. (2.104) and (2.105) can be rewritten as

$$\partial\mathcal{B}_0 = \partial\mathcal{B}_0^{\boldsymbol{\varphi}} \cup \partial\mathcal{B}_0^{\boldsymbol{t}} \qquad \text{with} \qquad \partial\mathcal{B}_0^{\boldsymbol{\varphi}} \cap \partial\mathcal{B}_0^{\boldsymbol{t}} = \emptyset \; , \tag{2.106}$$

$$\partial\mathcal{B}_0 = \partial\mathcal{B}_0^{\theta} \cup \partial\mathcal{B}_0^{\boldsymbol{Q}} \qquad \text{with} \qquad \partial\mathcal{B}_0^{\theta} \cap \partial\mathcal{B}_0^{\boldsymbol{Q}} = \emptyset \; . \tag{2.107}$$

With this at hand, the boundary conditions are prescribed on their respective referential

Box 2.1: Thermo-mechanically coupled framework for large deformations in material form.

Unknown fields

$\boldsymbol{\varphi}(\boldsymbol{X},t)$	deformation map
$\theta(\boldsymbol{X},t)$	temperature

Local strong forms of balance equations in material form

$$\rho_0\,\ddot{\boldsymbol{\varphi}} = \nabla_{\boldsymbol{X}}\cdot\boldsymbol{P} + \rho_0\,\boldsymbol{f} \qquad \text{balance of linear momentum}$$

$$c_0\,\dot{\theta} = \theta\,\frac{\partial \boldsymbol{P}}{\partial\theta} : \dot{\boldsymbol{F}} + \rho_0\,r - \nabla_{\boldsymbol{X}}\cdot\boldsymbol{Q} + \left[\boldsymbol{\kappa} - \theta\,\frac{\partial\boldsymbol{\kappa}}{\partial\theta}\right]\circ\dot{\boldsymbol{k}} \qquad \text{heat equation}$$

Constitutive relations in hyperelastic form

$\Psi(\boldsymbol{F},\theta,\boldsymbol{k})$	Helmholtz free energy function
$\boldsymbol{P} = \rho_0\,\dfrac{\partial\Psi}{\partial\boldsymbol{F}}$	Piola stresses
$\boldsymbol{\kappa} = -\,\rho_0\,\dfrac{\partial\Psi}{\partial\boldsymbol{k}}$	driving forces for evolution of internal variables
$c_0 = -\,\rho_0\,\theta\,\dfrac{\partial^2\Psi}{\partial\theta^2}$	heat capacity
$\mathcal{D}_{\text{int}}^{\text{red}} = \boldsymbol{\kappa}\circ\dot{\boldsymbol{k}} \geq 0$	evolution equations must satisfy reduced dissipation inequality
$\boldsymbol{Q}(\boldsymbol{F},\theta,\nabla_{\boldsymbol{X}}\theta)$	heat flux must satisfy Fourier's inequality, cf. Eq. (2.89)

Boundary conditions

$\boldsymbol{t}_0 = \boldsymbol{P}\cdot\boldsymbol{N} = \bar{\boldsymbol{t}}_0$	on $\partial\mathcal{B}_0^{\boldsymbol{t}}$	Neumann
$\boldsymbol{\varphi} = \bar{\boldsymbol{\varphi}}$	on $\partial\mathcal{B}_0^{\boldsymbol{\varphi}}$	Dirichlet
$Q = -\boldsymbol{Q}\cdot\boldsymbol{N} = \bar{Q}$	on $\partial\mathcal{B}_0^{Q}$	Neumann
$\theta = \bar{\theta}$	on $\partial\mathcal{B}_0^{\theta}$	Dirichlet

boundaries

$$\boldsymbol{\varphi} = \bar{\boldsymbol{\varphi}} \qquad \text{on} \qquad \partial\mathcal{B}_0^{\boldsymbol{\varphi}}\,, \tag{2.108}$$

$$\boldsymbol{t}_0 = \boldsymbol{P}\cdot\boldsymbol{N} = \bar{\boldsymbol{t}}_0 \qquad \text{on} \qquad \partial\mathcal{B}_0^{\boldsymbol{t}}\,, \tag{2.109}$$

$$\theta = \bar{\theta} \qquad \text{on} \qquad \partial\mathcal{B}_0^{\theta}\,, \tag{2.110}$$

$$Q = -\boldsymbol{Q}\cdot\boldsymbol{N} = \bar{Q} \qquad \text{on} \qquad \partial\mathcal{B}_0^{Q}\,, \tag{2.111}$$

Box 2.2: Thermo-mechanically coupled framework for small deformations.

Unknown fields

$\boldsymbol{u}(\boldsymbol{x},t)$	displacements
$\theta(\boldsymbol{x},t)$	temperature

Local strong forms of balance equations

$$\rho\,\ddot{\boldsymbol{u}} = \nabla_{\boldsymbol{x}}\cdot\boldsymbol{\sigma} + \rho\,\boldsymbol{f} \qquad \text{balance of linear momentum}$$

$$c\,\dot{\theta} = \theta\,\frac{\partial\boldsymbol{\sigma}}{\partial\theta} : \dot{\boldsymbol{\varepsilon}} + \rho\,r - \nabla_{\boldsymbol{x}}\cdot\boldsymbol{q} + \left[\boldsymbol{\kappa} - \theta\,\frac{\partial\boldsymbol{\kappa}}{\partial\theta}\right]\circ\dot{\boldsymbol{k}} \qquad \text{heat equation}$$

Constitutive relations in hyperelastic form

$\Psi(\boldsymbol{\varepsilon},\theta,\boldsymbol{k})$	Helmholtz energy
$\boldsymbol{\sigma} = \rho\,\dfrac{\partial\Psi}{\partial\boldsymbol{\varepsilon}}$	Piola stresses
$\boldsymbol{\kappa} = -\,\rho\,\dfrac{\partial\Psi}{\partial\boldsymbol{k}}$	driving forces
$c = -\,\rho\,\theta\,\dfrac{\partial^2\Psi}{\partial\theta^2}$	heat capacity
$\mathcal{D}_{\text{int}}^{\text{red}} = \boldsymbol{\kappa}\circ\dot{\boldsymbol{k}} \geq 0$	restriction of evolution equations
$\boldsymbol{q}(\theta,\nabla_{\boldsymbol{x}}\theta)$	heat flux must satisfy Fourier's inequality, cf. Eq. (2.89)

Boundary conditions

$\boldsymbol{t} = \boldsymbol{\sigma}\cdot\boldsymbol{n} = \bar{\boldsymbol{t}}$	on $\partial\mathcal{B}^{\boldsymbol{t}}$	Neumann
$\boldsymbol{u} = \bar{\boldsymbol{u}}$	on $\partial\mathcal{B}^{\boldsymbol{u}}$	Dirichlet
$q = -\boldsymbol{q}\cdot\boldsymbol{n} = \bar{q}$	on $\partial\mathcal{B}^{q}$	Neumann
$\theta = \bar{\theta}$	on $\partial\mathcal{B}^{\theta}$	Dirichlet

with $\boldsymbol{N}$ being the outward unit normal vector on the referential surface. Mathematically speaking, Dirichlet boundary conditions are classified as homogeneous ($\bar{\boldsymbol{\varphi}} = \boldsymbol{0}$, $\bar{\theta} = 0$) and inhomogeneous ($\bar{\boldsymbol{\varphi}} \neq \boldsymbol{0}$, $\bar{\theta} \neq 0$) boundary conditions. The same applies to Neumann boundary conditions where homogeneous mechanical boundary conditions ($\bar{\boldsymbol{t}}_0 = \boldsymbol{0}$) are often denoted as "free surfaces" and where homogeneous thermal boundary conditions ($\bar{Q} = 0$) are often introduced as "adiabatic". Prescribed forces or heat fluxes can either

Box 2.3: Framework for a rigid heat conductor.

Unknown field

$\theta(\boldsymbol{x}, t)$ temperature

Local strong form of the heat equation

$$c\,\dot{\theta} = \rho\, r - \nabla_{\boldsymbol{x}} \cdot \boldsymbol{q}$$

Constitutive relations in hyperelastic form

$\Psi(\theta)$	Helmholtz free energy function
$c = -\rho\,\theta\,\dfrac{\partial^2 \Psi}{\partial \theta^2}$	heat capacity
$\boldsymbol{q}(\theta, \nabla_{\boldsymbol{x}}\theta)$	heat flux must satisfy Fourier's inequality, cf. Eq. (2.89)

Boundary conditions

$q = -\boldsymbol{q} \cdot \boldsymbol{n} = \bar{q}$	on $\partial\mathcal{B}^q$	Neumann
$\theta = \bar{\theta}$	on $\partial\mathcal{B}^\theta$	Dirichlet

be "classic" Neumann boundary conditions, which are then simply prescribed ($\bar{\boldsymbol{t}}_0 \neq \boldsymbol{0}$, $\bar{Q} \neq 0$), or they can be dependent on the respective fields. The latter are also often denoted as Robin boundary conditions. For illustration purposes, the different types of boundary conditions are sketched in Fig. 2.3.

For a concise overview of the unknown fields, the underlying balance equations, the constitutive relations to be defined as well as the respective boundary conditions are collated in Box 2.1 for a heat conductor which undergoes finite deformations. Analogously, the governing equations for a deformable heat conductor within a geomentrically linearised setting are collated in Box 2.2. Here, reference and current configuration of a body are no longer distinguished between, so that $\mathcal{B}$ denotes the body at all times, the boundary of the body is denoted by $\partial\mathcal{B}$ and the coordinates of material points are denoted by $\boldsymbol{x}$ for all times. The deformation map field is replaced by the displacement field $\boldsymbol{u}(\boldsymbol{x}, t)$ and the strain measure is the infinitesimal strain tensor $\boldsymbol{\varepsilon}$, cf. Eq. (2.62). Consequently, the Helmholtz energy function depends on $\boldsymbol{\varepsilon}$, θ and $\boldsymbol{k}$, i.e. $\Psi = \Psi(\boldsymbol{\varepsilon}, \theta, \boldsymbol{k})$. Due to the absence of different configurations, the stress measure is written as $\boldsymbol{\sigma}$. For a rigid heat conductor, the remaining field is the temperature $\theta(\boldsymbol{x}, t)$ such that only the heat equation has to be solved. The reduced set of relations is summarised in Box 2.3.

In this thesis, the initial boundary value problems given in Boxes 2.1 to 2.3 are solved by means of the finite element method. For this purpose, a finite element programme written in C++ was developed in the framework of the research work related to this thesis. The related derivations for the most general case treated within this thesis, the deformable heat conductor at finite deformations according to Box 2.1, are summarised in Appendix A. For the sake of convenience, the finite element discretisation for the frameworks discussed within the following chapters is briefly summarised within each of the chapters. Hereby, Chapters 3 and 4 deal with research work based on the governing equations of a rigid heat conductor, cf. Box 2.3. The thermo-mechanical homogenisation framework discussed in Chapter 5 relies on the equations for a deformable heat conductor within a geometrically linearised setting according to Box 2.2, and the thermo-mechanical homogenisation framework introduced in Chapter 6 rests upon the equations for a deformable heat conductor at finite deformations summarised in Box 2.1.

3 Simulation of non-linear heat transfer during thermal spraying of complex workpieces

From the modelling perspective, thermal spraying represents a combination of several complex processes. Pre-treated hard material powder is partly molten and accelerated to the surface of the substrate where the single agglomerated powder particles form splats which solidify due to quenching and form the coating as the final result. The fluid flow simulation itself is a challenging task which is briefly discussed in Section 1.1.1. Further challenging questions are the thermo-mechanical state of the pre-treated hard material powder before it is molten by the thermal spray gun, while the powder partly melts and the condition after impact on the surface as well as the subsequent quenching. Apart from all the challenging questions regarding the physics of the different stages of the coating process, a modelling framework is required which geometrically accounts for the thermal spray gun movement and the area which is covered by the gun flame. Such a geometrical framework is part of the research within the doctoral thesis of Wiederkehr [190].

During thermal spraying, especially pronounced within workpieces with complex geometries, residual stresses occur which may lead to lower coating qualities or a reduced service life of the coated workpieces. In order to understand the occurring effects and to advance the planning of coating processes, simulations of the highly transient thermal energy flux of the HVOF spray gun into the substrate are of great value. In this chapter, a novel software framework for the simulation of non-linear heat transfer during (HVOF) thermal spraying is presented. One part of this framework employs an efficient GPU-based simulation algorithm to compute the time-dependent input boundary conditions for a spray gun that moves along a complex workpiece of arbitrary shape. The other part employs a finite-element model for a rigid heat conductor adhering to the computed boundary conditions. The model is derived from the fundamental equations of continuum thermodynamics where non-linear temperature-depending heat conduction is assumed.

The following two sections describe the fundamental equations of continuum thermodynamics for a rigid heat conductor and the resulting finite element discretisation.

Section 3.3 outlines the functionality of the robot guided spray simulation, Wiederkehr et al. [188], and provides important details regarding the GPU-accelerated computation of the input boundary conditions. Section 3.4 presents a demonstration of the software tool for the simulation of a real work piece. The material parameters of the underlying constitutive relations – the heat capacity c as well as the heat conduction coefficient λ – are represented by suitable functions which are fitted to experimental data.

3.1 Continuum thermodynamical framework

The governing equations of a thermo-mechanically coupled heat conductor are discussed in Chapter 2 within Sections 2.3 and 2.4 where the heat equation, cf. Eq. (2.103), was finally obtained as the balance equation related to the temperature field. When solely the heat conduction is modelled, and hence the deformation of the heat conducting body $\mathcal{B}$ is not considered, such a heat conductor is often denoted as a rigid heat conductor to express the absence of a field which describes the deformation. The initial boundary value problem of a rigid heat conductor, where the only present physical field is the temperature field $\theta(\boldsymbol{x}, t)$, is summarised in Box 2.3. Within this chapter, the heat equation

$$c\,(\theta)\,\dot{\theta} = -\,\nabla_{\boldsymbol{x}} \cdot \boldsymbol{q} + \rho\, r\ , \tag{3.1}$$

is used in order to model non-linear heat conduction within a body that is subjected to heat input via a thermal spray gun as well as to heat transfer via its surface. Furthermore, both the heat capacity, $c(\theta) = -\rho\,\theta\,(\partial^2\Psi)/(\partial\theta^2)$, as well as the heat flux, $\boldsymbol{q}(\theta)$, are assumed to be temperature dependent. The specific temperature dependency is discussed in Section 3.3. The heat equation, Eq. (3.1), is solved by means of the finite element framework elaborated in the following section. For this purpose, the boundary $\partial\mathcal{B}$ of the body $\mathcal{B}$ is decomposed into three disjoint parts, i.e., $\partial\mathcal{B}^{\mathrm{D}} \cup \partial\mathcal{B}^{\mathrm{N}} \cup \partial\mathcal{B}^{\mathrm{R}} = \partial\mathcal{B}$ with $\partial\mathcal{B}^{\mathrm{D}} \cap \partial\mathcal{B}^{\mathrm{N}} = \emptyset$, $\partial\mathcal{B}^{\mathrm{D}} \cap \partial\mathcal{B}^{\mathrm{R}} = \emptyset$ and $\partial\mathcal{B}^{\mathrm{N}} \cap \partial\mathcal{B}^{\mathrm{R}} = \emptyset$. On $\partial\mathcal{B}^{\mathrm{D}}$ Dirichlet boundary conditions are prescribed for the temperature θ, whereas Neumann and Robin boundary conditions are prescribed for the heat flux $\boldsymbol{q}$ on $\partial\mathcal{B}^{\mathrm{N}}$ respectively $\partial\mathcal{B}^{\mathrm{R}}$:

$$\theta = \bar{\theta} \quad \text{on} \quad \partial\mathcal{B}^{\mathrm{D}}, \qquad -\boldsymbol{q}\cdot\boldsymbol{n} = \bar{q}^{\mathrm{N}} \quad \text{on} \quad \partial\mathcal{B}^{\mathrm{N}}, \qquad -\boldsymbol{q}\cdot\boldsymbol{n} \ = \bar{q}^{\mathrm{R}}(\theta) \quad \text{on} \quad \partial\mathcal{B}^{\mathrm{R}}\ . \tag{3.2}$$

3.2 Finite element discretisation

The different representations of the energy balance equation derived above are given in strong form. To calculate a solution for the desired field of the temperature by means of the finite element method in the context of inhomogeneous initial boundary value

problems, the temperature-based balance of energy has to be reformulated in weak form. Therefore, we transfer Eq. (3.1) to a residual form,

$$0 = \delta\theta \left[c\,\dot{\theta} + \nabla_{\boldsymbol{x}} \cdot \boldsymbol{q} - \rho\, r \right] , \tag{3.3}$$

where $\delta\theta$ is a scalar-valued test function which can be interpreted as the virtual temperature and which is 0 at Dirichlet boundaries $\partial\mathcal{B}^{\mathrm{D}}$, see Lewis et al. [107] for detailed background information. This relation also holds under integration over the volume of a body $\mathcal{B}$,

$$0 = \int_{\mathcal{B}} \delta\theta \left[c\,\dot{\theta} + \nabla_{\boldsymbol{x}} \cdot \boldsymbol{q} - \rho\, r \right] \mathrm{d}v . \tag{3.4}$$

The divergence of the heat flux in Eq. (3.4) can be reformulated by the application of Gauß's theorem and integration by parts,

$$0 = \int_{\mathcal{B}} \delta\theta\, c\,\dot{\theta}\, \mathrm{d}v + \int_{\mathcal{B}} -\nabla_{\boldsymbol{x}}\delta\theta \cdot \boldsymbol{q}\, \mathrm{d}v - \int_{\mathcal{B}} \delta\theta\, \rho\, r\, \mathrm{d}v - \int_{\partial\mathcal{B}} -\delta\theta\, \boldsymbol{q} \cdot \boldsymbol{n}\, \mathrm{d}a . \tag{3.5}$$

Here, $\boldsymbol{n}$ denotes the outward unit vector on the boundary of the body $\mathcal{B}$. Eq. (3.5) represents the virtual temperature problem and can be written in terms of dynamic, volume, internal and surface terms

$$g(\delta\theta;\, \theta, \nabla_{\boldsymbol{x}}\theta) = \mathrm{w}_{\mathrm{dyn}} + \mathrm{w}_{\mathrm{int}} - \mathrm{w}_{\mathrm{vol}} - \mathrm{w}_{\mathrm{sur}} = 0 \quad \forall\, \delta\theta , \tag{3.6}$$

which, in turn, are defined by

$$\begin{aligned} \mathrm{w}_{\mathrm{dyn}} &= \int_{\mathcal{B}} \delta\theta\, c\,\dot{\theta}\, \mathrm{d}v , & \mathrm{w}_{\mathrm{vol}} &= \int_{\mathcal{B}} \delta\theta\, \rho\, r\, \mathrm{d}v , \\ \mathrm{w}_{\mathrm{int}} &= \int_{\mathcal{B}} -\nabla_{\boldsymbol{x}}\delta\theta \cdot \boldsymbol{q}\, \mathrm{d}v , & \mathrm{w}_{\mathrm{sur}} &= \int_{\partial\mathcal{B}} -\delta\theta\, \boldsymbol{q} \cdot \boldsymbol{n}\, \mathrm{d}a . \end{aligned} \tag{3.7}$$

Eq. (3.6) is the weak form of the initial boundary value problem of a rigid heat conductor which now has to be discretised in time and space, following the procedure outlined, e.g., in Bergheau and Fortunier [15] or Kuhl et al. [101]. For time discretisation, a differential-quotient-based Backward Euler integration scheme is applied, see, e.g., Vujičić [186],

$$\frac{\partial\,[\bullet]}{\partial t} \approx \frac{[\bullet]_{n+1} - [\bullet]_n}{\Delta t} , \tag{3.8}$$

where $[\bullet]$ symbolises an arbitrary quantity of interest and Δt denotes the time increment $t_{n+1} - t_n$. Subscript $n+1$ denotes a quantity at the actual time step t_{n+1}, whereas subscript n denotes a quantity at the previous time step t_n. Application of Eq. (3.8) to the temperature θ results in

$$\dot{\theta} = \frac{\theta_{n+1} - \theta_n}{\Delta t} \ . \tag{3.9}$$

In addition to the Backward Euler method applied in this work, recent works which address thermal problems use the Crank-Nicolson method, cf. Palani and Kim [133], or energy-momentum consistent schemes in the context of thermo-elastodynamics, cf. Gross and Betsch [67]. At time t_{n+1}, Eq. (3.9) leads to the relation

$$g(\delta\theta;\, \theta_{n+1}, \theta_n) = \mathrm{w}_{\mathrm{dyn}} + \mathrm{w}_{\mathrm{int}} - \mathrm{w}_{\mathrm{vol}} - \mathrm{w}_{\mathrm{sur}} = 0 \quad \forall\, \delta\theta \ , \tag{3.10}$$

for the unknown temperature θ_{n+1}. In view of the discretisation in space, it has to be taken into account that Robin boundary conditions require additional effort, since they represent one type of temperature dependent loads. For a review on the implementation and algorithmic treatment of deformation dependent loads, the reader is referred to the textbook by Bonet and Wood [29] and references cited therein. For that purpose, on the one hand the body $\mathcal{B}$ is approximated by a finite number of $n_{el}^{\mathcal{B}}$ volume elements $\mathcal{B}_{\mathcal{B}}^{e}$ and, on the other hand, the Robin boundary $\partial\mathcal{B}^{\mathrm{R}}$ of the body $\mathcal{B}$ is approximated by $n_{el}^{\partial\mathcal{B}}$ surface elements $\mathcal{B}_{\partial\mathcal{B}}^{e}$, i.e.

$$\mathcal{B} \approx \mathcal{B}^h = \bigcup_{e=1}^{n_{el}^{\mathcal{B}}} \mathcal{B}_{\mathcal{B}}^{e} \ , \quad \partial\mathcal{B}^{\mathrm{R}} \approx \partial\mathcal{B}^{\mathrm{R}\,h} = \bigcup_{e=1}^{n_{el}^{\partial\mathcal{B}}} \mathcal{B}_{\partial\mathcal{B}}^{e} \ . \tag{3.11}$$

Following the spirit of the isoparametric concept, the geometry of the body, in terms of position vectors $\boldsymbol{x}$, as well as the temperature of the body θ and the virtual temperature $\delta\theta$ are interpolated element-wise by shape functions $N^i_{\boldsymbol{x},\,\mathcal{B}}$ respectively $N^i_{\boldsymbol{x},\,\partial\mathcal{B}}$ and discrete node point positions $\boldsymbol{x}_i$ of $i = 1, ..., n_{en}^{\mathcal{B}}$ respectively $i = 1, ..., n_{en}^{\partial\mathcal{B}}$ element nodes, i.e.

$$\begin{aligned}
\boldsymbol{x}_{\mathcal{B}} \approx \boldsymbol{x}_{\mathcal{B}}^h = \bigcup_{i=1}^{n_{en}^{\mathcal{B}}} N^i_{\boldsymbol{x},\,\mathcal{B}}\, \boldsymbol{x}_i \ , \qquad & \boldsymbol{x}_{\partial\mathcal{B}} \approx \boldsymbol{x}_{\partial\mathcal{B}}^h = \bigcup_{i=1}^{n_{en}^{\partial\mathcal{B}}} N^i_{\boldsymbol{x},\,\partial\mathcal{B}}\, \boldsymbol{x}_i \ , \\
\theta_{\mathcal{B}} \approx \theta_{\mathcal{B}}^h = \bigcup_{i=1}^{n_{en}^{\mathcal{B}}} N^i_{\boldsymbol{x},\,\mathcal{B}}\, \theta_i \ , \qquad & \theta_{\partial\mathcal{B}} \approx \theta_{\partial\mathcal{B}}^h = \bigcup_{i=1}^{n_{en}^{\partial\mathcal{B}}} N^i_{\boldsymbol{x},\,\partial\mathcal{B}}\, \theta_i \ , \\
\delta\theta_{\mathcal{B}} \approx \delta\theta_{\mathcal{B}}^h = \bigcup_{i=1}^{n_{en}^{\mathcal{B}}} N^i_{\boldsymbol{x},\,\mathcal{B}}\, \delta\theta_i \ , \qquad & \delta\theta_{\partial\mathcal{B}} \approx \delta\theta_{\partial\mathcal{B}}^h = \bigcup_{i=1}^{n_{en}^{\partial\mathcal{B}}} N^i_{\boldsymbol{x},\,\partial\mathcal{B}}\, \delta\theta_i \ .
\end{aligned} \tag{3.12}$$

Hence, the gradients $\nabla_{\boldsymbol{x}}\boldsymbol{x}$, $\nabla_{\boldsymbol{x}}\theta$ and $\nabla_{\boldsymbol{x}}\delta\theta$ are approximated as

$$\begin{aligned}
\nabla_{\boldsymbol{x}}\boldsymbol{x}_{\mathcal{B}} &\approx \nabla_{\boldsymbol{x}}\boldsymbol{x}^h_{\mathcal{B}} = \bigcup_{i=1}^{n^{\mathcal{B}}_{en}} \boldsymbol{x}_i \otimes \nabla_{\boldsymbol{x}} N^i_{\boldsymbol{x},\mathcal{B}} \;, & \nabla_{\boldsymbol{x}}\boldsymbol{x}_{\partial\mathcal{B}} &\approx \nabla_{\boldsymbol{x}}\boldsymbol{x}^h_{\partial\mathcal{B}} = \bigcup_{i=1}^{n^{\partial\mathcal{B}}_{en}} \boldsymbol{x}_i \otimes \nabla_{\boldsymbol{x}} N^i_{\boldsymbol{x},\partial\mathcal{B}} \;, \\
\nabla_{\boldsymbol{x}}\theta_{\mathcal{B}} &\approx \nabla_{\boldsymbol{x}}\theta^h_{\mathcal{B}} = \bigcup_{i=1}^{n^{\mathcal{B}}_{en}} \theta_i \; \nabla_{\boldsymbol{x}} N^i_{\boldsymbol{x},\mathcal{B}} \;, & \nabla_{\boldsymbol{x}}\theta_{\partial\mathcal{B}} &\approx \nabla_{\boldsymbol{x}}\theta^h_{\partial\mathcal{B}} = \bigcup_{i=1}^{n^{\partial\mathcal{B}}_{en}} \theta_i \; \nabla_{\boldsymbol{x}} N^i_{\boldsymbol{x},\partial\mathcal{B}} \;, \\
\nabla_{\boldsymbol{x}}\delta\theta_{\mathcal{B}} &\approx \nabla_{\boldsymbol{x}}\delta\theta^h_{\mathcal{B}} = \bigcup_{i=1}^{n^{\mathcal{B}}_{en}} \delta\theta_i \; \nabla_{\boldsymbol{x}} N^i_{\boldsymbol{x},\mathcal{B}} \;, & \nabla_{\boldsymbol{x}}\delta\theta_{\partial\mathcal{B}} &\approx \nabla_{\boldsymbol{x}}\delta\theta^h_{\partial\mathcal{B}} = \bigcup_{i=1}^{n^{\partial\mathcal{B}}_{en}} \delta\theta_i \; \nabla_{\boldsymbol{x}} N^i_{\boldsymbol{x},\partial\mathcal{B}} \;.
\end{aligned} \tag{3.13}$$

The insertion of the approximations given by Eqs. (3.12) and (3.13) into Eq. (3.10) leads to the fully discretised balance of energy in terms of the unknown temperature θ_{n+1}

$$\underline{\mathbf{r}}^h\left(\theta^h_{n+1}\right) = \underline{\mathbf{f}}_{\text{dyn}} + \underline{\mathbf{f}}_{\text{int}} - \underline{\mathbf{f}}_{\text{vol}} - \underline{\mathbf{f}}_{\text{sur}} = 0 \;, \tag{3.14}$$

where the discrete inertia, volume, internal and surface fluxes are expressed by

$$\begin{aligned}
\mathrm{f}_{\text{dyn}I} &= \mathop{\mathbf{A}}_{e=1}^{n^{\mathcal{B}}_{el}} \int_{\mathcal{B}^e_{\mathcal{B}}} N^i_{\boldsymbol{x},\mathcal{B}}\, c(\theta)\, \frac{\theta_{n+1}-\theta_n}{\Delta t}\, \mathrm{d}v \;, \\
\mathrm{f}_{\text{vol}I} &= \mathop{\mathbf{A}}_{e=1}^{n^{\mathcal{B}}_{el}} \int_{\mathcal{B}^e_{\mathcal{B}}} N^i_{\boldsymbol{x},\mathcal{B}}\, q\, \mathrm{d}V \;, \\
\mathrm{f}_{\text{int}I} &= \mathop{\mathbf{A}}_{e=1}^{n^{\mathcal{B}}_{el}} \int_{\mathcal{B}^e_{\mathcal{B}}} \nabla_{\boldsymbol{x}} N^i_{\boldsymbol{x},\mathcal{B}} \cdot \boldsymbol{q}\, \mathrm{d}V \;, \\
\mathrm{f}_{\text{sur}I} &= \mathop{\mathbf{A}}_{e=1}^{n^{\mathcal{B}}_{el}} \int_{\partial\mathcal{B}^e_{\mathcal{B}}} -N^i_{\boldsymbol{x},\partial\mathcal{B}}\, \bar{q}^{\mathrm{N}}\, \mathrm{d}A \;+\; \mathop{\mathbf{A}}_{e=1}^{n^{\partial\mathcal{B}}_{el}} \int_{\mathcal{B}^e_{\partial\mathcal{B}}} -N^j_{\boldsymbol{x},\partial\mathcal{B}}\, \bar{q}^{\mathrm{R}}(\theta)\, \mathrm{d}A \;.
\end{aligned} \tag{3.15}$$

In the above equations, $\mathbf{A}$ represents the assembly operator over all $e = 1, ..., n^{\mathcal{B}}_{el}$ volume element contributions and all $e = 1, ..., n^{\partial\mathcal{B}}_{el}$ surface element contributions at $i = 1, ..., n^{\mathcal{B}}_{en}$ respectively $j = 1, ..., n^{\partial\mathcal{B}}_{en}$ element nodes to the global node points $I = 1, ..., n_{np}$. Note, that q and $\bar{q}^{\mathrm{N}}$ are assumed to be temperature-independent throughout this work. With the definitions in Eq. (3.15), Eq. (3.14) represents the discretised nonlinear temperature field equation. The solution is performed by an incremental Newton-Raphson scheme, see De Borst et al. [44] for detailed background information in the context of the finite element method. For that purpose, the Jacobian of the residual with respect to the

temperature θ has to be determined. Therefore, the iterative scheme can be expressed as

$$\mathrm{r}_{I,n+1}^{h,k+1} = \mathrm{r}_{I,n+1}^{h,k} + \mathrm{d}\mathrm{r}_I \quad \forall I = 1, ..., n_{np} \ , \tag{3.16}$$

wherein $\mathrm{d}\mathrm{r}_I$ is approximated by the linear term of a Taylor series expansion,

$$\mathrm{d}\mathrm{r}_I = \sum_{J=1}^{n_{np}} K_{IJ} \, \mathrm{d}\theta_J \quad \forall I = 1, ..., n_{np} \ . \tag{3.17}$$

The derivative $K_{IJ} = \partial \mathrm{r}_I / \partial \theta_J$ is assembled to the global tangent operator

$$\begin{aligned} K_{IJ} = & \mathop{\mathsf{A}}_{e=1}^{n_{el}^{\mathcal{B}}} \int_{\mathcal{B}_{\mathcal{B}}^e} N_{\boldsymbol{x},\mathcal{B}}^i \left[c(\theta) \, \frac{1}{\Delta t} + \frac{\partial c(\theta)}{\partial \theta} \, \frac{\theta_{n+1} - \theta_n}{\Delta t} \right] N_{\boldsymbol{x},\mathcal{B}}^j \, \mathrm{d}V \\ & + \mathop{\mathsf{A}}_{e=1}^{n_{el}^{\mathcal{B}}} \int_{\mathcal{B}_{\mathcal{B}}^e} \nabla_{\boldsymbol{x}} N_{\boldsymbol{x},\mathcal{B}}^i \cdot \frac{\partial \boldsymbol{q}}{\partial \, \nabla_{\boldsymbol{x}} \theta} \cdot \nabla_{\boldsymbol{x}} N_{\boldsymbol{x},\mathcal{B}}^j \, \mathrm{d}V - \mathop{\mathsf{A}}_{e=1}^{n_{el}^{\partial\mathcal{B}}} \int_{\mathcal{B}_{\partial\mathcal{B}}^e} -N_{\boldsymbol{x},\partial\mathcal{B}}^i \, \frac{\partial \bar{q}^{\mathrm{R}}(\theta)}{\partial \theta} \, N_{\boldsymbol{x},\partial\mathcal{B}}^j \, \mathrm{d}A \ . \end{aligned} \tag{3.18}$$

The first term represents the dynamic contribution and therefore characterises the time-dependency of the problem, whereas the second term corresponds to the internal heat flux where the constitutive relation for the heat flux $\boldsymbol{q}$ still has to be defined. The third term reflects the surface element contribution by Robin boundary conditions $\bar{q}^{\mathrm{R}}(\theta)$.

3.3 Implementation

Two aspects are vital for the computer aided planning of thermal spray processes: the prediction of the coating thickness distribution on the surface of a workpiece and the prediction of the temperatures reached in the workpiece during the process. For the simulation of the coating thickness, an efficient GPU-accelerated, C++ based simulation was developed in Wiederkehr et al. [188]. In the present work, this framework is modified so as to compute a time dependent temperature distribution θ^{∞} on the surface of the discretised workpiece mesh which serves as an input for the finite element framework developed in the previous section. In order to model the energy input of the unloaded flame of the spray gun into the workpiece, the surface heat flux is assumed to be applied by convection and radiation. An unloaded flame means that the problem at hand is restricted to heat transfer only, without accounting for mass transport phenomena. One simple approach to mathematically cover the convective heat contribution is the introduction of a so-called film condition

$$\bar{q}_c = -h_c \, [\theta - \theta^{\infty}] \ , \tag{3.19}$$

wherein h_c denotes the convective heat transfer coefficient which is assumed to be a constant, and where θ^∞ denotes the environmental temperature which either represents the HVOF spray gun or the room temperature. It should be noted that h_c represents a rather complex fluid mechanical process, not captured by the finite element approach as this work proceeds. The heat radiation is modelled by

$$\bar{q}_r = -\alpha_r \, [\theta - \theta^\infty] \quad \text{with} \quad \alpha_r \; = \varepsilon \, \sigma \, \left[\theta^2 + \theta^{\infty 2}\right] \, [\theta - \theta^\infty] \; , \tag{3.20}$$

where ε is the emissivity and σ represents the Stefan-Boltzmann constant, cf. Comini et al. [41]. Both, $\bar{q}_c$ and $\bar{q}_r$, are Robin boundary conditions in view of Eq. (3.2), i.e. $\bar{q}^{\mathrm{R}}(\theta) = \bar{q}_c(\theta) + \bar{q}_r(\theta)$. For implementation, the heat capacity is specified by a cubic polynomial

$$c\,(\theta) = a_0 + a_1\,\theta + a_2\,\theta^2 + a_3\,\theta^3 \; . \tag{3.21}$$

To guarantee thermal stability as discussed above, it has to be ensured that $c\,(\theta) > 0$ holds for arbitrary (positive) values of the absolute temperature θ. Furthermore, the heat conduction is modelled by Fourier's law

$$\boldsymbol{q} = -\boldsymbol{\Lambda}\,(\theta) \cdot \nabla_{\boldsymbol{x}}\theta \; , \tag{3.22}$$

where $\boldsymbol{\Lambda}(\theta)$ has to be positive semi-definite for any θ, see e.g. Liu [108], and is thus represented by

$$\boldsymbol{\Lambda}(\theta) = \Lambda(\theta)\,\boldsymbol{I} \quad \text{with} \quad \Lambda(\theta) = b_0 + \sum_{i=1}^{4} b_{i,1} \, \exp\left(-\left[\frac{\theta - b_{i,2}}{b_{i,3}}\right]^2\right) \; , \tag{3.23}$$

where $\boldsymbol{I}$ is the second order identity tensor and $\Lambda(\theta) > 0$ is the heat conduction coefficient. The assumption of $\boldsymbol{\Lambda}(\theta)$ being proportional to $\boldsymbol{I}$ leads to an isotropic heat conduction model. The non-linear heat conduction model specified via Eqs. (3.19) to (3.23) is implemented in C++ as part of the already mentioned simulation framework. The remaining part of this section describes the computation of the film condition parameters θ_i^∞ for all boundary triangles of the tetrahedron volume mesh representing the workpiece.

Apart from the triangulated workpiece mesh, the simulation approach takes a robot guided spray gun movement path as an input, which is represented as a sequence of 3-tuples $\boldsymbol{p}_i = \{\boldsymbol{x}_i, \boldsymbol{q}_i, t_i\}$ for $i = 1, \ldots, n$ discrete robot path positions. Therein, $\boldsymbol{x}_i$ is the spray gun position in global coordinates and $\boldsymbol{q}_i$ is a quaternion describing the orientation of the spray gun at time t_i. For detailed background information on quaternions the reader is referred to Argyris [4], Betsch et al. [26], Altmann [3] and the references cited therein.

During the simulation a virtual spray gun is moved along the given path in discrete time steps Δt, where positions are interpolated linearly and where quaternion slerp interpolation is used for the orientations, see Shoemake [158]. For every gun position $\boldsymbol{p}_i$

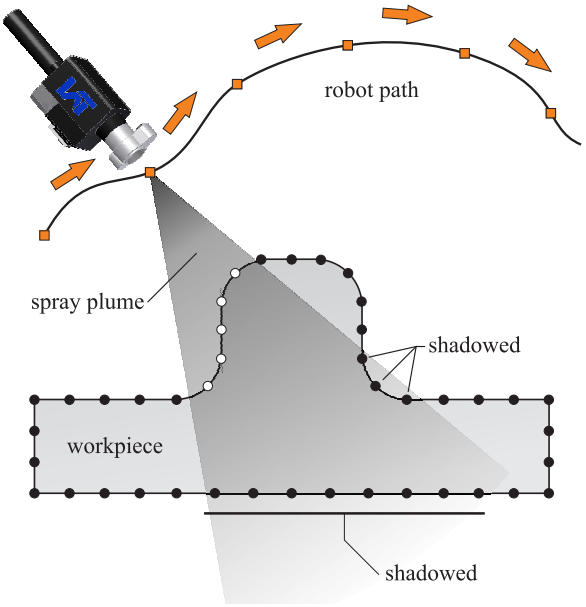

Figure 3.1: Visibility computation to determine the nodes of the workpiece to be coated and to receive a heat flux from the gun (white nodes). Nodes outside the spray cone or nodes that are shadowed from the gun by parts of the workpiece are not coated.

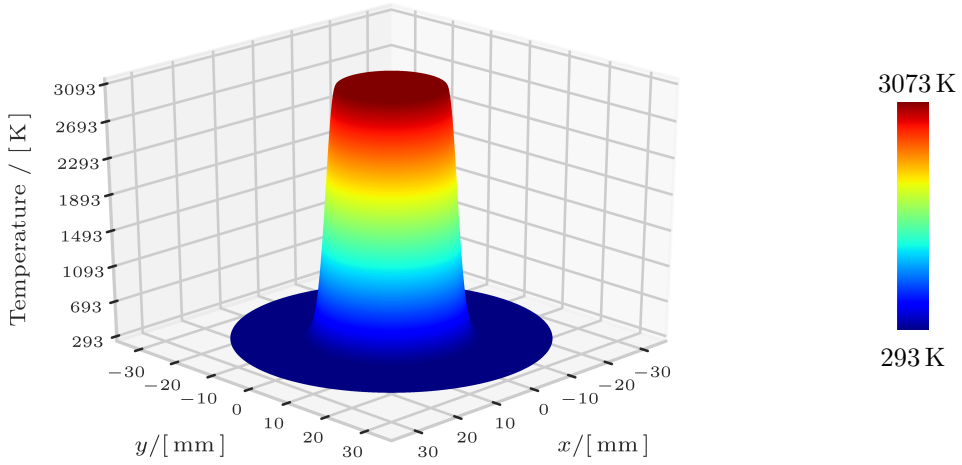

Figure 3.2: Shape of the radially symmetric load function $\theta^{\infty}_{\text{node}}$ which is used in the benchmark simulations; Eq. (3.24).

the following computations, where steps 1–3 are entirely GPU-based and implemented in OpenGL and the OpenGL Shading Language (GLSL), are performed:

1. *Compute the subset N_{loaded} of nodes of the workpiece mesh that receive a heat flux from the current spray gun position.*

   This is defined to be the subset of nodes, the coordinates of which are inside the spray plume, approximated by a (spray) cone which expands from the gun center position $\boldsymbol{x}(t)$, see Fig. 3.1. Only those nodes visible from the spray gun center are considered; nodes on the back side of the workpiece or nodes shadowed by other parts of the workpiece do not receive a high temperature load.

   This visibility computation for arbitrary meshes with potentially hundreds of thousands of nodes and faces can be efficiently implemented by exploiting the computational power of modern graphics cards, tailored by design to perform visibility computations on large triangle meshes in real-time. For the rendering of virtual scenes consisting of triangle meshes, the graphics card projects the three dimensional nodes of the mesh in a perspective correct manner onto a two-dimensional image plane.

   In the first visibility computation step, projected nodes outside the rectangular screen area are discarded, limiting the remaining nodes to the ones inside a pyramidal viewing frustum as depicted in Fig. 3.1. In an additional step, the graphics hardware uses the depth-buffer algorithm, see Catmull [34], to remove any nodes that are shadowed by the geometry for the particular viewpoint considered.

   For the current spray gun position, first, the opening angle of the viewing frustum of the virtual camera is adjusted to match the desired opening angle of the spray cone. Subsequently, the workpiece mesh is rendered and the desired nodes that receive a heat flux from the gun are determined. Since the viewing frustum is rectangular, the next step involves the correction to a circular spray cone.

2. *For every node in the subset N_{loaded} determine the thermal load $\theta^{\infty}_{\text{node}}$ in order to set up Robin type boundary conditions.*

   The nodes are projected onto a plane orthogonal to the central axis of the spray cone at the stand off distance d_{SOD} from the gun center. The thermal load for every node is then computed based on its distance r_{no} from the cone center axis. Due to the lack of precise measurement data, the load function is modelled as a

rotationally symmetric Gaussian with standard deviation s and amplitude $\theta_{\max}$ which is offset by r_{in} in order to cover a larger circular area of magnitude $\theta_{\max}$:

$$\theta^{\infty}_{\text{node}} = \begin{cases} \theta_{\max} & , \text{ if } r_{\text{no}} < r_{\text{in}} \\ \theta_{\text{amb}} & , \text{ if } r_{\max} \leq r_{\text{no}} \\ \theta_{\Delta\text{ma}} \ \exp\left(-\frac{1}{2}\left[\frac{r_{\text{no}} - r_{\text{in}}}{s}\right]^2\right) + \theta_{\text{amb}} & , \text{ else} \end{cases} \tag{3.24}$$

with $\theta_{\Delta\text{ma}} = \theta_{\max} - \theta_{\text{amb}}$. The threshold $r_{\max}$ is used to limit the function to a circular radius thereby transforming the rectangular viewing frustum into the desired circular spray plume approximation. For the simulations presented in this work, an HVOF spraying process is assumed and the values $d_{\text{SOD}} = 170\,\text{mm}$, $\theta_{\max} = \theta^{\infty}_{\text{gun}}$, $r_{\text{in}} = 10\,\text{mm}$, $r_{\max} = 66\,\text{mm}$ and $s = 2\,\text{mm}$ are used. The shape of the load function is shown in Fig. 3.2.

3. *The remaining nodes are set to receive an ambient thermal load $\theta^{\infty}_{\text{amb}}$ in order to set up Robin type boundary conditions.*

4. *The thermodynamic model is evaluated.*

   For each Newton iteration, the C++ implementation of the thermodynamic model assembles the global iterative residual vector r_I and the global tangent matrix K_{IJ} according to Eqs. (3.17) and (3.18), and then employs a conjugate gradient iterative solver with Jacobi (diagonal) preconditioning (pCG) to solve the system.

5. *The simulation time index is increased by Δt.*

This scheme is iterated until the end of the robot guided path is reached. For convenience, the flow chart of this scheme is illustrated in Algorithm 3.1. A key aspect for the efficient computation of the boundary conditions is the similarity of the geometric relationships of the spray plume expanding from the gun nozzle towards the workpiece on the one hand, and the geometry-projection process towards a virtual camera center in the visibility computation on the other. Due to this similarity, the first three steps can easily be performed by exploiting GPU acceleration techniques and are implemented in OpenGL and the OpenGL Shading Language (GLSL) within our framework.

Algorithm 3.1: Flow chart of the finite element framework.

initialisation of boundary value problem

time loop

while $t < t_{max}$ **do**

  compute current spray gun position from the predefined robot path

  foreach $N \in \partial\mathcal{B}$ **do**

    determine θ^{∞} of the surface node

    if $N \in N_{\text{loaded}}$ **then**

      compute θ^{∞}–value of the node according to Eq. (3.24)

    end

    else

      set $\theta^{\infty} = \theta_{\text{amb}}$

    end

  end

  Newton-Raphson loop

  while $\|\boldsymbol{r}\| \geq tol$ **do**

    loop over volume elements

    for $e = 1, ..., n_{el}^{\mathcal{B}}$ **do**

      volume element level computations

    end

    loop over surface elements

    for $se = 1, ..., n_{el}^{\partial\mathcal{B}}$ **do**

      surface element level computations

    end

    assemble and solve system of equations

  end

  postprocessing of current time step

  increase time step: $t \leftarrow t + \Delta t$

end

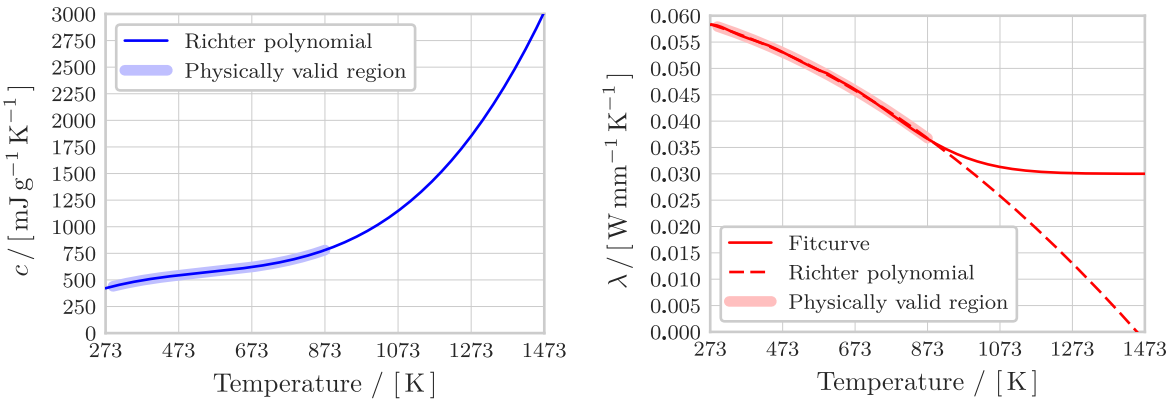

(a) Heat capacity $c(\theta)$.

(b) Heat conduction coefficient $\Lambda(\theta)$.

Figure 3.3: (a) Richter polynomial of the heat capacity $c(\theta)$. (b) Fitted curve and the Richter polynomial of the heat conduction coefficient $\Lambda(\theta)$; see Richter [142] for further details.

3.4 Examples

The implemented framework is now applied to carry out simulations of a realistic deep drawing tool in order to demonstrate the capabilities of the novel software. The starting temperature $\theta\big|_{t_0}$ of the material is considered to coincide with the room temperature $\theta^{\infty}_{\text{amb}} = 293\,\text{K}$ whereas the temperature of the spray gun is set to $\theta^{\infty}_{\text{gun}} = 3073\,\text{K}$. The steel material is St 35.8 (1.0305), the physical properties of which have been investigated by Richter, see Richter [141, 142], up to a temperature of 873 K. The parameters for Eq. (3.21), the polynomial of the heat capacity, are taken from Richter [141, 142] and summarised in Table 3.1. Note, that the polynomial is parameterised in °C not in K. For the sake of completeness, the polynomial is depicted with a K-scale in Fig. 3.3(a). It can be seen that the parameter set is not valid for temperatures beyond the interval $\theta = [293;\ 873]\,\text{K}$. Since $c(\theta) > 0$ is guaranteed within the temperature range of interest, $\theta \geq 293\,\text{K}$, the implemented framework remains thermally stable even when the physical valid temperature range is exceeded. This turns out to be helpful for the testing of the algorithmic framework.

Furthermore, the parameters for the heat conduction coefficient $\Lambda(\theta)$, which is given by Eq. (3.23), are also summarised in Table 3.1. Because the parameters are the result of fitting a polynomial of Richter [142], both functions are depicted in Fig. 3.3(b). The solid line represents the fitted function and, in contrast, the dashed line represents the polynomial taken from Richter [142]. Obviously, the fit is very good within the physical valid temperature range. Beyond this range, the fitted curve asymptotically tends move towards to a positive limit while the Richter polynomial has a root at $\theta = 1451.58\,\text{K}$. As an advantage, the fitted function guarantees $\Lambda(\theta) > 0$ for any θ, thereby avoiding numerical problems while testing the algorithmic framework. To complete the set of parameters, values for the convective heat transfer coefficients h_c^{air} and h_c^{gun} as well as for the emissivity ε and the Stefan-Boltzmann constant σ are summarised in Table 3.2.

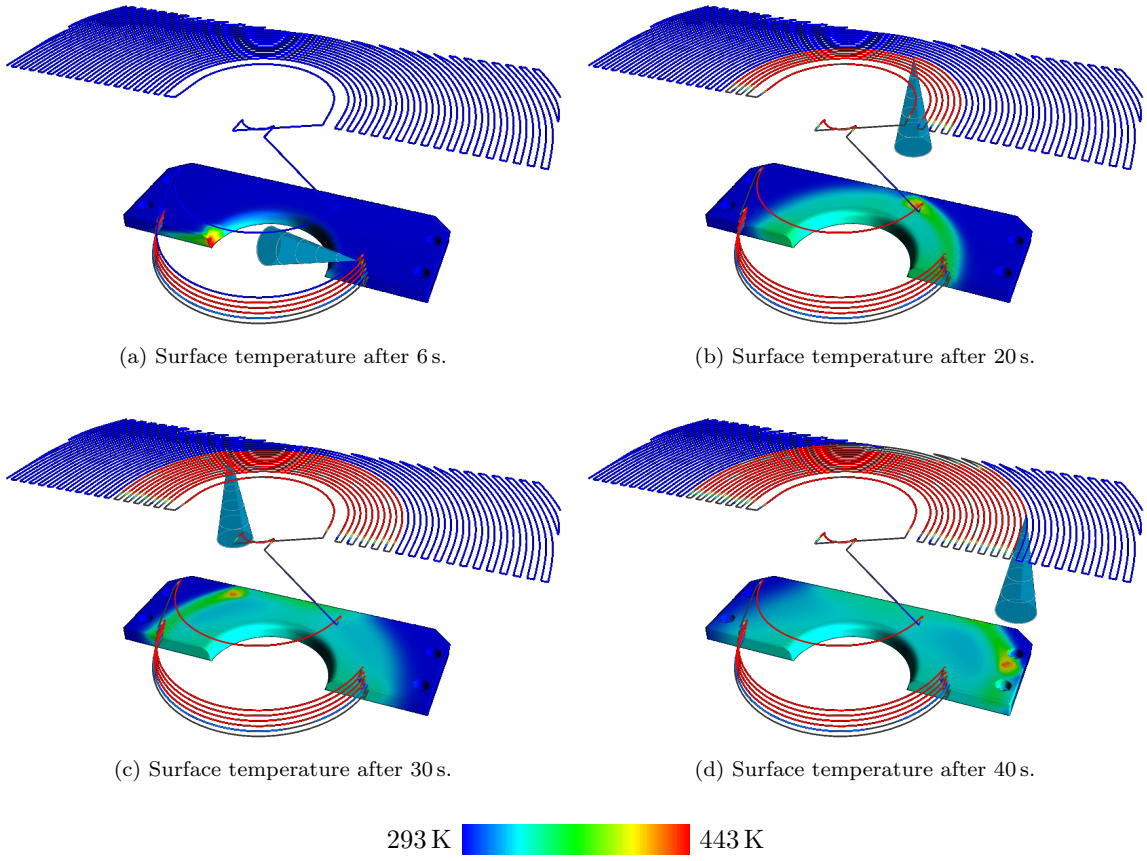

(a) Surface temperature after 6 s.

(b) Surface temperature after 20 s.

(c) Surface temperature after 30 s.

(d) Surface temperature after 40 s.

Figure 3.4: Simulated deep drawing workpiece and the employed robot movement path. The surface colors represent the surface temperatures and the path colors the temperature load after (a) 6 s, (b) 20 s, (c) 30 s and (d) 40 s of the medium gun speed simulation run. Blue path segments have not yet been processed.

We assume the surface surrounded by air to be exposed to natural convection, as the surface loaded by the HVOF spray gun is assumed to be charged with forced convection.

The integrated coating and thermodynamic simulation is carried out to predict the workpiece temperature for the manufacturing of thermal sprayed sheet metal forming tools. In this regard, the heat transport into a deep drawing tool of a moving and unloaded HVOF thermal spray gun is simulated using a complex robot tool path at three different movement speeds. The fastest simulation run completes the tool path within 40 s, the medium speed simulation in 80 s and the slowest run within 160 s. The tool path of the spray gun movement is depicted in Fig. 3.4. The colours of the robot path represent the temperature load resulting from the respective gun position. For the robot path, the blue regions on the right and left parts have not been processed yet, since the gun started at the lower end of the path proceeding upwards along the circular opening of the workpiece onto the plain surface on top. For the path already processed, the colouring represents the surface load temperatures induced by the gun, where grey

Table 3.1: Parameters for $c(\theta)$ introduced in Eq. (3.21) and $\Lambda(\theta)$ introduced in Eq. (3.23). The values are valid within $\theta = [293; 873]\,\mathrm{K}$; see Richter [142] for further details.

Quantity	Description	Symbol	Value	Unit
$c(\theta)$	Constant term	a_0	4.22×10^{2}	$\mathrm{mJ\,g^{-1}\,K^{-1}}$
	Linear coefficient	a_1	9.31×10^{-1}	$\mathrm{mJ\,g^{-1}\,K^{-2}}$
	Quadratic coefficient	a_2	-2.14×10^{-3}	$\mathrm{mJ\,g^{-1}\,K^{-3}}$
	Cubic coefficient	a_3	2.64×10^{-6}	$\mathrm{mJ\,g^{-1}\,K^{-4}}$
$\Lambda(\theta)$	Constant term	b_0	3.000×10^{-2}	$\mathrm{W\,mm^{-1}\,K^{-1}}$
	First scaling term	$b_{1,1}$	1.549×10^{-2}	$\mathrm{W\,mm^{-1}\,K^{-1}}$
	First numerator term	$b_{1,2}$	2.342×10^{2}	K
	First denominator term	$b_{1,3}$	1.051×10^{2}	K
	Second scaling term	$b_{2,1}$	8.527×10^{-3}	$\mathrm{W\,mm^{-1}\,K^{-1}}$
	Second numerator term	$b_{2,2}$	3.717×10^{2}	K
	Second denominator term	$b_{2,3}$	1.357×10^{2}	K
	Third scaling term	$b_{3,1}$	2.091×10^{-4}	$\mathrm{W\,mm^{-1}\,K^{-1}}$
	Third numerator term	$b_{3,2}$	5.916×10^{2}	K
	Third denominator term	$b_{3,3}$	1.518×10^{1}	K
	Fourth scaling term	$b_{4,1}$	1.888×10^{-2}	$\mathrm{W\,mm^{-1}\,K^{-1}}$
	Fourth numerator term	$b_{4,2}$	5.389×10^{2}	K
	Fourth denominator term	$b_{4,3}$	3.266×10^{2}	K

Table 3.2: Values for the convective heat transfer coefficients h_c^{air} and h_c^{gun}, the emissivity ε and the Stefan-Boltzmann constant σ.

Description	Symbol	Value	Unit
Film condition coefficient of air	h_c^{air}	1.0×10^{-5}	$\mathrm{W\,mm^{-2}\,K^{-1}}$
Film condition coefficient of spray gun	h_c^{gun}	1.4×10^{-4}	$\mathrm{W\,mm^{-2}\,K^{-1}}$
Emissivity coefficient of gray radiator	ε	0.81	
Stefan-Boltzmann constant	σ	5.670×10^{-14}	$\mathrm{W\,mm^{-2}\,K^{-4}}$

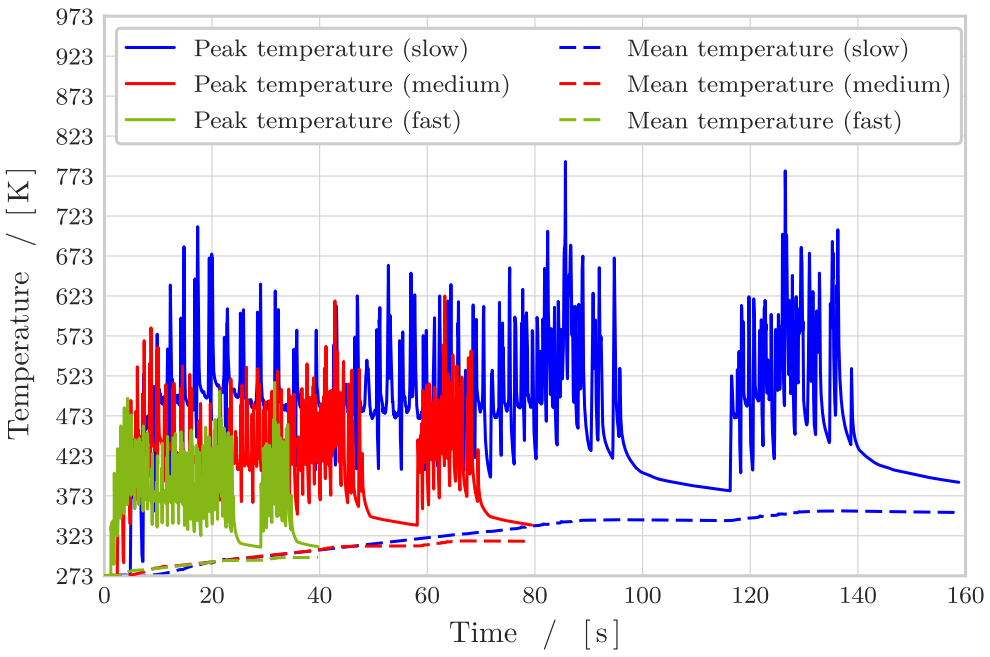

Figure 3.5: Simulated development of peak and mean workpiece temperature of the workpiece shown in Fig. 3.4. The temperatures are depicted for the three gun speed simulation runs.

areas represent zero thermal load. In other words, these grey parts represent positions of the spray gun where the spray cone does not intersect with the workpiece. The surface colours represent the surface temperature at different time steps for the medium gun speed simulation run.

The simulation keeps track of the volume-averaged temperature and the peak workpiece temperature both with respect to time to identify critical sections of the path, which may cause an overheating of the workpiece. Fig. 3.5 shows the simulated temperatures averaged over the entire workpiece volume and the peak temperature occurring in the workpiece – both plotted versus time – for the three gun speed simulation runs. The spraying process can be divided into four sections – compare Fig. 3.4: First, the spray gun aims at the front radius working its way up to the plain surface, which is then coated in circular arc movements from left to right and back. During this process, peak temperatures are reached when the gun approaches the border of the workpiece and turns around for the next arc in opposite direction. The fluctuations of the peak temperature curves are due to the gun leaving and entering the workpiece at the borders. The third and fourth distinguishable sections are the right and left border areas of the workpiece including the screw holes for mounting the part. At the beginning of these sections, the peak and average temperatures increase considerably, because the large screw holes provide a significantly larger surface area that is heated by the spray gun. Afterwards the temperatures drop again when the gun gradually leaves the workpiece area. It can be seen that, for the considered robot tool path, the slowest simulated gun

movement speed leads to the highest mean temperature of the workpiece as well as to the highest surface peak temperatures. The heat output to the environment through the surface is lower than the heat input by the spray gun.

4 Finite element simulation of coating-induced heat transfer: Application to thermal spraying processes

In the previous chapter, a finite element framework for a rigid-heat conductor for non-linear heat conduction was presented which is embedded, as a physics module, into a geometry based simulation framework for the planning of robot controlled thermal spray gun movement paths. As already stated, the geometry based simulation framework was developed as part of the research documented in Wiederkehr [190] and the combined framework represents joint work, [20]. Within this combined framework, a robot guided thermal spray gun path is pre-defined and discretised in time, whereby the spray gun is represented by a camera which observes the surface of the workpiece to be coated by means of a cone shaped display window. The projected intersection of the workpiece surface which is visible to the camera is interpreted as the area that is affected by the gun flame of the spray gun and is modelled to be subjected to heat input by the gun flame via radiation as well as enforced convection considered by film-condition type Robin boundary conditions. The remaining surface is subjected to natural convection such that the heated workpiece is quenched until the modelled workpiece reaches the ambient temperature after the modelled heat input was stopped. Thus, this extended framework thereby enables a realistic prediction of the heat input by the flame of a thermal spray gun which does not transport molten hard material to the surface of the considered workpiece.

Hence, an essential aspect of thermal spraying has so far not been included in the extended thermal spraying framework discussed in the previous chapter, namely the deposition of the hard material coating itself. However, the optimisation of the thermal spraying process with respect to temperature or temperature induced residual stress states requires a numerical framework for the simulation of the coating itself as well as of the quenching procedure after the application of additional material. Therefore, this chapter presents a novel approach for thermodynamical consistent modelling of mass deposition for a non-linear rigid heat conductor in the framework of continuous Galerkin

methods. The approach of handling the dynamic problem size within the finite element framework is highlighted with a focus on the thermodynamical consistency of the derived model. Since a continuous Galerkin method is applied, the temperature of newly added mass has to satisfy a continuous temperature distribution and no temperature jumps are allowed at a single distinct finite element node. We overcome this problem by the introduction of internal heat sources which shall ensure conservation of energy.

The following section describes the underlying equations of continuum thermodynamics by adopting the basics which are discussed in Section 2.3 of Chapter 2, extended for a domain which grows in the sense of mass which is added to the considered rigid heat conductor. The resulting finite element framework is subsequently described in Section 4.2. Section 4.3 presents academic numerical examples in order to show the capabilities of the developed framework, whereby the material parameters used are fitted to experimental data.

4.1 Continuum thermodynamical framework

From a continuum thermodynamics point of view, the underlying problem represents an open system where mass is deployed on the surface of a body $\mathcal{B}$. Thus, the configuration of the considered body may change with time t. Since temperature is the only physical field considered within the presented framework, we do not distinguish between reference placements $\boldsymbol{X}$ and current placements $\boldsymbol{x}$ in the context of continuum mechanics. Specifically speaking, we consider a rigid heat conductor as summarised in Box 2.3, but with a time dependent configuration that may expand by mass application.

The application of mass represents a special case within this thesis which is only accounted for in this chapter with respect to a rigid heat conductor and is therefore not discussed in the framework of large deformations in Section 2.3. Hence, some steps are adopted from Section 2.3 within this section and further extended according to the textbook of Hutter [85] with the simplification of non-moving placements $\boldsymbol{x}$. In analogy to Section 2.3, a global physical quantity $\mathcal{G}$ at time t is determined by

$$\mathcal{G}(t) = \int_{\mathcal{B}} \gamma(\boldsymbol{x}, t)\, \mathrm{d}v \;, \tag{4.1}$$

where $\gamma(\boldsymbol{x}, t)$ is the density of the respective quantity at $\boldsymbol{x}$ and t. The rate of $\mathcal{G}$ can be expressed as

$$\frac{\mathrm{d}\mathcal{G}}{\mathrm{d}t} = \frac{\mathrm{d}}{\mathrm{d}t} \int_{\mathcal{B}} \gamma(\boldsymbol{x}, t)\, \mathrm{d}v = \int_{\mathcal{B}} [\, \pi_\gamma(\boldsymbol{x}, t) + \sigma_\gamma(\boldsymbol{x}, t)\,]\, \mathrm{d}v - \int_{\partial\mathcal{B}} \boldsymbol{\phi}_\gamma(\boldsymbol{x}, t) \cdot \boldsymbol{n}\, \mathrm{d}a \;. \tag{4.2}$$

Here, π_γ denotes the production and σ_γ represents the supply of $\mathcal{G}$ within the body $\mathcal{B}$, whereas $\boldsymbol{\phi}_\gamma$ represents the flux of $\mathcal{G}$ via the surface $\partial\mathcal{B}$ of the body with surface normal $\boldsymbol{n}$,

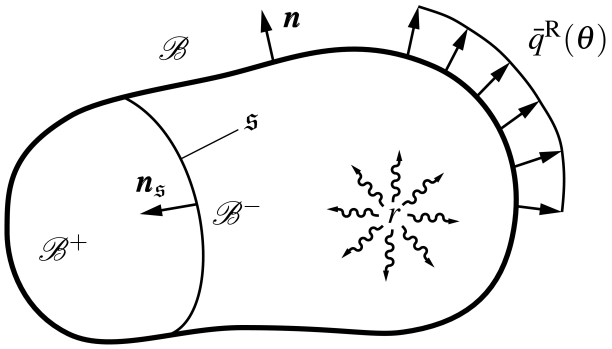

Figure 4.1: Body $\mathcal{B}$ divided into $\mathcal{B}^+$ and $\mathcal{B}^-$ by the singular surface $\mathfrak{s}$.

cf. Hutter [85]. So far, Eqs. (4.1) and (4.2) are analogous to Eqs. (2.64) and (2.68) but merely written in lower case letters which are not related to a current configuration since this differentiation, as already mentioned, is not necessary for a rigid heat conductor. Next, consider that the quantity $\mathcal{G}$ has a jump through a singular surface $\mathfrak{s}$ which divides the body $\mathcal{B}$ into $\mathcal{B}^+$ and $\mathcal{B}^-$ as illustrated in Fig. 4.1. Such a jump shall be denoted as $[\![\, \mathcal{G} \,]\!] := \mathcal{G}^+ - \mathcal{G}^-$. With this at hand, the change of $\mathcal{G}$ in time modifies Eq. (4.2) to

$$\begin{aligned}
\frac{\mathrm{d}\mathcal{G}}{\mathrm{d}t} &= \frac{\mathrm{d}}{\mathrm{d}t} \int\limits_{\mathcal{B}^+} \gamma(\boldsymbol{x},t)\,\mathrm{d}v + \frac{\mathrm{d}}{\mathrm{d}t} \int\limits_{\mathcal{B}^-} \gamma(\boldsymbol{x},t)\,\mathrm{d}v \\
&= \int\limits_{\mathcal{B}^+} \dot{\gamma}\,\mathrm{d}v - \int\limits_{\mathfrak{s}} \gamma^+\,\boldsymbol{w}^+ \cdot \boldsymbol{n}_{\mathfrak{s}}\,\mathrm{d}a + \int\limits_{\mathcal{B}^-} \dot{\gamma}\,\mathrm{d}v + \int\limits_{\mathfrak{s}} \gamma^-\,\boldsymbol{w}^- \cdot \boldsymbol{n}_{\mathfrak{s}}\,\mathrm{d}a \\
&= \int\limits_{\mathcal{B}} \dot{\gamma}\,\mathrm{d}v - \int\limits_{\mathfrak{s}} [\![\, \gamma\,\boldsymbol{w} \cdot \boldsymbol{n}_{\mathfrak{s}} \,]\!]\,\mathrm{d}a \;.
\end{aligned} \tag{4.3}$$

Within the above equation $\boldsymbol{w}$ denotes the interface velocity and $\boldsymbol{n}_{\mathfrak{s}}$ represents the singular surface normal which points from the "−"-side to the "+"-side. For the computation of the flux of a physical quantity g, surface $\partial\mathcal{B}$ is divided into positive $\partial\mathcal{B}^+ \cap \mathfrak{s}$ and negative $\partial\mathcal{B}^- \cap \mathfrak{s}$ parts. Application of the divergence theorem renders the flux relation

$$\int\limits_{\partial\mathcal{B}} \boldsymbol{\phi}_\gamma \cdot \boldsymbol{n}\,\mathrm{d}a = \int\limits_{\mathcal{B}^+} \nabla_{\boldsymbol{x}} \cdot \boldsymbol{\phi}_\gamma\,\mathrm{d}v + \int\limits_{\mathcal{B}^-} \nabla_{\boldsymbol{x}} \cdot \boldsymbol{\phi}_\gamma\,\mathrm{d}v + \int\limits_{\mathfrak{s}} [\![\, \boldsymbol{\phi}_\gamma \cdot \boldsymbol{n}_{\mathfrak{s}} \,]\!]\,\mathrm{d}a \;, \tag{4.4}$$

see Hutter [85]. In the case of vanishing production and supply terms within the singular surface, the general balance equation results in

$$\begin{aligned}\int_{\mathfrak{s}} [\![\, \gamma\, \boldsymbol{w}_{\mathfrak{s}} \cdot \boldsymbol{n}_{\mathfrak{s}} - \boldsymbol{\phi}_{\gamma} \cdot \boldsymbol{n}_{\mathfrak{s}} \,]\!]\, \mathrm{d}a = &\int_{\mathcal{B}^+} \left[\, \dot{\gamma} + \nabla_{\boldsymbol{x}} \cdot \boldsymbol{\phi}_{\gamma} - \pi_{\gamma} - \sigma_{\gamma} \,\right] \mathrm{d}v \\ &+ \int_{\mathcal{B}^-} \left[\, \dot{\gamma} + \nabla_{\boldsymbol{x}} \cdot \boldsymbol{\phi}_{\gamma} - \pi_{\gamma} - \sigma_{\gamma} \,\right] \mathrm{d}v \;.\end{aligned} \tag{4.5}$$

Consider a part of body $\mathcal{B}$ not containing the singular surface. Then the right hand side of the above equation vanishes and the equation reduces for each part, i.e. $\mathcal{B}^+$ and $\mathcal{B}^-$, to the local form

$$\dot{\gamma} + \nabla_{\boldsymbol{x}} \cdot \boldsymbol{\phi}_{\gamma} - \pi_{\gamma} - \sigma_{\gamma} = 0 \;. \tag{4.6}$$

On the singular surface, the left hand side of Eq. (4.5) vanishes and yields the local form

$$[\![\, \gamma\, \boldsymbol{w}_{\mathfrak{s}} - \boldsymbol{\phi}_{\gamma} \,]\!] \cdot \boldsymbol{n}_{\mathfrak{s}} = 0 \;. \tag{4.7}$$

This general representation of balance equation is next applied to different quantities of interest, such as mass and energy.

In view of the balance of mass, we use Eqs. (4.6) and (4.7) with $\gamma = \rho$, whereby ρ represents the mass density. Moreover, we assume $\pi_{\rho} = \sigma_{\rho} = 0$ and $\boldsymbol{\phi}_{\rho} = \boldsymbol{0}$, so that the above mentioned equations related to balance of mass read

$$\dot{\rho} = 0 \;, \tag{4.8}$$

$$[\![\, \rho\, \boldsymbol{w}_{\mathfrak{s}} \,]\!] \cdot \boldsymbol{n}_{\mathfrak{s}} = 0 \;, \tag{4.9}$$

whereby Eq. (4.8) coincides with Eq. (2.80).

Concerning the energy balance, Eqs. (4.6) and (4.7) include the internal energy $\gamma = \mathcal{E} = \rho\, e$, the supply of energy $\pi_{\mathcal{E}} = \rho\, r$ and the heat flux $\boldsymbol{\phi}_{\mathcal{E}} = \boldsymbol{q}$, cf. Section 2.3.3. Moreover, the kinetic part of the energy as well as surface tractions are neglected in the framework of a rigid heat conductor. Inserting these relations into the general representation of balance equations as well as taking into account the mass conservation Eq. (4.8) yields the local balance of energy as

$$\rho\, \dot{e} = \rho\, r - \nabla_{\boldsymbol{x}} \cdot \boldsymbol{q} \;, \tag{4.10}$$

$$[\![\, \rho\, e\, \boldsymbol{w}_{\mathfrak{s}} - \boldsymbol{q} \,]\!] \cdot \boldsymbol{n}_{\mathfrak{s}} = 0 \,. \tag{4.11}$$

Finally, the balance of entropy has to be taken into account. Application of Eqs. (4.6) and (4.7) now include the entropy $\gamma = \rho\, s$, the production of entropy $\pi_s = \mathcal{D} \geq 0$, the entropy supply $\sigma_s = \rho\, r/\theta$ as well as that the entropy flux $\boldsymbol{\phi}_s = \boldsymbol{q}/\theta$, cf. Section 2.3.4. Here, it is assumed that the entropy supply is proportional to the supply of energy ρr and the entropy flux is proportional to the heat flux $\boldsymbol{q}$ which is in line with Coleman and Noll [40]. For an outline on a different choice of the entropy flux the interested reader is referred to the text books of Müller [121] and Liu [108], as well as to the references cited therein. In the present framework, the local form of entropy balance and entropy jump then read

$$\rho\, \dot{s} + \nabla_{\boldsymbol{x}} \cdot \left(\frac{\boldsymbol{q}}{\theta} \right) - \frac{\rho\, r}{\theta} = \mathcal{D} \geq 0 \,, \tag{4.12}$$

$$\left[\!\!\left[\rho\, s\, \boldsymbol{w}_{\mathfrak{s}} - \frac{\boldsymbol{q}}{\theta} \right]\!\!\right] \cdot \boldsymbol{n}_{\mathfrak{s}} = -\mathfrak{p}_{\mathfrak{s}} \leq 0 \,, \tag{4.13}$$

where Eq. (4.12) coincides with Eq. (2.86) and where $\mathfrak{p}_{\mathfrak{s}}$ is the surface production of entropy within the singular surface according to Hutter [85].

In the special case of a time dependent configuration $\boldsymbol{x}(t)$ of a rigid heat conductor, the interface velocities $\boldsymbol{w}_{\mathfrak{s}}^{+} = \boldsymbol{w}_{\mathfrak{s}}^{-} = \boldsymbol{w}_{\mathfrak{s}} = \boldsymbol{0}$ vanish such that the jump conditions, Eqs. (4.9) and (4.11), are trivially fulfilled. It is furthermore assumed that no entropy is produced within the singular surface, i.e. $\mathfrak{p}_{\mathfrak{s}} = 0$, such that the set of balance equations reduces to the same balance equations as in Chapter 3.

As outlined in Section 2.3.4, Eq. (4.12) reduces to the the Fourier's inequality, cf. Eq. (2.86), which is fulfilled by Fourier's law

$$\boldsymbol{q} = -\boldsymbol{\Lambda}(\theta) \cdot \nabla_{\boldsymbol{x}}\, \theta \,. \tag{4.14}$$

In the above equation, $\boldsymbol{\Lambda}(\theta)$ is the temperature dependent positive semi-definite thermal conductivity tensor, [108]. The energy balance, Eq. (4.11), can be formulated in form of the heat equation

$$c(\theta)\, \dot{\theta} = \rho\, r - \nabla_{\boldsymbol{x}} \cdot [\, -\boldsymbol{\Lambda}(\theta) \cdot \nabla_{\boldsymbol{x}}\, \theta \,] \,, \tag{4.15}$$

where $c(\theta) = \rho\, \partial e/\partial \theta \geq 0$ is the temperature dependent heat capacity and where Eq. (4.14) is inserted.

Solutions of (4.15) are automatically thermodynamical consistent as long as the restrictions for $c(\theta)$ and $\boldsymbol{\Lambda}(\theta)$ are satisfied. The considered initial boundary value problem requires the definition of an initial state of the body $\mathcal{B}$ and the definition of proper

boundary conditions on $\partial\mathcal{B}$. Throughout this work, the only boundary conditions to be applied are adiabatic or Robin type boundary conditions, i.e.

$$\begin{aligned} -\boldsymbol{q}\cdot\boldsymbol{n} &= 0 \qquad\quad \text{on} \quad \partial\mathcal{B}\,, \\ -\boldsymbol{q}\cdot\boldsymbol{n} &= \bar{q}^{\mathrm{R}}(\theta) \quad \text{on} \quad \partial\mathcal{B} = \partial\mathcal{B}^{\mathrm{R}}\,, \end{aligned} \tag{4.16}$$

which are related the heat flux $\boldsymbol{q}$ on $\partial\mathcal{B} = \partial\mathcal{B}^{\mathrm{R}}$.

4.2 Finite element implementation

In order to solve the balance of energy by means of the finite element method, the strong form given by Eq. (4.15) must be reformulated in weak form. Therefore, the energy balance is written in residual form, multiplied by the virtual temperature $\delta\theta$ as a test function and integrated over the volume of the body $\mathcal{B}$, i.e.

$$0 = \int_{\mathcal{B}} \delta\theta \left[c(\theta)\,\dot{\theta} + \nabla_{\boldsymbol{x}}\cdot\left[\,-\boldsymbol{\Lambda}(\theta)\cdot\nabla_{\boldsymbol{x}}\,\theta\,\right] - \rho\, r \right] \mathrm{d}v\,. \tag{4.17}$$

The application of the divergence theorem and the use of Eqs. (4.14) and (4.16) leads to

$$0 = \int_{\mathcal{B}} \delta\theta\, c(\theta)\,\dot{\theta}\,\mathrm{d}v - \int_{\partial\mathcal{B}^{\mathrm{R}}} \delta\theta\,\bar{q}^{\mathrm{R}}(\theta)\,\mathrm{d}a + \int_{\mathcal{B}} \nabla_{\boldsymbol{x}}\,\delta\theta\cdot\boldsymbol{\Lambda}(\theta)\cdot\nabla_{\boldsymbol{x}}\,\theta\,\mathrm{d}v - \int_{\mathcal{B}} \delta\theta\,\rho\, r\,\mathrm{d}v\,. \tag{4.18}$$

The different terms in the above equation can be interpreted as dynamic, volume, internal and surface contributions,

$$\begin{aligned} \mathrm{w}_{\mathrm{dyn}} &= \int_{\mathcal{B}} \delta\theta\, c(\theta)\,\dot{\theta}\,\mathrm{d}v\,, & \mathrm{w}_{\mathrm{vol}} &= \int_{\mathcal{B}} \delta\theta\,\rho\, r\,\mathrm{d}v\,, \\ \mathrm{w}_{\mathrm{int}} &= \int_{\mathcal{B}} \nabla_{\boldsymbol{x}}(\delta\theta)\cdot\boldsymbol{\Lambda}(\theta)\cdot\nabla_{\boldsymbol{x}}\,\theta\,\mathrm{d}v\,, & \mathrm{w}_{\mathrm{sur}} &= \int_{\partial\mathcal{B}^{\mathrm{R}}} \delta\theta\,\bar{q}^{\mathrm{R}}(\theta)\,\mathrm{d}a\,, \end{aligned} \tag{4.19}$$

such that Eq. (4.18) can be rewritten as

$$0 = \mathrm{w}_{\mathrm{dyn}} + \mathrm{w}_{\mathrm{int}} - \mathrm{w}_{\mathrm{vol}} - \mathrm{w}_{\mathrm{sur}}\,. \tag{4.20}$$

In this form, the heat equation is basically suitable for the solution by means of the finite element method. Since Robin boundary conditions represent a kind of temperature dependent load, not only the considered body $\mathcal{B}$ but also the Robin boundary $\partial\mathcal{B}^{\mathrm{R}}$ must be discretised, see e.g. Lewis et al. [107] or Bonet and Wood [29] with application to

deformation dependent loads such as pressure. Therefore, a finite number of $n_{\mathrm{el}}^{\mathcal{B}}$ volume elements $\mathcal{B}_{\mathcal{B}}^{e}$ as well as a finite number of $n_{\mathrm{el}}^{\partial\mathcal{B}^{\mathrm{R}}}$ Robin boundary elements $\mathcal{B}_{\partial\mathcal{B}^{\mathrm{R}}}^{e}$,

$$\mathcal{B} \approx \mathcal{B}^{h} = \bigcup_{e=1}^{n_{\mathrm{el}}^{\mathcal{B}}} \mathcal{B}_{\mathcal{B}}^{e} \,, \qquad \partial\mathcal{B}^{\mathrm{R}} \approx \partial\mathcal{B}^{\mathrm{R}\,h} = \bigcup_{e=1}^{n_{\mathrm{el}}^{\partial\mathcal{B}^{\mathrm{R}}}} \mathcal{B}_{\partial\mathcal{B}^{\mathrm{R}}}^{e} \,, \tag{4.21}$$

approximate the body $\mathcal{B}$ and the Robin boundary $\partial\mathcal{B}^{\mathrm{R}}$. Eq. (4.20) can be rewritten as the sum over all element integrals

$$\mathrm{w} \approx \mathrm{w}^{h} = \sum_{e=1}^{n_{\mathrm{el}}^{\mathcal{B}}} \left[\mathrm{w}_{\mathrm{dyn}}^{e} + \mathrm{w}_{\mathrm{int}}^{e} - \mathrm{w}_{\mathrm{vol}}^{e} \right] - \sum_{e=1}^{n_{\mathrm{el}}^{\partial\mathcal{B}^{\mathrm{R}}}} \left[\mathrm{w}_{\mathrm{sur}}^{e} \right] \,. \tag{4.22}$$

By application of isoparametric finite elements, the spatial discretisation of the node positions $\boldsymbol{x}^{h} \approx \boldsymbol{x}$ as well as the dicretisation of the temperature $\theta^{h} \approx \theta$ and the virtual temperature $\delta\theta^{h} \approx \delta\theta$ is carried out by the same set of shape functions $N_{\boldsymbol{x},\,\mathcal{B}}^{i}$ respectively $N_{\boldsymbol{x},\,\partial\mathcal{B}^{\mathrm{R}}}^{j}$ for $i = 1, ..., n_{\mathrm{en}}^{\mathcal{B}}$ volume element nodes and $j = 1, ..., n_{\mathrm{en}}^{\partial\mathcal{B}^{\mathrm{R}}}$ boundary element nodes, i.e.

$$\begin{aligned}
\boldsymbol{x}_{\mathcal{B}}^{h} &= \bigcup_{i=1}^{n_{\mathrm{en}}^{\mathcal{B}}} N_{\boldsymbol{x},\,\mathcal{B}}^{i}\, \boldsymbol{x}_{i} \,, & \boldsymbol{x}_{\partial\mathcal{B}^{\mathrm{R}}}^{h} &= \bigcup_{j=1}^{n_{\mathrm{en}}^{\partial\mathcal{B}^{\mathrm{R}}}} N_{\boldsymbol{x},\,\partial\mathcal{B}^{\mathrm{R}}}^{j}\, \boldsymbol{x}_{j} \,, \\
\theta_{\mathcal{B}}^{h} &= \bigcup_{i=1}^{n_{\mathrm{en}}^{\mathcal{B}}} N_{\boldsymbol{x},\,\mathcal{B}}^{i}\, \theta_{i} \,, & \theta_{\partial\mathcal{B}^{\mathrm{R}}}^{h} &= \bigcup_{j=1}^{n_{\mathrm{en}}^{\partial\mathcal{B}^{\mathrm{R}}}} N_{\boldsymbol{x},\,\partial\mathcal{B}^{\mathrm{R}}}^{j}\, \theta_{j} \,, \\
\delta\theta_{\mathcal{B}}^{h} &= \bigcup_{i=1}^{n_{\mathrm{en}}^{\mathcal{B}}} N_{\boldsymbol{x},\,\mathcal{B}}^{i}\, \delta\theta_{i} \,, & \delta\theta_{\partial\mathcal{B}^{\mathrm{R}}}^{h} &= \bigcup_{j=1}^{n_{\mathrm{en}}^{\partial\mathcal{B}^{\mathrm{R}}}} N_{\boldsymbol{x},\,\partial\mathcal{B}^{\mathrm{R}}}^{j}\, \delta\theta_{j} \,.
\end{aligned} \tag{4.23}$$

Accordingly, the approximations of the gradients $\nabla_{\boldsymbol{x}}\, \boldsymbol{x} \approx \nabla_{\boldsymbol{x}}\, \boldsymbol{x}^{h}$, $\nabla_{\boldsymbol{x}}\, \theta \approx \nabla_{\boldsymbol{x}}\, \theta^{h}$ and $\nabla_{\boldsymbol{x}}\, \delta\theta \approx \nabla_{\boldsymbol{x}}\, \delta\theta^{h}$ are discretised.

The last level of discretisation of the problem is the time discretisation of Eq. $(4.19)_1$. The current state of the implementation of the presented framework makes use of the Backward Euler time integration scheme which reads

$$\dot{\theta} = \frac{\theta_{n+1} - \theta_{n}}{\Delta t} \,, \tag{4.24}$$

for the temperature with $\Delta t = t_{n+1} - t_n > 0$. The system of nonlinear equations is to be solved at each discrete time step finally reads

$$\begin{aligned}\mathbf{w}^{h\Delta t} = &\mathop{\mathbf{A}}_{e=1}^{n_{\mathrm{el}}^{\mathcal{B}}} \Big[\sum_{i=1}^{n_{\mathrm{en}}^{\mathcal{B}}} \Big[\int_{\mathcal{B}_{\mathcal{B}}^e} N_{\boldsymbol{x},\mathcal{B}}^i \, c(\theta) \, \frac{\theta_{n+1} - \theta_n}{\Delta t} \, \mathrm{d}v - \int_{\mathcal{B}_{\mathcal{B}}^e} N_{\boldsymbol{x},\mathcal{B}}^i \, \rho \, r \, \mathrm{d}v \\ &+ \int_{\mathcal{B}_{\mathcal{B}}^e} \nabla_{\boldsymbol{x}} \, N_{\boldsymbol{x},\mathcal{B}}^i \cdot \boldsymbol{\Lambda}(\theta) \cdot \nabla_{\boldsymbol{x}} \, \theta \, \mathrm{d}v \Big] \Big] \\ &- \mathop{\mathbf{A}}_{e=1}^{n_{\mathrm{el}}^{\partial\mathcal{B}^{\mathrm{R}}}} \Big[\sum_{j=1}^{n_{\mathrm{en}}^{\partial\mathcal{B}^{\mathrm{R}}}} \Big[\int_{\partial\mathcal{B}^{\mathrm{R}}} N_{\boldsymbol{x},\partial\mathcal{B}^{\mathrm{R}}}^j \, \bar{q}^{\mathrm{R}}(\theta) \, \mathrm{d}a \Big] \Big] \, . \end{aligned} \tag{4.25}$$

In the above relation $\mathbf{w}^{h\Delta t}$ is an algebraic vector which depends on the nodal temperatures $\boldsymbol{\theta}_{n+1}$ and $\boldsymbol{\theta}_n$. The dimension of these vectors is $[\, n_{\mathrm{np}} \times 1 \,]$ where n_{np} is the number of the (current) global node points. Symbol $\mathbf{A}$ in Eq. (4.25) represents the assembly operator over all $e = 1, ..., n_{\mathrm{el}}^{\partial\mathcal{B}}$ volume elements and all $e = 1, ..., n_{\mathrm{el}}^{\partial\mathcal{B}^{\mathrm{R}}}$ boundary elements. Equation $\mathbf{w}^{h\Delta t}(\boldsymbol{\theta}_{n+1}, \boldsymbol{\theta}_n) = \mathbf{0}$ is solved by means of a Newton-Raphson scheme, Chapter 3, so that the update of the nodal temperatures at the current time step $\Delta\boldsymbol{\theta}$ is calculated via

$$\underline{\underline{\mathbf{K}}}^{h\Delta t}(\boldsymbol{\theta}_{n+1}, \boldsymbol{\theta}_n) \cdot \Delta\boldsymbol{\theta} = -\mathbf{w}^{h\Delta t}(\boldsymbol{\theta}_{n+1}, \boldsymbol{\theta}_n) \, . \tag{4.26}$$

In the above equation, $\underline{\underline{\mathbf{K}}}^{h\Delta t}(\boldsymbol{\theta}_{n+1}, \boldsymbol{\theta}_n)$ represents the tangent matrix which is the derivative of the algebraic residual $\mathbf{w}^{h\Delta t}$ with respect to the current nodal temperatures $\boldsymbol{\theta}_{n+1}$,

$$\begin{aligned}\underline{\underline{\mathbf{K}}}^{h\Delta t}(\boldsymbol{\theta}_{n+1}, \boldsymbol{\theta}_n) &= \frac{\partial \mathbf{w}^{h\Delta t}(\boldsymbol{\theta}_{n+1}, \boldsymbol{\theta}_n)}{\partial \boldsymbol{\theta}_{n+1}} \\ &= \mathop{\mathbf{A}}_{e=1}^{n_{\mathrm{el}}^{\mathcal{B}}} \Big[\sum_{i=1}^{n_{\mathrm{en}}^{\mathcal{B}}} \sum_{j=1}^{n_{\mathrm{en}}^{\mathcal{B}}} \Big[\int_{\mathcal{B}_{\mathcal{B}}^e} N_{\boldsymbol{x},\mathcal{B}}^i \Big[\frac{c(\theta)}{\Delta t} + \frac{\partial c(\theta)}{\partial \theta} \frac{\theta_{n+1} - \theta_n}{\Delta t} \Big] N_{\boldsymbol{x},\mathcal{B}}^j \, \mathrm{d}v \\ &\quad + \int_{\mathcal{B}_{\mathcal{B}}^e} \nabla_{\boldsymbol{x}} \, N_{\boldsymbol{x},\mathcal{B}}^i \cdot \boldsymbol{\Lambda}(\theta) \cdot \nabla_{\boldsymbol{x}} \, N_{\boldsymbol{x},\mathcal{B}}^j \, \mathrm{d}v + \int_{\mathcal{B}_{\mathcal{B}}^e} \nabla_{\boldsymbol{x}} \, N_{\boldsymbol{x},\mathcal{B}}^i \, \frac{\partial \boldsymbol{\kappa}(\theta)}{\partial \theta} \, \nabla_{\boldsymbol{x}} \, \theta^j \, \mathrm{d}v \Big] \Big] \\ &\quad - \mathop{\mathbf{A}}_{e=1}^{n_{\mathrm{el}}^{\partial\mathcal{B}^{\mathrm{R}}}} \Big[\sum_{k=1}^{n_{\mathrm{en}}^{\partial\mathcal{B}^{\mathrm{R}}}} \sum_{l=1}^{n_{\mathrm{en}}^{\partial\mathcal{B}^{\mathrm{R}}}} \Big[\int_{\partial\mathcal{B}^{\mathrm{R}}} N_{\boldsymbol{x},\partial\mathcal{B}^{\mathrm{R}}}^k \, \frac{\partial \bar{q}^{\mathrm{R}}(\theta)}{\partial \theta} \, N_{\boldsymbol{x},\partial\mathcal{B}^{\mathrm{R}}}^l \, \mathrm{d}a \Big] \Big] \, . \end{aligned} \tag{4.27}$$

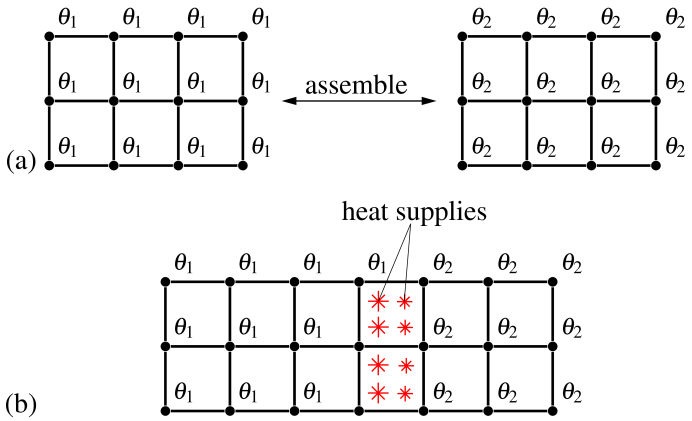

Figure 4.2: (a) Configuration of elements with different temperatures before the connection. (b) Configuration of the elements after the connection.

Compared to standard finite element implementations, a crucial detail of the presented framework is that the configuration $\boldsymbol{x}(t)$ changes with time because of mass application such that $n_{\mathrm{np}} \neq \text{const}$. This means that an existing discretisation $(\,\mathcal{B}^{h\Delta t}, \partial\mathcal{B}^{\mathrm{R}\,h\Delta t}\,)_n$ at a discrete time step t_n has to be updated to a discretisation $(\,\mathcal{B}^{h\Delta t}, \partial\mathcal{B}^{\mathrm{R}\,h\Delta t}\,)_{n+1}$ at time step t_{n+1} if the configuration has changed in that particular time step. In the particular case of adding particles with coating temperature θ_{coat} on a surface which possesses a different temperature, a method for the numerical treatment of the connection procedure must be chosen. At first, we assume that the total amount of stored energy within the existing body and the particles to be added to that body does not change by any dissipation effects during the deposition of the particles on the body's surface. Thus, the energy of an adiabatic system has to remain conserved by the assembly process.

As already mentioned in the introduction, several options exist in order to handle the extension of an existing mesh of finite elements by additional finite elements. One possibility is the application of discontinuous Galerkin methods, Baumann and Oden [12], Engel et al. [50], Hu et al. [82]. Another possibility is the use of interface elements, Fagerstrom and Larsson [52], Fleischhauer et al. [56], Steinmann and Häsner [165], Utzinger et al. [183]. In contrast, the spirit of our current approach is to use continuous volume elements for the body and to use surface elements to capture the Robin boundary conditions. As a consequence, existing elements and added elements share connectivity nodes. However, existing nodes have a defined temperature which results from the solution path up to the moment of connecting new elements to existing elements. We resolve that problem by fixing the temperature value of each existing node that is occupied by a new element which can, of course, have a different temperature than the temperature of the newly connected existing node. Thus, in general, the energy

conservation is violated by a change of the total thermal energy of an element which is computed by the expression

$$E^e = \int_{\mathcal{B}^e} \int_{\theta_0}^{\theta^e} c(\theta)\, \mathrm{d}\theta\, \mathrm{d}v \;, \tag{4.28}$$

wherein θ_0 represents the reference temperature and where θ^e is the temperature of the element. This is illustrated by Fig. 4.2, where elements with different temperature distributions are connected. As depicted, an energy source is introduced in order to conserve the energy. In each added element that shares one or more nodes with previously existing elements, an energy difference, $\Delta E^e_* = E^e - E^e_*$, occurs after its connection. This energy difference must be induced into the system in order to compensate the error in total thermal energy such that thermodynamical consistency is ensured. For this reason a heat supply term

$$\begin{aligned} \int_{\mathcal{B}^e} \frac{\rho\, r}{\Delta t}\, \mathrm{d}v \doteq \Delta E^e_* = E^e - E^e_* &= \int_{\mathcal{B}^e} \left[\int_{\theta_0}^{\theta^e} c(\theta)\, \mathrm{d}\theta - \int_{\theta_0}^{\theta^e_*} c(\theta)\, \mathrm{d}\theta \right] \mathrm{d}v \\ &= \int_{\mathcal{B}^e} \int_{\theta^e_*}^{\theta^e} c(\theta)\, \mathrm{d}\theta\, \mathrm{d}v \end{aligned} \tag{4.29}$$

is introduced which is taken into account within the heat supply contribution of Eq. (4.15) or rather in its weak form Eq. (4.19), respectively the discritised weak form Eq. (4.25). In Eq. (4.29), θ^e_* is the temperature of an element after the assembling of elements and θ^e is the temperature before assembling. In the case of "old" elements, $\theta^e_* = \theta^e$ holds true such that no heat supply term is induced. In the case of "new" elements $\theta^e_* \neq \theta^e$ may occur such that a heat supply term is induced in the particular time step.

The solution procedure of the developed framework is not standard. Algorithm 4.1 provides a flow chart of the related finite element implementation. In each time step it is checked whether the configuration remains constant or not. Thus, in the first time step or if new elements are added, volume elements and surface elements are identified and the global system is either initialised (first time step) or reorganised. If new degrees of freedom are introduced, the values of the new degrees of freedom are set to the temperature θ_{coat} of the newly connected mass. With an updated configuration, the Newton-Raphson solution algorithm is applied in order to obtain a solution of the nonlinear system of equations.

Algorithm 4.1: Flow chart of the finite element framework.

initialisation of boundary value problem

time loop

while $t < t_{\max}$ **do**

  if *new elements are introduced* **then**

    identify new volume elements

    identify new surface elements

    modify $n_{\mathrm{el}}^{\mathcal{B}}$ and $n_{\mathrm{el}}^{\partial\mathcal{B}}$

    reorganisation of global system of equations

    set new degrees of freedom to θ_{coat}

  end

  Newton-Raphson loop

  while $\|\underline{\mathbf{r}}\| \geq tol$ **do**

    loop over volume elements

    for $e = 1, ..., n_{\mathrm{el}}^{\mathcal{B}}$ **do**

      volume element level computations

    end

    loop over surface elements

    for $se = 1, ..., n_{\mathrm{el}}^{\partial\mathcal{B}}$ **do**

      surface element level computations

    end

    assemble system of equations

    solve system of equations

  end

  postprocessing of current time step

  increase time step

  $t \leftarrow t + \Delta t$

end

4.3 Numerical examples

The proposed framework is applied to the simulation of initial boundary values problems in order to show the capabilities of the developed finite element software tool. For this purpose, the coating of an existing body with an initial temperature of $\theta_{\text{init}} = 293.15\,\text{K}$ is simulated. The temperature of the hot particles is assumed as $\theta_{\text{coat}} = 1873.15\,\text{K}$ which is in good agreement with particle temperatures during the HVOF thermal spraying process, [71]. Some of the examples include the use of the aforementioned adiabatic boundaries, Eq. $(4.16)_1$, whereas in the other examples Robin boundary conditions, Eq. $(4.16)_2$, are involved.

Two different mechanisms are modelled with the help of Robin boundary conditions. The first mechanism is convection which is captured by a film condition

$$\bar{q}_c^{\,\text{R}} = -\,h_c\,[\theta - \theta_\infty]\;. \tag{4.30}$$

In the above equation, h_c is the film condition coefficient, θ_∞ represents the environmental temperature and θ is the temperature of the modelled surface. Such boundary conditions are different for the case of an accelerated gun flame as they are for the case of quasi non-moving surrounding air. In order to capture this difference, h_c^{gun} and h_c^{air} are chosen differently as given in Table 4.1.

The second mechanism is radiation which is modelled by the expression

$$\bar{q}_r^{\,\text{R}} = -\,\varepsilon\,\sigma\,\left[\theta^4 - {\theta_\infty}^4\right]\;, \tag{4.31}$$

wherein σ denotes the Stefan Boltzmann constant and where ε is the emissivity which is chosen to model a grey body. The values chosen are summarised in Table 4.1. Note, that radiation inherently leads to a nonlinearity and therefore must be taken into account within the consistent linearisation of the finite element framework.

The heat conduction tensor is assumed to be isotropic

$$\boldsymbol{\Lambda}(\theta) = \Lambda(\theta)\,\boldsymbol{I}\;, \tag{4.32}$$

where $\Lambda(\theta)$ is the heat conduction coefficient and where $\boldsymbol{I}$ represents the second order identity. In order to capture the non-linear temperature dependency of the heat capacity as well as the heat conduction coefficient, the same type of function

$$c(\vartheta) = \rho\,\left[\,a_0 + a_1\,\arctan\left(a_2 + a_3\,\vartheta\right)\right] \tag{4.33}$$

$$\Lambda(\vartheta) = b_0 + b_1\,\arctan\left(b_2 + b_3\,\vartheta\right) \tag{4.34}$$

in dependence of the temperature ϑ in °C is chosen and fitted to experimental data for both steel and WC-Co, Delfosse et al. [46], Hussainova et al. [84], Toparli et al. [180]. A summary of the parameters fitted is given in Table 4.2. For the purpose of illustration,

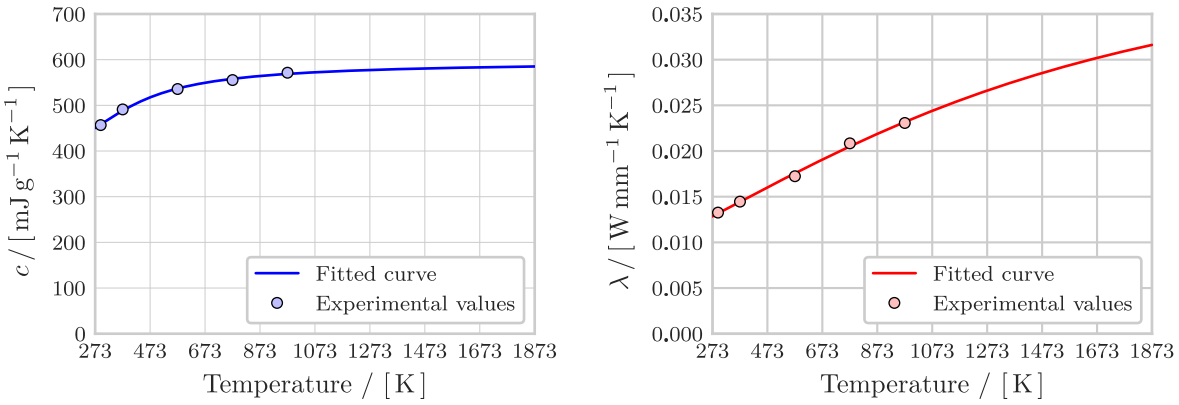

(a) Heat capacity of steel $c^{\mathrm{S}}(\vartheta)$.

(b) Heat conduction coefficient of steel $\Lambda^{\mathrm{S}}(\vartheta)$.

Figure 4.3: (a) Fitted curve of the heat capacity of steel $c^{\mathrm{S}}(\vartheta)$. (b) Fitted curve of the heat conduction coefficient of steel $\Lambda^{\mathrm{S}}(\vartheta)$. The values are taken from Delfosse et al. [46], Hussainova et al. [84], Nomura et al. [126], Toparli et al. [180].

Table 4.1: Values for the convective heat transfer coefficients h_c^{air} and h_c^{gun}, the emissivity ε, the Stefan-Boltzmann constant σ and the mass densities of steel ρ^{S} as well as of WC-Co ρ^{C}.

Description	Symbol	Value	Unit
Film condition coefficient of air	h_c^{air}	1.0×10^{-5}	$\mathrm{W\,mm^{-2}\,K^{-1}}$
Film condition coefficient of spray gun	h_c^{gun}	1.4×10^{-4}	$\mathrm{W\,mm^{-2}\,K^{-1}}$
Emissivity coefficient of gray radiator	ε	0.81	
Stefan-Boltzmann constant	σ	5.670×10^{-14}	$\mathrm{W\,mm^{-2}\,K^{-4}}$
Mass density of steel	ρ^{S}	8.031×10^{-3}	$\mathrm{g\,mm^{-3}}$
Mass density of WC-Co	ρ^{C}	1.390×10^{-2}	$\mathrm{g\,mm^{-3}}$

the resulting functions are plotted with respect to the K-scale, whereby Fig. 4.2 refers to steel and Fig. 4.3 to WC-Co.

Some of the example simulations are carried out with constant values of the heat capacity as well as of the heat conduction coefficient. In these cases, the functions are evaluated at 293.15 K (20 °C).

4.3.1 Two-element simulations – 2d

A simple academic example to demonstrate the applicability of the developed framework is based on one element with a homogeneous initial temperature θ_1 that is assembled to another element with a homogeneous temperature $\theta_2 \neq \theta_1$. The elements can represent either the same material or different materials. In total, four different scenarios are simulated. The first and second examples involve two elements, the underlying

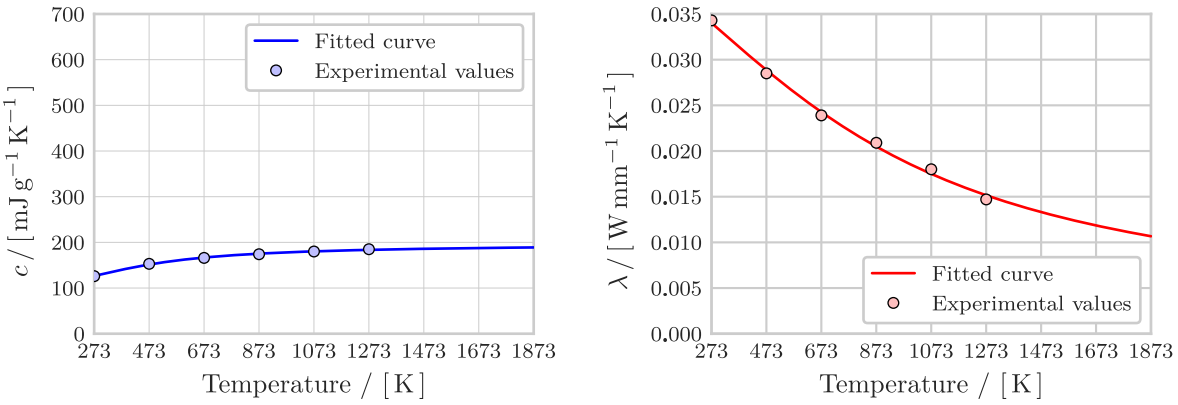

(a) Heat capacity of WC-Co $c^{\mathrm{C}}(\vartheta)$.

(b) Heat conduction coefficient of WC-Co $\Lambda^{\mathrm{C}}(\vartheta)$.

Figure 4.4: (a) Fitted curve of the heat capacity of WC-Co $c^{\mathrm{C}}(\vartheta)$. (b) Fitted curve of the heat conduction coefficient of WC-Co $\Lambda^{\mathrm{C}}(\vartheta)$. The values are taken from Delfosse et al. [46], Hussainova et al. [84], Nomura et al. [126], Toparli et al. [180].

material of which refer to steel. Within the first example, c^{S} and Λ^{S} are chosen to be constant, whereas for the second example c^{S} and Λ^{S} are temperature dependent as given by Eqs. (4.33) and (4.34). The third and fourth examples each involve one steel-related element with θ_1 and one WC-Co-related element with θ_2. Analogously, c^{S} and Λ^{S} as well as c^{C} and Λ^{C} are constant within the third example and temperature dependent within the fourth example. For all four examples, an adiabatic boundary is modelled and the temperatures are set to $\theta_1 = 293.15\,\mathrm{K}$ and $\theta_2 = 1873.15\,\mathrm{K}$. The examples are carried out in two dimensional space with four-noded bilinear elements of $1\,\mathrm{mm}^2$ size. The simulations start at time $t = 0$ and end at time $t = 5000\,\mathrm{ms}$. The second element is assembled to the first at $t = 1000\,\mathrm{ms}$. Furthermore, each of the four examples are simulated with two different time step sizes, namely $\Delta t = 10\,\mathrm{ms}$ and $\Delta t = 100\,\mathrm{ms}$.

The results of the first two-element example are depicted in Fig. 4.5. The energy of the system versus time is shown in Fig. 4.5(a). Evaluation of Eq. (4.28) gives the total energy of the system before, denoted as “Analytical (low)”, and after, referred to as “Analytical (high)”, the element assembly as analytic values. It can be seen that the stored energy which is computed by the finite element programme exactly reaches these values for both time step sizes. Fig. 4.5(b) shows the maximum and minimum temperatures for both time step sizes versus time and, additionally, the analytically determined temperature value for $t \to \infty$. It is obvious that for both time step sizes the analytical temperature is computed by the finite element code for $t \geq 1800\,\mathrm{ms}$. At time step $t = 1000\,\mathrm{ms}$ the simulation run with the $\Delta t = 10\,\mathrm{ms}$ shows an underestimation of the lowest possible temperature and an overestimation of the highest possible temperature – there is no physical reason for $\theta_{\min} \leq 293\,\mathrm{K}$ or $\theta_{\max} \geq 1873\,\mathrm{K}$. For the larger time step size, neither underestimation nor overestimation are observed. In Fig. 4.5(c) temperature plots of the one element before assembly and the two elements after assembly at specific time steps are depicted. As additional information, the minimum and maximum value of the

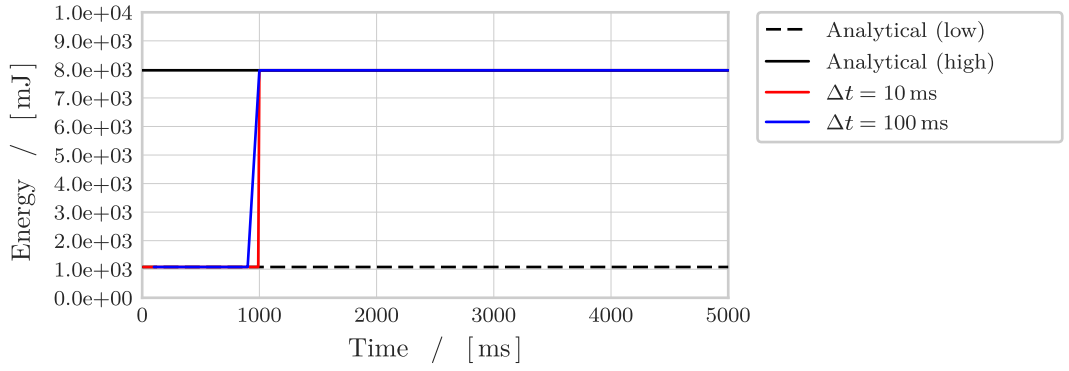

(a) Total thermal energy versus time of two assembled steel elements.

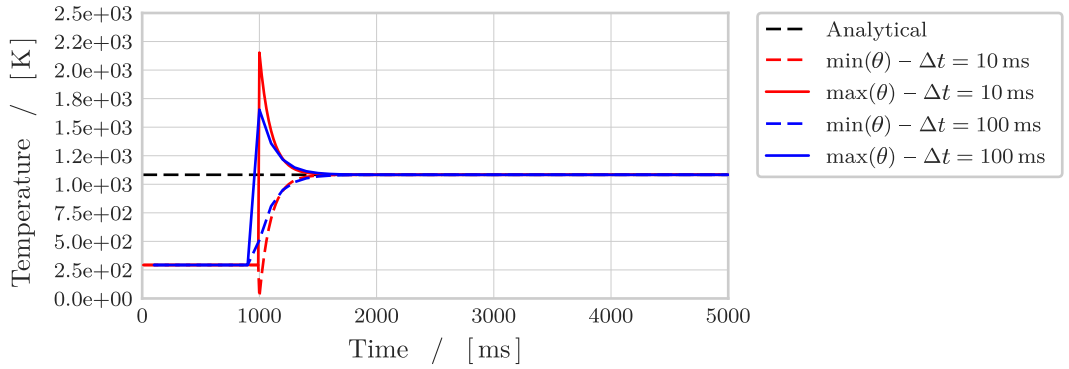

(b) Maximum and minimum values of the temperature versus time.

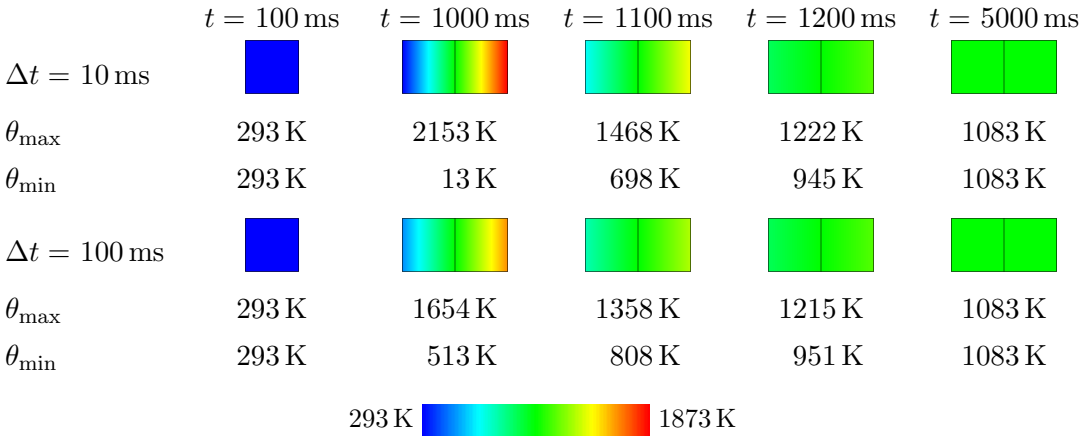

(c) Plot of the temperature of two assembled elements.

Figure 4.5: (a) Total thermal energy versus time of two assembled elements which refer to steel ($\theta_1 = 293\,\mathrm{K}$ and $\theta_2 = 1873\,\mathrm{K}$). Comparison of the total thermal energy for two different time step sizes ($\Delta t = 10\,\mathrm{ms}$ and $\Delta t = 100\,\mathrm{ms}$) with the analytical values. (b) Maximum and minimum values of the temperature versus time for two different time step sizes ($\Delta t = 10\,\mathrm{ms}$ and $\Delta t = 100\,\mathrm{ms}$). (c) Plot of the temperature of one element ($t = 100\,\mathrm{ms}$) and of two assembled elements ($t \geq 1000\,\mathrm{ms}$) at different time steps.

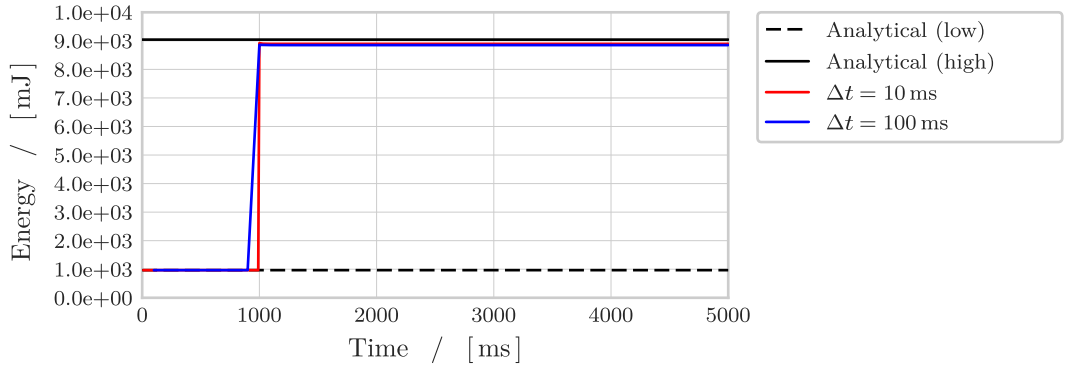

(a) Total thermal energy versus time of two assembled steel elements.

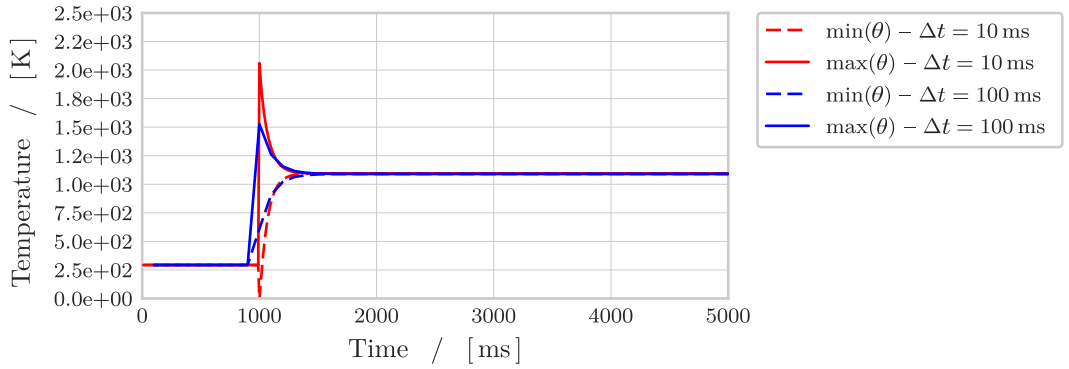

(b) Maximum and minimum values of the temperature versus time.

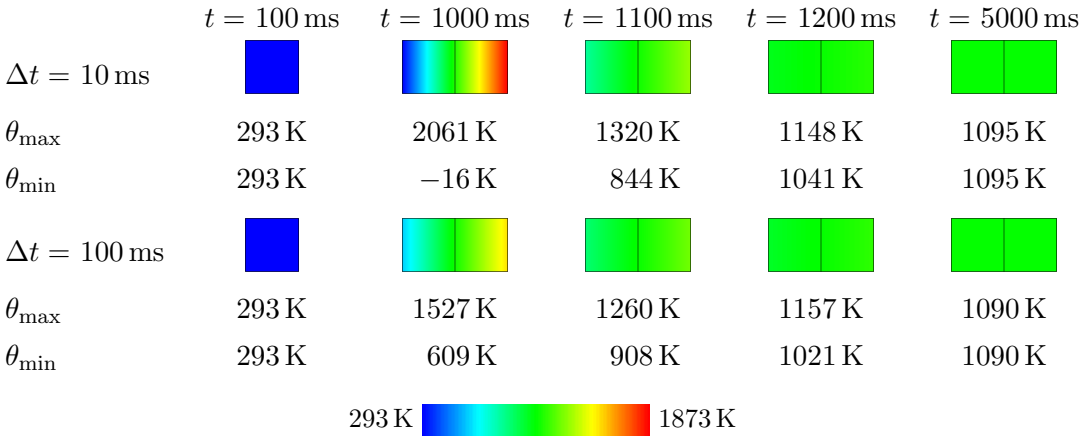

(c) Plot of the temperature of two assembled elements.

Figure 4.6: (a) Total thermal energy versus time of two assembled elements which refer to steel ($\theta_1 = 293\,\mathrm{K}$ and $\theta_2 = 1873\,\mathrm{K}$). Comparison of the total thermal energy for two different time step sizes ($\Delta t = 10\,\mathrm{ms}$ and $\Delta t = 100\,\mathrm{ms}$) with the analytical values. (b) Maximum and minimum values of the temperature versus time for two different time step sizes ($\Delta t = 10\,\mathrm{ms}$ and $\Delta t = 100\,\mathrm{ms}$). (c) Plot of the temperature of one element ($t = 100\,\mathrm{ms}$) and of two assembled elements ($t \geq 1000\,\mathrm{ms}$) at different time steps.

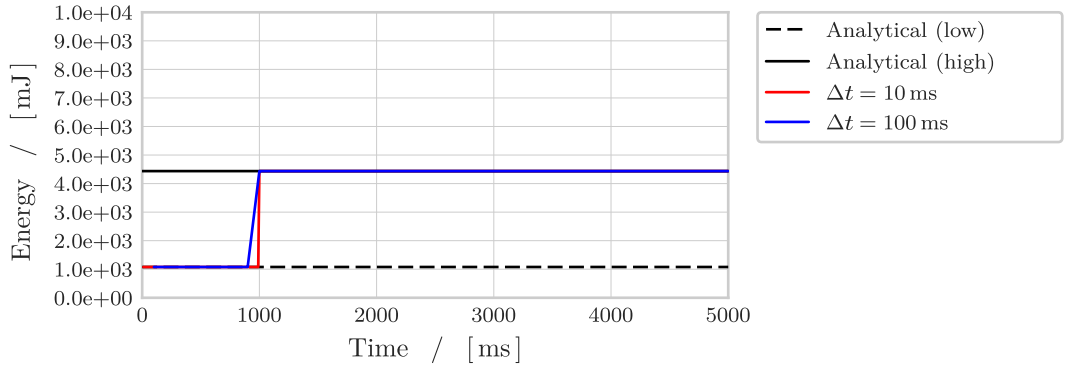

(a) Total thermal energy versus time of two assembled elements. WC-Co is assembled to steel.

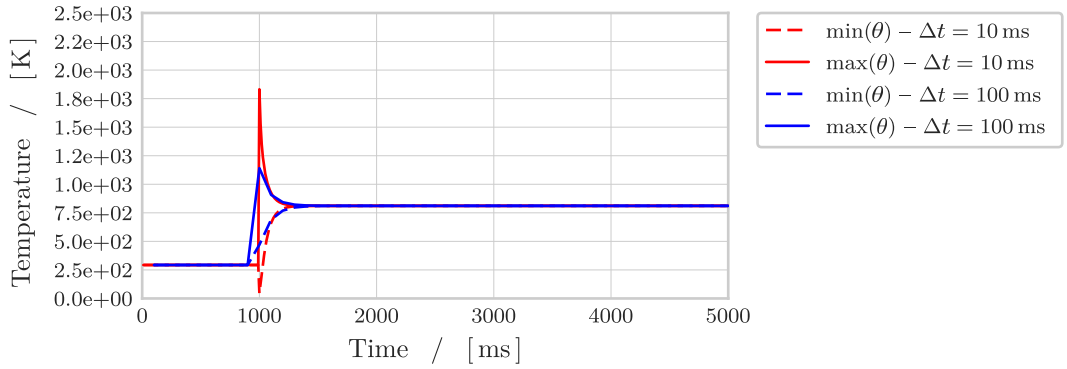

(b) Maximum and minimum values of the temperature versus time.

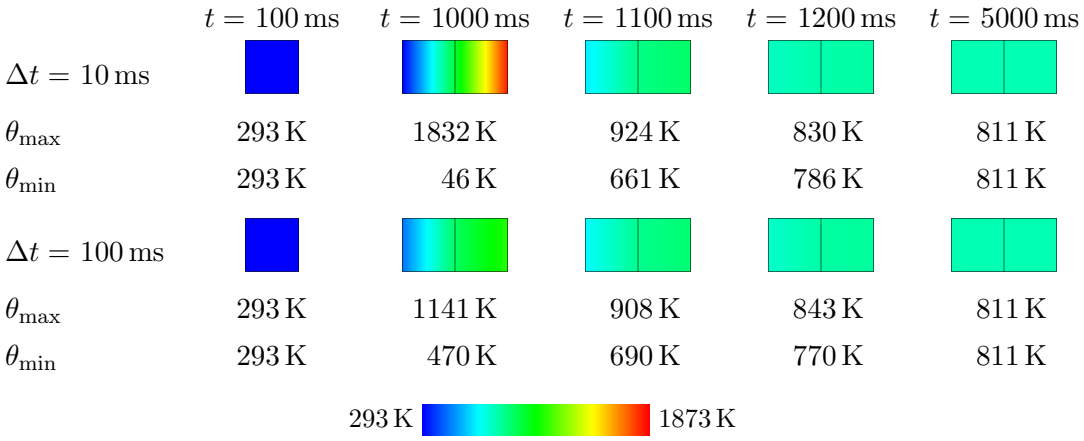

(c) Plot of the temperature of two assembled elements.

Figure 4.7: (a) Total thermal energy versus time of two assembled elements which refer to steel ($\theta_1 = 293\,\mathrm{K}$ and $\theta_2 = 1873\,\mathrm{K}$). Comparison of the total thermal energy for two different time step sizes ($\Delta t = 10\,\mathrm{ms}$ and $\Delta t = 100\,\mathrm{ms}$) with the analytical values. (b) Maximum and minimum values of the temperature versus time for two different time step sizes ($\Delta t = 10\,\mathrm{ms}$ and $\Delta t = 100\,\mathrm{ms}$). (c) Plot of the temperature of one element ($t = 100\,\mathrm{ms}$) and of two assembled elements ($t \geq 1000\,\mathrm{ms}$) at different time steps.

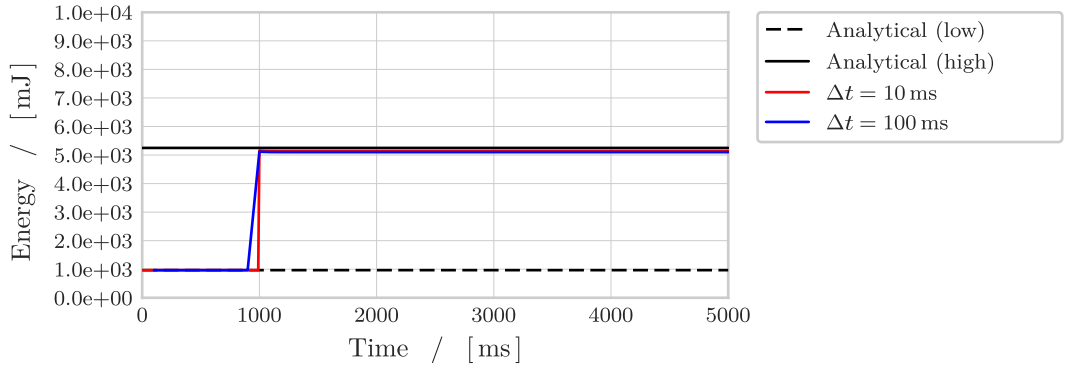

(a) Total thermal energy versus time of two assembled elements. WC-Co is assembled to steel.

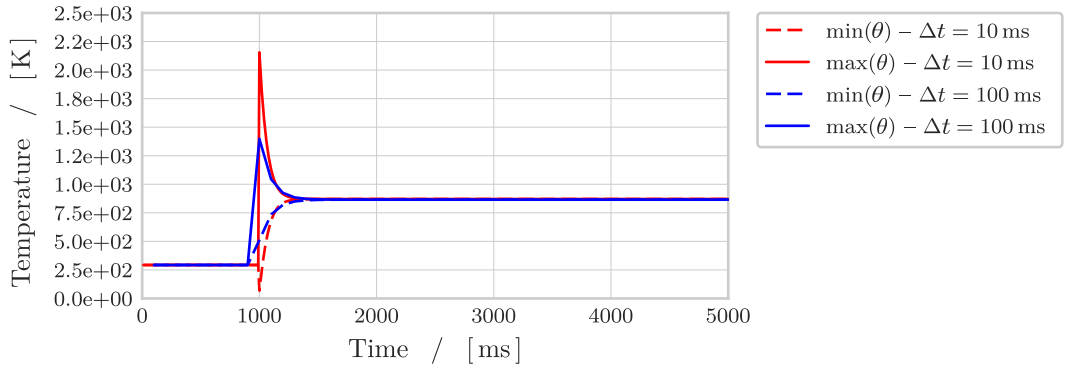

(b) Maximum and minimum values of the temperature versus time.

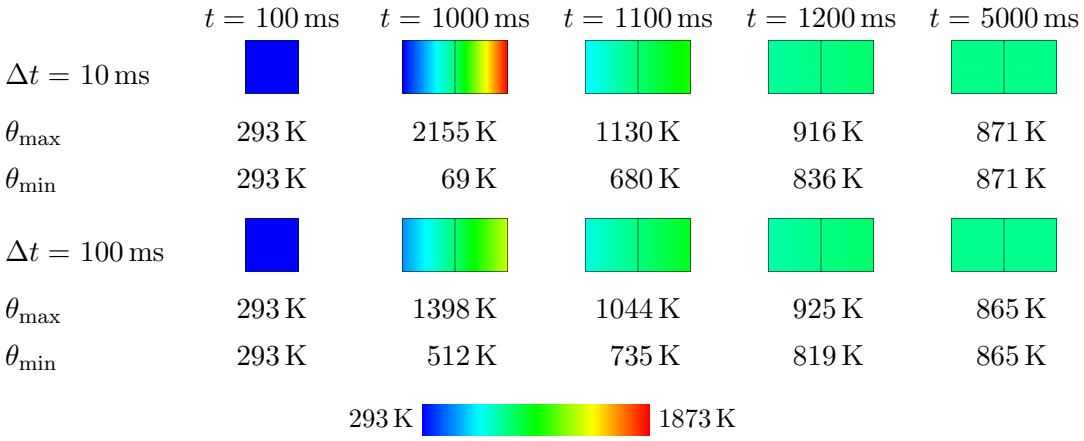

(c) Plot of the temperature of two assembled elements.

Figure 4.8: (a) Total thermal energy versus time of two assembled elements which refer to steel ($\theta_1 = 293\,\mathrm{K}$ and $\theta_2 = 1873\,\mathrm{K}$). Comparison of the total thermal energy for two different time step sizes ($\Delta t = 10\,\mathrm{ms}$ and $\Delta t = 100\,\mathrm{ms}$) with the analytical values. (b) Maximum and minimum values of the temperature versus time for two different time step sizes ($\Delta t = 10\,\mathrm{ms}$ and $\Delta t = 100\,\mathrm{ms}$). (c) Plot of the temperature of one element ($t = 100\,\mathrm{ms}$) and of two assembled elements ($t \geq 1000\,\mathrm{ms}$) at different time steps.

Table 4.2: Parameters for $c(\vartheta)$ introduced in Eq. (4.33) and $\Lambda(\vartheta)$ introduced in Eq. (4.34). See Delfosse et al. [46], Hussainova et al. [84], Nomura et al. [126], Toparli et al. [180] for further details.

Quantity	Description	Symbol	Value	Unit
$c^{\mathrm{S}}(\theta)$	Constant term	a_0	4.57×10^{2}	$\mathrm{mJ\,g^{-1}\,K^{-1}}$
	Scaling coefficient	a_1	8.94×10^{1}	$\mathrm{mJ\,g^{-1}\,K^{-1}}$
	Constant argument coefficient	a_2	-6.79×10^{-2}	
	Linear argument coefficient	a_3	4.34×10^{-3}	$\mathrm{K^{-1}}$
$c^{\mathrm{C}}(\theta)$	Constant term	a_0	1.26×10^{2}	$\mathrm{mJ\,g^{-1}\,K^{-1}}$
	Scaling coefficient	a_1	4.60×10^{1}	$\mathrm{mJ\,g^{-1}\,K^{-1}}$
	Constant argument coefficient	a_2	1.17×10^{-2}	
	Linear argument coefficient	a_3	3.04×10^{-3}	$\mathrm{K^{-1}}$
$\Lambda^{\mathrm{S}}(\theta)$	Constant term	b_0	1.33×10^{-2}	$\mathrm{W\,mm^{-1}\,K^{-1}}$
	Scaling coefficient	b_1	-2.11×10^{-2}	$\mathrm{W\,mm^{-1}\,K^{-1}}$
	Constant argument coefficient	b_2	1.90×10^{-2}	
	Linear argument coefficient	b_3	-7.53×10^{-4}	$\mathrm{K^{-1}}$
$\Lambda^{\mathrm{C}}(\theta)$	Constant term	b_0	3.43×10^{-2}	$\mathrm{W\,mm^{-1}\,K^{-1}}$
	Scaling coefficient	b_1	-2.14×10^{-2}	$\mathrm{W\,mm^{-1}\,K^{-1}}$
	Constant argument coefficient	b_2	1.33×10^{-2}	
	Linear argument coefficient	b_3	1.23×10^{-3}	$\mathrm{K^{-1}}$

temperature at each time step are listed. The time step size influences the temperature values at times that are close to the point in time of assembly. As already mentioned, the temperature tends, with increasing time, to exactly the same value for both time step sizes.

In Fig. 4.6, the results of the second example simulation are shown. The difference to the first example is that c^{S} and Λ^{S} are now temperature dependent. The analytical value of the stored total energy in the system is higher than in the previous case since c^{S} increases with increasing θ. For this non-linear case, the finite element code produces an error of $\approx 1.5\%$ for $\Delta t = 10\,\mathrm{ms}$ and an error of $\approx 2\%$ for $\Delta t = 100\,\mathrm{ms}$. For $t \to \infty$, this results in a temperature of 1095 K for $\Delta t = 10\,\mathrm{ms}$ and a temperature of 1090 K for $\Delta t = 100\,\mathrm{ms}$. As above, for $\Delta t = 10\,\mathrm{ms}$ an underestimation of the lowest temperature as well as an overestimation of the highest temperature is observed at $t = 1000\,\mathrm{ms}$. The loss in stored energy might result from the Backward Euler integration scheme known for not being energy conserving.

Fig. 4.7 illustrates the results of the third two-element example. The total stored energy of the system versus time plot shows that for this example the analytical total energy value is captured by the finite element programme for both time step sizes. Since $c^{\mathrm{C}} < c^{\mathrm{S}}$, the energy value is smaller than the one observed in the first example. For the example at hand, an underestimation of $\theta_{\min}$ but no overestimation of $\theta_{\max}$ occurs for $\Delta t = 10\,\mathrm{ms}$. Both time step sizes lead to $\theta = 811\,\mathrm{K}$ for $t \to \infty$.

The results of the fourth example are depicted in Fig. 4.8. Analogously to the error in the total energy value within the second example, the finite element code produces an error of $\approx 1.8\%$ for $\Delta t = 10\,\mathrm{ms}$ and an error of $\approx 2.5\%$ for $\Delta t = 100\,\mathrm{ms}$. Since c^{C} also increases with increasing θ, the stored energy value is higher than for the third example with constant material parameters. In contrast to the third example, both an underestimation of $\theta_{\min}$ and an overestimation of $\theta_{\max}$ are observed for $\Delta t = 10\,\mathrm{ms}$. For $t \to \infty$, a temperature of $\theta = 871\,\mathrm{K}$ is observed for $\Delta t = 10\,\mathrm{ms}$ as well as a temperature of $\theta = 865\,\mathrm{K}$ for $\Delta t = 100\,\mathrm{ms}$.

4.3.2 Coating of a plate – 2d

As a more complex academic example, the two dimensional problem which is depicted in Fig. 4.9(a) is considered. The 2d-representation of a plate is considered to be 30 mm wide and 3 mm high. The discretisation is performed with squared four-noded elements of $0.25\,\mathrm{mm}^2$ size. The material is considered to represent steel and has an initial temperature of $\theta_{\mathrm{init}} = 293\,\mathrm{K}$. The time step size is $\Delta t = 10\,\mathrm{ms}$ and the material behaviour is supposed to be temperature dependent. Every 100 ms, a HVOF spray gun applies 6 mm by 0.5 mm – twelve by one elements – WC-Co-splats, the material behaviour of which is also considered to be temperature dependent, onto the substrate. The temperature of the WC-Co-splats before the assembly with the existing system is $\theta_{\mathrm{coat}} = 1873\,\mathrm{K}$. Two different configurations of gun movement are simulated. In one setting, the HVOF gun always begins on the left hand side of the system and applies material until the right hand side is reached. This is called the "one-direction"-setting. For the other setting, the HVOF gun begins from left to right and continues mass application from the right to the left and so on. This is called the "two-direction"-setting. The arrows in Figs. 4.9(b) and 4.9(c) clarify the difference. The spray gun moves on for a total of six paths so that finally half of the plate consists of "old" steel substrate and the other half consists of "new" applied WC-Co coating as depicted in Fig. 4.9(d).

At first, the boundary of the system is considered to be adiabatic and simulations are carried out for both gun movement paths. The results of the simulation are depicted in Figs. 4.10 and 4.11 at which the temperature plots refer to time steps directly before the WC-Co-splat is applied – after $t = 1090\,\mathrm{ms}$, $t = 2090\,\mathrm{ms}$ and $t = 3090\,\mathrm{ms}$ – as well as at the final time step at $t = 10\,000\,\mathrm{ms}$. As far as the eyes can catch, the temperature plots for the "one-direction" setting, Fig. 4.10, as well as the "two-direction" setting, Fig. 4.11, look "mirrored". The only difference appears when $\theta_{\min}$ and $\theta_{\max}$ of the two different gun movement paths are compared. Naturally, the "one-direction" path leads

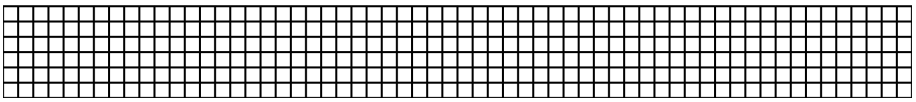

(a) Initial configuration of the steel substrate.

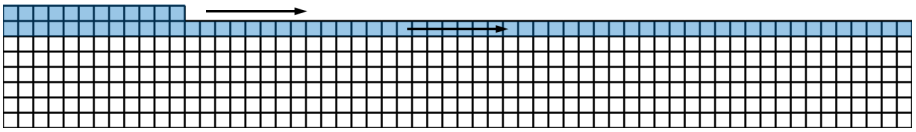

(b) The arrows indicate the gun direction of the "one-direction"-setting.

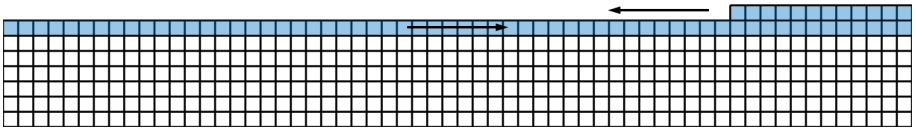

(c) The arrows indicate the gun direction of the "two-direction"-setting.

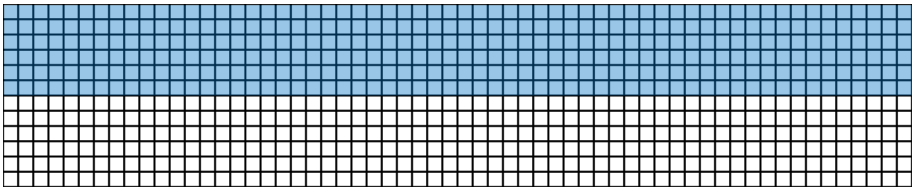

(d) Configuration after the coating procedure.

Figure 4.9: Coating of a 2d plate. White elements are related to steel and blue elements are related to WC-Co. (a) Initial configuration of the steel substrate. (b) The first WC-Co-splat of the second path for the "one-direction"-setting is depicted. The arrows indicate the direction of the HVOF gun. (c) The first WC-Co-splat of the second path for the "two-direction"-setting is depicted. The arrows indicate the direction of the HVOF gun. (d) Configuration after the coating procedure.

to lower $\theta_{\min}$ and higher $\theta_{\max}$ but the difference is only a few Kelvin. At the end of the simulation, thermal equilibrium is almost reached in both cases ($\theta \approx 880\,\mathrm{K}$).

In a second comparison, the boundary of the body is considered to be a Robin boundary with convective and radiative heat transfer via the surface. The environmental temperature of the surrounding air is the room temperature $\theta_\infty^{\mathrm{air}} = 293\,\mathrm{K}$. The top side of the additionally applied (twelve by one) elements is exposed to the HVOF gun which is assumed to have a temperature of $\theta_\infty^{\mathrm{gun}} = 3073\,\mathrm{K}$. The results are shown in Figs. 4.12 and 4.13. The points in time at which the results are visualised are chosen analogously to the previous example. Again, the temperature plots appear "mirrored" for the two gun movement paths. The comparison of $\theta_{\min}$ and of $\theta_{\max}$ for the two gun movement paths again leads to a slightly higher (only a few Kelvin) difference for the "one-direction" path, Fig. 4.12. Since the boundary heat flux that is caused by convection and radiation leads to cooling of the body, the temperature plots show lower temperatures than those observed in Figs. 4.10 and 4.11. Obviously, the boundary heat flux induced by the gun flame during the coating procedure does not lead to a significant heating. Thermal equilibrium is expected for $t \to \infty$ when the temperature of the body is the same as the

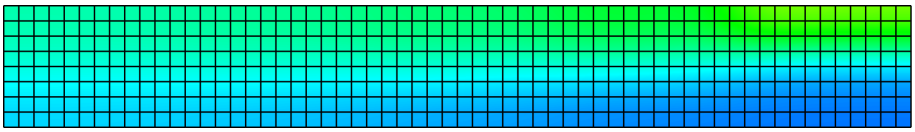

(a) Temperature distribution of the “one-direction” setting after 1090 ms.

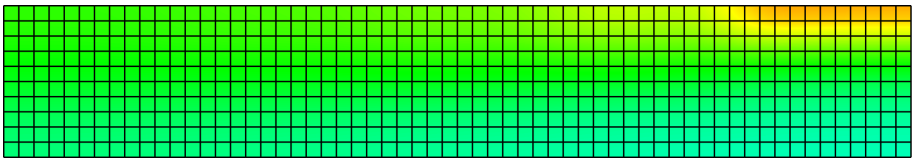

(b) Temperature distribution of the “one-direction” setting after 2090 ms.

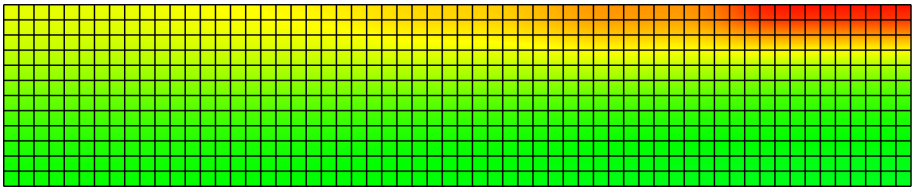

(c) Temperature distribution of the “one-direction” setting after 3090 ms.

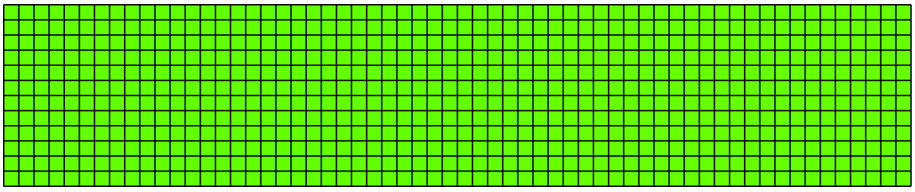

(d) Temperature distribution of the “one-direction” setting after 10 000 ms.

Figure 4.10: Simulation of coating of a 2d-plate with adiabatic boundary and the “one-direction” gun movement path. Temperature distribution after (a) 1090 ms, (b) 2090 ms, (c) 3090 ms and (d) 10 000 ms.

temperature of the surrounding air. At the final time step considered, the temperature of the body is in the range of $\approx [740; 750]$ K for both gun movement paths.

4.3.3 Coating of a plate – 3d

The examples above involve application of mass in the same order of magnitude as the size of the initial configuration. To be precise, the added material occupies the same bulk as the initial configuration such that the total bulk is finally doubled. In reality, a comparatively small amount of hard material is deposited on an existing tool or workpiece. Therefore, in order to give a more realistic example, a three dimensional plate which is depicted in Fig. 4.14 is considered. The dimension of the plate is 180 mm × 180 mm × 30 mm in $x-$, $y-$ and $z-$direction. The discretisation is performed with eight-noded hexahedral elements of different sizes. In $z-$direction, three layers of elements are used to discretise the range of $z = [0; 29]$ mm and ten layers of elements discretise the range of

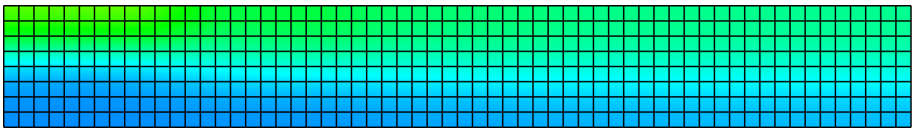

(a) Temperature distribution of the "two-direction" setting after 1090 ms.

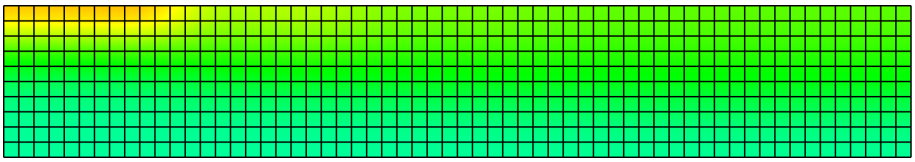

(b) Temperature distribution of the "two-direction" setting after 2090 ms.

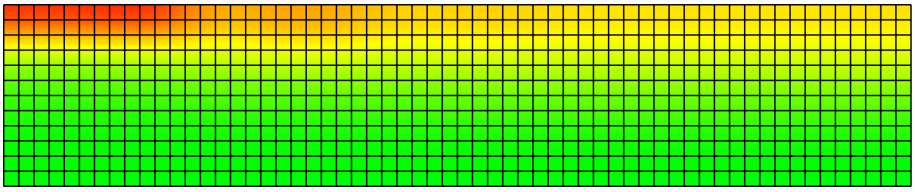

(c) Temperature distribution of the "two-direction" setting after 3090 ms.

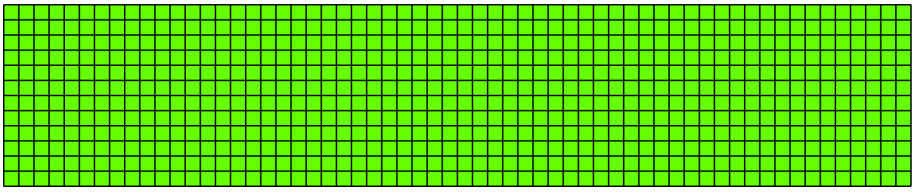

(d) Temperature distribution of the "two-direction" setting after 10 000 ms.

Figure 4.11: Simulation of coating of a 2d-plate with adiabatic boundary and the "two-direction" gun movement path. Temperature distribution after (a) 1090 ms, (b) 2090 ms, (c) 3090 ms and (d) 10 000 ms.

$z = (29;\, 30]$ mm. This results in a fine discretisation near the surface at $z = 30$ mm where the coating is applied. In $x-$ and $y-$direction the discretisation is performed with 6 mm edge-length which results in comparatively strong distorted elements for $z > 29$ mm. This is a trade off, since the substrate is in this way discretised by 11700 elements before any mass is newly applied. The initial temperature of the steel substrate is set to $\theta_{\text{init}} = 293\,\text{K}$. The material deposition is illustrated in Fig. 4.14(b). In discrete time steps of $\Delta t = 100$ ms, the HVOF gun applies 30 mm $\times$ 30 mm $\times$ 1 mm WC-Co-splats with a temperature of $\theta_{\text{coat}} = 1873\,\text{K}$ onto the substrate. The material properties are chosen to be constant throughout the simulation. In order to model the surface heat flux, surrounding air with an ambient temperature of $\theta_{\text{air}} = 293\,\text{K}$ is employed and a HVOF gun temperature of $\theta_{\text{gun}} = 3073\,\text{K}$ is used in order to occupy the $z = 31$ mm surface of the newly applied WC-Co splat. After 36 time steps, the coating is fully applied such that the configuration is discretised by a total of 20700 elements. Cooling in air is simulated up to the final time step $t = 10\,000$ ms. In Fig. 4.15, the resulting temperature plots for

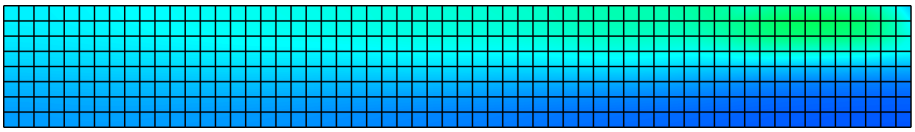

(a) Temperature distribution of the "one-direction" setting after 1090 ms.

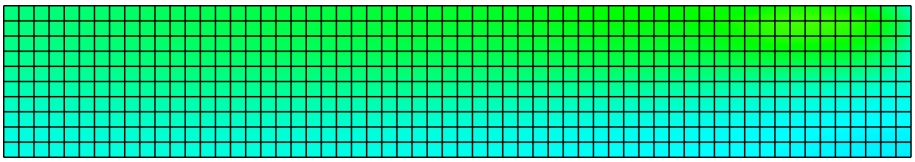

(b) Temperature distribution of the "one-direction" setting after 2090 ms.

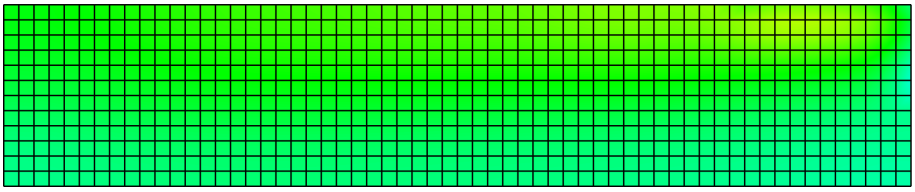

(c) Temperature distribution of the "one-direction" setting after 3090 ms.

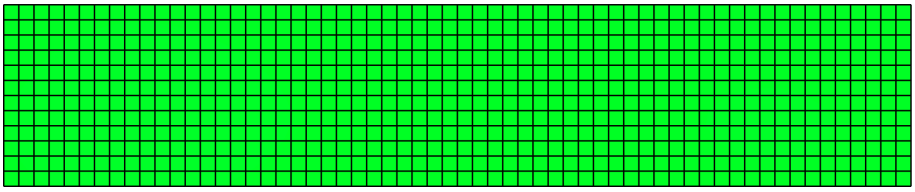

(d) Temperature distribution of the "one-direction" setting after 10 000 ms.

Figure 4.12: Simulation of coating of a 2d-plate with Robin boundary (convection and radiation) and the "one-direction" gun movement path. Temperature distribution after (a) 1090 ms, (b) 2090 ms, (c) 3090 ms and (d) 10 000 ms.

four different time steps are depicted. Since the volume of the newly added material is small in relation to the substrate, it is plausible that the temperature increase is observed near the area of mass application, see Figs. 4.15(a) and 4.15(b). Fig. 4.15(c) shows the time step of the application of the last WC-Co-splat. At that time step, the temperature increase in deeper regions of the plate due to heat conduction can be observed in areas where the simulation of mass deposition started. Fig. 4.15(d) shows the temperature state of the plate after 10 000 ms. Due to heat conduction to the regions of the plate as well as the cooling by the surrounding air, the maximum temperature is not more than $\approx 380\,\mathrm{K}$. During the simulation, under- and overestimation of the temperature occurs. Related to Figs. 4.15(b) and 4.15(c), it can be observed that a newly applied WC-Co-splat leads to a drop of the temperature within the already applied splats next to it. As for the 2d example with Robin boundary, thermal equilibrium is expected for $t \to \infty$ when the temperature of the body is $\theta_{\mathrm{air}} = 293\,\mathrm{K}$.

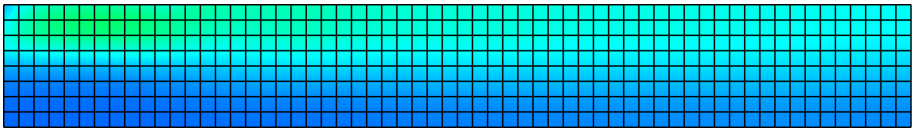

(a) Temperature distribution of the “two-direction” setting after 1090 ms.

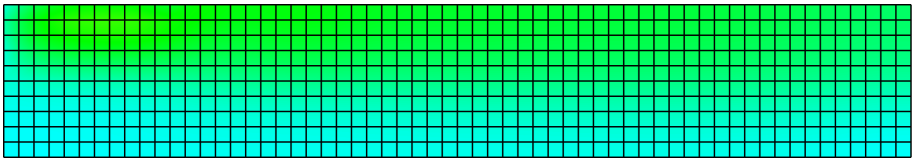

(b) Temperature distribution of the “two-direction” setting after 2090 ms.

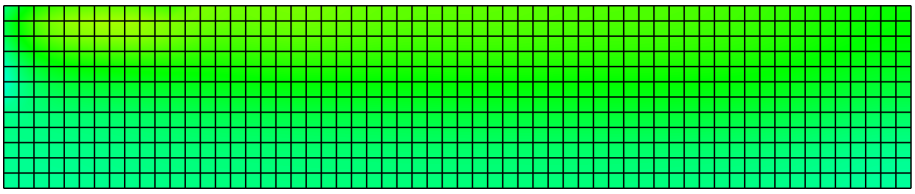

(c) Temperature distribution of the “two-direction” setting after 3090 ms.

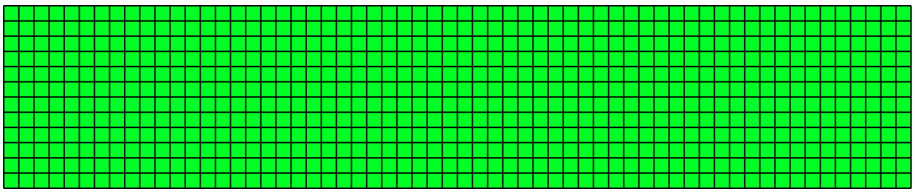

(d) Temperature distribution of the “two-direction” setting after 10 000 ms.

Figure 4.13: Simulation of coating of a 2d-plate with Robin boundary (convection and radiation) and the “two-direction” gun movement path. Temperature distribution after (a) 1090 ms, (b) 2090 ms, (c) 3090 ms and (d) 10 000 ms.

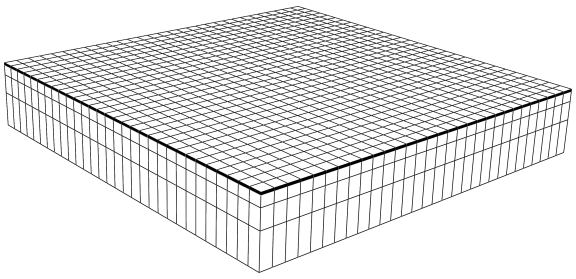

(a) Initial configuration of the steel substrate.

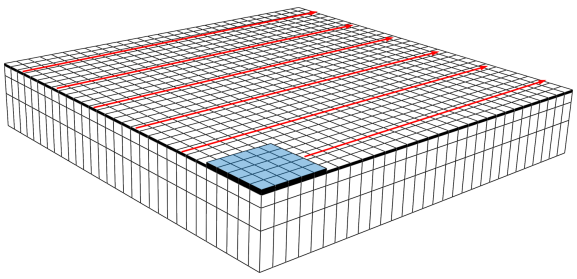

(b) The first WC-Co-splat is depicted and the arrows visualise the direction of the HVOF gun.

Figure 4.14: Coating of a 3d plate. White elements are related to steel and blue elements are related to WC-Co. (a) Initial configuration of the steel substrate. (b) The first WC-Co-splat is depicted. The arrows visualise the direction of the HVOF gun.

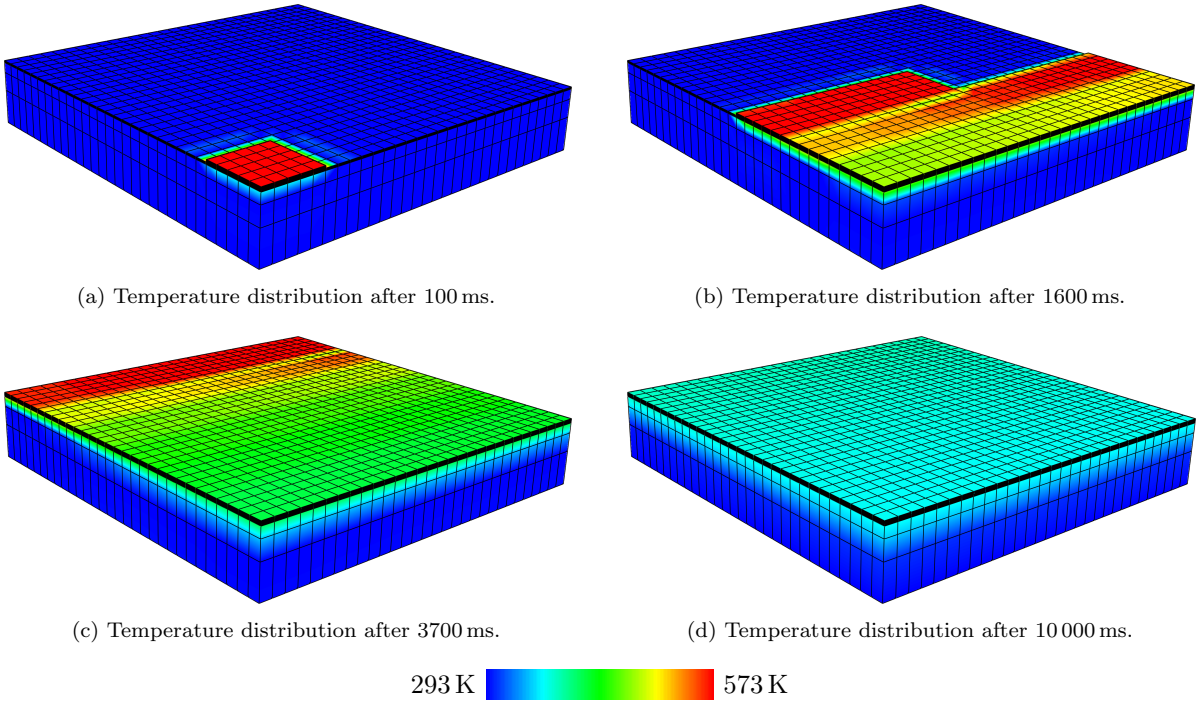

(a) Temperature distribution after 100 ms.

(b) Temperature distribution after 1600 ms.

(c) Temperature distribution after 3700 ms.

(d) Temperature distribution after 10 000 ms.

Figure 4.15: Simulation of coating of a 3d-plate with Robin boundary conditions which cover convective and radiative heat transfer. Temperature distribution after (a) 100 ms, (b) 1600 ms, (c) 3700 ms and (d) 10 000 ms.

5 Computational homogenisation for thermo-viscoplastic composites: Small strain formulation and application to thermally sprayed coatings

The previous two chapters dealt with the finite element modelling of thermal spraying processes under consideration of the heat input by a robot guided spray gun as well as the modelling of mass deposition in the framework of a rigid heat conductor. Since deformation is neglected within Chapters 3 and 4, residual stresses during quenching have consequently so far not been studied due to the fact that, within a rigid heat conductor, no field is present which describes the deformation. An extension of the framework discussed in Chapter 4 with respect to a thermo-mechanically coupled mass deposition framework requires constitutive relations valid for the hard material which is applied as wear protection and which generally consists of multiple constituents. The mathematical procedure when the effective behaviour of two or more different materials is determined is often denoted as *homogenisation*. In this as well as in the following chapter, the so-called FE^2 method is applied where the effective material behaviour of a heterogeneous material on a *upper scale* is captured by means of a *representative volume element (RVE)*, the effective behaviour of which is determined by means of the finite element solution under appropriate boundary conditions on a *lower scale*.

The objective of this chapter is to discuss and apply a thermo-mechanically coupled simulation framework which captures the heterogeneity of the deposited coating material. Therefore, a two-scale finite element framework for the solution of non-linear thermo-mechanically coupled problems is elaborated and applied to the simulation of thermoviscoplastic material behaviour including non-linear thermal softening in a geometrically linearised setting, cf. Box 2.2. The finite element framework and material model is demonstrated by means of numerical examples.

This chapter is structured as follows: In Section 5.1, the two-scale continuum thermo-mechanical framework is summarised. The two-scale finite element framework is subse-

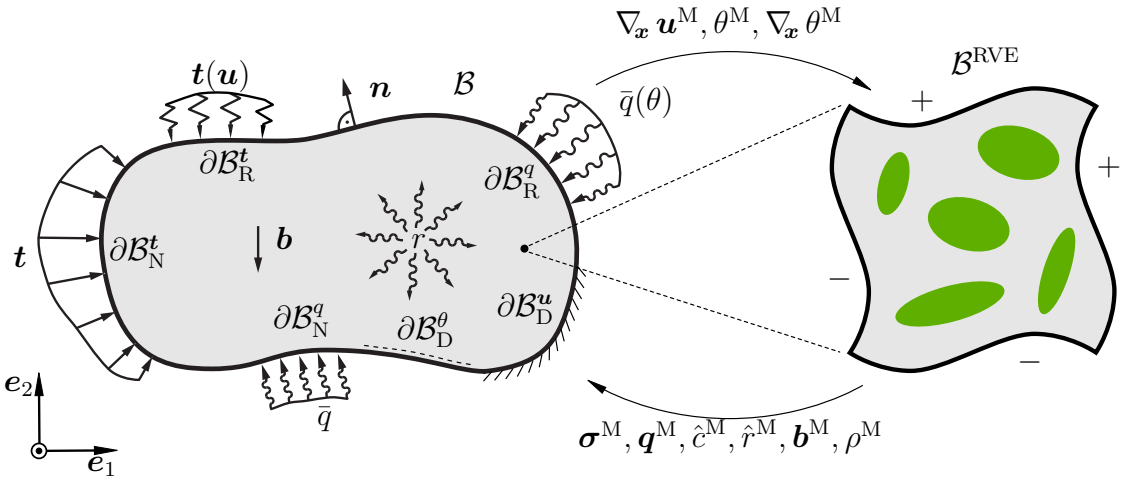

Figure 5.1: Deformable heat conductor $\mathcal{B}$. The effective behaviour is determined by the underlying heterogeneous meso-structure of the material. In each material point on the macro-scale, a RVE $\mathcal{B}^{\mathrm{RVE}}$ is considered.

quently outlined in Section 5.2. Details regarding the thermoviscoplastic material model are given in Section 5.3 followed by numerical examples in Section 5.4.

5.1 Continuum thermomechanics

This section provides a summary of the governing equations of continuum thermodynamics of the presented thermo-mechanical multiscale finite element framework. On the macro-scale, a deformable heat conductor $\mathcal{B}$ according to Box 2.2 is considered. However, on the meso-scale, the heat conductor is assumed to be heterogeneous. The heterogeneous mesostructure is incorporated by a so-called representative volume element (RVE) considered as a deformable heat conductor $\mathcal{B}^{\mathrm{RVE}}$ on the lower scale. The heterogeneous nature of $\mathcal{B}^{\mathrm{RVE}}$ determines the effective material behaviour which is observable on the macro-scale. Thereby it is assumed that the characteristic length on the macro-scale is much larger than the characteristic length on the meso-scale, i.e. $l^{\mathrm{M}} \gg l^{\mathrm{m}}$. The two separated scales are illustrated in Fig. 5.1. Throughout this chapter we consider a first order homogenisation scheme which implies that the thermomechanical response on the lower scale is steady state.

5.1.1 Macro-scale

The deformable heat conductor depicted in Fig. 5.1 represents a thermo-mechanical initial boundary value problem (IBVP) where the bulk of the body considered is denoted by $\mathcal{B}$ and where the boundary of the body $\partial\mathcal{B}$ is distinguished in a displacement boundary $\partial\mathcal{B}^{\boldsymbol{u}}$ as well as in a temperature boundary $\partial\mathcal{B}^{\theta}$. The balance equations needed in order to obtain a solution for the displacement field $\boldsymbol{u}$ and the temperature field θ are the

balance of linear momentum and the energy balance equation, as represented by the heat equation,

$$\rho^{\mathrm{M}}\,\ddot{\boldsymbol{u}}^{\mathrm{M}} = \nabla_{\boldsymbol{x}}\cdot\boldsymbol{\sigma}^{\mathrm{M}} + \rho^{\mathrm{M}}\,\boldsymbol{b}^{\mathrm{M}}\ , \tag{5.1}$$

$$[\,\rho\,c\,]^{\mathrm{M}}\,\dot{\theta}^{\mathrm{M}} = -\,\nabla_{\boldsymbol{x}}\cdot\,\boldsymbol{q}^{\mathrm{M}} + \hat{r}^{\mathrm{M}}\ , \tag{5.2}$$

here in local strong form. In the above equations, ρ^{M} is the mass density and $\nabla_{\boldsymbol{x}}$ is the nabla operator. Furthermore, in Eq. (5.1) $\ddot{\boldsymbol{u}}^{\mathrm{M}}$ is the acceleration, $\boldsymbol{\sigma}^{\mathrm{M}}$ is the stress tensor and $\boldsymbol{b}^{\mathrm{M}}$ is the body force vector per unit volume. Moreover, in Eq. (5.2) $[\,\rho\,c\,]^{\mathrm{M}}$ is the heat capacity, $\dot{\theta}^{\mathrm{M}}$ is the rate of temperature, $\boldsymbol{q}^{\mathrm{M}}$ is the heat flux vector and $\hat{r}^{\mathrm{M}}$ is the sum of the external heat supply and the mechanical heat supply. The solution of the IBVP requires an initial state at time t_0 and the definition of boundary conditions. For both balance equations, three different types of boundary conditions are considered by splitting the boundary into three disjoint parts

$$\partial\mathcal{B}^{\boldsymbol{u}} = \partial\mathcal{B}^{\boldsymbol{u}}_{\mathrm{D}} \cup \partial\mathcal{B}^{\boldsymbol{t}}_{\mathrm{N}} \cup \partial\mathcal{B}^{\boldsymbol{t}}_{\mathrm{R}} \text{ with } \partial\mathcal{B}^{\boldsymbol{u}}_{\mathrm{D}} \cap \partial\mathcal{B}^{\boldsymbol{t}}_{\mathrm{N}} = \partial\mathcal{B}^{\boldsymbol{u}}_{\mathrm{D}} \cap \partial\mathcal{B}^{\boldsymbol{t}}_{\mathrm{R}} = \partial\mathcal{B}^{\boldsymbol{t}}_{\mathrm{N}} \cap \partial\mathcal{B}^{\boldsymbol{t}}_{\mathrm{R}} = \emptyset \tag{5.3}$$

and

$$\partial\mathcal{B}^{\theta} = \partial\mathcal{B}^{\theta}_{\mathrm{D}} \cup \partial\mathcal{B}^{q}_{\mathrm{N}} \cup \partial\mathcal{B}^{q}_{\mathrm{R}} \text{ with } \partial\mathcal{B}^{\theta}_{\mathrm{D}} \cap \partial\mathcal{B}^{q}_{\mathrm{N}} = \partial\mathcal{B}^{\theta}_{\mathrm{D}} \cap \partial\mathcal{B}^{q}_{\mathrm{R}} = \partial\mathcal{B}^{q}_{\mathrm{N}} \cap \partial\mathcal{B}^{q}_{\mathrm{R}} = \emptyset \tag{5.4}$$

onto which the following conditions are prescribed for the mechanical problem

$$\begin{aligned}
\boldsymbol{u} &= \bar{\boldsymbol{u}} && \text{on} && \partial\mathcal{B}^{\boldsymbol{u}}_{\mathrm{D}}\ ,\\
\boldsymbol{\sigma}\cdot\boldsymbol{n} &= \bar{\boldsymbol{t}} && \text{on} && \partial\mathcal{B}^{\boldsymbol{t}}_{\mathrm{N}}\ ,\\
\boldsymbol{\sigma}\cdot\boldsymbol{n} &= \bar{\boldsymbol{t}}(\boldsymbol{u}) && \text{on} && \partial\mathcal{B}^{\boldsymbol{t}}_{\mathrm{R}}\ ,
\end{aligned} \tag{5.5}$$

as well as for the thermal problem

$$\begin{aligned}
\theta &= \bar{\theta} && \text{on} && \partial\mathcal{B}^{\theta}_{\mathrm{D}}\ ,\\
-\,\boldsymbol{q}\cdot\boldsymbol{n} &= \bar{q} && \text{on} && \partial\mathcal{B}^{q}_{\mathrm{N}}\ ,\\
-\,\boldsymbol{q}\cdot\boldsymbol{n} &= \bar{q}(\theta) && \text{on} && \partial\mathcal{B}^{q}_{\mathrm{R}}\ ,
\end{aligned} \tag{5.6}$$

with $\boldsymbol{n}$ denoting the outward unit vector. Boundaries $\partial\mathcal{B}^{\boldsymbol{u}}_{\mathrm{D}}$ and $\partial\mathcal{B}^{\theta}_{\mathrm{D}}$ are denoted as Dirichlet boundaries at which the field variables themselves are prescribed. In contrast, the flux terms are prescribed on the so-called Neumann boundaries $\partial\mathcal{B}^{\boldsymbol{t}}_{\mathrm{N}}$ and $\partial\mathcal{B}^{q}_{\mathrm{N}}$ as well as on the Robin boundaries $\partial\mathcal{B}^{\boldsymbol{t}}_{\mathrm{R}}$ and $\partial\mathcal{B}^{q}_{\mathrm{R}}$. The formal difference of a Robin boundary to a Neumann boundary is that a Robin boundary condition is dependent on the respective field variable. As special cases of the Neumann boundary conditions, Eq. $(5.5)_2$ and

Eq. $(5.6)_2$, free mechanical surfaces, $\boldsymbol{\sigma} \cdot \boldsymbol{n} = \mathbf{0}$, and adiabatic thermal boundaries, $-\boldsymbol{q} \cdot \boldsymbol{n} = 0$, are included.

5.1.2 Meso-scale

In one-scale (macroscopic) frameworks, stress $\boldsymbol{\sigma}^{\mathrm{M}}$ and heat flux $\boldsymbol{q}^{\mathrm{M}}$ are straightforwardly obtained by the evaluation of an underlying constitutive model with strain tensor $\boldsymbol{\varepsilon}^{\mathrm{M}}$, temperature θ^{M} and temperature gradient $\nabla_{\boldsymbol{x}}\, \theta^{\mathrm{M}}$. This also applies to mass density ρ^{M}, body force $\boldsymbol{b}^{\mathrm{M}}$, heat capacity $[\,\rho\, c\,]^{\mathrm{M}}$ as well as to the heat supply $\hat{r}^{\mathrm{M}}$.

In contrast to this, in a two-scale framework, the material behaviour is obtained by the solution of an underlying problem at a lower scale. For this purpose, balance equations are required and $\boldsymbol{\varepsilon}^{\mathrm{M}}$, θ^{M} as well as $\nabla_{\boldsymbol{x}}\, \theta^{\mathrm{M}}$ are passed from the macro-scale to the meso-scale. When it is assumed that the material at the meso-scale reacts instantaneously, the mesoscopic counterparts of balance equations, Eqs. (5.1) and (5.2), read

$$\mathbf{0} = \nabla_{\boldsymbol{x}} \cdot \boldsymbol{\sigma}^{\mathrm{m}} \,, \tag{5.7}$$

$$0 = -\nabla_{\boldsymbol{x}} \cdot \boldsymbol{q}^{\mathrm{m}} \,. \tag{5.8}$$

The effective material behaviour is obtained by a homogenisation procedure outlined in Sengupta et al. [157].

5.2 Finite Element Framework

The fully coupled thermo-mechanical two-scale problem is monolithically solved by means of the finite element method. The leading equations are summarised in Section 5.2.1 and then subsequently applied in the two-scale framework which is outlined in Section 5.2.2 including details regarding the scale-transition, the meso-scale boundary conditions, as well as the homogenisation procedure. Finally, Section 5.2.3 gives some details regarding the implementation.

5.2.1 General thermomechanical framework

The local strong forms of the considered balance equations, Eqs. (5.1) and (5.2), are rewritten in residual form and weighted by admissible test functions $\delta\boldsymbol{u}$ and $\delta\theta$. Subse-

quent integration over the volume of the considered body $\mathcal{B}$ results in the global weak forms

$$0 = \int_{\mathcal{B}} \delta\boldsymbol{u} \cdot [\, \nabla_{\boldsymbol{x}} \cdot \boldsymbol{\sigma} + \rho\, \boldsymbol{b} - \rho\, \ddot{\boldsymbol{u}} \,]\, \mathrm{d}v \;, \tag{5.9}$$

$$0 = \int_{\mathcal{B}} \delta\theta \, \Big[- \nabla_{\boldsymbol{x}} \cdot \boldsymbol{q} + \hat{r} - (\rho\, c)\, \dot{\theta} \Big]\, \mathrm{d}v \;. \tag{5.10}$$

Subsequently, integration by parts of the divergence terms as well as the application of Gauß's divergence theorem with $\partial\mathcal{B}^{\boldsymbol{t}} = \partial\mathcal{B}^{\boldsymbol{t}}_{\mathrm{N}} \cup \partial\mathcal{B}^{\boldsymbol{t}}_{\mathrm{R}}$ and $\partial\mathcal{B}^{q} = \partial\mathcal{B}^{q}_{\mathrm{N}} \cup \partial\mathcal{B}^{q}_{\mathrm{R}}$ leads to the global residual relations

$$\mathrm{w}^{\boldsymbol{u}}(\delta\boldsymbol{u}; \boldsymbol{u}, \theta) = \mathrm{w}^{\boldsymbol{u}}_{\mathrm{dyn}} + \mathrm{w}^{\boldsymbol{u}}_{\mathrm{int}} - \mathrm{w}^{\boldsymbol{u}}_{\mathrm{vol}} - \mathrm{w}^{\boldsymbol{u}}_{\mathrm{sur}} = 0 \;, \tag{5.11}$$

$$\mathrm{w}^{\theta}(\delta\theta; \boldsymbol{u}, \theta) = \mathrm{w}^{\theta}_{\mathrm{dyn}} + \mathrm{w}^{\theta}_{\mathrm{int}} - \mathrm{w}^{\theta}_{\mathrm{vol}} - \mathrm{w}^{\theta}_{\mathrm{sur}} = 0 \;, \tag{5.12}$$

with the contributions

$$\begin{aligned} \mathrm{w}^{\boldsymbol{u}}_{\mathrm{dyn}} &= \int_{\mathcal{B}} \rho\, \delta\boldsymbol{u} \cdot \ddot{\boldsymbol{u}}\, \mathrm{d}v \;, \quad \mathrm{w}^{\boldsymbol{u}}_{\mathrm{int}} = \int_{\mathcal{B}} \nabla_{\boldsymbol{x}}\, \delta\boldsymbol{u} : \boldsymbol{\sigma}\, \mathrm{d}v \;, \\ \mathrm{w}^{\boldsymbol{u}}_{\mathrm{vol}} &= \int_{\mathcal{B}} \rho\, \delta\boldsymbol{u} \cdot \boldsymbol{b}\, \mathrm{d}v \;, \quad \mathrm{w}^{\boldsymbol{u}}_{\mathrm{sur}} = \int_{\partial\mathcal{B}^{\boldsymbol{t}}} \delta\boldsymbol{u} \cdot \bar{\boldsymbol{t}}\, \mathrm{d}a \;, \end{aligned} \tag{5.13}$$

and

$$\begin{aligned} \mathrm{w}^{\theta}_{\mathrm{dyn}} &= \int_{\mathcal{B}} \rho\, c\, \delta\theta\, \dot{\theta}\, \mathrm{d}v \;, \quad \mathrm{w}^{\theta}_{\mathrm{int}} = \int_{\mathcal{B}} - \nabla_{\boldsymbol{x}}\, \delta\theta \cdot \boldsymbol{q}\, \mathrm{d}v \;, \\ \mathrm{w}^{\theta}_{\mathrm{vol}} &= \int_{\mathcal{B}} \delta\theta\, \hat{r}\, \mathrm{d}v \;, \quad \mathrm{w}^{\boldsymbol{u}}_{\mathrm{sur}} = \int_{\partial\mathcal{B}^{q}} \delta\theta\, \bar{q}\, \mathrm{d}a \;. \end{aligned} \tag{5.14}$$

In the above equations, index "dyn" denotes the dynamic contributions, index "int" indicates the internal contributions, index "vol" means the volumetric contributions and index "sur" denotes the surface contributions. Eqs. (5.11) and (5.12) are suitable for the solution by means of the finite element method. Therefore, the considered body $\mathcal{B}$ is approximated by a finite number of n_{el} volume elements and, furthermore, the Robin boundaries $\partial\mathcal{B}^{\boldsymbol{t}}_{\mathrm{R}}$ and $\partial\mathcal{B}^{q}_{\mathrm{R}}$ are approximated by $n^{\boldsymbol{t}}_{sel}$ respectively n^{q}_{sel} surface elements. As a consequence, the integral terms in Eqs. (5.11) and (5.12) are approximated by the sum over all volume and surface element integrals

$$\mathrm{w}^{\boldsymbol{u}} \approx \mathrm{w}^{\boldsymbol{u}\,h} = \sum_{e=1}^{n_{el}} \big[\, \mathrm{w}^{\boldsymbol{u}\,e}_{\mathrm{dyn}} + \mathrm{w}^{\boldsymbol{u}\,e}_{\mathrm{int}} - \mathrm{w}^{\boldsymbol{u}\,e}_{\mathrm{vol}} \,\big] + \sum_{i=1}^{n^{\boldsymbol{t}}_{sel}} \big[\, -\mathrm{w}^{\boldsymbol{u}\,i}_{\mathrm{sur}} \,\big] = 0 \;, \tag{5.15}$$

and

$$\mathrm{w}^{\theta} \approx \mathrm{w}^{\theta\,h} = \sum_{e=1}^{n_{el}} \left[\mathrm{w}^{\theta\,e}_{\mathrm{dyn}} + \mathrm{w}^{\theta\,e}_{\mathrm{int}} - \mathrm{w}^{\theta\,e}_{\mathrm{vol}} \right] + \sum_{j=1}^{n^{\theta}_{sel}} \left[-\mathrm{w}^{\theta\,j}_{\mathrm{sur}} \right] = 0 \,. \tag{5.16}$$

The spatial discretisation follows the concept of isoparametric finite elements where geometry $\boldsymbol{x}$, test functions $\delta\boldsymbol{u}$ and $\delta\theta$ as well as field variables $\boldsymbol{u}$ and θ are interpolated by the same set of shape functions. In general, different shape functions can be chosen for the different fields. To account for this, the shape functions for the mechanical problem are denoted by $N^A(\boldsymbol{\xi})$ and the shape functions for the thermal problem are denoted by $N^C(\boldsymbol{\xi})$ such that the nodal points are numbered element-wise, i.e., $A = 1, ..., n^{\boldsymbol{u}}_{en}$ and $C = 1, ..., n^{\theta}_{nen}$. However, it should be noted that the implementation is carried out with $N^A(\boldsymbol{\xi}) = N^C(\boldsymbol{\xi})$ and $n^{\boldsymbol{u}}_{nen} = n^{\theta}_{nen}$.

The spatial discretisation of Eqs. (5.15) and (5.16) in combination with the arbitrariness of the discretised test functions leads to a semidiscrete system of nonlinear equations

$$\underline{\mathbf{f}}^{\boldsymbol{u}}_{\mathrm{dyn}} + \underline{\mathbf{f}}^{\boldsymbol{u}}_{\mathrm{int}} - \underline{\mathbf{f}}^{\boldsymbol{u}}_{\mathrm{vol}} - \underline{\mathbf{f}}^{\boldsymbol{u}}_{\mathrm{sur}} = \underline{\mathbf{0}} \,, \tag{5.17}$$

$$\underline{\mathbf{f}}^{\theta}_{\mathrm{dyn}} + \underline{\mathbf{f}}^{\theta}_{\mathrm{int}} - \underline{\mathbf{f}}^{\theta}_{\mathrm{vol}} - \underline{\mathbf{f}}^{\theta}_{\mathrm{sur}} = \underline{\mathbf{0}} \,. \tag{5.18}$$

These global equations are assembled from the nodal element contributions

$$\begin{aligned} \boldsymbol{f}^{\boldsymbol{u}\,eA}_{\mathrm{dyn}} &= \int_{\mathcal{B}_e} \rho\, N^A\, \ddot{\boldsymbol{u}}\, \mathrm{d}v \,, \quad \boldsymbol{f}^{\boldsymbol{u}\,eA}_{\mathrm{int}} = \int_{\mathcal{B}_e} \boldsymbol{\sigma} \cdot \nabla_{\boldsymbol{x}} N^A\, \mathrm{d}v \,, \\ \boldsymbol{f}^{\boldsymbol{u}\,eA}_{\mathrm{vol}} &= \int_{\mathcal{B}_e} \rho\, N^A\, \boldsymbol{b}\, \mathrm{d}v \,, \quad \boldsymbol{f}^{\boldsymbol{u}\,eA}_{\mathrm{sur}} = \int_{\partial\mathcal{B}^{\boldsymbol{t}}_e} N^A\, \bar{\boldsymbol{t}}\, \mathrm{d}a \,, \end{aligned} \tag{5.19}$$

and

$$\begin{aligned} f^{\theta\,eC}_{\mathrm{dyn}} &= \int_{\mathcal{B}_e} \rho\, c\, N^C\, \dot{\theta}\, \mathrm{d}v \,, \quad f^{\theta\,eC}_{\mathrm{int}} = \int_{\mathcal{B}_e} -\nabla_{\boldsymbol{x}} N^C \cdot \boldsymbol{q}\, \mathrm{d}v \,, \\ f^{\theta\,eC}_{\mathrm{vol}} &= \int_{\mathcal{B}_e} N^C\, \hat{r}\, \mathrm{d}v \,, \quad f^{\theta\,eC}_{\mathrm{sur}} = \int_{\partial\mathcal{B}^{q}_e} N^C\, \bar{q}\, \mathrm{d}a \,, \end{aligned} \tag{5.20}$$

with $e = 1, ..., n_{el}$ as well as the mechanical, $A = 1, ..., n^{\boldsymbol{u}}_{en}$, and the thermal, $C = 1, ..., n^{\theta}_{en}$, node contributions. By introducing a global vector of all degrees of freedom,

$$\underline{\mathbf{d}} = \left[\boldsymbol{u}_1 \;\; \theta_1 \;\; \boldsymbol{u}_2 \;\; \theta_2 \;\; \ldots \;\; \boldsymbol{u}_{n_{np}} \;\; \theta_{n_{np}} \right]^{\mathrm{t}} \,, \tag{5.21}$$

Eqs. (5.17) and (5.18) can be written as

$$\underline{\mathbf{r}}(\underline{\mathbf{d}}, \dot{\underline{\mathbf{d}}}, \ddot{\underline{\mathbf{d}}}) = \underline{\mathbf{f}}_{\mathrm{dyn}} + \underline{\mathbf{f}}_{\mathrm{int}} - \underline{\mathbf{f}}_{\mathrm{vol}} - \underline{\mathbf{f}}_{\mathrm{sur}} = \underline{\mathbf{0}} \,. \tag{5.22}$$

The residual depends on the field variables represented by the degrees of freedom $\underline{\mathbf{d}}$ and the respective time derivatives $\dot{\underline{\mathbf{d}}}$ and $\ddot{\underline{\mathbf{d}}}$.

In this chapter, inertia forces, mechanical volume forces and mechanical Robin boundary conditions (follower forces) are neglected. Furthermore, the time discretisation is carried out with the Backward Euler method ($\dot{\underline{\mathbf{d}}} = [\underline{\mathbf{d}}_{n+1} - \underline{\mathbf{d}}_n]/\Delta t$) such that the discrete residual equation reads

$$\underline{\mathbf{r}}(\underline{\mathbf{d}}_{n+1}, \underline{\mathbf{d}}_n) = \underline{\mathbf{f}}_{\mathrm{dyn}}(\underline{\mathbf{d}}_{n+1}, \underline{\mathbf{d}}_n) + \underline{\mathbf{f}}_{\mathrm{int}}(\underline{\mathbf{d}}_{n+1}, \underline{\mathbf{d}}_n) - \underline{\mathbf{f}}_{\mathrm{vol}}(\underline{\mathbf{d}}_{n+1}, \underline{\mathbf{d}}_n) - \underline{\mathbf{f}}_{\mathrm{sur}}(\underline{\mathbf{d}}_{n+1}) = \underline{\mathbf{0}} \,. \tag{5.23}$$

This system of non-linear equations is solved iteratively by means of the Newton-Raphson method, i.e.

$$\begin{aligned} \underline{\underline{\mathbf{J}}}(\underline{\mathbf{d}}^m_{n+1}) \cdot \Delta\underline{\mathbf{d}} &= -\underline{\mathbf{r}}(\underline{\mathbf{d}}^m_{n+1}, \underline{\mathbf{d}}_n) \,, \\ \underline{\mathbf{d}}^{m+1}_{n+1} &= \underline{\mathbf{d}}^m_{n+1} + \Delta\underline{\mathbf{d}} \,, \\ m &\leftarrow m + 1 \,. \end{aligned} \tag{5.24}$$

In the above equation, $\underline{\underline{\mathbf{J}}}$ is the Jacobian of the global Newton-Raphson scheme

$$\underline{\underline{\mathbf{J}}}(\underline{\mathbf{d}}^m_{n+1}) = \frac{\mathrm{d}\underline{\mathbf{r}}(\underline{\mathbf{d}}^m_{n+1}, \underline{\mathbf{d}}_n)}{\mathrm{d}\underline{\mathbf{d}}^m_{n+1}} \,, \tag{5.25}$$

which depends on the current unknown state of equilibrium.

5.2.2 Thermomechanical two-scale framework

The thermomechanical finite element framework derived in the previous section is applied on the macro-scale

$$\underline{\mathbf{r}}^{\mathrm{M}} = \underline{\mathbf{f}}^{\mathrm{M}}_{\mathrm{dyn}} + \underline{\mathbf{f}}^{\mathrm{M}}_{\mathrm{int}} - \underline{\mathbf{f}}^{\mathrm{M}}_{\mathrm{vol}} - \underline{\mathbf{f}}^{\mathrm{M}}_{\mathrm{sur}} = \underline{\mathbf{0}} \,. \tag{5.26}$$

According to the balance equations of the meso-scale problems, Eqs. (5.7) and (5.8), the meso-scale residual equation reduces to the steady state problem

$$\underline{\mathbf{r}}^{\mathrm{m}} = \underline{\mathbf{f}}^{\mathrm{m}}_{\mathrm{int}} = \underline{\mathbf{0}} \,. \tag{5.27}$$

In order to relate the macro-scale and meso-scale quantities, the macro homogeneity conditions

$$\boldsymbol{\sigma}^{\mathrm{M}} : \boldsymbol{\varepsilon}^{\mathrm{M}} = \frac{1}{v} \int_{\mathcal{B}} \boldsymbol{\sigma}^{\mathrm{m}} : \boldsymbol{\varepsilon}^{\mathrm{m}} \, \mathrm{d}v \, , \tag{5.28}$$

$$\boldsymbol{q}^{\mathrm{M}} \cdot \nabla_{\boldsymbol{x}} \, \theta^{\mathrm{M}} = \frac{1}{v} \int_{\mathcal{B}} \boldsymbol{q}^{\mathrm{m}} \cdot \nabla_{\boldsymbol{x}} \, \theta^{\mathrm{m}} \, \mathrm{d}v \, , \tag{5.29}$$

are applied and are fulfilled for linear displacement boundary conditions, periodic boundary conditions as well as for uniform tractions or, respectively, heat fluxes. In this work, periodic boundary conditions are applied such that

$$\begin{aligned} \boldsymbol{u}^{+} &= \boldsymbol{u}^{-} + \boldsymbol{\varepsilon}^{\mathrm{M}} \cdot [\boldsymbol{x}^{+} - \boldsymbol{x}^{-}] \, , \\ \boldsymbol{t}^{+} &= -\, \boldsymbol{t}^{-} \, , \\ \theta^{+} &= \theta^{-} + \nabla_{\boldsymbol{x}} \, \theta^{\mathrm{M}} \cdot [\boldsymbol{x}^{+} - \boldsymbol{x}^{-}] \, , \\ \boldsymbol{q}^{+} \cdot \boldsymbol{n}^{+} &= -\, \boldsymbol{q}^{-} \cdot \boldsymbol{n}^{-} \, , \end{aligned} \tag{5.30}$$

are enforced on the meso-scale. The above set of equations does not define, how the macro-scale temperature is dealt with at the meso-scale. However, the effective material response explicitly depends on the temperature due to, e.g., temperature dependent material properties or due to thermal softening. Eq. $(5.30)_3$ shows that the macro-scale temperature gradient $\nabla_{\boldsymbol{x}} \, \theta^{\mathrm{M}}$ as well as the size of the underlying RVE determines the temperature at the meso-scale. As a consequence, the meso-scale temperature θ^{m} might largely differ from the macro-scale temperature θ^{M} for high temperature gradients or large RVEs. Therefore, it must be ensured that the RVE is small compared to the meso-scale so that the separation of scales assumption holds true. This is the θ^{m}–approach which is applied in, e.g., Özdemir et al. [132] and Sengupta et al. [157]. The meso-scale temperature is thereby assumed to be the macro-scale temperature in the centre of the considered RVE. As already mentioned, the θ^{M}–approach was proposed by Temizer and Wriggers [172]. Here, all temperature dependent quantities are explicitly evaluated at the macro-scale temperature θ^{M}. The meso-scale temperature field resulting from equation Eq. $(5.30)_3$ is only used in order to induce a temperature gradient $\nabla_{\boldsymbol{x}} \, \theta^{\mathrm{m}}$ at the meso-scale. With this approach, the size of the RVE does not affect the effective material behaviour. In practice, this appears to be convenient since a discretised RVE can be used for multi-scale analysis without taking mesh dimensions and unit systems into consideration. From a continuum thermodynamics point of view, this approach a priori meets the restriction of the separation of scales assumption, Temizer and Wriggers [172]. Both approaches will briefly be discussed on the basis of numerical examples in Section 5.4.1.

For the fully coupled multiscale finite element framework, the material model as well as the respective tangent terms have to be extracted from the meso-scale finite element solution. Following the procedure outlined in Sengupta et al. [157], the effective stress and heat flux are obtained by

$$\boldsymbol{\sigma}^{\mathrm{M}} = \frac{1}{v} \sum_{I=1}^{n_{\mathrm{ext}}} \boldsymbol{x}^I \otimes \underline{\mathbf{r}}_{\boldsymbol{u}}^I \;, \quad \boldsymbol{q}^{\mathrm{M}} = \frac{1}{v} \sum_{I=1}^{n_{\mathrm{ext}}} - \boldsymbol{x}^I \otimes \underline{\mathbf{r}}_{\theta}^I \;. \tag{5.31}$$

In the above equation, v is the volume occupied by the RVE and $I = 1, \ldots, n_{\mathrm{ext}}$ represents the boundary nodes of the RVE discretisation on $\partial\mathcal{B}^{\mathrm{RVE}}$. In general, this boundary includes the external boundary as well as internal boundaries like voids or cracks. However, throughout this work we assume traction free and adiabatic internal boundaries. Furthermore, in the above equation, $\underline{\mathbf{r}}_{\boldsymbol{u}}^I$ is the reaction force vector at the boundary related to the displacements, and $\underline{\mathbf{r}}_{\theta}^I$ is the reaction flux vector at the boundary related to the temperature. The effective value of volume related quantities is obtained by a volume average over the RVE, i.e.

$$\begin{aligned} \boldsymbol{b}^{\mathrm{M}} &= \frac{1}{v} \int_{\mathcal{B}^{\mathrm{RVE}}} \boldsymbol{b}^{\mathrm{m}} \, \mathrm{d}v \;, \quad \rho^{\mathrm{M}} = \frac{1}{v} \int_{\mathcal{B}^{\mathrm{RVE}}} \rho^{\mathrm{m}} \, \mathrm{d}v \;, \\ \hat{r}^{\mathrm{M}} &= \frac{1}{v} \int_{\mathcal{B}^{\mathrm{RVE}}} \hat{r}^{\mathrm{m}} \, \mathrm{d}v \;, \quad [\,\rho\, c\,]^{\mathrm{M}} = \frac{1}{v} \int_{\mathcal{B}^{\mathrm{RVE}}} [\,\rho\, c\,]^{\mathrm{m}} \, \mathrm{d}v \;. \end{aligned} \tag{5.32}$$

The tangent terms which are needed to evaluate the macro-scale Jacobian are obtained by

$$\begin{aligned} \frac{\mathrm{d}\boldsymbol{\sigma}^{\mathrm{M}}}{\mathrm{d}\boldsymbol{\varepsilon}^{\mathrm{M}}} &= \frac{1}{v} \sum_{I=1}^{n_{\mathrm{ext}}} \sum_{J=1}^{n_{\mathrm{ext}}} \boldsymbol{x}^I \otimes \underline{\underline{\mathbf{C}}}_{\boldsymbol{u}\boldsymbol{u}}^{IJ} \otimes \boldsymbol{x}^J \;, \quad \frac{\mathrm{d}\boldsymbol{\sigma}^{\mathrm{M}}}{\mathrm{d}\theta^{\mathrm{M}}} = \frac{1}{v} \sum_{I=1}^{n_{\mathrm{ext}}} \sum_{J=1}^{n_{\mathrm{ext}}} \boldsymbol{x}^I \otimes \underline{\underline{\mathbf{C}}}_{\boldsymbol{u}\theta}^{IJ} \;, \\ \frac{\mathrm{d}\boldsymbol{q}^{\mathrm{M}}}{\mathrm{d}\,\nabla_{\boldsymbol{x}}\,\theta^{\mathrm{M}}} &= \frac{1}{v} \sum_{I=1}^{n_{\mathrm{ext}}} \sum_{J=1}^{n_{\mathrm{ext}}} \boldsymbol{x}^I \otimes \left[\, \boldsymbol{x}^J - \boldsymbol{x}^{\mathrm{c}} \,\right] \mathrm{C}_{\theta\theta}^{IJ} \;, \\ \frac{\mathrm{d}\hat{r}^{\mathrm{M}}}{\mathrm{d}\boldsymbol{\varepsilon}^{\mathrm{M}}} &= \frac{1}{v} \sum_{I=1}^{n_{\mathrm{ext}}} \boldsymbol{x}^I \otimes \left[\hat{\underline{\mathbf{r}}}_{\boldsymbol{u}}^I - \sum_{J=1}^{n_{\mathrm{int}}} \underline{\underline{\mathbf{D}}}_{\boldsymbol{u}\boldsymbol{u}}^{JI} \cdot \hat{\underline{\mathbf{r}}}_{\boldsymbol{u}}^J \right] , \\ \frac{\mathrm{d}\hat{r}^{\mathrm{M}}}{\mathrm{d}\theta^{\mathrm{M}}} &= \frac{1}{v} \sum_{I=1}^{n_{\mathrm{ext}}} \left[\hat{\underline{\mathbf{r}}}_{\theta}^I - \sum_{J=1}^{n_{\mathrm{int}}} \hat{\underline{\mathbf{r}}}_{\theta}^J \, \mathrm{D}_{\theta\theta}^{JI} + \hat{\underline{\mathbf{r}}}_{\boldsymbol{u}}^J \cdot \underline{\underline{\mathbf{D}}}_{\boldsymbol{u}\theta}^{JI} \right] , \end{aligned} \tag{5.33}$$

with the center point of the RVE $\boldsymbol{x}^{\mathrm{c}}$ and the following expressions

Algorithm 5.1: Sketch of the two-scale finite element framework.

Data: Read input files and initialise the boundary value problem at the macro-scale as well as all mesoscale boundary value problems.
while $t < t_{\max}$ **do** // Time loop
  while $\|\underline{\mathbf{r}}^{\mathrm{M}}\| \geq tol$ **do** // Macro-scale Newton-Raphson loop
    for $e = 1, ..., n_{el}^{\mathrm{M}}$ **do** // Macro-scale element loop
      extract element values $\underline{\mathbf{d}}_e$ from the global $\underline{\mathbf{d}}$-vector, cf. Eq. (5.21)
      for $q = 1, ..., n_{qp}$ **do** // Macro-scale quadrature point loop
        compute $\boldsymbol{\varepsilon}^{\mathrm{M}}$, θ^{M} and $\nabla_{\boldsymbol{x}}\,\theta^{\mathrm{M}}$ at q from $\underline{\mathbf{d}}_e$ and pass the values to the RVE
        load internal variables of the RVE belonging to the last state of equilibrium
        apply the constraints, cf. Eq. (5.30), to enforce periodic boundary conditions
        while $\|\underline{\mathbf{r}}^{\mathrm{m}}\| \geq tol$ **do** // Meso-scale Newton-Raphson loop
          for $e = 1, ..., n_{el}^{\mathrm{m}}$ **do** // Meso-scale element loop
            extract element values $\underline{\mathbf{d}}_e$ from the global $\underline{\mathbf{d}}$-vector, cf. Eq. (5.21)
            for $q = 1, ..., n_{qp}$ **do** // Meso-scale quadrature point loop
              determine the material reaction $\boldsymbol{\sigma}^{\mathrm{m}}$ and $\boldsymbol{q}^{\mathrm{m}}$, $\boldsymbol{b}^{\mathrm{m}}$, ρ^{m}, $\hat{r}^{\mathrm{m}}$ and $[\rho\, c]^{\mathrm{m}}$
              determine the tangent terms $\frac{\mathrm{d}\boldsymbol{\sigma}}{\mathrm{d}\boldsymbol{\varepsilon}}$, $\frac{\mathrm{d}\boldsymbol{\sigma}}{\mathrm{d}\theta}$, $\frac{\mathrm{d}\boldsymbol{q}}{\mathrm{d}\,\nabla_{\boldsymbol{x}}\,\theta}$, $\frac{\mathrm{d}\hat{r}}{\mathrm{d}\boldsymbol{\varepsilon}}$ as well as $\frac{\mathrm{d}\hat{r}}{\mathrm{d}\theta}$
            end
            evaluate elemental force/flux contributions, cf. Eqs. (5.19) and (5.20)
            compute the respective elemental tangent terms
          end
          assemble the meso-scale residual $\underline{\mathbf{r}}^{\mathrm{m}}$ and the respective Jacobian $\underline{\underline{\mathbf{J}}}^{\mathrm{m}}$
          solve the system of equations to determine $\Delta\underline{\mathbf{d}}^{\mathrm{m}}$, cf. Eq. (5.24)
        end
        perform the homogenisation procedure on the converged state, cf. Eq. (5.34)
        subsequently evaluate Eqs. (5.31) to (5.33)
        return $\boldsymbol{\sigma}^{\mathrm{M}}$ and $\boldsymbol{q}^{\mathrm{M}}$ as well as the effective tangents terms to macro-scale q
      end
      evaluate elemental force/flux contributions, cf. Eqs. (5.19) and (5.20)
      compute the respective elemental tangent terms
    end
    assemble the macro-scale residual $\underline{\mathbf{r}}^{\mathrm{M}}$ and the respective Jacobian $\underline{\underline{\mathbf{J}}}^{\mathrm{M}}$
    solve the system of equations to determine $\Delta\underline{\mathbf{d}}^{\mathrm{M}}$, cf. Eq. (5.24)
  end
  save the internal variables of the converged state of each RVE for the next time step
  evaluate postprocessing routines for the current time step
  increase time step
  $t \leftarrow t + \Delta t^{\mathrm{M}}$
end

$$\underline{\underline{\mathbf{D}}}^{LJ} = [\underline{\underline{\mathbf{J}}}^{KL}]^{-1} \cdot \underline{\underline{\mathbf{J}}}^{KJ} \ , \quad \underline{\underline{\mathbf{C}}}^{IJ} = \underline{\underline{\mathbf{J}}}^{IJ} - \underline{\underline{\mathbf{J}}}^{IL} \cdot \underline{\underline{\mathbf{D}}}^{LJ} \ ,$$
$$\hat{\underline{\mathbf{r}}}_{\boldsymbol{u}} = \mathop{\mathbf{A}}_{e=1}^{n_{el}} \int_{\mathcal{B}^{\mathrm{RVE}}} \frac{\mathrm{d}\hat{r}}{\mathrm{d}\boldsymbol{\varepsilon}} \, \mathrm{d}v \ , \quad \hat{\underline{\mathbf{r}}}_{\theta} = \mathop{\mathbf{A}}_{e=1}^{n_{el}} \int_{\mathcal{B}^{\mathrm{RVE}}} \frac{\mathrm{d}\hat{r}}{\mathrm{d}\theta} \, \mathrm{d}v \ . \tag{5.34}$$

In the above equation, $\underline{\underline{\mathbf{J}}}$ is the Jacobian which is introduced in Eq. (5.25). Details regarding the derivation can be found in Sengupta et al. [157]. With the above equations at hand, a two-scale finite element framework is implemented as described in detail in the following section.

5.2.3 Implementation for parallel computing

The two-scale finite element framework outlined in the above sections is implemented in C++. Parallelisation on the macro-scale is achieved with the help of suitable OpenMP[1] pragmas. The tangent stiffness matrices are treated as sparse matrices with the help of the linear algebra library Eigen[2]. In order to solve the resulting non-linear systems of equations, UMFPACK from the SuiteSparse[3] library is used as a direct solver. For performance purposes, the code is linked with the highly optimised BLAS implementation OpenBLAS[4].

Algorithm 5.1 demonstrates the structure of the code. After reading the input files, the macro-scale as well as meso-scale problems are initialised and the macro-scale time loop is started. At each load step, a Newton-Raphson loop is run, wherein equations Eqs. (5.23) and (5.25) are evaluated. Therefore, it is necessary to perform RVE computations at each quadrature point of the respective macro-scale elements, for which $\boldsymbol{\varepsilon}^{\mathrm{M}}$, θ^{M} and $\nabla_{\boldsymbol{x}} \theta^{\mathrm{M}}$ are passed to the RVE. At the meso-scale, each underlying RVE is subjected to periodic boundary conditions, cf. Eq. (5.30), and for one time step (with Δt^{M}) another Newton-Raphson loop is performed. Schematically, this procedure equals a local iteration within the algorithmic treatment of a nonlinear constitutive relation. Hence, all internal variables of the macro-scale state of equilibrium of a particular RVE have to be stored in the main memory of the computer performing the simulation.

After convergence is achieved at the meso-scale computation, Eqs. (5.31) to (5.33) are evaluated and the homogenised quantities are returned to the macro-scale. After all meso-scale computations have been processed, the Newton-Raphson updates are computed at the macro-scale until the current state of equilibrium is found, and the simulation continues with the next macro-scale load increment.

[1] http://www.openmp.org
[2] http://eigen.tuxfamily.org
[3] http://faculty.cse.tamu.edu/davis/suitesparse.html
[4] http://www.openblas.net

5.3 Thermoviscoplasticity

In order to demonstrate the general nonlinear two-scale finite element framework derived above, a thermoviscoplastic constitutive relation with nonlinear thermal softening is proposed in this section. Here, a viscous ansatz according to Hohenemser and Prager [80] is applied within a thermoplastic constitutive framework and a geometrically linear setting following, e.g., Simo and Miehe [164], Simo and Hughes [160], Rosakis et al. [144], Bertram and Krawietz [25].

5.3.1 Constitutive relations

We assume a free energy function $\hat{\Psi}(\boldsymbol{\varepsilon}, \theta, \underline{\mathbf{z}})$ wherein $\underline{\mathbf{z}}$ represents a vector valued set of internal variables. A further assumption made is the additive decomposition of the strain tensor into an elastic and a plastic part

$$\boldsymbol{\varepsilon} = \boldsymbol{\varepsilon}^{\mathrm{e}} + \boldsymbol{\varepsilon}^{\mathrm{p}} \ . \tag{5.35}$$

It is further assumed that only elastic strains evoke stresses such that the free energy function is a function of the elastic strains $\boldsymbol{\varepsilon}^{\mathrm{e}}$, the temperature θ and the set of internal variables $\underline{\mathbf{z}}$, so that $\Psi(\boldsymbol{\varepsilon}^{\mathrm{e}}, \theta, \underline{\mathbf{z}})$. From this form of free energy function, following, e.g., Liu [108], the definitions of the stress $\boldsymbol{\sigma}$ and the entropy s follow

$$\boldsymbol{\sigma} = \rho \, \frac{\partial \Psi(\boldsymbol{\varepsilon}^{\mathrm{e}}, \theta, \underline{\mathbf{z}})}{\partial \boldsymbol{\varepsilon}^{\mathrm{e}}} \ , \tag{5.36}$$

$$s = -\frac{\partial \Psi(\boldsymbol{\varepsilon}^{\mathrm{e}}, \theta, \underline{\mathbf{z}})}{\partial \theta} \ , \tag{5.37}$$

and the driving forces $\underline{\mathbf{y}}$ are obtained by

$$\underline{\mathbf{y}} = -\rho \, \frac{\partial \Psi(\boldsymbol{\varepsilon}^{\mathrm{e}}, \theta, \underline{\mathbf{z}})}{\partial \underline{\mathbf{z}}} \ . \tag{5.38}$$

In this chapter, the set of internal variables $\underline{\mathbf{z}} = \{\boldsymbol{\varepsilon}^{\mathrm{p}}, k\}$ includes the plastic part of the strain tensor $\boldsymbol{\varepsilon}^{\mathrm{p}}$ as well as the accumulated plastic strain k and the respective driving forces are denoted as $\underline{\mathbf{y}} = \{\boldsymbol{\sigma}, \kappa\}$. The thermoviscoplastic material considered shall be characterised by an additively decomposed free energy function

$$\Psi(\boldsymbol{\varepsilon}^{\mathrm{e}}, \theta, \underline{\mathbf{z}}) = \Psi^{\mathrm{e}}_{\mathrm{vol}}(\boldsymbol{\varepsilon}^{\mathrm{e}}) + \Psi^{\mathrm{e}}_{\mathrm{dev}}(\boldsymbol{\varepsilon}^{\mathrm{e}}_{\mathrm{dev}}) + \Psi^{\mathrm{e}\,\theta}_{\mathrm{vol}}(\boldsymbol{\varepsilon}^{\mathrm{e}}, \theta) + \Psi^{\theta}(\theta) + \Psi^{\mathrm{p}\,\theta}_{\mathrm{dev}}(\theta, k) \ , \tag{5.39}$$

with the elastic volumetric, $\Psi^{\mathrm{e}}_{\mathrm{vol}}$, the elastic deviatoric, $\Psi^{\mathrm{e}}_{\mathrm{dev}}$, the thermoelastic coupling, $\Psi^{\mathrm{e}\,\theta}_{\mathrm{vol}}$, the thermal, Ψ^{θ}, as well as the thermoplastic, $\Psi^{\mathrm{p}\,\theta}_{\mathrm{dev}}$, parts. In order to limit admissible

thermoelastic states, in Bertram and Krawietz [25] a yield function of the form $\Phi(\boldsymbol{\varepsilon}, \theta, \underline{\mathbf{z}})$ with yield condition

$$\Phi(\boldsymbol{\varepsilon}, \theta, \underline{\mathbf{z}}) = 0 \,, \tag{5.40}$$

and loading condition

$$\frac{\partial \Phi}{\partial \boldsymbol{\varepsilon}} : \dot{\boldsymbol{\varepsilon}} + \frac{\partial \Phi}{\partial \theta}\, \dot{\theta} > 0 \,, \tag{5.41}$$

is proposed. If both conditions are fulfilled, yielding occurs, $\dot{\underline{\mathbf{z}}} \neq \underline{\mathbf{0}}$. Otherwise, the thermodynamic state is thermoelastic and the rate of the internal variables vanishes, $\dot{\underline{\mathbf{z}}} = \underline{\mathbf{0}}$. Application of the postulate of maximum dissipation as outlined in, e.g., Simo and Hughes [160], Simo [161] yields the associated evolution equations

$$\dot{\boldsymbol{\varepsilon}}^{\mathrm{p}} = \dot{\lambda}\, \frac{\partial \Phi}{\partial \boldsymbol{\sigma}} \,, \qquad \dot{k} = \dot{\lambda}\, \frac{\partial \Phi}{\partial \kappa} \,, \tag{5.42}$$

with $\Phi = 0$ and the plastic multiplier $\dot{\lambda} > 0$ in case of inelastic loading. Further information regarding the Kuhn-Tucker conditions can be found in Luenberger and Ye [109] as well as in Simo and Hughes [160] and the references cited therein. The rate dependency is included in the model by an ansatz which was proposed by Hohenemser and Prager [80]

$$\dot{\lambda} = \frac{\langle \Phi \rangle}{2\,\eta} \,, \tag{5.43}$$

where η is a viscous damper-like constant.

The single contributions of Eq. (5.39) are specified by

$$\Psi^{\mathrm{e}}_{\mathrm{vol}}(\boldsymbol{\varepsilon}^{\mathrm{e}}) = \frac{1}{\rho}\, K\, \mathrm{tr}^2(\boldsymbol{\varepsilon}^{\mathrm{e}}) \,, \tag{5.44}$$

$$\Psi^{\mathrm{e}}_{\mathrm{dev}}(\boldsymbol{\varepsilon}^{\mathrm{e}}_{\mathrm{dev}}) = \frac{1}{\rho}\, G\, \boldsymbol{\varepsilon}^{\mathrm{e}}_{\mathrm{dev}} : \boldsymbol{\varepsilon}^{\mathrm{e}}_{\mathrm{dev}} \,, \tag{5.45}$$

$$\Psi^{\mathrm{e}\,\theta}_{\mathrm{vol}}(\boldsymbol{\varepsilon}^{\mathrm{e}}, \theta) = \frac{1}{\rho}\, 3\,\alpha\, K \left[\theta - \theta_0\right]\, \mathrm{tr}(\boldsymbol{\varepsilon}^{\mathrm{e}}) \,, \tag{5.46}$$

$$\Psi^{\theta}(\theta) = c \left[\left[\theta - \theta_0\right] - \theta\, \ln\left(\frac{\theta}{\theta_0}\right) \right] \,, \tag{5.47}$$

$$\Psi^{\mathrm{p}\,\theta}_{\mathrm{dev}}(\theta, k) = \left[1 - r\right] \left[y_\infty(\theta) - y_0(\theta)\right] \left[k + k_0 \exp\left(-\frac{k}{k_0}\right) \right] + \frac{r}{2}\, h(\theta)\, k^2 \,. \tag{5.48}$$

In the above equations, $\boldsymbol{\varepsilon}^{\mathrm{e}}_{\mathrm{dev}}$ is the elastic deviatoric part of the strain tensor, K is the bulk modulus, G is the shear modulus, α is the thermal expansion coefficient, θ_0 is the reference temperature and k is the accumulated plastic strain from $\underline{\mathbf{z}}$ which is introduced above. Furthermore, k_0 represents an exponential saturation coefficient and $r \in [0,1]$ is a mixing parameter. The temperature dependent initial yield stress $y_0(\theta)$, saturation yield stress $y_\infty(\theta)$ as well as the linear hardening modulus $h(\theta)$ are defined as

$$y_0(\theta) = a_{y0} \left[\arctan\left(-\frac{\theta - b_{y0}}{c_{y0}} \right) + d_{y0} \right] , \tag{5.49}$$

$$y_\infty(\theta) = a_{y\infty} \left[\arctan\left(-\frac{\theta - b_{y\infty}}{c_{y\infty}} \right) + d_{y\infty} \right] , \tag{5.50}$$

$$h(\theta) = a_h \left[\arctan\left(-\frac{\theta - b_h}{c_h} \right) + d_h \right] , \tag{5.51}$$

which, in the case of appropriate parameter choices, lead to so-called thermal softening as discussed, e.g., in Simo [163]. With this at hand, the evaluation of Eqs. (5.36) and (5.38) yields

$$\boldsymbol{\sigma} = K \left[\operatorname{tr}(\boldsymbol{\varepsilon}^{\mathrm{e}}) - 3\,\alpha \left[\theta - \theta_0 \right] \right] \boldsymbol{I} + 2\,G\,\boldsymbol{\varepsilon}^{\mathrm{e}}_{\mathrm{dev}} , \tag{5.52}$$

$$\kappa = \left[r - 1 \right] \left[y_\infty(\theta) - y_0(\theta) \right] \left[1 - \exp\left(-\frac{k}{k_0} \right) \right] - r\,h(\theta)\,k , \tag{5.53}$$

where $\boldsymbol{I}$ is the second order identity tensor. A von Mises type yield function

$$\Phi = \| \boldsymbol{\sigma}_{\mathrm{dev}} \| - \sqrt{\frac{2}{3}} \left[y_0(\theta) - \kappa(k) \right] , \tag{5.54}$$

is chosen such that the Perzyna type evolution equations, Eq. (5.42), evaluate to

$$\dot{\boldsymbol{\varepsilon}}^{\mathrm{p}} = \dot{\lambda}\,\boldsymbol{\nu} \quad \text{with} \quad \boldsymbol{\nu} = \frac{\partial \Phi}{\partial \boldsymbol{\sigma}} = \frac{\boldsymbol{\sigma}_{\mathrm{dev}}}{\| \boldsymbol{\sigma}_{\mathrm{dev}} \|} , \tag{5.55}$$

$$\dot{k} = \sqrt{\frac{2}{3}}\,\dot{\lambda} . \tag{5.56}$$

The viscoplastic yield function $\widetilde{\Phi}$ is obtained by inserting Eq. (5.54) in Eq. (5.43)

$$\widetilde{\Phi} = \left\langle \| \boldsymbol{\sigma}_{\mathrm{dev}} \| - \sqrt{\frac{2}{3}} \left[y_0(\theta) - \kappa(k) \right] \right\rangle - 2\,\eta\,\dot{\lambda} . \tag{5.57}$$

From the Clausius-Duhem inequality, the heat production rate with elastic and plastic contributions follows

$$\hat{r} = -\,3\,\alpha\,K\,\theta\;\mathrm{tr}(\dot{\boldsymbol{\varepsilon}}) + \left[\,\|\boldsymbol{\sigma}_{\mathrm{dev}}\| + \sqrt{\frac{2}{3}}\left[\,\kappa - \theta\,\frac{\partial\kappa}{\partial\theta}\,\right]\right]\dot{\lambda}\;. \tag{5.58}$$

Details regarding the derivation of the dissipation from the Clausius-Duhem inequality can be found in Bertram and Krawietz [25]. In this chapter, the so-called Fourier heat conduction law

$$\boldsymbol{q} = -\boldsymbol{\Lambda}\cdot\nabla_{\boldsymbol{x}}\,\theta = -\Lambda\,\boldsymbol{I}\cdot\nabla_{\boldsymbol{x}}\,\theta\;, \tag{5.59}$$

is considered which maintains the Fourier inequality for semi-definite heat conductivity tensors $\boldsymbol{\Lambda}$, Liu [108]. The chosen isotropic representation involves the heat conduction coefficient Λ which has to be a positive number.

5.3.2 Radial return mapping

With the above constitutive equations at hand, a radial return mapping algorithm is applied in the case of plastic yielding at a time $t \in [0, t_{\mathrm{end}}]$ where the values of the internal variables $\{\boldsymbol{\varepsilon}^{\mathrm{p}}_n, k_n\}$ of the previous time step t_n are assumed to be known, and where the current values of $\boldsymbol{\varepsilon}$, θ as well as $\nabla_{\boldsymbol{x}}\,\theta$ are provided by the finite element method. First, an elastic trial step is carried out

$$\boldsymbol{\varepsilon}^{\mathrm{e\,tr}} = \boldsymbol{\varepsilon} - \boldsymbol{\varepsilon}^{\mathrm{p}}_n\;, \tag{5.60}$$

$$k^{\mathrm{tr}} = k_n\;, \tag{5.61}$$

and, subsequently, Eqs. (5.52) and (5.53) are evaluated with the elastic trial strain $\boldsymbol{\varepsilon}^{\mathrm{e\,tr}}$ as well as with the hardening functions, Eqs. (5.49) to (5.51). The resulting trial stress $\boldsymbol{\sigma}^{\mathrm{tr}}$ is subjected to a volumetric-deviatoric split so that the trial constitutive material answer reads

$$\boldsymbol{\sigma}_{\mathrm{vol}} = K\left[\;\mathrm{tr}\left(\boldsymbol{\varepsilon}^{\mathrm{e\,tr}}\right) - 3\,\alpha\,[\,\theta - \theta_0\,]\;\right]\boldsymbol{I}\;, \tag{5.62}$$

$$\boldsymbol{\sigma}^{\mathrm{tr}}_{\mathrm{dev}} = 2\,G\,\boldsymbol{\varepsilon}^{\mathrm{e\,tr}}_{\mathrm{dev}}\;, \tag{5.63}$$

$$\kappa^{\mathrm{tr}} = [\,r-1\,]\,[\,y_\infty(\theta) - y_0(\theta)\,]\left[\,1 - \exp\left(-\frac{k_n}{k_0}\right)\,\right] - r\,h(\theta)\,k_n\;. \tag{5.64}$$

Next, the yield function, Eq. (5.54), is evaluated. If $\Phi \leq 0$ holds, the current state $\{\boldsymbol{\varepsilon}, \theta, \nabla_{\boldsymbol{x}}\,\theta\}$ is thermoelastic. If not, viscoplastic yielding occurs where a Backward Euler

scheme is used for the constitutive integration of the evolution equations, Eqs. (5.55) and (5.56), which then, with the definition $\Delta\lambda := \Delta t\,\dot{\lambda}$, read

$$\boldsymbol{\varepsilon}^{\mathrm{p}} = \boldsymbol{\varepsilon}^{\mathrm{p}}_n + \Delta\lambda\,\boldsymbol{\nu}\;, \tag{5.65}$$

$$k = k_n + \sqrt{\frac{2}{3}}\,\Delta\lambda\;. \tag{5.66}$$

The thermoviscoplastic yield function, Eq. (5.57), must be fulfilled, i.e.

$$\widetilde{\Phi} = \|\boldsymbol{\sigma}^{\mathrm{tr}}_{\mathrm{dev}}\| - 2\,G\,\Delta\lambda - \sqrt{\frac{2}{3}}\left[\,y_0(\theta) - \kappa(k)\,\right] - 2\,\eta\,\frac{\Delta\lambda}{\Delta t} = 0\;. \tag{5.67}$$

This, in turn, is a nonlinear relation and can be solved iteratively with k as well as $\Delta\lambda$ unknown. Eqs. (5.66) and (5.67) can therefore be formulated in the vector valued residual form

$$\underline{\mathbf{r}}_{\mathrm{loc}} = \begin{bmatrix} \widetilde{\Phi}(\tilde{\underline{\mathbf{z}}}) \\ k_n + \sqrt{\frac{2}{3}}\,\Delta\lambda - k \end{bmatrix} \stackrel{!}{=} \underline{\mathbf{0}}\;, \quad \text{with} \quad \tilde{\underline{\mathbf{z}}} = \begin{bmatrix} \Delta\lambda \\ k \end{bmatrix}\;. \tag{5.68}$$

In order to solve this local nonlinear system of equations, we apply the Newton Raphson method, cf. Eq. (5.24), where the local Jacobian

$$\underline{\underline{\mathbf{J}}}_{\mathrm{loc}} = \frac{\mathrm{d}\underline{\mathbf{r}}_{\mathrm{loc}}}{\mathrm{d}\tilde{\underline{\mathbf{z}}}} = \begin{bmatrix} \dfrac{\mathrm{d}r_{\Delta\lambda}}{\mathrm{d}\Delta\lambda} & \dfrac{\mathrm{d}r_{\Delta\lambda}}{\mathrm{d}k} \\ \dfrac{\mathrm{d}r_k}{\mathrm{d}\Delta\lambda} & \dfrac{\mathrm{d}r_k}{\mathrm{d}k} \end{bmatrix}\;, \tag{5.69}$$

has to be determined. After convergence of the local Newton Raphson algorithm, the current stress as well as dissipation rate can be evaluated. Furthermore, the total derivatives of the thermoviscoplastic terms are needed in order to compute the finite element Jacobian. The consistent linearisation of the stress as well as of the mechanical heat production is therefore outlined in Appendix C.1. In addition, Algorithm C.1, found in Appendix C.1, summarises all necessary equations to be implemented for the radial return algorithm, including the evaluated local Jacobian, cf. Eq. (5.69).

5.4 Numerical examples

The two-scale finite element framework elaborated in Section 5.2 is applied with the thermoviscoplastic material model outlined in the previous section. Due to the compu-

tational cost of rather large multi-scale simulations, a cluster with 4 Intel Xeon E5-4650 CPUs and main memory of 512 GB RAM has been used.

This section is partitioned into three subsections in order to demonstrate different aspects of the thermo-mechanically, fully coupled two-scale finite element framework. The first subsection, Section 5.4.1, shows the difference of the θ^{m}– and θ^{M}–approaches, respectively the handling of the macroscopic temperature at the meso-scale, as discussed in Section 5.2.1. Therefore, a meso-structure with a circular inclusion is considered under a given macroscopic load. In the second subsection, Section 5.4.2, a plane plate with a hole perforated with small voids is studied. Thereby, one-scale finite element analyses with the explicit dissolution of the geometry are compared with two-scale finite element analyses, wherein the macro-scale is coarsely meshed and the voids are modelled within the respective RVEs. Finally, in the third subsection, Section 5.4.3, the results of a quenching simulation of a coated steel radius are shown. Here, the coating consists of tungsten carbide (WC) as well as cobalt (Co). The respective two dimensional WC-Co-RVE is generated from an electron micrograph which was already depicted in Fig. 1.3.

5.4.1 Circular inclusion

In this example, the θ^{m}– and θ^{M}–approaches are compared with each other for a given macroscopic load

$$\begin{aligned} \boldsymbol{\varepsilon}^{\mathrm{M}} &= 0.01\big[\,\boldsymbol{I} + \boldsymbol{e}_1 \otimes \boldsymbol{e}_2 + \boldsymbol{e}_2 \otimes \boldsymbol{e}_1\,\big]\ , \\ \theta^{\mathrm{M}} &= 293\,\mathrm{K}\ , \\ \nabla_{\boldsymbol{x}}\,\theta^{\mathrm{M}} &= \big[\,0.05\,\boldsymbol{e}_1 - 0.1\,\boldsymbol{e}_2\,\big]\,\mathrm{K\,mm^{-1}}\ , \\ \theta_0 &= 293\,\mathrm{K}\ , \end{aligned} \tag{5.70}$$

with the Cartesian basis vectors $\{\boldsymbol{e}_1, \boldsymbol{e}_2\}$. These values are passed from the macro-scale of the two-scale finite element framework to the meso-scale, together with a time increment of $\Delta t = 1\,\mathrm{s}$. The initial values of the internal variables at the meso-scale are zero, hence $k^{\mathrm{m}} = 0$ and $\boldsymbol{\varepsilon}^{\mathrm{p\,m}} = \boldsymbol{0}$. Fig. 5.2 shows the discretisation of the RVE. The grey domain represents cobalt as the matrix material, and the green domain represents tungsten carbide in form of a circular inclusion. In Tables 5.1 and 5.2, the thermo-mechanical material parameters are summarised. The WC phase is modelled as purely thermoelastic material such that no yielding occurs. For demonstration purposes, the initial yield limit function, Eq. (5.49), of the cobalt matrix is chosen to have the intentionally artificial course of the function

$$y_0(\theta) = 500\ \big[\,\arctan\left(-\theta/\mathrm{K} + 293\right) + 2\,\big]\ \mathrm{MPa}\ . \tag{5.71}$$

Consequently, the turning point of the function is at $\theta = 293\,\mathrm{K}$ and is therefore equal to the macroscopic temperature θ^{M} of this example. Furthermore, the saturation term in

Table 5.1: Thermo-mechanical material parameters for cobalt (Co), tungsten carbide (WC) and steel.

Material	Description	Symbol	Value	Unit
Co	Young's modulus	E	2.11×10^{2}	GPa
	Poisson ratio	ν	3.10×10^{-1}	
	Mass density	ρ	8.90×10^{-3}	$\mathrm{g\,mm^{-3}}$
	Heat capacity	c	4.56×10^{2}	$\mathrm{mJ\,g^{-1}\,K^{-1}}$
	Heat expansion	α	1.25×10^{-6}	$\mathrm{K^{-1}}$
	Heat conduction	Λ	1.00×10^{-1}	$\mathrm{W\,mm^{-1}\,K^{-1}}$
WC	Young's modulus	E	7.05×10^{2}	GPa
	Poisson ratio	ν	1.94×10^{-1}	
	Mass density	ρ	1.57×10^{-2}	$\mathrm{g\,mm^{-3}}$
	Heat capacity	c	3.43×10^{2}	$\mathrm{mJ\,g^{-1}\,K^{-1}}$
	Heat expansion	α	1.02×10^{-6}	$\mathrm{K^{-1}}$
	Heat conduction	Λ	8.40×10^{-2}	$\mathrm{W\,mm^{-1}\,K^{-1}}$
Steel	Young's modulus	E	2.10×10^{2}	GPa
	Poisson ratio	ν	3.00×10^{-1}	
	Mass density	ρ	7.85×10^{-3}	$\mathrm{g\,mm^{-3}}$
	Heat capacity	c	4.21×10^{2}	$\mathrm{mJ\,g^{-1}\,K^{-1}}$
	Heat expansion	α	1.30×10^{-6}	$\mathrm{K^{-1}}$
	Heat conduction	Λ	1.00×10^{-1}	$\mathrm{W\,mm^{-1}\,K^{-1}}$

Eq. (5.53) is deactivated with $r = 1$ and the hardening modulus is chosen to be constant $h = 6\,\mathrm{GPa}$ instead of function, Eq. (5.51).

In order to demonstrate the difference of the two approaches, the mesh size of the RVE depicted in Fig. 5.2 is scaled to different sizes by keeping the geometry. The chosen edge lengths are 100 µm, 1 mm and 3 m. The different sizes only affect the thermal part of the considered problem since the mechanical part is only influenced by the symmetric part of the displacement gradient, $\boldsymbol{\varepsilon}^{\mathrm{m}}$. However, the thermal part of the problem is influenced by the temperature θ^{m} itself as well as by the temperature gradient $\nabla_{\boldsymbol{x}}\,\theta^{\mathrm{m}}$. Eq. $(5.30)_3$ reveals the size dependence of the meso-scale problem for the case of using the meso-scale temperature θ^{m} for the evaluation of temperature dependent quantities. In the θ^{m}–approach this temperature is used to evaluate temperature dependent quantities.

Fig. 5.3 shows plots of the temperature, the hardening variable, the mechanical heat production rate and the von Mises stress for the three different RVE sizes. It can be observed that the two rather small RVE sizes qualitatively show the same results for all

Table 5.2: Thermoviscoplastic material parameters for cobalt (Co).

Material	Description	Symbol	Value	Unit
Co	Dynamic viscosity	η	9.63×10^{5}	MPa s
	Mixing parameter	r	8.00×10^{-1}	
	Exponential hardening parameter	k_0	1.15×10^{-2}	
	Initial yield parameter	a_{y0}	1.80×10^{2}	MPa
	Initial yield parameter	b_{y0}	5.50×10^{2}	K
	Initial yield parameter	c_{y0}	2.50×10^{2}	K
	Initial yield parameter	d_{y0}	2.00×10^{1}	
	Saturation yield parameter	$a_{y\infty}$	2.50×10^{2}	MPa
	Saturation yield parameter	$b_{y\infty}$	5.50×10^{2}	K
	Saturation yield parameter	$c_{y\infty}$	2.50×10^{2}	K
	Saturation yield parameter	$d_{y\infty}$	2.00×10^{1}	
	Hardening parameter	a_h	2.00×10^{3}	MPa
	Hardening parameter	b_h	4.50×10^{2}	K
	Hardening parameter	c_h	1.00×10^{2}	K
	Hardening parameter	d_h	2.00×10^{1}	

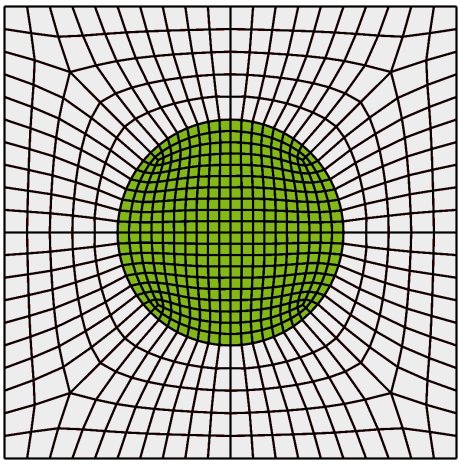

Figure 5.2: Discretisation of the circular inclusion RVE with quadrilateral elements. The grey domain represents cobalt and the green domain represents tungsten carbide. The volume fraction of tungsten carbide is approximately 19.6 %.

quantities under consideration of the chosen scales. In the case of the largest RVE size, it is not surprising that the temperature either falls below or exceeds the temperature scale due to its large size. Due to the evaluation of temperature dependent terms at θ^{m}, the

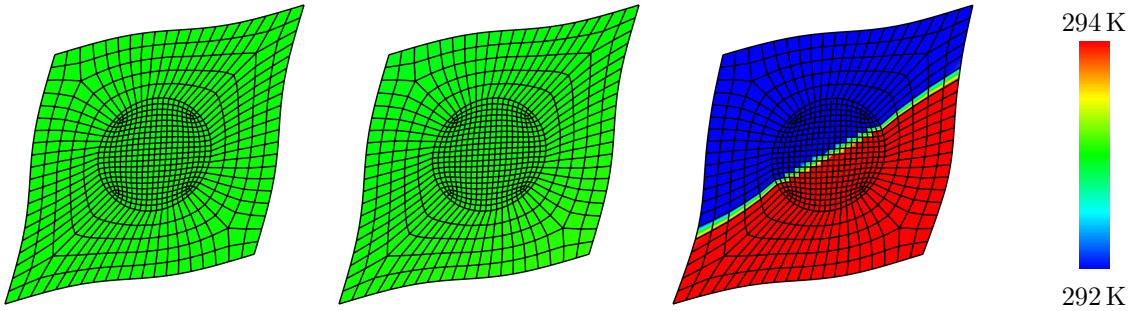

(a) θ^{m} contour plots for RVE edge lengths of (left) 100 µm, (middle) 1 mm and (right) 3 m.

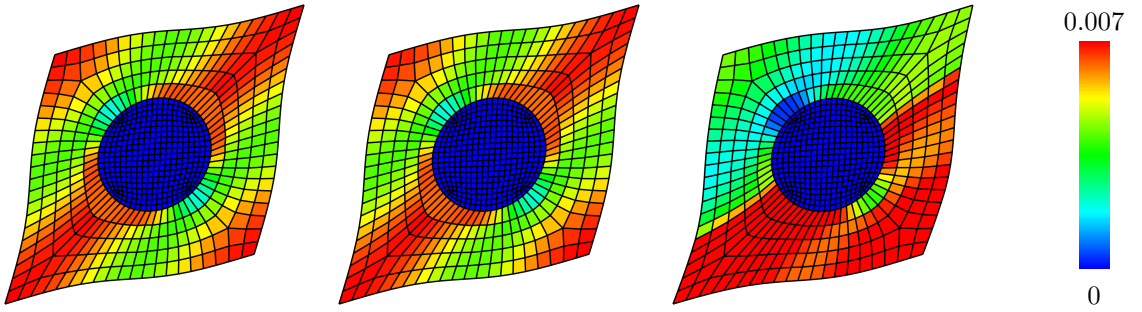

(b) k^{m} contour plots for RVE edge lengths of (left) 100 µm, (middle) 1 mm and (right) 3 m.

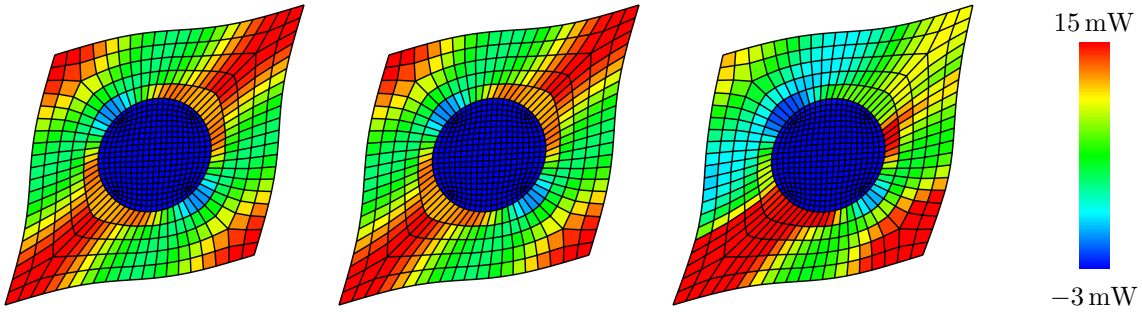

(c) r^{m} contour plots for RVE edge lengths of (left) 100 µm, (middle) 1 mm and (right) 3 m.

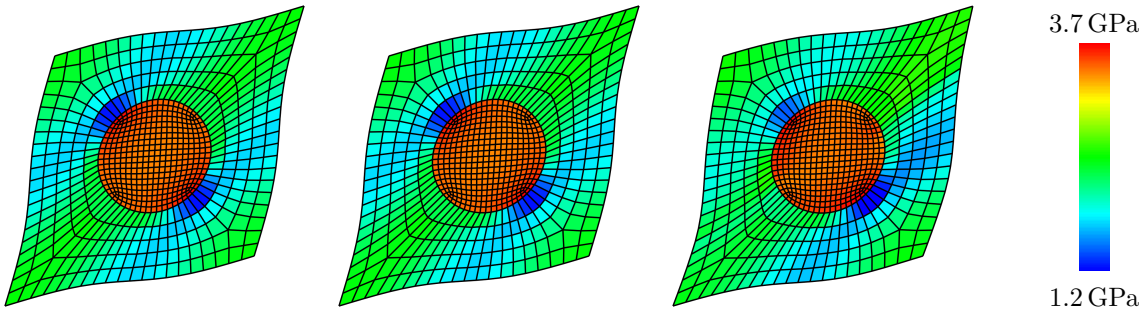

(d) $\sqrt{\frac{3}{2}}\,\|\boldsymbol{\sigma}^{\mathrm{m}}_{\mathrm{dev}}\|$ contour plots for RVE edge lengths of (left) 100 µm, (middle) 1 mm and (right) 3 m.

Figure 5.3: Contour plots of the circular inclusion for the θ^{m}-approach. In table form, (a) the temperature θ^{m}, (b) the hardening variable k^{m}, (c) the heat production rate r^{m} and (d) the von Mises stress are shown for different RVE sizes. The displacements are scaled by factor 25.

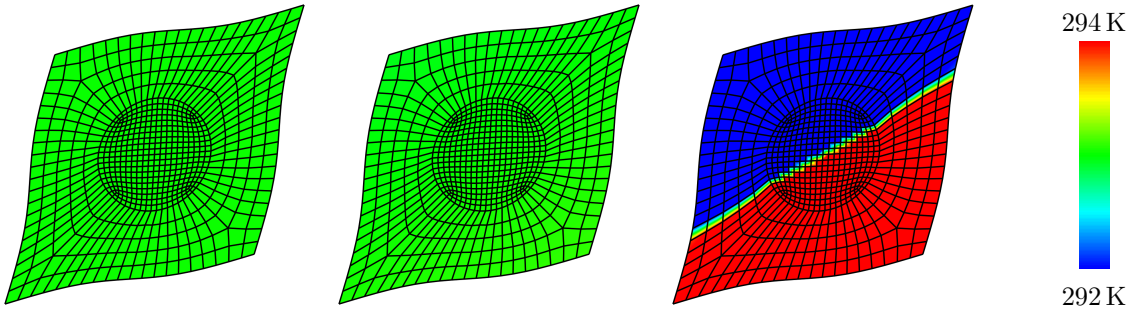

(a) θ^{m} contour plots for RVE edge lengths of (left) 100 µm, (middle) 1 mm and (right) 3 m.

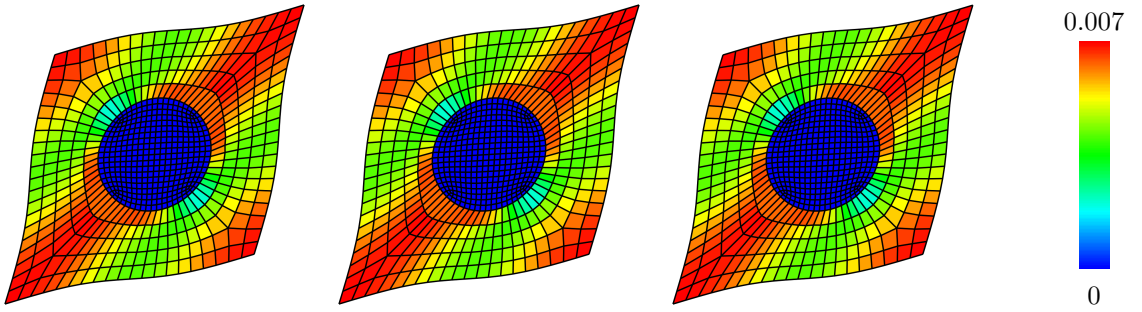

(b) k^{m} contour plots for RVE edge lengths of (left) 100 µm, (middle) 1 mm and (right) 3 m.

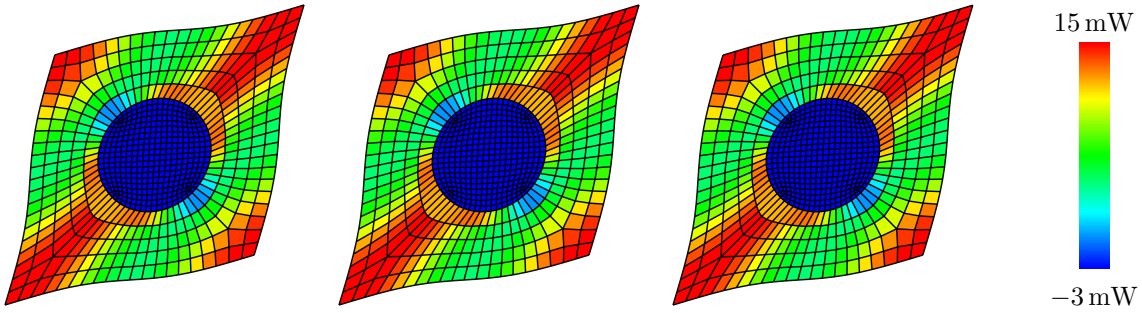

(c) r^{m} contour plots for RVE edge lengths of (left) 100 µm, (middle) 1 mm and (right) 3 m.

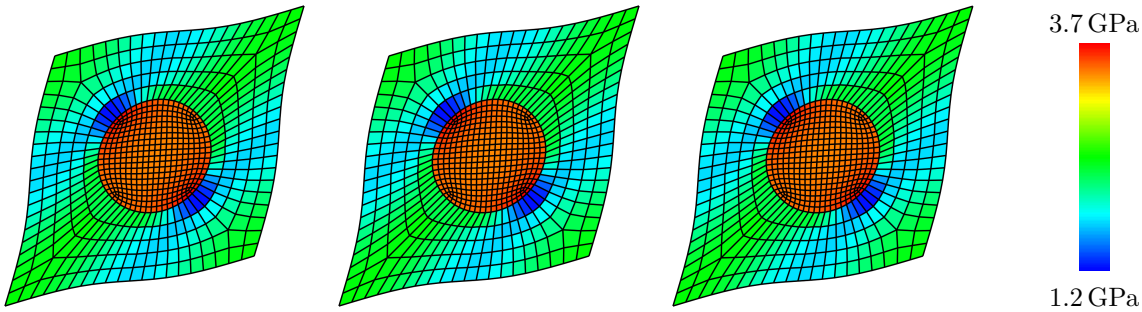

(d) $\sqrt{\frac{3}{2}}\,\|\boldsymbol{\sigma}^{\mathrm{m}}_{\mathrm{dev}}\|$ contour plots for RVE edge lengths of (left) 100 µm, (middle) 1 mm and (right) 3 m.

Figure 5.4: Contour plots of the circular inclusion for the θ^{M}-approach. In table form, (a) the temperature θ^{m}, (b) the hardening variable k^{m}, (c) the heat production rate r^{m} and (d) the von Mises stress are shown for different RVE sizes. The displacements are scaled by factor 25.

Table 5.3: Thermo-mechanical material parameters for cobalt (Co) and tungsten carbide (WC). Tensorial coefficients refer to a Cartesian base system $\{\boldsymbol{e}_1, \boldsymbol{e}_2\}$.

	Quantity	Edge length 100 µm	Edge length 1 mm	Edge length 3 m
θ^{m}–appr.	$\boldsymbol{\sigma}^{\mathrm{M}}$ / MPa	$\begin{bmatrix} 4640.5 & 1320.9 \\ 1320.9 & 4640.5 \end{bmatrix}$	$\begin{bmatrix} 4640.5 & 1320.9 \\ 1320.9 & 4640.5 \end{bmatrix}$	$\begin{bmatrix} 4650.8 & 1329.7 \\ 1329.7 & 4649.8 \end{bmatrix}$
	$\hat{r}^{\mathrm{M}}$ / W	0.006645	0.006645	0.006295
	$\frac{\mathrm{d}\hat{r}^{\mathrm{M}}}{\mathrm{d}\boldsymbol{\varepsilon}^{\mathrm{M}}}$	$\begin{bmatrix} 0.0924 & 0.8748 \\ 0.8748 & 0.0924 \end{bmatrix}$	$\begin{bmatrix} 0.0924 & 0.8748 \\ 0.8748 & 0.0924 \end{bmatrix}$	$\begin{bmatrix} 0.0851 & 0.8778 \\ 0.8726 & 0.0886 \end{bmatrix}$
θ^{M}–appr.	$\boldsymbol{\sigma}^{\mathrm{M}}$ / MPa	$\begin{bmatrix} 4640.5 & 1320.9 \\ 1320.9 & 4640.5 \end{bmatrix}$	$\begin{bmatrix} 4640.5 & 1320.9 \\ 1320.9 & 4640.5 \end{bmatrix}$	$\begin{bmatrix} 4640.5 & 1320.9 \\ 1320.9 & 4640.5 \end{bmatrix}$
	$\hat{r}^{\mathrm{M}}$ / W	0.006645	0.006645	0.006645
	$\frac{\mathrm{d}\hat{r}^{\mathrm{M}}}{\mathrm{d}\boldsymbol{\varepsilon}^{\mathrm{M}}}$	$\begin{bmatrix} 0.0924 & 0.8748 \\ 0.8748 & 0.0924 \end{bmatrix}$	$\begin{bmatrix} 0.0924 & 0.8748 \\ 0.8748 & 0.0924 \end{bmatrix}$	$\begin{bmatrix} 0.0924 & 0.8748 \\ 0.8748 & 0.0924 \end{bmatrix}$

hardening variable k^{m} and consequently the heat production rate $\hat{r}^{\mathrm{m}}$ are affected which result in different contour plots than for the smaller mesh sizes. On closer examination, the von Mises stress plot as well as the deformed shape of the RVE differ from those of the smaller mesh sizes. Furthermore in Table 5.3, the homogenised values of the stress $\boldsymbol{\sigma}^{\mathrm{M}}$, heat production rate $\hat{r}^{\mathrm{M}}$ as well as the respective tangent modulus $\boldsymbol{\gamma}^{\mathrm{M}}_{\mathrm{alg}}$ are summarised for the three different mesh sizes. The floating point precision is thereby chosen to show four significant positions of the respectively rounded values. It appears that the two smaller mesh sizes show the quasi-identical homogenised material response, whereas the largest RVE size yields deviating values. Moreover, it turns out that $\boldsymbol{\gamma}^{\mathrm{M}}_{\mathrm{alg}}$ loses its symmetry for the largest RVE size as a result of the gradient of $\hat{r}^{\mathrm{m}}$ which is observable Fig. 5.3(c). It should be noted that the Gough Joule effect results in elastic cooling in the WC-phase as the blue colour within the $\hat{r}^{\mathrm{m}}$ contour plots indicates. This result does not affect the homogenised value $\hat{r}^{\mathrm{M}}$ since the temperature enters Eq. (5.58) directly and also indirectly, via Eq. (5.52), each in a linear manner. As a consequence, the homogenised $\hat{r}^{\mathrm{M}}$ is not influenced by the local temperature θ^{m} in the WC phase at the meso-scale.

In contrast, Fig. 5.4 shows the contour plots of the temperature, the hardening variable, the heat production rate and the von Mises stress for the three considered RVE sizes and the θ^{M}–approach. Herein, the temperature dependent quantities are evaluated at the macroscopic temperature θ^{M} which is passed to the RVE from the higher scale.

The local temperature θ^{m} induces the meso-scale heat flux $\nabla_{\boldsymbol{x}}\,\theta^{\mathrm{m}}$ which is needed to evaluate heat flux dependent quantities. Therefore, it is not surprising that the meso-scale temperature contour plot looks exactly the same as the one for the θ^{m}–approach in Fig. 5.3. The comparison of the other plots reveals that all plots are identical, since the local temperature θ^{m} does not influence the results. A closer examination of the deformed shapes of the RVEs shows that the shapes of all RVEs coincide for all the different sizes. In consequence, the homogenised values of the stress $\boldsymbol{\sigma}^{\mathrm{M}}$, the heat production rate $\hat{r}^{\mathrm{M}}$ as well as the respective tangent modulus $\boldsymbol{\gamma}^{\mathrm{M}}_{\mathrm{alg}}$ take exactly the same values for all RVE sizes, cf. Table 5.3. As expected, the symmetry of $\boldsymbol{\gamma}^{\mathrm{M}}_{\mathrm{alg}}$ is therefore also met for the largest RVE size.

5.4.2 Perforated plane plate with hole

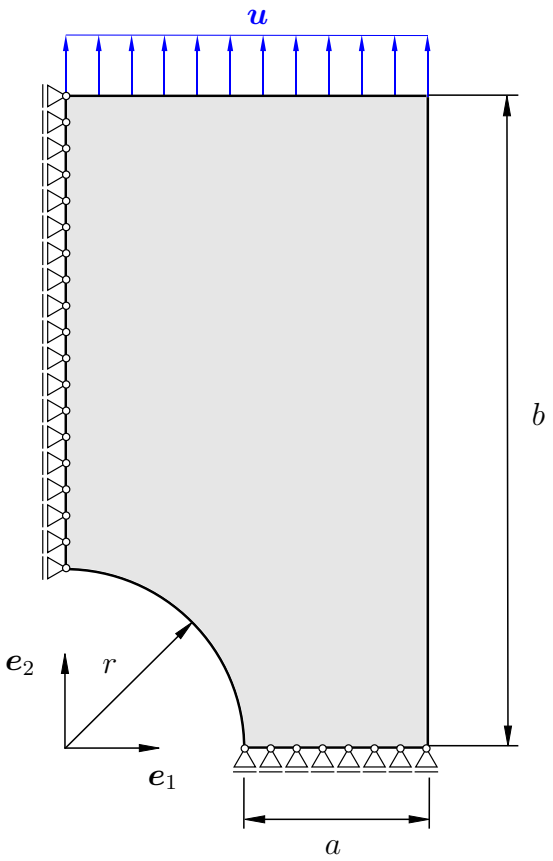

Figure 5.5: Plane plate with a hole. Symmetry is utilised and displacements are prescribed.

The second numerical example is a planar plate with a hole as depicted in Fig. 5.5, cf. Oñate and Owen [127]. In this example, symmetry of the problem is assumed and indicated by the bearing symbols. The radius of the hole is indicated by r and set to 5 mm, the width of the fillet next to the hole is denoted by a and also chosen to be 5 mm

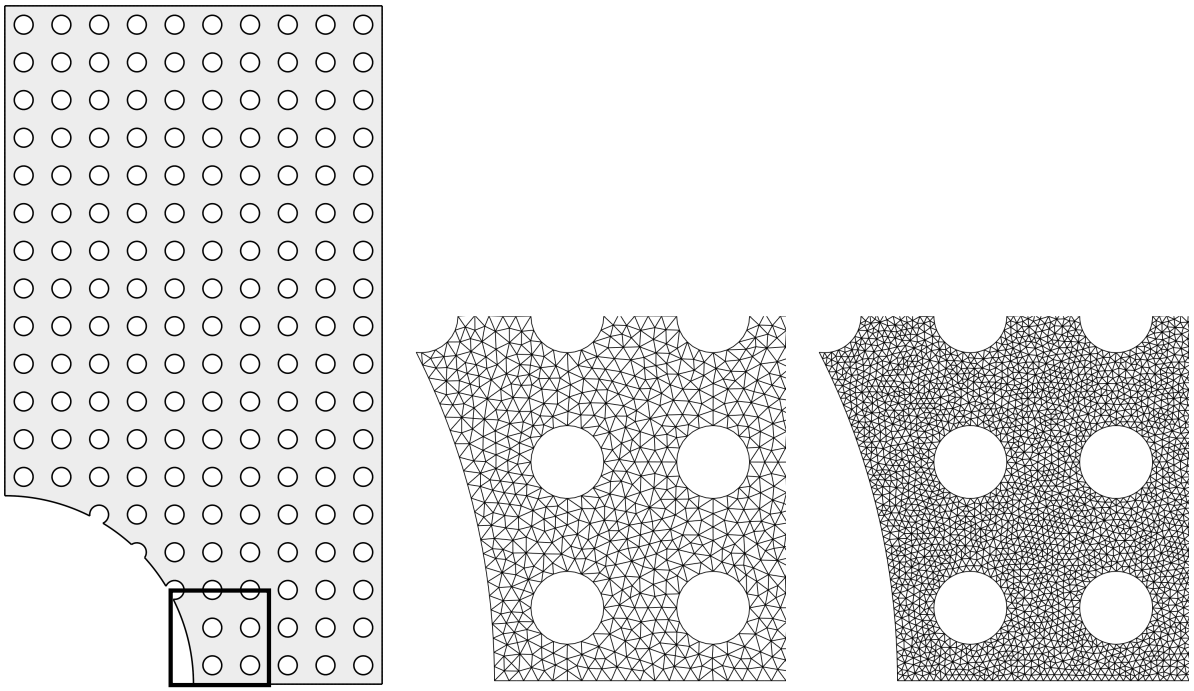

(a) Perforated plate with hole. (b) Coarse FE discretisation. (c) Fine FE discretisation.

Figure 5.6: (a) Periodically perforated plane plate with a hole. (b) Coarse FE discretisation. (c) Fine FE discretisation.

and the half height by b which is 18 mm. The top edge is loaded by a prescribed vertical displacement $\boldsymbol{u}$ in form of inhomogeneous Dirichlet boundary conditions.

The perforation of the plate is regular with equally sized voids with a diameter of 0.5 mm as shown in Fig. 5.6(a). Hence, the voids represent a periodic mesostructure. In order to compare the two-scale finite element framework (FE^2) with the results of a single-scale finite element programme (FE), two different discretisations are utilised for the FE as well as for the FE^2 solution of the problem. In all the different simulation setups, the voids as well as the hole are assumed to be traction free and adiabatic. The FE discretisations are shown in Figs. 5.6(b) and 5.6(c) as magnifications of the quadrilateral area marked in Fig. 5.6(a). The discretisation is performed with six-noded triangular elements with three integration points and quadratic shape functions for the displacement and temperature fields. The coarse discretisation consists of 72 811 nodes which leads to 218 433 degrees of freedom (`ndf`) and 35 120 elements (`nel`). The fine FE discretisation involves 285 869 nodes and therefore yields 857 607 degrees of freedom and 140 288 elements.

The FE^2 discretisations are shown in Fig. 5.7. The coarse discretisation consists of 98 nodes (294 degrees of freedom) and 41 volume elements as well as 3 surface elements on the macro-scale, cf. Fig. 5.7(a). The coarse meso-scale discretisation is shown in Fig. 5.7(b) and consists of 520 nodes (1560 degrees of freedom) and 232 elements. The

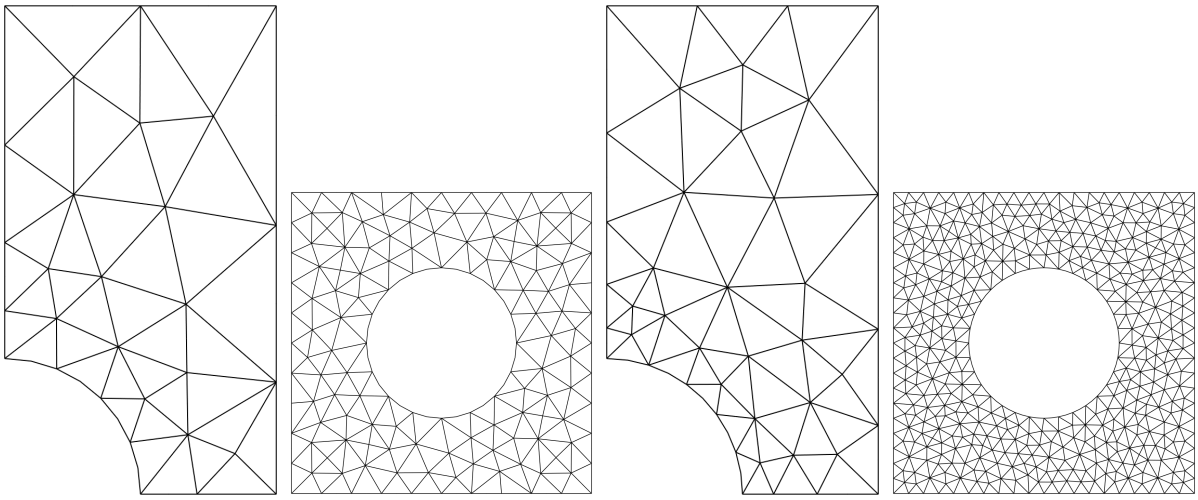

(a) Coarse Macro-scale. (b) Coarse Meso-scale. (c) Fine Macro-scale. (d) Fine Meso-scale.

Figure 5.7: (a) Coarse macro-scale discretisation. (b) Coarse meso-scale discretisation. (c) Fine macro-scale discretisation. (d) Fine meso-scale discretisation.

fine FE^2 discretisation consists of 145 nodes (435 degrees of freedom), 62 volume and

Table 5.4: Summary of the numbers of degrees of freedom and numbers of elements of the FE and FE^2 discretisations. In the case of FE^2 discretisations, the first entries represent the macro-scale values, whereas the second ones represent the meso-scale values.

	`ndf`	`nel`
FE coarse	218 433	35 120
FE fine	857 607	140 288
FE^2 coarse	294 / 1560	41 / 232
FE^2 fine	435 / 5472	62 / 856

4 surface elements at the macro-scale. At the meso-scale, 1824 nodes (5472 degrees of freedom) build a mesh of 856 elements. A summary of all `ndf` and `nel` numbers can be found in Table 5.4. The displacement $\boldsymbol{u}$ is increased linearly from 0 to 1 mm in 10 s and a time increment of $\Delta t = 0.5$ s. After this point in time is reached, the displacement is held constant for another 90 s by keeping $\Delta t = 0.5$ s. One set of simulations is carried out with an adiabatic boundary of the plane plate, the other set of simulations is carried out with an assumed ambient temperature of 293 K such that the initial state of the unloaded specimen is in thermal equilibrium. In the non-adiabatic setup, the right hand side edge of the perforated plate is the Robin boundary on which convective heat transfer is modelled. The heat exchange is thereby realised via surface element and a film condition, see Chapter 4 for further details. The film coefficient is assumed to

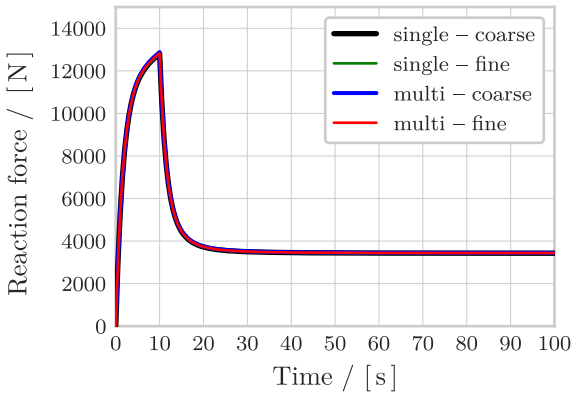

(a) Reaction force plot.

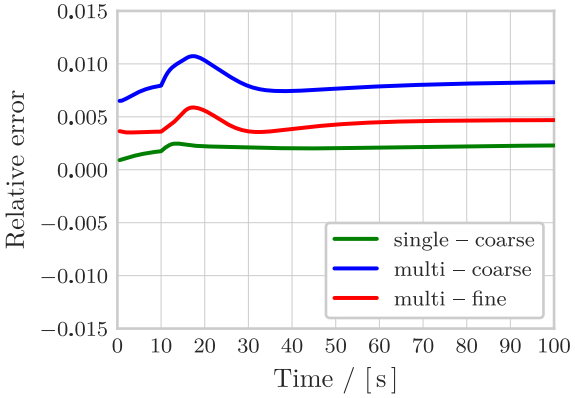

(b) Relative error of the reaction force.

Figure 5.8: Adiabatic perforated plane plate with a hole simulations. (a) Reaction force plot. (b) Relative error of the reaction forces related to the fine FE discretisation results.

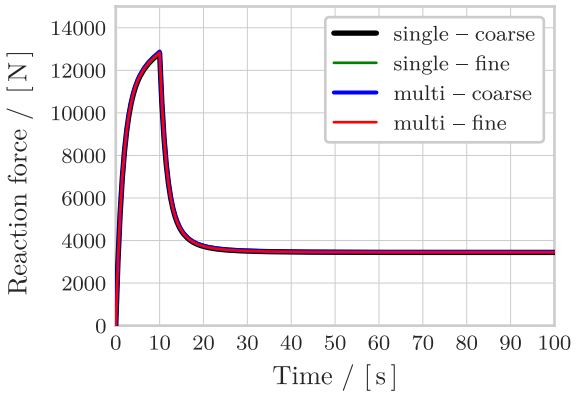

(a) Reaction force plot.

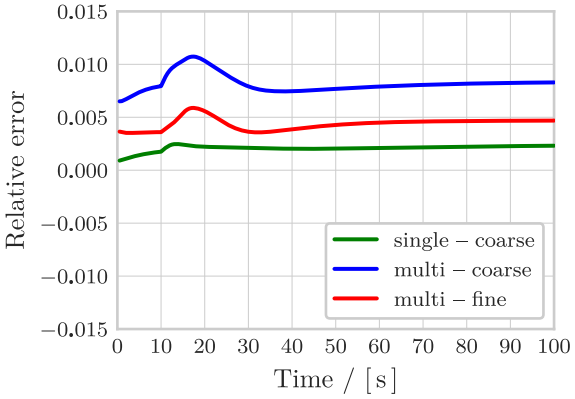

(b) Relative error of the reaction force.

Figure 5.9: Non-adiabatic perforated plane plate with a hole simulations. (a) Reaction force plot. (b) Relative error of the reaction forces related to the fine FE discretisation results.

be $h_c = 10 \times 10^{-4}$. During the simulation, the reaction force $\underline{\mathbf{r}}_{\text{top}}$ at the displacement controlled edge is recorded for the two FE as well as for the two FE^2–setups. In Fig. 5.8, the reaction force of the adiabatic simulations is plotted versus time, and the relative error

$$e_{\text{rel}} = \frac{\|\underline{\mathbf{r}}^{\bullet}_{\text{top}}\| - \|\underline{\mathbf{r}}^{\text{fine}}_{\text{top}}\|}{\|\underline{\mathbf{r}}^{\text{fine}}_{\text{top}}\|} \,, \tag{5.72}$$

of the reaction force of the FE^2 simulations and the coarse FE simulation related to the fine FE simulation are shown. The reaction force plot shows a very good agreement of the FE and FE^2 results and exhibits the viscoplastic behaviour of the presented material model. While the load is increased during the first 10 s, the reaction force increases in a nonlinear manner up to 12 783 N and drops significantly during the following 10 s.

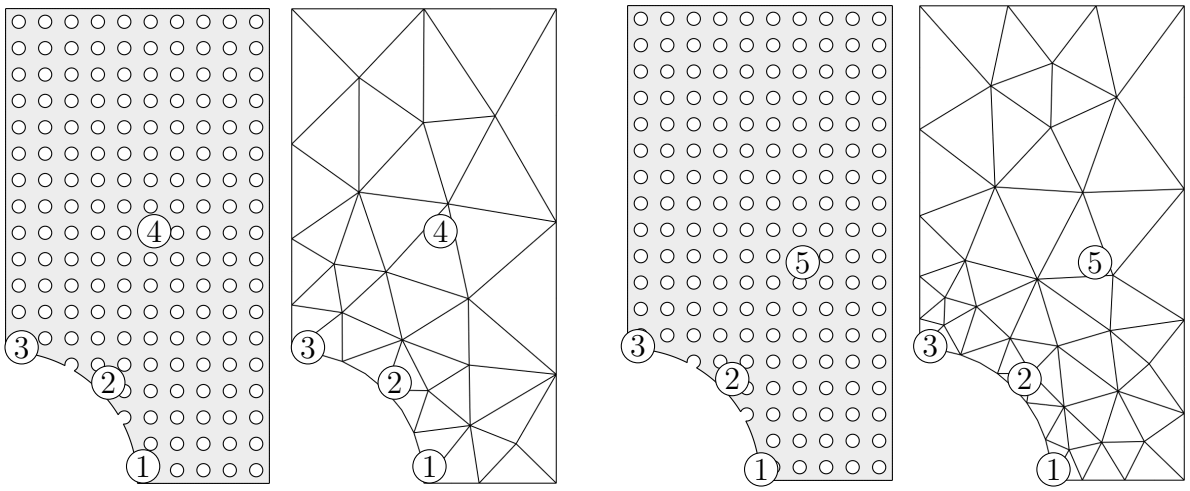

(a) Macro-scale quadrature point positions of the coarse FE^2–discretisation.

(b) Macro-scale quadrature point positions of the fine FE^2–discretisation.

Figure 5.10: Positions of the macro-scale quadrature points of the (a) coarse and (b) fine FE^2–discretisations related to the position of the single scale problem. The coordinates of the positions in the coordinate system defined in Fig. 5.5 are enlisted in Table 5.5.

Table 5.5: Coordinate values of the positions in Fig. 5.10(a) within the upper block and in Fig. 5.10(b) within the lower block, related to the $\{\boldsymbol{e}_1, \boldsymbol{e}_2\}$ base system introduced in Fig. 5.5.

Position	$\boldsymbol{e}_1$-direction	$\boldsymbol{e}_2$-direction
①	5.23 mm	0.68 mm
②	3.91 mm	3.85 mm
③	0.64 mm	5.18 mm
④	5.64 mm	9.57 mm
①	5.07 mm	0.45 mm
②	3.97 mm	3.86 mm
③	0.41 mm	5.11 mm
⑤	6.64 mm	8.27 mm

Subsequently, the force level remains more or less constant while the force still slowly decreases to 3421 N at the end of the simulation. The relative error plot confirms the good agreement of the different simulations. The relative error of the coarse FE^2 discretisation is between 0.6 % and 1.1 %, the relative error of the fine FE^2 discretisation is between 0.4 % and 0.6 %. The coarse FE discretisation is closest to the fine FE discretisation results with an error of 0.1 % to 0.2 %.

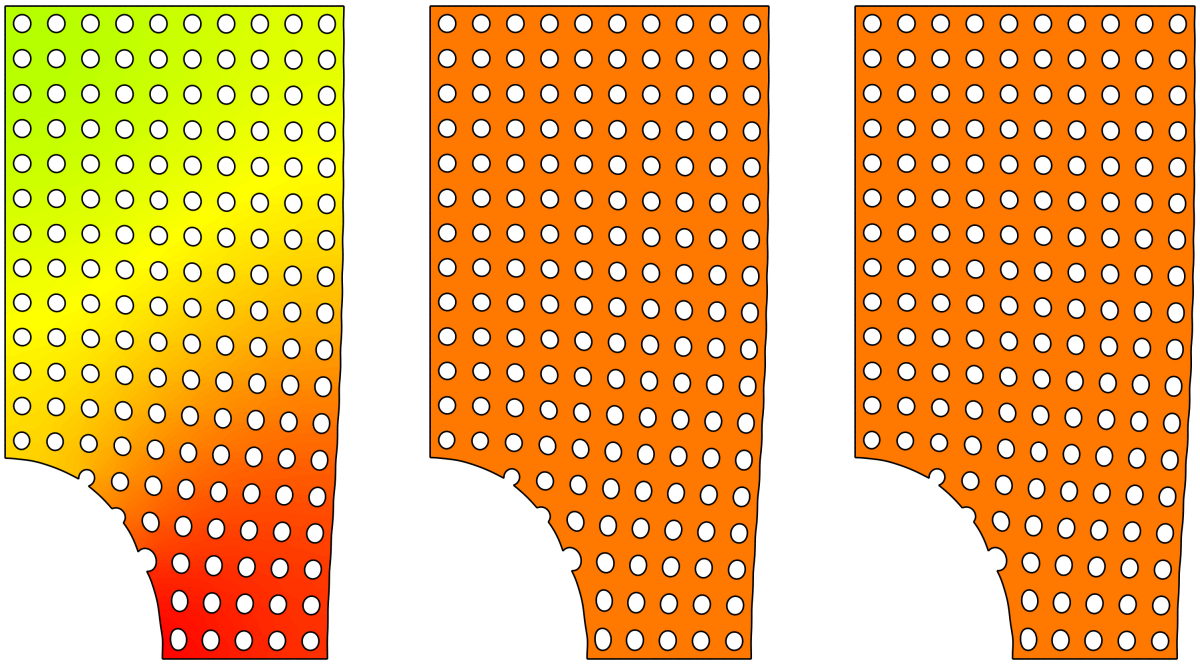

(a) Temperature contour plots of the coarse FE discretisation of the adiabatic perforated plane plate with a hole after (left) 10 s, (middle) 50 s and (right) 100 s.

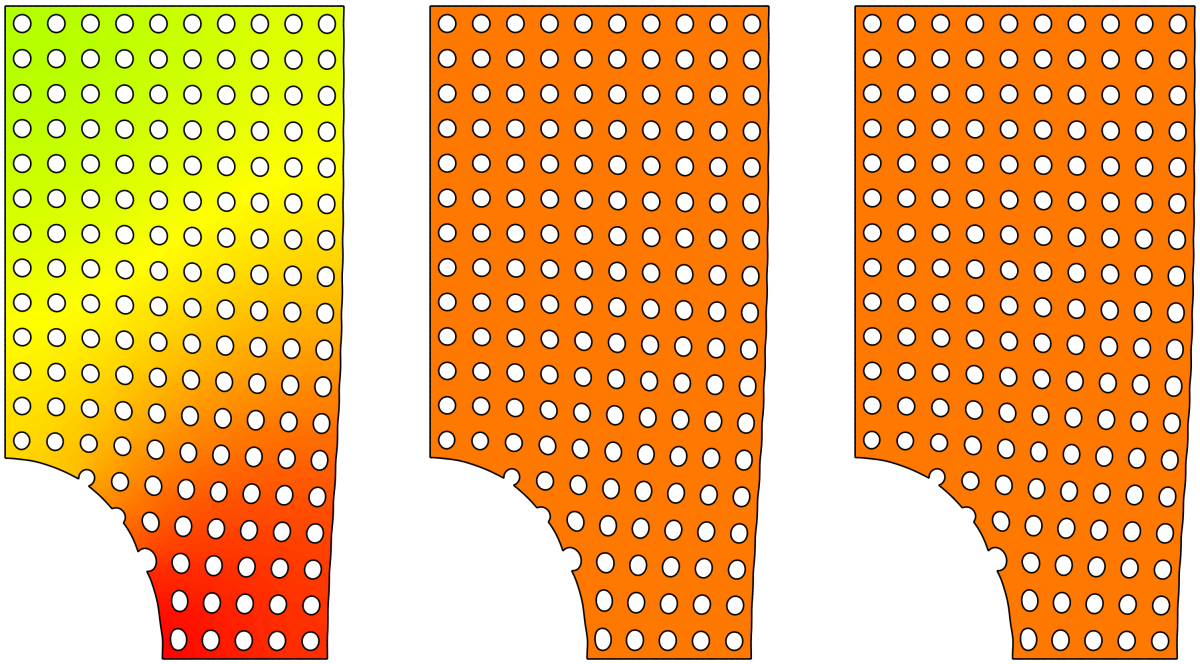

(b) Temperature contour plots of the fine FE discretisation of the adiabatic perforated plane plate with a hole after (left) 10 s, (middle) 50 s and (right) 100 s.

Figure 5.11: Temperature field of the adiabatic perforated plane plate with a hole simulation at different time steps. For a better view, the FE mesh ist omitted for the (a) coarse and (b) fine FE discretisations.

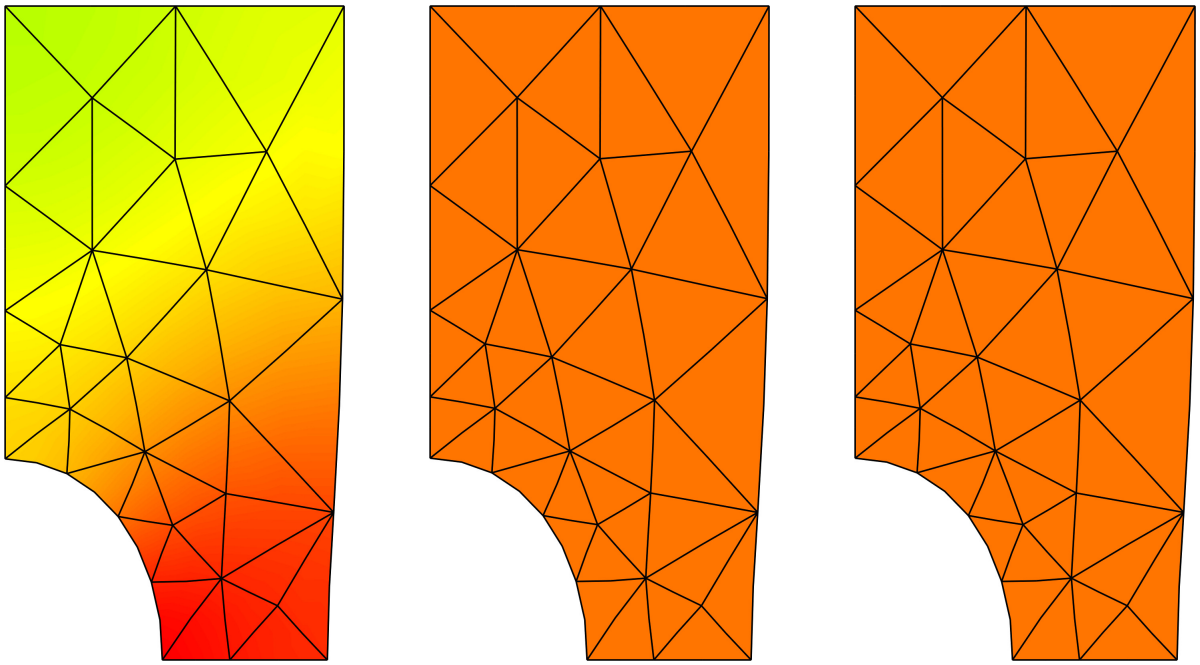

(a) Macroscale temperature contour plots of the coarse FE^2 discretisation of the adiabatic perforated plane plate with a hole after (left) 10 s, (middle) 50 s and (right) 100 s.

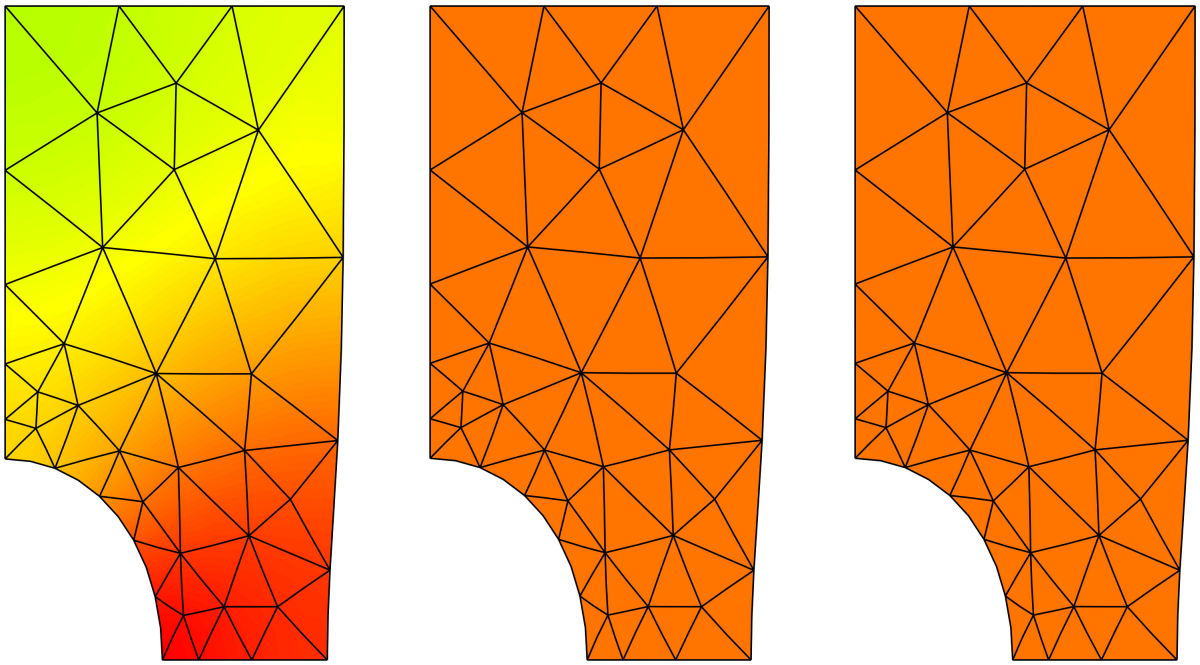

(b) Macroscale temperature contour plots of the fine FE^2 discretisation of the adiabatic perforated plane plate with a hole after (left) 10 s, (middle) 50 s and (right) 100 s.

Figure 5.12: Macroscale temperature field of the (a) coarse and (b) fine discretisations of the adiabatic perforated plane plate with a hole FE^2-simulation at different time steps.

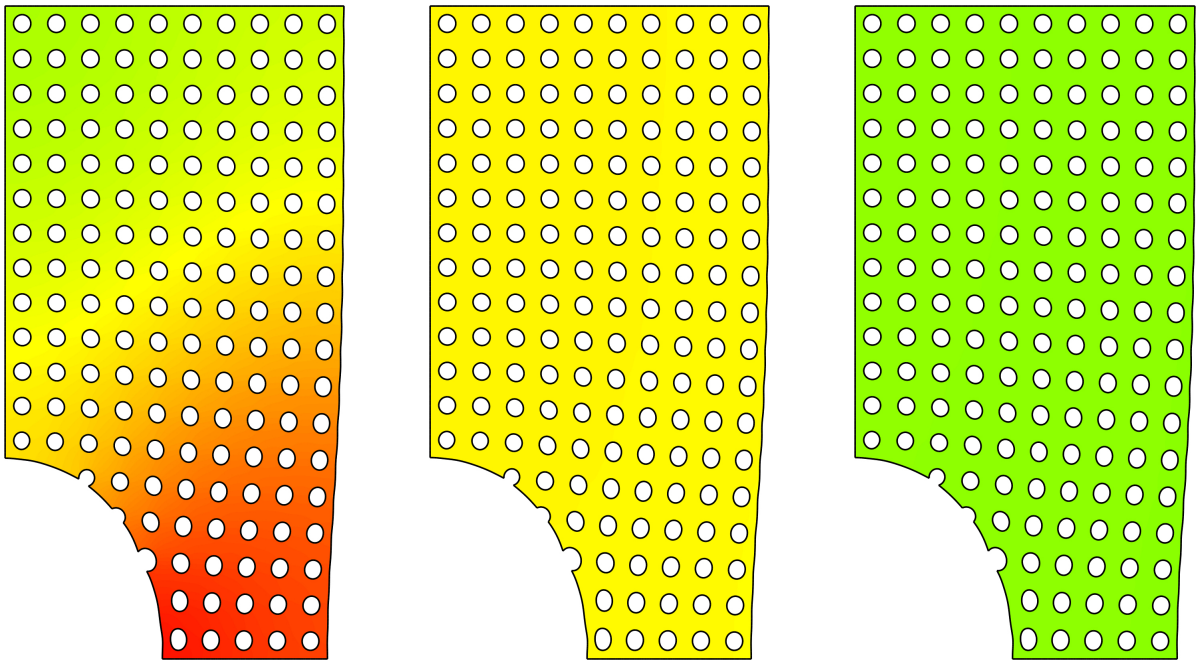

(a) Temperature contour plots of the coarse FE discretisation of the non-adiabatic perforated plane plate with a hole after (left) 10 s, (middle) 50 s and (right) 100 s.

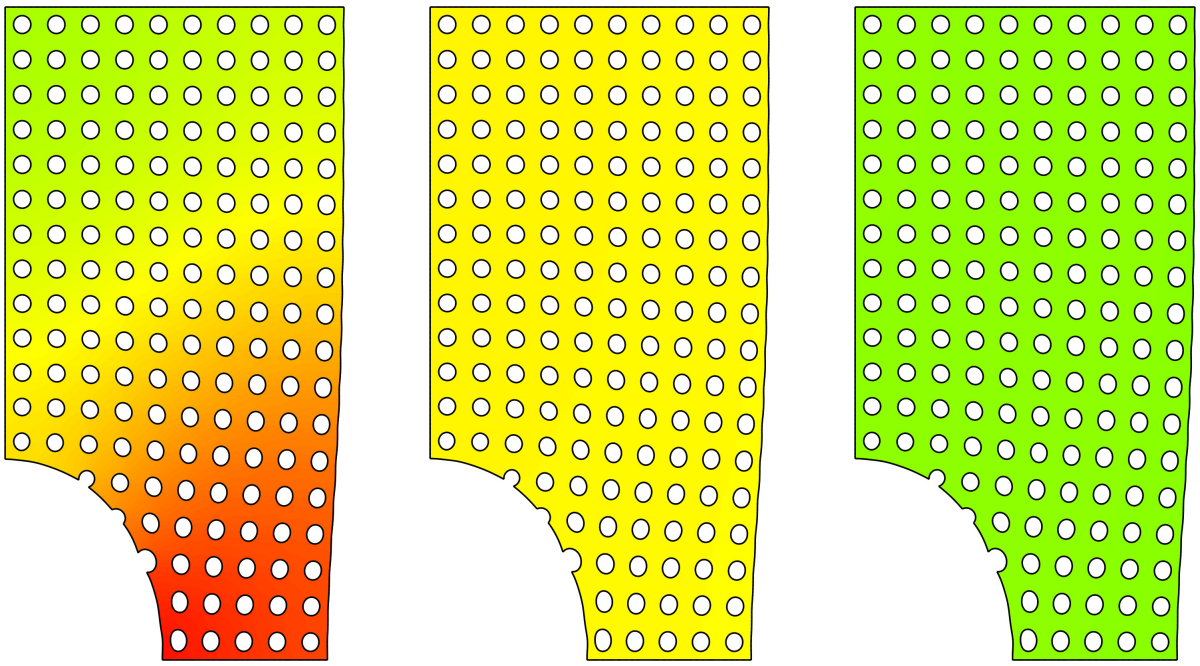

(b) Temperature contour plots of the fine FE discretisation of the non-adiabatic perforated plane plate with a hole after (left) 10 s, (middle) 50 s and (right) 100 s.

Figure 5.13: Temperature field of the non-adiabatic perforated plane plate with a hole simulation at different time steps. For a better view, the FE mesh ist omitted for the (a) coarse and (b) fine FE discretisations.

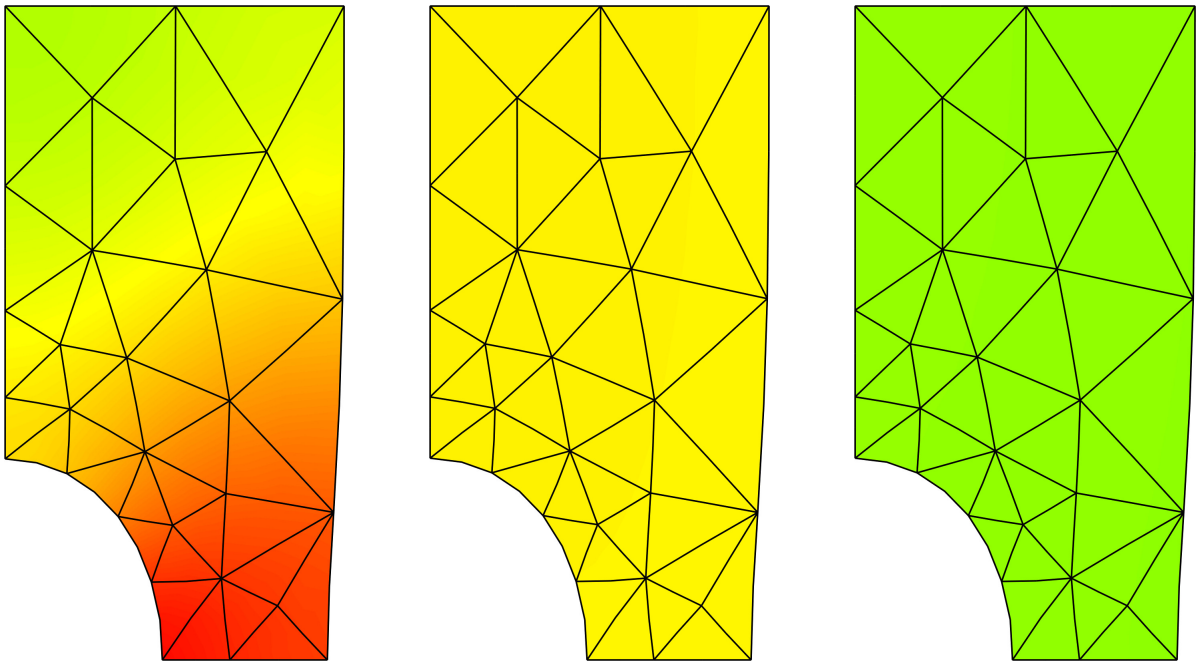

(a) Macroscale temperature contour plots of the coarse FE^2 discretisation of the non-adiabatic perforated plane plate with a hole after (left) 10 s, (middle) 50 s and (right) 100 s.

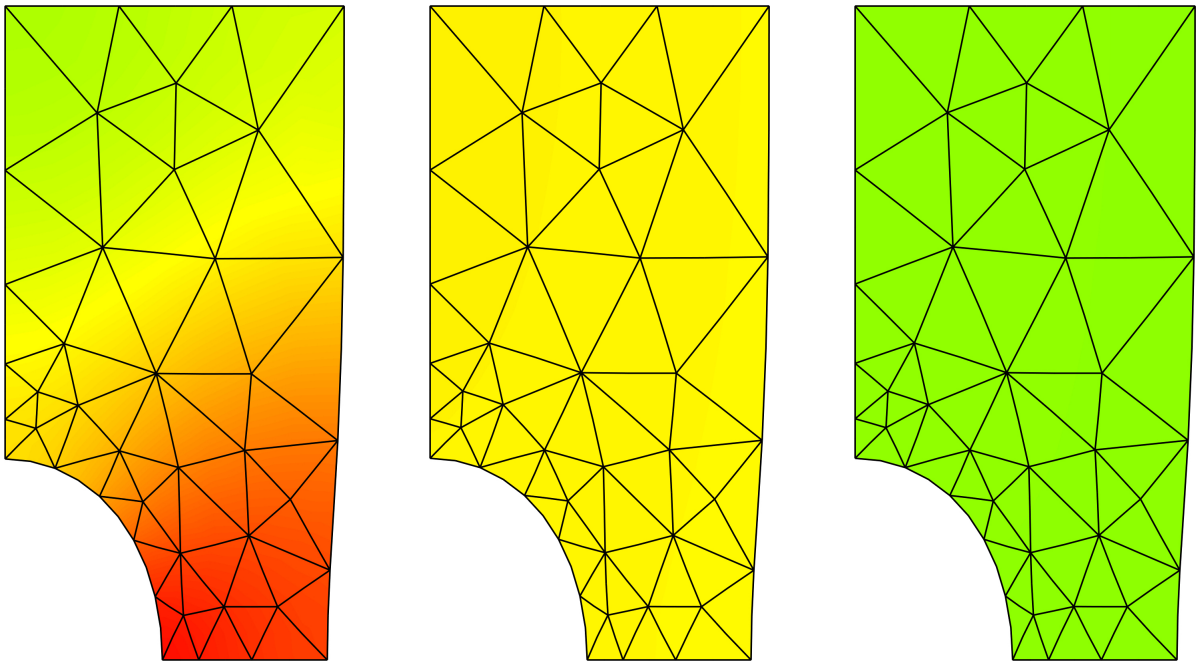

(b) Macroscale temperature contour plots of the fine FE^2 discretisation of the non-adiabatic perforated plane plate with a hole after (left) 10 s, (middle) 50 s and (right) 100 s.

Figure 5.14: Macroscale temperature field of the (a) coarse and (b) fine discretisations of the non-adiabatic perforated plane plate with a hole FE^2-simulation at different time steps.

In Fig. 5.9, the analogous results are shown for the non-adiabatic simulations with heat transfer via the boundary. The reaction force plots of the FE as well as of the FE^2 simulations are also in good agreement with each other. At first glance, the results look quasi identical and close to the adiabatic simulation setup. The maximum reaction force is 12 784 N after 10 s and therefore 1 N higher than the maximum reaction force of the adiabatic setup. The reason for this is the thermal softening which is included in the material model. Figs. 5.11 to 5.14 show the temperature evolution due to plastic heating for all four discretisations of the adiabatic and the non-adiabatic setups at different time steps. For both setups, the temperature fields appear to coincide for all discretisations. As expected, the temperature level of the adiabatic simulations is higher than the temperature level of the non-adiabatic simulations due to the considered convective heat transfer. Hence, the material remains stiffer in the non-adiabatic simulations. As in the adiabatic simulations, the reaction force significantly drops to a quasi constant level after 20 s. At the end of the simulation, the reaction force is 3433 N which is 12 N higher than in the adiabatic case due to less thermal softening. The relative error of the residual forces of the non-adiabatic simulations in Fig. 5.9(b) shows the same good results as Fig. 5.8(b) does for the adiabatic cases. A more comprehensive comparison of the FE and FE^2 simulations is only possible by comparing simulation results of distinct positions of the single scale results with RVE results of appropriate quadrature point positions. For this purpose, in Fig. 5.10 macro-scale quadrature point coordinates of the FE^2-simulations are labelled related to their positions in the single scale simulations. The coordinate values in the $\{\boldsymbol{e}_1, \boldsymbol{e}_2\}$ coordinate system, cf. Fig. 5.5, are enlisted in Table 5.5.

The first three positions, ①–③, are approximately the same for both FE^2–discretisations. Position ④ is related to the coarse FE^2–mesh and position ⑤ to the fine FE^2–discretisation. For the adiabatic simulation setup, in Figs. 5.15 to 5.19, the hardening variable k and the von Mises stress are depicted after 10 s as well as after 100 s for the fine FE–discretisation and both RVE mesh sizes of the two FE^2–discretisations for all five positions ①–⑤. The scales of the respective quantities are identical for better comparability. Fig. 5.15 is related to position ① which is located next to the hole and near the point of the highest load, $[5\,\boldsymbol{e}_1, 0\,\boldsymbol{e}_2]$, cf. Fig. 5.5. In Figs. 5.15(a) and 5.15(b), the hardening variable k is depicted after (a) 10 s as well as after (b) 100 s. The comparison of these two states shows that the effective plastic strain k evolves from $t = 10\,\mathrm{s}$ to $t = 100\,\mathrm{s}$ which is in line with the reaction force relaxation for $t > 10\,\mathrm{s}$, cf. the reaction force–time plot in Fig. 5.8(a) – the material flows. Furthermore, it can clearly be seen that the principle spatial distribution of k for both depicted points in time coincides very well for the finely discretised single scale result compared to the two RVE discretisations of both two–scale results. Since periodic boundary conditions are chosen, cf. Eq. (5.30), the deformed shape of the RVEs naturally leads to a locally slightly different distribution of k. Nevertheless, the absolute values of k, the deformed shape of the hole as well as the vertical band-like area of almost zero k do agree very well. The von Mises stress contour plots of position ① in Figs. 5.15(c) and 5.15(d) show the same good agreement

of the principle spatial distribution of the von Mises stress as well as the same good agreement of the absolute value of the von Mises stress for both depicted time steps.

Again, a vertical band-like area of lesser values of now the von Mises stress occurs in all plots. The comparison of the two points in time reveals that the von Mises stress decreases for $t > 10\,\mathrm{s}$ which coincides with the reaction force relaxation, cf. Fig. 5.8(a), and the evolution of k, cf. Figs. 5.15(a) and 5.15(b) as discussed above. Moreover, the comparison of the contour plots of the coarse RVE with those of the fine RVE indicates the increasing accuracy of RVE test computations with increasing mesh density.

Fig. 5.16 is related to position ②. At this point, the load is not as high as it is at position ① such that the hardening variable k at position ② does not evolve as pronounced as it does at position ①. This can clearly be seen by comparison of Figs. 5.15(a) and 5.15(b) with Figs. 5.16(a) and 5.16(b). Nonetheless, a closer examination of Figs. 5.16(a) and 5.16(b) reveals that k evolves at position ② from $t = 10\,\mathrm{s}$ to $t = 100\,\mathrm{s}$. As a consequence, the von Mises stress relaxes from $t = 10\,\mathrm{s}$ to $t = 100\,\mathrm{s}$ as depicted in Figs. 5.16(c) and 5.16(d). As discussed above for position ①, the agreement of the single scale and multi–scale results is very good which is not surprising when taking the reaction force relative error plot, Fig. 5.8(b), into account.

Fig. 5.17 is related to position ③ which is near to the point $[0\,\boldsymbol{e}_1, 5\,\boldsymbol{e}_2]$, cf. Fig. 5.5, at the top of the hole of the plate. The equivalent plastic strain k also evolves from $t = 10\,\mathrm{s}$ to $t = 100\,\mathrm{s}$ as shown in Figs. 5.17(a) and 5.17(b) where a horizontal band of almost zero k can be observed both, in the single scale result as well as in the two–scale results. The same band-like structure of lesser von Mises stresses appears in Figs. 5.17(c) and 5.17(d) wherein the relaxation of the stress level from $t = 10\,\mathrm{s}$ to $t = 100\,\mathrm{s}$ is demonstrated for position ③. Especially the comparison of the left image of Fig. 5.17(c) with the right image of Fig. 5.17(c) shows the good agreement of the absolute values of the von Mises stress in the single scale and multi–scale simulations. Once more, the local difference induced by the periodic boundary conditions at the meso-scale is obvious on closer inspection of the figure.

Fig. 5.18 related to position ④ and Fig. 5.19 related to position ⑤ both show different positions inside the "bulk" of the plane plate. Both positions refer to quadrature point coordinates that almost coincide with holes of the single scale analysis with explicit dissolution of the holes. As a consequence, in the case of Fig. 5.18 only the coarse FE^2 analysis is compared to the finely discretised single scale analysis and, likewise, in Fig. 5.19 only the fine FE^2 analysis is compared to the single scale analysis. In both cases, the evolution of k in time can be observed analogously to the previously discussed positions, cf. Figs. 5.18(a) and 5.18(b) as well as respectively Figs. 5.19(a) and 5.19(b). Furthermore, the relaxation of the stress level of both positions between the points in time $t = 10\,\mathrm{s}$ and $t = 100\,\mathrm{s}$ can be seen in Figs. 5.18(c) and 5.18(d) and Figs. 5.19(c) and 5.19(d).

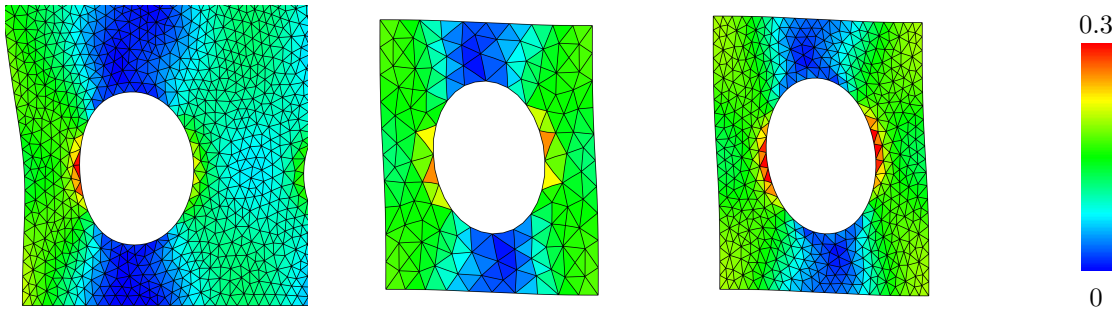

(a) Hardening variable k of position ① after 10 s. Left to right: Fine FE, coarse RVE, fine RVE.

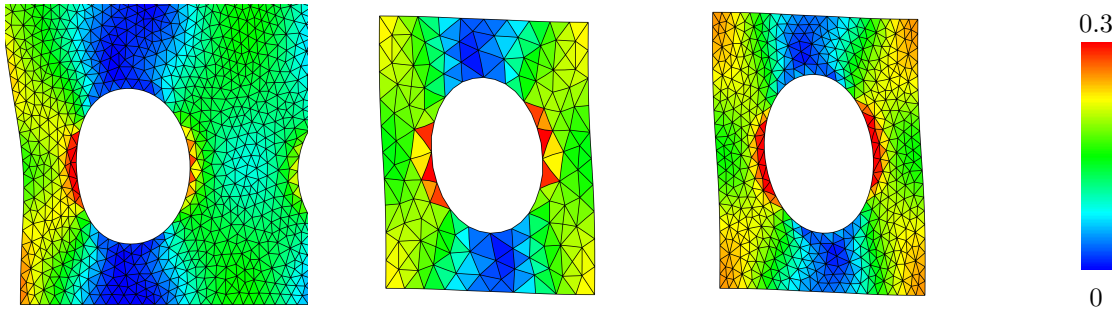

(b) Hardening variable k of position ① after 100 s. Left to right: Fine FE, coarse RVE, fine RVE.

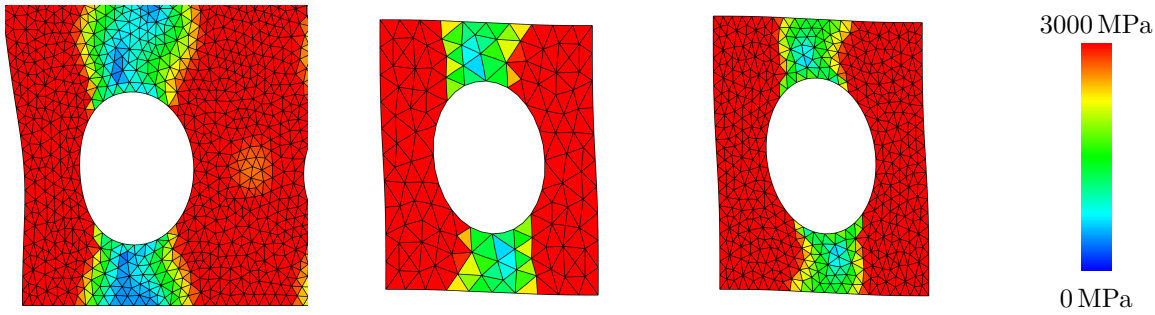

(c) Von Mises stress $\sqrt{\frac{3}{2}}\,\|\boldsymbol{\sigma}_{\mathrm{dev}}\|$ of position ① after 10 s. Left to right: Fine FE, coarse RVE, fine RVE.

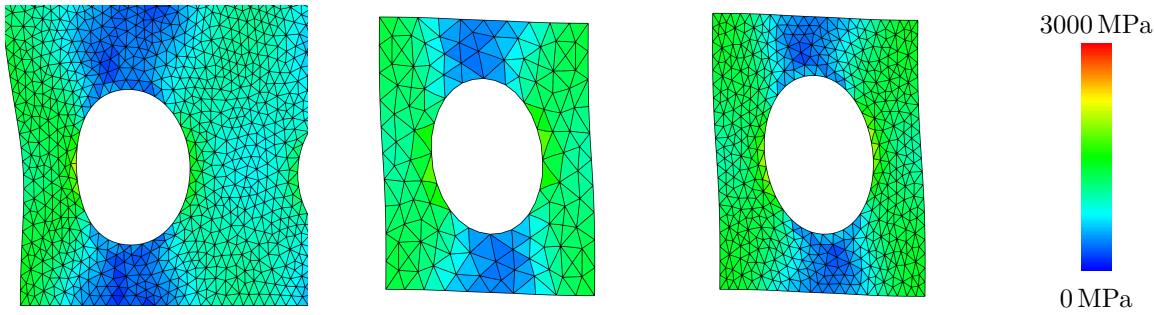

(d) Von Mises stress $\sqrt{\frac{3}{2}}\,\|\boldsymbol{\sigma}_{\mathrm{dev}}\|$ of position ① after 100 s. Left to right: Fine FE, coarse RVE, fine RVE.

Figure 5.15: Contour plots of position ① for the adiabatic simulation. The hardening variable k is shown after (a) 10 s and (b) 100 s as well as the von Mises stress $\sqrt{\frac{3}{2}}\,\|\boldsymbol{\sigma}_{\mathrm{dev}}\|$ after (c) 10 s and (d) 100 s.

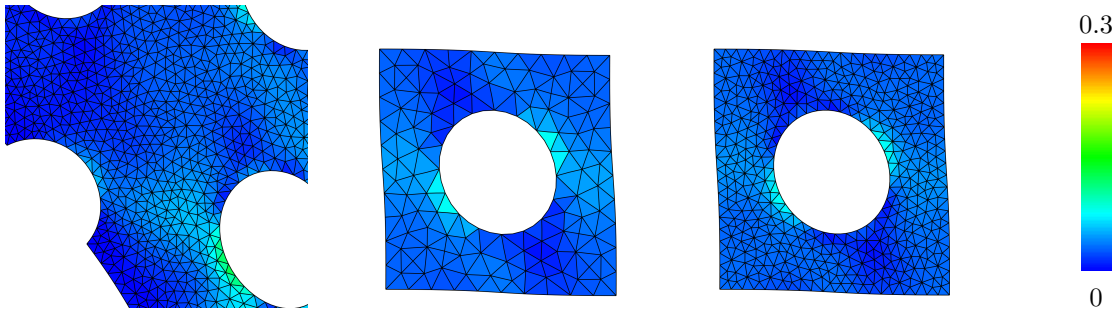

(a) Hardening variable k of position ② after 10 s. Left to right: Fine FE, coarse RVE, fine RVE.

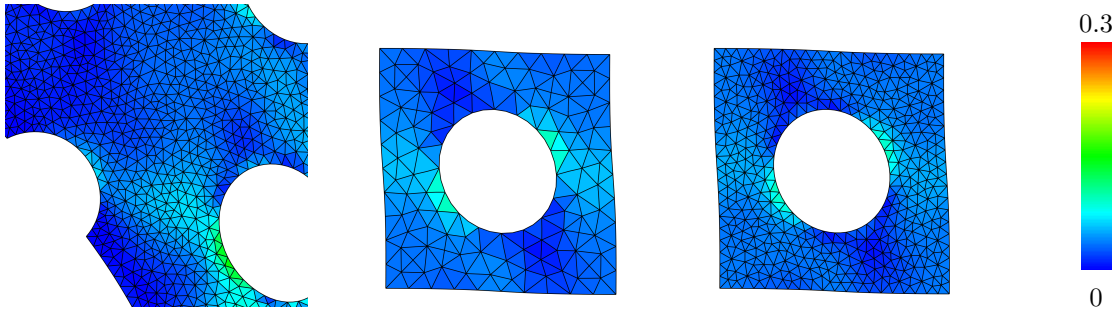

(b) Hardening variable k of position ② after 100 s. Left to right: Fine FE, coarse RVE, fine RVE.

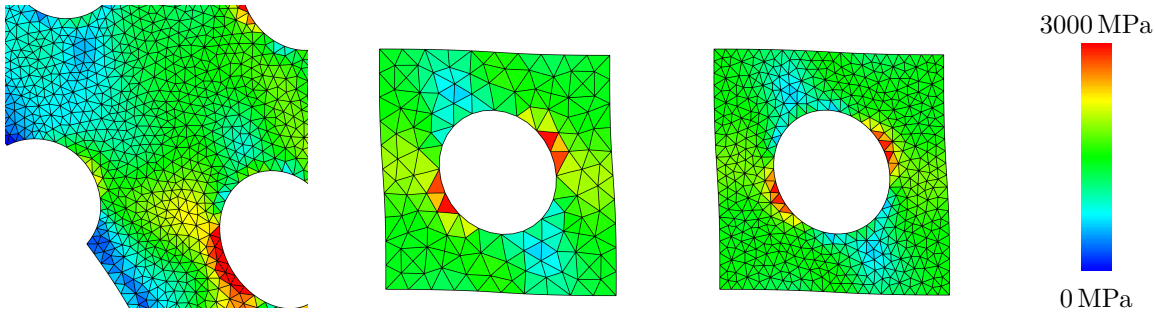

(c) Von Mises stress $\sqrt{\frac{3}{2}}\,\|\boldsymbol{\sigma}_{\mathrm{dev}}\|$ of position ② after 10 s. Left to right: Fine FE, coarse RVE, fine RVE.

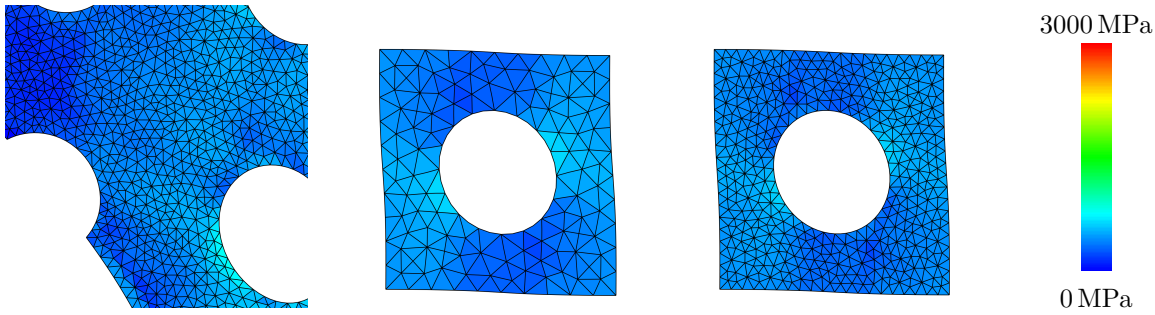

(d) Von Mises stress $\sqrt{\frac{3}{2}}\,\|\boldsymbol{\sigma}_{\mathrm{dev}}\|$ of position ② after 100 s. Left to right: Fine FE, coarse RVE, fine RVE.

Figure 5.16: Contour plots of position ② for the adiabatic simulation. The hardening variable k is shown after (a) 10 s and (b) 100 s as well as the von Mises stress $\sqrt{\frac{3}{2}}\,\|\boldsymbol{\sigma}_{\mathrm{dev}}\|$ after (c) 10 s and (d) 100 s.

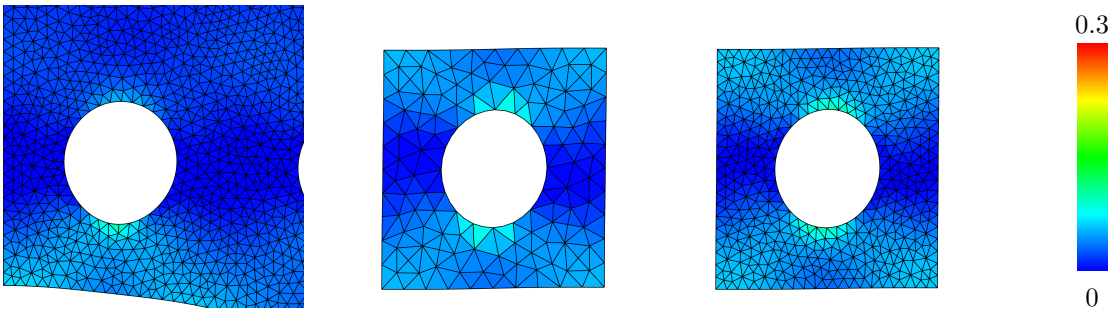

(a) Hardening variable k of position ③ after 10 s. Left to right: Fine FE, coarse RVE, fine RVE.

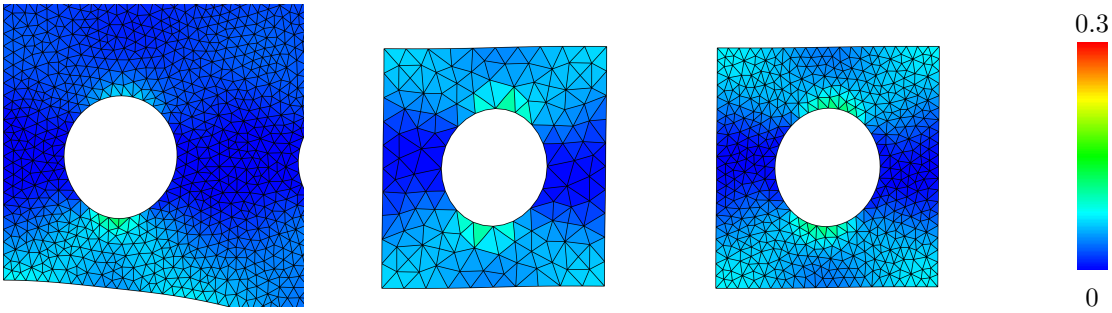

(b) Hardening variable k of position ③ after 100 s. Left to right: Fine FE, coarse RVE, fine RVE.

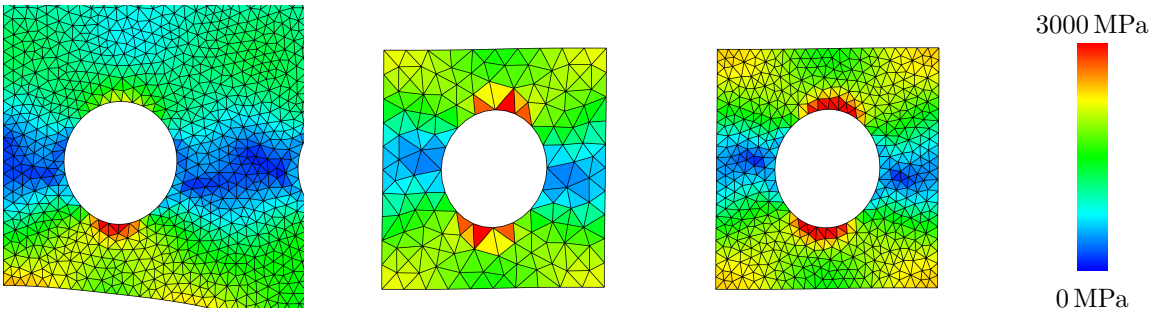

(c) Von Mises stress $\sqrt{\frac{3}{2}}\,\|\boldsymbol{\sigma}_{\mathrm{dev}}\|$ of position ③ after 10 s. Left to right: Fine FE, coarse RVE, fine RVE.

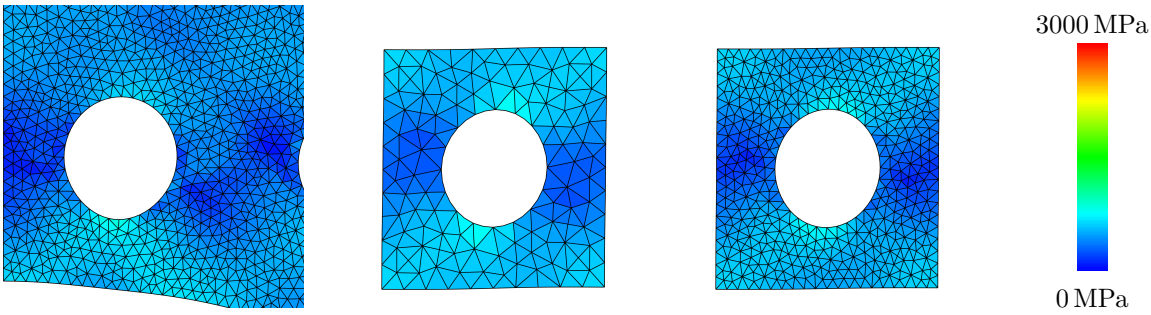

(d) Von Mises stress $\sqrt{\frac{3}{2}}\,\|\boldsymbol{\sigma}_{\mathrm{dev}}\|$ of position ③ after 100 s. Left to right: Fine FE, coarse RVE, fine RVE.

Figure 5.17: Contour plots of position ③ for the adiabatic simulation. The hardening variable k is shown after (a) 10 s and (b) 100 s as well as the von Mises stress $\sqrt{\frac{3}{2}}\,\|\boldsymbol{\sigma}_{\mathrm{dev}}\|$ after (c) 10 s and (d) 100 s.

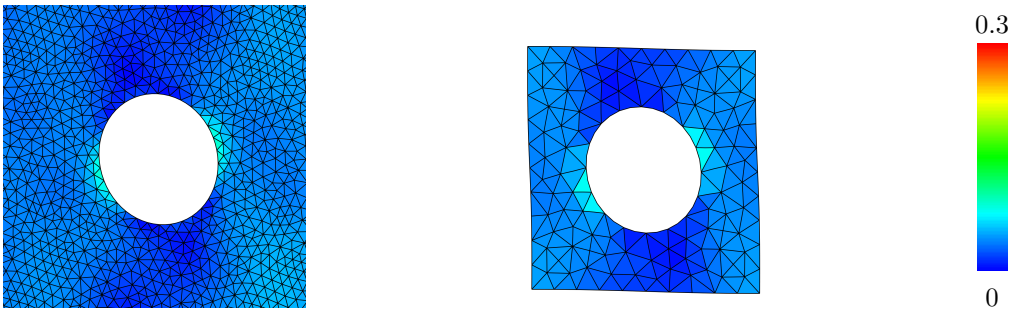

(a) Hardening variable k of position ④ after 10 s. Left to right: Fine FE, coarse RVE.

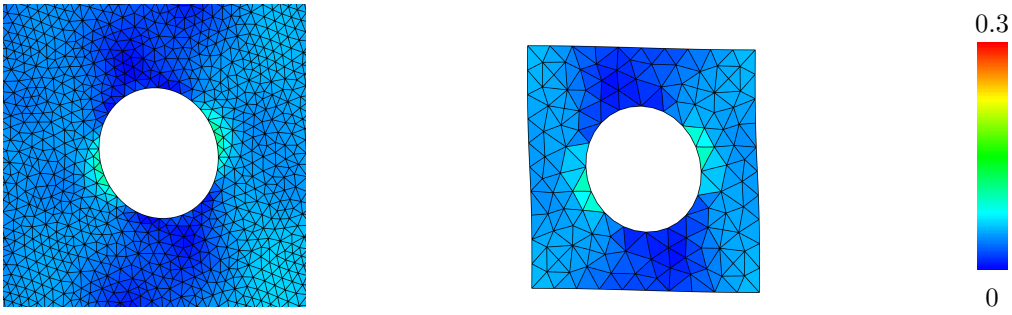

(b) Hardening variable k of position ④ after 100 s. Left to right: Fine FE, coarse RVE.

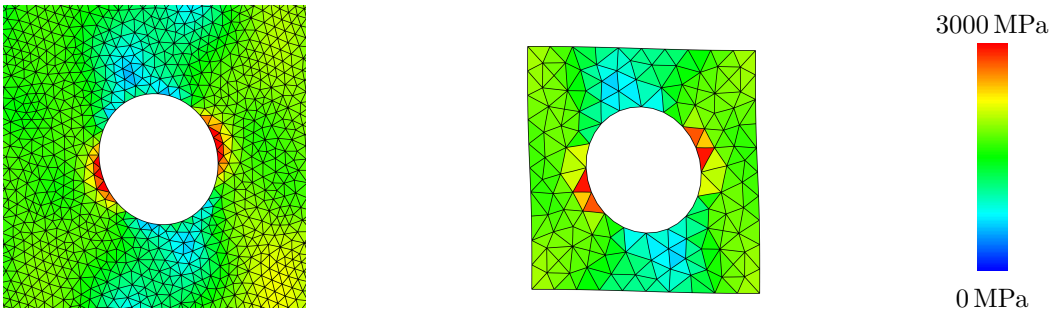

(c) Von Mises stress $\sqrt{\frac{3}{2}}\,\|\boldsymbol{\sigma}_{\mathrm{dev}}\|$ of position ④ after 10 s. Left to right: Fine FE, coarse RVE.

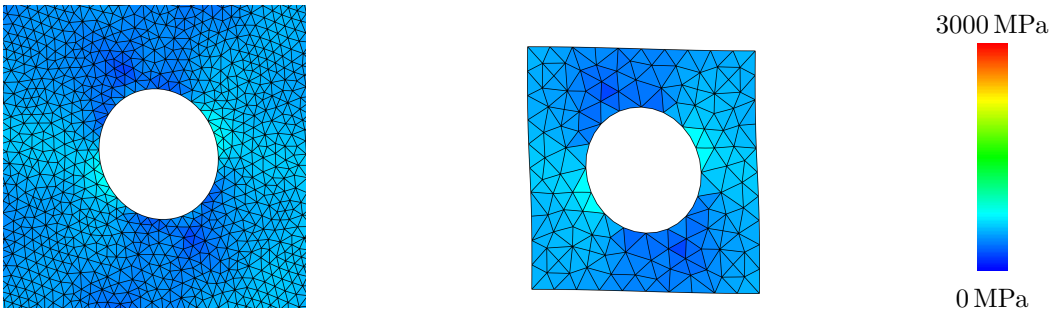

(d) Von Mises stress $\sqrt{\frac{3}{2}}\,\|\boldsymbol{\sigma}_{\mathrm{dev}}\|$ of position ④ after 100 s. Left to right: Fine FE, coarse RVE.

Figure 5.18: Contour plots of position ④ for the adiabatic simulation. The hardening variable k is shown after (a) 10 s and (b) 100 s as well as the von Mises stress $\sqrt{\frac{3}{2}}\,\|\boldsymbol{\sigma}_{\mathrm{dev}}\|$ after (c) 10 s and (d) 100 s.

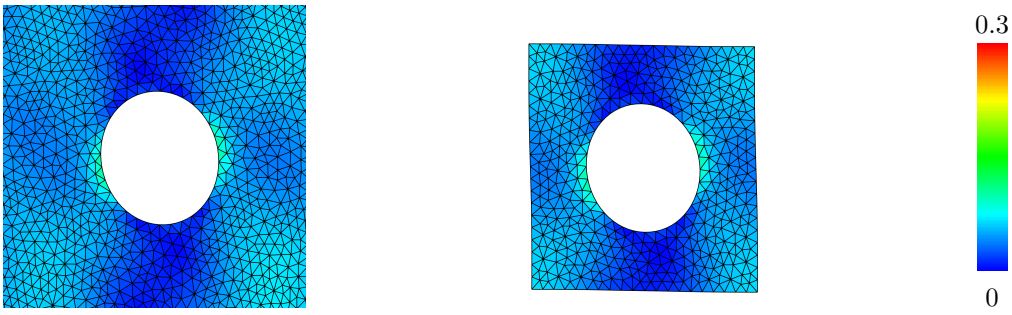

(a) Hardening variable k of position ⑤ after 10 s. Left to right: Fine FE, fine RVE.

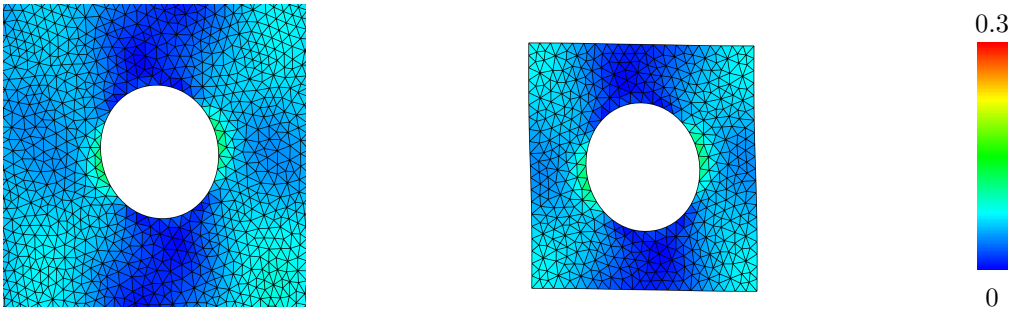

(b) Hardening variable k of position ⑤ after 100 s. Left to right: Fine FE, fine RVE.

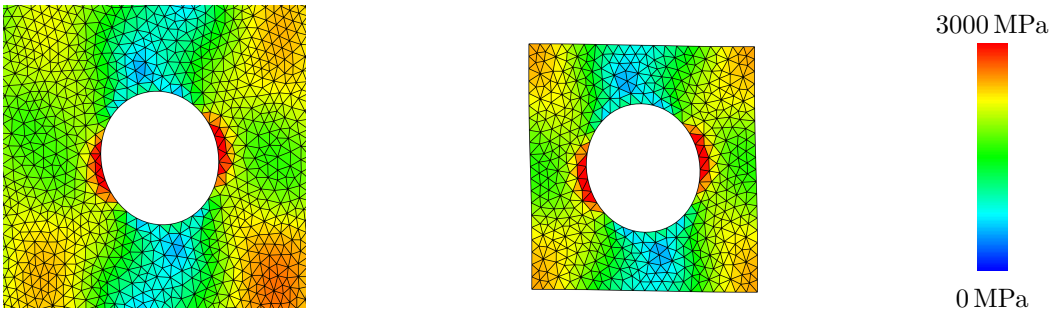

(c) Von Mises stress $\sqrt{\frac{3}{2}}\,\|\boldsymbol{\sigma}_{\mathrm{dev}}\|$ of position ⑤ after 10 s. Left to right: Fine FE, fine RVE.

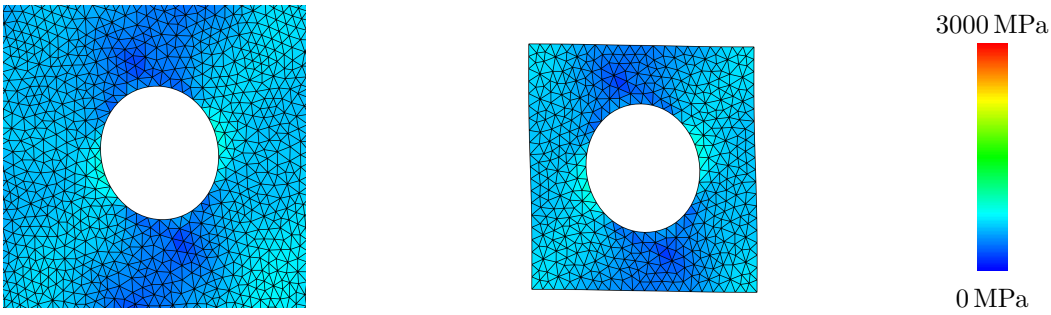

(d) Von Mises stress $\sqrt{\frac{3}{2}}\,\|\boldsymbol{\sigma}_{\mathrm{dev}}\|$ of position ⑤ after 100 s. Left to right: Fine FE, fine RVE.

Figure 5.19: Contour plots of position ⑤ for the adiabatic simulation. The hardening variable k is shown after (a) 10 s and (b) 100 s as well as the von Mises stress $\sqrt{\frac{3}{2}}\,\|\boldsymbol{\sigma}_{\mathrm{dev}}\|$ after (c) 10 s and (d) 100 s.

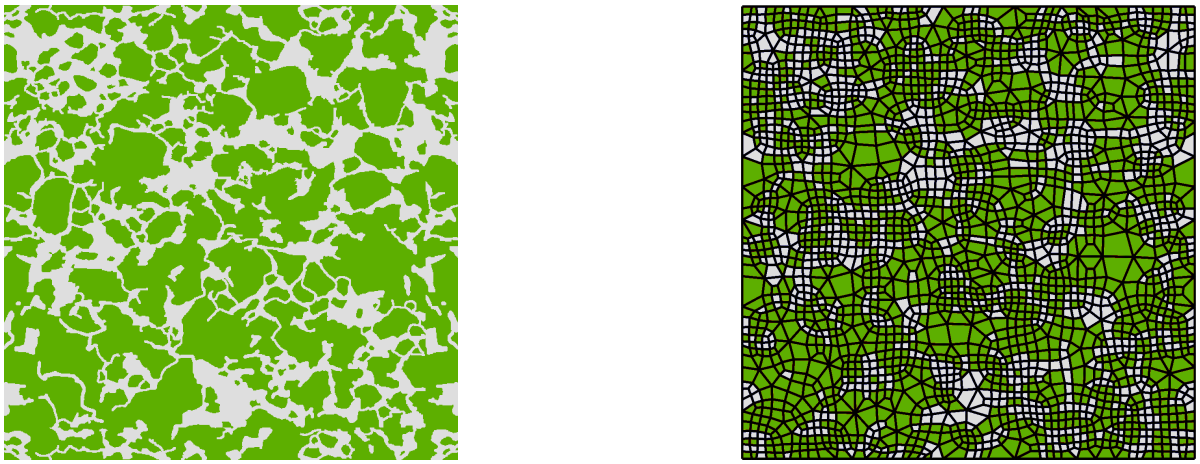

(a) Periodic binary image.

(b) Respective FE discretisation.

Figure 5.20: (a) Periodic binary image. (b) FE discretisation of the periodic binary image.

5.4.3 Coated radius

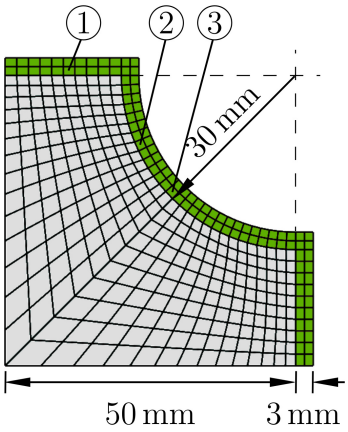

Figure 5.21: FE discretisation of the steel radius (grey) and the WC-Co coating (green) before quenching.

The third numerical example follows a practical application of coating tool surfaces for metal forming with wear-resistant hard materials such as WC-Co. During the development of coating technology, academic examples like the coating of a radius are examined. Here, due to residual stresses during quenching after the coating procedure, delamination of the coating can occur, cf. Fig. 1.5. In order to model the quenching procedure, the radius is discretised as depicted in Fig. 5.21. The grey area represents steel, whereas the green area is the applied WC-Co coating which is heterogeneous in nature. The steel is modelled as thermoelastic material and the coating is represented by an RVE. At RVE level, the proposed thermoviscoplastic model is applied for the Co-phase, whereas WC is modelled as thermoelastic material. In total, 104 quadrilateral two–scale elements with four integration points and bi-linear shape functions are involved in this analysis. The two dimensional RVE is generated on the basis of a binary analysis of an SEM image, cf. Fig. 1.3. Since periodic boundary conditions are applied at the meso-scale, the RVE also has to be periodic and therefore the binary image is manually made periodic as shown in Fig. 5.20(a) and subsequently meshed with the help of the software oof2, cf. Reid

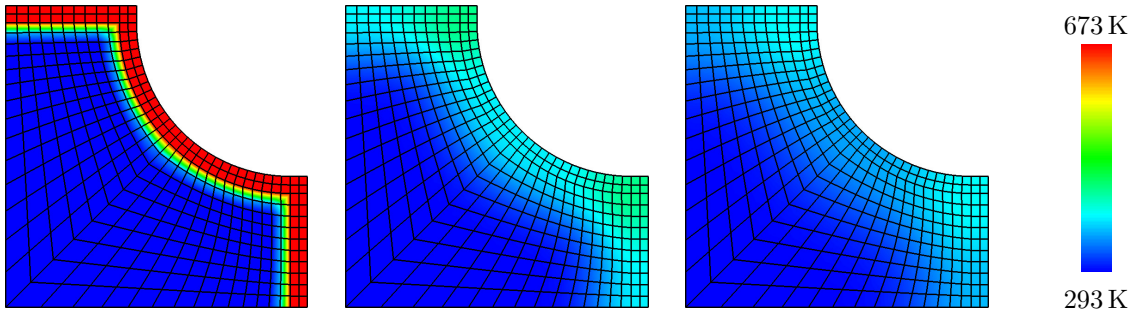

(a) Temperature of the coated radius after (left) 0 s, (middle) 5 s and (right) 10 s.

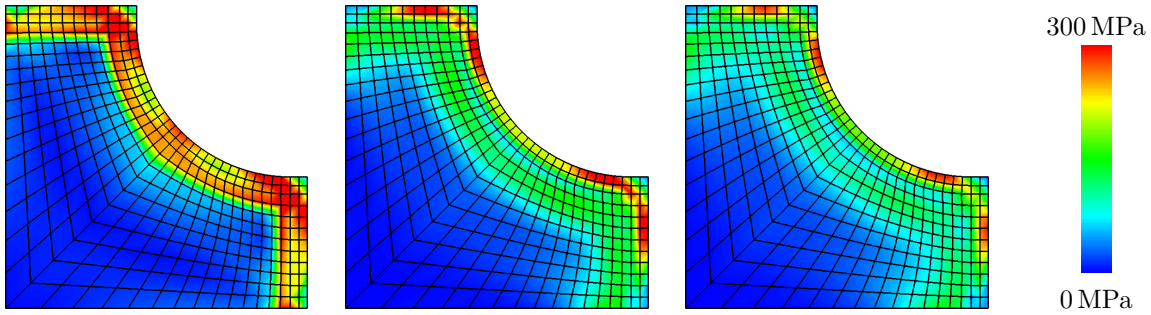

(b) Von Mises stress of the coated radius after (left) 0 s, (middle) 5 s and (right) 10 s.

Figure 5.22: Macroscale contour plots of (a) the temperature and (b) the von Mises stress of the coated radius after (left) 0 s, (middle) 5 s and (right) 10 s.

et al. [139]. The resulting mesh is depicted in Fig. 5.20(b). It consists of 2855 nodes and 2770 elements and shows overall isotropic effective behaviour. The initial temperature of the steel substrate is 293 K and the coating is assumed to have an initial temperature of 673 K. In order to model quenching, the ambient temperature is set to 293 K such that the body is cooled down via convective heat transfer. The material parameters are taken from Table 5.1. The simulation is carried out from $t = 0$ to $t = 10\,\mathrm{s}$ with $\Delta t = 0.1\,\mathrm{s}$.

The temperature field of the simulation is depicted in Fig. 5.22(a) at the beginning of the simulation, after 5 s and at the end. It can be observed that the steel substrate is heated near the coating due to heat conduction. The heat is partly led away via the surface as a consequence of the modelling of convective heat transfer. The different thermo-mechanical material properties induce residual stresses, as the plot of the von Mises stress indicates for the three chosen points in time, see Fig. 5.22(b). It shows that the von Mises stress in the coating near the sharp edge of the radius is relatively high at the beginning of the simulation. Here, as observed in Fig. 1.5, the coating would delaminate. Since no damage modelling is involved, the bonding remains perfect in the simulations presented in this work. With proceeding cooling, the von Mises stress shows risen values in the steel substrate near the interface of the substrate and the coating. High values near the sharp radius edges are observed up to the end of the simulation, although the overall area with high von Mises stress decreases.

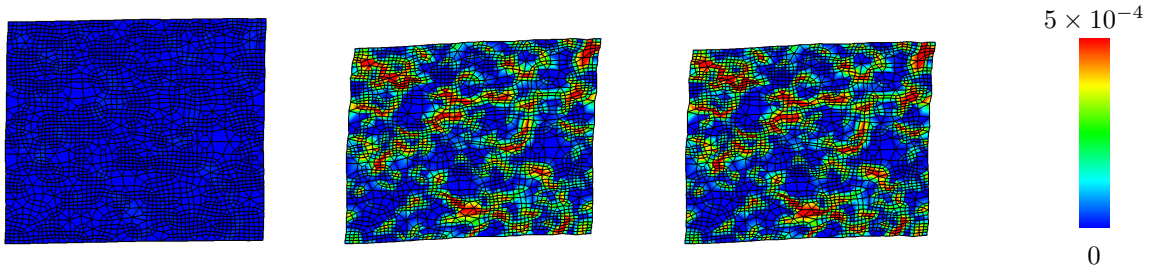

(a) Hardening variable k of the RVE at position ① after (left) 0 s, (middle) 5 s and (right) 10 s.

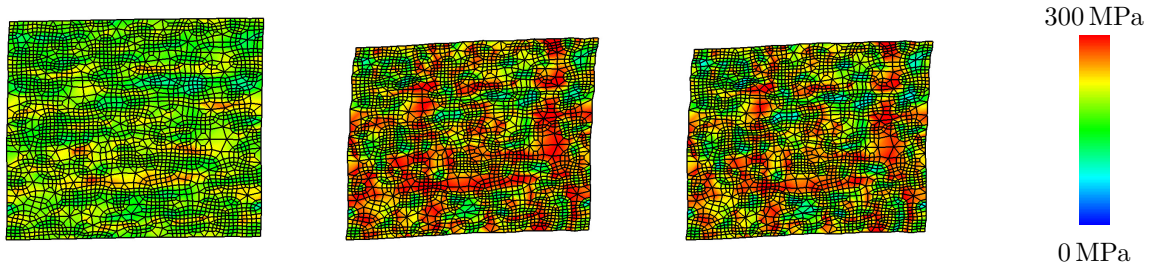

(b) Von Mises stress of the RVE at position ① after (left) 0 s, (middle) 5 s and (right) 10 s.

Figure 5.23: Mesoscale contour plots of (a) the Hardening variable k and (b) the von Mises stress of the RVE at position ① after (left) 0 s, (middle) 5 s and (right) 10 s.

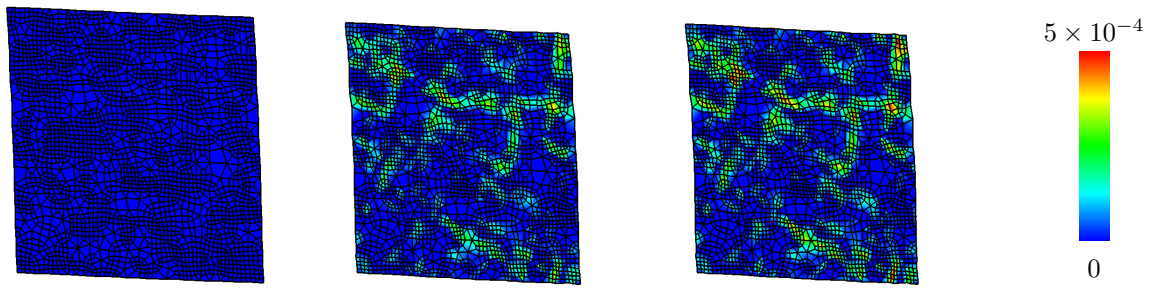

(a) Hardening variable k of the RVE at position ② after (left) 0 s, (middle) 5 s and (right) 10 s.

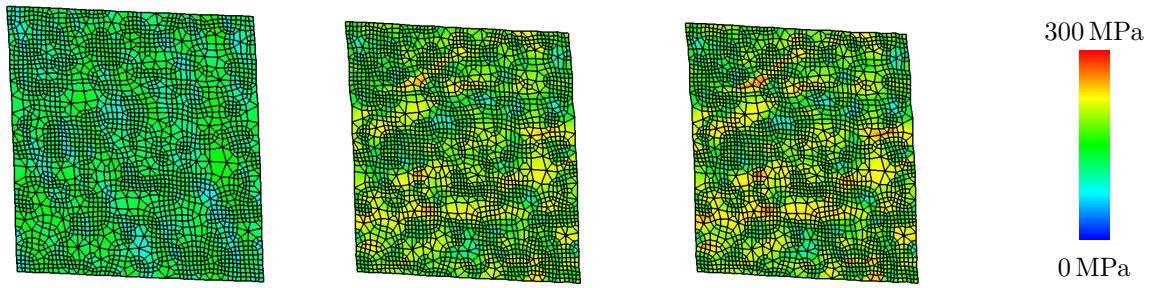

(b) Von Mises stress of the RVE at position ② after (left) 0 s, (middle) 5 s and (right) 10 s.

Figure 5.24: Mesoscale contour plots of (a) the Hardening variable k and (b) the von Mises stress of the RVE at position ② after (left) 0 s, (middle) 5 s and (right) 10 s.

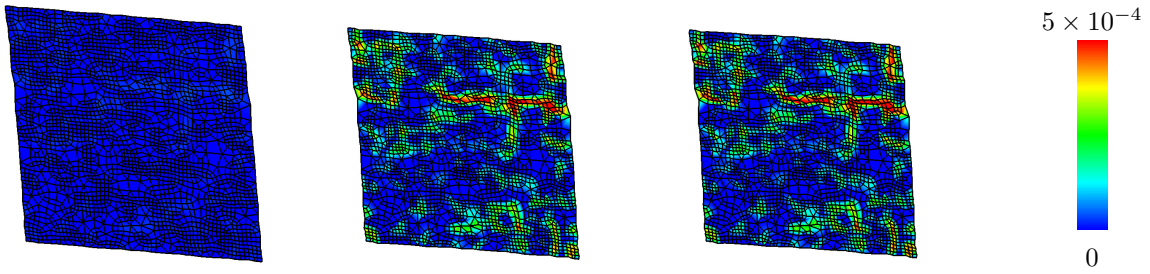

(a) Hardening variable k of the RVE at position ③ after (left) 0 s, (middle) 5 s and (right) 10 s.

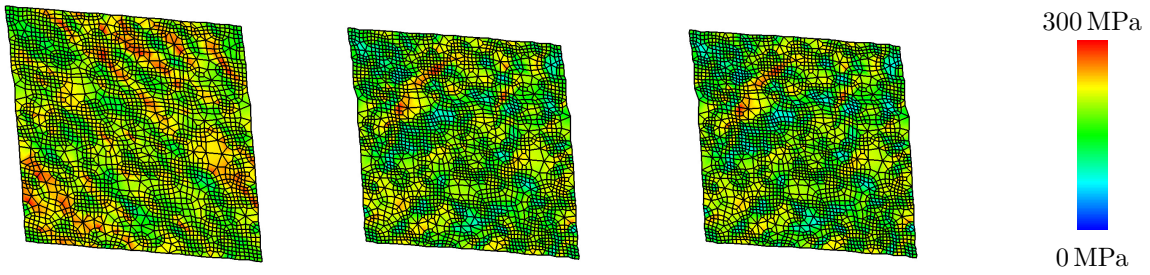

(b) Von Mises stress of the RVE at position ③ after (left) 0 s, (middle) 5 s and (right) 10 s.

Figure 5.25: Mesoscale contour plots of (a) the Hardening variable k and (b) the von Mises stress of the RVE at position ③ after (left) 0 s, (middle) 5 s and (right) 10 s.

The behaviour of the coating material is determined by the behaviour of the WC and Co phases on the meso-scale. In order to show the evolution of plastic deformation and the resulting stress state at the meso-scale, RVEs from three different positions are plotted with a constant displacement exaggeration factor of 250. The positions are shown in Fig. 5.21. The RVE at position ① is compressed further and further during the quenching and plastic deformation evolves in the Co phase, as can be seen in Fig. 5.23(a). The level of the von Mises stress is shown in Fig. 5.23(b) and reaches its (depicted) maximum at $t = 5\,\mathrm{s}$. This coincides with the macro-scale von Mises plot, cf. Fig. 5.22(b), of the respective position.

The RVE at position ② shows less plastic deformation, as can bee seen in Fig. 5.24(a), and a lower von Mises stress state, as Fig. 5.24(b) shows, which causes the observable macro-scale result. At position ③, plastic deformation evolves during the first 5 s of the simulation and remains more or less constant afterwards, cf. Fig. 5.25(a). The von Mises stress is depicted in Fig. 5.25(b) and is comparatively high at the beginning. During the last 5 s of the simulation, the von Mises stress shows a quasi constant level at position ③ which is also observable in the homogenised plot in Fig. 5.22(b).

6 Computational homogenisation for thermo-viscoplastic composites: Large strain formulation and weak micro-periodicity

This chapter deals with a first order two-scale finite element framework for fully coupled thermo-mechanical problems at finite deformations. In this respect, this chapter represents the extension of the geometrically linearised framework discussed in the previous chapter. The scale bridging is achieved by the application of Hill-Mandel condition based boundary conditions at the lower scale. A further emphasis of this chapter is the extension of the concept of weak micro-periodicity, cf. Larsson et al. [104], to thermo-mechanically coupled problems. With this formulation at hand, uniform traction, respectively heat flux boundary conditions as well as the classic periodic boundary conditions are captured as well as a transition in between them. The governing equations of continuum thermodynamics, the scale-bridging across the two scales as well as a thermo-viscoplastic constitutive model for finite deformations are summarised in Section 6.1. Subsequently in Section 6.2, the two-scale finite element implementation is briefly recapitulated with the focus on the algorithmic handling of the novel thermo-mechanical weak micro-periodicity constraints. Finally, the performance of the proposed boundary conditions in comparison to the classic Hill-Mandel based boundary conditions is shown by means of simulations of a single representative volume element as well as by means of multi-scale simulations in Section 6.3.

6.1 Continuum thermodynamical background

In this section, the thermodynamical background of the proposed thermo-mechanically coupled multi-scale framework is presented. The governing equations and main assumptions of this large deformation framework are summarised in Section 6.1.1, whereby equations which are discussed in Chapter 2 are repeated for the sake of convenience. Subsequently, Section 6.1.2 presents the scale transition between the two scales considered,

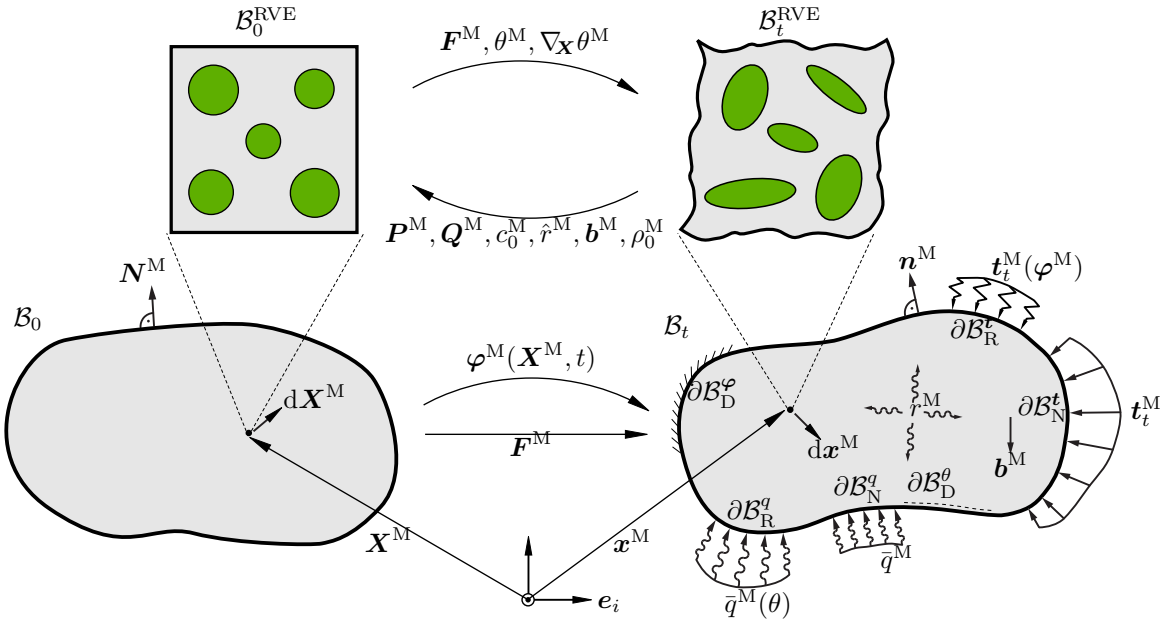

Figure 6.1: Reference configuration $\mathcal{B}_0$ and current configuration $\mathcal{B}_t$ of a deformable heat conductor. The effective material behaviour of the body is defined by the heterogeneous meso-structure.

whereby the upper scale is denoted as the "macro-scale" and the lower scale is denoted as the "meso-scale". Note that this lower scale is often denoted as the micro-scale. Within this work, however, we shall denote this scale as meso-scale since its respective constituents may possess further, even smaller scales. In order to carry out exemplary numerical simulations where inelastic effects as well as inelastic heating is considered, a thermo-viscoplastic constitutive model is presented in Section 6.1.3 for demonstration purposes.

6.1.1 Continuum thermo-mechanics at two separated length scales

In this chapter, a deformable transient heat conductor at large deformations is considered, cf. Box 2.1 in Section 2.4. It is assumed that the considered body with configurations $\mathcal{B}_0$ and $\mathcal{B}_t$ is observable at the so-called macro-scale (superscript "M") with the characteristic lengths $L^{\mathrm{M}} \in \mathcal{B}_0$ and, respectively, $l^{\mathrm{M}} \in \mathcal{B}_t$. At a lower scale, which is denoted as the meso-scale (superscript "m") in this work, heterogeneities might be observed which are captured by representative volume elements (RVE) $\mathcal{B}_0^{\mathrm{RVE}}$ at a point $\boldsymbol{X}^{\mathrm{M}} \in \mathcal{B}_0$. According to the deformation map $\boldsymbol{\varphi}^{\mathrm{M}}(\boldsymbol{X}^{\mathrm{M}}, t)$, the current configuration of the RVE at the corresponding point $\boldsymbol{x}^{\mathrm{M}} \in \mathcal{B}_t$ is denoted by $\mathcal{B}_t^{\mathrm{RVE}}$, cf. Fig. 6.1 for an illustration. At the macro-scale, transient thermo-mechanical initial boundary value problems (IBVP) are solved in order to obtain the solution of the unknown current placements $\boldsymbol{x}^{\mathrm{M}}$ as well as the unknown absolute temperature $\theta^{\mathrm{M}} > 0$ for a given load at current time step t. The underlying balance equations are the balance of linear momentum

$$\rho_0^{\mathrm{M}}\,\ddot{\boldsymbol{\varphi}}^{\mathrm{M}} = \nabla_{\boldsymbol{X}}\cdot\boldsymbol{P}^{\mathrm{M}} + \rho_0^{\mathrm{M}}\,\boldsymbol{b}^{\mathrm{M}}\,, \tag{6.1}$$

and the energy balance equation, represented by the rate of the temperature equation

$$c_0^{\mathrm{M}}\,\dot{\theta}^{\mathrm{M}} = -\,\nabla_{\boldsymbol{X}}\cdot\boldsymbol{Q}^{\mathrm{M}} + \rho_0^{\mathrm{M}}\,\hat{r}^{\mathrm{M}}\,, \tag{6.2}$$

in their referential local strong forms, cf. Eqs. (2.82) and (2.101). In the above equations, ρ_0^{M} is the (conserved) referential mass density, $\ddot{\boldsymbol{\varphi}}^{\mathrm{M}}$ is the acceleration, $\boldsymbol{P}^{\mathrm{M}}$ are the Piola stresses and $\boldsymbol{b}^{\mathrm{M}}$ is the body force vector. Moreover, in Eq. (6.2) c_0^{M} is the referential heat capacity, $\dot{\theta}^{\mathrm{M}}$ is the rate of the temperature, $\boldsymbol{Q}^{\mathrm{M}}$ is the referential heat flux vector and $\hat{r}^{\mathrm{M}}$ is the sum of all local, internal heat sources per referential unit volume. The two unknown fields, $\boldsymbol{\varphi}^{\mathrm{M}}$ and θ^{M}, coexist at each material point of the deformable heat conductor. The different types of boundary conditions which are necessary to define the IBVP are illustrated in Fig. 6.1. In this framework, the current load at the macro-scale is related to the reference configuration

$$\boldsymbol{\varphi}^{\mathrm{M}} = \bar{\boldsymbol{\varphi}}^{\mathrm{M}} \qquad \text{on} \qquad \partial\mathcal{B}_0^{\boldsymbol{\varphi}}\,, \tag{6.3}$$

$$\boldsymbol{t}_0^{\mathrm{M}} = \boldsymbol{P}^{\mathrm{M}}\cdot\boldsymbol{N}^{\mathrm{M}} = \bar{\boldsymbol{t}}_0^{\mathrm{M}} \qquad \text{on} \qquad \partial\mathcal{B}_0^{\boldsymbol{t}}\,, \tag{6.4}$$

$$\theta^{\mathrm{M}} = \bar{\theta}^{\mathrm{M}} \qquad \text{on} \qquad \partial\mathcal{B}_0^{\theta}\,, \tag{6.5}$$

$$Q^{\mathrm{M}} = -\boldsymbol{Q}^{\mathrm{M}}\cdot\boldsymbol{N}^{\mathrm{M}} = \bar{Q}^{\mathrm{M}} \qquad \text{on} \qquad \partial\mathcal{B}_0^{Q}\,, \tag{6.6}$$

according to Eqs. (2.104) to (2.107) and Box 2.1.

An important assumption made is that the characteristic lengths at the lower meso-scale $L^{\mathrm{m}} \in \mathcal{B}_0^{\mathrm{RVE}}$ and $l^{\mathrm{m}} \in \mathcal{B}_t^{\mathrm{RVE}}$ are much smaller than those at the upper macro-scale, such that $L^{\mathrm{M}} \gg L^{\mathrm{m}}$ and $l^{\mathrm{M}} \gg l^{\mathrm{m}}$. As a consequence, the two length scales are separated from each other. With this at hand, we apply a first order homogenisation procedure which implicates an instantaneous constitutive response at the meso-scale. At all macroscopic referential points $\boldsymbol{X}^{\mathrm{M}}$ where an RVE determines the effective constitutive behaviour, the current macroscopic state of deformation in terms of the deformation gradient $\boldsymbol{F}^{\mathrm{M}}$, the temperature θ^{M} as well as the referential temperature gradient $\nabla_{\boldsymbol{X}}\theta^{\mathrm{M}}$ is transferred to the meso-scale. With the given macroscopic deformation state at hand and under further assumptions specified as this work proceeds, particular boundary conditions can be derived in order to obtain the effective response of the RVE referred to $\boldsymbol{X}^{\mathrm{M}}$ with reference configuration $\mathcal{B}_0^{\mathrm{RVE}}$. As outlined above, the unknown fields are assumed to evolve instantaneously at the meso-scale. Therefore, the mesoscopic equivalents of Eqs. (6.1) and (6.2) to be solved are

$$\boldsymbol{0} = \nabla_{\boldsymbol{X}}\cdot\boldsymbol{P}^{\mathrm{m}}\,, \tag{6.7}$$

$$0 = -\,\nabla_{\boldsymbol{X}}\cdot\boldsymbol{Q}^{\mathrm{m}}\,. \tag{6.8}$$

The aforementioned assumptions and resulting boundary conditions as well as the homogenisation procedure are summarised in the next section.

6.1.2 Scale bridging between two separated length scales

The effective macroscopic material behaviour is obtained according to Eqs. (6.7) and (6.8) which are solved at the mesoscale for given $\boldsymbol{F}^{\mathrm{M}}$, θ^{M} and $\nabla_{\boldsymbol{X}}\theta^{\mathrm{M}}$. In order to ensure equivalence of the macroscopic and mesoscopic internal work as well as equivalence of the macroscopic and mesoscopic entropy increase, we follow the approach by Özdemir et al. [132] and use the Hill-Mandel-type macro-meso homogeneity conditions

$$\boldsymbol{P}^{\mathrm{M}} : \boldsymbol{F}^{\mathrm{M}} = \frac{1}{V^{\mathrm{RVE}}} \int\limits_{\mathcal{B}_0^{\mathrm{RVE}}} \boldsymbol{P}^{\mathrm{m}} : \boldsymbol{F}^{\mathrm{m}} \, \mathrm{d}V \ , \tag{6.9}$$

$$\boldsymbol{Q}^{\mathrm{M}} \cdot \nabla_{\boldsymbol{X}}\theta^{\mathrm{M}} = \frac{1}{V^{\mathrm{RVE}}} \int\limits_{\mathcal{B}_0^{\mathrm{RVE}}} \boldsymbol{Q}^{\mathrm{m}} \cdot \nabla_{\boldsymbol{X}}\theta^{\mathrm{m}} \, \mathrm{d}V \ , \tag{6.10}$$

with

$$V^{\mathrm{RVE}} = \int\limits_{\mathcal{B}_0^{\mathrm{RVE}}} \mathrm{d}V \ , \tag{6.11}$$

for the scale-bridging, although Eq. (6.10) does not fully describe the meso-scale entropy production as commented on in Sengupta et al. [157]. The volumetric average of an arbitrary mesoscale quantity $(\bullet)^{\mathrm{m}}$ is defined as

$$\langle \, (\bullet)^{\mathrm{m}} \, \rangle = \frac{1}{V^{\mathrm{RVE}}} \int\limits_{\mathcal{B}_0^{\mathrm{RVE}}} (\bullet)^{\mathrm{m}} \, \mathrm{d}V \ , \tag{6.12}$$

which represents the average of the respective quantity over the RVE domain. For extensive quantities, the above equation yields the effective macro-scale quantity, such that $(\bullet)^{\mathrm{M}} = \langle \, (\bullet)^{\mathrm{m}} \, \rangle$. However, as e.g. discussed in Sengupta et al. [157], neither $\boldsymbol{P}$ and $\boldsymbol{F}$ nor $\boldsymbol{Q}$ and $\nabla_{\boldsymbol{X}}\theta$ are extensive quantities. As a consequence, Eqs. (6.9) and (6.10) are only valid under further assumptions, since in general $\langle (\bullet)^{\mathrm{m}} \rangle \neq (\bullet)^{\mathrm{M}}$ for non-extensive quantities $(\bullet)$. As outlined in, e.g., Kouznetsova et al. [98] or Sengupta et al. [157],

the averages of the quantities in Eqs. (6.9) and (6.10) are computed via Eq. (6.12) and subsequently transformed into boundary integrals

$$\begin{aligned}
\langle \boldsymbol{F}^{\mathrm{m}} \rangle &= \frac{1}{V^{\mathrm{RVE}}} \int\limits_{\mathcal{B}_0^{\mathrm{RVE}}} \boldsymbol{F}^{\mathrm{m}} \,\mathrm{d}V = \frac{1}{V^{\mathrm{RVE}}} \int\limits_{\mathcal{B}_0^{\mathrm{RVE}}} \nabla_{\boldsymbol{X}} \otimes \boldsymbol{x}^{\mathrm{m}} \,\mathrm{d}V \\
&= \frac{1}{V^{\mathrm{RVE}}} \int\limits_{\mathcal{B}_0^{\mathrm{RVE}}} \nabla_{\boldsymbol{X}}\, \boldsymbol{x}^{\mathrm{m}} \,\mathrm{d}V = \frac{1}{V^{\mathrm{RVE}}} \int\limits_{\mathcal{B}_0^{\mathrm{RVE}}} \nabla_{\boldsymbol{X}} \cdot \big[\, \boldsymbol{x}^{\mathrm{m}} \otimes \boldsymbol{I} \,\big] \,\mathrm{d}V \\
&= \frac{1}{V^{\mathrm{RVE}}} \int\limits_{\partial\mathcal{B}_0^{\mathrm{RVE}}} \big[\, \boldsymbol{x}^{\mathrm{m}} \otimes \boldsymbol{I} \,\big] \cdot \boldsymbol{N} \,\mathrm{d}A = \frac{1}{V^{\mathrm{RVE}}} \int\limits_{\partial\mathcal{B}_0^{\mathrm{RVE}}} \boldsymbol{x}^{\mathrm{m}} \otimes \boldsymbol{N}^{\mathrm{m}} \,\mathrm{d}A \,,
\end{aligned} \tag{6.13}$$

$$\begin{aligned}
\langle \boldsymbol{P}^{\mathrm{m}} \rangle &= \frac{1}{V^{\mathrm{RVE}}} \int\limits_{\mathcal{B}_0^{\mathrm{RVE}}} \boldsymbol{P}^{\mathrm{m}} \,\mathrm{d}V = \frac{1}{V^{\mathrm{RVE}}} \int\limits_{\mathcal{B}_0^{\mathrm{RVE}}} \nabla_{\boldsymbol{X}} \cdot \big[\, \boldsymbol{P}^{\mathrm{m}} \otimes \boldsymbol{X}^{\mathrm{m}} \,\big] \,\mathrm{d}V \\
&= \frac{1}{V^{\mathrm{RVE}}} \int\limits_{\partial\mathcal{B}_0^{\mathrm{RVE}}} [\, \boldsymbol{P}^{\mathrm{m}} \cdot \boldsymbol{N} \,] \otimes \boldsymbol{X}^{\mathrm{m}} \,\mathrm{d}A = \frac{1}{V^{\mathrm{RVE}}} \int\limits_{\partial\mathcal{B}_0^{\mathrm{RVE}}} \boldsymbol{t}_0^{\mathrm{m}} \otimes \boldsymbol{X}^{\mathrm{m}} \,\mathrm{d}A \,,
\end{aligned} \tag{6.14}$$

as well as

$$\begin{aligned}
\langle \nabla_{\boldsymbol{X}} \theta^{\mathrm{m}} \rangle &= \frac{1}{V^{\mathrm{RVE}}} \int\limits_{\mathcal{B}_0^{\mathrm{RVE}}} \nabla_{\boldsymbol{X}} \theta^{\mathrm{m}} \,\mathrm{d}V = \frac{1}{V^{\mathrm{RVE}}} \int\limits_{\mathcal{B}_0^{\mathrm{RVE}}} \nabla_{\boldsymbol{X}} \cdot \big[\, \theta^{\mathrm{m}} \boldsymbol{I} \,\big] \,\mathrm{d}V \\
&= \frac{1}{V^{\mathrm{RVE}}} \int\limits_{\partial\mathcal{B}_0^{\mathrm{RVE}}} \big[\, \theta^{\mathrm{m}} \boldsymbol{I} \,\big] \cdot \boldsymbol{N} \,\mathrm{d}A = \frac{1}{V^{\mathrm{RVE}}} \int\limits_{\partial\mathcal{B}_0^{\mathrm{RVE}}} \theta^{\mathrm{m}} \boldsymbol{N}^{\mathrm{m}} \,\mathrm{d}A \,,
\end{aligned} \tag{6.15}$$

$$\begin{aligned}
\langle \boldsymbol{Q}^{\mathrm{m}} \rangle &= \frac{1}{V^{\mathrm{RVE}}} \int\limits_{\mathcal{B}_0^{\mathrm{RVE}}} \boldsymbol{Q}^{\mathrm{m}} \,\mathrm{d}V = \frac{1}{V^{\mathrm{RVE}}} \int\limits_{\mathcal{B}_0^{\mathrm{RVE}}} \nabla_{\boldsymbol{X}} \cdot \big[\, \boldsymbol{Q}^{\mathrm{m}} \otimes \boldsymbol{X}^{\mathrm{m}} \,\big] \,\mathrm{d}V \\
&= \frac{1}{V^{\mathrm{RVE}}} \int\limits_{\partial\mathcal{B}_0^{\mathrm{RVE}}} [\, \boldsymbol{Q}^{\mathrm{m}} \cdot \boldsymbol{N} \,] \otimes \boldsymbol{X}^{\mathrm{m}} \,\mathrm{d}A = \frac{1}{V^{\mathrm{RVE}}} \int\limits_{\partial\mathcal{B}_0^{\mathrm{RVE}}} Q^{\mathrm{m}} \boldsymbol{X}^{\mathrm{m}} \,\mathrm{d}A \,.
\end{aligned} \tag{6.16}$$

In Eqs. (6.14) and (6.16), the vanishing divergence of $\boldsymbol{P}^{\mathrm{m}}$ is used, as well as the vanishing divergence of $\boldsymbol{Q}^{\mathrm{m}}$, as given by Eqs. (6.7) and (6.8) for an equilibrium state at the meso-scale whereby no internal surfaces such as cracks are considered. A framework which

takes internal surfaces into account can e.g. be found in [91]. Furthermore, the volume integrals of Eqs. (6.9) and (6.10) are transformed into boundary integrals

$$\begin{aligned}
&\frac{1}{V^{\mathrm{RVE}}} \int\limits_{\mathcal{B}_0^{\mathrm{RVE}}} \boldsymbol{P}^{\mathrm{m}} \colon \boldsymbol{F}^{\mathrm{m}} \, \mathrm{d}V = \frac{1}{V^{\mathrm{RVE}}} \int\limits_{\mathcal{B}_0^{\mathrm{RVE}}} \boldsymbol{P}^{\mathrm{m}} \colon [\, \boldsymbol{x}^{\mathrm{m}} \otimes \nabla_{\boldsymbol{X}} \,] \, \mathrm{d}V \\
&= \frac{1}{V^{\mathrm{RVE}}} \int\limits_{\mathcal{B}_0^{\mathrm{RVE}}} \boldsymbol{P}^{\mathrm{m}} \colon \nabla_{\boldsymbol{X}} \, \boldsymbol{x}^{\mathrm{m}} \, \mathrm{d}V = \frac{1}{V^{\mathrm{RVE}}} \int\limits_{\mathcal{B}_0^{\mathrm{RVE}}} [\, \boldsymbol{x}^{\mathrm{m}} \cdot \boldsymbol{P}^{\mathrm{m}} \,] \cdot \nabla_{\boldsymbol{X}} \, \mathrm{d}V \\
&= \frac{1}{V^{\mathrm{RVE}}} \int\limits_{\partial\mathcal{B}_0^{\mathrm{RVE}}} \boldsymbol{x}^{\mathrm{m}} \cdot \boldsymbol{P}^{\mathrm{m}} \cdot \boldsymbol{N}^{\mathrm{m}} \, \mathrm{d}A = \frac{1}{V^{\mathrm{RVE}}} \int\limits_{\partial\mathcal{B}_0^{\mathrm{RVE}}} \boldsymbol{x}^{\mathrm{m}} \cdot \boldsymbol{t}_0^{\mathrm{m}} \, \mathrm{d}A \, ,
\end{aligned} \tag{6.17}$$

$$\begin{aligned}
&\frac{1}{V^{\mathrm{RVE}}} \int\limits_{\mathcal{B}_0^{\mathrm{RVE}}} \boldsymbol{Q}^{\mathrm{m}} \cdot \nabla_{\boldsymbol{X}} \theta^{\mathrm{m}} \, \mathrm{d}V = \frac{1}{V^{\mathrm{RVE}}} \int\limits_{\mathcal{B}_0^{\mathrm{RVE}}} [\, \boldsymbol{Q}^{\mathrm{m}} \, \theta^{\mathrm{m}} \,] \cdot \nabla_{\boldsymbol{X}} \, \mathrm{d}V \\
&= \frac{1}{V^{\mathrm{RVE}}} \int\limits_{\partial\mathcal{B}_0^{\mathrm{RVE}}} [\, \boldsymbol{Q}^{\mathrm{m}} \, \theta^{\mathrm{m}} \,] \cdot \boldsymbol{N}^{\mathrm{m}} \, \mathrm{d}A = \frac{1}{V^{\mathrm{RVE}}} \int\limits_{\partial\mathcal{B}_0^{\mathrm{RVE}}} Q^{\mathrm{m}} \, \theta^{\mathrm{m}} \, \mathrm{d}A \, .
\end{aligned} \tag{6.18}$$

Following Nemat-Nasser and Hori [124], the calculations summarised in Appendix B.1 can be carried out and yield

$$\begin{aligned}
&\frac{1}{V^{\mathrm{RVE}}} \int\limits_{\partial\mathcal{B}_0^{\mathrm{RVE}}} \boldsymbol{x}^{\mathrm{m}} \cdot \boldsymbol{t}_0^{\mathrm{m}} \, \mathrm{d}A - \langle \boldsymbol{F}^{\mathrm{m}} \rangle \colon \langle \boldsymbol{P}^{\mathrm{m}} \rangle \\
&= \frac{1}{V^{\mathrm{RVE}}} \int\limits_{\partial\mathcal{B}_0^{\mathrm{RVE}}} [\, \boldsymbol{x}^{\mathrm{m}} - \langle \boldsymbol{F}^{\mathrm{m}} \rangle \cdot \boldsymbol{X}^{\mathrm{m}} \,] \cdot [\, \boldsymbol{t}_0^{\mathrm{m}} - \langle \boldsymbol{P}^{\mathrm{m}} \rangle \cdot \boldsymbol{N}^{\mathrm{m}} \,] \, \mathrm{d}A \, ,
\end{aligned} \tag{6.19}$$

$$\frac{1}{V^{\mathrm{RVE}}} \int\limits_{\partial \mathcal{B}_0^{\mathrm{RVE}}} \theta^{\mathrm{m}}\, Q^{\mathrm{m}}\, \mathrm{d}A - \langle \nabla_{\boldsymbol{X}} \theta^{\mathrm{m}} \rangle \cdot \langle \boldsymbol{Q}^{\mathrm{m}} \rangle$$

$$= \frac{1}{V^{\mathrm{RVE}}} \int\limits_{\partial \mathcal{B}_0^{\mathrm{RVE}}} \left[\theta^{\mathrm{m}} - \langle \nabla_{\boldsymbol{X}} \theta^{\mathrm{m}} \rangle \cdot \boldsymbol{X}^{\mathrm{m}} \right] \left[Q^{\mathrm{m}} - \langle \boldsymbol{Q}^{\mathrm{m}} \rangle \cdot \boldsymbol{N}^{\mathrm{m}} \right] \mathrm{d}A \,. \tag{6.20}$$

From these two equations it follows that the Hill-Mandel-type macro-homogeneity conditions, Eqs. (6.9) and (6.10), with $\boldsymbol{F}^{\mathrm{M}} = \langle \boldsymbol{F}^{\mathrm{m}} \rangle$, $\boldsymbol{P}^{\mathrm{M}} = \langle \boldsymbol{P}^{\mathrm{m}} \rangle$, $\nabla_{\boldsymbol{X}} \theta^{\mathrm{M}} = \langle \nabla_{\boldsymbol{X}} \theta^{\mathrm{m}} \rangle$ and $\boldsymbol{Q}^{\mathrm{M}} = \langle \boldsymbol{Q}^{\mathrm{m}} \rangle$ are fulfilled for

$$0 = \frac{1}{V^{\mathrm{RVE}}} \int\limits_{\partial \mathcal{B}_0^{\mathrm{RVE}}} \left[\boldsymbol{x}^{\mathrm{m}} - \boldsymbol{F}^{\mathrm{M}} \cdot \boldsymbol{X}^{\mathrm{m}} \right] \cdot \left[\boldsymbol{t}_0^{\mathrm{m}} - \boldsymbol{P}^{\mathrm{M}} \cdot \boldsymbol{N}^{\mathrm{m}} \right] \mathrm{d}A \,, \tag{6.21}$$

$$0 = \frac{1}{V^{\mathrm{RVE}}} \int\limits_{\partial \mathcal{B}_0^{\mathrm{RVE}}} \left[\theta^{\mathrm{m}} - \nabla_{\boldsymbol{X}} \theta^{\mathrm{M}} \cdot \boldsymbol{X}^{\mathrm{m}} \right] \left[Q^{\mathrm{m}} - \boldsymbol{Q}^{\mathrm{M}} \cdot \boldsymbol{N}^{\mathrm{m}} \right] \mathrm{d}A \,. \tag{6.22}$$

Possible solutions for Eqs. (6.21) and (6.22) are given for Dirichlet type boundary conditions at the meso-scale, i.e.

$$\boldsymbol{x}^{\mathrm{m}} = \boldsymbol{F}^{\mathrm{M}} \cdot \boldsymbol{X}^{\mathrm{m}} \,, \tag{6.23}$$

$$\theta^{\mathrm{m}} = \theta^{\mathrm{M}} + \nabla_{\boldsymbol{X}} \theta^{\mathrm{M}} \cdot \left[\boldsymbol{X}^{\mathrm{m}} - \boldsymbol{X}_{\mathrm{c}}^{\mathrm{m}} \right] , \tag{6.24}$$

whereby $\boldsymbol{X}_{\mathrm{c}}^{\mathrm{m}}$ denotes the geometric center of gravity of the considered RVE, cf. Fig. 6.2. Furthermore, Eqs. (6.21) and (6.22) are fulfilled for constant Neumann type boundary conditions at the meso-scale, namely

$$\boldsymbol{t}_0^{\mathrm{m}} = \quad \boldsymbol{P}^{\mathrm{M}} \cdot \boldsymbol{N}^{\mathrm{m}} \,, \tag{6.25}$$

$$Q^{\mathrm{m}} = -\boldsymbol{Q}^{\mathrm{M}} \cdot \boldsymbol{N}^{\mathrm{m}} \,. \tag{6.26}$$

as well as for periodic boundary conditions at the meso-scale represented by

$$\boldsymbol{x}_+^{\mathrm{m}} = \boldsymbol{x}_-^{\mathrm{m}} + \boldsymbol{F}^{\mathrm{M}} \cdot \left[\boldsymbol{X}_+^{\mathrm{m}} - \boldsymbol{X}_-^{\mathrm{m}} \right] , \qquad \boldsymbol{t}_{0+}^{\mathrm{m}} = -\, \boldsymbol{t}_{0-}^{\mathrm{m}} \,, \tag{6.27}$$

$$\theta_+^{\mathrm{m}} = \theta_-^{\mathrm{m}} + \nabla_{\boldsymbol{X}} \theta^{\mathrm{M}} \cdot \left[\boldsymbol{X}_+^{\mathrm{m}} - \boldsymbol{X}_-^{\mathrm{m}} \right] , \qquad Q_+^{\mathrm{m}} = -\, Q_-^{\mathrm{m}} \,, \tag{6.28}$$

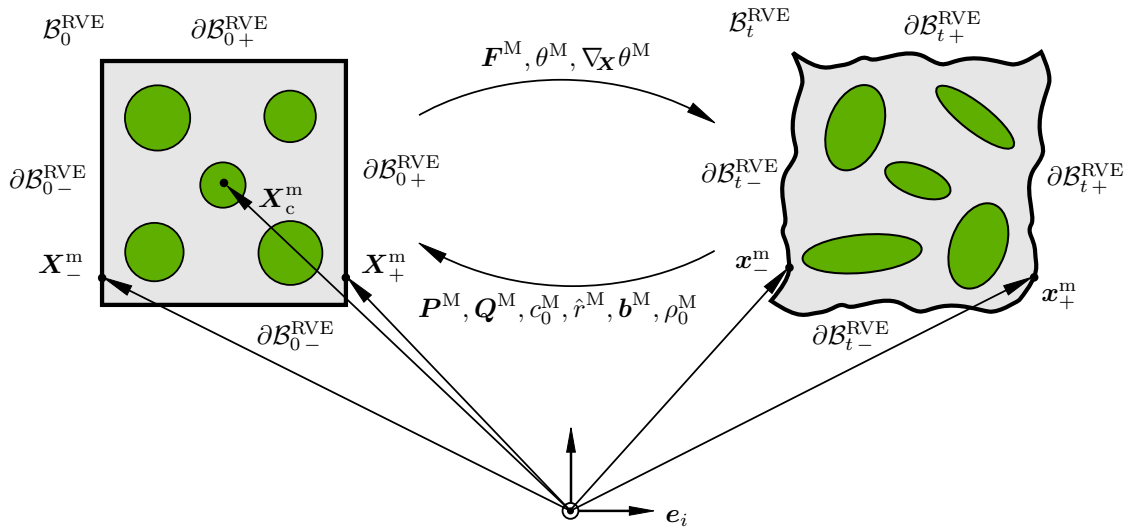

Figure 6.2: Reference configuration $\mathcal{B}_0^{\mathrm{RVE}}$ and current configuration $\mathcal{B}_t^{\mathrm{RVE}}$ of a RVE. The RVE boundary $\partial\mathcal{B}_0^{\mathrm{RVE}}$ ($\partial\mathcal{B}_t^{\mathrm{RVE}}$) is decomposed into a "+"-side $\partial\mathcal{B}_{0+}^{\mathrm{RVE}}$ ($\partial\mathcal{B}_{t+}^{\mathrm{RVE}}$) and a "−"-side $\partial\mathcal{B}_{0-}^{\mathrm{RVE}}$ ($\partial\mathcal{B}_{t-}^{\mathrm{RVE}}$). The geometric centre of gravity of the RVE is denoted by $\boldsymbol{X}_{\mathrm{c}}^{\mathrm{m}}$.

where subscripts "+" and "−" identify quantities related to opposing RVE boundary sections, cf. Fig. 6.2. The above periodicity constraints can be fulfilled either in a strong or in a weak sense as outlined in Section 6.2.
As discussed above, for extensive quantities, Eq. (6.12) is used in order to obtain the effective quantity. With respect to the thermo-mechanical framework considered in this work, the volume averages are

$$\rho_0^{\mathrm{M}} = \frac{1}{V^{\mathrm{RVE}}} \int\limits_{\mathcal{B}_0^{\mathrm{RVE}}} \rho_0^{\mathrm{m}} \, \mathrm{d}V \ , \tag{6.29}$$

$$\rho_0^{\mathrm{M}} \, \boldsymbol{b}^{\mathrm{M}} = \frac{1}{V^{\mathrm{RVE}}} \int\limits_{\mathcal{B}_0^{\mathrm{RVE}}} \rho_0^{\mathrm{m}} \, \boldsymbol{b}^{\mathrm{m}} \, \mathrm{d}V \ , \tag{6.30}$$

$$c_0^{\mathrm{M}} = \frac{1}{V^{\mathrm{RVE}}} \int\limits_{\mathcal{B}_0^{\mathrm{RVE}}} c_0^{\mathrm{m}} \, \mathrm{d}V = \frac{1}{V^{\mathrm{RVE}}} \int\limits_{\mathcal{B}_0^{\mathrm{RVE}}} \rho_0^{\mathrm{m}} \, c^{\mathrm{m}} \, \mathrm{d}V \ , \tag{6.31}$$

$$\rho_0^{\mathrm{M}} \, \hat{r}^{\mathrm{M}} = \frac{1}{V^{\mathrm{RVE}}} \int\limits_{\mathcal{B}_0^{\mathrm{RVE}}} \rho_0^{\mathrm{m}} \, \hat{r}^{\mathrm{m}} \, \mathrm{d}V \ . \tag{6.32}$$

In Section 6.2, the discretisation of the framework by means of a thermo-mechanical finite element formulation is summarised including aspects of implementation of weak periodic boundary conditions for thermo-mechanically coupled problems.

6.1.3 A thermo-viscoplastic constitutive model for large deformations

In this work, a phenomenological thermo-viscoplastic material model, [25], for large deformations is derived as the straightforward extension of the model already introduced for small deformations in Chapter 5 and applied for the simulations in Section 6.3. These constitutive relations are on the one hand directly applied at the macro-scale, cf. the modelling of the steel substrate in Section 6.3.3, and on the other hand also applied for different meso-scale constituents. In order to simplify notation, the superscripts "m" and "M" shall be omitted in this subsection.

We assume the multiplicative decomposition of the deformation gradient

$$\boldsymbol{F} = \boldsymbol{F}_{\mathrm{e}} \cdot \boldsymbol{F}_{\mathrm{p}} \ , \tag{6.33}$$

into an elastic $\boldsymbol{F}_{\mathrm{e}}$ and a plastic $\boldsymbol{F}_{\mathrm{p}}$ part, [161, 162]. The underlying Helmholtz free energy density is additively decomposed into an elastic and a plastic part

$$\Psi = \Psi_{\mathrm{e}}(\boldsymbol{F}_{\mathrm{e}}, \theta) + \Psi_{\mathrm{p}}(k, \theta) \ . \tag{6.34}$$

The elastic part of the Helmholtz energy density is specified by

$$\begin{aligned} \Psi_{\mathrm{e}}(\boldsymbol{F}_{\mathrm{e}}, \theta) = \frac{1}{2}\,\mu \left[\ \mathrm{tr}(\overline{\boldsymbol{C}}_{\mathrm{e}}) - 3 \ \right] + \frac{1}{2}\,K \left[\frac{1}{2} \left[\ {J_{\mathrm{e}}}^2 - 1 \ \right] - \ln\left(J_{\mathrm{e}}\right) \ \right] \\ - \frac{3\,\alpha_0\,K}{2} \left[\ \theta - \theta_0 \ \right] \left[\ J_{\mathrm{e}} - \frac{1}{J_{\mathrm{e}}} \ \right] + c_0 \left[\ \left[\ \theta - \theta_0 \ \right] - \theta \ \ln\left(\frac{\theta}{\theta_0}\right) \ \right] , \end{aligned} \tag{6.35}$$

where μ is the shear modulus, K is the bulk modulus, $J_{\mathrm{e}} = \det(\boldsymbol{F}_{\mathrm{e}})$ is the determinant of $\boldsymbol{F}_{\mathrm{e}}$, $\overline{\boldsymbol{C}}_{\mathrm{e}} = J_{\mathrm{e}}^{-2/3}\,\boldsymbol{C}_{\mathrm{e}}$ is the isochoric part of the elastic right Cauchy-Green deformation tensor $\boldsymbol{C}_{\mathrm{e}} = \boldsymbol{F}_{\mathrm{e}}^{\mathrm{t}} \cdot \boldsymbol{F}_{\mathrm{e}}$, α_0 is the thermal expansion coefficient and $\theta_0 > 0$ is the reference temperature. The plastic part of the Helmholtz free energy density is determined by

$$\Psi_{\mathrm{p}}(k, \theta) = x\,\frac{1}{2}\,h(\theta)\,k^2 + \left[\ 1 - x \ \right] \left[\ y_\infty(\theta) - y_0(\theta) \ \right] \left[\ k + k_0 \ \exp\left(-\frac{k}{k_0}\right) \ \right] , \tag{6.36}$$

where k is a proportional hardening internal variable, k_0 represents an exponential saturation coefficient and where $x \in [\,0, 1\,]$ is a parameter in order to interpolate between linear and saturation type hardening. Furthermore, the temperature dependent initial

yield stress $y_0(\theta)$, the temperature dependent saturation yield stress $y_\infty(\theta)$ and the temperature dependent linear hardening modulus $h(\theta)$ are defined by

$$y_0(\theta) = a_{y0} \left[\arctan\left(-\frac{\theta - b_{y0}}{c_{y0}} \right) + d_{y0} \right] , \tag{6.37}$$

$$y_\infty(\theta) = a_{y\infty} \left[\arctan\left(-\frac{\theta - b_{y\infty}}{c_{y\infty}} \right) + d_{y\infty} \right] , \tag{6.38}$$

$$h(\theta) = a_h \left[\arctan\left(-\frac{\theta - b_h}{c_h} \right) + d_h \right] . \tag{6.39}$$

The governing quantities of the thermo-mechanical deformation state are the deformation gradient $\boldsymbol{F}$, the temperature θ as well as the temperature gradient $\nabla_{\boldsymbol{X}}\theta$. In addition, Eqs. (6.35) and (6.36) depend on internal variables which are introduced as $\{\boldsymbol{F}_\mathrm{p}, k\}$. Without further specifying the respective contributions to the dissipation inequality, we adopt the common framework of rational mechanics. Within this framework, the quantities driving plastic evolution are the Mandel stress tensor

$$\begin{aligned} \boldsymbol{M} &= \boldsymbol{F}_\mathrm{e}^\mathrm{t} \cdot \frac{\partial \Psi}{\partial \boldsymbol{F}_\mathrm{e}} = \boldsymbol{F}_\mathrm{e}^\mathrm{t} \cdot \boldsymbol{P} \cdot \boldsymbol{F}_\mathrm{p}^\mathrm{t} \\ &= \mu \left[\overline{\boldsymbol{C}}_\mathrm{e} - \frac{1}{3}\, \mathrm{tr}(\overline{\boldsymbol{C}}_\mathrm{e})\, \boldsymbol{I} \right] + \frac{1}{2} K \left[J_\mathrm{e}^2 - 1 \right] \boldsymbol{I} - \frac{3\,\alpha_0\, K}{2} \left[\theta - \theta_0 \right] \left[J_\mathrm{e} - J_\mathrm{e}^{-1} \right] \boldsymbol{I} , \end{aligned} \tag{6.40}$$

with its deviatoric part

$$\boldsymbol{M}_\mathrm{dev} = \mu \left[\overline{\boldsymbol{C}}_\mathrm{e} - \frac{1}{3}\, \mathrm{tr}(\overline{\boldsymbol{C}}_\mathrm{e})\, \boldsymbol{I} \right] , \tag{6.41}$$

as well as a stress like quantity driving proportional hardening, i.e.

$$\kappa = -\frac{\partial \Psi}{\partial k} = -x\, h(\theta)\, k - \left[1 - x \right] \left[y_\infty(\theta) - y_0(\theta) \right] \left[1 - \exp\left(-\frac{k}{k_0} \right) \right] . \tag{6.42}$$

In order to decide whether a state of deformation is either thermo-elastic oder thermo-plastic, a von Mises type yield function

$$\Phi = \| \boldsymbol{M}_\mathrm{dev} \| - \left[y_0(\theta) - \kappa(k) \right] , \tag{6.43}$$

is applied. If plastic loading occurs, the associated evolution equations

$$\boldsymbol{L}_{\mathrm{p}} = \dot{\lambda}\,\frac{\partial \Phi}{\partial \boldsymbol{M}} = \dot{\boldsymbol{F}}_{\mathrm{p}} \cdot \boldsymbol{F}_{\mathrm{p}}^{-1} = \dot{\lambda}\,\frac{\boldsymbol{M}_{\mathrm{dev}}}{\|\boldsymbol{M}_{\mathrm{dev}}\|}\;, \tag{6.44}$$

$$\dot{k} = \dot{\lambda}\,\frac{\partial \Phi}{\partial \kappa} = \dot{\lambda}\;, \tag{6.45}$$

are evaluated with $\dot{\lambda}$ the multiplier related to the Karush-Kuhn-Tucker conditions

$$\dot{\lambda} \geq 0\;, \quad \Phi \leq 0\;, \quad \dot{\lambda}\,\Phi = 0 \quad \text{together with} \quad \dot{\lambda}\,\dot{\Phi} = 0\;. \tag{6.46}$$

As this work proceeds, the yield function, Eq. (6.43), is enriched by a viscous ansatz following Hohenemser and Prager [80] which results in

$$\widetilde{\Phi} = \left\langle\, \|\boldsymbol{M}_{\mathrm{dev}}\| - \left[\, y_0(\theta) - \kappa(k,\theta) \,\right] \right\rangle - 2\,\eta\,\dot{\lambda}\;, \tag{6.47}$$

where η is a relaxation-type constant.

Assuming that admissible values for $\boldsymbol{F}_{\mathrm{p}}$ and k are found for a given state of deformation, the constitutive relation for the Piola stress tensor $\boldsymbol{P}$ is obtained as

$$\begin{aligned}
\boldsymbol{P} &= \frac{\partial \Psi}{\partial \boldsymbol{F}_{\mathrm{e}}} \cdot \boldsymbol{F}_{\mathrm{p}}^{-\mathrm{t}} \\
&= G\,J^{-2/3}\,\boldsymbol{F} \cdot \boldsymbol{C}_{\mathrm{p}}^{-1} + \left[-\frac{1}{3}\,G\,J^{-2/3}\,\boldsymbol{C} : \boldsymbol{C}_{\mathrm{p}}^{-1} + \frac{1}{2}\,K\,\left[\, J^2 - 1 \,\right] \right] \boldsymbol{F}^{-\mathrm{t}} \\
&\quad - \frac{3\,\alpha_0\,K}{2}\,\left[\, \theta - \theta_0 \,\right]\,\left[\, J + J^{-1} \,\right]\,\boldsymbol{F}^{-\mathrm{t}}\;,
\end{aligned} \tag{6.48}$$

and the specification of the internal heat source results in

$$\begin{aligned}\hat{r}_0 = \rho_0\,\hat{r} = \rho_0\,r + \theta\,\frac{\partial \boldsymbol{P}}{\partial \theta} : \dot{\boldsymbol{F}} + \left[\kappa - \theta\,\frac{\partial \kappa}{\partial \theta}\right]\dot{k}\\ = \theta\,\frac{\partial \boldsymbol{P}}{\partial \theta} : \dot{\boldsymbol{F}} + \left[-\frac{\partial \Psi}{\partial k} + \theta\,\frac{\partial^2 \Psi}{\partial k \partial \theta}\right]\dot{k} + \left[-\frac{\partial \Psi}{\partial \boldsymbol{F}_\mathrm{p}} + \theta\,\frac{\partial^2 \Psi}{\partial \boldsymbol{F}_\mathrm{p} \partial \theta}\right] : \dot{\boldsymbol{F}}_\mathrm{p}\\ = -\frac{3\,\alpha_0\,K\,\theta}{2}\,\left[1 + J^{-2}\right]\,\dot{J} + \left[\kappa - \theta\,\frac{\partial \kappa}{\partial \theta}\right]\,\dot{\lambda}\\ + G\,J^{-2/3}\,\left[\boldsymbol{F}_\mathrm{p}^{-\mathrm{t}} \cdot \boldsymbol{C} \cdot \boldsymbol{C}_\mathrm{p}^{-1}\right] : \dot{\boldsymbol{F}}_\mathrm{p}\,,\end{aligned} \tag{6.49}$$

wherein $r = 0$ is assumed. In the above equations, the isochoric characteristics of the plasticity model are used in such a way that $J = J_\mathrm{e}$, i.e. $\det(\boldsymbol{F}_\mathrm{p}) = J_\mathrm{p} = 1$. Furthermore, $\boldsymbol{C}_\mathrm{p} = \boldsymbol{F}_\mathrm{p}^\mathrm{t} \cdot \boldsymbol{F}_\mathrm{p}$ is introduced to simplify the above expressions. The algorithmic treatment of the above equations by means of a return mapping algorithm is carried out in complete analogy to Chapter 5 and [47] as this chapter proceeds.

The constitutive relation considered for the heat flux is Fourier's law of heat conduction in referential format

$$\boldsymbol{Q} = -\boldsymbol{\Lambda}_0 \cdot \nabla_{\boldsymbol{X}}\theta\,, \tag{6.50}$$

where $\boldsymbol{\Lambda}_0$ is the positive-semidefinite heat conduction tensor which is assumed to be isotropic, $\boldsymbol{\Lambda}_0 = \Lambda_0\,\boldsymbol{I}$, and does therefore only depend on the scalar heat conduction coefficient Λ_0. Here and in the following, $\boldsymbol{I}$ represents the second order identity tensor.

Remark 6.1.1 (Thermal softening) *It should be remarked that no additional regularisation techniques with regard to thermal softening are considered within the present framework. In case of considerably small heat flux contributions, this consequently leads to localisation analogous to non-regularised damage formulations. This may occur, e.g., for very high deformation rates when heat conduction is very slow compared to heat generation. Within the numerical examples considered later on in this chapter, however, such localisation phenomena turn out not to be problematic.*

6.2 Multi-scale finite element framework

So far, the continuum mechanical background of the multi-scale framework, together with the related first-order homogenisation scheme, as well as thermo-mechanically coupled constitutive relations have been presented. Within this chapter, the resulting equations are to be solved by means of the finite element method. For doing so, in Section 6.2.1, the balance equations from Section 6.1.1 are transformed to be applicable for the finite

element method. This finite element framework is subsequently applied at two separated length scales. The specification of the equations related to the respective scales are summarised in Section 6.2.2. Finally, the implementation of the meso-scale boundary conditions with an emphasis on weak meso-scale periodicity is commented on in Section 6.2.3.

6.2.1 Thermo-mechanical finite element framework

For the solution procedure, the local strong forms Eqs. (6.1) and (6.2) and Eqs. (6.7) and (6.8) are multiplied by admissible test functions $\delta\boldsymbol{\varphi}$ and $\delta\theta$ in a standard manner and subsequently integrated over the volume of the body $\mathcal{B}_0$ with its boundary $\partial\mathcal{B}_0$. With the help of the divergence theorem, Eqs. (6.1) and (6.2) read

$$0 = \int_{\mathcal{B}_0} \rho_0\, \delta\boldsymbol{\varphi} \cdot \ddot{\boldsymbol{\varphi}}\, \mathrm{d}V + \int_{\mathcal{B}_0} \nabla_{\boldsymbol{X}} \delta\boldsymbol{\varphi} : \boldsymbol{P}\, \mathrm{d}V - \int_{\mathcal{B}_0} \rho_0\, \delta\boldsymbol{\varphi} \cdot \boldsymbol{b}\, \mathrm{d}V - \int_{\partial\mathcal{B}_0^{\boldsymbol{t}}} \delta\boldsymbol{\varphi} \cdot \bar{\boldsymbol{t}}_0\, \mathrm{d}A\,, \tag{6.51}$$

$$0 = \int_{\mathcal{B}_0} c_0\, \delta\theta\, \dot{\theta}\, \mathrm{d}V + \int_{\mathcal{B}_0} -\nabla_{\boldsymbol{X}} \delta\theta \cdot \boldsymbol{Q}\, \mathrm{d}V - \int_{\mathcal{B}_0} \delta\theta\, \hat{r}_0\, \mathrm{d}V - \int_{\partial\mathcal{B}_0^{Q}} \delta\theta\, \bar{Q}\, \mathrm{d}A\,. \tag{6.52}$$

The above equations may be rewritten as global residual relations

$$\mathrm{w}^{\boldsymbol{\varphi}}(\delta\boldsymbol{\varphi}; \boldsymbol{\varphi}, \theta) = \mathrm{w}^{\boldsymbol{\varphi}}_{\mathrm{dyn}} + \mathrm{w}^{\boldsymbol{\varphi}}_{\mathrm{int}} - \mathrm{w}^{\boldsymbol{\varphi}}_{\mathrm{vol}} - \mathrm{w}^{\boldsymbol{\varphi}}_{\mathrm{sur}} = 0\,, \tag{6.53}$$

$$\mathrm{w}^{\theta}(\delta\theta, \nabla_{\boldsymbol{X}}\delta\theta; \boldsymbol{\varphi}, \theta, \nabla_{\boldsymbol{X}}\theta) = \mathrm{w}^{\theta}_{\mathrm{dyn}} + \mathrm{w}^{\theta}_{\mathrm{int}} - \mathrm{w}^{\theta}_{\mathrm{vol}} - \mathrm{w}^{\theta}_{\mathrm{sur}} = 0\,, \tag{6.54}$$

where the respective contributions are the dynamic contributions with the subscript "dyn"

$$\mathrm{w}^{\boldsymbol{\varphi}}_{\mathrm{dyn}} = \int_{\mathcal{B}_0} \rho_0\, \delta\boldsymbol{\varphi} \cdot \ddot{\boldsymbol{\varphi}}\, \mathrm{d}V\,, \qquad \mathrm{w}^{\theta}_{\mathrm{dyn}} = \int_{\mathcal{B}_0} c_0\, \delta\theta\, \dot{\theta}\, \mathrm{d}V\,, \tag{6.55}$$

the internal contributions denoted by the subscript "int"

$$\mathrm{w}^{\boldsymbol{\varphi}}_{\mathrm{int}} = \int_{\mathcal{B}_0} \nabla_{\boldsymbol{X}} \delta\boldsymbol{\varphi} : \boldsymbol{P}\, \mathrm{d}V\,, \qquad \mathrm{w}^{\theta}_{\mathrm{int}} = \int_{\mathcal{B}_0} -\nabla_{\boldsymbol{X}} \delta\theta \cdot \boldsymbol{Q}\, \mathrm{d}V\,, \tag{6.56}$$

the volumetric contributions denoted by the subscript "vol"

$$\mathrm{w}^{\boldsymbol{\varphi}}_{\mathrm{vol}} = \int_{\mathcal{B}_0} \rho_0\, \delta\boldsymbol{\varphi} \cdot \boldsymbol{b}\, \mathrm{d}V\,, \qquad \mathrm{w}^{\theta}_{\mathrm{vol}} = \int_{\mathcal{B}_0} \delta\theta\, \hat{r}_0\, \mathrm{d}V\,, \tag{6.57}$$

and the surface contributions are indicated by the subscript "sur"

$$\mathrm{w}^{\boldsymbol{\varphi}}_{\mathrm{sur}} = \int\limits_{\partial\mathcal{B}^{\boldsymbol{t}}_0} \delta\boldsymbol{\varphi} \cdot \bar{\boldsymbol{t}}_0 \,\mathrm{d}A \;, \qquad \mathrm{w}^{\theta}_{\mathrm{sur}} = \int\limits_{\partial\mathcal{B}^{Q}_0} \delta\theta\, \bar{Q} \,\mathrm{d}A \;. \tag{6.58}$$

Since these equations are suitable for the solution by means of the finite element method, the body $\mathcal{B}_0$ is approximated by a finite number of n_{el} volume elements as well as $n^{\boldsymbol{t}}_{\mathrm{sel}}$ and n^{Q}_{sel} surface elements in order to capture Robin boundary conditions for the respective fields. Eventually, the integral terms in Eqs. (6.53) and (6.54) are approximated by the sums over all volume element integrals as well as all respective surface element integrals

$$\mathrm{w}^{\boldsymbol{\varphi}} \approx \mathrm{w}^{\boldsymbol{\varphi}\,h} = \sum_{e=1}^{n_{\mathrm{el}}} \Big[\mathrm{w}^{\boldsymbol{\varphi}\,e}_{\mathrm{dyn}} + \mathrm{w}^{\boldsymbol{\varphi}\,e}_{\mathrm{int}} - \mathrm{w}^{\boldsymbol{\varphi}\,e}_{\mathrm{vol}} \Big] + \sum_{i=1}^{n^{\boldsymbol{t}}_{\mathrm{sel}}} \Big[- \mathrm{w}^{\boldsymbol{\varphi}\,i}_{\mathrm{sur}} \Big] = 0 \;, \tag{6.59}$$

$$\mathrm{w}^{\theta} \approx \mathrm{w}^{\theta\,h} = \sum_{e=1}^{n_{\mathrm{el}}} \Big[\mathrm{w}^{\theta\,e}_{\mathrm{dyn}} + \mathrm{w}^{\theta\,e}_{\mathrm{int}} - \mathrm{w}^{\theta\,e}_{\mathrm{vol}} \Big] + \sum_{j=1}^{n^{Q}_{\mathrm{sel}}} \Big[- \mathrm{w}^{\theta\,j}_{\mathrm{sur}} \Big] = 0 \;. \tag{6.60}$$

The above expressions are spatially discretised by iso-parametric finite elements, cf. [191], where the placements $\boldsymbol{X}$ are interpolated by the same kind of shape functions as the field variables, $\boldsymbol{\varphi}$ and θ, and the respective test functions, $\delta\boldsymbol{\varphi}$ and $\delta\theta$. Consequently, this chapter is limited to the same shape functions $N^A(\boldsymbol{\xi})$ for all fields where $\boldsymbol{\xi}$ are referred to as the natural coordinates of the chosen element, [83], and $A = 1 \ldots n_{\mathrm{en}}$ are the element nodes, with n_{en} representing the number of nodes of the respective element. Each discrete node point of the finite element discretisation stores the field variable value as well as the test function value. Hence, the global vector of all field variables is introduced as

$$\underline{\mathbf{d}} = \big[\, \boldsymbol{\varphi}^{\mathrm{t}}_1 \quad \theta_1 \quad \boldsymbol{\varphi}^{\mathrm{t}}_2 \quad \theta_2 \quad \ldots \quad \boldsymbol{\varphi}^{\mathrm{t}}_{n_{\mathrm{np}}} \quad \theta_{n_{\mathrm{np}}} \,\big]^{\mathrm{t}} \;, \tag{6.61}$$

and the global vector of test functions is introduced in analogy as

$$\delta\underline{\mathbf{d}} = \big[\, \delta\boldsymbol{\varphi}^{\mathrm{t}}_1 \quad \delta\theta_1 \quad \delta\boldsymbol{\varphi}^{\mathrm{t}}_2 \quad \delta\theta_2 \quad \ldots \quad \delta\boldsymbol{\varphi}^{\mathrm{t}}_{n_{\mathrm{np}}} \quad \delta\theta_{n_{\mathrm{np}}} \,\big]^{\mathrm{t}} \;. \tag{6.62}$$

The global test function vector $\delta\underline{\mathbf{d}}$ is connected to the local element values by means of appropriate Boolean matrices and vectors. The definition of an assembly operator $\mathbf{A}$, cf. [101], in combination with the arbitrariness of the admissible test functions yields a semi-discrete residual system of nonlinear equations

$$\underline{\mathbf{r}}(\underline{\mathbf{d}}, \dot{\underline{\mathbf{d}}}, \ddot{\underline{\mathbf{d}}}) = \underline{\mathbf{f}}_{\mathrm{dyn}} + \underline{\mathbf{f}}_{\mathrm{int}} - \underline{\mathbf{f}}_{\mathrm{vol}} - \underline{\mathbf{f}}_{\mathrm{sur}} = \underline{\mathbf{0}} \;, \tag{6.63}$$

with the element related contributions

$$\begin{aligned} \boldsymbol{f}^{\boldsymbol{\varphi}\,e\,A}_{\text{dyn}} &= \int_{\mathcal{B}^e_0} \rho_0\, N^A\, \ddot{\boldsymbol{\varphi}}\, \mathrm{d}V\ , \qquad \boldsymbol{f}^{\boldsymbol{\varphi}\,e\,A}_{\text{int}} = \int_{\mathcal{B}^e_0} \boldsymbol{P}\cdot\nabla_{\boldsymbol{X}} N^A\, \mathrm{d}V\ , \\ \boldsymbol{f}^{\boldsymbol{\varphi}\,e\,A}_{\text{vol}} &= \int_{\mathcal{B}^e_0} \rho_0\, N^A\, \boldsymbol{b}\, \mathrm{d}V\ , \qquad \boldsymbol{f}^{\boldsymbol{\varphi}\,e\,A}_{\text{sur}} = \int_{\partial\mathcal{B}^{\boldsymbol{t}\,e}_0} N^A\, \bar{\boldsymbol{t}}_0\, \mathrm{d}A\ , \end{aligned} \tag{6.64}$$

as well as

$$\begin{aligned} f^{\theta\,e\,A}_{\text{dyn}} &= \int_{\mathcal{B}^e_0} c_0\, N^A\, \dot{\theta}\, \mathrm{d}V\ , \qquad f^{\theta\,e\,A}_{\text{int}} = \int_{\mathcal{B}^e_0} -\nabla_{\boldsymbol{X}} N^A\cdot\boldsymbol{Q}\, \mathrm{d}V\ , \\ f^{\theta\,e\,A}_{\text{vol}} &= \int_{\mathcal{B}^e_0} \rho_0\, N^A\, \hat{r}\, \mathrm{d}V\ , \qquad f^{\theta\,e\,A}_{\text{sur}} = \int_{\partial\mathcal{B}^{q\,e}_t} -N^A\, h_{\text{c}}\, [\,\theta-\theta_\infty\,]\, \mathrm{d}a\ . \end{aligned} \tag{6.65}$$

In order to model heat transfer via the boundary, a so-called film condition is used in this work analogous to Chapter 4 – this type of boundary condition is of Robin type as discussed in Section 2.4. For modelling purposes, the scalar film condition coefficient h_{c} is introduced in the above equation wherein θ_∞ represents the environmental temperature. In contrast to all other integral terms, the surface integration is performed within the current configuration, cf. [135] for further details.

Residual Eq. (6.63) depends on the field variables $\underline{\mathbf{d}}$ themselves as well as on the time derivatives $\dot{\underline{\mathbf{d}}}$ and $\ddot{\underline{\mathbf{d}}}$. In the following, mechanical inertia terms, mechanical volume forces as well as mechanical Robin boundary conditions are neglected. Therefore, the semi-discrete residual reduces to

$$\underline{\mathbf{r}}(\underline{\mathbf{d}},\dot{\underline{\mathbf{d}}}) = \underline{\mathbf{f}}_{\text{dyn}}(\underline{\mathbf{d}},\dot{\underline{\mathbf{d}}}) + \underline{\mathbf{f}}_{\text{int}}(\underline{\mathbf{d}},\dot{\underline{\mathbf{d}}}) - \underline{\mathbf{f}}_{\text{vol}}(\underline{\mathbf{d}},\dot{\underline{\mathbf{d}}}) - \underline{\mathbf{f}}_{\text{sur}}(\underline{\mathbf{d}}) = \underline{\mathbf{0}}\ , \tag{6.66}$$

and is subsequently discretised in time by means of the Backward Euler method

$$\dot{\underline{\mathbf{d}}}_{n+1} \approx \frac{\underline{\mathbf{d}}_{n+1} - \underline{\mathbf{d}}_n}{\Delta t}\ , \tag{6.67}$$

where $\Delta t = t_{n+1} - t_n > 0$ is the time increment. The fully discretised residual equation is

$$\underline{\mathbf{r}}(\underline{\mathbf{d}}_{n+1},\underline{\mathbf{d}}_n) = \underline{\mathbf{f}}_{\text{dyn}}(\underline{\mathbf{d}}_{n+1},\underline{\mathbf{d}}_n) + \underline{\mathbf{f}}_{\text{int}}(\underline{\mathbf{d}}_{n+1},\underline{\mathbf{d}}_n) - \underline{\mathbf{f}}_{\text{vol}}(\underline{\mathbf{d}}_{n+1},\underline{\mathbf{d}}_n) - \underline{\mathbf{f}}_{\text{sur}}(\underline{\mathbf{d}}_{n+1}) = \underline{\mathbf{0}}\ . \tag{6.68}$$

The above system of non-linear equations is solved by means of the Newton-Raphson method.

6.2.2 Thermo-mechanical FEM at two separated length scales

The thermo-mechanical finite element framework which is summarised in the previous section is applied on two scales. On the macro-scale, Eqs. (6.51) and (6.52) read

$$\begin{aligned} 0 = &\int_{\mathcal{B}_0} \rho_0^{\mathrm{M}}\, \delta\boldsymbol{\varphi}^{\mathrm{M}} \cdot \ddot{\boldsymbol{\varphi}}^{\mathrm{M}}\, \mathrm{d}V + \int_{\mathcal{B}_0} \nabla_{\boldsymbol{X}} \delta\boldsymbol{\varphi}^{\mathrm{M}} : \boldsymbol{P}^{\mathrm{M}}\, \mathrm{d}V \\ &- \int_{\mathcal{B}_0} \rho_0^{\mathrm{M}}\, \delta\boldsymbol{\varphi}^{\mathrm{M}} \cdot \boldsymbol{b}^{\mathrm{M}}\, \mathrm{d}V - \int_{\partial\mathcal{B}_0^{\boldsymbol{t}}} \delta\boldsymbol{\varphi}^{\mathrm{M}} \cdot \bar{\boldsymbol{t}}_0^{\mathrm{M}}\, \mathrm{d}A\,, \end{aligned} \tag{6.69}$$

$$\begin{aligned} 0 = &\int_{\mathcal{B}_0} c_0^{\mathrm{M}}\, \delta\theta^{\mathrm{M}}\, \dot{\theta}^{\mathrm{M}}\, \mathrm{d}V + \int_{\mathcal{B}_0} -\nabla_{\boldsymbol{X}} \delta\theta^{\mathrm{M}} \cdot \boldsymbol{Q}^{\mathrm{M}}\, \mathrm{d}V \\ &- \int_{\mathcal{B}_0} \delta\theta^{\mathrm{M}}\, \hat{r}_0^{\mathrm{M}}\, \mathrm{d}V - \int_{\partial\mathcal{B}_t^{q}} \delta\theta^{\mathrm{M}}\, \bar{q}^{\mathrm{M}}\, \mathrm{d}a\,, \end{aligned} \tag{6.70}$$

cf. Eqs. (6.1) and (6.2), where superscript "M" denotes macro-scale quantities. Hence, the residual system of non-linear equations, Eq. (6.68), turns into

$$\underline{\mathbf{r}}^{\mathrm{M}}(\underline{\mathbf{d}}_{n+1}^{\mathrm{M}}, \underline{\mathbf{d}}_n^{\mathrm{M}}) = \underline{\mathbf{f}}_{\mathrm{dyn}}^{\mathrm{M}}(\underline{\mathbf{d}}_{n+1}^{\mathrm{M}}, \underline{\mathbf{d}}_n^{\mathrm{M}}) + \underline{\mathbf{f}}_{\mathrm{int}}^{\mathrm{M}}(\underline{\mathbf{d}}_{n+1}^{\mathrm{M}}, \underline{\mathbf{d}}_n^{\mathrm{M}}) - \underline{\mathbf{f}}_{\mathrm{vol}}^{\mathrm{M}}(\underline{\mathbf{d}}_{n+1}^{\mathrm{M}}, \underline{\mathbf{d}}_n^{\mathrm{M}}) - \underline{\mathbf{f}}_{\mathrm{sur}}^{\mathrm{M}}(\underline{\mathbf{d}}_{n+1}^{\mathrm{M}}) = \underline{\mathbf{0}}\,. \tag{6.71}$$

At the meso-scale, dynamic and volume contributions are neglected and therefore Eqs. (6.51) and (6.52) formally reduce to

$$0 = \int_{\mathcal{B}_0^{\mathrm{RVE}}} \nabla_{\boldsymbol{X}} \delta\boldsymbol{\varphi}^{\mathrm{m}} : \boldsymbol{P}^{\mathrm{m}}\, \mathrm{d}V - \int_{\partial\mathcal{B}_0^{\mathrm{RVE}\,\boldsymbol{t}}} \delta\boldsymbol{\varphi}^{\mathrm{m}} \cdot \bar{\boldsymbol{t}}_0^{\mathrm{m}}\, \mathrm{d}A\,, \tag{6.72}$$

$$0 = \int_{\mathcal{B}_0^{\mathrm{RVE}}} -\nabla_{\boldsymbol{X}} \delta\theta^{\mathrm{m}} \cdot \boldsymbol{Q}^{\mathrm{m}}\, \mathrm{d}V - \int_{\partial\mathcal{B}_0^{\mathrm{RVE}\,Q}} \delta\theta^{\mathrm{m}}\, \bar{Q}^{\mathrm{m}}\, \mathrm{d}A\,, \tag{6.73}$$

cf. Eqs. (6.7) and (6.8), where the superscript "m" indicates meso-scale quantities. The residual system of equations therefore reduces to

$$\underline{\mathbf{r}}^{\mathrm{m}}(\underline{\mathbf{d}}_{n+1}^{\mathrm{m}}, \underline{\mathbf{d}}_n^{\mathrm{m}}; \boldsymbol{F}^{\mathrm{M}}, \theta^{\mathrm{M}}, \nabla_{\boldsymbol{X}}\theta^{\mathrm{M}}) = \underline{\mathbf{f}}_{\mathrm{int}}^{\mathrm{m}}(\underline{\mathbf{d}}_{n+1}^{\mathrm{m}}, \underline{\mathbf{d}}_n^{\mathrm{m}}) - \underline{\mathbf{f}}_{\mathrm{sur}}^{\mathrm{m}}(\underline{\mathbf{d}}_{n+1}^{\mathrm{m}}; \boldsymbol{F}^{\mathrm{M}}, \theta^{\mathrm{M}}, \nabla_{\boldsymbol{X}}\theta^{\mathrm{M}}) = \underline{\mathbf{0}}\,, \tag{6.74}$$

and is also likewise solved by means of an iterative Newton-Raphson scheme. In the above equation, the dependency of the meso-scale surface term $\underline{\mathbf{f}}_{\mathrm{sur}}^{\mathrm{m}}$ on the macro-scale deformation gradient $\boldsymbol{F}^{\mathrm{M}}$, the macro-scale temperature θ^{M} as well as on the macro-scale

temperature gradient $\nabla_{\boldsymbol{X}}\theta^{\mathrm{M}}$ shall indicate the boundary conditions which are essential for the scale bridging within the presented homogenisation framework. The consistent linearisation of the two-scale framework is carried out by analogy with the presentation in [157] and Chapter 5.

Remark 6.2.1 (Inertia terms) *Note that general homogenisation schemes for dynamical problems need very careful treatment. First order homogenisation frameworks are valid for dynamic processes only when the size of the RVE is sufficiently small in comparison to the wavelength of the dynamical loading. As this chapter proceeds, however, inertia contributions (as well as mechanical volume forces) shall be neglected.*

6.2.3 Algorithmic treatment of mesoscale boundary conditions

In this work, established boundary conditions are compared against weak periodic boundary conditions. The displacement type boundary conditions, cf. Eqs. (6.23) and (6.24), are abbreviated with "LN" and the strongly enforced periodic boundary conditions, cf. Eqs. (6.27) and (6.28), are denoted with "PR". The implementation follows the work by Sengupta et al. [157], whereby the linear constraints regarding the PR boundary conditions are based on the work of Kouznetsova et al. [98]. The third type of established boundary conditions are the uniform flux boundary conditions, cf. Eqs. (6.25) and (6.26), which are denoted "UF" in the following. Algorithmically, these boundary conditions are treated by means of the Lagrange multiplier method according to the work of Miehe and Koch [115], whereby the additional term given by Eq. (6.26) is considered as additional constraint equation regarding the thermal part of the coupled problem at hand. In the following, the algorithmic treatment of weak meso-periodic boundary conditions is outlined as the thermo-mechanical extension of the idea of mechanical weak meso-periodic boundary conditions according to Larsson et al. [104]. This type of boundary conditions will be abbreviated by "WK" followed by a characteristic number clarified in what follows.

Throughout the literature, PR boundary conditions are often denoted as the most natural choice in Hill-Mandel-type-condition based homogenisation frameworks. Following the mentioned suggestion made in Sengupta et al. [157], only 16 degrees of freedom – namely the degrees of freedom of four edge nodes each of which possesses three displacements and one temperature degrees of freedom – have to be prescribed together with linear constraints formulated in terms of the meso-scale degrees of freedom $\underline{\mathbf{d}}^{\mathrm{m}}_{n+1}$, the macro-scale temperature θ^{M} as well as the macro-scale gradients $\boldsymbol{F}^{\mathrm{M}}$ and $\nabla_{\boldsymbol{X}}\theta^{\mathrm{M}}$ in order to define the whole meso-scale problem. Apparently, however, the obvious drawback of the strong enforcement of meso-scale periodicity is the requirement of perfectly periodic meshes with distinct node pairs on the "−"-sides and "+"-sides of the considered RVE discretisation. To overcome the necessity of periodic meshes, the constraints given by Eqs. (6.21) and (6.22) can be enforced weakly as proposed by Larsson et al. [104] for purely mechanical problems or by Sandström et al. [149] for diffusion problems.

With respect to the underlying thermo-mechanically coupled problem considered in this work, Eq. (6.21) is reformulated in terms of displacements and, subsequently, Eqs. (6.21) and (6.22) are written in residual form

$$\mathbf{0} = \boldsymbol{u}^{\mathrm{m}}_{+} - \boldsymbol{u}^{\mathrm{m}}_{-} - \boldsymbol{H}^{\mathrm{M}} \cdot \left[\boldsymbol{X}^{\mathrm{m}}_{+} - \boldsymbol{X}^{\mathrm{m}}_{-} \right] \,, \tag{6.75}$$

$$0 = \theta^{\mathrm{m}}_{+} - \theta^{\mathrm{m}}_{-} - \nabla_{\boldsymbol{X}} \theta^{\mathrm{M}} \cdot \left[\boldsymbol{X}^{\mathrm{m}}_{+} - \boldsymbol{X}^{\mathrm{m}}_{-} \right] \,, \tag{6.76}$$

with $\boldsymbol{u}^{\mathrm{m}} = \boldsymbol{x}^{\mathrm{m}} - \boldsymbol{X}^{\mathrm{m}}$ formally denoting the displacement field and the macro-scale displacement gradient $\boldsymbol{H}^{\mathrm{M}} = \boldsymbol{F}^{\mathrm{M}} - \boldsymbol{I}$. Subsequently, these two equations are multiplied with test functions $\delta\boldsymbol{\varphi}^{\mathrm{m}}$ as well as $\delta\theta^{\mathrm{m}}$, and an integration over the "+"-boundary of the RVE is carried out, cf. Fig. 6.2 for an illustration of the partition of the RVE boundary $\partial\mathcal{B}^{\mathrm{RVE}}_{0}$ into a "+"-side $\partial\mathcal{B}^{\mathrm{RVE}}_{0+}$ as well as the corresponding "−"-side $\partial\mathcal{B}^{\mathrm{RVE}}_{0-}$. Furthermore, the displacement jump, $[\![\, \boldsymbol{u}^{\mathrm{m}} \,]\!] = \boldsymbol{u}^{\mathrm{m}}_{+} - \boldsymbol{u}^{\mathrm{m}}_{-}$, as well as the temperature jump, $[\![\, \theta^{\mathrm{m}} \,]\!] = \theta^{\mathrm{m}}_{+} - \theta^{\mathrm{m}}_{-}$, and the reference coordinate difference, $[\![\, \boldsymbol{X}^{\mathrm{m}} \,]\!] = \boldsymbol{X}^{\mathrm{m}}_{+} - \boldsymbol{X}^{\mathrm{m}}_{-}$, are introduced. Thus, the above equations transform into

$$0 = \int\limits_{\partial\mathcal{B}^{\mathrm{RVE}}_{0+}} \delta\boldsymbol{\varphi}^{\mathrm{m}} \cdot \Big[[\![\, \boldsymbol{u}^{\mathrm{m}} \,]\!] - \boldsymbol{H}^{\mathrm{M}} \cdot [\![\, \boldsymbol{X}^{\mathrm{m}} \,]\!] \Big] \, \mathrm{d}A \,, \tag{6.77}$$

$$0 = \int\limits_{\partial\mathcal{B}^{\mathrm{RVE}}_{0+}} \delta\theta \Big[[\![\, \theta^{\mathrm{m}} \,]\!] - \nabla_{\boldsymbol{X}} \theta^{\mathrm{M}} \cdot [\![\, \boldsymbol{X}^{\mathrm{m}} \,]\!] \Big] \, \mathrm{d}A \,. \tag{6.78}$$

With regard to the finite element method, the "+"-boundary of the RVE is discretised by means of n_{pel} "+"-boundary elements

$$0 = \sum_{i=1}^{n_{\mathrm{pel}}} \int\limits_{\partial\mathcal{B}^{\mathrm{RVE}\,i}_{0+}} \delta\boldsymbol{\varphi}^{\mathrm{m}} \cdot \Big[[\![\, \boldsymbol{u}^{\mathrm{m}} \,]\!] - \boldsymbol{H}^{\mathrm{M}} \cdot [\![\, \boldsymbol{X}^{\mathrm{m}} \,]\!] \Big] \, \mathrm{d}A \,, \tag{6.79}$$

$$0 = \sum_{j=1}^{n_{\mathrm{pel}}} \int\limits_{\partial\mathcal{B}^{\mathrm{RVE}\,j}_{0+}} \delta\theta^{\mathrm{m}} \Big[[\![\, \theta^{\mathrm{m}} \,]\!] - \nabla_{\boldsymbol{X}} \theta^{\mathrm{M}} \cdot [\![\, \boldsymbol{X}^{\mathrm{m}} \,]\!] \Big] \, \mathrm{d}A \,. \tag{6.80}$$

In analogy to the procedure outlined in Section 6.2.1, the test functions are element-wisely approximated by means of shape functions $N^{A}(\boldsymbol{\xi})$. Application of the assembly operator for the "+"-boundary elements yields the vector valued constraints

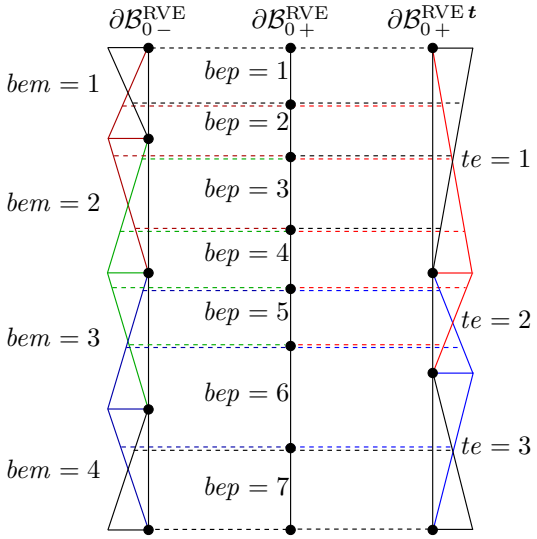

Figure 6.3: Indicated differing discretisations of the RVE "+"- and "−"-sides and the "reduced flux boundary". The interpolation is carried out by means of Lagrange polynomials on the "+"-boundary on which the weak periodicity constraints are evaluated, cf. Fig. 6.2 for an illustration of the partition of the RVE boundary $\partial\mathcal{B}_0^{\mathrm{RVE}}$ into a "+"-side $\partial\mathcal{B}_{0+}^{\mathrm{RVE}}$ as well as the corresponding "−"-side $\partial\mathcal{B}_{0-}^{\mathrm{RVE}}$.

$$\underline{\mathbf{g}}^{\boldsymbol{\varphi}} = \mathop{\mathbf{A}}_{i=1}^{n_{\mathrm{pel}}} \int_{\partial\mathcal{B}_{0+}^{\mathrm{RVE}\,i}} N^A \left[[\![\boldsymbol{u}^{\mathrm{m}}]\!] - \boldsymbol{H}^{\mathrm{M}} \cdot [\![\boldsymbol{X}^{\mathrm{m}}]\!] \right] \mathrm{d}A \,, \tag{6.81}$$

$$\underline{\mathbf{g}}^{\theta} = \mathop{\mathbf{A}}_{j=1}^{n_{\mathrm{pel}}} \int_{\partial\mathcal{B}_{0+}^{\mathrm{RVE}\,j}} N^A \left[[\![\theta^{\mathrm{m}}]\!] - \nabla_{\boldsymbol{X}}\theta^{\mathrm{M}} \cdot [\![\boldsymbol{X}^{\mathrm{m}}]\!] \right] \mathrm{d}A \,. \tag{6.82}$$

The above constraint equations affect the "+"-boundary nodes as well the corresponding "−"-boundary via the jumps in the displacement and temperature fields. Hence, the vectors $\underline{\mathbf{g}}^{\boldsymbol{\varphi}}$ and $\underline{\mathbf{g}}^{\theta}$ have non-zero entries for the global equation numbers of the respective degrees of freedom in the assembled system of non-linear equations at the meso-scale, cf. Eq. (6.74). Hence, an appropriate surface force contribution $\underline{\mathbf{f}}_{\mathrm{sur}}^{\mathrm{m}}(\underline{\mathbf{d}}_{n+1}^{\mathrm{m}}; \boldsymbol{F}^{\mathrm{M}}, \theta^{\mathrm{M}}, \nabla_{\boldsymbol{X}}\theta^{\mathrm{M}})$ is desired in order to meet the constraints to obtain the effective material behaviour. The above constraints are both enforced by means of Lagrange multipliers, $\boldsymbol{\lambda}^{\boldsymbol{t}_0} \in \partial\mathcal{B}_{0+}^{\mathrm{RVE}\,\boldsymbol{t}}$ as traction like multipliers and $\boldsymbol{\lambda}^{Q} \in \partial\mathcal{B}_{0+}^{\mathrm{RVE}\,Q}$ as heat flux like multipliers such that

$$0 = \boldsymbol{\lambda}^{\boldsymbol{t}_0} \cdot \underline{\mathbf{g}}^{\boldsymbol{\varphi}} \,, \tag{6.83}$$

$$0 = \boldsymbol{\lambda}^{Q} \cdot \underline{\mathbf{g}}^{\theta} \,, \tag{6.84}$$

must hold. The two additionally introduced boundaries, $\partial\mathcal{B}_{0+}^{\mathrm{RVE}\,\boldsymbol{t}}$ and $\partial\mathcal{B}_{0+}^{\mathrm{RVE}\,Q}$, are discrete flux boundaries and represent the (reduced) space of the constraints in analogy to the so-called "reduced traction meshes" in Larsson et al. [104] – in the context of the present work, this terminology might be extended to "reduced flux meshes". An immediate consequence of a reduced space of unknown flux variables related to unknown displacements or temperature is that Eqs. (6.83) and (6.84) are not valid without further assumptions, since vectors $\boldsymbol{\lambda}^{\boldsymbol{t}_0}$ and $\underline{\mathbf{g}}^{\boldsymbol{\varphi}}$ are no longer of the same dimension. Analogously, vectors $\boldsymbol{\lambda}^{Q}$ and $\underline{\mathbf{g}}^{\theta}$ are also of different dimension in the case of reduced boundary heat fluxes.

One possibility to link the constraint space to the degrees of freedom space is to interpolate the effect of one constraint node on a degree of freedom node by means of a Lagrange polynomial similar to the interpolation from node points to integration points in finite elements as visualised in Fig. 6.3. The most simple flux boundary represents constant fluxes throughout the whole boundary representation which is equivalent to UF boundary conditions. This is realised in such a way that one traction-like vector valued Lagrange multiplier as well as one heat flux-like Lagrange multiplier is introduced for the (two, respectively three) vertex nodes (in two-, respectively three-dimensional case), cf. Figs. 6.4(a) and 6.4(c). By taking more flux boundary nodes into account, the set of Lagrange multipliers is appropriately extended, cf. Figs. 6.4(b) and 6.4(d), which leads to a stiffer effective RVE response. The limit case would be to choose the same amount of flux boundary nodes as nodes on the degree of freedom boundary mesh as this scenario represents the strong PR boundary conditions.

Therefore, the WK boundary conditions are one kind of tool to interpolate between UF and PR boundary conditions, cf. the numerical examples in Section 6.3. The interpolation mentioned above and sketched by the interpolation lines in Fig. 6.3 leads to weights within the interval $[\,0\,,\,1\,]$ for each Lagrange multiplier with respect to each degree of freedom. Mathematically, this can be written in terms of weight matrices, $\underline{\underline{\mathbf{P}}}^{\boldsymbol{\varphi}\,i\,A}$ and $\underline{\underline{\mathbf{P}}}^{\theta\,i\,A}$, for each element $\partial\mathcal{B}_{0+}^{\mathrm{RVE}\,i} \in \partial\mathcal{B}_{0+}^{\mathrm{RVE}}$. With these weight matrices at hand, Eqs. (6.83) and (6.84) can be rewritten as

$$0 = \sum_{i=1}^{n_{\mathrm{pel}}} \sum_{A=1}^{n_{\mathrm{en}}} \underbrace{\boldsymbol{\lambda}^{\boldsymbol{t}_0} \cdot \underline{\underline{\mathbf{P}}}^{\boldsymbol{\varphi}\,i\,A}}_{=:\,\boldsymbol{\lambda}^{\boldsymbol{\varphi}\,i\,A}} \cdot \left[\int\limits_{\partial\mathcal{B}_{0+}^{\mathrm{RVE}\,i}} N^A \left[\left[\!\left[\boldsymbol{u}^{\mathrm{m}} \right]\!\right] - \boldsymbol{H}^{\mathrm{M}} \cdot \left[\!\left[\boldsymbol{X}^{\mathrm{m}} \right]\!\right] \right] \mathrm{d}A \right], \tag{6.85}$$

$$0 = \sum_{i=1}^{n_{\mathrm{pel}}} \sum_{A=1}^{n_{\mathrm{en}}} \underbrace{\boldsymbol{\lambda}^{Q} \cdot \underline{\underline{\mathbf{P}}}^{\theta\,i\,A}}_{=:\,\lambda^{\theta\,i\,A}} \cdot \left[\int\limits_{\partial\mathcal{B}_{0+}^{\mathrm{RVE}\,i}} N^A \left[\left[\!\left[\theta^{\mathrm{m}} \right]\!\right] - \nabla_{\boldsymbol{X}} \theta^{\mathrm{M}} \cdot \left[\!\left[\boldsymbol{X}^{\mathrm{m}} \right]\!\right] \right] \mathrm{d}A \right]. \tag{6.86}$$

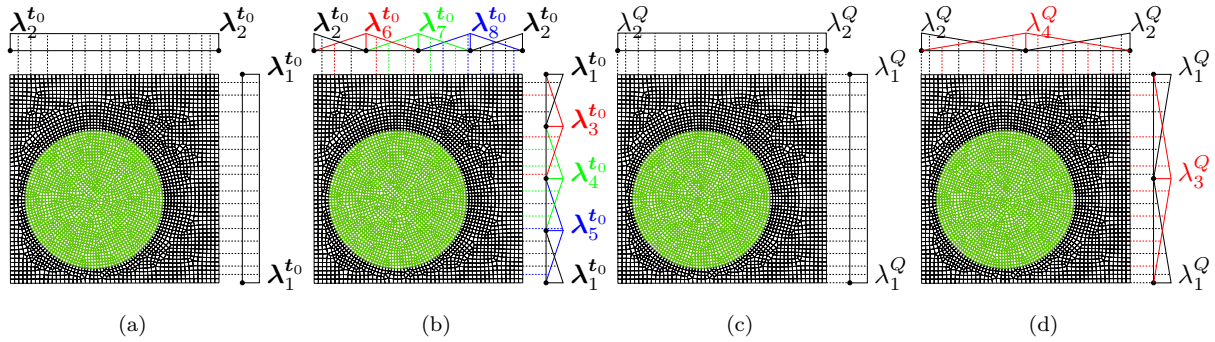

Figure 6.4: (a) Minimal traction boundaries with two nodes which is equivalent to constant traction boundary conditions. (b) Exemplary traction boundaries with five equally distributed nodes. (c) Minimal heat flux boundaries with two nodes which is equivalent to constant heat flux boundary conditions. (d) Exemplary heat flux boundaries with three equally distributed nodes.

From these two equations, the surface force contributions result as derivations of the respective terms with respect to the related degrees of freedoms, i.e.

$$\underline{\mathbf{f}}^{\boldsymbol{\varphi}}_{\text{sur}} = \frac{\partial}{\partial \underline{\boldsymbol{\varphi}}} \sum_{i=1}^{n_{\text{pel}}} \underbrace{\sum_{A=1}^{n_{\text{en}}} N^A \, \boldsymbol{\lambda}^{\boldsymbol{\varphi}\, i\, A}}_{=:\, \boldsymbol{\lambda}^{\boldsymbol{\varphi}\, i}} \cdot \left[\int_{\partial \mathcal{B}_{0+}^{\text{RVE}\, i}} \left[\left[\!\left[\boldsymbol{u}^{\text{m}} \right]\!\right] - \boldsymbol{H}^{\text{M}} \cdot \left[\!\left[\boldsymbol{X}^{\text{m}} \right]\!\right] \right] \mathrm{d}A \right]$$

$$= \mathop{\mathbf{A}}_{i=1}^{n_{\text{pel}}} \int_{\partial \mathcal{B}_{0+}^{\text{RVE}\, i}} \left[\!\left[\pm \right]\!\right] N^B \, \boldsymbol{\lambda}^{\boldsymbol{\varphi}\, i} \, \mathrm{d}A \,, \tag{6.87}$$

$$\underline{\mathbf{f}}^{\theta}_{\text{sur}} = \frac{\partial}{\partial \underline{\boldsymbol{\theta}}} \sum_{i=1}^{n_{\text{pel}}} \underbrace{\sum_{A=1}^{n_{\text{en}}} N^A \, \lambda^{\theta\, i\, A}}_{=:\, \lambda^{\theta\, i}} \left[\int_{\partial \mathcal{B}_{0+}^{\text{RVE}\, i}} \left[\left[\!\left[\theta^{\text{m}} \right]\!\right] - \nabla_{\boldsymbol{X}} \theta^{\text{M}} \cdot \left[\!\left[\boldsymbol{X}^{\text{m}} \right]\!\right] \right] \mathrm{d}A \right]$$

$$= \mathop{\mathbf{A}}_{i=1}^{n_{\text{pel}}} \int_{\partial \mathcal{B}_{0+}^{\text{RVE}\, i}} \left[\!\left[\pm \right]\!\right] N^B \, \lambda^{\theta\, i} \, \mathrm{d}A \,, \tag{6.88}$$

with

$$\underline{\boldsymbol{\varphi}} = \left[\boldsymbol{\varphi}_1^{\text{t}} \quad \boldsymbol{\varphi}_2^{\text{t}} \quad \dots \quad \boldsymbol{\varphi}_{n_{\text{np}}}^{\text{t}} \right]^{\text{t}} , \qquad \underline{\boldsymbol{\theta}} = \left[\theta_1 \quad \theta_2 \quad \dots \quad \theta_{n_{\text{np}}} \right]^{\text{t}} . \tag{6.89}$$

In the above equations, the "$[\![\pm]\!]$"-sign indicates that the resulting flux contribution is added with a positive sign to the corresponding nodes on the "+"-side as well as with a negative sign to the corresponding nodes on the "−"-side. This obviously results in

self-equilibrated boundary forces/fluxes. Furthermore, different boundary discretisations of $\partial\mathcal{B}_{0+}^{\mathrm{RVE}}$ and $\partial\mathcal{B}_{0-}^{\mathrm{RVE}}$ can be considered, as indicated by Fig. 6.3. Such cases can be dealt with once more introducing weight matrices, $\underline{\underline{\mathbf{P}}}^{\boldsymbol{\varphi}\,i\,A-}$ and $\underline{\underline{\mathbf{P}}}^{\theta\,i\,A-}$, for each "+"-side element $\partial\mathcal{B}_{0+}^{\mathrm{RVE}\,i} \in \partial\mathcal{B}_{0+}^{\mathrm{RVE}}$ stemming from interpolation. Inserting these weighting matrices into Eqs. (6.87) and (6.88) yields the modified self-equilibrated surface force, respectively flux terms. In the following section, numerical examples are carried out and the different boundary conditions – UF, WK, PR and UF – are compared. Since matching "+"- and "−"-sides are essential for PR boundary conditions, the case of non-matching opposite boundary representations is omitted in the examples shown.

Remark 6.2.2 (PR vs. WK boundary conditions) *In cases where "perfect" periodicity is desired at the meso-scale, it is numerically favorable to apply PR boundary conditions which are enforced strongly by Dirichlet boundary conditions. WK boundary conditions which identically represent PR boundary conditions due to the appropriate flux boundary choice yield larger non-linear systems of equations and, additionally, tend to need more Newton Raphson iteration steps to converge.*

Remark 6.2.3 (Temperature dependent quantities at the meso-scale) *The macro-scale temperature gradient $\nabla_{\boldsymbol{X}}\theta^{\mathrm{M}}$, together with the macro-scale temperature θ^{M}, induces a temperature field at the meso-scale inside the RVE which depends on the applied boundary conditions as discussed above. Different from the constitutive relations of purely mechanical meso-scale problems which solely depend on the deformation gradient $\boldsymbol{F}^{\mathrm{m}}$ in case of elasticity, the meso-scale temperature field θ^{m}, which depends on the macro-scale temperature gradient $\nabla_{\boldsymbol{X}}\theta^{\mathrm{M}}$ and the RVE size, explicitly arises in the thermal part of the problem as well as within the thermo-mechanical coupling terms of the mechanical problem. Consequently, the size of the RVE may seriously influence the effective macroscopic response. In the case of considerable large RVEs, the meso-scale temperature θ^{m} may notably differ from the macro-scale temperature θ^{M} as discussed in Chapter 5. A similar effect may occur for very high temperature gradients. Furthermore, a connection of the meso-scale quantities – such as stresses, heat capacity, heat source, etc. – with the meso-scale temperature obtained from Eq.* (6.28) *leads to macro-scale quantities that are connected with the macro-scale temperature gradient. Consequently, the effective Helmholtz energy would depend on the macro-scale temperature gradient which should be excluded. For this reason and, accordingly, to decouple the thermal part of the constitutive problem from the RVE size which yields a complete separation of scales, Temizer and Wriggers [172] evaluate temperature dependent quantities at the meso-scale in terms of the macro-scale temperature θ^{M}. For further detailed discussions the reader is referred to Temizer [169], wherein an asymptotic expansion framework for finite thermo-elasticity is elaborated. Computational comparisons between the evaluation of meso-scale quantities at θ^{m} and θ^{M} are discussed in Chapter 5. For all simulations shown in Section 6.3, however, the approach of Temizer and Wriggers [172] is chosen such that all temperature dependent quantities at the meso-scale are evaluated at θ^{M}.*

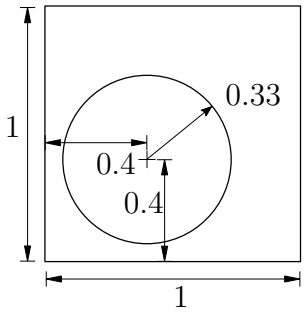

(a) Quadrilateral RVE domain with an eccentric circular inclusion.

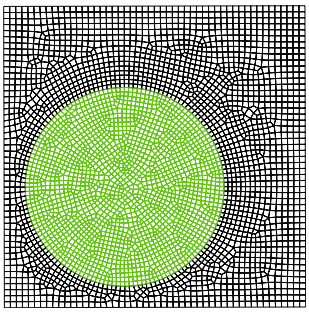

(b) RVE discretisation with quadrilateral finite elements ($n_{\text{el}} = 2112$ for the matrix, $n_{\text{el}} = 1817$ for the inclusion).

Figure 6.5: (a) RVE with a thermo-viscoplastic matrix and an eccentric thermo-elastic inclusion. (b) The RVE is discretised by quadrilateral elements with bi-linear shape functions. The eccentric circular inclusion is depicted in green coloured mesh, the matrix' mesh is coloured black.

Note that similar problems may occur whenever constitutive relations depend on the degrees of freedom and gradients thereof such as typical diffusion problems, in contrast to established FE² formulations for, e.g., electro- and magneto-mechanical coupling, [88, 93].

6.3 Numerical examples

The multi-scale finite element framework proposed in the previous sections is illustrated by several numerical examples which are summarised in this section. The section is subdivided into three subsections. In Section 6.3.1, a comparison of the WK boundary conditions with the LN boundary conditions, UF boundary conditions and PR boundary conditions is discussed by means of a prescribed state of deformation on a single RVE. In Section 6.3.2, a two-scale simulation is carried out, where the upper scale is represented by four quadrilateral elements. For different loading velocities, the deformation is prescribed on the macro-scale in such a way that an inhomogeneous state of deformation is induced. The influence of the chosen boundary conditions on the effective macroscopic response is studied. Finally, in Section 6.3.3, the result of a three-dimensional quenching simulation of a coated steel radius is shown. The WC-Co coating is thereby represented by artificially generated three-dimensional RVEs.

6.3.1 Boundary condition benchmark – Meso-scale simulation

In this example, the different established boundary conditions are compared to the WK boundary conditions which have been introduced in Section 6.2.3. For all RVE

test computations, two different states of deformation under plane strain conditions are prescribed. The first load case is defined by

$$\begin{aligned} \boldsymbol{F}^{\mathrm{M}} &= \boldsymbol{I} + 0.1\,[\,\boldsymbol{e}_1 \otimes \boldsymbol{e}_1 + \boldsymbol{e}_1 \otimes \boldsymbol{e}_2 + \boldsymbol{e}_2 \otimes \boldsymbol{e}_1 + \boldsymbol{e}_2 \otimes \boldsymbol{e}_2\,]\ , \\ \theta^{\mathrm{M}} &= 293\,\mathrm{K}\ , \\ \nabla_{\boldsymbol{X}}\theta^{\mathrm{M}} &= 1000\,[\,\boldsymbol{e}_1 + \boldsymbol{e}_2\,]\,\mathrm{K\,mm^{-1}}\ , \\ \theta_0 &= 293\,\mathrm{K}\ , \end{aligned} \tag{6.90}$$

Table 6.1: Thermo-mechanical material parameters for cobalt (Co), tungsten carbide (WC) and steel, [48, 138].

Material	Description	Symbol	Value	Unit
Co	Young's modulus	E	2.11×10^{2}	GPa
	Poisson ratio	ν	3.10×10^{-1}	
	Mass density	ρ_0	8.90×10^{-3}	$\mathrm{g\,mm^{-3}}$
	Heat capacity	c	4.56×10^{2}	$\mathrm{mJ\,g^{-1}\,K^{-1}}$
	Heat expansion	α_0	1.25×10^{-6}	$\mathrm{K^{-1}}$
	Heat conduction	Λ_0	1.00×10^{-1}	$\mathrm{W\,mm^{-1}\,K^{-1}}$
WC	Young's modulus	E	7.05×10^{2}	GPa
	Poisson ratio	ν	1.94×10^{-1}	
	Mass density	ρ_0	1.57×10^{-2}	$\mathrm{g\,mm^{-3}}$
	Heat capacity	c	3.43×10^{2}	$\mathrm{mJ\,g^{-1}\,K^{-1}}$
	Heat expansion	α_0	1.02×10^{-6}	$\mathrm{K^{-1}}$
	Heat conduction	Λ_0	8.40×10^{-2}	$\mathrm{W\,mm^{-1}\,K^{-1}}$
Steel	Young's modulus	E	2.10×10^{2}	GPa
	Poisson ratio	ν	3.00×10^{-1}	
	Mass density	ρ_0	7.85×10^{-1}	$\mathrm{g\,mm^{-3}}$
	Heat capacity	c	4.21×10^{2}	$\mathrm{mJ\,g^{-1}\,K^{-1}}$
	Heat expansion	α_0	1.30×10^{-6}	$\mathrm{K^{-1}}$
	Heat conduction	Λ_0	1.00×10^{-1}	$\mathrm{W\,mm^{-1}\,K^{-1}}$

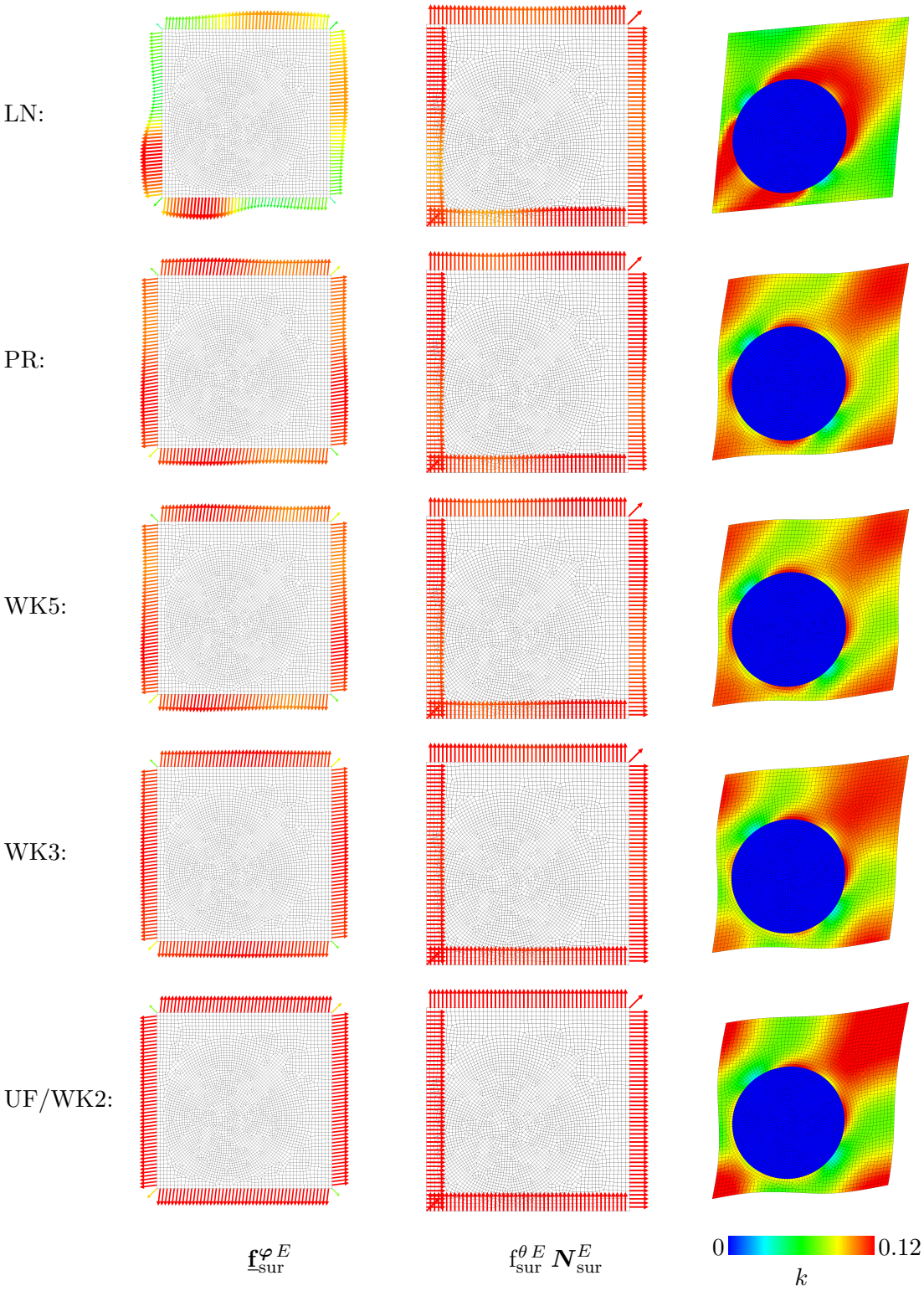

Figure 6.6: Comparison of the different types of boundary conditions for the first load case. From top to bottom, the rows show the results for the stiffest boundary conditions (LN) down to the weakest boundary conditions (UF). Strong periodic boundary conditions (PR) and weak periodic boundary conditions (WK5, WK3) are in between.

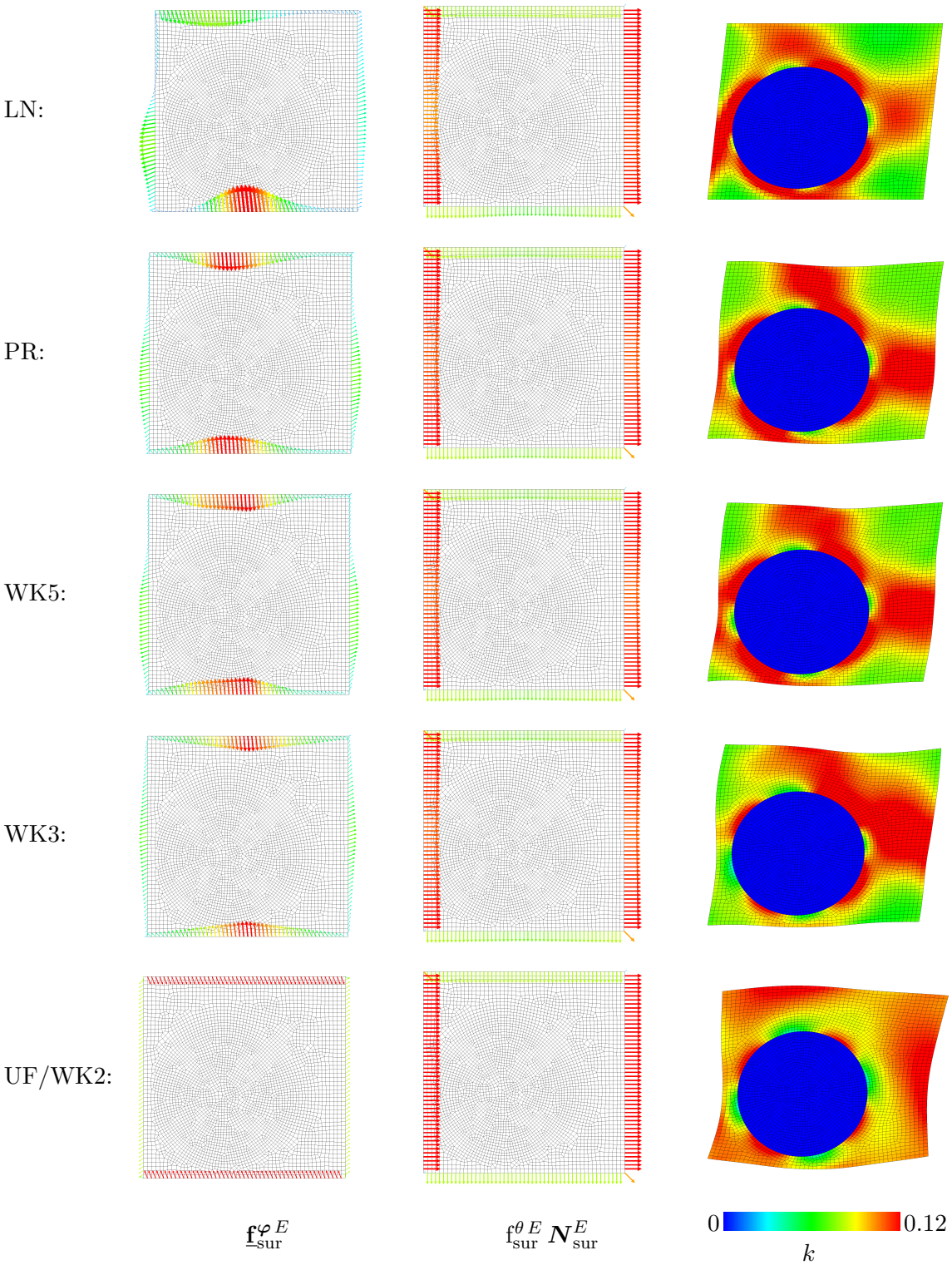

Figure 6.7: Comparison of the different types of boundary conditions for the second load case. From top to bottom, the rows show the results for the stiffest boundary conditions (LN) down to the weakest boundary conditions (UF). Strong periodic boundary conditions (PR) and weak periodic boundary conditions (WK5, WK3) are in between.

Table 6.2: Thermoviscoplastic material parameters for cobalt (Co), [24].

Material	Description	Symbol	Value	Unit
Co	Relaxation-type constant	η	9.63×10^5	MPa s
	Mixing parameter	x	1.00×10^{-1}	
	Exponential hardening parameter	k_0	1.15×10^{-2}	
	Initial yield parameter	a_{y0}	1.80×10^2	MPa
	Initial yield parameter	b_{y0}	5.50×10^2	K
	Initial yield parameter	c_{y0}	2.50×10^2	K
	Initial yield parameter	d_{y0}	2.00×10^1	
	Saturation yield parameter	$a_{y\infty}$	2.50×10^2	MPa
	Saturation yield parameter	$b_{y\infty}$	5.50×10^2	K
	Saturation yield parameter	$c_{y\infty}$	2.50×10^2	K
	Saturation yield parameter	$d_{y\infty}$	2.00×10^1	
	Hardening parameter	a_h	2.00×10^3	MPa
	Hardening parameter	b_h	4.50×10^2	K
	Hardening parameter	c_h	1.00×10^2	K
	Hardening parameter	d_h	2.00×10^1	

with $\{\boldsymbol{e}_i\}$ an orthonormal basis system, whereas the second load case is characterised by

$$\begin{aligned} \boldsymbol{F}^{\mathrm{M}} &= 1.1\,\boldsymbol{e}_1 \otimes \boldsymbol{e}_1 + 0.1\,\boldsymbol{e}_1 \otimes \boldsymbol{e}_2 + 0.9\,\boldsymbol{e}_2 \otimes \boldsymbol{e}_2 \;, \\ \theta^{\mathrm{M}} &= 293\,\mathrm{K} \;, \\ \nabla_{\boldsymbol{X}} \theta^{\mathrm{M}} &= [\,0.05\,\boldsymbol{e}_1 - 0.1\,\boldsymbol{e}_2\,]\;\mathrm{K\,mm^{-1}} \;, \\ \theta_0 &= 293\,\mathrm{K} \;. \end{aligned} \tag{6.91}$$

Both states of deformation are prescribed within a time increment of $\Delta t = 1\,\mathrm{s}$. The RVE as well as its discretisation are depicted in Fig. 6.5. The RVE domain is of quadratic shape with an edge of unit length. The radius of the eccentrically positioned circular inclusion is $r = 0.33$ unit length and the center of the inclusion is located at $[\,0.4, 0.4\,]$, cf. Fig. 6.5(a). The matrix is considered to be thermo-viscoplastic, whereas the inclusion is modelled as thermo-elastic phase. Hence, the parameters of the matrix material are taken from Table 6.1 (Co) as well as Table 6.2 and the model parameters of the inclusion from Table 6.1 (WC). Closer inspection of Fig. 6.5(b) exhibits the "+"- and "−"-boundaries of the RVE to be discretised with 50 equidistantly distributed nodes. As already discussed

Table 6.3: Norm of the homogenised Piola stress $\|\boldsymbol{P}^{\mathrm{M}}\|$ and norm of the homogenised heat flux $\|\boldsymbol{Q}^{\mathrm{M}}\|$ for the two studied load cases and different types of boundary conditions.

Load case	Quantity	LN	PR	WK5	WK3	UF/WK2
1	$\|\boldsymbol{P}^{\mathrm{M}}\|$ / MPa	70117.40	69715.09	69703.93	69199.35	68944.75
	$\|\boldsymbol{Q}^{\mathrm{M}}\|$ / K mm^{-1}	133.3053	133.2632	133.2625	133.1904	133.1835
2	$\|\boldsymbol{P}^{\mathrm{M}}\|$ / MPa	27757.95	25622.90	25526.17	24012.71	21342.62
	$\|\boldsymbol{Q}^{\mathrm{M}}\|$ / K mm^{-1}	1.699733	1.698779	1.698776	1.698730	1.698218

in the previous section, such a discretisation is essential in order to compare the WK boundary conditions to the strongly enforced PR boundary conditions. The bulk of the RVE is discretised with 3929 quadrilateral elements with bi-linear shape functions, from which 2112 elements represent the matrix material and 1817 elements represent the inclusion. For the weak boundary conditions, two different flux boundaries with equally distributed discrete nodes are used: the one with three flux nodes (WK3) and the other with five flux nodes (WK5).

Fig. 6.6 shows RVE results of the first prescribed load case in table form, sorted from the top to the bottom row from the stiffest boundary conditions (LN) to the weakest boundary conditions (UF). The intermediate boundary conditions in decreasing order are the strongly enforced periodic boundary conditions (PR), the weakly enforced periodic boundary conditions with five equally distributed flux nodes (WK5) as well as weakly enforced periodic boundary conditions with three equally distributed flux nodes (WK3). In the left column, the RVE mesh is shown with a plot of the resulting mechanical reaction forces at the RVE boundary nodes. In the middle column, the RVE mesh is shown together with the surface normal vector weighted by the resulting thermal reaction flux at the RVE boundary nodes. All vector plots in Fig. 6.6 are scaled column-wise to the same scale in order to achieve comparability. The right column shows equivalent plastic strain plots as well as the deformed shapes of the RVE under the prescribed load. The comparison of the flux plots, either mechanical or thermal, reveals that only the LN boundary conditions show, as expected, non-periodic boundary fluxes. All other boundary conditions, the strong periodic as well as the weakly enforced periodic boundary conditions with reduced flux boundaries, show periodical fluxes on the opposite boundaries – this can be interpreted as kinetic compatibility. Examination of the deformed shapes of the RVE for the different boundary conditions shows, that the opposite RVE boundaries deform periodically for the LN and PR boundary conditions – this can be seen as kinematic compatibility. In contrast, the weakly enforced boundary conditions with reduced flux boundaries yield deformations which do not match on opposite surfaces. Hence, solely the strongly enforced periodic boundary conditions yield

kinematic as well as kinetic compatibility. It is furthermore observed that the resulting distribution of the equivalent plastic strain k depends on the chosen type of boundary conditions. While the resulting k-plot for the LN boundary conditions apparently differs a lot compared to the result obtained for PR boundary conditions, the k-distribution for UF/WK2 boundary conditions looks similar to the PR result. By increasing the number of boundary flux nodes (WK3, WK5), the deformed RVE shape as well as the k-distribution tends towards the PR result.

In contrast to the first load case, the second load case includes an unsymmetrical shear component as well as a compression component. The RVE benchmark results for the second load case are depicted in Fig. 6.7. Analogously to the first load case, the resulting plots are organised in table form, sorted from the top to the bottom row from the stiffest boundary conditions (LN) to the weakest boundary conditions (UF). Again, the intermediary boundary conditions are, in decreasing order, the PR, WK5 as well as WK3 periodic boundary conditions. In the left column, the mesh of the RVE is plotted together with the resulting mechanical reaction force vectors. In the middle column, the RVE mesh is shown with the surface normal vector weighted by the resulting thermal reaction flux. Again, the vectors in all plots are scaled column-wise to the same scale for comparison purposes. The right column shows equivalent plastic strain plots as well as the deformed shapes of the RVE under the prescribed load. Of course, the comparison of the mechanical and thermal flux plots as well as the deformed RVE shapes shows the same findings as before with regard to kinetic and kinematic compability. It is noteworthy that the differences with regard to k-distribution as well as the deformed shapes between WK und PR boundary conditions are more pronounced for the second load case than they are for the first load case.

To prove the statement already made, as well as to meet the expectation that LN boundary conditions are stiffer than PR boundary conditions, which themselves are stiffer than WK boundary conditions with reduced flux boundary nodes, the norms of the homogenised Piola stress $\|\boldsymbol{P}^{\mathrm{M}}\|$ as well as of the homogenised heat flux $\|\boldsymbol{Q}^{\mathrm{M}}\|$ are compared in Table 6.3 for both load cases. The former conclusion is proven by comparison of the numbers, whereby the fact stands out that the relative difference is more pronounced for the mechanical part of the problem than it is for the thermal part of the problem. The relative deviation of the weakest boundary conditions (UF) to the stiffest (LN) with respect to $\|\boldsymbol{P}^{\mathrm{M}}\|$ is approximately 1.7 % in case of load case 1, and approximately 23.1 % in case of load case 2. In constrast, the relative deviation of UF to LN boundary conditions with respect to $\|\boldsymbol{Q}^{\mathrm{M}}\|$ is about 9.0×10^{-4} for both load cases. The reason for this observation is the fact that the thermal model parameters of tungsten carbide and cobalt are quite close to each other. The mismatch of the heat conduction coefficients is just $\Lambda_0^{\mathrm{WC}}/\Lambda_0^{\mathrm{Co}} = 0.84$ and therefore close to 1, whereas the mismatch of the Young's moduli is $E^{\mathrm{WC}}/E^{\mathrm{Co}} = 3.34$, cf. Table 6.1.

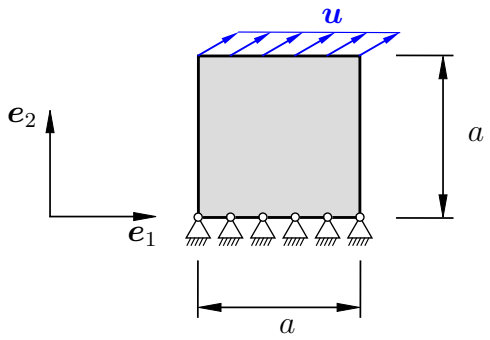

(a) Plane quadrilateral plate which is supported at the bottom edge and subject to prescribed displacements at the top edge.

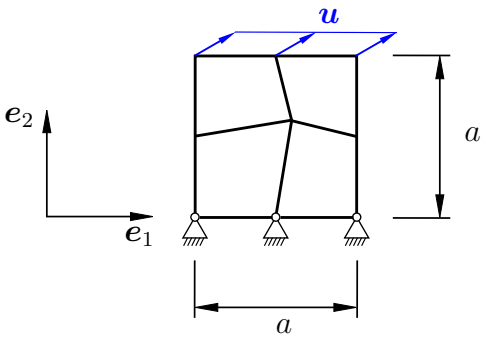

(b) Discretisation of the plane quadrilateral plate by means of four fully integrated quadrilateral finite elements with bi-linear shape functions.

Figure 6.8: Macroscale boundary value problem of a plane quadrilateral plate which is (a) subject to displacement boundary conditions as well as adiabatic thermal boundary conditions and (b) discretised by means of four fully integrated quadrilateral finite elements with bi-linear shape functions.

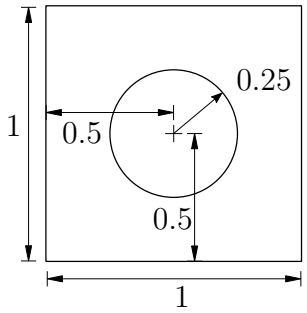

(a) Quadrilateral RVE domain with a centric circular inclusion.

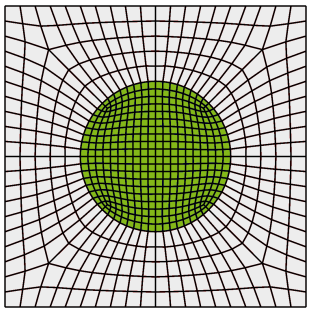

(b) RVE discretisation with quadrilateral finite elements ($n_{\mathrm{el}} = 336$ for the matrix, $n_{\mathrm{el}} = 384$ for the inclusion).

Figure 6.9: (a) RVE with a thermo-viscoplastic matrix and a centric thermo-elastic inclusion. (b) The RVE is discretised by quadrilateral elements with bi-linear shape functions. The centric circular inclusion is depicted in green colour, the matrix is coloured light grey.

6.3.2 Boundary condition benchmark – Multi-scale simulation

The second numerical example involves two scales, a macro-scale boundary value problem to be solved as well as a meso-scale problem at every macro-scale integration point in order to capture the effective thermo-mechanical behaviour of the underlying RVE in the macro-scale analysis. The two-dimensional macro-scale problem is a quadratic plate under plane strain conditions with an edge length $a = 2\,\mathrm{mm}$ that is clamped at its bottom edge. At the top edge, displacements are prescribed, $\boldsymbol{u} = b(t)\,[\,0.3\,\boldsymbol{e}_1 + 0.1\,\boldsymbol{e}_2\,]$ mm, whereby the factor $b(t)$ is linearly increased in time from 0 to 1 within three different time intervals, namely 10 s, 30 s and 50 s. When $b = 1$ is reached, this loading factor remains constant during the remaining analysis. The boundary of the whole domain is considered to be adiabatic. Fig. 6.8(a) illustrates the boundary value problem. The time increment is

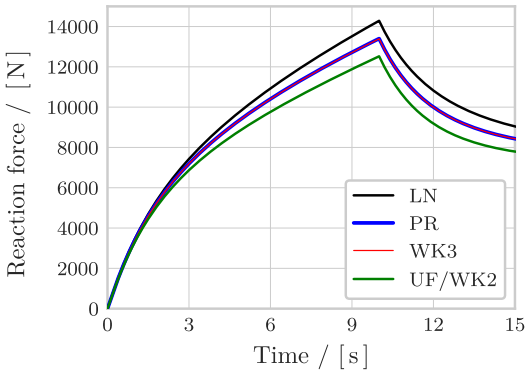

(a) Macroscale reaction force vs. time plot.

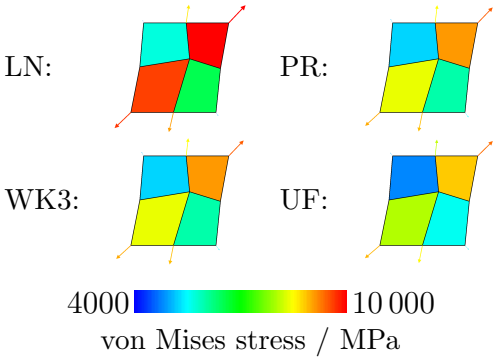

(b) Macroscale von Mises stress plots after 10 s.

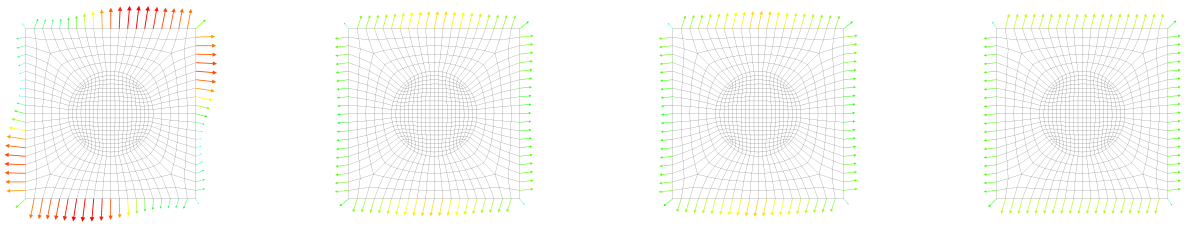

(c) Mesoscale plot of the boundary node forces after 10 s. From *left* to *right* LN, PR, WK3, UF boundary conditions.

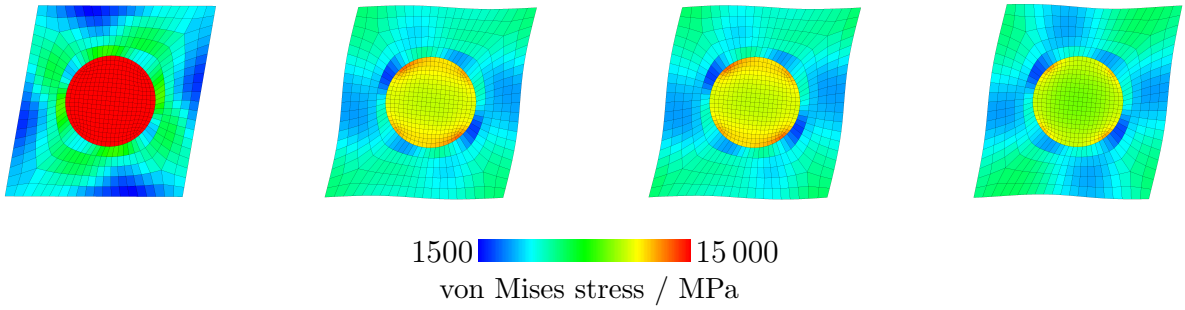

(d) Mesoscale von Mises stress plot after 10 s. From *left* to *right* LN, PR, WK3, UF boundary conditions.

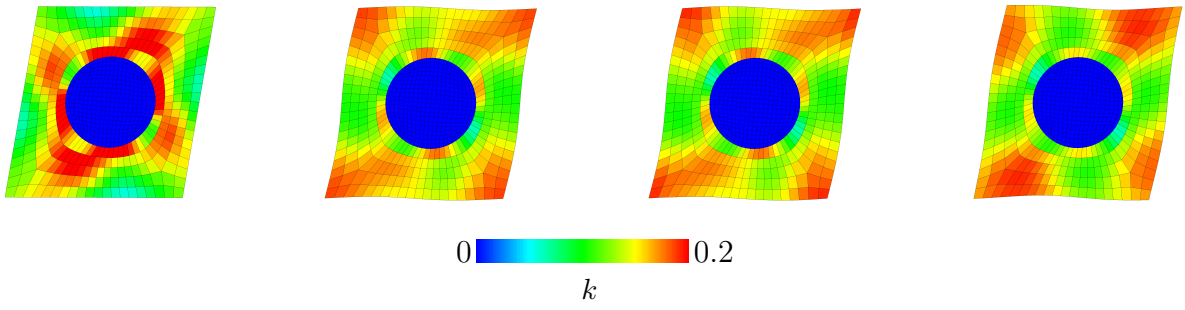

(e) Mesoscale equivalent plastic strain plot after 10 s. From *left* to *right* LN, PR, WK3, UF boundary conditions.

Figure 6.10: Results from the plane quadratic plate multi-scale simulations with the centric circular inclusion RVE. The maximum displacement is prescribed after 10 s. (a) Macroscale reaction force vs. time plot. (b) Macroscale von Mises stress plot and reaction forces after 10 s. Mesoscale plots with (c) the boundary node forces, (d) von Mises stresses and (e) equivalent plastic strains after 10 s.

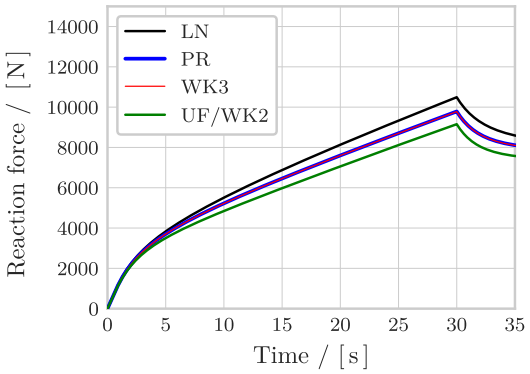

(a) Macroscale reaction force vs. time plot.

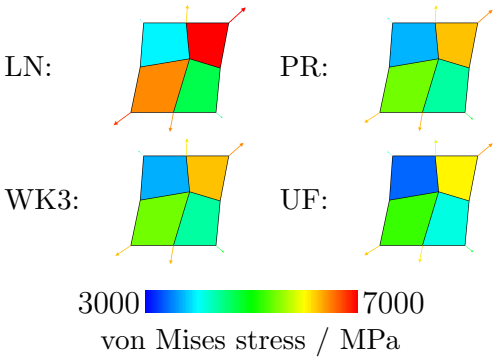

(b) Macroscale von Mises stress plots after 30 s.

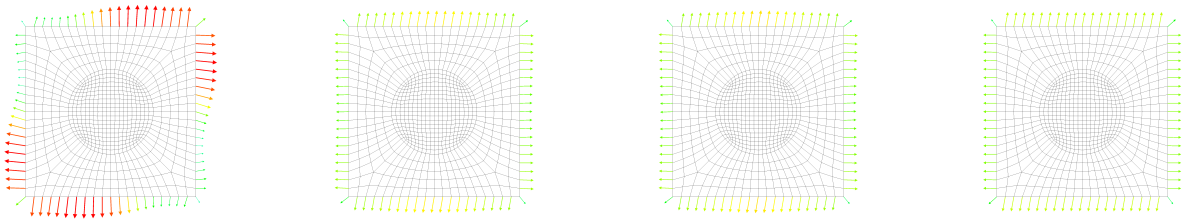

(c) Mesoscale plot of the boundary node forces after 30 s. From *left* to *right* LN, PR, WK3, UF boundary conditions.

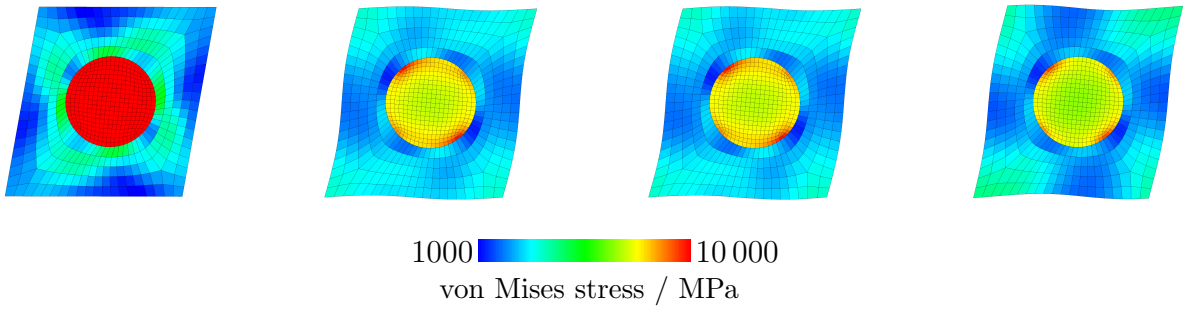

(d) Mesoscale von Mises stress plot after 30 s. From *left* to *right* LN, PR, WK3, UF boundary conditions.

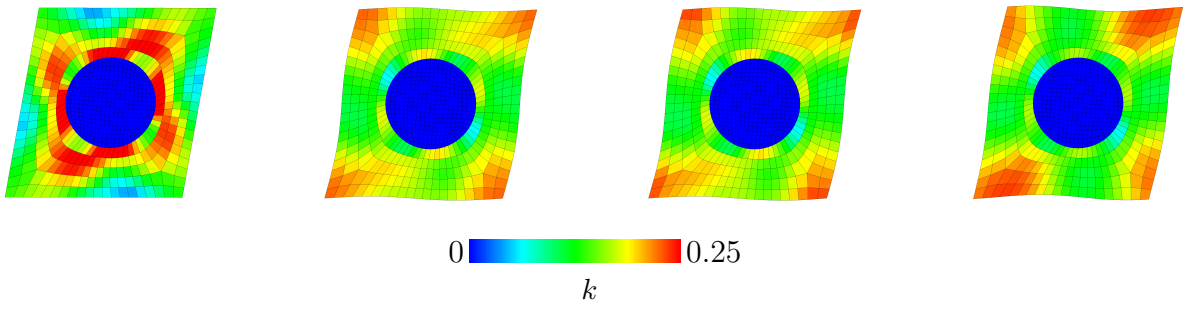

(e) Mesoscale equivalent plastic strain plot after 30 s. From *left* to *right* LN, PR, WK3, UF boundary conditions.

Figure 6.11: Results from the plane quadratic plate multi-scale simulations with the centric circular inclusion RVE. The maximum displacement is prescribed after 30 s. (a) Macroscale reaction force vs. time plot. (b) Macroscale von Mises stress plot and reaction forces after 30 s. Mesoscale plots with (c) the boundary node forces, (d) von Mises stresses and (e) equivalent plastic strains after 30 s.

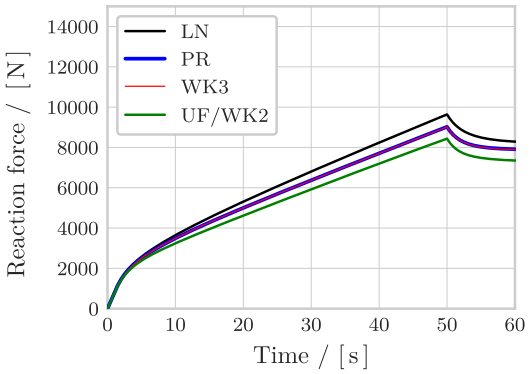

(a) Macroscale reaction force vs. time plot.

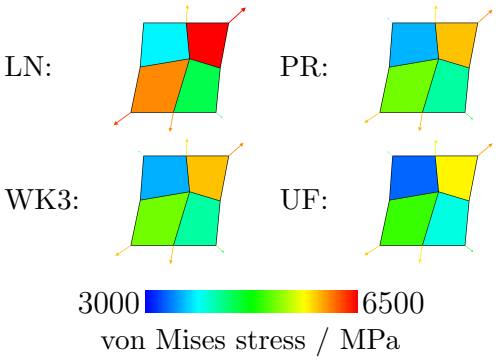

(b) Macroscale von Mises stress plots after 50 s.

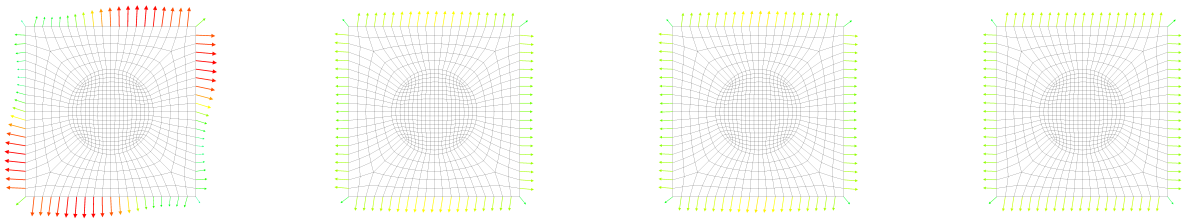

(c) Mesoscale plot of the boundary node forces after 50 s. From *left* to *right* LN, PR, WK3, UF boundary conditions.

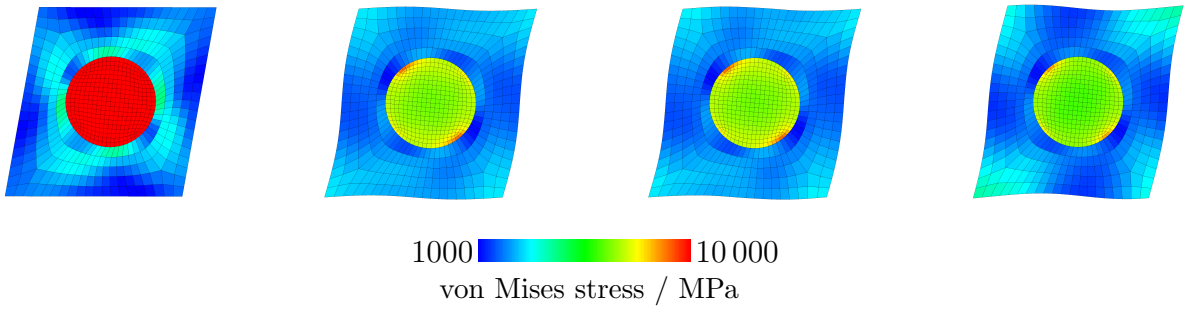

(d) Mesoscale von Mises stress plot after 50 s. From *left* to *right* LN, PR, WK3, UF boundary conditions.

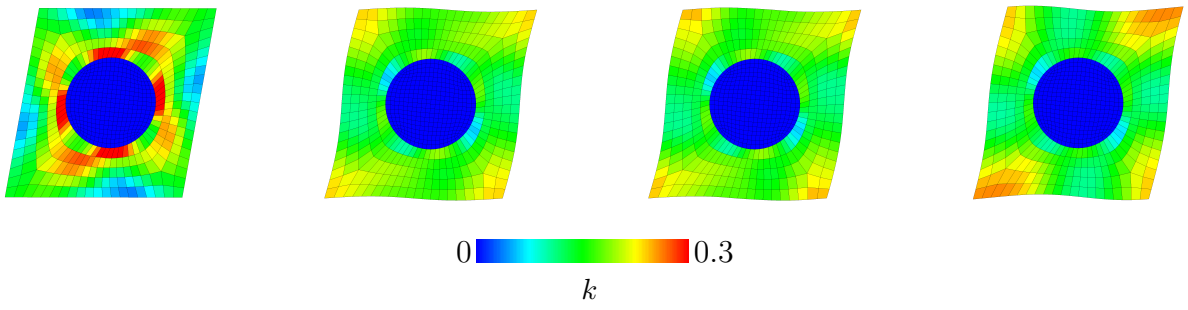

(e) Mesoscale equivalent plastic strain plot after 50 s. From *left* to *right* LN, PR, WK3, UF boundary conditions.

Figure 6.12: Results from the plane quadratic plate multi-scale simulations with the centric circular inclusion RVE. The maximum displacement is prescribed after 50 s. (a) Macroscale reaction force vs. time plot. (b) Macroscale von Mises stress plot and reaction forces after 50 s. Mesoscale plots with (c) the boundary node forces, (d) von Mises stresses and (e) equivalent plastic strains after 50 s.

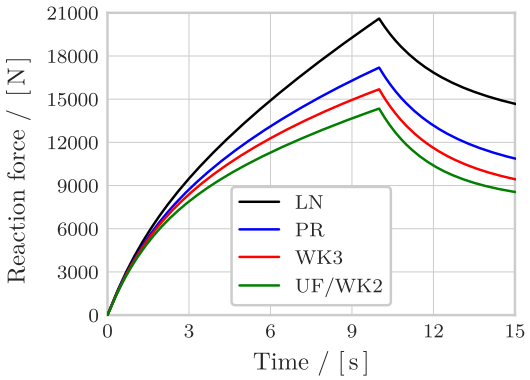

(a) Macroscale reaction force vs. time plot.

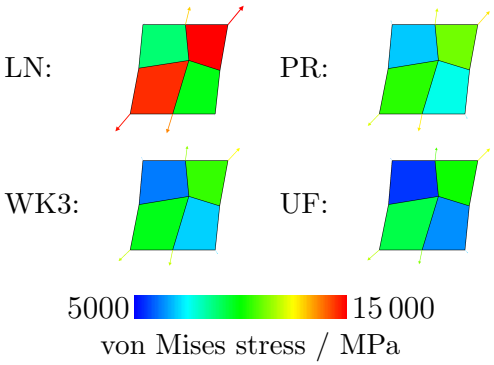

(b) Macroscale von Mises stress plots after 10 s.

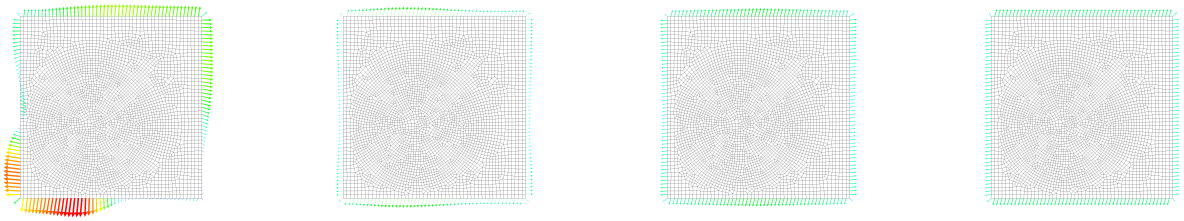

(c) Mesoscale plot of the boundary node forces after 10 s. From *left* to *right* LN, PR, WK3, UF boundary conditions.

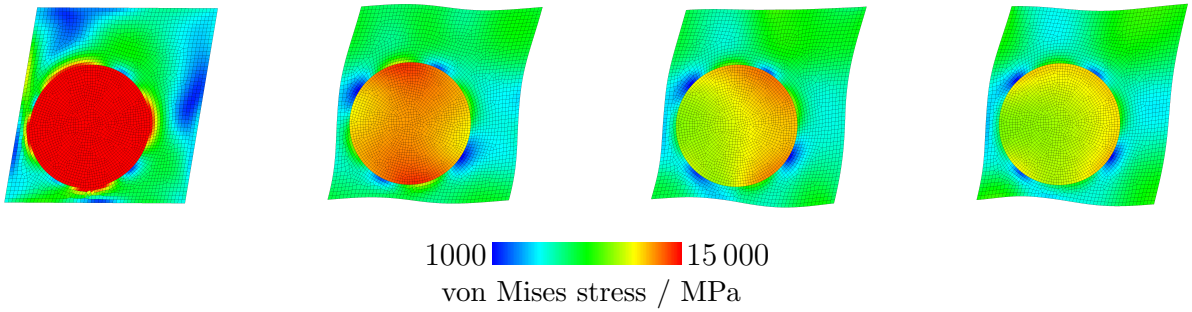

(d) Mesoscale von Mises stress plot after 10 s. From *left* to *right* LN, PR, WK3, UF boundary conditions.

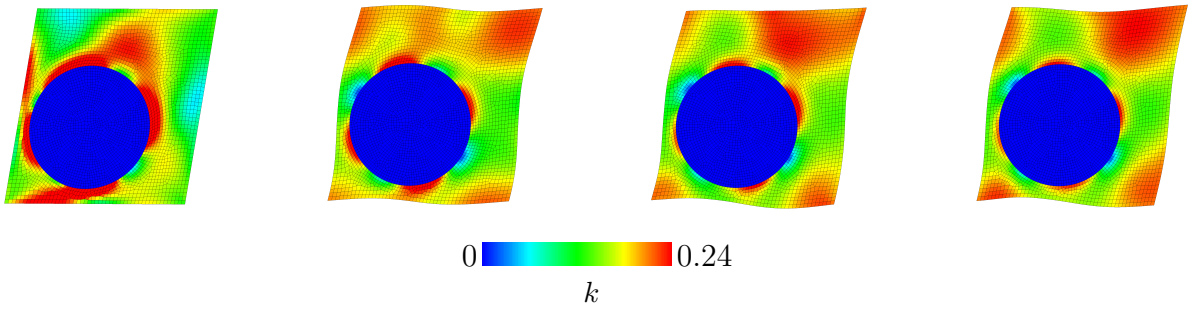

(e) Mesoscale hardening variable plot after 10 s. From *left* to *right* LN, PR, WK3, UF boundary conditions.

Figure 6.13: Results from the plane quadratic plate multi-scale simulations with the eccentric circular inclusion RVE. The maximum displacement is prescribed after 10 s. (a) Macroscale reaction force vs. time plot. (b) Macroscale von Mises stress plot and reaction forces after 10 s. Mesoscale plots with (c) the boundary node forces, (d) von Mises stresses and (e) equivalent plastic strains after 10 s.

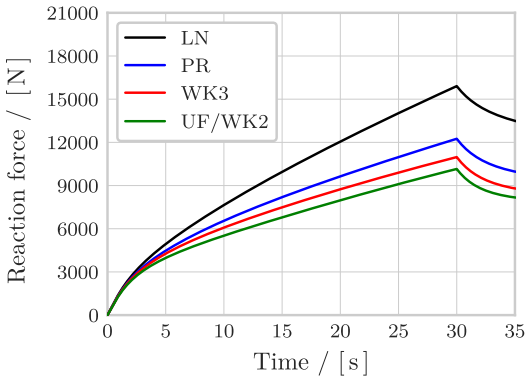

(a) Macroscale reaction force vs. time plot.

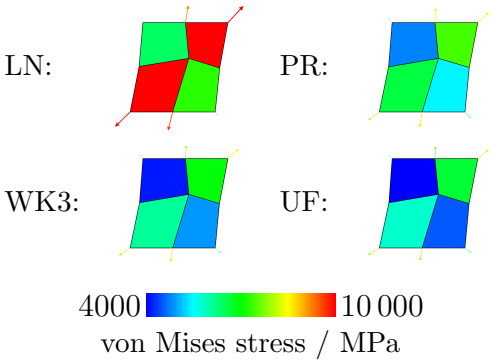

(b) Macroscale von Mises stress plots after 30 s.

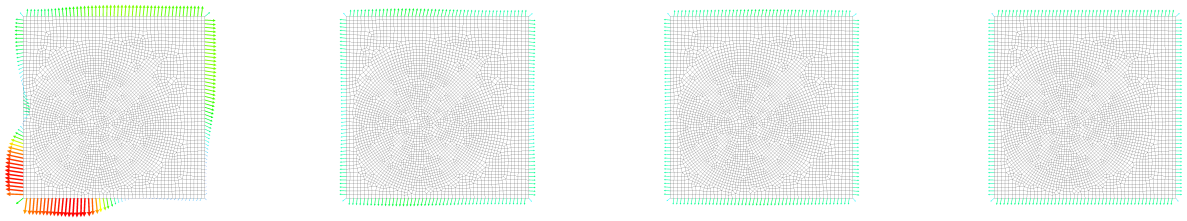

(c) Mesoscale plot of the boundary node forces after 30 s. From *left* to *right* LN, PR, WK3, UF boundary conditions.

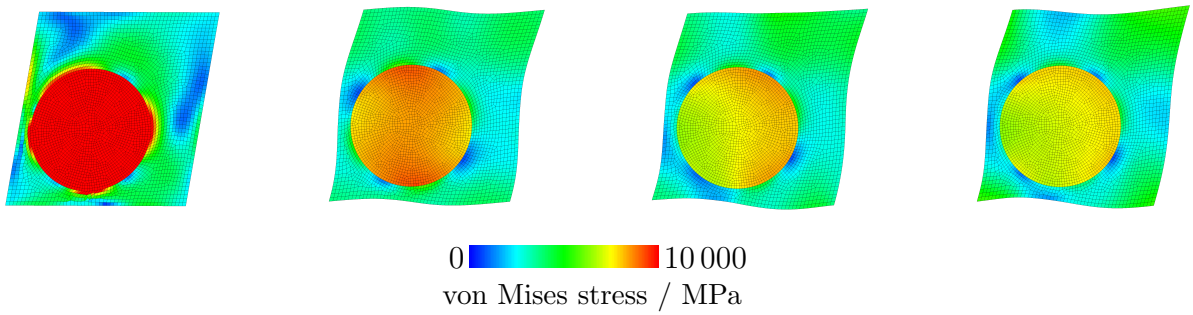

(d) Mesoscale von Mises stress plot after 30 s. From *left* to *right* LN, PR, WK3, UF boundary conditions.

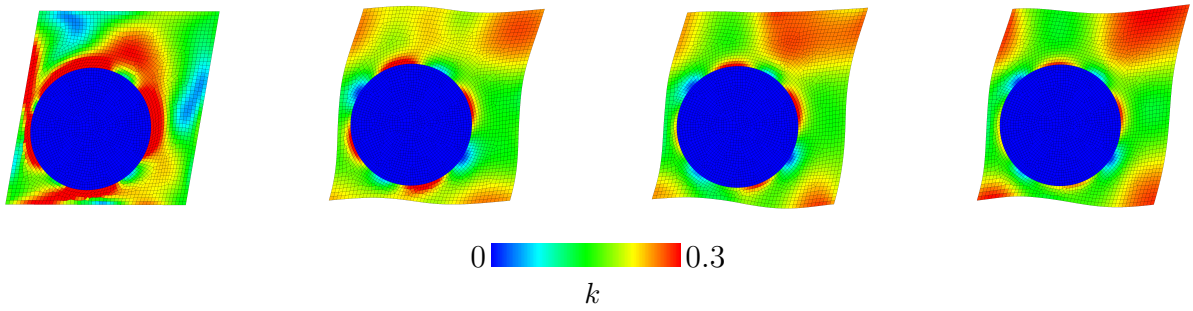

(e) Mesoscale hardening variable plot after 30 s. From *left* to *right* LN, PR, WK3, UF boundary conditions.

Figure 6.14: Results from the plane quadratic plate multi-scale simulations with the eccentric circular inclusion RVE. The maximum displacement is prescribed after 30 s. (a) Macroscale reaction force vs. time plot. (b) Macroscale von Mises stress plot and reaction forces after 30 s. Mesoscale plots with (c) the boundary node forces, (d) von Mises stresses and (e) equivalent plastic strains after 30 s.

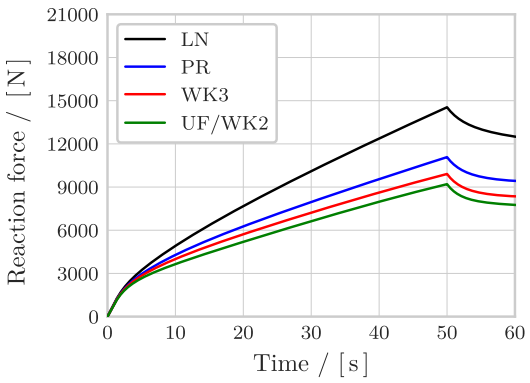

(a) Macroscale reaction force vs. time plot.

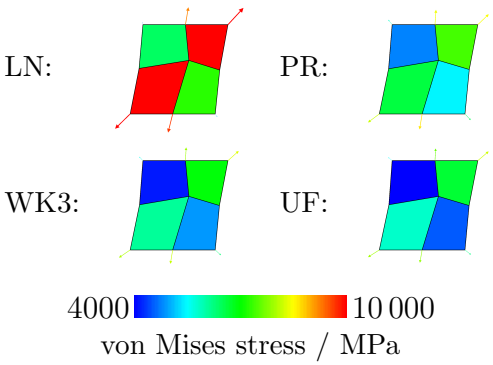

(b) Macroscale von Mises stress plots after 50 s.

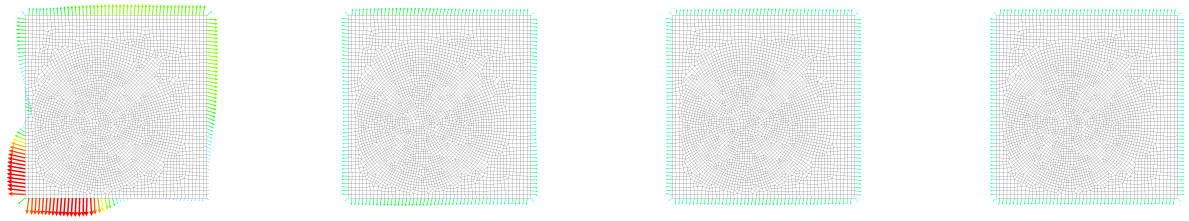

(c) Mesoscale plot of the boundary node forces after 50 s. From *left* to *right* LN, PR, WK3, UF boundary conditions.

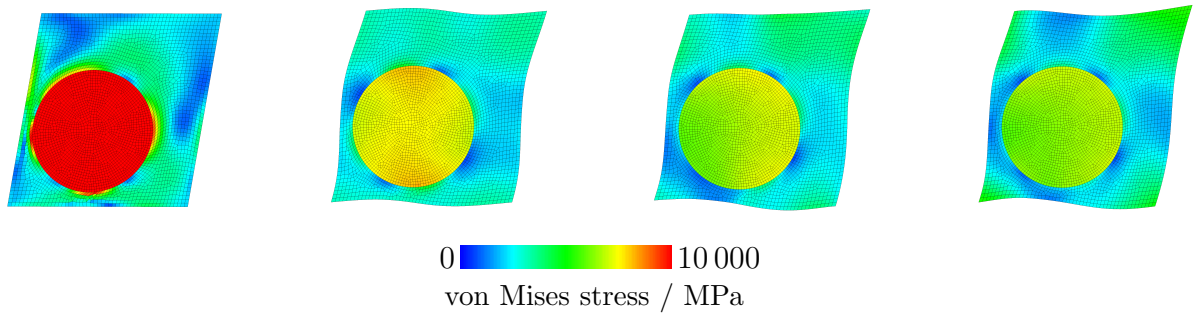

(d) Mesoscale von Mises stress plot after 50 s. From *left* to *right* LN, PR, WK3, UF boundary conditions.

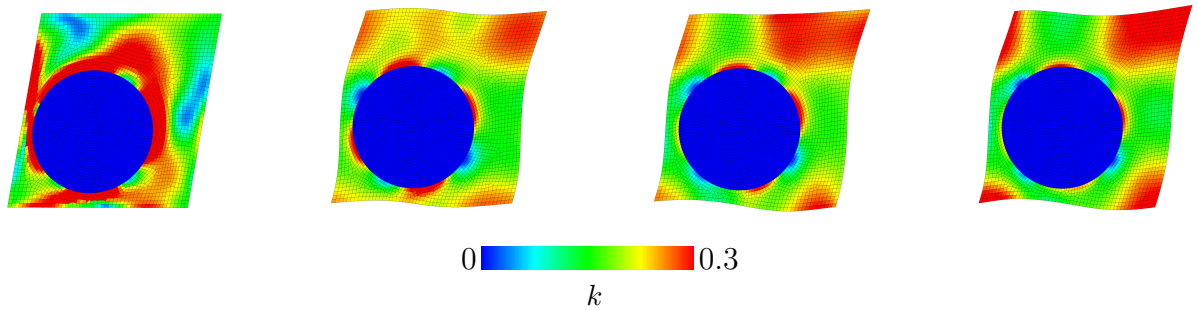

(e) Mesoscale equivalent plastic strain plot after 50 s. From *left* to *right* LN, PR, WK3, UF boundary conditions.

Figure 6.15: Results from the plane quadratic plate multi-scale simulations with the eccentric circular inclusion RVE. The maximum displacement is prescribed after 50 s. (a) Macroscale reaction force vs. time plot. (b) Macroscale von Mises stress plot and reaction forces after 50 s. Mesoscale plots with (c) the boundary node forces, (d) von Mises stresses and (e) equivalent plastic strains after 50 s.

chosen to be $\Delta t = 100\,\text{ms}$ and the analysis ends at $T = 100\,\text{s}$ in order to be able to observe relaxation effects due to the visco-plastic character of the material model at RVE level. As depicted in Fig. 6.8(b), the macro-scale configuration is irregularly discretised by four bi-linear quadrilateral elements where the same RVE at each integration point is used for each boundary condition benchmark series. For this purpose, two different RVEs are considered so that in total six different series of boundary condition benchmarks are carried out – three different loading velocities and two different RVEs. The first RVE considered is depicted in Fig. 6.9. The RVE domain is quadratic width an edge of unit length and a centric inclusion with $r = 0.25$, cf. Fig. 6.9(a). The matrix is considered to be thermo-viscoplastic, cf. model parameters for Co in Tables 6.1 and 6.2, whereas the inclusion is assumed to be thermo-elastic, cf. model parameters for WC in Table 6.1. The second RVE is identical to the one considered in the previous example in Section 6.3.2, an eccentric inclusion with a radius of $r = 0.33$ unit length, cf. Fig. 6.5. Within each of these six benchmark simulation series, four different settings of boundary conditions are investigated, i.e., LN, PR, weak periodic boundary conditions with three equidistantly distributed boundary flux nodes (WK3) as well as UF boundary conditions. Hence, a total of 24 simulations each with 1000 macro-scale load steps have been carried out on 2.4 GHz Intel Xeon E5-2640v4 CPUs, whereby four physical cores have been used for each simulation, see Chapter 5 for further details regarding the parallelised implementation. The computation time for one single simulation was approximately 1 to 2 days.

In Figs. 6.10 to 6.12 the results of the two-scale benchmark simulations with the centric inclusion RVE, cf. Fig. 6.9, are shown and in Figs. 6.13 to 6.15 the results of the benchmark simulations with the eccentric inclusion RVE, cf. Fig. 6.5 are depicted. Figs. 6.10(a), 6.11(a), 6.12(a), 6.13(a), 6.14(a) and 6.15(a) show the norm of the integrated reaction force at the upper edge plotted over time. It is observed that the reaction force increases nonlinearly until the maximum prescribed displacement is reached. After this point in time, the prescribed displacements remain constant and relaxation is observed in the macro-scale reaction force plots. Due to the deformation rate dependent material model, faster loading velocities show higher macro-scale reaction forces. The slower the loading velocity is chosen, the lower the observed macro-scale reaction force is. As expected, LN boundary conditions yield the stiffest effective material response while UF/WK2 boundary conditions show the weakest response. In the case of the centric inclusion RVE, cf. Figs. 6.10(a), 6.11(a) and 6.12(a), the effective responses of PR as well as WK3 boundary conditions remarkably do indeed coincide, whereas in the case of the eccentric inclusion, cf. Figs. 6.13(a), 6.14(a) and 6.15(a), the reaction force of the WK3 boundary condition simulations lies somewhere between the PR and UF/WK2 results. Hence, WK3 boundary conditions show a weaker effective behaviour than PR boundary conditions which is generally expected. The reason for coinciding effective behaviour of PR as well as of WK3 boundary conditions in the case of the centric inclusion might be that the respective third constraint node lies on the middle of the respective RVE boundary, and that therefore both additional constraint nodes lie on the centre lines of

the RVE with centric inclusion. The location of the constraint nodes is analogous to Fig. 6.4(d).

Figs. 6.10(b), 6.11(b), 6.12(b), 6.13(b), 6.14(b) and 6.15(b) show macro-scale von Mises stress plots on a deformed mesh at the point in time when the maximum prescribed displacement is reached, thus after 10 s, 30 s or respectively 50 s. Furthermore, the reaction force vectors are shown. The plots are in line with the reaction force vs. time plots, as the plots show the highest von Mises stress values for LN boundary conditions at the meso-scale and the lowest values for UF boundary conditions at the meso-scale. In the case of the centric circular inclusion RVE, cf. Figs. 6.10(b), 6.11(b) and 6.12(b), the plots related to PR and WK3 boundary conditions look identical, whereas in the case of the eccentric circular inclusion RVE, cf. Figs. 6.13(b), 6.14(b) and 6.15(b), the PR simulations show higher von Mises stresses than the WK3 simulations. Obviously, the macro-scale boundary value problem shows the intended inhomogeneous behaviour, so that all underlying RVEs considered undergo different loading paths. To further investigate meso-scale results we highlight plots referred to the integration point which is located closest to the right and top corner node of the macro-scale domain.

In Figs. 6.10(c), 6.11(c), 6.12(c), 6.13(c), 6.14(c) and 6.15(c), the boundary node forces of the RVE are shown for the different meso-scale boundary conditions after 10 s, 30 s and 50 s, depending on the loading velocity. As before in the first example, the highest reaction force values are observed in the case of LN boundary conditions whereas, the PR, WK3 and UF setups show lower maximum values. In the case of the centric inclusion RVE, cf. Figs. 6.10(c), 6.11(c) and 6.12(c), the reaction force curves of the WK3 and PR boundary conditions coincide and therefore approve the previously mentioned observation of identical von Mises stress plots. Figs. 6.10(d), 6.11(d), 6.12(d), 6.13(d), 6.14(d) and 6.15(d) as well as Figs. 6.10(e), 6.11(e), 6.12(e), 6.13(e), 6.14(e) and 6.15(e) show plots of the von Mises stresses and the hardening variable k on the deformed mesh of the RVE. In the case of LN boundary conditions the von Mises stresses show the highest values as expected, and the hardening variable evolves in particular around the inclusion. In the case of PR, WK3 and UF boundary conditions at the meso-scale, the observed von Mises stress values are lower compared to LN. As expected, it is furthermore observed that PR boundary conditions are – in the case of the eccentric inclusion – stiffer than WK3 which, moreover, are stiffer than UF boundary conditions. In the case of the centric inclusion, the von Mises stress and hardening variable plots of PR and WK3 boundary conditions agree with each other which is in line with the other results discussed above. In contrast to the behaviour of the LN setups, the plastic strain tends to evolve in the corners of the RVE for PR, WK3 and UF boundary conditions.

6.3.3 Multi-scale quenching simulation

The third example highlights the expansion of the two-dimensional quenching simulation discussed in [24] to the three-dimensional case. Experimental investigations of HVOF spraying processes for the coating of curved steel components at LWT, TU Dortmund,

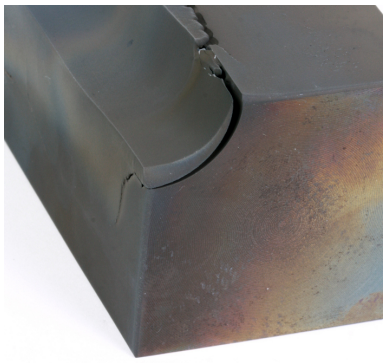

(a) Delamination of a WC-Co coating from a steel radius. The sample is kindly provided by LWT, TU Dortmund.

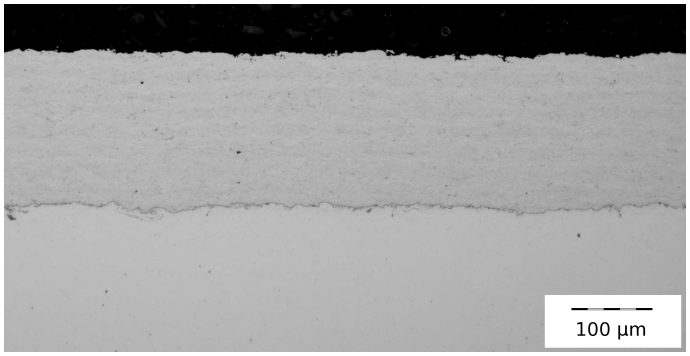

(b) Polished micrograph section of a WC-Co coating (top) with characteristic layers on steel substrate (bottom). The sample is kindly provided by LWT, TU Dortmund.

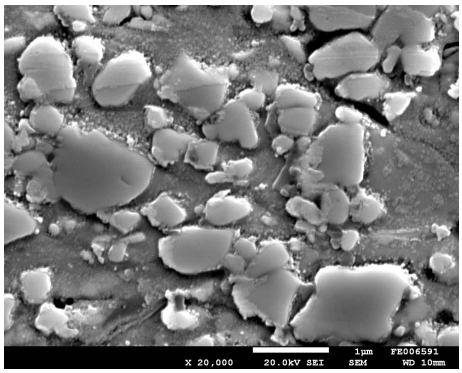

(c) Electron micrograph of WC particles inside of a Co matrix. The sample is kindly provided by LWT, TU Dortmund.

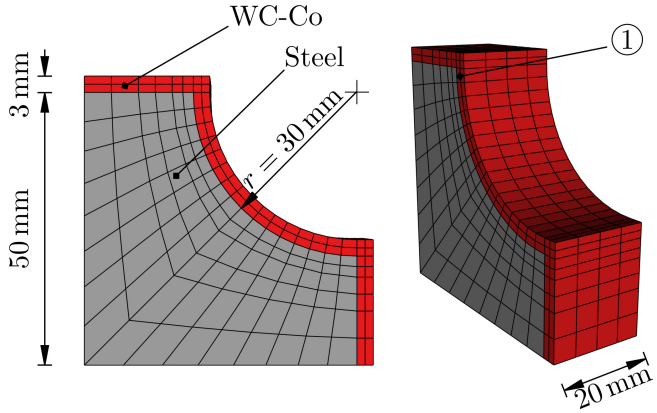

(d) Dimensions and discretisation of the steel radius (gray) which is coated by HVOF spraying with WC-Co (red) and subsequently quenched.

Figure 6.16: (a) Delamination from a WC-Co coating from a steel radius. (b) Polished micrograph section of a characteristic WC-Co coating with layers of multiple HVOF gun passovers (top) on steel substrate (bottom). (c) Electron micrograph of WC particles embedded into an Co matrix. (d) Dimensions and discretisation of the steel radius (gray) which is coated by HVOF spraying with WC-Co (red) and subsequently quenched. The samples are kindly provided by LWT, TU Dortmund.

have shown, that delamination of the produced coating can occur during quenching after the coating procedure, cf. Fig. 6.16(a). A possible explanation for this behaviour could be the residual stresses which arise while the coating as well as the substrate are cooling down. A closer inspection of HVOF coatings by means of a metallographic microscope reveals the heterogeneous nature of such coatings, cf. Fig. 6.16(b), which characteristically consist of multiple coating layers as a result from multiple HVOF gun passovers. An even closer look to the structure of the coating with the help of a scanning electron microscope, cf. Fig. 6.16(c), shows the single sharp edged WC particles which are embedded into the Co matrix. In order to investigate the quenching by means of a finite element simulation, the proposed FE^2-framework is applied to the initial

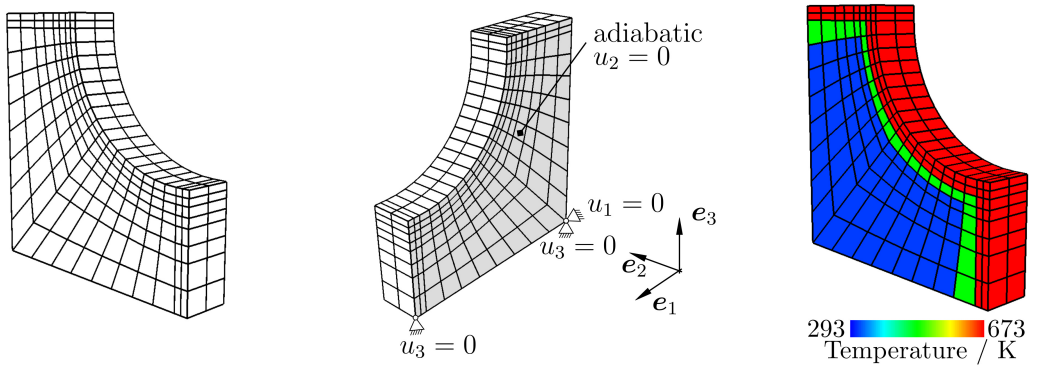

(a) Half specimen. (b) Boundary conditions. (c) Initial temperature.

Figure 6.17: The discretisation of the steel radius is (a) halved in order to reduce computation time. (b) Symmetry boundary conditions are applied. Within the gray plane, the displacements are therefore restricted in 2−direction and adiabatic (homogeneous Neumann) boundary conditions are applied for the temperature field. (c) The steel substrate has an initial temperature of 293 K, the WC-Co coating has an initial temperature of 673 K.

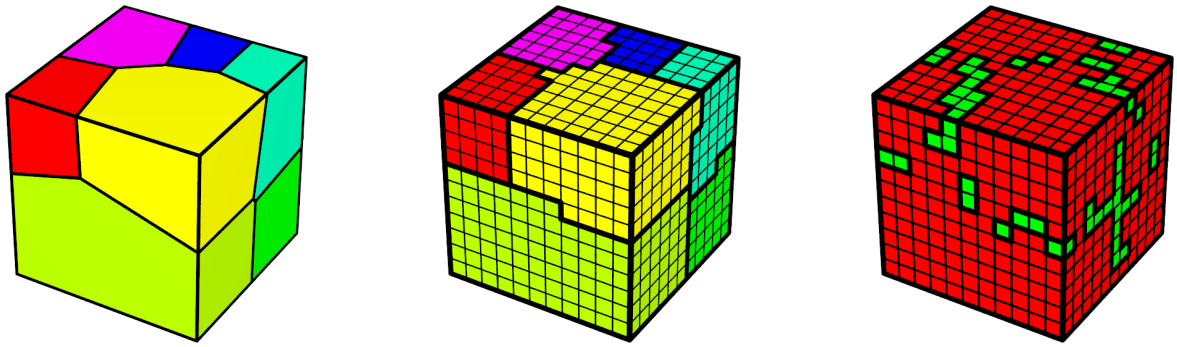

(a) Neper generated grains. (b) Brick element mesh. (c) Processed mesh.

Figure 6.18: Artificially generated RVE which consists of (a) eight grains generated with Neper, [137]. The grains are (b) discretised by 1331 linear brick elements. (c) The mesh is processed in order to meet the volume percentage of WC (red) and Co (green).

boundary value problem depicted in Fig. 6.16(d). The steel substrate is considered to be a 50 mm × 50 mm × 20 mm block with a concavity with a radius of 30 mm and the coating is chosen to be 3 mm thick. In order to reduce the computation time, only half of the specimen is discretised, where the symmetry of the initial boundary value problem is used, cf. Fig. 6.16(d) as well as Fig. 6.17(a) and Fig. 6.17(b). With this at hand, the steel substrate is modelled by 192 linear brick elements, whereby the material is assumed to show thermo-elastic behaviour. The model parameters are taken from Table 6.1. The coating is discretised by 112 linear brick elements, the constitutive relations of which are determined by the FE^2 approach proposed based on the WC-Co RVE-related meso-structure specified as this work proceeds. The symmetry conditions are included via appropriate boundary conditions which are depicted in Fig. 6.17(b). Within the gray

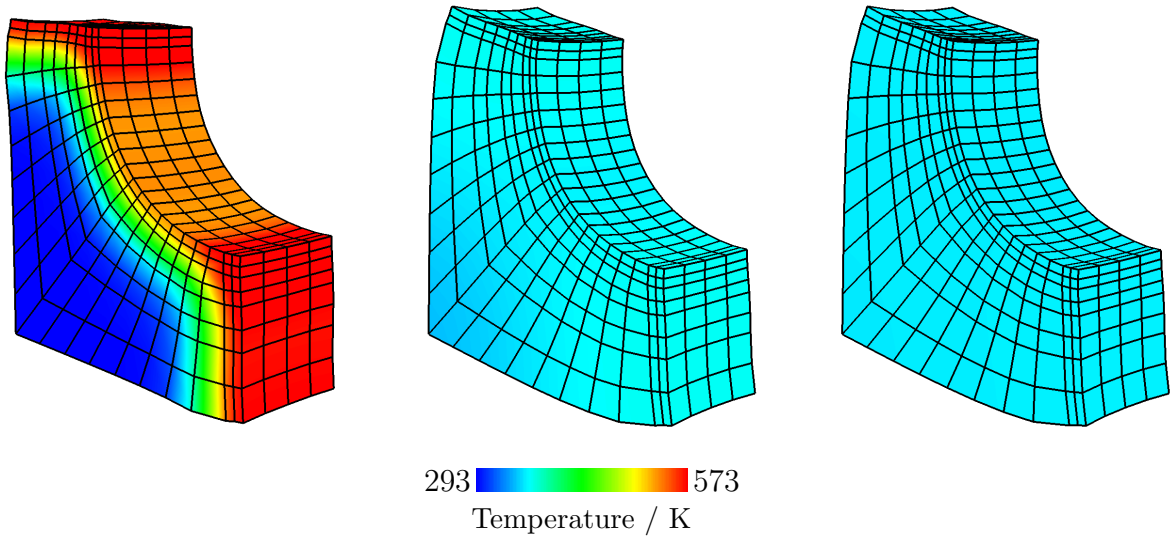

(a) Macro-scale temperature plots of the coated radius after, from *left* to *right*, 0.5 s, 17.5 s and 35 s.

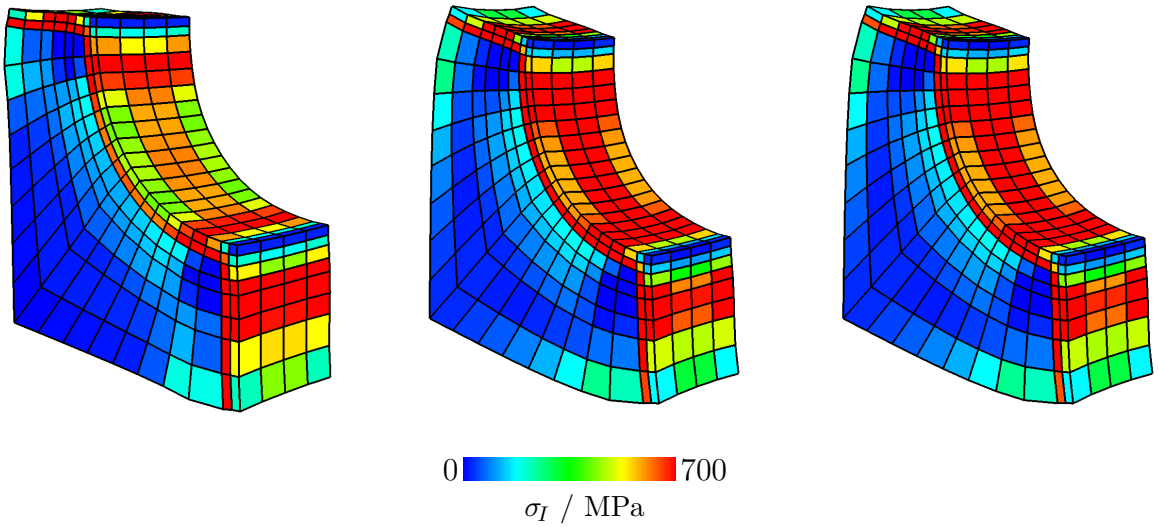

(b) Macro-scale first principal Cauchy stress plots of the coated radius after, from *left* to *right*, 0.5 s, 17.5 s and 35 s.

Figure 6.19: Macro-scale plots of the coated radius. The displacements are scaled by factor 50.

plane, the displacements are restricted in $\boldsymbol{e}_2-$direction and the temperature field is subject to homogeneous Neumann boundary conditions in order to model an adiabatic plane. The bearing symbols visualise the remaining restrictions of the displacements such that the mechanical part of the initial boundary problem represents a statically determined system. The initial temperature of all nodes which belong to the coating is

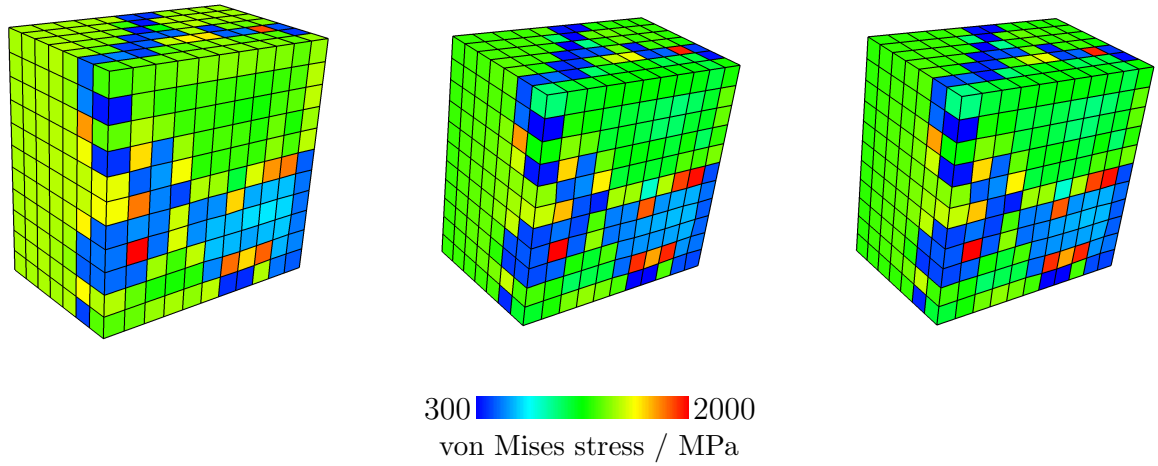

(a) Meso-scale von Mises stress plot of the RVE at position 1 after, from *left* to *right*, 0.5 s, 17.5 s and 35 s.

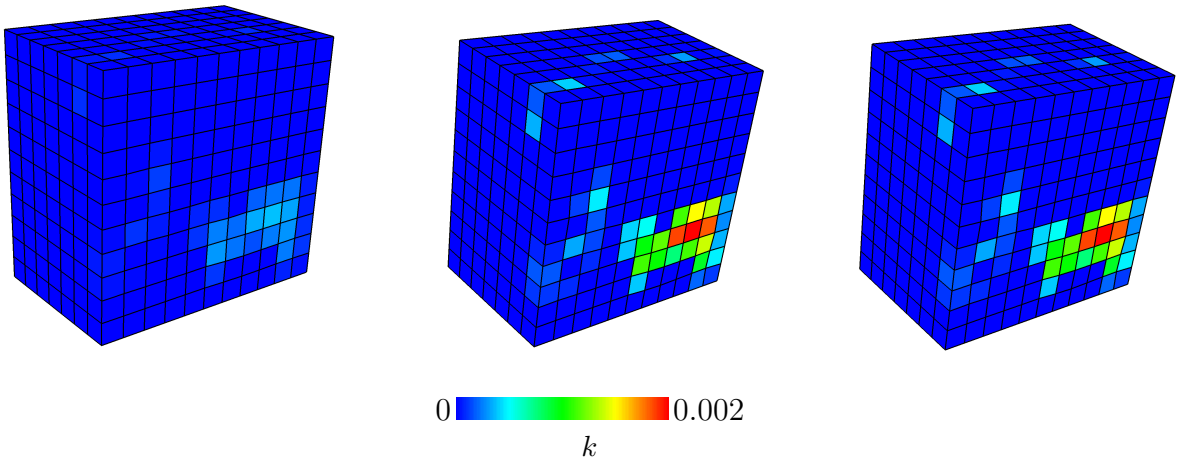

(b) Meso-scale plot of the distribution of the hardening variable within RVE at position 1 after, from *left* to *right*, 0.5 s, 17.5 s and 35 s.

Figure 6.20: Meso-scale plots of the RVE at position 1. The displacements are scaled by factor 50.

673 K, whereas the substrate temperature is 293 K which also coincides with the ambient temperature θ_∞, cf. Fig. 6.17(c). To capture quenching by convective heat transfer, the film condition coefficient is set to $h_\mathrm{c} = 1 \times 10^{-5}\,\mathrm{W\,K^{-1}\,mm^{-2}}$, cf. Eq. (6.65), and the whole boundary, except the gray plane in Fig. 6.17(b), is discretised by four-noded quadrilateral surface elements. While the steel substrate is modelled by means of a single scale material model, the effective behaviour of the WC-Co coating is captured with the help of an artificially generated RVE which represents the hard material consisting of 88 wt.-% tungsten carbide and 12 wt.-% cobalt. In a first step, an artificial grain structure is generated with the help of the software Neper [137], cf. Fig. 6.18(a), which

is subsequently discretised by linear brick elements, cf. Fig. 6.18(b). In order to end up with a mesh which represents large tungsten carbide particles glued together with the cobalt matrix, the "grains" are interpreted as tungsten carbide. Subsequently, the elements at the "grain boundaries" are identified and redefined to represent cobalt. This procedure is repeated until the volume percentage of the two phases is approximately met – here, 12 wt.-% cobalt correspond to approximately 19.4 vol.-%. For more sophisticated particle reinforced RVE generation algorithms, the reader is referred to the work of Fritzen and Böhlke [59]. The finally obtained RVE is depicted in Fig. 6.18(c). As in the previous examples, cobalt is assumed to be thermo-viscoplastic, tungsten carbide to be thermo-elastic, cf. Tables 6.1 and 6.2 for the model parameters. For postprocessing purposes, the RVE results of position 1, cf. Fig. 6.16(d), are stored. The RVE is subject to LN boundary conditions. The simulation is carried out for 35 s with a constant time increment of $\Delta t = 0.5$ s. For postprocessing, the obtained results are mirrored at the symmetry plane in order to show the complete boundary volume problem which has been solved.

The simulated macro-scale temperature field is depicted in Fig. 6.19(a) for different points in time, after 0.5 s, 17.5 s and 35 s. The heat is on the one hand conducted into the steel substrate which does heat up until after 35 s when a quasi homogeneous temperature distribution is reached in the coated steel radius. On the other hand, heat is convected out of the coating as well as out of the heated steel substrate via the free surfaces. Due to the inhomogeneous initial temperature distribution as well as the different thermo-mechanical material parameters, residual stresses occur during quenching of the coated radius. The simulated first principal Cauchy stress σ_I is shown in Fig. 6.19(b). Note, that the residual stresses are induced by the inhomogeneous quenching only, since only essential mechanical boundary conditions are used which do not prevent the modelled body from deforming. Although the chosen model is coarsely discretised, the basic result of the analysis is that the highest principal Cauchy stress values occur at the edges of the coated steel radius inside the coating near the interface where delamination is initially observed in the experiment, cf. Fig. 6.16(a). During cooling, the first principal Cauchy stress increases within the coating. Within the steel substrate, the first principal Cauchy stress shows higher values near the interface between substrate and coating. The effective material behaviour of the coating is determined by the RVE shown in Fig. 6.18(c). The von Mises stress as well as the distribution of the hardening variable within the RVE at position 1, cf. Fig. 6.16(d), are depicted in Fig. 6.20 for the same three points in time as the previously shown macro-scale results, i.e. after 0.5 s, 17.5 s and 35 s. The von Mises stress distribution results from shear deformations induced by the different thermal expansion behaviour of Co and WC on the one hand and the different properties and initial temperatures of the substrate and the coating on the other. For the RVE at position 1 it is observable in Fig. 6.20(a) that the von Mises stress decreases within the bulk of the WC particles, whereas it increases near the interface to Co. Within the Co phase, comparatively low von Mises stress values are observed. In Fig. 6.20(b), the evolution of the hardening variable k is shown in the Co phase. Beginning with the first

time step, the hardening variable continuously increases in the inelastic zone. The rather low absolute value of the hardening variable results from the relatively small induced shear deformation.

7 Concluding remarks

In this thesis, research results are presented which address two different objectives of Project B6 of the expired SFB 708: The development of a simulation framework for thermal spraying processes, cf. Chapters 3 and 4, as well as the development of a non-linear two-scale framework for thermo-mechanically coupled boundary value problems, cf. Chapters 5 and 6. Both frameworks are implemented as thermodynamically consistent finite element frameworks based on fundamental balance equations summarised in **Chapter 2** which therefore collocates the continuum thermodynamical basis of this work.

7.1 Modelling of thermal spraying

With respect to the simulation of thermal spraying processes, **Chapter 3** presents a novel integrated simulation approach for the computation of the workpiece temperature development during thermal spraying. In collaboration with Dr. Thomas Wiederkehr who carried out the re-implementation of the developed finite element programme into his geometric modelling tool, [190], the newly created framework is suited for large and arbitrarily complex shaped components. As its core, a thermodynamically consistent non-linear rigid heat conductor based on the balance of energy in form of the temperature rate equation is employed. The balance equation obtained is transformed into its weak form that represents the underlying equation of the presented non-linear finite-element-framework, re-implemented into the C++–based GPGPU framework. The material parameters are adjusted to experimental data by fitting suitable functions, and the parameters of the Robin boundary conditions are chosen in order to model realistic heat transfer by means of convection as well as radiation. The presented simulations of a complex shaped deep drawing tool demonstrate a possible field of application for the novel software tool.

Subsequently, in **Chapter 4**, the finite element framework of a non-linear rigid heat conductor mentioned above is further extended to a novel finite element tool for the simulation of material deposition of hot particles which therefore additionally contribute to the evolution of the workpiece temperature during thermal spraying. The key aspect of this chapter is the novel mass deposition ansatz where internal heat sources are intro-

duced in order to ensure conservation of energy in the framework of continuous Galerkin finite element methods. With this at hand, the proposed simulation approach can be implemented in established continuous Galerkin finite element codes. A set of example simulations demonstrates the numerical application of the implemented framework. The material parameters involved have been fitted to experimental data, and the coefficients for convective and radiative heat transfer have been chosen to model conditions close to reality. The examples indicate that the time discretisation noticeably influences the solution of the temperature field near the point in time of mass deposition. For non-linear simulations, comparatively small errors occur in the value of the total energy. A possible reason might be the use of the Backward Euler time integration scheme. Nonetheless, in summary the present work contributes an easy-to-implement novel finite element approach for a non-linear rigid heat conductor with mass deposition.

A possible scenario for future work might be the use of the developed thermal spraying simulation framework within the optimisation software developed by Kout and Müller [97] in order to be able to optimise the thermal spraying process with respect to temperature related goal functions. Such a physics based optimisation framework would represent a further step forward in terms of the vision of SFB 708. Another aspect of future research is the extension towards a thermo-mechanically coupled framework which will enable the analysis of residual stresses and damage due to thermal spraying as discussed in, e.g., Boehmer et al. [28] or Fagerstrom and Larsson [52]. Depending on the considered materials, the modelling of phase transformations should be taken into account. With respect to energy consistency of the mass deposition framework, the time integration scheme could be modified in future work, e.g., to a Galerkin-based time integrator. In the field of elastodynamics, i.e., energy-momentum consistent time integration schemes are applied, cf. Gross and Betsch [67]. In addition, experimental investigations for calibration, verification and validation should be made so that reliable simulations can be carried out.

7.2 Homogenisation of thermo-mechanical problems

The emphasis of this thesis is on computational homogenisation of thermo-mechanical problems. In **Chapter 5**, a thermo-mechanically fully coupled two-scale finite element framework in monolithic structure is presented. The developed framework is applicable for the simulation of inelastic material behaviour in a geometrically linearised setting. An established framework from Sengupta et al. [157] is used and extended with a thermodynamically consistent homogenisation scheme proposed by Temizer and Wriggers [172] for non-linear constitutive models. The implementation is carried out in a tailored C++-Code along with the libraries Eigen, SparseSuite and OpenBLAS. Robin type boundary conditions are applied in order to model convective heat transfer via the boundary. Furthermore, this chapter proposes a thermo-viscoplastic material model with non-linear thermal softening. The capabilities of the developed two-scale finite

element framework are shown by means of various finite element simulations. Thereby, the advantage of explicitly enforcing the macroscopic temperature at the meso-scale, even for non-linear geometrically linearised problems, is discussed. Further simulations show the performance of the two-scale implementation compared with equivalent single scale simulations. Finally, a simulation of the quenching of steel radius coated by tungsten-carbide-cobalt is presented.

The two-scale finite element framework mentioned above is extended to a geometrically non-linear two-scale framework in **Chapter 6**. The novel key contribution of this chapter is the development of weak micro-periodic boundary conditions for thermo-mechanically coupled problems at the lower scale which represent the extension of the weak micro-periodicity concept for mechanical problems of Larsson et al. [104]. The weak micro-periodicity constraint is enforced by means of traction and heat flux like Lagrange multipliers which are allowed to be discretised independently from the displacement problem as well as the temperature problem. The proposed boundary conditions are implemented into the thermo-mechanically coupled FE^2-framework for finite deformations, and descriptive numerical examples show the performance of the developed boundary conditions compared to boundary conditions which are established in Hill–Mandel condition based homogenisation frameworks. For demonstration purposes, a thermo-viscoplastic material model for large deformations is derived and implemented. It is shown that the thermo-mechanical weak-periodicity constraints result in a response in between strong periodic boundary conditions and uniform traction/heat flux boundary conditions.

Future work could include the extension of the presented finite element framework with the coating simulation framework proposed in Chapter 4 by means of the presented thermo-mechanically coupled two-scale framework. In this context, the consideration of interface elements between the substrate and the applied coating should be taken into account in order to model possible delamination processes of the coating. In addition, more advanced constitutive models taking account of temperature dependency of the heat capacity, $c(\theta)$, or the viscous behaviour, $\eta(\theta)$, shall be considered. This will render the possibility of capturing the residual stress state based on homogenised non-linear material behaviour during the coating process itself. Therefore, parameter identification should be carried out with the help of appropriate experimental investigations, followed by a validation procedure. However, in the case of large thermo-mechanically coupled coating simulations, a full FE^2 coating simulation might be prohibitive computationally expensive. In this connection, the presented two-scale framework could be used in order to carry out virtual experiments, the results of which may subsequently be applied to adjust a phenomenological constitutive model for single scale simulations. Further reasonable extensions of the presented framework are, amongst others, a different algorithmic treatment of boundary conditions at RVE level, cf. Javili et al. [90], or the application of the Irving-Kirkwood procedure, cf. Mercer et al. [114] for the purely mechanical treatment. As discussed, the presented framework does not account for additional regularisation techniques with regard to thermal softening which might lead to mesh dependent simulation results for initial boundary value problems. In future work,

an additional field analogous to gradient-enhanced plasticity formulations as proposed by [134, 187] may be introduced to overcome this problem.

A Implementation of the finite element method

In this appendix, the derivation of a thermo-mechanically coupled finite element framework with monolithic structure is summarised. Even though a subset of the following equations is already included within the previous chapters, the entire derivation is briefly discussed for the readers convenience. However, some details and especially the fundamental mathematical basis of the finite element method are omitted in order to keep the content of this appendix concise. For a broad overview of the finite element method, there exist numerous references throughout the literature. Amongst others, the interested reader is referred to the textbooks of Bonet and Wood [29], Belytschko et al. [13], Bathe [11], Hughes [83], De Borst et al. [44], Wriggers [191] as well as Zienkiewicz et al. [192]. In Appendix A.1, the derivation of the framework is summarised, followed by its consistent linearisation outlined in Appendix A.2.

A.1 Thermo-mechanically coupled finite element framework

The thermo-mechanically coupled finite element framework is based on the balance equations

$$\rho_0 \, \ddot{\boldsymbol{\varphi}} = \nabla_{\boldsymbol{X}} \cdot \boldsymbol{P} + \rho_0 \, \boldsymbol{b} \, , \tag{A.1}$$

$$c_0 \, \dot{\theta} = \theta \, \frac{\partial \boldsymbol{P}}{\partial \theta} : \dot{\boldsymbol{F}} + \rho_0 \, r - \nabla_{\boldsymbol{X}} \cdot \boldsymbol{Q} + \left[\boldsymbol{\kappa} - \theta \, \frac{\partial \boldsymbol{\kappa}}{\partial \theta} \right] \circ \dot{\boldsymbol{k}} \, , \tag{A.2}$$

which are already introduced in Chapter 2 and summarised in Eqs. (2.102) and (2.103) as well as in Box 2.1. The first of the above equations is the balance of linear momentum and the second equation is denoted as the energy balance represented by the rate of the temperature equation. Weighting the strong forms, Eqs. (A.1) and (A.2), of the balance equations with test functions — namely the virtual displacements $\delta\boldsymbol{\varphi}$ and virtual

temperatures $\delta\theta$ — which have to be (kinematically) admissible yield, after integration over the reference domain $\mathcal{B}_0$, the global weak forms

$$0 = \int_{\mathcal{B}_0} \delta\boldsymbol{\varphi} \cdot \Big[\nabla_{\boldsymbol{X}} \cdot \boldsymbol{P} + \rho_0 \, [\, \boldsymbol{b} - \ddot{\boldsymbol{\varphi}} \,] \Big] \, \mathrm{d}V \tag{A.3}$$

$$0 = \int_{\mathcal{B}_0} \delta\theta \Big[- \nabla_{\boldsymbol{X}} \cdot \boldsymbol{Q} + \hat{r}_0 - c_0 \, \dot{\theta} \Big] \, \mathrm{d}V \tag{A.4}$$

wherein the abbreviation

$$\hat{r}_0 = \rho_0 \, r + \theta \, \frac{\partial \boldsymbol{P}}{\partial \theta} : \dot{\boldsymbol{F}} + \left[\boldsymbol{\kappa} - \theta \, \frac{\partial \boldsymbol{\kappa}}{\partial \theta} \right] \circ \dot{\boldsymbol{k}} \, , \tag{A.5}$$

is used. Integration by parts of the divergence terms yields

$$\int_{\mathcal{B}_0} \delta\boldsymbol{\varphi} \cdot [\, \nabla_{\boldsymbol{X}} \cdot \boldsymbol{P} \,] \, \mathrm{d}V = \int_{\mathcal{B}_0} \Big[\, \nabla_{\boldsymbol{X}} \cdot [\, \delta\boldsymbol{\varphi} \cdot \boldsymbol{P} \,] - \nabla_{\boldsymbol{X}} \, \delta\boldsymbol{\varphi} : \boldsymbol{P} \Big] \, \mathrm{d}V \, , \tag{A.6}$$

$$\int_{\mathcal{B}_0} \delta\theta \; \nabla_{\boldsymbol{X}} \cdot \boldsymbol{Q} \, \mathrm{d}V = \int_{\mathcal{B}_0} \Big[\, \nabla_{\boldsymbol{X}} \cdot [\, \delta\theta \, \boldsymbol{Q} \,] - \nabla_{\boldsymbol{X}} \, \delta\theta \cdot \boldsymbol{Q} \Big] \, \mathrm{d}V \, , \tag{A.7}$$

where the Gauß theorem can be applied on the divergence terms of the right hand sides of the above equations

$$\int_{\mathcal{B}_0} \nabla_{\boldsymbol{X}} \cdot [\, \delta\boldsymbol{\varphi} \cdot \boldsymbol{P} \,] \, \mathrm{d}V = \int_{\partial\mathcal{B}_0} \delta\boldsymbol{\varphi} \cdot \boldsymbol{P} \cdot \boldsymbol{N} \, \mathrm{d}A = \int_{\partial\mathcal{B}_0^{\boldsymbol{t}}} \delta\boldsymbol{\varphi} \cdot \bar{\boldsymbol{t}}_0 \, \mathrm{d}A \, , \tag{A.8}$$

$$\int_{\mathcal{B}_0} \nabla_{\boldsymbol{X}} \cdot [\, \delta\theta \, \boldsymbol{Q} \,] \, \mathrm{d}V = \int_{\partial\mathcal{B}_0} \delta\theta \, \boldsymbol{Q} \cdot \boldsymbol{N} \, \mathrm{d}A = \int_{\partial\mathcal{B}_0^{q}} \delta\theta \, \bar{Q} \, \mathrm{d}A \, . \tag{A.9}$$

With these equations at hand, Eqs. (A.3) and (A.4) can be rewritten as

$$\begin{aligned} \mathrm{w}^{\boldsymbol{\varphi}} = & \int_{\mathcal{B}_0} \rho_0 \, \delta\boldsymbol{\varphi} \cdot \ddot{\boldsymbol{\varphi}} \, \mathrm{d}V + \int_{\mathcal{B}_0} \nabla_{\boldsymbol{X}} \, \delta\boldsymbol{\varphi} : \boldsymbol{P} \, \mathrm{d}V \\ & - \int_{\mathcal{B}_0} \rho_0 \, \delta\boldsymbol{\varphi} \cdot \boldsymbol{b} \, \mathrm{d}V - \int_{\partial\mathcal{B}_0^{\boldsymbol{t}}} \delta\boldsymbol{\varphi} \cdot \bar{\boldsymbol{t}}_0 \, \mathrm{d}A = 0 \, , \end{aligned} \tag{A.10}$$

as well as

$$\begin{aligned} \mathrm{w}^{\theta} = & \int_{\mathcal{B}_0} c_0 \, \delta\theta \, \dot{\theta} \, \mathrm{d}V + \int_{\mathcal{B}_0} - \nabla_{\boldsymbol{X}} \, \delta\theta \cdot \boldsymbol{Q} \, \mathrm{d}V \\ & - \int_{\mathcal{B}_0} \delta\theta \, \hat{r}_0 \, \mathrm{d}V - \int_{\partial\mathcal{B}_0^q} \delta\theta \, \bar{Q} \, \mathrm{d}A = 0 \, . \end{aligned} \tag{A.11}$$

In order to compute the global integral terms within the above equations, the reference domain $\mathcal{B}_0$ is approximated by n_{el} finite elements $\mathcal{B}_0^e$

$$\mathcal{B}_0 \approx \bigcup_{e=1}^{n_{el}} \mathcal{B}_0^e \, , \tag{A.12}$$

such that the Eqs. (A.10) and (A.11) are written as sums over all element integrals

$$\begin{aligned} \mathrm{w}^{\boldsymbol{\varphi}} \approx \sum_{e=1}^{n_{el}} \Bigg[& \int_{\mathcal{B}_0^e} \rho_0 \, \delta\boldsymbol{\varphi} \cdot \ddot{\boldsymbol{\varphi}} \, \mathrm{d}V + \int_{\mathcal{B}_0^e} \nabla_{\boldsymbol{X}} \, \delta\boldsymbol{\varphi} : \boldsymbol{P} \, \mathrm{d}V \\ & - \int_{\mathcal{B}_0^e} \rho_0 \, \delta\boldsymbol{\varphi} \cdot \boldsymbol{b} \, \mathrm{d}V - \int_{\partial\mathcal{B}_0^{e\,\boldsymbol{t}}} \delta\boldsymbol{\varphi} \cdot \bar{\boldsymbol{t}}_0 \, \mathrm{d}A \Bigg] = 0 \, , \end{aligned} \tag{A.13}$$

$$\begin{aligned} \mathrm{w}^{\theta} \approx \sum_{e=1}^{n_{el}} \Bigg[& \int_{\mathcal{B}_0^e} c_0 \, \delta\theta \, \dot{\theta} \, \mathrm{d}V + \int_{\mathcal{B}_0^e} - \nabla_{\boldsymbol{X}} \, \delta\theta \cdot \boldsymbol{Q} \, \mathrm{d}V \\ & - \int_{\mathcal{B}_0^e} \delta\theta \, \hat{r}_0 \, \mathrm{d}V - \int_{\partial\mathcal{B}_0^{e\,q}} \delta\theta \, \bar{Q} \, \mathrm{d}A \Bigg] = 0 \, . \end{aligned} \tag{A.14}$$

Furthermore, the reference placements $\boldsymbol{X}^e$ of the element and the current placements $\boldsymbol{x}^e = \boldsymbol{\varphi}^e$ of the element are approximated by

$$\boldsymbol{X}^e(\boldsymbol{\xi}) = \sum_{A=1}^{n_{en}} \boldsymbol{X}^{e\,A} \, N^A(\boldsymbol{\xi}) \, , \tag{A.15}$$

$$\boldsymbol{\varphi}^e(\boldsymbol{\xi}) = \sum_{A=1}^{n_{en}} \boldsymbol{\varphi}^{e\,A} \, N^A(\boldsymbol{\xi}) \, , \tag{A.16}$$

where $\boldsymbol{X}^{e\,A}$ represents the reference position of element node A, $\boldsymbol{\varphi}^{e\,A}$ is the current position of element node A and $N^A(\boldsymbol{\xi})$ is the shape function belonging to element node A. The shape functions are defined on the master element domain $\mathcal{B}_{\boldsymbol{\xi}}$, so that $\boldsymbol{\xi} \in \mathcal{B}_{\boldsymbol{\xi}}$. In the same fashion, the temperature θ^e of the element is approximated by

$$\theta^e(\boldsymbol{\xi}) = \sum_{C=1}^{n_{en}} \theta^{e\,C}\, N^C(\boldsymbol{\xi}) \,, \tag{A.17}$$

where formally a different set of element nodes C is introduced to indicate that different shape functions $N^C(\boldsymbol{\xi})$ can be chosen. In order to deal with the gradients in physical space, the element Jacobian

$$\boldsymbol{J}_0^e = \frac{\partial \boldsymbol{X}^e}{\partial \boldsymbol{\xi}} = \sum_{A=1}^{n_{en}} \boldsymbol{X}^{e\,A} \otimes \nabla_{\boldsymbol{\xi}}\, N^A(\boldsymbol{\xi}) \,, \tag{A.18}$$

is determined and the chain rule is applied such that the material gradient of a quantity $[\bullet]$ reads

$$\nabla_{\boldsymbol{X}}[\bullet] = \nabla_{\boldsymbol{\xi}}[\bullet] \cdot \boldsymbol{J}_0^{e-1} \,. \tag{A.19}$$

With this at hand, the deformation gradient is approximated by

$$\begin{aligned} \boldsymbol{F} \approx \boldsymbol{F}^e = \nabla_{\boldsymbol{X}}\, \boldsymbol{\varphi}^e(\boldsymbol{\xi}) &= \sum_{A=1}^{n_{en}} \boldsymbol{\varphi}^{e\,A} \otimes \nabla_{\boldsymbol{\xi}}\, N^A(\boldsymbol{\xi}) \cdot \boldsymbol{J}_0^{e-1} \\ &= \sum_{A=1}^{n_{en}} \boldsymbol{\varphi}^{e\,A} \otimes \nabla_{\boldsymbol{X}}\, N^A(\boldsymbol{\xi}) \,. \end{aligned} \tag{A.20}$$

Furthermore, the virtual placements $\delta\boldsymbol{\varphi}$, the referential gradient of the virtual placements $\nabla_{\boldsymbol{X}}\, \delta\boldsymbol{\varphi}$, the virtual temperature $\delta\theta$ as well as the referential gradient of the virtual temperature $\nabla_{\boldsymbol{X}}\, \delta\theta$ are now approximated by

$$\delta\boldsymbol{\varphi} \approx \bigcup_{e=1}^{n_{el}} \delta\boldsymbol{\varphi}^e(\boldsymbol{\xi}) \qquad \text{with} \qquad \delta\boldsymbol{\varphi}^e = \sum_{A=1}^{n_{en}} \delta\boldsymbol{\varphi}^{e\,A}\, N^A(\boldsymbol{\xi}) \,, \tag{A.21}$$

$$\nabla_{\boldsymbol{X}}\, \delta\boldsymbol{\varphi} \approx \bigcup_{e=1}^{n_{el}} \nabla_{\boldsymbol{X}}\, \delta\boldsymbol{\varphi}^e(\boldsymbol{\xi}) \quad \text{with} \quad \nabla_{\boldsymbol{X}}\, \delta\boldsymbol{\varphi}^e = \sum_{A=1}^{n_{en}} \delta\boldsymbol{\varphi}^{e\,A} \otimes \nabla_{\boldsymbol{X}}\, N^A(\boldsymbol{\xi}) \,, \tag{A.22}$$

$$\delta\theta \approx \bigcup_{e=1}^{n_{el}} \delta\theta^e(\boldsymbol{\xi}) \qquad \text{with} \qquad \delta\theta^e = \sum_{C=1}^{n_{en}} \delta\theta^{e\,C}\, N^C(\boldsymbol{\xi}) \,, \tag{A.23}$$

$$\nabla_{\boldsymbol{X}}\, \delta\theta \approx \bigcup_{e=1}^{n_{el}} \nabla_{\boldsymbol{X}}\, \delta\theta^e(\boldsymbol{\xi}) \quad \text{with} \quad \nabla_{\boldsymbol{X}}\, \delta\theta^e = \sum_{C=1}^{n_{en}} \delta\theta^{e\,C}\, \nabla_{\boldsymbol{X}}\, N^C(\boldsymbol{\xi}) \,. \tag{A.24}$$

Insertion of the above discretisations into Eqs. (A.13) and (A.14) yields

$$\begin{aligned} \mathrm{w}^{\boldsymbol{\varphi}} \approx \sum_{e=1}^{n_{el}} \sum_{A=1}^{n_{en}} \delta\boldsymbol{\varphi}^{e\,A} \cdot \Bigg[& \int_{\mathcal{B}_0^e} \rho_0\, N^A\, \ddot{\boldsymbol{\varphi}}\, \mathrm{d}V + \int_{\mathcal{B}_0^e} \boldsymbol{P} \cdot \nabla_{\boldsymbol{X}}\, N^A\, \mathrm{d}V \\ & - \int_{\mathcal{B}_0^e} \rho_0\, N^A\, \boldsymbol{b}\, \mathrm{d}V - \int_{\partial\mathcal{B}_0^{e\,\boldsymbol{t}}} N^A\, \bar{\boldsymbol{t}}_0\, \mathrm{d}A \Bigg] = 0 \,, \end{aligned} \tag{A.25}$$

$$\begin{aligned} \mathrm{w}^{\theta} \approx \sum_{e=1}^{n_{el}} \sum_{C=1}^{n_{en}} \delta\theta^{e\,C} \Bigg[& \int_{\mathcal{B}_0^e} c_0\, N^C\, \dot{\theta}\, \mathrm{d}V + \int_{\mathcal{B}_0^e} -\nabla_{\boldsymbol{X}}\, N^C \cdot \boldsymbol{Q}\, \mathrm{d}V \\ & - \int_{\mathcal{B}_0^e} N^C\, \hat{r}_0\, \mathrm{d}V - \int_{\partial\mathcal{B}_0^{e\,q}} N^C\, \bar{Q}\, \mathrm{d}A \Bigg] = 0 \,. \end{aligned} \tag{A.26}$$

The single contributions of the above equations are interpreted as elemental force

$$\boldsymbol{f}_{\mathrm{dyn}}^{\boldsymbol{\varphi}\,e\,A} = \int_{\mathcal{B}_0^e} \rho_0\, N^A\, \ddot{\boldsymbol{\varphi}}\, \mathrm{d}V \,, \tag{A.27}$$

$$\boldsymbol{f}_{\mathrm{int}}^{\boldsymbol{\varphi}\,e\,A} = \int_{\mathcal{B}_0^e} \boldsymbol{P} \cdot \nabla_{\boldsymbol{X}}\, N^A\, \mathrm{d}V \,, \tag{A.28}$$

$$\boldsymbol{f}_{\mathrm{vol}}^{\boldsymbol{\varphi}\,e\,A} = \int_{\mathcal{B}_0^e} \rho_0\, N^A\, \boldsymbol{b}\, \mathrm{d}V \,, \tag{A.29}$$

$$\boldsymbol{f}_{\mathrm{sur}}^{\boldsymbol{\varphi}\,e\,A} = \int_{\partial\mathcal{B}_0^{e\,\boldsymbol{t}}} N^A\, \bar{\boldsymbol{t}}_0\, \mathrm{d}A \,, \tag{A.30}$$

and flux terms

$$f_{\mathrm{dyn}}^{\theta\, e\, C} = \int\limits_{\mathcal{B}_0^e} c_0\, N^C\, \dot{\theta}\, \mathrm{d}V \;, \tag{A.31}$$

$$f_{\mathrm{int}}^{\theta\, e\, C} = \int\limits_{\mathcal{B}_0^e} -\nabla_{\boldsymbol{X}}\, N^C \cdot \boldsymbol{Q}\, \mathrm{d}V \;, \tag{A.32}$$

$$f_{\mathrm{vol}}^{\theta\, e\, C} = \int\limits_{\mathcal{B}_0^e} N^C\, \hat{r}_0\, \mathrm{d}V \;, \tag{A.33}$$

$$f_{\mathrm{sur}}^{\theta\, e\, C} = \int\limits_{\partial\mathcal{B}_0^{e\, q}} N^C\, \bar{Q}\, \mathrm{d}A \;. \tag{A.34}$$

For the implementation in terms of a computer programme, the global degrees of freedom are organised in a vector,

$$\underline{\mathbf{d}} = \left[\boldsymbol{\varphi}_1{}^{\mathrm{t}} \;\; \theta_1 \;\; \boldsymbol{\varphi}_2{}^{\mathrm{t}} \;\; \theta_2 \;\; \ldots \;\; \boldsymbol{\varphi}_{n_{np}}{}^{\mathrm{t}} \;\; \theta_{n_{np}} \right]^{\mathrm{t}} , \tag{A.35}$$

which has to be connected to the elemental degrees of freedom by appropriate matrices $\underline{\underline{\mathbf{L}}}^{\boldsymbol{\varphi}\, e\, A}$ and, respectively, vectors $\underline{\mathbf{l}}^{\theta\, e\, C}$ such that

$$\boldsymbol{\varphi}^{e\, A} = \underline{\mathbf{d}}^{\mathrm{t}} \cdot \left[\underline{\underline{\mathbf{L}}}^{\boldsymbol{\varphi}\, e\, A} \right]^{\mathrm{t}} , \qquad \delta\boldsymbol{\varphi}^{e\, A} = \delta\underline{\mathbf{d}}^{\mathrm{t}} \cdot \left[\underline{\underline{\mathbf{L}}}^{\boldsymbol{\varphi}\, e\, A} \right]^{\mathrm{t}} , \tag{A.36}$$

$$\theta^{e\, C} = \underline{\mathbf{d}}^{\mathrm{t}} \cdot \left[\underline{\mathbf{l}}^{\theta\, e\, C} \right]^{\mathrm{t}} , \qquad \delta\theta^{e\, C} = \delta\underline{\mathbf{d}}^{\mathrm{t}} \cdot \left[\underline{\mathbf{l}}^{\theta\, e\, C} \right]^{\mathrm{t}} . \tag{A.37}$$

Inserting Eqs. (A.36) and (A.37) into Eqs. (A.25) and (A.26), together with Eqs. (A.27) to (A.30) as well as Eqs. (A.31) to (A.34), yields

$$\mathrm{w}^{\boldsymbol{\varphi}} \approx \delta\underline{\mathbf{d}}^{\mathrm{t}} \cdot \left[\sum_{e=1}^{n_{el}} \sum_{A=1}^{n_{en}} \left[\underline{\underline{\mathbf{L}}}^{\boldsymbol{\varphi}\, e\, A} \right]^{\mathrm{t}} \cdot \left[\boldsymbol{f}_{\mathrm{dyn}}^{\boldsymbol{\varphi}\, e\, A} + \boldsymbol{f}_{\mathrm{int}}^{\boldsymbol{\varphi}\, e\, A} - \boldsymbol{f}_{\mathrm{vol}}^{\boldsymbol{\varphi}\, e\, A} - \boldsymbol{f}_{\mathrm{sur}}^{\boldsymbol{\varphi}\, e\, A} \right] \right] = 0 \;, \tag{A.38}$$

$$\mathrm{w}^{\theta} \approx \delta\underline{\mathbf{d}}^{\mathrm{t}} \cdot \left[\sum_{e=1}^{n_{el}} \sum_{C=1}^{n_{en}} \left[\underline{\mathbf{l}}^{\theta\, e\, C} \right]^{\mathrm{t}} \left[f_{\mathrm{dyn}}^{\theta\, e\, C} + f_{\mathrm{int}}^{\theta\, e\, C} - f_{\mathrm{vol}}^{\theta\, e\, C} - f_{\mathrm{sur}}^{\theta\, e\, C} \right] \right] = 0 \;. \tag{A.39}$$

Both equations hold for all admissible test function values $\delta\underline{\mathbf{d}}$. In order to further simplify the notation, the assembly operator

$$\mathop{\mathbf{A}}_{e=1}^{n_{el}}(\bullet)^{\varphi\, e\, A} = \sum_{e=1}^{n_{el}}\sum_{A=1}^{n_{en}} [\underline{\underline{\mathbf{L}}}^{\varphi\, e\, A}]^{\mathrm{t}} \cdot (\bullet)^{\varphi\, e\, A} \,, \tag{A.40}$$

$$\mathop{\mathbf{A}}_{e=1}^{n_{el}}(\bullet)^{\theta\, e\, C} = \sum_{e=1}^{n_{el}}\sum_{C=1}^{n_{en}} [\underline{\mathbf{l}}^{\theta\, e\, C}]^{\mathrm{t}}\, (\bullet)^{\varphi\, e\, C} \,, \tag{A.41}$$

is defined such that the elemental force and flux contributions, Eqs. (A.27) to (A.34), can be assembled to

$$\underline{\mathbf{f}}_{\mathrm{dyn}} = \underline{\mathbf{f}}^{\varphi}_{\mathrm{dyn}} + \underline{\mathbf{f}}^{\theta}_{\mathrm{dyn}} = \mathop{\mathbf{A}}_{e=1}^{n_{el}} \boldsymbol{f}^{\varphi\, e\, A}_{\mathrm{dyn}} + \mathop{\mathbf{A}}_{e=1}^{n_{el}} \boldsymbol{f}^{\theta\, e\, C}_{\mathrm{dyn}} \,, \tag{A.42}$$

$$\underline{\mathbf{f}}_{\mathrm{int}} = \underline{\mathbf{f}}^{\varphi}_{\mathrm{int}} + \underline{\mathbf{f}}^{\theta}_{\mathrm{int}} = \mathop{\mathbf{A}}_{e=1}^{n_{el}} \boldsymbol{f}^{\varphi\, e\, A}_{\mathrm{int}} + \mathop{\mathbf{A}}_{e=1}^{n_{el}} \boldsymbol{f}^{\theta\, e\, C}_{\mathrm{int}} \,, \tag{A.43}$$

$$\underline{\mathbf{f}}_{\mathrm{vol}} = \underline{\mathbf{f}}^{\varphi}_{\mathrm{vol}} + \underline{\mathbf{f}}^{\theta}_{\mathrm{vol}} = \mathop{\mathbf{A}}_{e=1}^{n_{el}} \boldsymbol{f}^{\varphi\, e\, A}_{\mathrm{vol}} + \mathop{\mathbf{A}}_{e=1}^{n_{el}} \boldsymbol{f}^{\theta\, e\, C}_{\mathrm{vol}} \,, \tag{A.44}$$

$$\underline{\mathbf{f}}_{\mathrm{sur}} = \underline{\mathbf{f}}^{\varphi}_{\mathrm{sur}} + \underline{\mathbf{f}}^{\theta}_{\mathrm{sur}} = \mathop{\mathbf{A}}_{e=1}^{n_{el}} \boldsymbol{f}^{\varphi\, e\, A}_{\mathrm{sur}} + \mathop{\mathbf{A}}_{e=1}^{n_{el}} \boldsymbol{f}^{\theta\, e\, C}_{\mathrm{sur}} \,. \tag{A.45}$$

Finally, Eqs. (A.38) and (A.39) reduce to one semi-discrete, vector valued residual equation

$$\underline{\mathbf{r}}(\underline{\mathbf{d}}, \dot{\underline{\mathbf{d}}}, \ddot{\underline{\mathbf{d}}}) = \underline{\mathbf{f}}_{\mathrm{dyn}} + \underline{\mathbf{f}}_{\mathrm{int}} - \underline{\mathbf{f}}_{\mathrm{vol}} - \underline{\mathbf{f}}_{\mathrm{sur}} = \underline{\mathbf{0}} \,, \tag{A.46}$$

which depends on the degrees of freedom $\underline{\mathbf{d}}$ and the respective time derivatives $\dot{\underline{\mathbf{d}}}$ and $\ddot{\underline{\mathbf{d}}}$ which are organised in vectors

$$\dot{\underline{\mathbf{d}}} = \begin{bmatrix} \mathbf{0}^{\mathrm{t}} & \dot{\theta}_1 & \mathbf{0}^{\mathrm{t}} & \dot{\theta}_2 & \dots & \mathbf{0}^{\mathrm{t}} & \dot{\theta}_{n_{np}} \end{bmatrix}^{\mathrm{t}} , \tag{A.47}$$

$$\ddot{\underline{\mathbf{d}}} = \begin{bmatrix} \ddot{\boldsymbol{\varphi}}_1{}^{\mathrm{t}} & 0 & \ddot{\boldsymbol{\varphi}}_2{}^{\mathrm{t}} & 0 & \dots & \ddot{\boldsymbol{\varphi}}_{n_{np}}{}^{\mathrm{t}} & 0 \end{bmatrix}^{\mathrm{t}} , \tag{A.48}$$

such as Eq. (A.35). The discretisation of the acceleration $\ddot{\boldsymbol{\varphi}}$ is carried out analogously to Eq. (A.16),

$$\ddot{\boldsymbol{\varphi}}^{e}(\boldsymbol{\xi}) = \sum_{B=1}^{n_{en}} \ddot{\boldsymbol{\varphi}}^{e\, B}\, N^{B}(\boldsymbol{\xi}) \,, \tag{A.49}$$

and the discretisation of $\dot{\theta}$ is performed analogously to Eq. (A.17),

$$\dot{\theta}^e(\boldsymbol{\xi}) = \sum_{D=1}^{n_{en}} \dot{\theta}^{e\,D}\, N^D(\boldsymbol{\xi}) \,. \tag{A.50}$$

The subsequent insertion of the resulting terms into Eqs. (A.27) and (A.31) yields

$$\begin{aligned} \boldsymbol{f}_{\mathrm{dyn}}^{\boldsymbol{\varphi}\,e\,A} &= \int_{\mathcal{B}_0^e} \rho_0\, N^A \left[\sum_{B=1}^{n_{en}} \ddot{\boldsymbol{\varphi}}^{e\,B}\, N^B \right] \mathrm{d}V \\ &= \left[\sum_{B=1}^{n_{en}} \left[\underbrace{\int_{\mathcal{B}_0^e} \rho_0\, N^A\, \boldsymbol{I}\, N^B \,\mathrm{d}V}_{=:\boldsymbol{M}^{e\,A\,B}} \right] \cdot \underline{\underline{\mathbf{L}}}^{\boldsymbol{\varphi}\,e\,B} \right] \cdot \underline{\ddot{\mathbf{d}}} \,, \end{aligned} \tag{A.51}$$

as well as

$$\begin{aligned} f_{\mathrm{dyn}}^{\theta\,e\,C} &= \int_{\mathcal{B}_0^e} c_0\, N^C \left[\sum_{D=1}^{n_{en}} \dot{\theta}^{e\,D}\, N^D \right] \mathrm{d}V \\ &= \left[\sum_{D=1}^{n_{en}} \left[\underbrace{\int_{\mathcal{B}_0^e} c_0\, N^C\, N^D \,\mathrm{d}V}_{=:C^{e\,C\,D}} \right] \underline{\mathbf{l}}^{\theta\,e\,D} \right] \cdot \underline{\dot{\mathbf{d}}} \,. \end{aligned} \tag{A.52}$$

In the above expressions, $\boldsymbol{M}^{e\,A\,B}$ is the element mass matrix and $C^{e\,C\,D}$ is the element heat capacity matrix contribution which both can be assembled to the global mass matrix

$$\underline{\underline{\mathbf{M}}} = \sum_{e=1}^{n_{el}} \sum_{A=1}^{n_{en}} \sum_{B=1}^{n_{en}} [\underline{\underline{\mathbf{L}}}^{\boldsymbol{\varphi}\,e\,A}]^{\mathrm{t}} \cdot \boldsymbol{M}^{e\,A\,B} \cdot \underline{\underline{\mathbf{L}}}^{\boldsymbol{\varphi}\,e\,B} = \mathop{\mathsf{A}}_{e=1}^{n_{el}} \boldsymbol{M}^{e\,A\,B} \,, \tag{A.53}$$

as well as to the global heat capacity matrix

$$\underline{\underline{\mathbf{C}}} = \sum_{e=1}^{n_{el}} \sum_{C=1}^{n_{en}} \sum_{D=1}^{n_{en}} [\underline{\mathbf{l}}^{\theta\,e\,C}]^{\mathrm{t}}\, C^{e\,C\,D} \cdot \underline{\mathbf{l}}^{\theta\,e\,D} = \mathop{\mathsf{A}}_{e=1}^{n_{el}} C^{e\,C\,D} \,. \tag{A.54}$$

With the global mass and heat capacity matrices, Eq. (A.46) can be rewritten as

$$\underline{\mathbf{r}}(\underline{\mathbf{d}}, \underline{\dot{\mathbf{d}}}, \underline{\ddot{\mathbf{d}}}) = \underline{\underline{\mathbf{M}}} \cdot \underline{\ddot{\mathbf{d}}} + \underline{\underline{\mathbf{C}}} \cdot \underline{\dot{\mathbf{d}}} + \underline{\mathbf{f}}_{\mathrm{int}} - \underline{\mathbf{f}}_{\mathrm{vol}} - \underline{\mathbf{f}}_{\mathrm{sur}} = \underline{\mathbf{0}} \,. \tag{A.55}$$

Before the semi-discrete set of non-linear equations is solved, the above expression is discretised in time. Within this thesis, the Backward Euler method is applied such that the time derivatives of $\underline{\mathbf{d}}$ are approximated by

$$\dot{\underline{\mathbf{d}}}_{n+1} \approx \frac{\underline{\mathbf{d}}_{n+1} - \underline{\mathbf{d}}_n}{\Delta t} \,, \qquad \ddot{\underline{\mathbf{d}}}_{n+1} \approx \frac{\dot{\underline{\mathbf{d}}}_{n+1} - \dot{\underline{\mathbf{d}}}_n}{\Delta t} = \frac{\underline{\mathbf{d}}_{n+1} - 2\,\underline{\mathbf{d}}_n + \underline{\mathbf{d}}_{n-1}}{\Delta t^2} \tag{A.56}$$

where Δt is the time increment and the abbreviations $\underline{\mathbf{d}}_\bullet = \underline{\mathbf{d}}(t_\bullet)$ are used. In this regard, "$n+1$" indicates the current/unknown discrete time step, whereas "n" identifies the previous time step and "$n-1$" denotes the second to previous time step. With this time discretisation at hand, Eq. (A.55) reads

$$\underline{\mathbf{r}}(\underline{\mathbf{d}}_{n+1}) = \underline{\underline{\mathbf{M}}} \cdot \frac{\underline{\mathbf{d}}_{n+1} - 2\,\underline{\mathbf{d}}_n + \underline{\mathbf{d}}_{n-1}}{\Delta t^2} + \underline{\underline{\mathbf{C}}} \cdot \frac{\underline{\mathbf{d}}_{n+1} - \underline{\mathbf{d}}_n}{\Delta t} + \underline{\mathbf{f}}_{\text{int}} - \underline{\mathbf{f}}_{\text{vol}} - \underline{\mathbf{f}}_{\text{sur}} = \underline{\mathbf{0}} \,. \tag{A.57}$$

This set of non-linear equation is iteratively solved by means of the Newton-Raphson method where the Jacobian of the system of equations

$$\underline{\underline{\mathbf{J}}}(\underline{\mathbf{d}}^k_{n+1}) = \frac{\mathrm{d}\underline{\mathbf{r}}(\underline{\mathbf{d}}^k_{n+1})}{\mathrm{d}\underline{\mathbf{d}}^k_{n+1}} = \frac{1}{\Delta t^2}\,\underline{\underline{\mathbf{M}}} + \frac{1}{\Delta t}\,\underline{\underline{\mathbf{C}}} + \frac{\mathrm{d}\left[\,\underline{\mathbf{f}}_{\text{int}}(\underline{\mathbf{d}}^k_{n+1}) - \underline{\mathbf{f}}_{\text{vol}}(\underline{\mathbf{d}}^k_{n+1})\,\right]}{\mathrm{d}\underline{\mathbf{d}}^k_{n+1}} \,, \tag{A.58}$$

needs to be evaluated at each k^{th} iteration step — below, the subscript "$n+1$" as well as the superscript "k" are omitted to keep the expressions clear.

A.2 Consistent linearisation

In Eq. (A.58), it is assumed that the heat capacity matrix $\underline{\underline{\mathbf{C}}}$ is constant and that the surface force and flux contributions $\underline{\mathbf{f}}_{\text{sur}}$ do not depend on the degrees of freedom — comments on the implementation of a framework that accounts for a temperature dependent heat capacity as well as for Robin boundary conditions are for instance given in Chapter 3. At this point, the total derivatives of the internal forces well as the volume forces are elaborated since these result in the coupling terms of the Jacobian. With Eqs. (A.28) and (A.32), the derivative of the internal force contribution with respect to the degrees of freedom reads

$$\begin{aligned}\frac{\mathrm{d}\underline{\mathbf{f}}_{\text{int}}(\underline{\mathbf{d}})}{\mathrm{d}\underline{\mathbf{d}}} = \frac{\mathrm{d}}{\mathrm{d}\underline{\mathbf{d}}} \Bigg[\sum_{e=1}^{n_{el}} \Bigg[\sum_{A=1}^{n_{en}} \Big[\big[\underline{\underline{\mathbf{L}}}^{\boldsymbol{\varphi}\,e\,A}\big]^{\mathrm{t}} \cdot \int_{\mathcal{B}_0^e} \boldsymbol{P}(\underline{\mathbf{d}}) \cdot \nabla_{\boldsymbol{X}}\, N^A \,\mathrm{d}V \Big] \\ + \sum_{C=1}^{n_{en}} \Big[\big[\underline{\mathbf{l}}^{\theta\,e\,C}\big]^{\mathrm{t}} \int_{\mathcal{B}_0^e} -\nabla_{\boldsymbol{X}}\, N^C \cdot \boldsymbol{Q}(\underline{\mathbf{d}}) \,\mathrm{d}V \Big] \Bigg] \Bigg] \,.\end{aligned} \tag{A.59}$$

The derivative of the first integral term of the above equation yields

$$\frac{\mathrm{d}\boldsymbol{f}_{\mathrm{int}}^{\boldsymbol{\varphi}\,e\,A}}{\mathrm{d}\underline{\mathbf{d}}} = \int\limits_{\mathcal{B}_0^e} \left[\nabla_{\boldsymbol{X}}\, N^A \circ \frac{\mathrm{d}\boldsymbol{P}}{\mathrm{d}\boldsymbol{F}} : \frac{\partial \boldsymbol{F}}{\partial \underline{\mathbf{d}}} + \nabla_{\boldsymbol{X}}\, N^A \circ \frac{\mathrm{d}\boldsymbol{P}}{\mathrm{d}\theta}\, \frac{\partial \theta}{\partial \underline{\mathbf{d}}} \right] \mathrm{d}V \;, \tag{A.60}$$

and the derivative of the second integral term yields

$$\frac{\mathrm{d}f_{\mathrm{int}}^{\theta\,e\,C}}{\mathrm{d}\underline{\mathbf{d}}} = \int\limits_{\mathcal{B}_0^e} -\nabla_{\boldsymbol{X}}\, N^C \cdot \frac{\mathrm{d}\boldsymbol{Q}}{\mathrm{d}\,\nabla_{\boldsymbol{X}}\,\theta} \cdot \frac{\partial\,\nabla_{\boldsymbol{X}}\,\theta}{\partial \underline{\mathbf{d}}}\,\mathrm{d}V \;. \tag{A.61}$$

With Eq. (A.33), the derivative of the volume force contribution with respect to the degrees of freedom reads

$$\frac{\mathrm{d}\underline{\mathbf{f}}_{\mathrm{vol}}(\underline{\mathbf{d}})}{\mathrm{d}\underline{\mathbf{d}}} = \frac{\mathrm{d}}{\mathrm{d}\underline{\mathbf{d}}} \left[\sum_{e=1}^{n_{el}} \left[\sum_{C=1}^{n_{en}} \left[\underline{\mathbf{l}}^{\theta\,e\,C} \right]^{\mathrm{t}} \int\limits_{\mathcal{B}_0^e} N^C\, \hat{r}_0\, \mathrm{d}V \right] \right] \;, \tag{A.62}$$

where the derivative of the integral reads

$$\frac{\mathrm{d}f_{\mathrm{vol}}^{\theta\,e\,C}}{\mathrm{d}\underline{\mathbf{d}}} = \int\limits_{\mathcal{B}_0^e} \left[N^C\, \frac{\mathrm{d}\hat{r}_0}{\mathrm{d}\boldsymbol{F}} \cdot \frac{\partial \boldsymbol{F}}{\partial \underline{\mathbf{d}}} + N^C\, \frac{\mathrm{d}\hat{r}_0}{\mathrm{d}\theta}\, \frac{\partial \theta}{\partial \underline{\mathbf{d}}} \right] \mathrm{d}V \;. \tag{A.63}$$

In order to evaluate the above equations, the partial derivatives of $\boldsymbol{F}$, θ and $\nabla_{\boldsymbol{X}}\theta$, cf. Eqs. (A.17), (A.20) and (A.24), with respect to $\underline{\mathbf{d}}$ must be determined via

$$\begin{aligned} \frac{\partial \boldsymbol{F}}{\partial \underline{\mathbf{d}}} &= \frac{\partial}{\partial \underline{\mathbf{d}}} \left[\sum_{B=1}^{n_{en}} \boldsymbol{\varphi}^{e\,B} \otimes \nabla_{\boldsymbol{X}}\, N^B \right] = \sum_{B=1}^{n_{en}} \underline{\underline{\mathbf{L}}}^{\boldsymbol{\varphi}\,e\,B} \cdot \frac{\partial \underline{\mathbf{d}}}{\partial \underline{\mathbf{d}}} \mathbin{\overline{\otimes}} \nabla_{\boldsymbol{X}}\, N^B \\ &= \sum_{B=1}^{n_{en}} \underline{\underline{\mathbf{L}}}^{\boldsymbol{\varphi}\,e\,B} \mathbin{\overline{\otimes}} \nabla_{\boldsymbol{X}}\, N^B \;, \end{aligned} \tag{A.64}$$

$$\frac{\partial \theta}{\partial \underline{\mathbf{d}}} = \frac{\partial}{\partial \underline{\mathbf{d}}} \left[\sum_{D=1}^{n_{en}} \theta^{e\,D}\, N^D \right] = \sum_{D=1}^{n_{en}} \underline{\mathbf{l}}^{\theta\,e\,D} \cdot \frac{\partial \underline{\mathbf{d}}}{\partial \underline{\mathbf{d}}}\, N^D = \sum_{D=1}^{n_{en}} \underline{\mathbf{l}}^{\theta\,e\,D}\, N^D \;,$$

as well as via

$$\begin{aligned}\frac{\partial\,\nabla_{\boldsymbol{X}}\,\theta}{\partial\underline{\mathbf{d}}} &= \frac{\partial}{\partial\underline{\mathbf{d}}}\Big[\sum_{D=1}^{n_{en}}\theta^{e\,D}\;\nabla_{\boldsymbol{X}}\,N^{D}\Big] = \sum_{D=1}^{n_{en}}\nabla_{\boldsymbol{X}}N^{D}\otimes\underline{\mathbf{l}}^{\theta\,e\,D}\cdot\frac{\partial\underline{\mathbf{d}}}{\partial\underline{\mathbf{d}}}\\ &= \sum_{D=1}^{n_{en}}\nabla_{\boldsymbol{X}}\,N^{D}\otimes\underline{\mathbf{l}}^{\theta\,e\,D}\,.\end{aligned} \tag{A.65}$$

Inserting these contributions into Eqs. (A.59) and (A.62) yields

$$\begin{aligned}\frac{\mathrm{d}\underline{\mathbf{f}}_{\mathrm{int}}(\underline{\mathbf{d}})}{\mathrm{d}\underline{\mathbf{d}}} &= \sum_{e=1}^{n_{\mathrm{el}}}\sum_{A=1}^{n_{\mathrm{en}}}\sum_{B=1}^{n_{\mathrm{en}}}[\underline{\underline{\mathbf{L}}}^{\boldsymbol{\varphi}\,e\,A}]^{\mathrm{t}}\cdot\Big[\int_{\mathcal{B}_0^e}\nabla_{\boldsymbol{X}}\,N^{A}\circ\frac{\mathrm{d}\boldsymbol{P}}{\mathrm{d}\boldsymbol{F}}\cdot\nabla_{\boldsymbol{X}}\,N^{B}\,\mathrm{d}V\Big]\cdot\underline{\underline{\mathbf{L}}}^{\boldsymbol{\varphi}\,e\,B}\\ &\quad+\sum_{e=1}^{n_{\mathrm{el}}}\sum_{A=1}^{n_{\mathrm{en}}}\sum_{D=1}^{n_{\mathrm{en}}}[\underline{\underline{\mathbf{L}}}^{\boldsymbol{\varphi}\,e\,A}]^{\mathrm{t}}\cdot\Big[\int_{\mathcal{B}_0^e}\nabla_{\boldsymbol{X}}\,N^{A}\circ\frac{\mathrm{d}\boldsymbol{P}}{\mathrm{d}\theta}\,N^{D}\,\mathrm{d}V\Big]\cdot\underline{\mathbf{l}}^{\theta\,e\,D}\\ &\quad+\sum_{e=1}^{n_{\mathrm{el}}}\sum_{C=1}^{n_{\mathrm{en}}}\sum_{D=1}^{n_{\mathrm{en}}}[\underline{\mathbf{l}}^{\theta\,e\,C}]^{\mathrm{t}}\Big[\int_{\mathcal{B}_0^e}-\nabla_{\boldsymbol{X}}N^{C}\cdot\frac{\mathrm{d}\boldsymbol{Q}}{\mathrm{d}\,\nabla_{\boldsymbol{X}}\theta}\cdot\nabla_{\boldsymbol{X}}N^{D}\,\mathrm{d}V\Big]\cdot\underline{\mathbf{l}}^{\theta\,e\,D}\,,\end{aligned} \tag{A.66}$$

and

$$\begin{aligned}\frac{\mathrm{d}\underline{\mathbf{f}}_{\mathrm{sur}}(\underline{\mathbf{d}})}{\mathrm{d}\underline{\mathbf{d}}} &= \sum_{e=1}^{n_{\mathrm{el}}}\sum_{C=1}^{n_{\mathrm{en}}}\sum_{B=1}^{n_{\mathrm{en}}}[\underline{\mathbf{l}}^{\theta\,e\,C}]^{\mathrm{t}}\Big[\int_{\mathcal{B}_0^e}N^{C}\,\frac{\mathrm{d}\hat{r}_0}{\mathrm{d}\boldsymbol{F}}\cdot\nabla_{\boldsymbol{X}}N^{B}\,\mathrm{d}V\Big]\cdot\underline{\underline{\mathbf{L}}}^{\boldsymbol{\varphi}\,e\,B}\\ &\quad+\sum_{e=1}^{n_{\mathrm{el}}}\sum_{C=1}^{n_{\mathrm{en}}}\sum_{D=1}^{n_{\mathrm{en}}}[\underline{\mathbf{l}}^{\theta\,e\,C}]^{\mathrm{t}}\Big[\int_{\mathcal{B}_0^e}N^{C}\,\frac{\mathrm{d}\hat{r}_0}{\mathrm{d}\theta}\,N^{D}\,\mathrm{d}V\Big]\cdot\underline{\mathbf{l}}^{\theta\,e\,D}\,.\end{aligned} \tag{A.67}$$

The two above expressions complete the Jacobian, cf. Eq. (A.58), for the considered thermo-mechanically coupled problems.

B Homogenisation

In this appendix, equations related to homogenisation are summarised. The thermo-mechanically coupled two-scale finite element framework which are elaborated in Chapters 5 and 6 are based on the so-called Hill Mandel macro-homogeneity condition. Equations related to the derivation of the condition are briefly discussed in Appendix B.1. Subsequently, in Appendix B.2, comments are given on the implementation of the resulting linear displacement, uniform flux as well as strong periodic boundary conditions.

B.1 Hill–Mandel macro-homogeneity condition related equations

As discussed in Section 6.1.2, the deformation gradient $\boldsymbol{F}$, the temperature gradient $\nabla_{\boldsymbol{X}}\theta$, the Piola stresses $\boldsymbol{P}$ and the heat flux $\boldsymbol{Q}$ are not extensive quantities. Consequently, the Hill-Mandel-type macro-homogeneity conditions, Eqs. (6.9) and (6.10), are only valid for particular boundary displacement and temperature values which result from boundary conditions for the RVE under consideration. Following [124, pp. 32–33], we find

$$\begin{aligned}
&[\,\boldsymbol{x}^{\mathrm{m}} - \langle \boldsymbol{F}^{\mathrm{m}} \rangle \cdot \boldsymbol{X}^{\mathrm{m}}\,] \cdot [\,\boldsymbol{t}_0^{\mathrm{m}} - \langle \boldsymbol{P}^{\mathrm{m}} \rangle \cdot \boldsymbol{N}^{\mathrm{m}}\,] \\
&= \boldsymbol{x}^{\mathrm{m}} \cdot \boldsymbol{t}_0^{\mathrm{m}} - \boldsymbol{x}^{\mathrm{m}} \cdot \langle \boldsymbol{P}^{\mathrm{m}} \rangle \cdot \boldsymbol{N}^{\mathrm{m}} \\
&\quad - \boldsymbol{t}^{\mathrm{m}} \cdot \langle \boldsymbol{F}^{\mathrm{m}} \rangle \cdot \boldsymbol{X}^{\mathrm{m}} + \left[\, \boldsymbol{X}^{\mathrm{m}} \otimes \boldsymbol{N}^{\mathrm{m}} \,\right] \colon \left[\, \langle \boldsymbol{F}^{\mathrm{m}\mathrm{t}} \rangle \cdot \langle \boldsymbol{P}^{\mathrm{m}} \rangle \,\right] .
\end{aligned} \tag{B.1}$$

Dividing by the RVE volume V^{RVE} and integration over the RVE surface $\partial\mathcal{B}_0^{\mathrm{RVE}}$ yields

$$\begin{aligned}
\frac{1}{V^{\mathrm{RVE}}} \int\limits_{\partial\mathcal{B}_0^{\mathrm{RVE}}} \Big[& \boldsymbol{x}^{\mathrm{m}} \cdot \boldsymbol{t}_0^{\mathrm{m}} - \boldsymbol{x}^{\mathrm{m}} \cdot \langle \boldsymbol{P}^{\mathrm{m}} \rangle \cdot \boldsymbol{N}^{\mathrm{m}} \\
& - \boldsymbol{t}^{\mathrm{m}} \cdot \langle \boldsymbol{F}^{\mathrm{m}} \rangle \cdot \boldsymbol{X}^{\mathrm{m}} + \left[\, \boldsymbol{X}^{\mathrm{m}} \otimes \boldsymbol{N}^{\mathrm{m}} \,\right] \colon \left[\, \langle \boldsymbol{F}^{\mathrm{m}\mathrm{t}} \rangle \cdot \langle \boldsymbol{P}^{\mathrm{m}} \rangle \,\right] \Big] \, \mathrm{d}A \,,
\end{aligned} \tag{B.2}$$

whereby the second term can be written as

$$
\begin{aligned}
-\frac{1}{V^{\mathrm{RVE}}} \int\limits_{\partial \mathcal{B}_0^{\mathrm{RVE}}} \boldsymbol{x}^{\mathrm{m}} \cdot \langle \boldsymbol{P}^{\mathrm{m}} \rangle \cdot \boldsymbol{N}^{\mathrm{m}} \, \mathrm{d}A &= - \underbrace{\left[\frac{1}{V^{\mathrm{RVE}}} \int\limits_{\partial \mathcal{B}_0^{\mathrm{RVE}}} \boldsymbol{x}^{\mathrm{m}} \otimes \boldsymbol{N}^{\mathrm{m}} \, \mathrm{d}A \right]}_{= \langle \boldsymbol{F}^{\mathrm{m}} \rangle} : \langle \boldsymbol{P}^{\mathrm{m}} \rangle \\
&= - \langle \boldsymbol{F}^{\mathrm{m}} \rangle : \langle \boldsymbol{P}^{\mathrm{m}} \rangle \, .
\end{aligned}
\tag{B.3}
$$

The third term in Eq. (B.2) transforms to

$$
\begin{aligned}
-\frac{1}{V^{\mathrm{RVE}}} \int\limits_{\partial \mathcal{B}_0^{\mathrm{RVE}}} \boldsymbol{t}_0^{\mathrm{m}} \cdot \langle \boldsymbol{F}^{\mathrm{m}} \rangle \cdot \boldsymbol{X}^{\mathrm{m}} \, \mathrm{d}A &= - \underbrace{\left[\frac{1}{V^{\mathrm{RVE}}} \int\limits_{\partial \mathcal{B}_0^{\mathrm{RVE}}} \boldsymbol{t}_0^{\mathrm{m}} \otimes \boldsymbol{X}^{\mathrm{m}} \, \mathrm{d}A \right]}_{= \langle \boldsymbol{P}^{\mathrm{m}} \rangle} : \langle \boldsymbol{F}^{\mathrm{m}} \rangle \\
&= - \langle \boldsymbol{P}^{\mathrm{m}} \rangle : \langle \boldsymbol{F}^{\mathrm{m}} \rangle \, ,
\end{aligned}
\tag{B.4}
$$

and the fourth term in Eq. (B.2) turns to

$$
\begin{aligned}
&\frac{1}{V^{\mathrm{RVE}}} \int\limits_{\partial \mathcal{B}_0^{\mathrm{RVE}}} \left[\, \boldsymbol{X}^{\mathrm{m}} \otimes \boldsymbol{N}^{\mathrm{m}} \, \right] : \left[\, \langle \boldsymbol{F}^{\mathrm{mt}} \rangle \cdot \langle \boldsymbol{P}^{\mathrm{m}} \rangle \, \right] \mathrm{d}A \\
&= \underbrace{\left[\frac{1}{V^{\mathrm{RVE}}} \int\limits_{\partial \mathcal{B}_0^{\mathrm{RVE}}} \boldsymbol{X}^{\mathrm{m}} \otimes \boldsymbol{N}^{\mathrm{m}} \, \mathrm{d}A \right]}_{= \boldsymbol{I}} : \left[\, \langle \boldsymbol{F}^{\mathrm{mt}} \rangle \cdot \langle \boldsymbol{P}^{\mathrm{m}} \rangle \, \right] = \langle \boldsymbol{P}^{\mathrm{m}} \rangle : \langle \boldsymbol{F}^{\mathrm{m}} \rangle \, .
\end{aligned}
\tag{B.5}
$$

Inserting the transformed terms from Eqs. (B.3) to (B.5) into Eq. (B.2), the expression

$$
\frac{1}{V^{\mathrm{RVE}}} \int\limits_{\partial \mathcal{B}_0^{\mathrm{RVE}}} \boldsymbol{x}^{\mathrm{m}} \cdot \boldsymbol{t}_0^{\mathrm{m}} \, \mathrm{d}A - \langle \boldsymbol{F}^{\mathrm{m}} \rangle : \langle \boldsymbol{P}^{\mathrm{m}} \rangle - \langle \boldsymbol{P}^{\mathrm{m}} \rangle : \langle \boldsymbol{F}^{\mathrm{m}} \rangle + \langle \boldsymbol{P}^{\mathrm{m}} \rangle : \langle \boldsymbol{F}^{\mathrm{m}} \rangle \tag{B.6}
$$

is obtained so that

$$\begin{aligned}&\frac{1}{V^{\mathrm{RVE}}}\int\limits_{\partial\mathcal{B}_0^{\mathrm{RVE}}}\boldsymbol{x}^{\mathrm{m}}\cdot\boldsymbol{t}_0^{\mathrm{m}}\,\mathrm{d}A-\langle\boldsymbol{F}^{\mathrm{m}}\rangle\colon\langle\boldsymbol{P}^{\mathrm{m}}\rangle\\ =&\frac{1}{V^{\mathrm{RVE}}}\int\limits_{\partial\mathcal{B}_0^{\mathrm{RVE}}}\left[\,\boldsymbol{x}^{\mathrm{m}}-\langle\boldsymbol{F}^{\mathrm{m}}\rangle\cdot\boldsymbol{X}^{\mathrm{m}}\,\right]\cdot\left[\,\boldsymbol{t}_0^{\mathrm{m}}-\langle\boldsymbol{P}^{\mathrm{m}}\rangle\cdot\boldsymbol{N}^{\mathrm{m}}\,\right]\mathrm{d}A\,,\end{aligned}\tag{B.7}$$

which results in Eq. (6.21) if Eq. (6.9) shall be valid.

For the thermal part of the problem, the analogue point of departure is

$$\begin{aligned}&\left[\,\theta^{\mathrm{m}}-\langle\nabla_{\boldsymbol{X}}\theta^{\mathrm{m}}\rangle\cdot\boldsymbol{X}^{\mathrm{m}}\,\right]\left[\,Q^{\mathrm{m}}-\langle\boldsymbol{Q}^{\mathrm{m}}\rangle\cdot\boldsymbol{N}^{\mathrm{m}}\,\right]\\ &=\theta^{\mathrm{m}}\,Q^{\mathrm{m}}-\theta^{\mathrm{m}}\,\langle\boldsymbol{Q}^{\mathrm{m}}\rangle\cdot\boldsymbol{N}^{\mathrm{m}}-Q^{\mathrm{m}}\,\langle\nabla_{\boldsymbol{X}}\theta^{\mathrm{m}}\rangle\cdot\boldsymbol{X}^{\mathrm{m}}+\left[\,\langle\nabla_{\boldsymbol{X}}\theta^{\mathrm{m}}\rangle\cdot\boldsymbol{X}^{\mathrm{m}}\,\right]\left[\,\langle\boldsymbol{Q}^{\mathrm{m}}\rangle\cdot\boldsymbol{N}^{\mathrm{m}}\,\right].\end{aligned}\tag{B.8}$$

Division of the right hand side above equation by the RVE volume V^{RVE} and integration over the RVE surface $\partial\mathcal{B}_0^{\mathrm{RVE}}$ yields

$$\begin{aligned}\frac{1}{V^{\mathrm{RVE}}}\int\limits_{\partial\mathcal{B}_0^{\mathrm{RVE}}}\Big[&\theta^{\mathrm{m}}\,Q^{\mathrm{m}}-\theta^{\mathrm{m}}\,\langle\boldsymbol{Q}^{\mathrm{m}}\rangle\cdot\boldsymbol{N}^{\mathrm{m}}\\ &-Q^{\mathrm{m}}\,\langle\nabla_{\boldsymbol{X}}\theta^{\mathrm{m}}\rangle\cdot\boldsymbol{X}^{\mathrm{m}}+\left[\,\langle\nabla_{\boldsymbol{X}}\theta^{\mathrm{m}}\rangle\cdot\boldsymbol{X}^{\mathrm{m}}\,\right]\left[\,\langle\boldsymbol{Q}^{\mathrm{m}}\rangle\cdot\boldsymbol{N}^{\mathrm{m}}\,\right]\Big]\,\mathrm{d}A\,,\end{aligned}\tag{B.9}$$

where the second term can be transformed as follows

$$\begin{aligned}-\frac{1}{V^{\mathrm{RVE}}}\int\limits_{\partial\mathcal{B}_0^{\mathrm{RVE}}}\theta^{\mathrm{m}}\,\langle\boldsymbol{Q}^{\mathrm{m}}\rangle\cdot\boldsymbol{N}^{\mathrm{m}}\,\mathrm{d}A&=-\underbrace{\left[\frac{1}{V^{\mathrm{RVE}}}\int\limits_{\partial\mathcal{B}_0^{\mathrm{RVE}}}\theta^{\mathrm{m}}\,\boldsymbol{N}^{\mathrm{m}}\,\mathrm{d}A\right]}_{=\langle\nabla_{\boldsymbol{X}}\theta^{\mathrm{m}}\rangle}\cdot\langle\boldsymbol{Q}^{\mathrm{m}}\rangle\\ &=-\langle\nabla_{\boldsymbol{X}}\theta^{\mathrm{m}}\rangle\cdot\langle\boldsymbol{Q}^{\mathrm{m}}\rangle\,.\end{aligned}\tag{B.10}$$

The third term of Eq. (B.9) can be written as

$$
\begin{aligned}
-\frac{1}{V^{\mathrm{RVE}}} \int\limits_{\partial\mathcal{B}_0^{\mathrm{RVE}}} Q^{\mathrm{m}} \left\langle \nabla_{\boldsymbol{X}} \theta^{\mathrm{m}} \right\rangle \cdot \boldsymbol{X}^{\mathrm{m}} \, \mathrm{d}A &= - \underbrace{\left[\frac{1}{V^{\mathrm{RVE}}} \int\limits_{\partial\mathcal{B}_0^{\mathrm{RVE}}} Q^{\mathrm{m}} \, \boldsymbol{X}^{\mathrm{m}} \, \mathrm{d}A \right]}_{= \langle \boldsymbol{Q}^{\mathrm{m}} \rangle} \cdot \left\langle \nabla_{\boldsymbol{X}} \theta^{\mathrm{m}} \right\rangle \\
&= - \langle \boldsymbol{Q}^{\mathrm{m}} \rangle \cdot \left\langle \nabla_{\boldsymbol{X}} \theta^{\mathrm{m}} \right\rangle \, ,
\end{aligned}
\tag{B.11}
$$

and the fourth term of Eq. (B.9) can be reformulated as

$$
\begin{aligned}
&\frac{1}{V^{\mathrm{RVE}}} \int\limits_{\partial\mathcal{B}_0^{\mathrm{RVE}}} \left[\left\langle \nabla_{\boldsymbol{X}} \theta^{\mathrm{m}} \right\rangle \cdot \boldsymbol{X}^{\mathrm{m}} \right] \left[\langle \boldsymbol{Q}^{\mathrm{m}} \rangle \cdot \boldsymbol{N}^{\mathrm{m}} \right] \\
&= \underbrace{\left[\frac{1}{V^{\mathrm{RVE}}} \int\limits_{\partial\mathcal{B}_0^{\mathrm{RVE}}} \boldsymbol{X}^{\mathrm{m}} \otimes \boldsymbol{N}^{\mathrm{m}} \, \mathrm{d}A \right]}_{= \boldsymbol{I}} : \left[\left\langle \nabla_{\boldsymbol{X}} \theta^{\mathrm{m}} \right\rangle \otimes \langle \boldsymbol{Q}^{\mathrm{m}} \rangle \right] \mathrm{d}A = \left\langle \nabla_{\boldsymbol{X}} \theta^{\mathrm{m}} \right\rangle \cdot \langle \boldsymbol{Q}^{\mathrm{m}} \rangle \, .
\end{aligned}
\tag{B.12}
$$

Inserting the transformed terms from Eqs. (B.10) to (B.12) into Eq. (B.9), the expression

$$
\frac{1}{V^{\mathrm{RVE}}} \int\limits_{\partial\mathcal{B}_0^{\mathrm{RVE}}} \theta^{\mathrm{m}} \, Q^{\mathrm{m}} \, \mathrm{d}A - \left\langle \nabla_{\boldsymbol{X}} \theta^{\mathrm{m}} \right\rangle \cdot \langle \boldsymbol{Q}^{\mathrm{m}} \rangle - \langle \boldsymbol{Q}^{\mathrm{m}} \rangle \cdot \left\langle \nabla_{\boldsymbol{X}} \theta^{\mathrm{m}} \right\rangle + \left\langle \nabla_{\boldsymbol{X}} \theta^{\mathrm{m}} \right\rangle \cdot \langle \boldsymbol{Q}^{\mathrm{m}} \rangle \tag{B.13}
$$

is obtained so that

$$
\begin{aligned}
&\frac{1}{V^{\mathrm{RVE}}} \int\limits_{\partial\mathcal{B}_0^{\mathrm{RVE}}} \theta^{\mathrm{m}} \, Q^{\mathrm{m}} \, \mathrm{d}A - \left\langle \nabla_{\boldsymbol{X}} \theta^{\mathrm{m}} \right\rangle \cdot \langle \boldsymbol{Q}^{\mathrm{m}} \rangle \\
&= \frac{1}{V^{\mathrm{RVE}}} \int\limits_{\partial\mathcal{B}_0^{\mathrm{RVE}}} \left[\theta^{\mathrm{m}} - \left\langle \nabla_{\boldsymbol{X}} \theta^{\mathrm{m}} \right\rangle \cdot \boldsymbol{X}^{\mathrm{m}} \right] \left[Q^{\mathrm{m}} - \langle \boldsymbol{Q}^{\mathrm{m}} \rangle \cdot \boldsymbol{N}^{\mathrm{m}} \right] \mathrm{d}A \, ,
\end{aligned}
\tag{B.14}
$$

which results in Eq. (6.22) if Eq. (6.10) shall be valid.

B.2 Algorithmic treatment of meso-scale boundary conditions

The algorithmic treatment of the established meso-scale boundary conditions follows the literature. The implementation of the linear displacement boundary conditions is briefly discussed in this section. For this, a RVE $\mathcal{B}_0^{\mathrm{RVE}}$ formed like a cube is considered. The opposite faces, the boundary $\partial\mathcal{B}_0^{\mathrm{RVE}}$, of that cube shall have a matching discretisation such that each meso-scale node on the one side $\boldsymbol{X}_-^{\mathrm{m}}$ is paired with a node on the other side $\boldsymbol{X}_+^{\mathrm{m}}$.

Displacement boundary conditions

The displacement boundary conditions are straight forwardly implemented as Dirichlet boundary conditions such that meso-scale displacements and temperatures are prescribed by

$$\boldsymbol{u}^{\mathrm{m}} = \boldsymbol{H}^{\mathrm{M}} \cdot \boldsymbol{X}^{\mathrm{m}} \qquad \text{on} \qquad \partial\mathcal{B}_0^{\mathrm{RVE}} \,, \tag{B.15}$$

$$\theta^{\mathrm{m}} = \nabla_{\boldsymbol{X}}\theta^{\mathrm{M}} \cdot [\, \boldsymbol{X}^{\mathrm{m}} - \boldsymbol{X}_{\mathrm{c}}^{\mathrm{m}} \,] \qquad \text{on} \qquad \partial\mathcal{B}_0^{\mathrm{RVE}} \,, \tag{B.16}$$

where $\boldsymbol{H}^{\mathrm{M}} = \boldsymbol{F}^{\mathrm{M}} - \boldsymbol{I}$ is the macro-scale displacement gradient and $\boldsymbol{X}_{\mathrm{c}}^{\mathrm{m}}$ is the geometric center of gravity of the considered RVE. By enforcing this strongly at each point of the meso-scale boundary, the weak expressions Eqs. (6.21) and (6.22) are automatically fulfilled. In this case, the meso-scale force vector vanishes, $\underline{\mathbf{f}}_{\mathrm{sur}}^{\mathrm{m}} = \underline{\mathbf{0}}$, such that the residual $\underline{\mathbf{r}}^{\mathrm{m}}$ contains the reaction force in order to extract the effective stress and heat flux.

Uniform flux boundary conditions

In order to solve the meso-scale problem for unknown constant boundary fluxes – tractions represent the linear momentum flux whereas the heat flux is the flux of the thermal energy –, the unknown macro-scale Piola stress $\boldsymbol{P}^{\mathrm{M}}$ and the unknown macro-scale heat flux $\boldsymbol{Q}^{\mathrm{M}}$ are inserted in Eqs. (6.21) and (6.22) such that the expressions

$$\boldsymbol{P}^{\mathrm{M}} \colon \boldsymbol{F}^{\mathrm{M}} = \frac{1}{V} \int\limits_{\partial\mathcal{B}_0^{\mathrm{RVE}}} \boldsymbol{x}^{\mathrm{m}} \cdot \boldsymbol{P}^{\mathrm{M}} \cdot \boldsymbol{N}^{\mathrm{m}} \, \mathrm{d}A \,, \tag{B.17}$$

$$\boldsymbol{Q}^{\mathrm{M}} \cdot \nabla_{\boldsymbol{X}}\theta^{\mathrm{M}} = \frac{1}{V} \int\limits_{\partial\mathcal{B}_0^{\mathrm{RVE}}} \theta\, \boldsymbol{Q}^{\mathrm{M}} \cdot \boldsymbol{N}^{\mathrm{m}} \, \mathrm{d}A \,, \tag{B.18}$$

are obtained. Since with this at hand, Eqs. (6.21) and (6.22) are fulfilled due to $\boldsymbol{t}_0 = \boldsymbol{P}^{\mathrm{M}} \cdot \boldsymbol{N}^{\mathrm{m}}$ as well as $Q = \boldsymbol{Q}^{\mathrm{M}} \cdot \boldsymbol{N}^{\mathrm{m}}$, the unknown macro-scale stress as well as the unknown

macro-scale heat flux can be interpreted as Lagrange multipliers for the deformation problem and the temperature problem in order to enforce the constraint

$$\underline{\mathbf{g}} = \frac{1}{V} \begin{bmatrix} \left[\int\limits_{\partial \mathcal{B}_0^{\mathrm{RVE}}} \boldsymbol{x}^{\mathrm{m}} \otimes \boldsymbol{N} \, \mathrm{d}A - \boldsymbol{F}^{\mathrm{M}} \right]^{\mathrm{Kel}} \\ \int\limits_{\partial \mathcal{B}_0^{\mathrm{RVE}}} \theta^{\mathrm{m}} \boldsymbol{N} \, \mathrm{d}A - \nabla_{\boldsymbol{X}} \theta^{\mathrm{M}} \end{bmatrix} = \underline{\mathbf{0}} \, . \tag{B.19}$$

In the above vector valued constraint equation, the Kelvin notation according to Eq. (2.34) is applied. The unknown effective stress is related to the first constraint within the above vector $\underline{\mathbf{g}}$ and can be seen as second-order tensor valued Lagrange multiplier $\boldsymbol{\lambda}_{\boldsymbol{\varphi}}$ with nine unknowns. In analogy, the unknown effective heat flux corresponds to the second constraint within vector $\underline{\mathbf{g}}$ and can be interpreted as vector valued Lagrange multiplier $\boldsymbol{\lambda}_{\theta}$ with three unknowns. The implementation is carried out in analogy to the framework of Miehe and Koch [115]. The boundary of the RVE is discretised by n_{sel} surface elements such that the meso-scale surface force term is computed by

$$\underline{\mathbf{f}}_{\mathrm{sur}} = \mathop{\mathbf{A}}_{se=1}^{n_{\mathrm{sel}}} \frac{1}{V} \int\limits_{\partial \mathcal{B}_0^{\mathrm{RVE}}} N^A \, \boldsymbol{\lambda} \cdot \boldsymbol{N} \, \mathrm{d}A \, . \tag{B.20}$$

In the above equation $\mathbf{A}$ is the assembly operator which assembles the surface element contributions to the global surface force vector. Furthermore, N^A is the value of the shape function belonging to node A of the surface element, $\boldsymbol{\lambda}$ are the twelve Lagrange multipliers

$$\boldsymbol{\lambda} = \left[\left[\boldsymbol{\lambda}_{\boldsymbol{\varphi}}^{\mathrm{Kel}} \right]^{\mathrm{t}}, \boldsymbol{\lambda}_{\theta}{}^{\mathrm{t}} \right]^{\mathrm{t}} , \tag{B.21}$$

and $\boldsymbol{N}$ is the referential outward surface normal vector. With Eq. (B.20) at hand, Eq. (6.74) turns to a self-equilibrated system of equations with $\underline{\mathbf{r}}^{\mathrm{m}} = \underline{\mathbf{0}}$ where rigid body motions must be suppressed. The system of non-linear equations to be solved is

$$\begin{bmatrix} \dfrac{\mathrm{d}\underline{\mathbf{r}}^{\mathrm{m}}}{\mathrm{d}\underline{\mathbf{d}}} & \dfrac{\mathrm{d}\underline{\mathbf{r}}^{\mathrm{m}}}{\mathrm{d}\boldsymbol{\lambda}} \\ \dfrac{\mathrm{d}\underline{\mathbf{g}}}{\mathrm{d}\underline{\mathbf{d}}} & \underline{\underline{\mathbf{0}}} \end{bmatrix} \cdot \begin{bmatrix} \Delta\underline{\mathbf{d}} \\ \Delta\boldsymbol{\lambda} \end{bmatrix} = - \begin{bmatrix} \underline{\mathbf{r}}^{\mathrm{m}} \\ \underline{\mathbf{g}} \end{bmatrix} , \tag{B.22}$$

where the additional Jacobian terms are

$$-\frac{\mathrm{d}\underline{\mathbf{r}}^{\mathrm{m}}}{\mathrm{d}\boldsymbol{\lambda}} = \frac{\mathrm{d}\underline{\mathbf{g}}}{\mathrm{d}\underline{\mathbf{d}}} = \mathop{\mathbf{A}}_{se=1}^{n_{\mathrm{sel}}} \frac{1}{V} \int\limits_{\partial\mathcal{B}_0^{\mathrm{RVE}}} N^A \, \frac{\mathrm{d}\big[\,\boldsymbol{\lambda}\cdot\boldsymbol{N}\,\big]}{\mathrm{d}\boldsymbol{\lambda}} \, \mathrm{d}A \; . \tag{B.23}$$

After the solution of the non-linear system of equations is obtained, the homogenised constitutive reaction can directly be extracted from the solution of the Lagrange multipliers, hence $\boldsymbol{P}^{\mathrm{M}} = \boldsymbol{\lambda}_{\boldsymbol{\varphi}}$ and $\boldsymbol{Q}^{\mathrm{M}} = \boldsymbol{\lambda}_{\theta}$.

Remark B.2.1 (Different cases of implementation) *The differential within the integral of Eq.* (B.23) *takes different values in dependence of the spatial dimension of the problem at hand. For two dimensional problems one obtains*

$$\frac{\mathrm{d}\big[\,\boldsymbol{\lambda}\cdot\boldsymbol{N}\,\big]}{\mathrm{d}\boldsymbol{\lambda}} = \begin{bmatrix} N_1 & N_2 & 0 & 0 & 0 & 0 \\ 0 & 0 & N_1 & N_2 & 0 & 0 \\ 0 & 0 & 0 & 0 & N_1 & N_2 \end{bmatrix} \; ,$$

whereas equivalent in three dimensional space reads

$$\frac{\mathrm{d}\big[\,\boldsymbol{\lambda}\cdot\boldsymbol{N}\,\big]}{\mathrm{d}\boldsymbol{\lambda}} = \begin{bmatrix} N_1 & N_2 & N_3 & 0 & 0 & 0 & 0 & 0 & 0 & 0 & 0 & 0 \\ 0 & 0 & 0 & N_1 & N_2 & N_3 & 0 & 0 & 0 & 0 & 0 & 0 \\ 0 & 0 & 0 & 0 & 0 & 0 & N_1 & N_2 & N_3 & 0 & 0 & 0 \\ 0 & 0 & 0 & 0 & 0 & 0 & 0 & 0 & 0 & N_1 & N_2 & N_3 \end{bmatrix} \; .$$

In the above expressions, N_i correspond to the Cartesian coefficients of the outward unit normal $\boldsymbol{N}$. In addition, the Kelvin notation for symmetric tensors, cf. Eq. (2.39)*, must be considered providing that the above equations are applied within a geometrically linearised framework. The differential within the integral of Eq.* (B.23) *then reads*

$$\frac{\mathrm{d}\big[\,\boldsymbol{\lambda}\cdot\boldsymbol{N}\,\big]}{\mathrm{d}\boldsymbol{\lambda}} = \begin{bmatrix} N_1 & 0 & \sqrt{2}\,N_2 & 0 & 0 \\ 0 & N_2 & \sqrt{2}\,N_1 & 0 & 0 \\ 0 & 0 & 0 & N_1 & N_2 \end{bmatrix} \; ,$$

in two dimensional problems and

$$\frac{\mathrm{d}\big[\,\boldsymbol{\lambda}\cdot\boldsymbol{N}\,\big]}{\mathrm{d}\boldsymbol{\lambda}} = \begin{bmatrix} N_1 & 0 & 0 & 0 & \sqrt{2}\,N_3 & \sqrt{2}\,N_2 & 0 & 0 \\ 0 & N_2 & 0 & \sqrt{2}\,N_3 & 0 & \sqrt{2}\,N_1 & 0 & 0 \\ 0 & 0 & N_3 & \sqrt{2}\,N_2 & \sqrt{2}\,N_1 & 0 & 0 & 0 \\ 0 & 0 & 0 & 0 & 0 & 0 & N_1 & N_2 \end{bmatrix} \; ,$$

in three dimensional space.

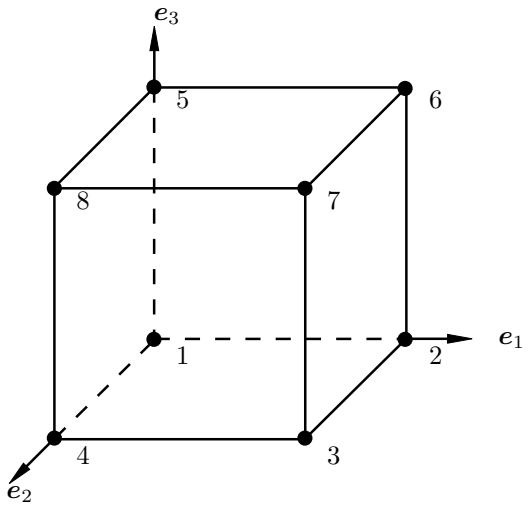

Figure B.1: Visualisation of the vertex numbers and master edges of an RVE.

Strong periodic boundary conditions

When each node on the "−"-boundary has a mirror-node on the "+"-boundary, the periodic boundary conditions can be implemented in a strong sense by means of linear constraints of the respective degrees of freedom. For this purpose, Eqs. (6.21) and (6.22) are enforced by means of

$$\boldsymbol{u}^{+} = \boldsymbol{u}^{-} + \boldsymbol{H}^{\mathrm{M}} \cdot \left[\boldsymbol{X}^{+} - \boldsymbol{X}^{-} \right] \,, \tag{B.24}$$

$$\theta^{+} = \theta^{-} + \nabla_{\boldsymbol{X}} \theta^{\mathrm{M}} \cdot \left[\boldsymbol{X}^{+} - \boldsymbol{X}^{-} \right] \,. \tag{B.25}$$

As outlined by Kouznetsova et al. [98] and extended by Özdemir et al. [132], the deformation and temperature is prescribed at the four vertex nodes 1, 2, 4 and 5, cf. Fig. B.1, which can formally be member of a set which is a subset of all vertex nodes

$$\texttt{vertex} = \{\boldsymbol{X}_i\} \,, \quad i = 1, \ldots, 8 \tag{B.26}$$

$$\texttt{vertex\_master} = \{\boldsymbol{X}_1, \boldsymbol{X}_2, \boldsymbol{X}_4, \boldsymbol{X}_5\} \,, \tag{B.27}$$

such that the current coordinates and temperatures of the "master" vertices can be computed by

$$\boldsymbol{x} = \boldsymbol{F}^{\mathrm{M}} \cdot \boldsymbol{X} \qquad \forall\, \boldsymbol{X} \in \texttt{vertex\_master} \,, \tag{B.28}$$

$$\theta = \theta^{\mathrm{M}} + \nabla_{\boldsymbol{X}} \theta^{\mathrm{M}} \cdot [\, \boldsymbol{X} - \boldsymbol{X}_{\mathrm{c}}^{\mathrm{m}} \,] \qquad \forall\, \boldsymbol{X} \in \texttt{vertex\_master} \,. \tag{B.29}$$

In order to set up the linear constraint equations for the remaining vertices, a set of dependent "slave" vertex nodes

$$\texttt{vertex\_slave} = \texttt{vertex} \setminus \texttt{vertex\_master} \,, \tag{B.30}$$

has to be defined. Subsequently, the three RVE edges in $\boldsymbol{e}_1$, $\boldsymbol{e}_2$ and $\boldsymbol{e}_3$ directions are defined as master edges

$$\texttt{me}_1 = \{\boldsymbol{X} \in [\,1\,2\,] \setminus \{\boldsymbol{X}_1, \boldsymbol{X}_2\}\} \,, \tag{B.31}$$

$$\texttt{me}_2 = \{\boldsymbol{X} \in [\,1\,4\,] \setminus \{\boldsymbol{X}_1, \boldsymbol{X}_4\}\} \,, \tag{B.32}$$

$$\texttt{me}_3 = \{\boldsymbol{X} \in [\,1\,5\,] \setminus \{\boldsymbol{X}_1, \boldsymbol{X}_5\}\} \,. \tag{B.33}$$

These sets contain all the respective edge nodes but without the vertex nodes. The three other edges in each of the $\boldsymbol{e}_i$-directions are defined as "slave"-edges

$$\texttt{se}_{11} = \{\boldsymbol{X} \in [\,3\,4\,] \setminus \{\boldsymbol{X}_3, \boldsymbol{X}_4\}\} \,, \qquad \texttt{se}_{12} = \{\boldsymbol{X} \in [\,7\,8\,] \setminus \{\boldsymbol{X}_7, \boldsymbol{X}_8\}\} \,, \tag{B.34}$$

$$\texttt{se}_{13} = \{\boldsymbol{X} \in [\,5\,6\,] \setminus \{\boldsymbol{X}_5, \boldsymbol{X}_6\}\} \,, \qquad \texttt{se}_{21} = \{\boldsymbol{X} \in [\,2\,3\,] \setminus \{\boldsymbol{X}_2, \boldsymbol{X}_3\}\} \,, \tag{B.35}$$

$$\texttt{se}_{22} = \{\boldsymbol{X} \in [\,6\,7\,] \setminus \{\boldsymbol{X}_6, \boldsymbol{X}_7\}\} \,, \qquad \texttt{se}_{23} = \{\boldsymbol{X} \in [\,5\,8\,] \setminus \{\boldsymbol{X}_5, \boldsymbol{X}_8\}\} \,, \tag{B.36}$$

$$\texttt{se}_{31} = \{\boldsymbol{X} \in [\,2\,6\,] \setminus \{\boldsymbol{X}_2, \boldsymbol{X}_6\}\} \,, \qquad \texttt{se}_{32} = \{\boldsymbol{X} \in [\,3\,7\,] \setminus \{\boldsymbol{X}_3, \boldsymbol{X}_7\}\} \,, \tag{B.37}$$

$$\texttt{se}_{33} = \{\boldsymbol{X} \in [\,4\,8\,] \setminus \{\boldsymbol{X}_4, \boldsymbol{X}_8\}\} \,, \tag{B.38}$$

where the first number of the subscript indicates the corresponding master edge. Finally, sets of the face nodes on the "$-$"-side ($\boldsymbol{N}_i = -\boldsymbol{e}_i$) are defined as master faces

$$\texttt{mf}_1 = \{\boldsymbol{X} \in [\,1\,4\,8\,5\,] \setminus [\,\{\boldsymbol{X}_1, \boldsymbol{X}_4, \boldsymbol{X}_5, \boldsymbol{X}_8\} \wedge \texttt{me}_2 \wedge \texttt{me}_3 \wedge \texttt{se}_{23} \wedge \texttt{se}_{33}\,]\} \,, \tag{B.39}$$

$$\texttt{mf}_2 = \{\boldsymbol{X} \in [\,1\,5\,6\,2\,] \setminus [\,\{\boldsymbol{X}_1, \boldsymbol{X}_2, \boldsymbol{X}_5, \boldsymbol{X}_6\} \wedge \texttt{me}_1 \wedge \texttt{me}_3 \wedge \texttt{se}_{13} \wedge \texttt{se}_{31}\,]\} \,, \tag{B.40}$$

$$\texttt{mf}_3 = \{\boldsymbol{X} \in [\,1\,2\,3\,4\,] \setminus [\,\{\boldsymbol{X}_1, \boldsymbol{X}_2, \boldsymbol{X}_3, \boldsymbol{X}_4\} \wedge \texttt{me}_1 \wedge \texttt{me}_2 \wedge \texttt{se}_{11} \wedge \texttt{se}_{21}\,]\} \,, \tag{B.41}$$

and their respective counterparts are defined as slave faces on the "$+$"-side ($\boldsymbol{N}_i = \boldsymbol{e}_i$) of the RVE boundary

$$\texttt{sf}_1 = \{\boldsymbol{X} \in [\,2\,6\,7\,3\,] \setminus [\,\{\boldsymbol{X}_2, \boldsymbol{X}_3, \boldsymbol{X}_6, \boldsymbol{X}_7\} \wedge \texttt{se}_{21} \wedge \texttt{se}_{22} \wedge \texttt{se}_{31} \wedge \texttt{se}_{32}\,]\} \,, \tag{B.42}$$

$$\texttt{sf}_2 = \{\boldsymbol{X} \in [\,3\,7\,8\,4\,] \setminus [\,\{\boldsymbol{X}_3, \boldsymbol{X}_4, \boldsymbol{X}_7, \boldsymbol{X}_8\} \wedge \texttt{se}_{11} \wedge \texttt{se}_{12} \wedge \texttt{se}_{32} \wedge \texttt{se}_{33}\,]\} \,, \tag{B.43}$$

$$\texttt{sf}_3 = \{\boldsymbol{X} \in [\,5\,8\,7\,6\,] \setminus [\,\{\boldsymbol{X}_5, \boldsymbol{X}_6, \boldsymbol{X}_7, \boldsymbol{X}_8\} \wedge \texttt{se}_{12} \wedge \texttt{se}_{13} \wedge \texttt{se}_{22} \wedge \texttt{se}_{23}\,]\} \,. \tag{B.44}$$

With these set definitions at hand, homogeneous linear constraints can be formulated for the different slave sets. Fur this purpose, the degrees of freedom per node are denoted by $\boldsymbol{d} = [\,\boldsymbol{u}\,,\ \theta\,]^{\mathrm{t}}$. The linear constraints for the $\mathtt{sf}_i$-sets read

$$\boldsymbol{d}^+ = \boldsymbol{d}^- + \boldsymbol{d}_2 - \boldsymbol{d}_1 \qquad \text{for node pairs } \boldsymbol{X}^+ \in \mathtt{sf}_1 \text{ and } \boldsymbol{X}^- \in \mathtt{mf}_1\ , \tag{B.45}$$

$$\boldsymbol{d}^+ = \boldsymbol{d}^- + \boldsymbol{d}_4 - \boldsymbol{d}_1 \qquad \text{for node pairs } \boldsymbol{X}^+ \in \mathtt{sf}_2 \text{ and } \boldsymbol{X}^- \in \mathtt{mf}_2\ , \tag{B.46}$$

$$\boldsymbol{d}^+ = \boldsymbol{d}^- + \boldsymbol{d}_5 - \boldsymbol{d}_1 \qquad \text{for node pairs } \boldsymbol{X}^+ \in \mathtt{sf}_3 \text{ and } \boldsymbol{X}^- \in \mathtt{mf}_3\ . \tag{B.47}$$

The linear constraints for the slave edges read

$$\boldsymbol{d}^+ = \boldsymbol{d}^- + \boldsymbol{d}_4 - \boldsymbol{d}_1 \qquad \text{for node pairs } \boldsymbol{X}^+ \in \mathtt{se}_{11} \text{ and } \boldsymbol{X}^- \in \mathtt{me}_1\ , \tag{B.48}$$

$$\boldsymbol{d}^+ = \boldsymbol{d}^- + \boldsymbol{d}_4 + \boldsymbol{d}_5 - 2\,\boldsymbol{d}_1 \qquad \text{for node pairs } \boldsymbol{X}^+ \in \mathtt{se}_{12} \text{ and } \boldsymbol{X}^- \in \mathtt{me}_1\ , \tag{B.49}$$

$$\boldsymbol{d}^+ = \boldsymbol{d}^- + \boldsymbol{d}_4 - \boldsymbol{d}_1 \qquad \text{for node pairs } \boldsymbol{X}^+ \in \mathtt{se}_{13} \text{ and } \boldsymbol{X}^- \in \mathtt{me}_1\ , \tag{B.50}$$

$$\boldsymbol{d}^+ = \boldsymbol{d}^- + \boldsymbol{d}_2 - \boldsymbol{d}_1 \qquad \text{for node pairs } \boldsymbol{X}^+ \in \mathtt{se}_{21} \text{ and } \boldsymbol{X}^- \in \mathtt{me}_2\ , \tag{B.51}$$

$$\boldsymbol{d}^+ = \boldsymbol{d}^- + \boldsymbol{d}_2 + \boldsymbol{d}_5 - 2\,\boldsymbol{d}_1 \qquad \text{for node pairs } \boldsymbol{X}^+ \in \mathtt{s1}_{22} \text{ and } \boldsymbol{X}^- \in \mathtt{me}_2\ , \tag{B.52}$$

$$\boldsymbol{d}^+ = \boldsymbol{d}^- + \boldsymbol{d}_5 - \boldsymbol{d}_1 \qquad \text{for node pairs } \boldsymbol{X}^+ \in \mathtt{se}_{23} \text{ and } \boldsymbol{X}^- \in \mathtt{me}_2\ , \tag{B.53}$$

$$\boldsymbol{d}^+ = \boldsymbol{d}^- + \boldsymbol{d}_2 - \boldsymbol{d}_1 \qquad \text{for node pairs } \boldsymbol{X}^+ \in \mathtt{se}_{11} \text{ and } \boldsymbol{X}^- \in \mathtt{me}_3\ , \tag{B.54}$$

$$\boldsymbol{d}^+ = \boldsymbol{d}^- + \boldsymbol{d}_2 + \boldsymbol{d}_4 - 2\,\boldsymbol{d}_1 \qquad \text{for node pairs } \boldsymbol{X}^+ \in \mathtt{se}_{12} \text{ and } \boldsymbol{X}^- \in \mathtt{me}_3\ , \tag{B.55}$$

$$\boldsymbol{d}^+ = \boldsymbol{d}^- + \boldsymbol{d}_4 - \boldsymbol{d}_1 \qquad \text{for node pairs } \boldsymbol{X}^+ \in \mathtt{se}_{13} \text{ and } \boldsymbol{X}^- \in \mathtt{me}_3\ . \tag{B.56}$$

The linear constraints for the `vertex_slave`-set finally read

$$\boldsymbol{d}_3 = \boldsymbol{d}_2 + \boldsymbol{d}_4 - \boldsymbol{d}_1 \qquad \text{for node } \boldsymbol{X}_3\ , \tag{B.57}$$

$$\boldsymbol{d}_6 = \boldsymbol{d}_2 + \boldsymbol{d}_5 - \boldsymbol{d}_1 \qquad \text{for node } \boldsymbol{X}_6\ , \tag{B.58}$$

$$\boldsymbol{d}_7 = \boldsymbol{d}_2 + \boldsymbol{d}_4 + \boldsymbol{d}_5 - 2\,\boldsymbol{d}_1 \qquad \text{for node } \boldsymbol{X}_7\ , \tag{B.59}$$

$$\boldsymbol{d}_8 = \boldsymbol{d}_4 + \boldsymbol{d}_5 - \boldsymbol{d}_1 \qquad \text{for node } \boldsymbol{X}_8\ . \tag{B.60}$$

These linear constraints are imposed to the assembled system of equations via the construction of a constraint matrix $\underline{\underline{\mathbf{T}}}$, see [42, 98] for further details. This matrix is multiplied with the residual as well as with the Jacobian matrix

$$\begin{aligned} \hat{\underline{\mathbf{r}}} &= \underline{\underline{\mathbf{T}}}^{\mathrm{t}} \cdot \underline{\mathbf{r}}\ , \\ \widehat{\underline{\underline{\mathbf{J}}}} &= \underline{\underline{\mathbf{T}}}^{\mathrm{t}} \cdot \underline{\underline{\mathbf{J}}} \cdot \underline{\underline{\mathbf{T}}}\ , \end{aligned} \tag{B.61}$$

in order to reduce the system of equations to the independent degrees of freedom. After the solution of the reduced system of equations, the solution of all degrees of freedom is recovered by $\underline{\mathbf{d}} = \underline{\underline{\mathbf{T}}} \cdot \hat{\underline{\mathbf{d}}}$.

C Implementation of thermo-viscoplasticity

In Chapters 5 and 6 thermo-viscoplastic constitutive models are applied for small as well as finite deformations. The shown numerical examples involve the iterative solution of non-linear systems of equations by means of the Newton-Raphson method. For this purpose it is necessary to consistenly linearise the material models. In this appendix, the equations which are necessary to implement the presented thermo-viscoplastic constitutive models are summarised. In Appendix C.1 the equations related to the small strain material model are collocated, followed by the equations related to the finite deformation variant in Appendix C.2.

C.1 Consistent linearisation of small strain thermo-viscoplasticity

In order to obtain the consistently linearised Jacobian of the finite element framework, Eq. (5.25), the total derivative of the stress $\boldsymbol{\sigma}$, Eq. (5.52), and the mechanical heat production $\hat{r}$, Eq. (5.58), with respect to strain $\boldsymbol{\varepsilon}$ at constant temperature θ must be determined

$$\begin{aligned} \mathrm{d}\boldsymbol{\sigma}\Big|_{\theta=\mathrm{fix}} &= \frac{\partial \boldsymbol{\sigma}}{\partial \boldsymbol{\varepsilon}} : \mathrm{d}\boldsymbol{\varepsilon} + \frac{\partial \boldsymbol{\sigma}}{\partial \underline{\tilde{\mathbf{z}}}} \bullet \mathrm{d}\underline{\tilde{\mathbf{z}}} = \mathbf{E}_{\mathrm{alg}} : \mathrm{d}\boldsymbol{\varepsilon} \\ \mathbf{E}_{\mathrm{alg}} &= \frac{\mathrm{d}\boldsymbol{\sigma}}{\mathrm{d}\boldsymbol{\varepsilon}}\Big|_{\theta=\mathrm{fix}} , \end{aligned} \tag{C.1}$$

$$\begin{aligned} \mathrm{d}\hat{r}\Big|_{\theta=\mathrm{fix}} &= \frac{\partial \hat{r}}{\partial \boldsymbol{\varepsilon}} : \mathrm{d}\boldsymbol{\varepsilon} + \frac{\partial \hat{r}}{\partial \underline{\tilde{\mathbf{z}}}} \bullet \mathrm{d}\underline{\tilde{\mathbf{z}}} = \boldsymbol{\gamma}_{\mathrm{alg}} : \mathrm{d}\boldsymbol{\varepsilon} \\ \boldsymbol{\gamma}_{\mathrm{alg}} &= \frac{\mathrm{d}\hat{r}}{\mathrm{d}\boldsymbol{\varepsilon}}\Big|_{\theta=\mathrm{fix}} , \end{aligned} \tag{C.2}$$

where $\bullet$ represents an appropriate contraction. Analogously, the total derivatives of the stress and the mechanical heat production with respect to the temperature at constant strain are defined as

$$\begin{aligned} \mathrm{d}\boldsymbol{\sigma}\Big|_{\boldsymbol{\varepsilon}=\mathrm{fix}} &= \frac{\partial \boldsymbol{\sigma}}{\partial \theta}\,\mathrm{d}\theta + \frac{\partial \boldsymbol{\sigma}}{\partial \underline{\tilde{\mathbf{z}}}} \bullet \mathrm{d}\underline{\tilde{\mathbf{z}}} = \boldsymbol{\beta}_{\mathrm{alg}}\,\mathrm{d}\theta \\ \boldsymbol{\beta}_{\mathrm{alg}} &= \frac{\mathrm{d}\boldsymbol{\sigma}}{\mathrm{d}\theta}\Big|_{\boldsymbol{\varepsilon}=\mathrm{fix}}\,, \end{aligned} \tag{C.3}$$

$$\begin{aligned} \mathrm{d}\hat{r}\Big|_{\boldsymbol{\varepsilon}=\mathrm{fix}} &= \frac{\partial \hat{r}}{\partial \theta}\,\mathrm{d}\theta + \frac{\partial \hat{r}}{\partial \underline{\tilde{\mathbf{z}}}} \bullet \mathrm{d}\underline{\tilde{\mathbf{z}}} = \zeta_{\mathrm{alg}}\,\mathrm{d}\theta \\ \zeta_{\mathrm{alg}} &= \frac{\mathrm{d}\hat{r}}{\mathrm{d}\theta}\Big|_{\boldsymbol{\varepsilon}=\mathrm{fix}}\,. \end{aligned} \tag{C.4}$$

In order to find a relation between $\mathrm{d}\underline{\tilde{\mathbf{z}}}$ and $\mathrm{d}\boldsymbol{\varepsilon}$ and, respectively, between $\mathrm{d}\underline{\tilde{\mathbf{z}}}$ and $\mathrm{d}\theta$, the linearisation of the local residual Eq. (5.68) at constant temperature as well as at constant strain must be carried out

$$\begin{aligned} \mathrm{d}\underline{\mathbf{r}}_{\mathrm{loc}}\Big|_{\theta=\mathrm{fix}} &= \frac{\partial \underline{\mathbf{r}}_{\mathrm{loc}}}{\partial \boldsymbol{\varepsilon}} : \mathrm{d}\boldsymbol{\varepsilon} + \frac{\partial \underline{\mathbf{r}}_{\mathrm{loc}}}{\partial \underline{\tilde{\mathbf{z}}}} \cdot \mathrm{d}\underline{\tilde{\mathbf{z}}} = \underline{\mathbf{0}} \\ \mathrm{d}\underline{\tilde{\mathbf{z}}}\Big|_{\theta=\mathrm{fix}} &= -\,\underline{\underline{\mathbf{J}}}_{\mathrm{loc}}^{-1} \cdot \frac{\partial \underline{\mathbf{r}}_{\mathrm{loc}}}{\partial \boldsymbol{\varepsilon}} : \mathrm{d}\boldsymbol{\varepsilon}\,, \end{aligned} \tag{C.5}$$

$$\begin{aligned} \mathrm{d}\underline{\mathbf{r}}_{\mathrm{loc}}\Big|_{\boldsymbol{\varepsilon}=\mathrm{fix}} &= \frac{\partial \underline{\mathbf{r}}_{\mathrm{loc}}}{\partial \theta}\,\mathrm{d}\theta + \frac{\partial \underline{\mathbf{r}}_{\mathrm{loc}}}{\partial \underline{\tilde{\mathbf{z}}}} \cdot \mathrm{d}\underline{\tilde{\mathbf{z}}} = \underline{\mathbf{0}} \\ \mathrm{d}\underline{\tilde{\mathbf{z}}}\Big|_{\boldsymbol{\varepsilon}=\mathrm{fix}} &= -\,\underline{\underline{\mathbf{J}}}_{\mathrm{loc}}^{-1} \cdot \frac{\partial \underline{\mathbf{r}}_{\mathrm{loc}}}{\partial \theta}\,\mathrm{d}\theta\,. \end{aligned} \tag{C.6}$$

In the above equations, the expression

$$\underline{\underline{\mathbf{J}}}_{\mathrm{loc}} = \begin{bmatrix} -2\,G - \dfrac{2\,\eta}{\Delta t} & -\sqrt{\dfrac{2}{3}}\,\dfrac{[\,1-r\,]\,[\,y_\infty(\theta) - y_0(\theta)\,]}{k_0}\,\exp\left(-\dfrac{k}{k_0}\right) - r\,h(\theta) \\ \sqrt{\dfrac{2}{3}} & -1 \end{bmatrix}, \tag{C.7}$$

which represents the specification of Eq. (5.69) is inserted. With this at hand, Eqs. (C.1) to (C.4) can be rewritten as

$$\mathbf{E}_{\mathrm{alg}} = \frac{\partial \boldsymbol{\sigma}}{\partial \boldsymbol{\varepsilon}} - \frac{\partial \boldsymbol{\sigma}}{\partial \underline{\tilde{\mathbf{z}}}} \cdot \underline{\underline{\mathbf{J}}}_{\mathrm{loc}}^{-1} \cdot \frac{\partial \underline{\mathbf{r}}_{\mathrm{loc}}}{\partial \boldsymbol{\varepsilon}} \,, \tag{C.8}$$

$$\boldsymbol{\gamma}_{\mathrm{alg}} = \frac{\partial \hat{r}}{\partial \boldsymbol{\varepsilon}} - \frac{\partial \hat{r}}{\partial \underline{\tilde{\mathbf{z}}}} \cdot \underline{\underline{\mathbf{J}}}_{\mathrm{loc}}^{-1} \cdot \frac{\partial \underline{\mathbf{r}}_{\mathrm{loc}}}{\partial \boldsymbol{\varepsilon}} \,, \tag{C.9}$$

$$\boldsymbol{\beta}_{\mathrm{alg}} = \frac{\partial \boldsymbol{\sigma}}{\partial \theta} - \frac{\partial \boldsymbol{\sigma}}{\partial \underline{\tilde{\mathbf{z}}}} \cdot \underline{\underline{\mathbf{J}}}_{\mathrm{loc}}^{-1} \cdot \frac{\partial \underline{\mathbf{r}}_{\mathrm{loc}}}{\partial \theta} \,, \tag{C.10}$$

$$\zeta_{\mathrm{alg}} = \frac{\partial \hat{r}}{\partial \theta} - \frac{\partial \hat{r}}{\partial \underline{\tilde{\mathbf{z}}}} \cdot \underline{\underline{\mathbf{J}}}_{\mathrm{loc}}^{-1} \cdot \frac{\partial \underline{\mathbf{r}}_{\mathrm{loc}}}{\partial \theta} \,, \tag{C.11}$$

such that, subsequently, merely the arising partial derivatives are required to evaluate the given expressions. The partial derivative of Eq. (5.52) with respect to the strain is

$$\frac{\partial \boldsymbol{\sigma}}{\partial \boldsymbol{\varepsilon}} = K\, \boldsymbol{I} \otimes \frac{\partial \operatorname{tr}(\boldsymbol{\varepsilon})}{\boldsymbol{\varepsilon}} + 2\, G\, \frac{\partial \boldsymbol{\varepsilon}_{\mathrm{dev}}}{\partial \boldsymbol{\varepsilon}} - 2\, G\, \Delta\lambda\, \frac{\partial \boldsymbol{\nu}}{\partial \boldsymbol{\varepsilon}} \tag{C.12}$$

with

$$\frac{\partial \boldsymbol{\nu}}{\partial \boldsymbol{\varepsilon}} = \frac{2\, G}{\| \boldsymbol{\sigma}_{\mathrm{dev}}^{\mathrm{tr}} \|} \left[\mathbf{I}^{\mathrm{dev}} - \boldsymbol{\nu} \otimes \boldsymbol{\nu} \right] , \tag{C.13}$$

wherein $\mathbf{I}^{\mathrm{dev}}$ denotes the deviatoric and symmetric fourth order identity tensor, it follows

$$\frac{\partial \boldsymbol{\sigma}}{\partial \boldsymbol{\varepsilon}} = K\, \boldsymbol{I} \otimes \boldsymbol{I} + \left[2\, G - \frac{4\, G^2\, \Delta\lambda}{\| \boldsymbol{\sigma}_{\mathrm{dev}}^{\mathrm{tr}} \|} \right] \mathbf{I}^{\mathrm{dev}} + \frac{4\, G^2\, \Delta\lambda}{\| \boldsymbol{\sigma}_{\mathrm{dev}}^{\mathrm{tr}} \|}\, \boldsymbol{\nu} \otimes \boldsymbol{\nu} \,. \tag{C.14}$$

Furthermore, the partial derivative of Eq. (5.52) with respect to the temperature is given by

$$\frac{\partial \boldsymbol{\sigma}}{\partial \theta} = -3\, \alpha\, K\, \boldsymbol{I} \,. \tag{C.15}$$

Finally, the partial derivative of equation (5.52) with respect to $\underline{\tilde{\mathbf{z}}}$ is

$$\frac{\partial \boldsymbol{\sigma}}{\partial \underline{\tilde{\mathbf{z}}}} = \begin{bmatrix} -2\,G\,\boldsymbol{\nu} \\ \\ \mathbf{0} \end{bmatrix} . \tag{C.16}$$

The partial derivative of the mechanical heat production, given by Eq. (5.58), with respect to the strain is

$$\frac{\partial \hat{r}}{\partial \boldsymbol{\varepsilon}} = -\frac{3\,\alpha\,K\,\theta}{\Delta t}\,\boldsymbol{I} + \frac{2\,G\,\Delta\lambda\,\boldsymbol{\nu}}{\Delta t} \tag{C.17}$$

The partial derivative of the mechanical heat production with respect to the temperature is

$$\frac{\partial \hat{r}}{\partial \theta} = -3\,\alpha\,K\ \mathrm{tr}(\dot{\boldsymbol{\varepsilon}}) + \sqrt{\frac{2}{3}}\,\frac{\partial \tilde{\kappa}}{\partial \theta}\,\frac{\Delta\lambda}{\Delta t}\ , \tag{C.18}$$

wherein the abbreviation

$$\tilde{\kappa} = \kappa - \theta\,\frac{\partial \kappa}{\partial \theta}\ , \tag{C.19}$$

is introduced. The partial derivative of the plastic mechanical heat production with respect to $\underline{\tilde{\mathbf{z}}}$ is

$$\frac{\partial \hat{r}}{\partial \underline{\tilde{\mathbf{z}}}} = \begin{bmatrix} \left[\|\boldsymbol{\sigma}^{\mathrm{tr}}_{\mathrm{dev}}\| - 4\,G\,\Delta\lambda + \sqrt{\frac{2}{3}}\,\tilde{\kappa} \right] \frac{1}{\Delta t} \\ \\ \sqrt{\frac{2}{3}}\,\frac{\partial \tilde{\kappa}}{\partial k}\,\frac{\Delta\lambda}{\Delta t} \end{bmatrix} . \tag{C.20}$$

The partial derivatives of the local residual, Eq. (5.68), with respect to the strain and as well to the temperature are

$$\frac{\partial \underline{\mathbf{r}}_{\mathrm{loc}}}{\partial \boldsymbol{\varepsilon}} = \begin{bmatrix} 2\,G\,\boldsymbol{\nu} \\ \\ \mathbf{0} \end{bmatrix} , \tag{C.21}$$

$$\frac{\partial \underline{\mathbf{r}}_{\mathrm{loc}}}{\partial \theta} = \begin{bmatrix} -\sqrt{\frac{2}{3}} \left[\frac{\partial y_0}{\partial \theta} - \frac{\partial \kappa}{\partial \theta} \right] \\ \\ 0 \end{bmatrix} . \tag{C.22}$$

With the above partial derivatives, the tangent moduli Eqs. (C.8) to (C.11) finally read

$$\mathsf{E}_{\mathrm{alg}} = K\,\boldsymbol{I} \otimes \boldsymbol{I} + \left[2\,G - \frac{4\,G^2\,\Delta\lambda}{\|\boldsymbol{\sigma}^{\mathrm{tr}}_{\mathrm{dev}}\|} \right] \mathsf{I}^{\mathrm{dev}} + \left[\frac{4\,G^2\,\Delta\lambda}{\|\boldsymbol{\sigma}^{\mathrm{tr}}_{\mathrm{dev}}\|} - \frac{4\,G^2}{\det(\underline{\underline{\mathbf{J}}}_{\mathrm{loc}})} \right] \boldsymbol{\nu} \otimes \boldsymbol{\nu} , \tag{C.23}$$

$$\begin{aligned} \boldsymbol{\gamma}_{\mathrm{alg}} = -\frac{3\,\alpha\,K\,\theta}{\Delta t}\,\boldsymbol{I} + \Bigg[& \frac{2\,G\,\Delta\lambda}{\Delta t} - \frac{2\,\mathrm{J}_{\mathrm{loc}\,22}\,G\left[\,\|\boldsymbol{\sigma}^{\mathrm{tr}}_{\mathrm{dev}}\| - 4\,G\,\Delta\lambda + \sqrt{2/3}\,\tilde{\kappa}\,\right]}{\Delta t\,\det(\underline{\underline{\mathbf{J}}}_{\mathrm{loc}})} \\ & + \frac{2\sqrt{6}\,\mathrm{J}_{\mathrm{loc}\,21}\,G\,\Delta\lambda}{3\,\Delta t\,\det(\underline{\underline{\mathbf{J}}}_{\mathrm{loc}})}\,\frac{\partial \tilde{\kappa}}{\partial k} \Bigg] \boldsymbol{\nu} , \end{aligned} \tag{C.24}$$

$$\boldsymbol{\beta}_{\mathrm{alg}} = -3\,\alpha\,K\,\boldsymbol{I} + \frac{2\,G}{\det(\underline{\underline{\mathbf{J}}}_{\mathrm{loc}})} \left[\mathrm{J}_{\mathrm{loc}\,12}\,\frac{\partial k}{\partial \theta} - \mathrm{J}_{\mathrm{loc}\,22}\sqrt{\frac{2}{3}} \left[\frac{\partial y_0}{\partial \theta} - \frac{\partial \kappa}{\partial \theta} \right] \right] \boldsymbol{\nu} , \tag{C.25}$$

$$\begin{aligned} \zeta_{\mathrm{alg}} = & -\frac{3\,\alpha\,K\,\theta\,[\mathrm{tr}(\boldsymbol{\varepsilon}) - \mathrm{tr}(\boldsymbol{\varepsilon}_n)]}{\Delta t} + \sqrt{\frac{2}{3}}\,\frac{\partial \tilde{\kappa}}{\partial \theta}\,\frac{\Delta\lambda}{\Delta t} \\ & - \frac{1}{\Delta t\,\det(\underline{\underline{\mathbf{J}}}_{\mathrm{loc}})} \Bigg[\left[\|\boldsymbol{\sigma}^{\mathrm{tr}}_{\mathrm{dev}}\| - 4\,G\,\Delta\lambda + \sqrt{\frac{2}{3}}\,\tilde{\kappa} \right] \\ & \qquad \left[\mathrm{J}_{\mathrm{loc}\,12}\,\frac{\partial k}{\partial \theta} - \sqrt{\frac{2}{3}}\,\mathrm{J}_{\mathrm{loc}\,22} \left[\frac{\partial y_0}{\partial \theta} - \frac{\partial \kappa}{\partial \theta} \right] \right] \Bigg] \\ & - \frac{1}{\Delta t\,\det(\underline{\underline{\mathbf{J}}}_{\mathrm{loc}})} \left[\left[\sqrt{\frac{2}{3}}\,\frac{\partial \tilde{\kappa}}{\partial k}\,\frac{\Delta\lambda}{\Delta t} \right] \left[-\mathrm{J}_{\mathrm{loc}\,11}\,\frac{\partial k}{\partial \theta} + \sqrt{\frac{2}{3}}\,\mathrm{J}_{\mathrm{loc}\,21} \left[\frac{\partial y_0}{\partial \theta} - \frac{\partial \kappa}{\partial \theta} \right] \right] \right] . \end{aligned} \tag{C.26}$$

Furthermore, the total derivative of the heat flux, Eq. (5.59), with respect to the temperature gradient $\nabla_{\boldsymbol{x}}\,\theta$ reads

$$\boldsymbol{L}_{\mathrm{alg}} = \frac{\mathrm{d}\boldsymbol{q}}{\mathrm{d}\,\nabla_{\boldsymbol{x}}\,\theta} = -\Lambda\,\boldsymbol{I}\ . \tag{C.27}$$

Details regarding the total derivative of the surface heat flux contribution, cf. Eq. $(5.4)_4$, can be found in Chapter 4.

Algorithm C.1: Radial return algorithm: Small strain thermo-viscoplasticity with von Mises type yield function and isotropic hardening.

Data: $\boldsymbol{\varepsilon}_{n+1}$, $\underline{\mathbf{z}}_n = [\,\boldsymbol{\varepsilon}^{\mathrm{p}}_n\,,\, k_n\,]^{\mathrm{t}}$, the strains of current time step and internal variables of previous state of equilibrium

compute trial values

$$\boldsymbol{\sigma}_{\mathrm{vol}\,n+1} = K\,\big[\,\mathrm{tr}\,(\boldsymbol{\varepsilon}_{n+1}) - 3\,\alpha\,[\,\theta - \theta_0\,]\,\big]\,\boldsymbol{I}\;,$$

$$\kappa^{\mathrm{tr}}_{n+1} = -[\,1-r\,]\,[\,y_\infty(\theta) - y_0(\theta)\,]\left[\,1 - \exp\left(-\frac{k_n}{k_0}\right)\,\right] - r\,h(\theta)\,k_n$$

$$\boldsymbol{\sigma}^{\mathrm{tr}}_{\mathrm{dev}\,n+1} = 2\,G\,\big[\,\boldsymbol{\varepsilon}^{\mathrm{dev}}_{n+1} - \boldsymbol{\varepsilon}^{\mathrm{p}}_n\,\big]\;,$$

$$\Phi^{\mathrm{tr}}_{n+1} = \|\boldsymbol{\sigma}^{\mathrm{tr}}_{\mathrm{dev}\,n+1}\| - \sqrt{\frac{2}{3}}\left[\,y_0(\theta) - \kappa^{\mathrm{tr}}_{n+1}\,\right]$$

check yield condition

if $\Phi^{\mathrm{tr}}_{n+1} \leq 0$ **then** Load step is thermoelastic

internal variables do not change during the current loadstep $\underline{\mathbf{z}}_{n+1} = \underline{\mathbf{z}}_n$

compute stresses $\boldsymbol{\sigma}_{n+1} = \boldsymbol{\sigma}_{\mathrm{vol}\,n+1} + \boldsymbol{\sigma}^{\mathrm{tr}}_{\mathrm{dev}\,n+1}$

compute tangent moduli

$$\mathsf{E}_{\mathrm{alg}\,n+1} = K\,\boldsymbol{I}\otimes\boldsymbol{I} + 2\,G\,\mathsf{I}^{\mathrm{dev}}\;, \qquad \boldsymbol{\gamma}_{\mathrm{alg}\,n+1} = -\frac{3\,\alpha\,K\,\theta}{\Delta t}\,\boldsymbol{I}$$

$$\boldsymbol{\beta}_{\mathrm{alg}\,n+1} = -3\,\alpha\,K\,\boldsymbol{I}\;, \qquad \zeta_{\mathrm{alg}\,n+1} = -\frac{3\,\alpha\,K\,\theta\,[\,\mathrm{tr}(\boldsymbol{\varepsilon}) - \mathrm{tr}(\boldsymbol{\varepsilon}_n)\,]}{\Delta t}$$

else Load step is thermoviscoplastic

set iteration counter $m = 0$ and hardening variable $k^0_{n+1} = k_n$

define the initial guess of set of local unknowns $\tilde{\underline{\mathbf{z}}}^0_{n+1} = \big[\,0\,,\, k^0_{n+1}\,\big]^{\mathrm{t}}$

formulate a residual vector $\underline{\mathbf{r}}^0_{\mathrm{loc}}(\tilde{\underline{\mathbf{z}}}^0_{n+1})$ according to Eq. (5.68)

while $\|\underline{\mathbf{r}}_{\mathrm{loc}}(\tilde{\underline{\mathbf{z}}}^m_{n+1})\| \geq$ `tol` **do** `// Newton-Raphson loop at constitutive level`

$$\text{solve} \quad \underline{\underline{\mathbf{J}}}_{\mathrm{loc}}(\tilde{\underline{\mathbf{z}}}^m_{n+1}) \cdot \Delta\tilde{\underline{\mathbf{z}}} = -\underline{\mathbf{r}}_{\mathrm{loc}}(\tilde{\underline{\mathbf{z}}}^m_{n+1})$$

$$\text{update} \quad \tilde{\underline{\mathbf{z}}}^{m+1}_{n+1} = \tilde{\underline{\mathbf{z}}}^m_{n+1} + \Delta\tilde{\underline{\mathbf{z}}}$$

$$\text{index} \quad m \leftarrow m+1$$

whereby the local Jacobian $\underline{\underline{\mathbf{J}}}_{\mathrm{loc}}$ is evaluated according to Eq. (C.7)

end

extract $\Delta\lambda_{n+1}$ and k_{n+1} from $\tilde{\underline{\mathbf{z}}}^m_{n+1}$ and calculate $\boldsymbol{\nu}_{n+1}$, cf. Eq. (5.55)

compute plastic strains $\boldsymbol{\varepsilon}^{\mathrm{p}}_{n+1} = \boldsymbol{\varepsilon}^{\mathrm{p}}_n + \Delta\lambda_{n+1}\,\boldsymbol{\nu}_{n+1}$

update internal variables $\underline{\mathbf{z}}_{n+1} = \big[\,\boldsymbol{\varepsilon}^{\mathrm{p}}_{n+1}\,,\, k_{n+1}\,\big]^{\mathrm{t}}$

compute the deviatoric part of the stresses $\boldsymbol{\sigma}_{\mathrm{dev}\,n+1} = \boldsymbol{\sigma}^{\mathrm{tr}}_{\mathrm{dev}\,n+1} - 2\,G\,\Delta\lambda_{n+1}\,\boldsymbol{\nu}_{n+1}$

compute stresses $\boldsymbol{\sigma}_{n+1} = \boldsymbol{\sigma}_{\mathrm{vol}\,n+1} + \boldsymbol{\sigma}_{\mathrm{dev}\,n+1}$

compute tangent moduli $\mathsf{E}_{\mathrm{alg}\,n+1}$, $\boldsymbol{\gamma}_{\mathrm{alg}\,n+1}$, $\boldsymbol{\beta}_{\mathrm{alg}\,n+1}$, $\zeta_{\mathrm{alg}\,n+1}$, cf. Eqs. (C.23) to (C.26)

end

save the internal variables $\underline{\mathbf{z}}_{n+1}$ for the next time step

computation of the heat flux and the thermal tangent moduli

$$\boldsymbol{q}_{n+1} = -\,\boldsymbol{\Lambda}\cdot\nabla_{\boldsymbol{x}}\,\theta_{n+1}\;, \qquad \boldsymbol{L}_{\mathrm{alg}\,n+1} = -\Lambda\,\boldsymbol{I}$$

C.2 Consistent linearisation of large strain thermo-viscoplasticity

In order to obtain the consistently linearised Jacobian of the finite element framework, the total derivative of the Piola stresses $\boldsymbol{P}$, Eq. (6.48) and the mechanical heat production $\hat{r}_0$, Eq. (6.49) with respect to the deformation gradient $\boldsymbol{F}$ at constant temperature θ must be determined

$$\begin{aligned} \mathrm{d}\boldsymbol{P}\Big|_{\theta=\mathrm{fix}} &= \frac{\partial \boldsymbol{P}}{\partial \boldsymbol{F}} : \mathrm{d}\boldsymbol{F} + \frac{\partial \boldsymbol{P}}{\partial \underline{\mathbf{z}}} \bullet \mathrm{d}\underline{\mathbf{z}} = \mathbf{A}_{\mathrm{alg}} : \mathrm{d}\boldsymbol{F} \\ \mathbf{A}_{\mathrm{alg}} &= \frac{\mathrm{d}\boldsymbol{P}}{\mathrm{d}\boldsymbol{F}}\Big|_{\theta=\mathrm{fix}} , \end{aligned} \tag{C.28}$$

$$\begin{aligned} \mathrm{d}\hat{r}_0\Big|_{\theta=\mathrm{fix}} &= \frac{\partial \hat{r}_0}{\partial \boldsymbol{F}} : \mathrm{d}\boldsymbol{F} + \frac{\partial \hat{r}_0}{\partial \underline{\mathbf{z}}} \bullet \mathrm{d}\underline{\mathbf{z}} = \boldsymbol{\Gamma}_{\mathrm{alg}} : \mathrm{d}\boldsymbol{F} \\ \boldsymbol{\Gamma}_{\mathrm{alg}} &= \frac{\mathrm{d}\hat{r}_0}{\mathrm{d}\boldsymbol{F}}\Big|_{\theta=\mathrm{fix}} , \end{aligned} \tag{C.29}$$

where $\bullet$ represents an appropriate contraction and $\underline{\mathbf{z}}$ is the vector of variables which are involved in the algorithm to obtain the solution of the return mapping algorithm. These variables are introduced below. Analogously to the above equations, the total derivatives of the Piola stresses ans the mechanical heat production with respect to the temperature at constant deformation are defined as

$$\begin{aligned} \mathrm{d}\boldsymbol{P}\Big|_{\boldsymbol{F}=\mathrm{fix}} &= \frac{\partial \boldsymbol{P}}{\partial \theta} : \mathrm{d}\theta + \frac{\partial \boldsymbol{P}}{\partial \underline{\mathbf{z}}} \bullet \mathrm{d}\underline{\mathbf{z}} = \boldsymbol{\beta}_{\mathrm{alg}}\, \mathrm{d}\theta \\ \boldsymbol{\beta}_{\mathrm{alg}} &= \frac{\mathrm{d}\boldsymbol{P}}{\mathrm{d}\theta}\Big|_{\boldsymbol{F}=\mathrm{fix}} , \end{aligned} \tag{C.30}$$

$$\begin{aligned} \mathrm{d}\hat{r}_0\Big|_{\boldsymbol{F}=\mathrm{fix}} &= \frac{\partial \hat{r}_0}{\partial \theta}\, \mathrm{d}\theta + \frac{\partial \hat{r}_0}{\partial \underline{\mathbf{z}}} \bullet \mathrm{d}\underline{\mathbf{z}} = \zeta_{\mathrm{alg}}\, \mathrm{d}\theta \\ \zeta_{\mathrm{alg}} &= \frac{\mathrm{d}\hat{r}_0}{\mathrm{d}\theta}\Big|_{\boldsymbol{F}=\mathrm{fix}} . \end{aligned} \tag{C.31}$$

The terms of the local residual of the return mapping algorithm result from Eqs. (6.44), (6.45) and (6.47) and read

$$\mathrm{r}_{\Delta\lambda} = \widetilde{\Phi}(\boldsymbol{M}_{\mathrm{dev}}^{n+1}, \kappa^{n+1}, \Delta\lambda) = \left\langle \, \|\boldsymbol{M}_{\mathrm{dev}}^{n+1}\| - \left[\, y_0(\theta) - \kappa^{n+1} \, \right] \right\rangle - 2\,\eta\,\Delta\lambda \,/\, \Delta t \;, \quad \text{(C.32)}$$

$$\underline{\mathbf{r}}_{\boldsymbol{F}_{\mathrm{p}}} = \left[\left[\boldsymbol{I} - \Delta\lambda \, \frac{\boldsymbol{M}_{\mathrm{dev}}^{n+1}}{\|\boldsymbol{M}_{\mathrm{dev}}^{n+1}\|} \right] \cdot \boldsymbol{F}_{\mathrm{p}}^{n+1} - \boldsymbol{F}_{\mathrm{p}}^{n} + \Delta\lambda_{\mathrm{iso}} \, J_{\mathrm{p}}^{n+1} \left[\boldsymbol{F}_{\mathrm{p}}^{n+1} \right]^{-\mathrm{t}} \right]^{\mathrm{Kel}} \;, \quad \text{(C.33)}$$

where the time integration is performed by means of the Backward Euler method and $\Delta\lambda_{\mathrm{iso}}$ is a Lagrange multiplier which enforces the restriction $J_{\mathrm{p}} = \det(\boldsymbol{F}_{\mathrm{p}}) = 1$. For doing so, an additional residual equation

$$\mathrm{r}_{\Delta\lambda_{\mathrm{iso}}} = J_{\mathrm{p}}^{n+1} - 1 \quad \text{(C.34)}$$

is introduced, cf. Denzer and Menzel [47]. In the remaining part of this section, the indication of the current time step "$n+1$" is omitted. It is implied that non-indicated variables are related to the current time step. The resulting residual is

$$\underline{\mathbf{r}}_{\mathrm{loc}} = \begin{bmatrix} \mathrm{r}_{\Delta\lambda} \\ \underline{\mathbf{r}}_{\boldsymbol{F}_{\mathrm{p}}} \\ \mathrm{r}_{\mathrm{iso}} \end{bmatrix} = \begin{bmatrix} 0 \\ \underline{\mathbf{0}} \\ 0 \end{bmatrix} \;, \quad \text{(C.35)}$$

and the corresponding vector of local variables is

$$\underline{\mathbf{z}} = \begin{bmatrix} \Delta\lambda \\ [\, \boldsymbol{F}_{\mathrm{p}} \,]^{\mathrm{Kel}} \\ \Delta\lambda_{\mathrm{iso}} \end{bmatrix} \;. \quad \text{(C.36)}$$

The local Jacobian which is needed to perform the iterative solution by means of a Newton-Raphson scheme is

$$\underline{\underline{\mathbf{J}}}_{\mathrm{loc}} = \frac{\mathrm{d}\underline{\mathbf{r}}_{\mathrm{loc}}}{\mathrm{d}\underline{\mathbf{z}}} = \begin{bmatrix} \dfrac{\partial \mathrm{r}_{\Delta\lambda}}{\partial \Delta\lambda} & \dfrac{\partial \mathrm{r}_{\Delta\lambda}}{\partial \boldsymbol{F}_{\mathrm{p}}} & \dfrac{\partial \mathrm{r}_{\Delta\lambda}}{\partial \Delta\lambda_{\mathrm{iso}}} \\ \dfrac{\partial \underline{\mathbf{r}}_{\boldsymbol{F}_{\mathrm{p}}}}{\partial \Delta\lambda} & \dfrac{\partial \underline{\mathbf{r}}_{\boldsymbol{F}_{\mathrm{p}}}}{\partial \boldsymbol{F}_{\mathrm{p}}} & \dfrac{\partial \underline{\mathbf{r}}_{\boldsymbol{F}_{\mathrm{p}}}}{\partial \Delta\lambda_{\mathrm{iso}}} \\ \dfrac{\partial \mathrm{r}_{\mathrm{iso}}}{\partial \Delta\lambda} & \dfrac{\partial \mathrm{r}_{\mathrm{iso}}}{\partial \boldsymbol{F}_{\mathrm{p}}} & \dfrac{\partial \mathrm{r}_{\mathrm{iso}}}{\partial \Delta\lambda_{\mathrm{iso}}} \end{bmatrix} \;. \quad \text{(C.37)}$$

When local convergence is achieved, the differential $\mathrm{d}\underline{\mathbf{z}}$ for fixed deformation as well as fixed temperature can be expressed by

$$\mathrm{d}\underline{\mathbf{z}}\Big|_{\theta=\mathrm{fix}} = -\underline{\underline{\mathbf{J}}}_{\mathrm{loc}}^{-1} \cdot \frac{\partial \underline{\mathbf{r}}_{\mathrm{loc}}}{\partial \boldsymbol{F}} : \mathrm{d}\boldsymbol{F} \,, \tag{C.38}$$

$$\mathrm{d}\underline{\mathbf{z}}\Big|_{\boldsymbol{F}=\mathrm{fix}} = -\underline{\underline{\mathbf{J}}}_{\mathrm{loc}}^{-1} \cdot \frac{\partial \underline{\mathbf{r}}_{\mathrm{loc}}}{\partial \theta} \,\mathrm{d}\theta \,. \tag{C.39}$$

With these relations at hand, the algorithmic moduli Eqs. (C.28) to (C.31) can be rewritten as

$$\mathbf{A}_{\mathrm{alg}} = \frac{\partial \boldsymbol{P}}{\partial \boldsymbol{F}} - \frac{\partial \boldsymbol{P}}{\partial \underline{\mathbf{z}}} \cdot \underline{\underline{\mathbf{J}}}_{\mathrm{loc}}^{-1} \cdot \frac{\partial \underline{\mathbf{r}}_{\mathrm{loc}}}{\partial \boldsymbol{F}} \,, \tag{C.40}$$

$$\boldsymbol{\Gamma}_{\mathrm{alg}} = \frac{\partial \hat{r}_0}{\partial \boldsymbol{F}} - \frac{\partial \hat{r}_0}{\partial \underline{\mathbf{z}}} \cdot \underline{\underline{\mathbf{J}}}_{\mathrm{loc}}^{-1} \cdot \frac{\partial \underline{\mathbf{r}}_{\mathrm{loc}}}{\partial \boldsymbol{F}} \,, \tag{C.41}$$

$$\boldsymbol{\beta}_{\mathrm{alg}} = \frac{\partial \boldsymbol{P}}{\partial \theta} - \frac{\partial \boldsymbol{P}}{\partial \underline{\mathbf{z}}} \cdot \underline{\underline{\mathbf{J}}}_{\mathrm{loc}}^{-1} \cdot \frac{\partial \underline{\mathbf{r}}_{\mathrm{loc}}}{\partial \theta} \,, \tag{C.42}$$

$$\zeta_{\mathrm{alg}} = \frac{\partial \hat{r}_0}{\partial \theta} - \frac{\partial \hat{r}_0}{\partial \underline{\mathbf{z}}} \cdot \underline{\underline{\mathbf{J}}}_{\mathrm{loc}}^{-1} \cdot \frac{\partial \underline{\mathbf{r}}_{\mathrm{loc}}}{\partial \theta} \,. \tag{C.43}$$

In the following, the partial derivatives for the considered material model are specified.

The local Jacobian terms related to $\mathrm{r}_{\Delta\lambda}$ are

$$\frac{\partial \mathrm{r}_{\Delta\lambda}}{\partial \Delta\lambda} = -\frac{2\,\eta}{\Delta t} \,, \tag{C.44}$$

$$\frac{\partial \mathrm{r}_{\Delta\lambda}}{\partial \boldsymbol{F}_{\mathrm{p}}} = \frac{\partial \|\boldsymbol{M}_{\mathrm{dev}}\|}{\partial \boldsymbol{M}} : \frac{\partial \boldsymbol{M}}{\partial \boldsymbol{F}_{\mathrm{e}}} : \frac{\partial \boldsymbol{F}_{\mathrm{e}}}{\partial \boldsymbol{F}_{\mathrm{p}}} \,, \tag{C.45}$$

$$\frac{\partial \mathrm{r}_{\Delta\lambda}}{\partial \Delta\lambda_{\mathrm{iso}}} = 0 \,, \tag{C.46}$$

with

$$\frac{\partial \boldsymbol{M}}{\partial \boldsymbol{F}_\mathrm{e}} = \mu\, [J_\mathrm{e}]^{-2/3} \left[[\boldsymbol{F}_\mathrm{e}]^\mathrm{t} \mathbin{\overline{\otimes}} \boldsymbol{I} + \boldsymbol{I} \mathbin{\underline{\otimes}} [\boldsymbol{F}_\mathrm{e}]^\mathrm{t} - \frac{2}{3} \boldsymbol{C}_\mathrm{e} \otimes [\boldsymbol{F}_\mathrm{e}]^{-\mathrm{t}} - \frac{2}{3} \boldsymbol{I} \otimes \left[\boldsymbol{F}_\mathrm{e} - \frac{1}{3}\, \mathrm{tr}\,(\boldsymbol{C}_\mathrm{e})\, [\boldsymbol{F}_\mathrm{e}]^{-\mathrm{t}} \right] \right] + K \left[[J_\mathrm{e}]^2 - \frac{3\,\alpha_0}{2}\, [\,\theta - \theta_0\,] \left[J_\mathrm{e} - \frac{1}{J_\mathrm{e}} \right] \right] \boldsymbol{I} \otimes [\boldsymbol{F}_\mathrm{e}]^{-\mathrm{t}} \,, \tag{C.47}$$

and

$$\frac{\partial \boldsymbol{F}_\mathrm{e}}{\partial \boldsymbol{F}_\mathrm{p}} = -\boldsymbol{F}_\mathrm{e} \mathbin{\overline{\otimes}} \boldsymbol{F}_\mathrm{p}{}^{-\mathrm{t}} \,. \tag{C.48}$$

The local Jacobian terms related to $\underline{\mathbf{r}}_{\boldsymbol{F}_\mathrm{p}}$ are

$$\frac{\partial \underline{\mathbf{r}}_{\boldsymbol{F}_\mathrm{p}}}{\partial \Delta\lambda} = -\frac{\boldsymbol{M}_\mathrm{dev}}{\|\boldsymbol{M}_\mathrm{dev}\|} \cdot \boldsymbol{F}_\mathrm{p} \,, \tag{C.49}$$

$$\frac{\partial \underline{\mathbf{r}}_{\boldsymbol{F}_\mathrm{p}}}{\partial \boldsymbol{F}_\mathrm{p}} = [\,\boldsymbol{I} - \Delta\lambda\, \boldsymbol{N}\,] \cdot \mathbf{I} - \Delta\lambda\, \frac{\partial \boldsymbol{N}}{\partial \boldsymbol{M}} : \frac{\partial \boldsymbol{M}}{\partial \boldsymbol{F}_\mathrm{e}} : \frac{\partial \boldsymbol{F}_\mathrm{e}}{\partial \boldsymbol{F}_\mathrm{p}} + J_\mathrm{p} \left[\boldsymbol{F}_\mathrm{p}{}^{-\mathrm{t}} \otimes \boldsymbol{F}_\mathrm{p}{}^{-\mathrm{t}} - \boldsymbol{F}_\mathrm{p}{}^{-\mathrm{t}} \mathbin{\underline{\otimes}} \boldsymbol{F}_\mathrm{p}{}^{-1} \right] \,, \tag{C.50}$$

$$\frac{\partial \underline{\mathbf{r}}_{\boldsymbol{F}_\mathrm{p}}}{\partial \Delta\lambda_\mathrm{iso}} = J_\mathrm{p}\, [\boldsymbol{F}_\mathrm{p}]^{-\mathrm{t}} \,, \tag{C.51}$$

with Eqs. (C.47) and (C.48) and

$$\frac{\partial \boldsymbol{N}_\mathrm{dev}}{\partial \boldsymbol{M}} = \frac{1}{\|\boldsymbol{M}_\mathrm{dev}\|} \left[\mathbf{I}^\mathrm{dev} - \boldsymbol{N} \otimes \boldsymbol{N} \right] \,. \tag{C.52}$$

The local Jacobian terms related to $\mathrm{r}_{\Delta\lambda_\mathrm{iso}}$ are

$$\frac{\partial \mathrm{r}_{\Delta\lambda_\mathrm{iso}}}{\partial \Delta\lambda} = 0 \,, \tag{C.53}$$

$$\frac{\partial \mathrm{r}_{\Delta\lambda_\mathrm{iso}}}{\partial \boldsymbol{F}_\mathrm{p}} = J_\mathrm{p}\, \boldsymbol{F}_\mathrm{p}{}^{-\mathrm{t}} \,, \tag{C.54}$$

$$\frac{\partial \mathrm{r}_{\Delta\lambda_\mathrm{iso}}}{\partial \Delta\lambda_\mathrm{iso}} = 0 \,, \tag{C.55}$$

The partial derivative of the Piola stresses with respect to the deformation gradient is

$$\begin{aligned}\frac{\partial \boldsymbol{P}}{\partial \boldsymbol{F}} &= G\,J^{-2/3}\,\boldsymbol{I}\,\overline{\otimes}\,\boldsymbol{C}_{\mathrm{p}}^{-1} - \frac{2}{3}\,G\,J^{-2/3}\,\left[\,\boldsymbol{F}\cdot\boldsymbol{C}_{\mathrm{p}}^{-1}\,\right]\otimes\boldsymbol{F}^{-\mathrm{t}} \\ &- \frac{2}{3}\,G\,J^{-2/3}\,\boldsymbol{F}^{-\mathrm{t}}\otimes\left[\,\boldsymbol{F}\cdot\boldsymbol{C}_{\mathrm{p}}^{-1}\,\right] + \left[\frac{1}{3}\,G\,J^{-2/3}\,\boldsymbol{C}:\boldsymbol{C}_{\mathrm{p}}^{-1}\right]\,\boldsymbol{F}^{-\mathrm{t}}\,\underline{\otimes}\,\boldsymbol{F}^{-1} \\ &+ \left[-\frac{1}{2}\,K\,\left[\,J^2-1\,\right] + \frac{3\,\alpha_0\,K}{2}\,\left[\,\theta-\theta_0\,\right]\,\left[\,J+J^{-1}\,\right]\right]\,\boldsymbol{F}^{-\mathrm{t}}\otimes\boldsymbol{F}^{-1} \\ &+ \left[\frac{2}{9}\,G\,J^{-2/3}\,\boldsymbol{C}:\boldsymbol{C}_{\mathrm{p}}^{-1} + K\,J^2 - \frac{3\,\alpha_0\,K}{2}\,\left[\,\theta-\theta_0\,\right]\,\left[\,J-J^{-1}\,\right]\right]\,\boldsymbol{F}^{-\mathrm{t}}\otimes\boldsymbol{F}^{-\mathrm{t}}\,.\end{aligned} \tag{C.56}$$

The partial derivative of the Piola stresses with respect to the temperature is

$$\frac{\partial \boldsymbol{P}}{\partial \theta} = -\frac{3\,\alpha_0\,K}{2}\,\left[J_{\mathrm{e}} + {J_{\mathrm{e}}}^{-1}\right]\,\boldsymbol{F}^{-\mathrm{t}}\,. \tag{C.57}$$

The partial derivative of the mechanical heat production with respect to the deformation gradient is

$$\begin{aligned}\frac{\partial \hat{r}_0}{\partial \boldsymbol{F}} &= \left[3\,\alpha_0\,K\,\theta\,\left[\,J^{-2}\,\dot{J} - \frac{1}{2}\,\left[\,J+J^{-1}\,\right]\,\frac{\partial \dot{J}}{\partial J}\right]\right]\,\boldsymbol{F}^{-\mathrm{t}} \\ &- \left[\frac{2}{3}\,G\,J^{-2/3}\,\left[\,\boldsymbol{F}_{\mathrm{p}}^{-\mathrm{t}}\cdot\boldsymbol{C}\cdot\boldsymbol{C}_{\mathrm{p}}^{-1}\,\right]:\dot{\boldsymbol{F}}_{\mathrm{p}}\right]\,\boldsymbol{F}^{-\mathrm{t}} + 2\,G\,J^{-2/3}\,\boldsymbol{F}_{\mathrm{e}}\cdot\boldsymbol{L}_{\mathrm{p}}\cdot\boldsymbol{F}_{\mathrm{p}}^{-\mathrm{t}}\,.\end{aligned} \tag{C.58}$$

The partial derivative of the mechanical heat production with respect to the temperature is

$$\frac{\partial \hat{r}_0}{\partial \theta} = -\frac{3\,\alpha_0\,K}{2}\,\left[\,1+J^{-2}\,\right]\,\dot{J} - \theta\,\frac{\partial^2 \kappa}{\partial \theta^2}\,\dot{\lambda}\,. \tag{C.59}$$

The partial derivative of the Piola stresses with respect to $\underline{\mathbf{z}}$ is

$$\frac{\partial \boldsymbol{P}}{\partial \underline{\mathbf{z}}} = \begin{bmatrix} \mathbf{0} \\ \left[\,\dfrac{\partial \boldsymbol{P}}{\partial \boldsymbol{F}_{\mathrm{p}}}\,\right]^{\mathrm{Kel}} \\ \mathbf{0} \end{bmatrix}\,, \tag{C.60}$$

with

$$\begin{aligned}\frac{\partial \boldsymbol{P}}{\partial \boldsymbol{F}_\mathrm{p}} = &- G\, J^{-2/3} && \boldsymbol{F}_\mathrm{e} \mathbin{\overline{\otimes}} \boldsymbol{C}_\mathrm{p}^{-1} \\ &- G\, J^{-2/3} && \left[\, \boldsymbol{F} \cdot \boldsymbol{C}_\mathrm{p}^{-1} \,\right] \mathbin{\underline{\otimes}} \boldsymbol{F}_\mathrm{p}^{-1} \\ &+ \frac{2}{3}\, G\, J^{-2/3} && \boldsymbol{F}^{-\mathrm{t}} \otimes \left[\, \boldsymbol{F}_\mathrm{p}^{-\mathrm{t}} \cdot \boldsymbol{C} \cdot \boldsymbol{C}_\mathrm{p}^{-1} \,\right] \,.\end{aligned} \tag{C.61}$$

The partial derivative of the mechanical heat production with respect to $\underline{\mathbf{z}}$ is

$$\frac{\partial \hat{r}_0}{\partial \underline{\mathbf{z}}} = \begin{bmatrix} \left[\dfrac{\partial \hat{r}}{\partial \Delta\lambda} \right]^{\mathrm{Kel}} \\ \dfrac{\partial \hat{r}}{\partial \boldsymbol{F}_\mathrm{p}} \\ 0 \end{bmatrix} \,, \tag{C.62}$$

with

$$\frac{\partial \hat{r}_0}{\partial \Delta\lambda} = \left[\kappa - \theta \frac{\partial \kappa}{\partial \theta} \right] \frac{\partial \dot{\lambda}}{\partial \Delta\lambda} \,, \tag{C.63}$$

and

$$\begin{aligned}\frac{\partial \hat{r}_0}{\partial \boldsymbol{F}_\mathrm{p}} = &\frac{G\, J^{-2/3}}{\Delta t} && \boldsymbol{F}_\mathrm{p}^{-\mathrm{t}} \cdot \boldsymbol{C} \cdot \boldsymbol{C}_\mathrm{p}^{-1} \\ &- G\, J^{-2/3} && \boldsymbol{F}_\mathrm{p}^{-\mathrm{t}} \cdot \boldsymbol{C} \cdot \boldsymbol{C}_\mathrm{p}^{-1} \cdot \boldsymbol{L}_\mathrm{p}^{\mathrm{t}} \\ &- G\, J^{-2/3} && \boldsymbol{F}_\mathrm{p}^{-\mathrm{t}} \cdot \boldsymbol{C} \cdot \boldsymbol{L}_\mathrm{p} \cdot \boldsymbol{C}_\mathrm{p}^{-1} \\ &- G\, J^{-2/3} && \boldsymbol{F}_\mathrm{p}^{-\mathrm{t}} \cdot \boldsymbol{L}_\mathrm{p}^{\mathrm{t}} \cdot \boldsymbol{C} \cdot \boldsymbol{C}_\mathrm{p}^{-1} \,.\end{aligned} \tag{C.64}$$

The partial derivative of the local residual with respect to the deformation gradient is

$$\frac{\partial \underline{\mathbf{r}}_\mathrm{loc}}{\partial \boldsymbol{F}} = \begin{bmatrix} \dfrac{\partial \mathrm{r}_{\Delta\lambda}}{\partial \boldsymbol{F}} \\ \dfrac{\partial \underline{\mathbf{r}}_{\boldsymbol{F}_\mathrm{p}}}{\partial \boldsymbol{F}} \\ 0 \end{bmatrix} \,, \tag{C.65}$$

with

$$\frac{\partial \mathrm{r}_{\Delta\lambda}}{\partial \boldsymbol{F}} = \boldsymbol{N} : \frac{\partial \boldsymbol{M}_\mathrm{dev}}{\partial \boldsymbol{F}} \,, \tag{C.66}$$

and, in index notation,

$$\frac{\partial \left[\underline{\mathbf{r}}_{\boldsymbol{F}_\mathrm{p}} \right]_{IJ}}{\partial F_{kL}} = -\Delta\lambda \frac{\partial N_{IM}}{\partial F_{kL}} \left[F_\mathrm{p}\right]_{MJ} = -\Delta\lambda \frac{\partial N_{IM}}{\partial [M_\mathrm{dev}]_{NO}} \frac{[M_\mathrm{dev}]_{NO}}{\partial F_{kL}} \left[F_\mathrm{p}\right]_{MJ} , \tag{C.67}$$

with

$$\begin{aligned} \frac{\partial \boldsymbol{M}_\mathrm{dev}}{\partial \boldsymbol{F}} &= G\, J^{-2/3} && \left[\boldsymbol{F}_\mathrm{p}^{-\mathrm{t}} \cdot \boldsymbol{F}^{\mathrm{t}} \right] \mathbin{\overline{\otimes}} \boldsymbol{F}_\mathrm{p}^{-\mathrm{t}} \\ &+ G\, J^{-2/3} && \boldsymbol{F}_\mathrm{p}^{-\mathrm{t}} \mathbin{\underline{\otimes}} \left[\boldsymbol{F}_\mathrm{p}^{-\mathrm{t}} \cdot \boldsymbol{F}^{\mathrm{t}} \right] \\ &- \frac{2}{3} G\, J^{-2/3} && \left[\boldsymbol{F}_\mathrm{p}^{-\mathrm{t}} \cdot \boldsymbol{C} \cdot \boldsymbol{F}_\mathrm{p}^{-1} \right] \otimes \boldsymbol{F}^{-\mathrm{t}} \\ &- \frac{2}{3} G\, J^{-2/3} && \boldsymbol{I} \otimes \left[\boldsymbol{F} \cdot \boldsymbol{C}_\mathrm{p}^{-1} \right] \\ &+ \frac{2}{9} \left[\boldsymbol{C} : \boldsymbol{C}_\mathrm{p}^{-1} \right] && \boldsymbol{I} \otimes \boldsymbol{F}^{-\mathrm{t}} . \end{aligned} \tag{C.68}$$

The partial derivative of the local residual with respect to the temperature is

$$\frac{\partial \underline{\mathbf{r}}_\mathrm{loc}}{\partial \theta} = \begin{bmatrix} \dfrac{\partial \mathrm{r}_{\Delta\lambda}}{\partial \theta} \\ \mathbf{0} \\ 0 \end{bmatrix} , \tag{C.69}$$

with

$$\frac{\partial \mathrm{r}_{\Delta\lambda}}{\partial \theta} = -\frac{\partial y_0(\theta)}{\partial \theta} + \frac{\partial \kappa(\theta)}{\partial \theta} . \tag{C.70}$$

Bibliography

[1] M. Aalami-Aleagha, S. Feli, and A. Eivani. FEM simulation of splatting of a molten metal droplet in thermal spray coating. *Computational Materials Science*, 48(1):65–70, 2010. ISSN 0927-0256. doi:10.1016/j.commatsci.2009.12.002.

[2] H. Altenbach. *Kontinuumsmechanik: Einführung in die materialunabhängigen und materialabhängigen Gleichungen*. Springer Vieweg, Berlin, Heidelberg, 3rd edition, 2015. ISBN 978-3-662-47070-1.

[3] S. Altmann. *Rotation, Quaternions and Double Groups*. Oxford University Press, 1986.

[4] J. Argyris. An excursion into large rotations. *Computer Methods in Applied Mechanics and Engineering*, 32(1-3):85–155, 1982. doi:10.1016/0045-7825(82)90069-X.

[5] G. Atefi and M. R. Talaee. Non-Fourier Temperature Field in a Solid Homogeneous Finite Hollow Cylinder. *Archive of Applied Mechanics*, 81(5):569–583, 2011. doi:10.1007/s00419-010-0436-5.

[6] J. Auriault. Effective macroscopic description for heat conduction in periodic composites. *International Journal of Heat and Mass Transfer*, 26(6):861–869, 1983. ISSN 0017-9310. doi:10.1016/S0017-9310(83)80110-0.

[7] I. Babuška. Homogenization Approach In Engineering. In M. Beckmann, H. P. Künzi, R. Glowinski, and J. L. Lions, editors, *Computing Methods in Applied Sciences and Engineering*, volume 134, pages 137–153. Springer, Berlin, Heidelberg, 1976. ISBN 978-3-642-85972-4. doi:10.1007/978-3-642-85972-4_8.

[8] N. Bakhvalov and G. Panasenko. The Concept of Asymptotic Expansion. A Model Example to Illustrate the Averaging Method. In M. Hazewinkel, editor, *Homogenisation: Averaging Processes in Periodic Media*, volume 36, pages 12–31. Springer Netherlands, Dordrecht, 1989. ISBN 978-94-010-7506-0. doi:10.1007/978-94-009-2247-1_2.

[9] D. Balzani, L. Scheunemann, D. Brands, and J. Schröder. Construction of two- and three-dimensional statistically similar RVEs for coupled micro-macro simulations. *Computational Mechanics*, 54(5):1269–1284, 2014. ISSN 1432-0924. doi:10.1007/s00466-014-1057-6.

[10] D. Balzani, A. Gandhi, M. Tanaka, and J. Schröder. Numerical calculation of thermo-mechanical problems at large strains based on complex step derivative approximation of tangent stiffness matrices. *Computational Mechanics*, 55(5):

861–871, 2015. ISSN 1432-0924. doi:10.1007/s00466-015-1139-0.

[11] K.-J. Bathe. *Finite Element Procedures*. Prentice Hall, Englewood Cliffs, N.J., 1996. ISBN 978-0-13-301458-7.

[12] C. E. Baumann and J. T. Oden. A discontinuous hp finite element method for convection—diffusion problems. *Computer Methods in Applied Mechanics and Engineering*, 175(3-4):311–341, 1999. ISSN 0045-7825. doi:10.1016/S0045-7825(98)00359-4.

[13] T. Belytschko, W. K. Liu, and B. Moran. *Nonlinear Finite Elements for Continua and Structures*. Wiley, Chichester, New York, 2000. ISBN 978-0-471-98773-4.

[14] A. Bensoussan, J.-L. Lions, and G. Papanicolaou. *Asymptotic Analysis for Periodic Structures*. Number v. 5 in Studies in Mathematics and Its Applications. Elsevier North-Holland, Amsterdam, New York, 1978. ISBN 978-0-444-85172-7.

[15] J.-M. Bergheau and R. Fortunier. *Finite Element Simulation of Heat Transfer (ISTE)*. Wiley-ISTE, 2008. ISBN 1-84821-053-1.

[16] H. Berns and W. Theisen. *Eisenwerkstoffe — Stahl und Gusseisen*. Springer, Berlin, Heidelberg, 2006. ISBN 978-3-540-29792-5.

[17] M. Bertagnolli, M. Marchese, and G. Jacucci. Modeling of particles impacting on a rigid substrate under plasma spraying conditions. *Journal of Thermal Spray Technology*, 4(1):41–49, 1995. ISSN 1544-1016. doi:10.1007/BF02648527.

[18] R. Berthelsen and A. Menzel. Computational homogenisation of thermo-viscoplastic composites: Large strain formulation and weak micro-periodicity. *Computer Methods in Applied Mechanics and Engineering*, 348:575–603, 2019. ISSN 0045-7825. doi:10.1016/j.cma.2018.12.032.

[19] R. Berthelsen, R. Denzer, and A. Menzel. Thermo-mechanical homogenisation - application to HVOF thermal-sprayed WC-Co coatings. *Proceedings in Applied Mathematics and Mechanics*, 14(1):583–584, 2014. ISSN 1617-7061. doi:10.1002/pamm.201410279.

[20] R. Berthelsen, T. Wiederkehr, R. Denzer, A. Menzel, and H. Müller. Efficient Simulation of Nonlinear Heat Transfer during Thermal Spraying of Complex Workpieces. *World Journal of Mechanics*, 4(9):289–301, 2014. ISSN 2160-0503. doi:10.4236/wjm.2014.49029.

[21] R. Berthelsen, D. Tomath, R. Denzer, and A. Menzel. Towards a finite element simulation of coating by means of thermal spraying. *Proceedings in Applied Mathematics and Mechanics*, 15(1):277–278, 2015. ISSN 1617-7061. doi:10.1002/pamm.201510129.

[22] R. Berthelsen, D. Tomath, R. Denzer, and A. Menzel. Finite element simulation of coating-induced heat transfer: Application to thermal spraying processes. *Meccanica*, 51(2):291–307, 2016. ISSN 1572-9648. doi:10.1007/s11012-015-0236-7.

[23] R. Berthelsen, H. Wilbuer, R. Holtermann, and A. Menzel. Computational modelling of wear - application to structured surfaces of elastoplastic tools. *GAMM-Mitteilungen*, 39(2):210–228, 2016. ISSN 0936-7195. doi:10.1002/gamm.201610013.

[24] R. Berthelsen, R. Denzer, P. Oppermann, and A. Menzel. Computational homogenisation for thermoviscoplasticity: Application to thermally sprayed coatings. *Computational Mechanics*, 60(5):739–766, 2017. ISSN 1432-0924. doi:10.1007/s00466-017-1436-x.

[25] A. Bertram and A. Krawietz. On the introduction of thermoplasticity. *Acta Mechanica*, 223(10):2257–2268, 2012. ISSN 1619-6937. doi:10.1007/s00707-012-0700-6.

[26] P. Betsch, A. Menzel, and E. Stein. On the parametrization of finite rotations in computational mechanics. *Computer Methods in Applied Mechanics and Engineering*, 155(3-4):273–305, 1998. doi:10.1016/S0045-7825(97)00158-8.

[27] K. Bobzin, N. Kopp, T. Warda, and M. Öte. Determination of the Effective Properties of Thermal Spray Coatings Using 2D and 3D Models. *Journal of Thermal Spray Technology*, 21(6):1269–1277, 2012. ISSN 1544-1016. doi:10.1007/s11666-012-9809-3.

[28] J. Boehmer, G. Funk, M. Jordan, and F. Fett. Strategies for coupled analysis of thermal strain history during continuous solidification processes. *Advances in Engineering Software*, 29(7-9):679–697, 1998. doi:10.1016/S0965-9978(98)00033-7.

[29] J. Bonet and R. D. Wood. *Nonlinear Continuum Mechanics for Finite Element Analysis*. Cambridge University Press, 2008. ISBN 0-521-83870-3.

[30] E. Bosco, V. G. Kouznetsova, and M. G. D. Geers. Multi-scale computational homogenization-localization for propagating discontinuities using X-FEM. *International Journal for Numerical Methods in Engineering*, 102(3-4):496–527, 2015. ISSN 0029-5981. doi:10.1002/nme.4838.

[31] E. Bosco, R. Peerlings, and M. Geers. Asymptotic homogenization of hygro-thermo-mechanical properties of fibrous networks. *International Journal of Solids and Structures*, 115-116:180–189, 2017. ISSN 0020-7683. doi:10.1016/j.ijsolstr.2017.03.015.

[32] L. Brassart and L. Stainier. Effective transient behaviour of heterogeneous media in diffusion problems with a large contrast in the phase diffusivities. *Journal of the Mechanics and Physics of Solids*, 124:366–391, 2019. ISSN 0022-5096. doi:10.1016/j.jmps.2018.10.021.

[33] I. N. Bronštejn and K. A. Semendjaev, editors. *Taschenbuch der Mathematik*. Deutsch, Frankfurt am Main, 6. edition, 2006. ISBN 978-3-8171-2006-2.

[34] E. Catmull. A subdivision algorithm for computer display of curved surfaces. Technical report, DTIC Document, 1974.

[35] P. Chadwick. *Continuum Mechanics: Concise Theory and Problems*. Dover Publications, Mineola, N.Y, 2nd edition, 1999. ISBN 978-0-486-40180-5.

[36] G. Chatzigeorgiou, A. Javili, and P. Steinmann. Unified magnetomechanical homogenization framework with application to magnetorheological elastomers. *Mathematics and Mechanics of Solids*, 19(2):193–211, 2014. ISSN 1741-3028. doi:10.1177/1081286512458109.

[37] G. Chatzigeorgiou, Y. Chemisky, and F. Meraghni. Computational micro to macro transitions for shape memory alloy composites using periodic homogenization. *Smart Materials and Structures*, 24(3):035009, 2015. ISSN 1361-665X. doi:10.1088/0964-1726/24/3/035009.

[38] G. Chatzigeorgiou, N. Charalambakis, Y. Chemisky, and F. Meraghni. Periodic homogenization for fully coupled thermomechanical modeling of dissipative generalized standard materials. *International Journal of Plasticity*, 81:18–39, 2016. ISSN 0749-6419. doi:10.1016/j.ijplas.2016.01.013.

[39] E. W. V. Chaves. *Notes on Continuum Mechanics*. Number 4 in Lecture Notes on Numerical Methods in Engineering and Sciences. CINME [u.a.], Barcelona, 1st edition, 2013. ISBN 978-94-007-5985-5.

[40] B. D. Coleman and W. Noll. The thermodynamics of elastic materials with heat conduction and viscosity. *Archive for Rational Mechanics and Analysis*, 13(1): 167–178, 1963. doi:10.1007/BF01262690.

[41] G. Comini, S. Del Guidice, R. W. Lewis, and O. C. Zienkiewicz. Finite element solution of non-linear heat conduction problems with special reference to phase change. *International Journal for Numerical Methods in Engineering*, 8(3):613–624, 1974. doi:10.1002/nme.1620080314.

[42] R. D. Cook, editor. *Concepts and Applications of Finite Element Analysis*. Wiley, New York, NY, 4th edition, 2002. ISBN 978-0-471-35605-9.

[43] R. de Boer. *Vektor- Und Tensorrechnung Für Ingenieure*. Hochschultext. Springer, Berlin, Heidelberg, 1982. ISBN 978-3-540-11834-3. OCLC: 251472017.

[44] R. De Borst, M. Crisfield, R. Remmers, and C. Verhoosel. *Nonlinear Finite Element Analysis of Solids and Structures (Wiley Series in Computational Mechanics)*. Wiley, 2012. ISBN 0-470-66644-7.

[45] L. De Lorenzis and P. Wriggers. Computational homogenization of rubber friction on rough rigid surfaces. *Computational Materials Science*, 77:264–280, 2013. ISSN 0927-0256. doi:10.1016/j.commatsci.2013.04.049.

[46] D. Delfosse, N. Cherradi, and B. Ilschner. Numerical and experimental determination of residual stresses in graded materials. *Composites Part B: Engineering*, 28 (1-2):127–141, 1997. ISSN 1359-8368. doi:10.1016/S1359-8368(96)00037-6.

[47] R. Denzer and A. Menzel. Configurational forces for quasi-incompressible large strain electro-viscoelasticity – Application to fracture mechanics. *European Journal of Mechanics - A/Solids*, 48:3–15, 2014. ISSN 0997-7538. doi:10.1016/j.euromechsol.2014.05.012.

[48] H. Doi, Y. Fujiwara, K. Miyake, and Y. Oosawa. A systematic investigation of elastic moduli of WC-Co alloys. *Metallurgical and Materials Transactions*, 1(5): 1417–1425, 1970. ISSN 0360-2133. doi:10.1007/BF02900264.

[49] E. Dongmo, R. Gadow, A. Killinger, and M. Wenzelburger. Modeling of Combustion as well as Heat, Mass, and Momentum Transfer During Thermal Spraying by HVOF and HVSFS. *Journal of Thermal Spray Technology*, 18(5-6):896–908, 2009. ISSN 1544-1016. doi:10.1007/s11666-009-9341-2.

[50] G. Engel, K. Garikipati, T. Hughes, M. Larson, L. Mazzei, and R. Taylor. Continuous/discontinuous finite element approximations of fourth-order elliptic problems in structural and continuum mechanics with applications to thin beams and plates, and strain gradient elasticity. *Computer Methods in Applied Mechanics and Engineering*, 191(34):3669–3750, 2002. ISSN 0045-7825. doi:10.1016/S0045-7825(02)00286-4.

[51] J. D. Eshelby. The determination of the elastic field of an ellipsoidal inclusion, and related problems. *Proceedings of the Royal Society of London. Series A. Mathematical and Physical Sciences*, 241(1226):376–396, 1957. ISSN 2053-9169. doi:10.1098/rspa.1957.0133.

[52] M. Fagerstrom and R. Larsson. A thermo-mechanical cohesive zone formulation for ductile fracture. *Journal of the Mechanics and Physics of Solids*, 56(10):3037–3058, 2008. doi:10.1016/j.jmps.2008.06.002.

[53] P. Fauchais, A. Vardelle, and B. Dussoubs. *Quo Vadis* Thermal Spraying? *Journal of Thermal Spray Technology*, 10(1):44–66, 2001. doi:10.1361/105996301770349510.

[54] F. Feyel and J.-L. Chaboche. FE2 multiscale approach for modelling the elastoviscoplastic behaviour of long fibre SiC/Ti composite materials. *Computer Methods in Applied Mechanics and Engineering*, 183(3-4):309–330, 2000. ISSN 0045-7825. doi:10.1016/S0045-7825(99)00224-8.

[55] S. Fillep, J. Orlik, Z. Bare, and P. Steinmann. Homogenization in periodically heterogeneous elastic bodies with multiple micro-contact. *Mathematics and Mechanics of Solids*, 19(8):1011–1021, 2014. ISSN 1741-3028. doi:10.1177/1081286513501104.

[56] R. Fleischhauer, R. Behnke, and M. Kaliske. A thermomechanical interface element formulation for finite deformations. *Computational Mechanics*, 52(5):1039–1058, 2013. ISSN 1432-0924. doi:10.1007/s00466-013-0862-7.

[57] R. Fleischhauer, M. Božić, and M. Kaliske. A novel approach to computational homogenization and its application to fully coupled two-scale thermomechanics. *Computational Mechanics*, 58(5):769–796, 2016. ISSN 1432-0924. doi:10.1007/s00466-

016-1315-x.

[58] G. A. Francfort. Homogenization and Linear Thermoelasticity. *SIAM Journal on Mathematical Analysis*, 14(4):696–708, 1983. ISSN 1095-7154. doi:10.1137/0514053.

[59] F. Fritzen and T. Böhlke. Periodic three-dimensional mesh generation for particle reinforced composites with application to metal matrix composites. *International Journal of Solids and Structures*, 48(5):706–718, 2011. ISSN 0020-7683. doi:10.1016/j.ijsolstr.2010.11.010.

[60] F. Fritzen and T. Böhlke. Reduced basis homogenization of viscoelastic composites. *Composites Science and Technology*, 76:84–91, 2013. ISSN 0266-3538. doi:10.1016/j.compscitech.2012.12.012.

[61] F. Fritzen, S. Marfia, and V. Sepe. Reduced order modeling in nonlinear homogenization: A comparative study. *Computers & Structures*, 157:114–131, 2015. ISSN 0045-7949. doi:10.1016/j.compstruc.2015.05.012.

[62] M. Geers, V. Kouznetsova, and W. Brekelmans. Multi-scale computational homogenization: Trends and challenges. *Journal of Computational and Applied Mathematics*, 234(7):2175–2182, 2010. ISSN 0377-0427. doi:10.1016/j.cam.2009.08.077.

[63] B. Gérard. Application of thermal spraying in the automobile industry. *Surface and Coatings Technology*, 201(5):2028–2031, 2006. ISSN 0257-8972. doi:10.1016/j.surfcoat.2006.04.050.

[64] S. Ghosh, K. Lee, and S. Moorthy. Two scale analysis of heterogeneous elastic-plastic materials with asymptotic homogenization and Voronoi cell finite element model. *Computer Methods in Applied Mechanics and Engineering*, 132(1-2):63–116, 1996. ISSN 0045-7825. doi:10.1016/0045-7825(95)00974-4.

[65] S. Gill and T. Clyne. Investigation of residual stress generation during thermal spraying by continuous curvature measurement. *Thin Solid Films*, 250(1-2):172–180, 1994. ISSN 0040-6090. doi:10.1016/0040-6090(94)90182-1.

[66] R. Greve. *Kontinuumsmechanik: ein Grundkurs für Ingenieure und Physiker*. Springer, Berlin, 2003. ISBN 978-3-540-00760-9.

[67] M. Gross and P. Betsch. Galerkin-based energy momentum consistent time-stepping algorithms for classical nonlinear thermo-elastodynamics. *Mathematics and Computers in Simulation*, 82(4):718–770, 2011. doi:10.1016/j.matcom.2011.10.009.

[68] M. Gurris, D. Kuzmin, and S. Turek. Implicit finite element schemes for stationary compressible particle-laden gas flows. *Journal of Computational and Applied Mathematics*, 235(17):5056–5077, 2011. ISSN 0377-0427. doi:10.1016/j.cam.2011.04.036.

[69] M. Gurris, D. Kuzmin, and S. Turek. Implicit finite element schemes for the stationary compressible Euler equations. *International Journal for Numerical*

Methods in Fluids, 69(1):1–28, 2012. ISSN 0271-2091. doi:10.1002/fld.2532.

[70] M. E. Gurtin, E. Fried, and L. Anand. *The Mechanics and Thermodynamics of Continua*. Cambridge University Press, New York, 2010. ISBN 978-0-521-40598-0.

[71] T. Hanson, C. Hackett, and G. Settles. Independent Control of HVOF Particle Velocity and Temperature. *Journal of Thermal Spray Technology*, 11(1):75–85, 2002. ISSN 1059-9630. doi:10.1361/105996302770349005.

[72] Z. Hashin and S. Shtrikman. On some variational principles in anisotropic and nonhomogeneous elasticity. *Journal of the Mechanics and Physics of Solids*, 10(4): 335–342, 1962. ISSN 0022-5096. doi:10.1016/0022-5096(62)90004-2.

[73] Z. Hashin and S. Shtrikman. A variational approach to the theory of the elastic behaviour of multiphase materials. *Journal of the Mechanics and Physics of Solids*, 11(2):127–140, 1963. ISSN 0022-5096. doi:10.1016/0022-5096(63)90060-7.

[74] P. Haupt. *Continuum Mechanics and Theory of Materials*. Springer, Berlin, Heidelberg, 2002. ISBN 978-3-662-04775-0.

[75] R. Hill. The Elastic Behaviour of a Crystalline Aggregate. *Proceedings of the Physical Society. Section A*, 65(5):349–354, 1952. ISSN 0370-1298. doi:10.1088/0370-1298/65/5/307.

[76] R. Hill. A self-consistent mechanics of composite materials. *Journal of the Mechanics and Physics of Solids*, 13(4):213–222, 1965. ISSN 0022-5096. doi:10.1016/0022-5096(65)90010-4.

[77] R. Hill. On macroscopic effects of heterogeneity in elastoplastic media at finite strain. *Mathematical Proceedings of the Cambridge Philosophical Society*, 95(03): 481, 1984. ISSN 1469-8064. doi:10.1017/S0305004100061818.

[78] C. Hirschberger, N. Sukumar, and P. Steinmann. Computational homogenization of material layers with micromorphic mesostructure. *Philosophical Magazine*, 88 (30-32):3603–3631, 2008. ISSN 1478-6443. doi:10.1080/14786430802502567.

[79] C. B. Hirschberger. *A Treatise on Micromorphic Continua: Theory, Homogenization, Computation*. Number 08-03 in UKL/LTM T. Techn. Univ., Lehrstuhl für Techn. Mechanik, Kaiserslautern, 2008. ISBN 978-3-939432-80-7.

[80] K. Hohenemser and W. Prager. Über die Ansätze der Mechanik isotroper Kontinua. *ZAMM - Zeitschrift für Angewandte Mathematik und Mechanik*, 12(4):216–226, 1932. ISSN 1521-4001. doi:10.1002/zamm.19320120403.

[81] G. A. Holzapfel. *Nonlinear Solid Mechanics: A Continuum Approach for Engineering*. Wiley, Chichester, New York, 2000. ISBN 978-0-471-82319-3.

[82] C. Hu, O. Lepsky, and C.-W. Shu. The Effect of the Least Square Procedure for Discontinuous Galerkin Methods for Hamilton-Jacobi Equations. In M. Griebel, D. E. Keyes, R. M. Nieminen, D. Roose, T. Schlick, B. Cockburn, G. E. Karniadakis, and C.-W. Shu, editors, *Discontinuous Galerkin Methods*, volume 11,

pages 343–348. Springer, Berlin, Heidelberg, 2000. ISBN 978-3-642-64098-8.

[83] T. J. R. Hughes. *The Finite Element Method: Linear Static and Dynamic Finite Element Analysis*. Dover Publications, Mineola, NY, 2000. ISBN 978-0-486-41181-1.

[84] I. Hussainova, J. Kubarsepp, and J. Pirso. Mechanical properties and features of erosion of cermets. *Wear*, 250(1-12):818–825, 2001. ISSN 0043-1648. doi:10.1016/S0043-1648(01)00737-2.

[85] K. Hutter. *Continuum Methods of Physical Modeling: Continuum Mechanics, Dimensional Analysis, Turbulence*. Springer, Berlin, New York, 2004. ISBN 3-540-20619-1.

[86] J. H. Irving and J. G. Kirkwood. The Statistical Mechanical Theory of Transport Processes. IV. The Equations of Hydrodynamics. *The Journal of Chemical Physics*, 18(6):817–829, 1950. ISSN 1089-7690. doi:10.1063/1.1747782.

[87] M. Itskov. *Tensor Algebra and Tensor Analysis for Engineers: With Applications to Continuum Mechanics*. Mathematical Engineering. Springer, Cham, 4th edition, 2015. ISBN 978-3-319-16341-3.

[88] A. Javili, G. Chatzigeorgiou, and P. Steinmann. Computational homogenization in magneto-mechanics. *International Journal of Solids and Structures*, 50(25-26): 4197–4216, 2013. ISSN 0020-7683. doi:10.1016/j.ijsolstr.2013.08.024.

[89] A. Javili, A. McBride, J. Mergheim, P. Steinmann, and U. Schmidt. Micro-to-macro transitions for continua with surface structure at the microscale. *International Journal of Solids and Structures*, 50(16-17):2561–2572, 2013. ISSN 0020-7683. doi:10.1016/j.ijsolstr.2013.03.022.

[90] A. Javili, S. Saeb, and P. Steinmann. Aspects of implementing constant traction boundary conditions in computational homogenization via semi-Dirichlet boundary conditions. *Computational Mechanics*, 59(1):21–35, 2017. ISSN 1432-0924. doi:10.1007/s00466-016-1333-8.

[91] A. Javili, G. Chatzigeorgiou, A. T. McBride, P. Steinmann, and C. Linder. Computational homogenization of nano-materials accounting for size effects via surface elasticity. *GAMM-Mitteilungen*, 38(2):285–312, 2015. ISSN 0936-7195. doi:10.1002/gamm.201510016.

[92] S. Kaessmair and P. Steinmann. Computational first-order homogenization in chemo-mechanics. *Archive of Applied Mechanics*, 88(1-2):271–286, 2018. ISSN 1432-0681. doi:10.1007/s00419-017-1287-0.

[93] M.-A. Keip, P. Steinmann, and J. Schröder. Two-scale computational homogenization of electro-elasticity at finite strains. *Computer Methods in Applied Mechanics and Engineering*, 278:62–79, 2014. ISSN 0045-7825. doi:10.1016/j.cma.2014.04.020.

[94] Z. F. Khisaeva and M. Ostoja-Starzewski. On the Size of RVE in Finite Elasticity of Random Composites. *Journal of Elasticity*, 85(2):153–173, 2006. ISSN 1573-2681. doi:10.1007/s10659-006-9076-y.

[95] B. Klusemann, R. Denzer, and B. Svendsen. Microstructure-Based Modeling of Residual Stresses in WC-12Co-Sprayed Coatings. *Journal of Thermal Spray Technology*, 21(1):96–107, 2012. ISSN 1544-1016. doi:10.1007/s11666-011-9690-5.

[96] J. Kochmann, S. Wulfinghoff, L. Ehle, J. Mayer, B. Svendsen, and S. Reese. Efficient and accurate two-scale FE-FFT-based prediction of the effective material behavior of elasto-viscoplastic polycrystals. *Computational Mechanics*, 2017. ISSN 1432-0924. doi:10.1007/s00466-017-1476-2.

[97] A. Kout and H. Müller. Parameter optimization for spray coating. *Advances in Engineering Software*, 40(10):1078–1086, 2009.

[98] V. Kouznetsova, W. A. M. Brekelmans, and F. P. T. Baaijens. An approach to micro-macro modeling of heterogeneous materials. *Computational Mechanics*, 27 (1):37–48, 2001. ISSN 1432-0924. doi:10.1007/s004660000212.

[99] V. Kouznetsova. *Computational Homogenization for the Multi-Scale Analysis of Multi-Phase Materials*. PhD thesis, Department of Mechanical Engineering, Technische Universiteit Eindhoven, 2002.

[100] V. Kouznetsova, M. Geers, and W. Brekelmans. Multi-scale second-order computational homogenization of multi-phase materials: A nested finite element solution strategy. *Computer Methods in Applied Mechanics and Engineering*, 193(48-51): 5525–5550, 2004. ISSN 0045-7825. doi:10.1016/j.cma.2003.12.073.

[101] E. Kuhl, R. Denzer, F. J. Barth, and P. Steinmann. Application of the material force method to thermo-hyperelasticity. *Computer Methods in Applied Mechanics and Engineering*, 193(30-32):3303–3325, 2004. doi:10.1016/j.cma.2003.09.021.

[102] S. Kuroda and T. Clyne. The quenching stress in thermally sprayed coatings. *Thin Solid Films*, 200(1):49–66, 1991. ISSN 0040-6090. doi:10.1016/0040-6090(91)90029-W.

[103] M. Labusch, J. Schröder, and M.-A. Keip. An FE2-Scheme for Magneto-Electro-Mechanically Coupled Boundary Value Problems. In J. Schröder and D. C. Lupascu, editors, *Ferroic Functional Materials*, volume 581, pages 227–262. Springer, Cham, 2018. ISBN 978-3-319-68881-7. doi:10.1007/978-3-319-68883-1_5.

[104] F. Larsson, K. Runesson, S. Saroukhani, and R. Vafadari. Computational homogenization based on a weak format of micro-periodicity for RVE-problems. *Computer Methods in Applied Mechanics and Engineering*, 200(1-4):11–26, 2011. ISSN 0045-7825. doi:10.1016/j.cma.2010.06.023.

[105] F. Larsson, K. Runesson, and F. Su. Variationally consistent computational homogenization of transient heat flow. *International Journal for Numerical Methods in Engineering*, pages 1659–1686, 2009. ISSN 1097-0207. doi:10.1002/nme.2747.

[106] M. Leuschner and F. Fritzen. Reduced order homogenization for viscoplastic composite materials including dissipative imperfect interfaces. *Mechanics of Materials*, 104:121–138, 2017. ISSN 0167-6636. doi:10.1016/j.mechmat.2016.10.008.

[107] R. W. Lewis, P. Nithiarasu, and K. Seetharamu. *Fundamentals of the Finite Element Method for Heat and Fluid Flow*. Wiley, 2004. ISBN 0-470-84788-3.

[108] I.-S. Liu. *Continuum Mechanics*. Springer, Berlin, Heidelberg, 2002. ISBN 978-3-662-05056-9.

[109] D. G. Luenberger and Y. Ye. *Linear and Nonlinear Programming*. International Series in Operations Research and Management Science. Springer, New York, NY, 3rd edition, 2008. ISBN 978-0-387-74502-2.

[110] K. K. Mandadapu, A. Sengupta, and P. Papadopoulos. A homogenization method for thermomechanical continua using extensive physical quantities. *Proceedings of the Royal Society A: Mathematical, Physical and Engineering Sciences*, 468(2142): 1696–1715, 2012. ISSN 1471-2946. doi:10.1098/rspa.2011.0578.

[111] J. E. Marsden and T. J. R. Hughes. *Mathematical Foundations of Elasticity*. Dover, New York, 1994. ISBN 978-0-486-67865-8.

[112] K. Matouš, M. G. Geers, V. G. Kouznetsova, and A. Gillman. A review of predictive nonlinear theories for multiscale modeling of heterogeneous materials. *Journal of Computational Physics*, 330:192–220, 2017. ISSN 0021-9991. doi:10.1016/j.jcp.2016.10.070.

[113] A. McBride, J. Mergheim, A. Javili, P. Steinmann, and S. Bargmann. Micro-to-macro transitions for heterogeneous material layers accounting for in-plane stretch. *Journal of the Mechanics and Physics of Solids*, 60(6):1221–1239, 2012. ISSN 0022-5096. doi:10.1016/j.jmps.2012.01.003.

[114] B. S. Mercer, K. K. Mandadapu, and P. Papadopoulos. Novel formulations of microscopic boundary-value problems in continuous multiscale finite element methods. *Computer Methods in Applied Mechanics and Engineering*, 286:268–292, 2015. ISSN 0045-7825. doi:10.1016/j.cma.2014.12.021.

[115] C. Miehe and A. Koch. Computational micro-to-macro transitions of discretized microstructures undergoing small strains. *Archive of Applied Mechanics*, 72(4-5): 300–317, 2002. ISSN 0939-1533. doi:10.1007/s00419-002-0212-2.

[116] C. Miehe, J. Schröder, and J. Schotte. Computational homogenization analysis in finite plasticity Simulation of texture development in polycrystalline materials. *Computer Methods in Applied Mechanics and Engineering*, 171(3-4):387–418, 1999. ISSN 0045-7825. doi:10.1016/S0045-7825(98)00218-7.

[117] C. Miehe, J. Schröder, and M. Becker. Computational homogenization analysis in finite elasticity: Material and structural instabilities on the micro- and macro-scales of periodic composites and their interaction. *Computer Methods in Applied Mechanics and Engineering*, 191(44):4971–5005, 2002. ISSN 0045-7825.

doi:10.1016/S0045-7825(02)00391-2.

[118] C. Miehe, D. Vallicotti, and S. Teichtmeister. Homogenization and multiscale stability analysis in finite magneto-electro-elasticity. Application to soft matter EE, ME and MEE composites. *Computer Methods in Applied Mechanics and Engineering*, 300:294–346, 2016. ISSN 0045-7825. doi:10.1016/j.cma.2015.10.013.

[119] O. Mierka and S. Turek. Numerical Simulation of Monodispersed Droplet Generation in Nozzles. In U. Fritsching, editor, *Process-Spray*, pages 493–516. Springer International Publishing, Cham, 2016. ISBN 978-3-319-32368-8. doi:10.1007/978-3-319-32370-1_13.

[120] T. Mori and K. Tanaka. Average stress in matrix and average elastic energy of materials with misfitting inclusions. *Acta Metallurgica*, 21(5):571–574, 1973. ISSN 0001-6160. doi:10.1016/0001-6160(73)90064-3.

[121] I. Müller. *Thermodynamik: Die Grundlagen der Materialtheorie*. Bertelsmann-Universitätsverlag, Düsseldorf, 1973. ISBN 3-571-09185-X.

[122] T. Mura. *Micromechanics of Defects in Solids*. Number 3 in Mechanics of Elastic and Inelastic Solids. M. Nijhoff ; Distributors for the U.S. and Canada, Kluwer Academic Publishers, Dordrecht, Netherlands; Boston, Hingham, MA, USA, 2nd, rev. ed edition, 1987. ISBN 978-90-247-3343-9.

[123] P. Neittaanmäki, S. I. Repin, T. Tiihonen, and T. Tuovinen, editors. *Numerical Methods for Differential Equations, Optimization, and Technological Problems: Dedicated to Professor P. Neittaanmäki on His 60th Birthday*. Number volume 27 in Computational Methods in Applied Sciences. Springer, Dordrecht, 2013. ISBN 978-94-007-5287-0.

[124] S. Nemat-Nasser and M. Hori. *Micromechanics: Overall Properties of Heterogeneous Materials*. Elsevier, Amsterdam, New York, 2nd edition, 1999. ISBN 978-0-444-50084-7.

[125] E. A. d. S. Neto, D. Perić, and D. R. J. Owen. *Computational Methods for Plasticity: Theory and Applications*. Wiley, Chichester, West Sussex, UK, 2008. ISBN 978-0-470-69452-7.

[126] T. Nomura, H. Moriguchi, K. Tsuda, K. Isobe, A. Ikegaya, and K. Moriyama. Material design method for the functionally graded cemented carbide tool. *International Journal of Refractory Metals and Hard Materials*, 17(6):397–404, November 1999. ISSN 0263-4368. doi:10.1016/S0263-4368(99)00029-3.

[127] E. Oñate and R. Owen, editors. *Computational Plasticity*. Number 7 in Computational Methods in Applied Sciences. Springer, Dordrecht, 2007. ISBN 978-1-4020-6576-7.

[128] R. W. Ogden. *Non-Linear Elastic Deformations*. Dover Publications, Mineola, N.Y, 1997. ISBN 978-0-486-69648-5.

[129] O. Oladijo, A. Venter, L. Cornish, and N. Sacks. X-ray diffraction measurement of residual stress in WC-Co thermally sprayed coatings onto metal substrates. *Surface and Coatings Technology*, 206(23):4725–4729, 2012. ISSN 0257-8972. doi:10.1016/j.surfcoat.2012.01.044.

[130] N. S. Ottosen and M. Ristinmaa. *The Mechanics of Constitutive Modeling*. Elsevier, Amsterdam, London, 2005. ISBN 978-0-08-044606-6.

[131] I. Özdemir, W. A. M. Brekelmans, and M. G. D. Geers. Computational homogenization for heat conduction in heterogeneous solids. *International Journal for Numerical Methods in Engineering*, 73(2):185–204, 2008. ISSN 1097-0207. doi:10.1002/nme.2068.

[132] I. Özdemir, W. Brekelmans, and M. Geers. Fe2 computational homogenization for the thermo-mechanical analysis of heterogeneous solids. *Computer Methods in Applied Mechanics and Engineering*, 198(3-4):602–613, 2008. ISSN 0045-7825. doi:10.1016/j.cma.2008.09.008.

[133] G. Palani and K.-Y. Kim. Numerical study on a vertical plate with variable viscosity and thermal conductivity. *Archive of Applied Mechanics*, 80(7):711–725, 2010. doi:10.1007/s00419-009-0336-8.

[134] J. Pamin, B. Wcisło, and K. Kowalczyk-Gajewska. Gradient-enhanced large strain thermoplasticity with automatic linearization and localization simulations. *Journal of Mechanics of Materials and Structures*, 12(1):123–146, 2017. ISSN 1559-3959. doi:10.2140/jomms.2017.12.123.

[135] H. Parisch. *Festkörper-Kontinuumsmechanik: von den Grundgleichungen zur Lösung mit Finiten Elementen*. Teubner Studienbücher Maschinenbau - Lehrbuch. Teubner, Stuttgart, 1st edition, 2003. ISBN 3-519-00434-8.

[136] J. Pina, V. Kouznetsova, and M. Geers. Thermo-mechanical analyses of heterogeneous materials with a strongly anisotropic phase: The case of cast iron. *International Journal of Solids and Structures*, 63:153–166, 2015. ISSN 0020-7683. doi:10.1016/j.ijsolstr.2015.02.048.

[137] R. Quey, P. Dawson, and F. Barbe. Large-scale 3D random polycrystals for the finite element method: Generation, meshing and remeshing. *Computer Methods in Applied Mechanics and Engineering*, 200(17-20):1729–1745, 2011. ISSN 0045-7825. doi:10.1016/j.cma.2011.01.002.

[138] R. R. Reeber and K. Wang. Thermophysical Properties of α-Tungsten Carbide. *Journal of the American Ceramic Society*, 82(1):129–135, 2004. ISSN 1551-2916. doi:10.1111/j.1151-2916.1999.tb01732.x.

[139] A. C. Reid, S. A. Langer, R. C. Lua, V. R. Coffman, S.-I. Haan, and R. E. García. Image-based finite element mesh construction for material microstructures. *Computational Materials Science*, 43(4):989–999, 2008. ISSN 0927-0256. doi:10.1016/j.commatsci.2008.02.016.

[140] A. Reuss. Berechnung der Fließgrenze von Mischkristallen auf Grund der Plastizitätsbedingung für Einkristalle. *ZAMM - Zeitschrift für Angewandte Mathematik und Mechanik*, 9(1):49–58, 1929. ISSN 1521-4001. doi:10.1002/zamm.19290090104.

[141] F. Richter. Die wichtigsten physikalischen Eigenschaften von 52 Eisenwerkstoffen. *Stahleisen-Sonderberichte, Duesseldorf: Verlag Stahleisen, 1973*, 1, 1973.

[142] F. Richter. *Physikalische Eigenschaften von Stahlen Und Ihre Temperaturabhängigkeit: Polynome Und Graphische Darstellungen: Mitteilung Aus Dem Forschungsinstitut Der Mannesmann AG*. Stahleisen, 1983.

[143] I. B. C. M. Rocha, F. P. van der Meer, R. P. L. Nijssen, and L. J. Sluys. A multiscale and multiphysics numerical framework for modelling of hygrothermal ageing in laminated composites. *International Journal for Numerical Methods in Engineering*, 2017. ISSN 0029-5981. doi:10.1002/nme.5542.

[144] P. Rosakis, A. Rosakis, G. Ravichandran, and J. Hodowany. A thermodynamic internal variable model for the partition of plastic work into heat and stored energy in metals. *Journal of the Mechanics and Physics of Solids*, 48(3):581–607, 2000. ISSN 0022-5096. doi:10.1016/S0022-5096(99)00048-4.

[145] A. Sadovoy. *Modeling and Offline Simulation of Thermal Spray Coating Process for Gas Turbine Applications*. PhD thesis, Department of Mechanical Engineering, TU Darmstadt, 2014.

[146] S. Sahraee. *Homogenization in Finite Thermo-Viscoplasticity*. Number 15,1 in Leibniz Universität Hannover, Institut Für Kontinuumsmechanik B. Institut für Kontinuumsmechanik, Leibniz Universität Hannover, Hannover, 2015. ISBN 978-3-941302-14-3. OCLC: 927405412.

[147] T. Sahraoui, N.-E. Fenineche, G. Montavon, and C. Coddet. Structure and wear behaviour of HVOF sprayed Cr3C2-NiCr and WC-Co coatings. *Materials & Design*, 24(5):309–313, 2003. doi:10.1016/S0261-3069(03)00059-1.

[148] E. Sanchez-Palencia. *Non-Homogeneous Media and Vibration Theory*. Number 127 in Lecture Notes in Physics. Springer, Berlin, 1980. ISBN 978-3-540-10000-3.

[149] C. Sandström, F. Larsson, and K. Runesson. Weakly periodic boundary conditions for the homogenization of flow in porous media. *Advanced Modeling and Simulation in Engineering Sciences*, 1(1), 2014. ISSN 2213-7467. doi:10.1186/s40323-014-0012-6.

[150] V. Savatorova, A. Talonov, and A. Vlasov. Homogenization of thermoelasticity processes in composite materials with periodic structure of heterogeneities. *ZAMM - Journal of Applied Mathematics and Mechanics / Zeitschrift für Angewandte Mathematik und Mechanik*, 93(8):575–596, 2013. ISSN 0044-2267. doi:10.1002/zamm.201200032.

[151] S. Schindler, J. Mergheim, M. Zimmermann, J. C. Aurich, and P. Steinmann. Numerical homogenization of elastic and thermal material properties for metal

matrix composites (MMC). *Continuum Mechanics and Thermodynamics*, 29(1): 51–75, 2017. ISSN 1432-0959. doi:10.1007/s00161-016-0515-0.

[152] J. Schröder. A numerical two-scale homogenization scheme: The FE2-method. In F. Pfeiffer, F. G. Rammerstorfer, E. Guazzelli, B. Schrefler, P. Serafini, J. Schröder, and K. Hackl, editors, *Plasticity and Beyond*, volume 550, pages 1–64. Springer Vienna, Vienna, 2014. ISBN 978-3-7091-1624-1. doi:10.1007/978-3-7091-1625-8_1.

[153] J. Schröder and M.-A. Keip. Two-scale homogenization of electromechanically coupled boundary value problems: Consistent linearization and applications. *Computational Mechanics*, 50(2):229–244, 2012. ISSN 1432-0924. doi:10.1007/s00466-012-0715-9.

[154] J. Schröder, D. Balzani, and D. Brands. Approximation of random microstructures by periodic statistically similar representative volume elements based on lineal-path functions. *Archive of Applied Mechanics*, 81(7):975–997, 2011. ISSN 1432-0681. doi:10.1007/s00419-010-0462-3.

[155] J. Schröder, A. Gandhi, and D. Balzani. Two-scale Modeling of DP Steel Incorporating Distributed Properties Inside Micro-constituents. *Procedia Engineering*, 81: 1390–1395, 2014. ISSN 1877-7058. doi:10.1016/j.proeng.2014.10.162.

[156] J. Schröder, M. Labusch, and M.-A. Keip. Algorithmic two-scale transition for magneto-electro-mechanically coupled problems. *Computer Methods in Applied Mechanics and Engineering*, 302:253–280, 2016. ISSN 0045-7825. doi:10.1016/j.cma.2015.10.005.

[157] A. Sengupta, P. Papadopoulos, and R. L. Taylor. A multiscale finite element method for modeling fully coupled thermomechanical problems in solids: Multiscale Modeling of Coupled Thermomechanical Response. *International Journal for Numerical Methods in Engineering*, 91(13):1386–1405, 2012. ISSN 0029-5981. doi:10.1002/nme.4320.

[158] K. Shoemake. Animating rotation with quaternion curves. *ACM SIGGRAPH Computer Graphics*, 19(3):245–254, 1985. doi:10.1145/325165.325242.

[159] M. Šilhavý. *The Mechanics and Thermodynamics of Continuous Media*. Springer, Berlin, Heidelberg, 1997. ISBN 978-3-642-08204-7.

[160] J. C. Simo and T. J. R. Hughes. *Computational Inelasticity*. Number v. 7 in Interdisciplinary Applied Mathematics. Springer, New York, 1998. ISBN 0-387-97520-9.

[161] J. Simo. A framework for finite strain elastoplasticity based on maximum plastic dissipation and the multiplicative decomposition: Part I. Continuum formulation. *Computer Methods in Applied Mechanics and Engineering*, 66(2):199–219, 1988. ISSN 0045-7825. doi:10.1016/0045-7825(88)90076-X.

[162] J. Simo. A framework for finite strain elastoplasticity based on maximum plastic dissipation and the multiplicative decomposition. Part II: Computational aspects.

Computer Methods in Applied Mechanics and Engineering, 68(1):1–31, 1988. ISSN 0045-7825. doi:10.1016/0045-7825(88)90104-1.

[163] J. Simo. Numerical analysis and simulation of plasticity. In *Handbook of Numerical Analysis*, volume 6, pages 183–499. Elsevier, 1998. ISBN 978-0-444-82569-8.

[164] J. Simo and C. Miehe. Associative coupled thermoplasticity at finite strains: Formulation, numerical analysis and implementation. *Computer Methods in Applied Mechanics and Engineering*, 98(1):41–104, 1992. ISSN 0045-7825. doi:10.1016/0045-7825(92)90170-O.

[165] P. Steinmann and O. Häsner. On material interfaces in thermomechanical solids. *Archive of Applied Mechanics*, 75(1):31–41, 2005. ISSN 1432-0681. doi:10.1007/s00419-005-0383-8.

[166] H. Tabbara and S. Gu. Computational simulation of liquid-fuelled HVOF thermal spraying. *Surface and Coatings Technology*, 204(5):676–684, 2009. ISSN 0257-8972. doi:10.1016/j.surfcoat.2009.09.005.

[167] M. R. Talaee and G. Atefi. Non-Fourier heat conduction in a finite hollow cylinder with periodic surface heat flux. *Archive of Applied Mechanics*, 81(12):1793–1806, 2011. doi:10.1007/s00419-011-0518-z.

[168] I. Temizer. Thermomechanical contact homogenization with random rough surfaces and microscopic contact resistance. *Tribology International*, 44(2):114–124, 2011. ISSN 0301-679X. doi:10.1016/j.triboint.2010.09.011.

[169] I. Temizer. On the asymptotic expansion treatment of two-scale finite thermoelasticity. *International Journal of Engineering Science*, 53:74–84, 2012. ISSN 0020-7225. doi:10.1016/j.ijengsci.2012.01.003.

[170] I. Temizer. Multiscale thermomechanical contact: Computational homogenization with isogeometric analysis. *International Journal for Numerical Methods in Engineering*, 97(8):582–607, 2014. ISSN 0029-5981. doi:10.1002/nme.4604.

[171] I. Temizer and P. Wriggers. On the computation of the macroscopic tangent for multiscale volumetric homogenization problems. *Computer Methods in Applied Mechanics and Engineering*, 198(3-4):495–510, 2008. ISSN 0045-7825. doi:10.1016/j.cma.2008.08.018.

[172] I. Temizer and P. Wriggers. Homogenization in finite thermoelasticity. *Journal of the Mechanics and Physics of Solids*, 59(2):344–372, 2011. ISSN 0022-5096. doi:10.1016/j.jmps.2010.10.004.

[173] I. Temizer and T. I. Zohdi. A numerical method for homogenization in nonlinear elasticity. *Computational Mechanics*, 40(2):281–298, 2007. ISSN 1432-0924. doi:10.1007/s00466-006-0097-y.

[174] M. L. Thorpe and H. J. Richter. A pragmatic analysis and comparison of HVOF processes. *Journal of Thermal Spray Technology*, 1(2):161–170, 1992.

doi:10.1007/BF02659017.

[175] E. Tikarrouchine, G. Chatzigeorgiou, F. Praud, B. Piotrowski, Y. Chemisky, and F. Meraghni. Three-dimensional FE 2 method for the simulation of non-linear, rate-dependent response of composite structures. *Composite Structures*, 193:165–179, 2018. ISSN 0263-8223. doi:10.1016/j.compstruct.2018.03.072.

[176] E. Tikarrouchine, G. Chatzigeorgiou, Y. Chemisky, and F. Meraghni. Fully coupled thermo-viscoplastic analysis of composite structures by means of multi-scale three-dimensional finite element computations. *International Journal of Solids and Structures*, 2019. ISSN 0020-7683. doi:10.1016/j.ijsolstr.2019.01.018.

[177] W. Tillmann and I. Baumann, editors. *6. Öffentliches Kolloquium – SFB 708*. Verl. Praxiswissen, Dortmund, 2013. ISBN 978-3-86975-086-6.

[178] W. Tillmann and J. Nebel, editors. *4. öffentliches Kolloquium – SFB 708*. Verl. Praxiswissen, Dortmund, 2011. ISBN 978-3-86975-052-1.

[179] W. Tillmann and J. Nebel, editors. *5. öffentliches Kolloquium – SFB 708*. Verl. Praxiswissen, Dortmund, 2012. ISBN 978-3-86975-071-2.

[180] M. Toparli, F. Sen, O. Culha, and E. Celik. Thermal stress analysis of HVOF sprayed WC–Co/NiAl multilayer coatings on stainless steel substrate using finite element methods. *Journal of Materials Processing Technology*, 190(1-3):26–32, 2007. ISSN 0924-0136. doi:10.1016/j.jmatprotec.2007.03.115.

[181] T. Totemeier and J. Wright. Residual stress determination in thermally sprayed coatings—a comparison of curvature models and X-ray techniques. *Surface and Coatings Technology*, 200(12-13):3955–3962, 2006. ISSN 0257-8972. doi:10.1016/j.surfcoat.2005.06.003.

[182] C. Truesdell. *The Elements of Continuum Mechanics*. Springer, Berlin, Heidelberg, 1984. ISBN 978-3-642-64976-9.

[183] J. Utzinger, M. Bos, M. Floeck, A. Menzel, E. Kuhl, R. Renz, K. Friedrich, A. K. Schlarb, and P. Steinmann. Computational modelling of thermal impact welded PEEK/steel single lap tensile specimens. *Computational Materials Science*, 41(3): 287–296, 2008. ISSN 0927-0256. doi:10.1016/j.commatsci.2007.04.015.

[184] R. A. van Tuijl, C. Harnish, K. Matouš, J. J. C. Remmers, and M. G. D. Geers. Wavelet based reduced order models for microstructural analyses. *Computational Mechanics*, 63(3):535–554, 2019. ISSN 1432-0924. doi:10.1007/s00466-018-1608-3.

[185] W. Voigt. Ueber die Beziehung zwischen den beiden Elasticitätsconstanten isotroper Körper. *Annalen der Physik*, 274(12):573–587, 1889. ISSN 1521-3889. doi:10.1002/andp.18892741206.

[186] M. R. Vujičić. Finite element solution of transient heat conduction using iterative solvers. *Engineering Computations*, 23(4):408–431, 2006. ISSN 0264-4401. doi:10.1108/02644400610661172.

[187] B. Wcisło and J. Pamin. Local and non-local thermomechanical modeling of elastic-plastic materials undergoing large strains. *International Journal for Numerical Methods in Engineering*, 109(1):102–124, 2017. ISSN 0029-5981. doi:10.1002/nme.5280.

[188] T. Wiederkehr, H. Müller, B. Krebs, and M. Abdulgader. A Deposition Model for Wire Arc Spraying and Its Computationally Efficient Simulation. In *Proceedings of the International Thermal Spray Conference*, pages 492–498, 2009.

[189] T. Wiederkehr, B. Klusemann, D. Gies, H. Müller, and B. Svendsen. An image morphing method for 3D reconstruction and FE-analysis of pore networks in thermal spray coatings. *Computational Materials Science*, 47(4):881–889, 2010. ISSN 0927-0256. doi:10.1016/j.commatsci.2009.11.019.

[190] T. Wiederkehr. *Effiziente, GPU-basierte Simulation thermischer Spritzprozesse*. PhD thesis, LS 07 Graphische Systeme, TU Dortmund, 2015.

[191] P. Wriggers. *Nonlinear Finite Element Methods*. Springer, Berlin, Heidelberg, 2008. ISBN 978-3-540-71000-4.

[192] O. C. Zienkiewicz, R. L. Taylor, and D. Fox. *The Finite Element Method for Solid and Structural Mechanics*. Elsevier/Butterworth-Heinemann, Amsterdam, Boston, 7th ed edition, 2014. ISBN 978-1-85617-634-7.

[193] T. I. Zohdi and P. Wriggers. *An Introduction to Computational Micromechanics*. Number v. 20 in Lecture Notes in Applied and Computational Mechanics. Springer, Berlin, 2008. ISBN 978-3-540-77482-2.

Publication series of the Institute of Mechanics

published to date:

2010/01 Palnau, V.: Implementierung eines netzfreien Diskretisierungsverfahrens und seine Anwendung auf die Scherbandanalyse. ISBN 978-3-921823-51-4

2010/02 Klusemann, B.: Application of homogenization methods and crystal plasticity to the modeling of heterogeneous materials of technological interest. ISBN 978-3-921823-53-8

2011/01 Hortig, C.: Local and non-local thermomechanical modeling and finite-element simulation of high-speed cutting. ISBN 978-3-921823-54-5

2011/02 Parvizian, F.: Modeling of microstructure evolution in aluminum alloys during hot extrusion. ISBN 978-3-921823-56-9

2011/03 Noman, M.: Characterization and model identification for the simulation of the forming behavior of ferritic steels. ISBN: 978-3-921823-55-2

2011/04 Kayser, T.: Characterization of microstructure in aluminum alloys based on electron backscatter diffraction. ISBN: 978-3-921823-57-6

2011/05 Bargmann, S.: Computational modeling of material behavior on different scales based on continuum mechanics. ISBN: 978-3-921823-58-3

2013/01 Waffenschmidt, T.: Modelling and simulation of adaptation and degradation in anisotropic biological tissues. ISBN: 978-3-921823-61-3

2015/01 Ostwald, R.: Modelling and simulation of phase-transformations in elasto-plastic polycrystals. ISBN: 978-3-921823-66-8

2016/01 Subramanian, M.: Phenomenological modelling and simulation of ferroelectric ceramics. ISBN: 978-3-921823-74-3

2016/02 Clausmeyer, T.: Evolution of plastic anisotropy in metals: Material models, experiments and applications. ISBN: 978-3-921823-76-7

2017/01 Holtermann, R.: Computational multiscale modelling of grinding processes. ISBN: 978-3-921823-86-6

2017/02 Bartels, A.: Modelling of evolving microstructures at different scales. ISBN: 978-3-921823-93-4

2017/03 Dusthakar Kumar Rao, D. K.: Computational modelling of single and poly-crystalline ferroelectric materials. ISBN: 978-3-921823-94-1
2019/01 Buckmann, K.: Microstructure evolution in functional magnetic materials. ISBN: 978-3-947323-09-8
2019/02 Kaiser, T.: Computational modelling of non-simple and anisotropic materials. ISBN: 978-3-921823-14-2
2019/03 Heitbreder, T.: Modelling of material interfaces at different length scales. ISBN: 978-3-947323-18-0
2020/01 Berthelsen, R.: Computational homogenisation of thermomechanical problems. ISBN: 978-3-947323-19-7